1995-96 ANNUAL REPORT

Reactions of Toxic Pollutants in Soil Systems

KEARNEY FOUNDATION OF SOIL SCIENCE
DIVISION OF AGRICULTURE AND NATURAL RESOURCES
UNIVERSITY OF CALIFORNIA

1995-96 ANNUAL REPORT

Reactions of Toxic Pollutants in Soil Systems

DR. ANDREW C. CHANG, DIRECTOR
KEARNEY FOUNDATION OF SOIL SCIENCE
DIVISION OF AGRICULTURE AND NATURAL RESOURCES
UNIVERSITY OF CALIFORNIA

Contents

Kearney Foundation of Soil Science -- A Brief Overview 1

Annual Progress Reports

Effect of Microscale Heterogeneity on Biodegradation of Pollutants in Soil 5

K. M. SCOW

Rhizosphere Effects on Degradation of Pesticides in Soil 41

D. E. CROWLEY

The Effects of a Chlorinated, Volatile Hydrocarbon (1,1,1-TCA) on the Diversity and Function of the Microbial Community in Surface and Subsurface Soil 55

M. K. FIRESTONE AND K. A. DUNKIN

Cometabolism of 1,1-dichloro-2,2-bis(4-chlorophenyl) ethylene (DDE) by *Pseudomonas acidovorans* M3GY Grown on Biphenyl 69

A. G. HAY AND D. D. FOCHT

Chemical Factors Affecting Colloid-Mediated Transport of Organic Pollutants in Soils 75

G. SPOSITO

Spectroscopic Studies of Herbicide-Humic Substance Complexes in Soils 87

G. SPOSITO

Factors Influencing Sorptive Properties of Carbonates for Trace Elements in Soils 103

M. ZAVARIN AND H. E. DONER

The Effects of a Hydrophobic Soil Layer on the Development of Unstable Flow 123

J. LETEY, M. CARRILLO, AND S. YATES

Rotational Conformers as Molecular Probes of Sorptive Interactions at Mineral and Organic Soil Surfaces 139

W. J. FARMER

Adsorption-Desorption Kinetics of VOCs onto Pure Clay Minerals 155

M. E. GRISMER AND F. MORRISSEY

Water Flow and Virus Transport in Weathered Bedrock 165

C. S. FRAZIER, R. C. GRAHAM, M. V. YATES, AND M. A. ANDERSON

Kinetics of Metal Fixation at Soil Carbonate Mineral Surfaces 173

W. H. CASEY AND P. A. ROCK

The Soil Chemistry of Iodine 185

J. A. WARNER, R. A. DAHLGREN, AND W. H. CASEY

A Spectroscopic Study of Bonding Structures and Redox Transformation of Arsenate and Arsenite on Goethite Surfaces 203

X. SUN AND H. E. DONER

A Geometric Approach to Soil Pollution 227

C. E. PUENTE

Macroscopic Dispersivity with a Linear Trend in the Log Conductivity 239

T. T. REID, R. B. LEIPNIK, H. A. LOAICIGA, AND M. A. MARINO

Development and Testing of a Micro-Tensiometer 251

J. W. HOPMANS AND T. C. HSIAO

Development of a Screening Model for Fate of Nonaqueous Phase Liquids in Soil 257

W. A. JURY

Uncertainty of Reactive DBCP Transport in Soils 273

T. HARTER, S. EZZEDINE AND K. K. TANJI

The Use of Conditional Simulation to Identify the Sensitive Areas for Nitrate Leaching 291

L. WU, W. A. JURY AND L. PAN

Development of a Sensor for Rapid Determination of Soil Mineral Nitrogen 309

S. K. UPADHYAHA AND D. SLAUGHTER

Composition and Distribution of Fugitive Dust from Central Valley Crop Management Systems 335

H. CLAUSNITZER, M. J. SINGER, AND R. J. SOUTHARD

Appendix

Charter, Kearney Foundation of Soil Science 355

Kearney Foundation Advisory Committee Members 358

Kearney Foundation Technical Committee Members 359

Principal Investigator Index 361

Kearney Foundation of Soil Science: A Brief Overview

The report that follows is the fifth in a series of five Annual Reports issued by the Kearney Foundation of Soil Science regarding its five-year research mission for 1991-96, **Reactions of Toxic Pollutants in Soil Systems**. This volume represents final progress on the research projects reported herein. The five-year mission on toxic pollutants concluded in June 1996. During the course of this mission, sixty three research projects were supported. They ranged in duration from one to five years and involved more than 50 faculty members and Cooperative Extension personnel. Many of the Foundation's research projects are funded for two to three years; thus, several investigators have referred to prior Annual Reports in this series with respect to research methodology and intermediate research results. Please refer to the Foundation's previous Annual Reports for this mission, as needed, for background information.

For more than 50 years, the M. Theodore Kearney Foundation of Soil Science at the University of California has established an impressive record in addressing critical research needs in the state and providing an intellectual forum for international leadership in soil science research. The Foundation has an endowment fund of more than $2 million, which supports, through a competitive grants process, fundamental and applied research by University faculty and Cooperative Extension personnel in the fields of soils, plant nutrition, and water science.

Mitigating the impacts of soil pollution is one of the major challenges facing California in the 1990s. Events that occur in soil have profound effects on surface water qualith and groundwater quality, but the dynamics of the relationship between soil quality and water quality need additional study. At present, scientists lack sufficient data from field situations on the movement, transformation, and fate of soil contaminants that influence water quality. Whether soil contamination arises from seepage of solvents used to clean aircraft at military bases, from leaking petroleum storage tanks at industrial sites, from normal application of fertilizers and pesticides in farming operations, from waste disposal, or from buildup of toxic levels of metals due to trace element-laden agricultural drainage water, University of California soil scientists are the experts who must develop the knowledge base to predict the fate of toxics, provide leadership in remediation strategies, and recommend scientifically sound techniques to prevent future degradation of soil and water quality in the state.

Pesticides provide a good example of soil contaminants requiring further study. Half of the pesticides used in the United States are applied in California, which ranks fifth worldwide in terms of agricultural revenue. The state accounts for 25% of the world's annual pesticide usage. The pressing need for additional scientific research about the transport and fate of toxic chemicals as they travel down the soil profile becomes unequivocal when such consumption of xenobiotic compounds is coupled with the state's dependence on irrigation agriculture and its public health mandate to sustain groundwater quality for domestic use.

Reactions of Toxic Pollutants in Soil Systems -- 1991-1996 Mission

The Foundation's research mission for 1991-96 **Reactions of Toxic Pollutants in Soil Systems**, which concluded recently, represented the first time the Foundation focused on examination of soil pollution problems rather than production of agricultural products. Environmental problems, such as soil pollution, are characterized by an intimate intertwining of physical, chemical, and biological processes that require multidisciplinary

research approaches. Many chemical sources of contamination are not miscible in water, but they can be transported, degraded, and transformed in soil. These soil processes need to be studied and managed for the protection of the state's natural resources and the public health of its citizens. The reactions, mechanisms, and interactions that occur in the soil's vadose region above the water table and in ground water under saturation conditions are not understood fully. The recently concluded five-year Kearney research mission focused only on soil pollution problems in the vadose zone as stated in the outline below:

I. Investigate soil mechanisms, processes, and interactions that control transport, degradation, transformation, and crop uptake of toxic pollutants

   Quantify and model soil processes that determine mobility and reactivity of pollutants in soil and the vadose zone, resulting in groundwater pollution.

   Investigate interactions of soil, water, rhizosphere, and pollutants

   For multi-phase and/or multi-pollutant systems, investigate physical, chemical, and biological reactions and porous media transport involved

II. Develop methodology for scaling up microscopic soil mechanisms and reactions to field-scale processes that apply to agricultural and urban soils

   Investigate spatial variation of physical, chemical, and biological reactions in soil and the vadose zone

   Improve predictive accuracy, including mathematical models' description of soil reactions

   Develop management strategies, including application of the Geographical Information System, to prevent soil and water pollution by toxic environmental pollutants.

The fundamental knowledge base on toxics developed by this mission, including remediation and management strategies, will be applicable throughout the state and will serve as a basis for developing application-related programs in agricultural and urban environments. Many soil science issues, such as the fate of toxics, know few boundaries between agricultural and urban soil.

History

The Kearney Foundation of Soil Science was established by the Regents of the University of California in 1954 to conduct research in soil science, plant nutrition and water science. Mr. M. Theodore Kearney, a prominent Fresno area farmer and founding member of the California Raisin Growers Association, died in 1906 and bequeathed his entire Fruit Vale Estate, worth close to $1.1 million, to the Regents of the University of California for agricultural research purposes. Over the years, Mr. Kearney had developed a fruitful working relationship with UC soil scientists whose advice regarding problems with drainage, salinity, and sodium had been essential to his ranch's success. Approximately 1,500 acres of Mr. Kearney's 5,000 acre Fruit Vale Estate had been planted to grapes for raisin production and the remainder was planted to alfalfa.

It was on Mr. Kearney's farm that University of California Professor W. P. Kelley conducted his classical experiments on alkali soil reclamation. UC Professor E. J. Wickson conducted field research on viticulture there. W. W. Mackie of the United States Department of Agriculture was the first to investigate land reclamation using a tile drainage system at the Kearney property in 1905. Mr. Kearney admired UC Professor E. Hilgard, widely regarded as the "father" of the California Agricultural Experiment Station. Dr. Hilgard began alkali soil studies in the San Joaquin Valley on horseback in 1877.

In 1908, the University took over management of the Kearney estate, located 10 miles west of Fresno, and operated it as a commercial farm until 1948, when the Regents authorized its sale. Income and proceeds from the sale of the farm resulted in the establishment of the Kearney Foundation of Soil Science in 1954 and the University's Kearney Agricultural Center in Parlier.

The early record shows that the in-house research staff of the Kearney Foundation was at the cutting edge of soils research. Their work had major spinoffs not only in agricultural production but also in human and animal health. For example, UC scientists funded by the Foundation studied the generation of radon gas in soils, discovered the importance of cobalt and molybdenum in nitrogen fixation, used ^{15}N isotopes for research, and determined selenium concentrations by X-ray fluorescence.

By the late 1960s, income from the endowment fund was insufficient to support the salaries and research programs of resident scientists, so the Foundation was reorganized to tackle new research missions every five years and to allocate research funds through a competitive grants process to existing faculty and Extension specialists, and farm advisors in the statewide Agricultural Experiment Station. The Foundation's research missions, established in five year cycles since 1970, have focused previously on nitrogen in the environment (1970-75), trace elements (1975-80), salinity (1980-85), and water penetration problems in irrigated soils (1986-91).

Administration

The Associate Vice President for Agriculture, Division of Agriculture and Natural Resources, appoints a Director of the Kearney Foundation from one of the three Agricultural Experiment Station campuses (Berkeley, Davis, or Riverside) to oversee carrying out the designated mission. A Technical Committee and an Advisory Committee are appointed by the Director to help establish research priorities, administer the competitive grants process, and ensure that sufficient research progress and information dissemination occur. Dr. Andrew C. Chang, Professor of Agricultural Engineering and Agricultural Engineer in the Citrus Research Center - Agricultural Experiment Station at Riverside, was Director of the 1991-1996 research mission. Members of the Technical and Advisory Committees for the 1991-1996 mission are listed in the Appendix.

Information Dissemination and Sponsored Activities

Since the 1980s, the Foundation has published an Annual Report of research progress. The Foundation also conducts workshops, holds seminars and technical conferences, and disseminates additional infoarmation, as needed, to fulfill each mission's research objectives and to communicate research accomplishments.

In June 1997, the Foundation will sponsor a special symposium on the UC Berkeley campus, **Phytoremediation of Trace Element-Contaminated Soil and Water**, which is one of five special symposia to be held in conjunction with the Fourth International Conference on the Biogeochemistry of Trace Elements. Approximately 400 scientists from 40 countries are participating in the conference. Twenty speakers will be presenting papers at the Kearney-sponsored symposium, and symposium organizers will publish a monograph of these papers as a special Kearney Foundation publication associated with the 1991-1996 mission.

The Foundation is also sponsoring an innovative study on the use of methyl bromide in soil fumigation that was undertaken by UC Cooperative Extension in Ventura County in conjunction with soil scientists at UCR. When the research project concludes, a special report will be issued and public meetings will be held for information dissemination.

In March 1996, the Foundation published **Background Concentrations of Trace and Major Elements in California Soils**, a special report that includes the first comprehensive, scientific database on total background concentrations of 46 trace and major elements in 50 benchmark soils selected from throughout the state. The database is essential to systematic, accurate assessments of anthropogenic and natural causes of elevated trace element concentrations and is useful to industries attempting to monitor their own effects on trace element levels in soils and to public agencies charged with assessing the severity of trace element pollution problems. The information in the report facilitates accurate interpretations of experimental and field data and facilitates scientifically defensible decisions by industries and policy makers. The Foundation continues to receive special requests for copies of this publication.

In September 1995, the Foundation sponsored an international conference, **Vadose Zone Hydrology: Cutting Across Disciplines**, and published the conference's Proceedings. The conference honored the research partnership of James W. Biggar and Donald R. Nielsen.

In September 1994, the Foundation hosted a Soil Science Conference that highlighted research progress on Foundation-funded projects; reviewed the roles of soil science at the University of California (UC); and made recommendations for the 1996-2001 Kearney research mission. Speakers included prinicpal investigators on Kearney projects, UC administrators, an industry colleague, and Kearney Foundation directors..

In June 1994, the Foundation jointly sponsored a Biosolids and Compost Workshop in conjunction with the Southern California Compost Coalition and the UC Cooperative Extension Waste Management Workgroup. The three agencies developed and published the first **Southern California Biosolids Resource Book** in 1995. It is available by request from the Cooperative Extension Office in the Department of Soil and Environmental Sciences at UC Riverside.

In June 1993, the Foundation convened a Soil Pollution Workshop, which focused on identifying research and development needs in California, ranking the state's most important soil pollution problems, and recommending applied research approaches. The Foundation issued a report summarizing the workshop results.

Additional copies of Annual Reports, the symposium monograph on Phytoremediation of Trace Element-Contaminated Soil and WAter, the special report on the use of methyl bromide in soil fumigation, the special report on Background Concentrations of Trace and Major Elements in California Soils, the Vadose Zone Hydrology Conference Proceedings, and the Soil Pollution Workshop Report are available upon request from the Office of the Kearney Foundation Director, Dr. Andrew C. Chang.

Effect of Microscale Heterogeneity on Biodegradation of Pollutants in Soil

KATE M. SCOW
Department of Land, Air and Water Resources, Davis Campus

Summary

The biodegradation kinetics of pollutants in soil are strongly impacted by the rates of mass transfer of pollutants from locations where they are sequestered to where microbial populations can biodegrade them. Phenanthrene movement in soil was initially very rapid and the chemical moved quickly off of aggregates onto which it was presorbed and into the surrounding soil in which these aggregates were mixed. Biodegradation of the same mass of phenanthrene was faster for soils which received phenanthrene dissolved in larger volumes of carrier solvent, possibly because a larger portion of these soils initially contacted the chemical. The Monod equation was modified to simulate degradation kinetics when different amounts of soil received the same mass of phenanthrene. When phenanthrene came in contact with a smaller mass of soil, the initial phenanthrene concentration was higher, and the kinetics were slower. A biphasic decline in the bioavailability of phenanthrene provided evidence that biodegradation rates were limited, not by the ability of populations to degrade phenanthrene, but by the chemical's availability in soil.

Key Words: biodegradation, sorption, desorption, pollutant, soil microbiology, coupled processes.

Project Objectives Addressed in 1995-1996

To determine the impact of soil spatial heterogeneity on rates of biodegradation of chemicals in soil and improve kinetic models describing biodegradation in heterogeneous systems under batch and column conditions.

Research Plans and Procedures

Heterogeneity in soil occurs on many different scales and involves many different phenomena. Even at the scale of the microcosm, at which many mechanistic biodegradation studies are carried out, the researcher must also consider the heterogeneous distribution of the added chemical within the soil, and how this uneven chemical distribution interacts with the soil's intrinsic biological and physical heterogeneity. In microcosm experiments, three different scales are of importance including that of: (1) the entire microcosm; (2) soil aggregates; (3) within a single aggregate. The factors and processes believed to be important in phenanthrene degradation kinetics ideally should be considered at each of these scales. These factors and processes include: (1) phenanthrene concentration; (2) phenanthrene movement (diffusion); (3) phenanthrene sorption; (4) microbial distribution; and, (5) microbial activity. Factors affecting phenanthrene concentration include the amount of chemical added to the microcosm and the distribution of the chemical among and within soil aggregates. Phenanthrene sorption equilibrium and kinetics are determined by the composition of the soil aggregates, soil moisture levels, soil aggregate size, phenanthrene concentration, and the chemical properties of the phenanthrene molecule. Phenanthrene diffusion is influenced by phenanthrene concentration, phenanthrene sorption, soil aggregate size, soil porosity, soil water content, and the physical and chemical properties of the phenanthrene molecule. Microbial distribution and activity on the aggregate and intra-aggregate scale is determined by the history of the soil, availability of nutrients and other carbon sources, soil water content, soil storage and treatment in the lab, the nature and ecology of the soil organisms, phenanthrene concentration, and microbial history with respect to previous exposure to phenanthrene. All these factors will contribute to the observed biodegradation kinetics. A number of experiments were performed to explore the influence of soil and chemical heterogeneity on phenanthrene biodegradation kinetics at the microcosm, aggregate, and intra-aggregate scales.

Biodegradation of phenanthrene was measured in modified biometer flasks using ^{14}C-radiolabeled chemical to determine the amount of $^{14}CO_2$ mineralized over time. Phenanthrene dissolved in a 100 µl of methylene chloride was added dropwise to 20 g dry weight soil. The soil was stirred for two minutes after phenanthrene addition and vented to the atmosphere for an additional five to ten minutes to allow methylene chloride to dissipate. Unless otherwise stated, 50 ng phenanthrene/g dry soil was added to each of triplicate microcosms. All soils were passed through a 2 mm sieve and moisture was approximately 1/3 bar moisture tension. Figure 1 shows biodegradation kinetics for seven soils spiked with 50 ng/g phenanthrene. All experiments

reported here involved one of these seven soils. Physical and chemical properties for these soils are listed in Table 1.

An investigation into the heterogeneity of chemical distribution in soil microcosms was performed using a water insoluble red dye as a surrogate for the radiolabeled chemical. Ten grams Yolo loam soil were amended with dye dissolved in either 20 µl or 1.5 ml of methylene chloride or acetone. Soil receiving 20 µl of solvent was stirred with a spatula for 1 minute after spiking. Soil receiving dye dissolved in 1.5 ml of solvent was completely saturated and could not be stirred without destroying the soil aggregate structure. After allowing the solvent to evaporate, the soil was divided into ten - 1 g subsamples. The dye from each subsample was extracted and quantitated spectrophotometrically. The amount of dye extracted from each subsample is reported as percent of total mass of dye added to the soil. This experiment was repeated several times.

To insure that toxicity of the solvent used to deliver phenanthrene, methylene chloride, did not affect experimental results, a comparison of degradation kinetics for phenanthrene dissolved in water, methylene chloride and hexane was also performed for Yolo and Tinker soils.

Phenanthrene movement between soil aggregates was investigated in a series of experiments in which phenanthrene was added to a small amount (3-5 g dry weight) of one soil (A) and then this phenanthrene spiked soil was mixed into a larger amount (15-17 g dry weight) of a second soil (B). The biodegradation kinetics obtained from these systems were compared with the biodegradation kinetics of the pure soils, A and B. They were also compared with biodegradation kinetics obtained from a third microcosm in which soils A and B were mixed before being spiked with phenanthrene. Table 2 lists the different combinations of soils A and B which were used. The actual mass of soil spiked and final soil mixture composition varied between experiments. After spiking, soils were allowed to sit from 5 min to one hour at room temperature before mixing with the second soil. To investigate the time dependence of phenanthrene transfer among soil aggregates, a soil mixing experiment was performed in which the spiked soil was incubated at 4°C for 20, 66, and 188 hours before mixing.. In total, seven different soil mixing experiments involving three different soil pairs were performed.

One approach to estimating diffusion of chemicals in soil was proposed by Jury et al. (1983) as part of a screening model used to compare transport of various pesticides in soil. Jury's approach assumes soil can be modeled as a homogenous matrix through which a chemical moves according to Fickian diffusion. Diffusion in both gas and water films is considered. An effective diffusion coefficient is calculated which contains both the aqueous and gas phase diffusion coefficients weighted by the equilibrium partitioning of the chemical between these phases. Equilibrium partitioning of the chemical into the immobile sorbed phase is also accounted for in the effective diffusion coefficients. Diffusion coefficients are reduced to account for the tortuous path chemicals must travel within the soil matrix. Estimates of phenanthrene

diffusion distances were calculated using the Jury approach for a strongly sorbing and less strongly sorbing soil.

The effect on biodegradation kinetics of the initial phenanthrene distribution in soil was investigated by adding the same mass (589 ng) of phenanthrene dissolved in either 21, 100, or 480 µl of methylene chloride to soil microcosms. Each jar thus received the same total mass of phenanthrene, but with a different initial distribution in the soil. Each microcosm also received the same total volume of methylene chloride to eliminate other potential influences of solvent volume.

The effect of phenanthrene concentration on biodegradation kinetics in Yolo soil was investigated using five phenanthrene concentrations: 6.2, 23.5, 40.7, 56, 90.1 ng/g dry soil. The influence of microbial populations on biodegradation kinetics was also investigated by exposing soil to phenanthrene which was not radiolabeled before adding the radioactive phenanthrene. Two different concentrations of unlabeled phenanthrene were used, 50 µg/g and 50 ng/g. Soils were spiked with the unlabeled phenanthrene in the same manner used with radiolabeled phenanthrene and incubated at 25°C for 116 and 610 hours, respectively, before radioactive phenanthrene was added. The length of the incubation times with unlabeled phenanthrene were chosen to maximize possible microbial growth on the added chemical. Previous experiments had shown that soils spiked with 50 ng/g phenanthrene reached maximum degradation rates after approximately 75-90 hours, and degradation rates for soil spiked with 50 µg/g phenanthrene leveled off after 610. Amounts of radioactive phenanthrene added were 50 ng/g for the jars spiked after 116 hours and 67 ng/g for the jars incubated for 610 hours. Control microcosms where also prepared. Control jars were treated in the same way as the other microcosms except they did not receive unlabeled phenanthrene.

The size distribution of soil aggregates was determined by sieving the soil under conditions determined by experimentation to produce reproducible results. Soils were air dried at room temperature for 48 hours prior to sieving. Subsamples, 7-11 g in weight, were placed on a stack of 5 tared 64 mm sieves plus a bottom pan. Care was taken to select as representative a soil subsample as possible. Sieve sizes were 1 mm, 0.5 mm, #60 mesh (250 µ), #140 mesh (106 µ), #300 mesh (50 µ), and a pan to catch soil which fell through all the sieves. Sieves were shaken for exactly four minutes on a sieve shaking machine (American Instrument Company, Silver springs MD). Care was taken to achieve reproducible shaking conditions. After shaking, each sieve plus soil was reweighed and the amount of soil collected in the sieve determined by difference. The aggregate distribution was determined using three separate subsamples for each soil. Soil masses were reported as air dried weights. Soil moisture values were measured for each size fraction for one subsample. The small amount of soil collected in each sieve prevented highly accurate moisture measurements; however, moisture contents between size fractions for the same soil did not appear to vary significantly. Results are reported as percent of total air dried soil mass retained in each sieve.

Throughout this report, biodegradation data are presented as both mineralization rate and cumulative amount mineralized versus time. In plots of mineralization rate, all experimental replicates are shown. In plots of cumulative amount mineralized, averages for experimental treatment are plotted and error bars equal to ± one standard deviation of the replicate data are included. In many graphs, the error bars are smaller than the size of the plot symbols.

Results

A. Phenanthrene distribution within microcosms

In microcosm biodegradation experiments, phenanthrene is added to the soil dissolved in a small amount of methylene chloride. This delivery method allows reproducible, accurate, and safe addition of the highly insoluble radiolabeled chemical to the soil. The methylene chloride carrier evaporates quickly from the soil minimizing its impact on the soil biota. After phenanthrene addition, jars are stirred for at least two minutes, but it is doubtful phenanthrene is homogeneously distributed among the soil particles even after stirring. Using an insoluble red dye as a surrogate for radiolabeled phenanthrene, a study was performed to compare the distribution of the dye in soils which was evenly saturated with solvent containing the dye and soils receiving the dye dissolved in 2 µl of solvent per gram dry soil. The ratio of 2 µl solvent/g dry soil was used for biodegradation experiments at the time of this study.

Figure 2 and Table 3 present the results obtained for this study. Assuming a normal distribution, 95% of the samples from the evenly saturated soil would contain between 8.8 - 11.2% of the total dye added. Only 34% and 37 % of the subsamples from soils receiving dye dissolved in 2 µl solvent per g soil would fall in this range. After this study, the spiking volume in microcosm experiments was increased to 5 µl solvent per g soil from the previously used 2 µl solvent per g soil. At the aggregate scale, it is likely that phenanthrene was distributed relatively uniformly in the microcosms at the beginning of the experiments.

B. Phenanthrene Movement between aggregates in soil--mixing experiments

When phenanthrene is added to soil, the vast majority of the relatively insoluble chemical will become bound to soil solids and thus rendered immobile. The immobility of phenanthrene in soil thus acts to preserve the initial heterogeneous distribution of the chemical following incorporation into soil. In the worst case, phenanthrene would remain bound only to the soil particles which came into direct contact with drops of the spiking solvent. To address this concern, a series of experiments was performed in which phenanthrene was initially added to one soil and after varying time intervals, this spiked soil was mixed with a second soil. The hypothesis was that if

phenanthrene remains bound to the soil to which it was originally added, the composition of the second soil would have no effect on biodegradation kinetics.

Results from soil mixing, experiment 2, are shown in Fig. 3. In experiment 2, 3 g of either Tinker or Forbes soil was spiked with phenanthrene. The soil was stirred for 1 minute, vented to the atmosphere for 10 minutes, and stored at 4°C for 14 hours before mixing into 17 g of either Forbes, Tinker, or no soil. Biodegradation kinetics of the microcosm containing 3 g spiked Tinker mixed into Forbes were much slower than microcosms containing 3 g spiked Tinker mixed into Tinker or 3 g of Tinker alone. The kinetics of jars containing spiked Tinker mixed into Forbes differed from the kinetics of microcosms containing 3 g spiked Forbes mixed into Forbes. The soil surrounding the spiked soil greatly influenced biodegradation kinetics, but the spiked soil itself also contributed to observed degradation rates. The microcosms containing 3 g spiked Forbes mixed into Tinker and 3 g spiked Tinker mixed into Tinker had nearly identical degradation kinetics. It is likely the very slow degradation kinetics exhibited by Forbes soil wre dwarfed by the fast kinetics exhibited by Tinker soil, so the two treatments give nearly identical results.

In soil mixing experiment 4, two soils were used in which both had relatively fast biodegradation kinetics, Yolo and Tinker. A third experiment (data not shown) gave results similar to that of experiment two for this new soil pair, that is, a small amount of Yolo soil spiked and mixed into a larger amount of Tinker soil exhibited biodegradation kinetics which did not match those of either the Yolo or Tinker soils. The same was true of a small amount of Tinker spiked and mixed into a larger amount of Yolo. In experiment 4, unlike experiment 2, the composition of the final soil mixture in the microcosms was kept constant at 3 g Tinker and 17 g Yolo. Examination of Fig. 4 shows there was only a slight difference in biodegradation kinetics depending on whether Yolo, Tinker, or a 3 g subsample of the soil mixture was spiked and stirred into the remaining soil. This data, and data from a similar experiment using a different soil pair, showed that the final soil composition is the most important determinant of biodegradation kinetics, not which soil originally received the phenanthrene. Letting the spiked soil sit for up to one hour at room temperature before stirring into the remaining soil did not alter this conclusion.

The results of the soil mixing experiments show that phenanthrene moves from soil aggregates which originally receive the chemical onto adjacent aggregates. This movement must happen relatively quickly, on the order of 12-24 hours, when the first data point is collected, or biodegradation kinetics measured for soil mixtures with the same final composition would not be relatively insensitive to which soil originally receives the phenanthrene.

As stated earlier, sorption processes are not instantaneous. The exact kinetics of phenanthrene sorption in soil are unknown. However, preliminary experiments suggest that a considerable amount of phenanthrene remains in the aqueous phase for at least one day after spiking. Stirring the soil during this period would thus result in distribution of phenanthrene throughout the soil by aggregate contact. Such a distribution mechanism might explain the results of

the soil mixing experiments. Eventually, migration to equilibrium and later to non-equilibrium sorption sites is expected to decrease the amount of chemical available to move through the soil by diffusion or any other mechanism. To determine if phenanthrene could travel between soil aggregates hours and days after addition to the soil, an experiment was performed in which mixing of the spiked soil into the remaining soil was delayed for 2, 20, 66, and 118 hours after spiking. To inhibit microbial processes during the incubation period, samples were kept at 4°C. No significant differences were noted between biodegradation kinetics of samples incubated for 20, 66, and 118 hours before mixing (Figs. 5 and 6).

The results of this experiment are surprising. Decreases in extraction efficiency and changes in biodegradation kinetics have been measured in our laboratory upon exposure of phenanthrene to soil for time scales similar to the incubation times used here. As phenanthrene becomes less available for chemical extraction, we expect a higher percentage of the chemical is bound to sorption sites from which desorption kinetics are slow. In general, biological processes are more strongly inhibited by lowering temperatures than are diffusion processes. It is possible, however, that incubation of the spiked soils at 4°C also inhibited diffusion to a greater degree than anticipated, perhaps through precipitation of phenanthrene as solid crystals. Both of these possibilities would complicate the interpretation of the results of the soil incubation experiment.

C. Calculations of phenanthrene diffusion in soil

Soil is a heterogeneous environment in which phenanthrene may exit in many forms. The chemical may be dissolved in fluid filled pores and water films. It may move as a vapor through inter-aggregate spaces, or it may become sorbed to organic matter or onto the surfaces of clay and mineral particles. Phenanthrene movement in soil will be dependent upon the relative amounts of the chemical partitioned into the gas, water, and solid phases. An accurate estimate of phenanthrene diffusion kinetics on the aggregate scale cannot be obtained because we cannot specify the exact composition and architecture of the soil environment on the aggregate and sub-aggregate scale. As an alternative, soil is usually modeled as a homogeneous medium. The diffusion coefficient of phenanthrene in this surrogate soil medium is calculated from the diffusion coefficients of the chemical in pure air and water. The pure air and water diffusion coefficients are reduced to account for the barriers to diffusive movement encountered in soil. The sum of these modified diffusion coefficients is weighted to reflect the equilibrium partitioning of the chemical between solid, air, and water phases. This weighted sum of modified air and water diffusion coefficients becomes the effective diffusion coefficient for transport through soil.

Diffusion calculations of the type described above were calculated for two soils, one similar to Yolo with a linear sorption coefficient of 200, and one similar to Tinker soil with a linear sorption coefficient of 2000. Assuming that phenanthrene diffuses spherically from a point source, the radius of a sphere which contains 95% of the chemical may be calculated as a function of time.

Table 4 contains a list of these radii. Examination of Table 4 shows that within a day, phenanthrene will extend through a sphere with a radius of several hundred microns. This amount of movement might be enough to cross water films linking aggregates which are in contact. This amount of movement might not be enough to include aggregates which are not immediately adjacent to the spiked aggregate. It is likely that the diffusion calculations presented here underestimate initial diffusion rates and overestimate diffusion rates at longer times. These diffusion distances were calculated assuming equilibrium partitioning between solid and aqueous phases. It is well known, however, that sorption is not instantaneous in soil (Pignatello & Xing, 1996). Thus, initially more phenanthrene will be in solution than would be accounted for by this diffusion estimate. At later times, phenanthrene may move into sorption sites from which desorption is very slow. Thus after longer exposure to the soil, less phenanthrene would be available for diffusion than assumed in the calculations reported here.

D. Effects of phenanthrene distribution on degradation kinetics

As discussed above, initially phenanthrene is not homogeneously distributed in the soil microcosms. Soil mixing experiments showed the chemical does move from aggregate to aggregate. Changes in phenanthrene extractability with time suggest phenanthrene diffusion would be important during the first week after phenanthrene addition to the soil. It is possible, however, that a homogeneous phenanthrene distribution is never obtained at any time during the biodegradation experiments.

The effect on biodegradation kinetics of the initial heterogeneous phenanthrene distribution in soil was investigated by adding the same mass of phenanthrene dissolved in differing volumes of methylene chloride to soil microcosms. The results are shown in Fig. 7. Biodegradation kinetics were faster for soils which received phenanthrene dissolved in larger volumes of methylene chloride. These curves cannot be superimposed upon one another after multiplication by a scaling factor. Each initial phenanthrene distribution produced a curve with a unique shape.

One hypothesis to explain the results obtained from the spiking solvent volume experiment is that only a subset of the soil in the microcosms is actually involved in biodegradation. The size of the active soil mass would change with the volume of spiking solvent used. When phenanthrene is delivered in less solvent, less soil comes into contact with phenanthrene. Diffusion processes and stirring would help distribute the chemical throughout the soil, but a homogeneous phenanthrene distribution is not achieved quickly enough (if it ever is) to prevent the initial heterogeneous distribution from affecting biodegradation kinetics. To explore the implications of this hypothesis, a common equation used to describe microbial degradation kinetics in liquid culture, the Monod equation, was modified to simulate perceived degradation kinetics when only a fraction of the total soil mass in the microcosm receives all the added phenanthrene. The Monod equation describes simultaneous growth and substrate degradation as a function of time. Biodegradation kinetics

obtained from this equation have differing shapes based on the relative concentrations of the substrate added, and the initial microbial population density, and the relative sizes of the initial substrate concentration, and a parameter, Ks, the Monod affinity constant. The Monod equation does not account for phenanthrene sorption to soil. The simulations presented here involving the Monod equation illustrate the potential effect on biological processes of reduced spiking volume in the absence of sorption.

The results of simulations using the modified Monod equation are shown in Figs. 8-10. Parameter values used in the simulations are listed in Tables 5 and 6. When not enough substrate is added to support growth, and Ks is much greater than the initial substrate concentration (plots a and b), changing the spiking volume has almost no effect on biodegradation kinetics. Kinetics in this case are known as first order kinetics (Simkins and Alexander, 1984). Spiking volume has no effect on first order kinetics because a decrease in initial chemical concentration is balanced by an increase in the number of microbes which can access the chemical. When enough substrate is added to support growth and this initial substrate concentration is much greater than Ks (plots c and d), the biodegradation curve has a different shape and the initial spiking volume will affect biodegradation kinetics. Degradation kinetics, under these circumstances, are termed logarithmic and are characteristic of unrestricted microbial growth. A third example (plots e and f), corresponds to an initial phenanthrene concentration large enough to support microbial growth but roughly equal to Ks. Degradation rates under these circumstances are termed Monod kinetics. The characteristic shape of Monod kinetics is exhibited by the simulation for a spiking volume of 3000 μl. At lower spiking solution volumes, the shape of the curve changes to become more like that seen for logarithmic growth. The shapes of degradation curves are sensitive to the concentration of the added substrate. Concentrating the same mass of phenanthrene onto a smaller mass of soil increases the initial phenanthrene concentration altering the biodegradation kinetics from Monod to logarithmic.

An investigation into the effect of relatively low phenanthrene concentrations on biodegradation rates was conducted for Yolo soil. Figure 11 shows the results of this study. Both initial and maximum degradation rates increase with increasing substrate concentration as would be expected for growing microorganisms. These results emphasize how strongly biodegradation kinetics are influenced by concentration, even at low substrate levels. They cast doubt on the common practice of assuming biodegradation kinetics in soil for low concentrations of pollutants follow first order, i.e. no growth, kinetics.

A second experiment was performed to investigate the effect of microbial growth on phenanthrene degradation kinetics. Phenanthrene that was not radiolabeled was added to soil to stimulate microbial growth before the addition of radiolabeled phenanthrene. Figure 12 shows the rates of radioactive carbon dioxide evolution from soils incubated with 50 μg phenanthrene/g soil for 621 hours prior to addition of radioactive phenanthrene and from soils incubated with 50 ng phenanthrene/g soil for 116 hours before addition of radioactive

phenanthrene. Also included in Fig. 12 are degradation rates for control microcosms which did not receive non-radioactive phenanthrene prior to spiking with radiolabeled phenanthrene. The rates of radioactive and nonradioactive phenanthrene mineralization cannot be determined, since only radioactive phenanthrene mineralization is measured by evolution of radioactive carbon dioxide. The shapes of the degradation curves, however, change from curves which initially exhibit increasing rates (control jars), to curves for which degradation kinetics continually decrease with time (jars pre-exposed to phenanthrene). Degradation kinetics which exhibit increasing rates are associated with microbial growth. Curves with constant or decreasing degradation rates suggest that microbial populations did not increase in number. Thus, it appeared that addition of the higher phenanthrene concentration supported increases in populations to the point where an additional 50 ng/g phenanthrene could not support further significant growth.

To test the hypothesis that toxicity of the carrier solvent may have influenced the rate of phenanthrene biodegradation, a comparison of degradation rates in Yolo and Tinker soils was performed using either hexane, water, or methylene chloride as the spiking solvent in which phenanthrene was dissolved. Figures 13 and 14 contain the results of a comparison of biodegradation kinetics for Yolo and Tinker soils when water, hexane, or methylene chloride were used to dissolve the phenanthrene added to the soil. For both Tinker and Yolo soils, biodegradation rates were initially higher when phenanthrene was dissolved in water. Degradation kinetics for phenanthrene dissolved in hexane or methylene chloride were the same for Tinker soil, while Yolo soils receiving phenanthrene dissolved in hexane had higher degradation rates than soils spiked using methylene chloride. By 150 hours after spiking, no difference in biodegradation rate remained between the different treatments. The total phenanthrene mineralized varied by a maximum of 6% for Yolo soils and 3% for Tinker soils among the differing treatments.

E. The effect of aging on the bioavailability of phenanthrene in soil.

The degradation rate of a sorbing chemical, such as phenanthrene, is limited by the availability to bacteria capable of metabolizing the compound in soil. The bioavailability of chemicals to bacteria in soil can be assessed by monitoring the degradation rate since only available compounds are metabolized. The relationship between the time phenanthrene was present in soil (residence time) and the bioavailability was investigated with a bioassay in a recalcitrant soil. Forbes is a soil collected from the Sierra Nevada foothills that contains a microbial population unable to rapidly degrade phenanthrene. The addition of strain RP17, an *Arthrobacter* sp., to phenanthrene-spiked Forbes soil at a concentration of 10^7 cfu/g soil results in a dramatic increase in the degradation rate and total amount of phenanthrene degraded. Phenanthrene degradation in such a bioaugmented soil is largely due to the inoculum. In this system phenanthrene can be aged for various lengths of time by delaying the inoculation of the soil microcosm. Furthermore, when the pollutant concentration in the soil is much below the affinity constant (Ks) of the inoculum, the degradation of available substrate will proceed according to first

order kinetics. Low concentration of carbon associated with either indigenous substrates or pollutants do not allow a population increase, thereby eliminating the complications of population growth in monitoring bioavailability.

Approximately 67 ng phenanthrene/g soil was spiked into microcosms containing 20 g dry weight Forbes soil. Different treatments were spiked at times ranging from 600 to 0.5 hours before the bacterial inoculum was added. All microcosms were inoculated at the same time with the same culture, and hence, all microcosms contained the same concentration of bacterial inoculum with an identical first order degradation rate constant (k_b) for phenanthrene degradation. After the maximum degradation rate was reached, which occurred approximately 24 hours after inoculation, the degradation rates of all treatments declined in a biphasic double exponential pattern. The difference among the treatments was greatest at the time of the maximum degradation rate. Subsequently, the rates converged, and 300 hours after inoculation, all degradation rates were similar (Fig. 15).

The degradation rates after the degradation rate maximum can be used to determine the change in bioavailability of phenanthrene to the bacterial inoculum over time. First order degradation kinetics are described by the equation:

$$\frac{dS}{dt} = \left(\frac{\mu_{max} * .}{K_s} \right.$$

where S is the concentration of bioavailable pollutant, and k_b is the first order rate constant. The ratio of the degradation rate of treatments with differentially aged phenanthrene is representative of the ratio of available substrate:

$$\left(\frac{dS}{dt}\right)_{rt1} \Big/ \left(\frac{dS}{dt}\right)_{rt2} = k_b(S)_{rt1} \Big/ k_b(S)_{rt2}$$

A curve representing the change in substrate availability was constructed by calculating the ratio of a rate at a given time for a specific treatment divided by the rate of the treatment with the shortest phenanthrene residence time. This normalized substrate availability curve declines in a biphasic double exponential pattern (Fig. 16). The biphasic decline in the bioavailability demonstrates the degradation rate in soil is not limited by the intrinsic ability of the microbial population to degrade phenanthrene, but rather by the availability of the chemical in soil.

Discussion

To summarize the main results presented here:

(1) Initial phenanthrene distributions in soil microcosms are heterogeneous.
(2) Phenanthrene movement in soil is large enough so that the composition of the soil surrounding the aggregate receiving phenanthrene almost completely determines the observed biodegradation kinetics. Inter-aggregate transfer of phenanthrene may be due to diffusion or aggregate contact when soils are mixed.
(3) Initial estimates of phenanthrene movement in soil by diffusion suggest phenanthrene may travel hundreds of microns in one day. Sorption will strongly influence phenanthrene diffusion in soil. Diffusion estimates which assume equilibrium partitioning probably underestimate diffusive movement immediately after phenanthrene addition to the soil and overestimate diffusion after phenanthrene has remained in the soil for some time.
(4) Phenanthrene degradation kinetics are highly concentration dependent and involve growth processes even at very low amounts of added chemical.
(5) Phenanthrene degradation kinetics are sensitive to initial phenanthrene distribution in the soil.

To this list must be added the observation that replicate microcosms almost always exhibit extremely reproducible biodegradation kinetics. Given the heterogeneity of soil, phenanthrene's uneven distribution in the microcosms, and the proven sensitivity of phenanthrene degradation kinetics to initial distribution in soil, such good reproducibility is surprising. Based on these observations, one may begin to construct a hypothetical picture of the behavior of phenanthrene at the scale of the soil aggregate.

Phenanthrene is initially heterogeneously distributed in the soil. Both biodegradation and diffusion processes begin immediately. By the time the first sampling point is taken, 12-24 hours after phenanthrene addition, phenanthrene has distributed far enough into the soil so that the entire composition of the soil is reflected in the observed biodegradation kinetics. Phenanthrene movement may occur through aggregate contact during stirring or diffusion. Either mechanism will be most effective immediately after phenanthrene addition due to non-instantaneous sorption kinetics. At this point, one must consider several different scenarios which experimental data to date cannot discriminate between. Does each pocket of phenanthrene cover a soil region which exhibits the same type of degradation kinetics, or do we observe the average of a distribution of differing degradation rates? Both scenarios could produce the highly reproducible results observed for replicate soil microcosms. That biodegradation kinetics observed in soil are actually the sum of a distribution of first order kinetics has been proposed previously (Gustafson and Holden, 1990). Phenanthrene will continue to diffuse through the soil, probably through distances on the order of hundreds of microns or millimeters. As time passes, diffusion processes will slow due to non-equilibrium sorption

kinetics fixing the heterogeneous phenanthrene distribution in space. The distance over which phenanthrene may be considered to travel quickly with respect to biodegradation kinetics will thus vary with time.

Phenanthrene diffusion kinetics will determine the scale over which soil processes can be modeled as a well-stirred reactor. Microbes in soil are not homogeneously distributed on the inter-aggregate and probably aggregate scale. If phenanthrene in soil moves quickly within and between aggregates, high local microbe populations can access phenanthrene from all portions of the soil, increasing overall degradation kinetics. As sorption slows, diffusion will isolate phenanthrene into small pockets which do not exchange the chemical, and only local conditions will affect biodegradation kinetics. Phenanthrene sorbed to aggregates with low microbial populations will degrade slowly, causing biodegradation kinetics to exhibit a long slow tail. Thus, distribution of microbes, phenanthrene, and movement of both the chemical and microbes in the soil are important to determining observed degradation kinetics.

References

Gustafson, D.I., and L. R. Holden. 1990. Nonlinear pesticide dissipation in soil: a new model based on spatial variability. Environ. Sci. Technol., 24:1032-1036.

Jury, W.A., W. F. Spencer and W. J. Farmer. 1983. Behavior Assessment Model for Trace Organics in Soil: I. Model Description. J. Environ. Qual., 12:558-564.

Pignatello, J.J. and B. Xing. B. 1996. Mechanisms of slow sorption of organic chemicals to natural particles. Environ. Sci. Technol. 30:1-11.

Simkins, S., and M. Alexander. 1984. Models for mineralization kinetics with the variables of substrate concentration and population density. Appl. Environ. Microbiol. 47:1299-1306.

Table 1. Soil properties.

Soil	Total carbon (%)	Texture class	pH	1/3 bar moisture %	Olsen Phosphorus (µg/g[b])	$N\text{-}NH_3$ (µg/g[b])	$N\text{-}NO_3$ (µg/g[b])	Freundlich sorption parameters Kf	n
Yolo	1.1[a]	loam	---	20.6	20[c]	3.6	43.9	560	0.77
Tinker	9.5	sandy loam	4.8	41.6	7	14.6	35.8	5000	0.72
Jocal	4.8	sandy loam	4.9	31.1	137	8.1	11	2200	0.71
Sobrante	6.4	loam	5.5	40.3	8	6.5	77.5	1300	0.91
Aiken	5.4	sandy loam	5.6	45.7	2	8.9	6.7	2700	0.70
Scott	3.6	loam	5.3	29.9	7	13.3	12.7	1500	0.82
Forbes	4.0	loam	5.6	40.3	2	4.9	6	2400	0.69

[a]Organic carbon content calculated from organic matter measured by Walkley-Black method. OC = OM/0.58.

[b]µg per gram air dried soil.

[c]Measured in July 1995. All other nutrient values measured in August 1994.

Table 2. Combinations used in soil mixing experiments

Spiked Soil:	Mix Spiked Soil Into Soil(s):	Final Soil Composition In Microcosm
3 g A	17 g A	20 g A
3 g B	17 g B	20 g B
3 g A	0 g B	3 g A
3 g B	0 g A	3 g B
3 g A	17 g B	3 g A + 17 g B
3 g B	17 g A	17 g A + 3 g B
3 g (B+A)	17 g (B+A)	17 g A + 3 g B
3 g A	14 g A + 3 g B	17 g A + 3 g B

Table 3. Dye distribution in soil subsamples

Subsample	% of total dye in subsample		
	150 ul per g soil	2 ul per g soil	2 ul per g soil
1	9.9	11.4	9.1
2	10.7	8.0	14.7
3	9.6	7.5	8.5
4	9.4	10.3	7.7
5	9.7	5.3	7.9
6	9.4	10.3	8.3
7	10.0	10.7	9.6
8	11.0	14.0	15.1
9	9.9	10.5	9.2
10	10.5	12.0	9.9
Average	10.0	10.0	10.0
Std. Deviation	0.6	2.5	2.7
Relative Std. Dev.	5.7%	24.9%	26.8%

Table 4. Radius of a sphere containing 95% of phenanthrene diffusing from a point source at the center of the sphere

Diffusion Time	Radius of sphere containing 95% of the phenanthrene	
	Kd[a] = 200	Kd[a] = 2000
1 min	14 um	4 um
1 hr	109 um	34 um
3 hr	188 um	60 um
12 hr	377 um	119 um
1 day	533 um	169 um
3 day	923 um	292 um
1 week	1.41 mm	446 um
1 month	2.92 mm	923 um
1 year	1.02 cm	3.22 mm

[a]Linear sorption partition coefficient

Table 5. Parameters used in simulations of the effect of spiking volume on the Monod equation

Parameter (units)	Symbol	(a) First order kinetics	(b) Logarithmic kinetics	(c) Monod kinetics
spiking volume (ul)	sv	3000 500 100	3000 500 100	3000 500 100
initial substrate concentration (ng phenanthrene/g dry soil)	Co	5E-03	5E+03	50
initial microbe concentration (cfu / g dry soil)	Bo	1E+04	1E+04	1E+03

Table 6. Parameters and variables used in all simulations

Parameter (units)	Symbol	Value	Sources
spiking volume which saturates soil (ul)	vtc	3000	observation from dye distribution experiment that 1.5 ml saturates 10 g soil
maximum specific growth rate (1/hr)	umax	0.07	growth rate during logarithmic growth of a mycobacterium sp. on phenanthrene (Boldrin, *et al.* 1993)
Monod affinity constant (ng phenanthrene/g dry soil)	Ks	20	0.1 ug/ml reasonable value based on Ks values for benzoate fit by Simkins, 1984. (0.1 ug/ml)(0.2 ml/g dry soil)(1000 ng/ug)
biomass yield (cfu/ng phenanthrene degraded)	Y	1E+04	yield for phenanthrene degrading bacterium RP17 in liquid culture (E. Schwartz)
carbon dioxide yield (ng CO_2 / ng phenanthrene degraded)	Z	1	value of 1 used to simplify interpretation of results. Actual value probably between 0.5-0.7.
mass dry soil (g dry soil)	D	20	experimental conditions
carbon dioxide evolved from biodegradation (ng CO_2/ g dry soil)	P	variable	
microbial biomass (cfu/g dry soil)	B	variable	
phenanthrene concentration (ng phenanthrene/g dry soil)	C	variable	

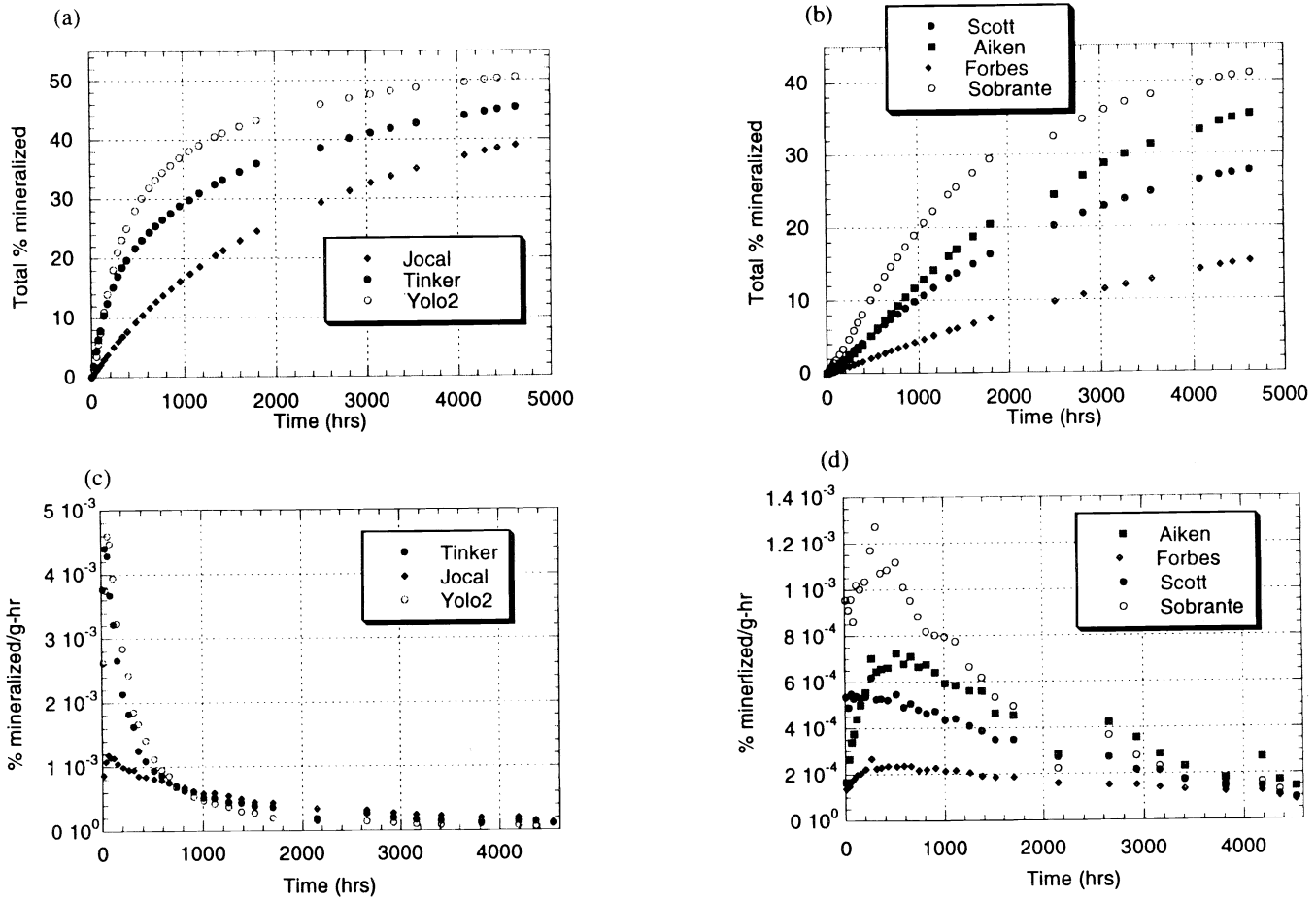

Figure 1. Phenanthrene biodegradation kinetics in seven soils. (a and b) Total percent mineralized versus time (% cumulative radioactivity evolved as $^{14}CO_2$ versus hours); (c and d) Mineralization rate versus time (% total radioactivity as $^{14}CO_2$ per g dry soil per hour versus hours).

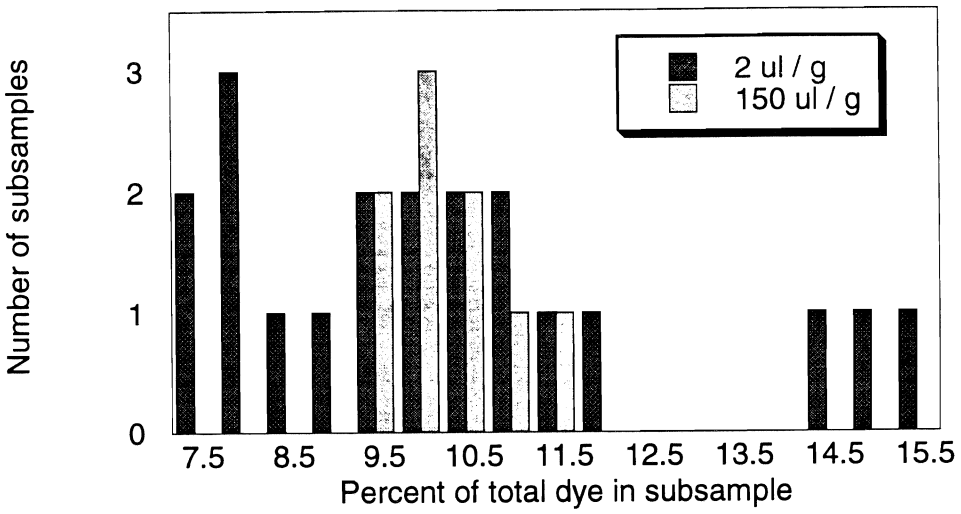

Figure 2. Distribution of dye in soils which receive dye in different volumes of solvent.

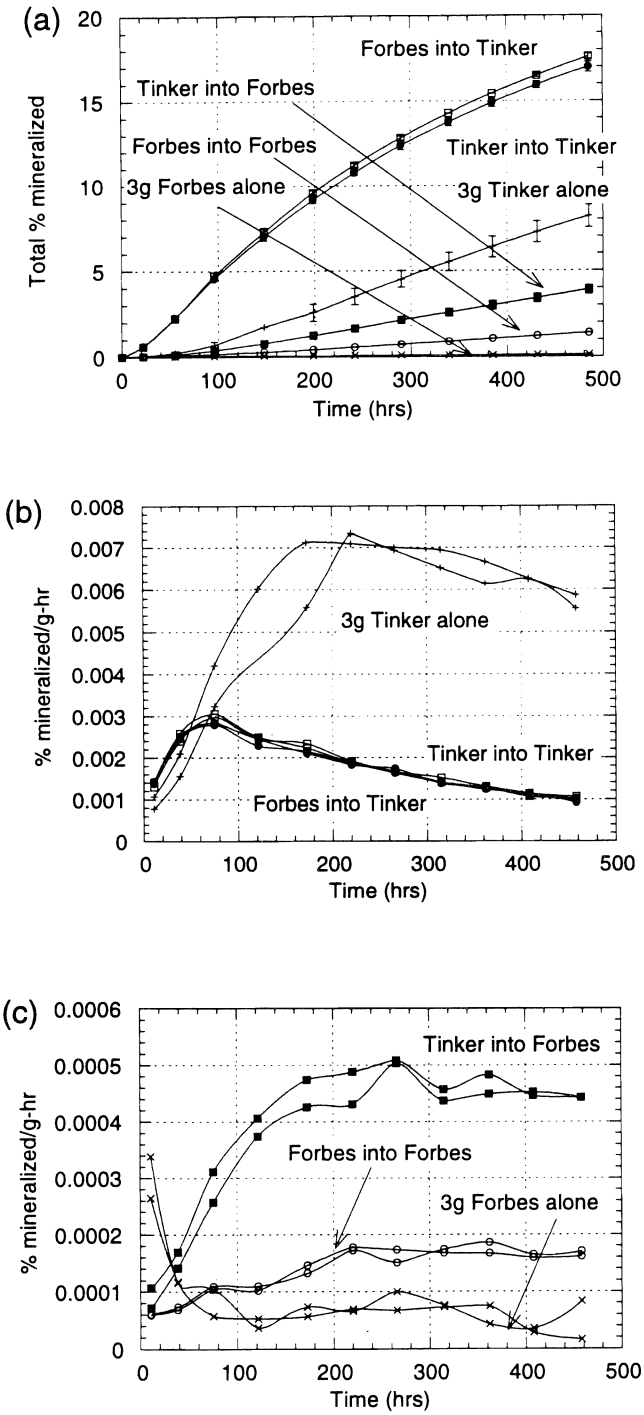

Figure 3. Results of soil mixing experiment 2. Three grams of Forbes or Tinker soil mixed into 17 g of Forbes or Tinker soil or not mixed into any other soil. Results presented as total % mineralized (a) or mineralization rate (b and c) versus time.

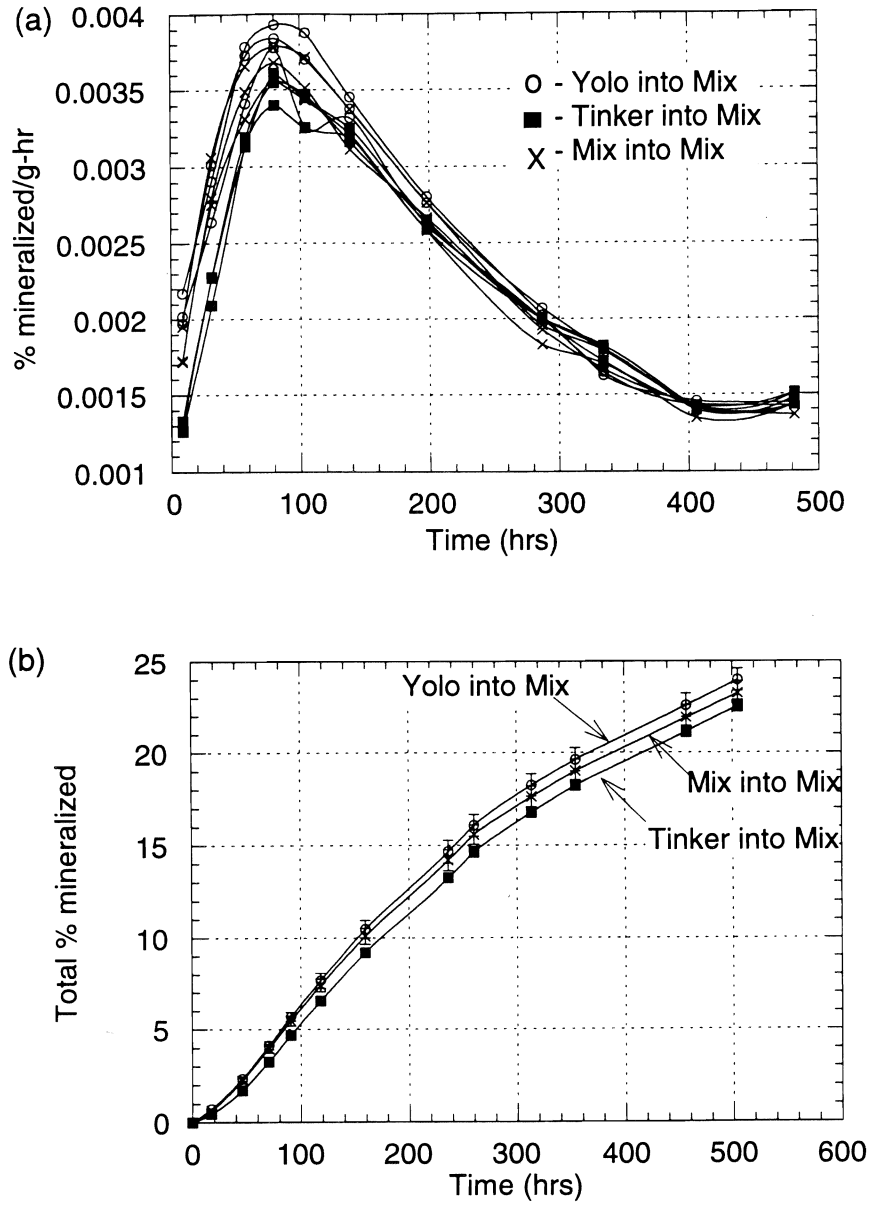

Figure 4. Results of soil mixing experiment 4. Overall soil composition the same for all microcosms, 3 g Tinker and 17 g soil. Spiked 3 g Tinker, Yolo, or mixture. (a) Total % mineralized; (b) MIneralization rate.

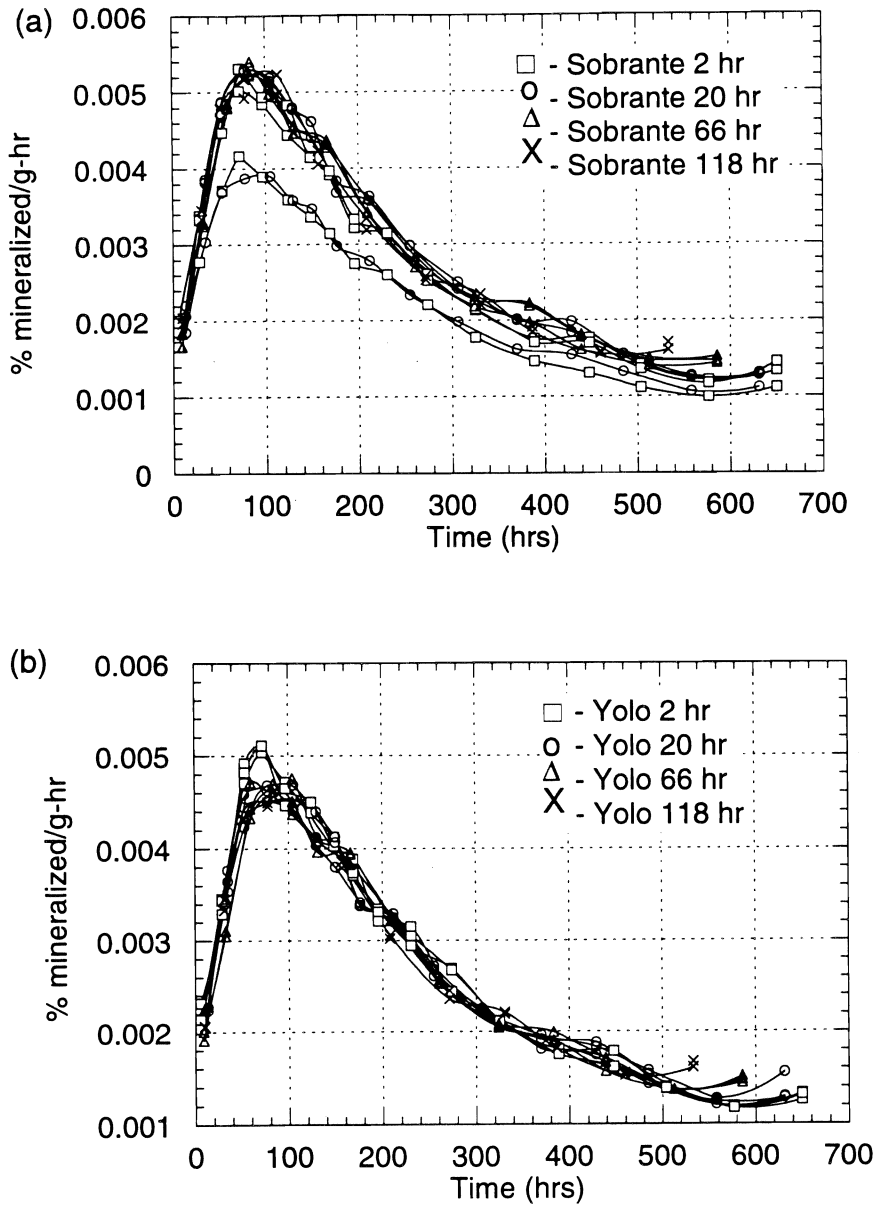

Figure 5. Effect of incubation on movement of phenanthrene from spiked aggregates. (a) Sobrante soil; (b) Yolo soil.

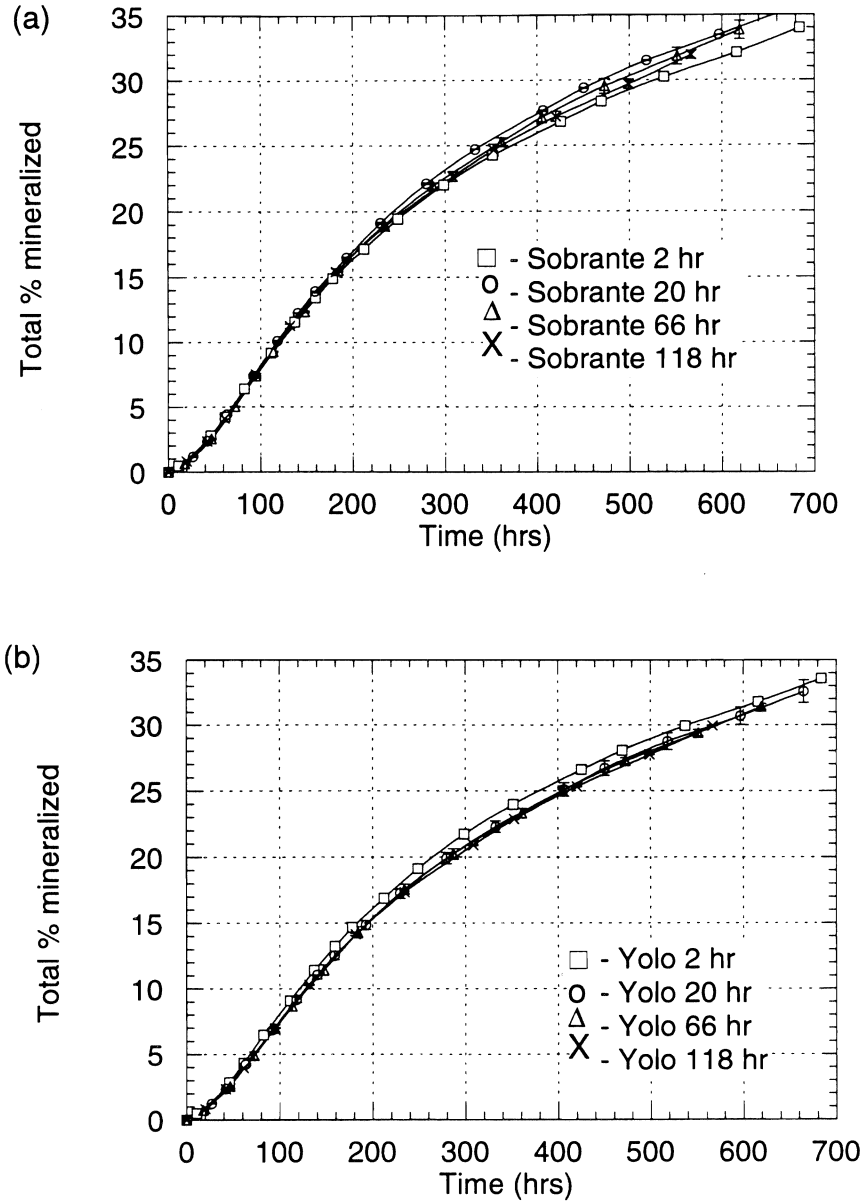

Figure 6. Effect of incubation on movement of phenanthrene from spiked aggregates. (a) Sobrante soil; (b) Yolo soil.

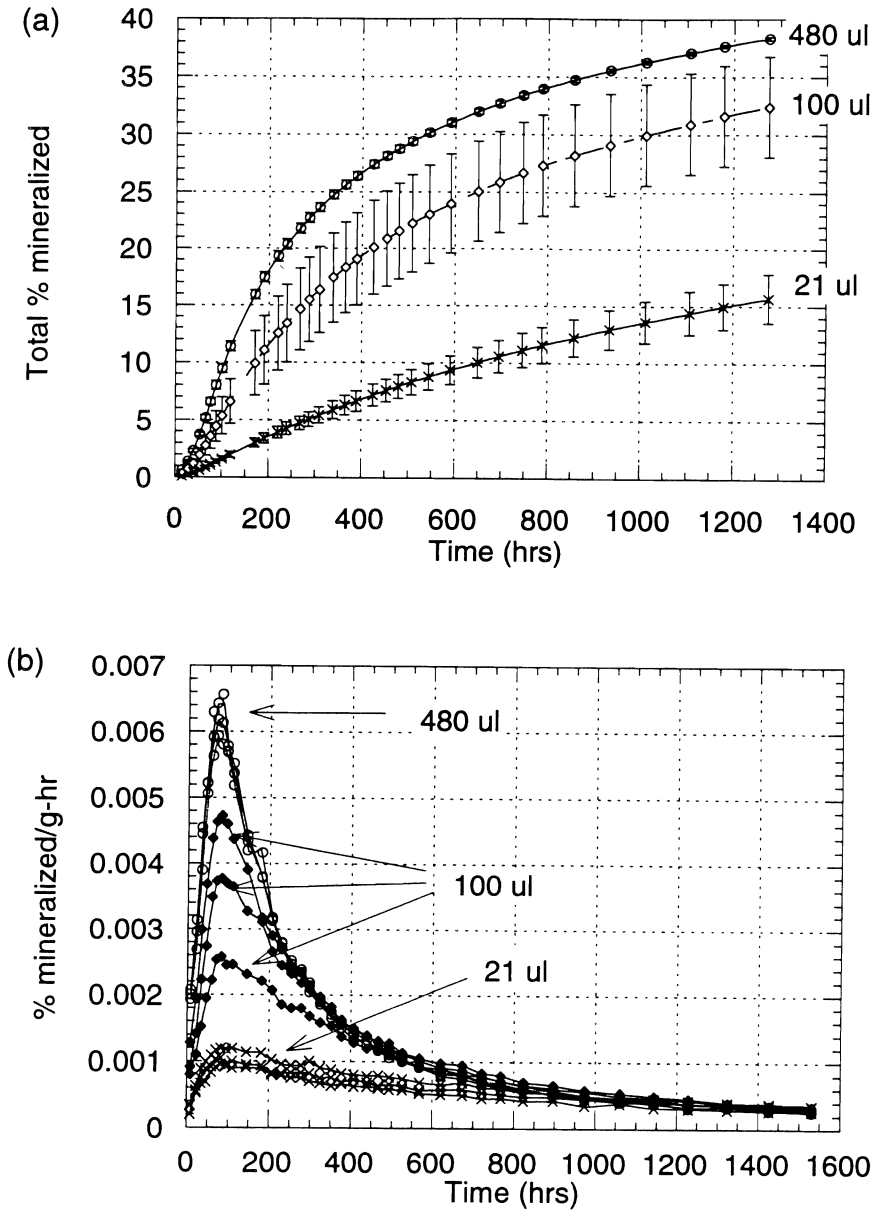

Figure 7. Effect of spiking solvent volume on phenanthrene biodegradation kinetics in Yolo soil. (a) Total % mineralized; (b) Mineralization rate.

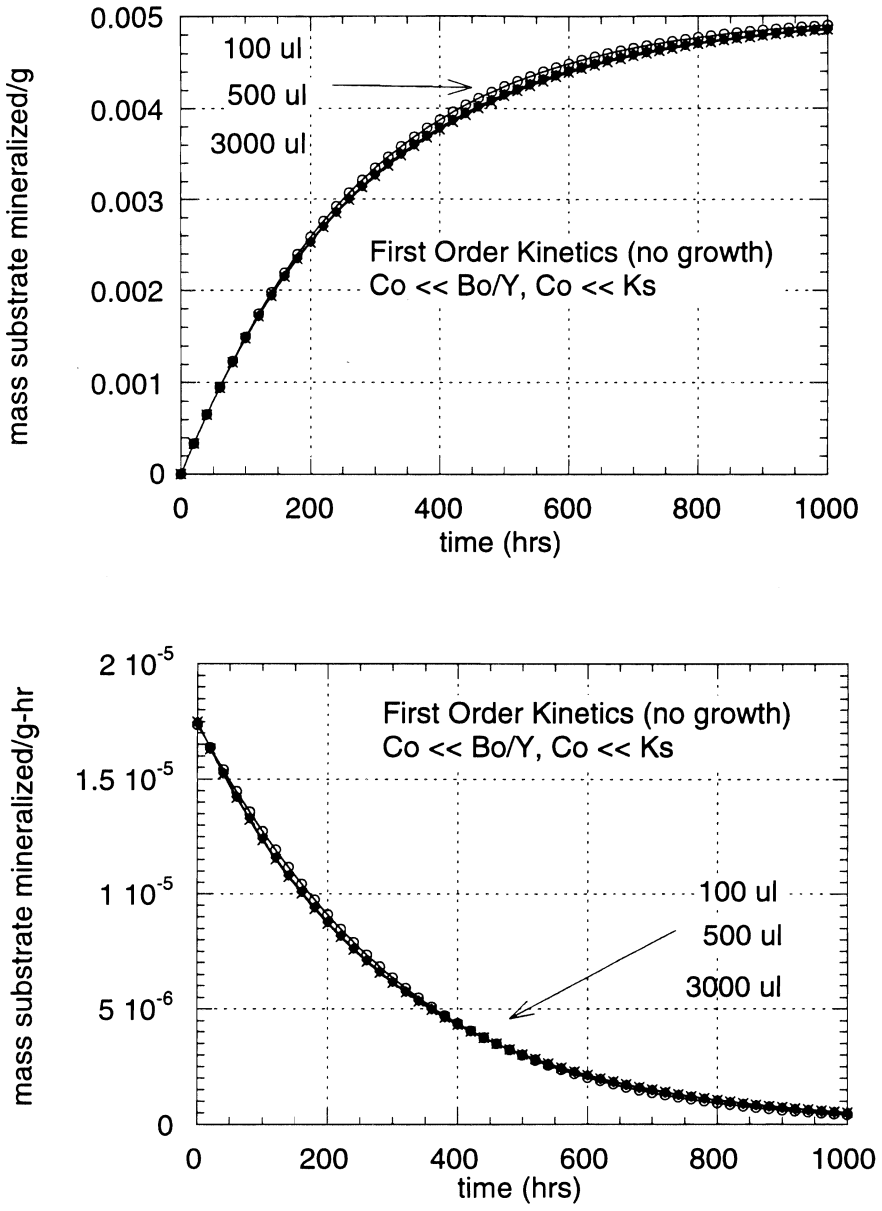

Figure 8. Simulation of the effect of spiking solvent volume on biodegradation kinetics using a modified Monod equation. First order kinetics.

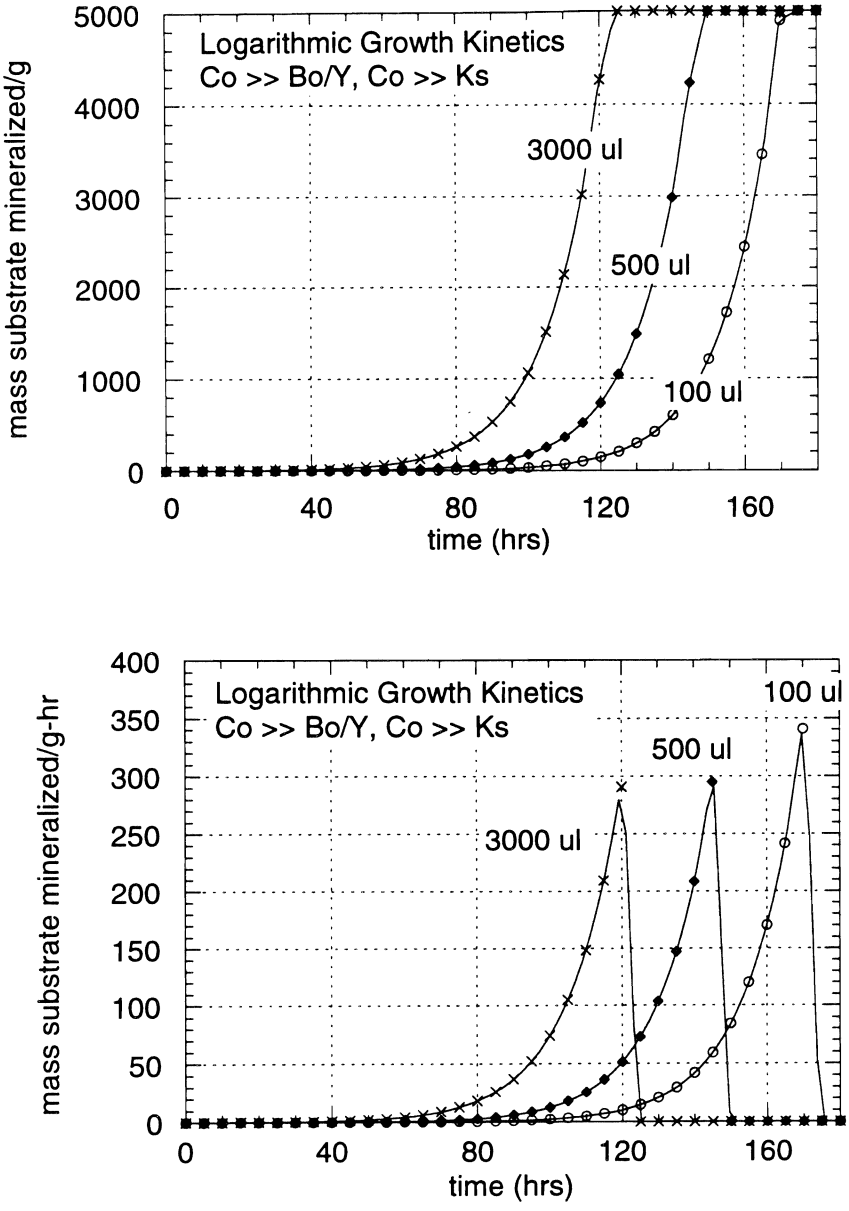

Figure 9. Simulation of the effect of spiking solvent volume on biodegradation kinetics using a modified Monod equation. Logarithmic kinetics.

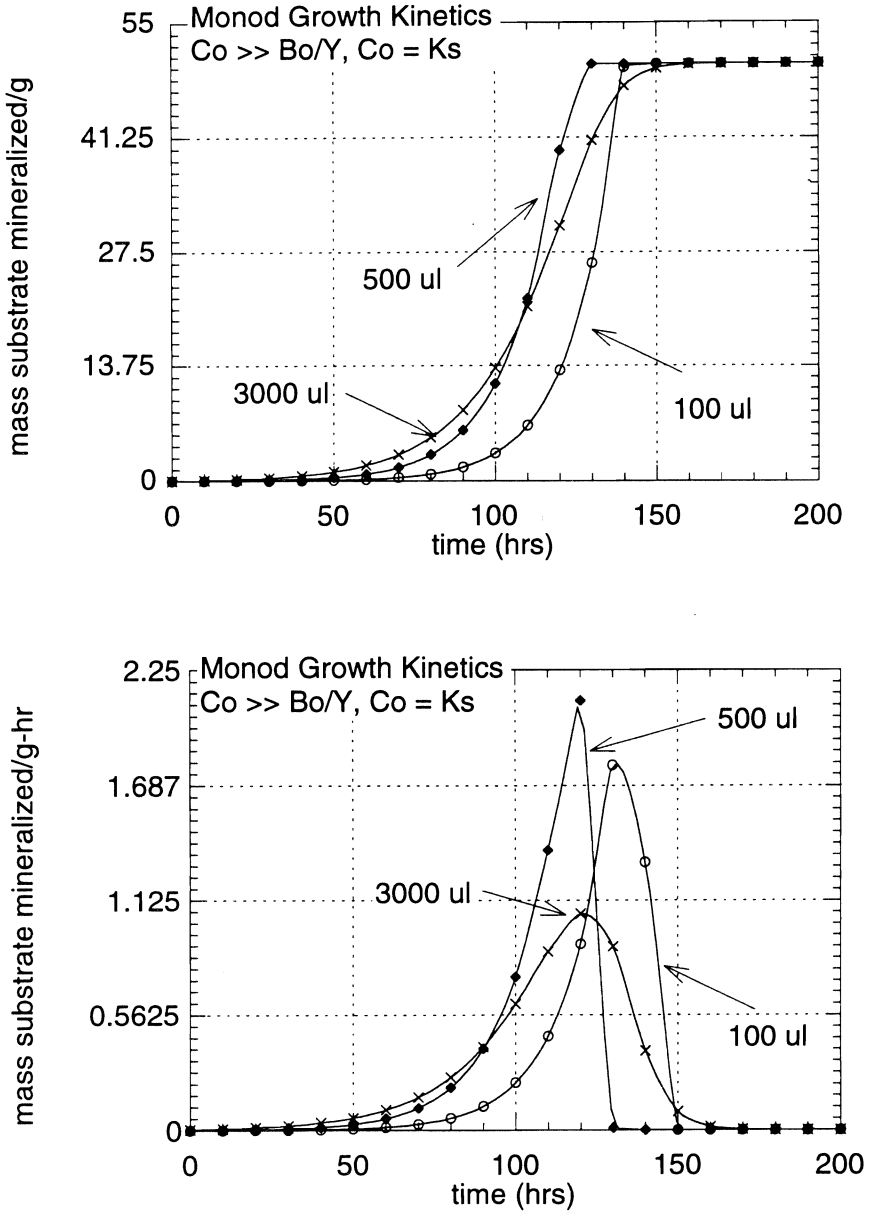

Figure 10. Simulation of the effect of spiking solvent volume on biodegradation kinetics using a modified Monod equation. Monod kinetics.

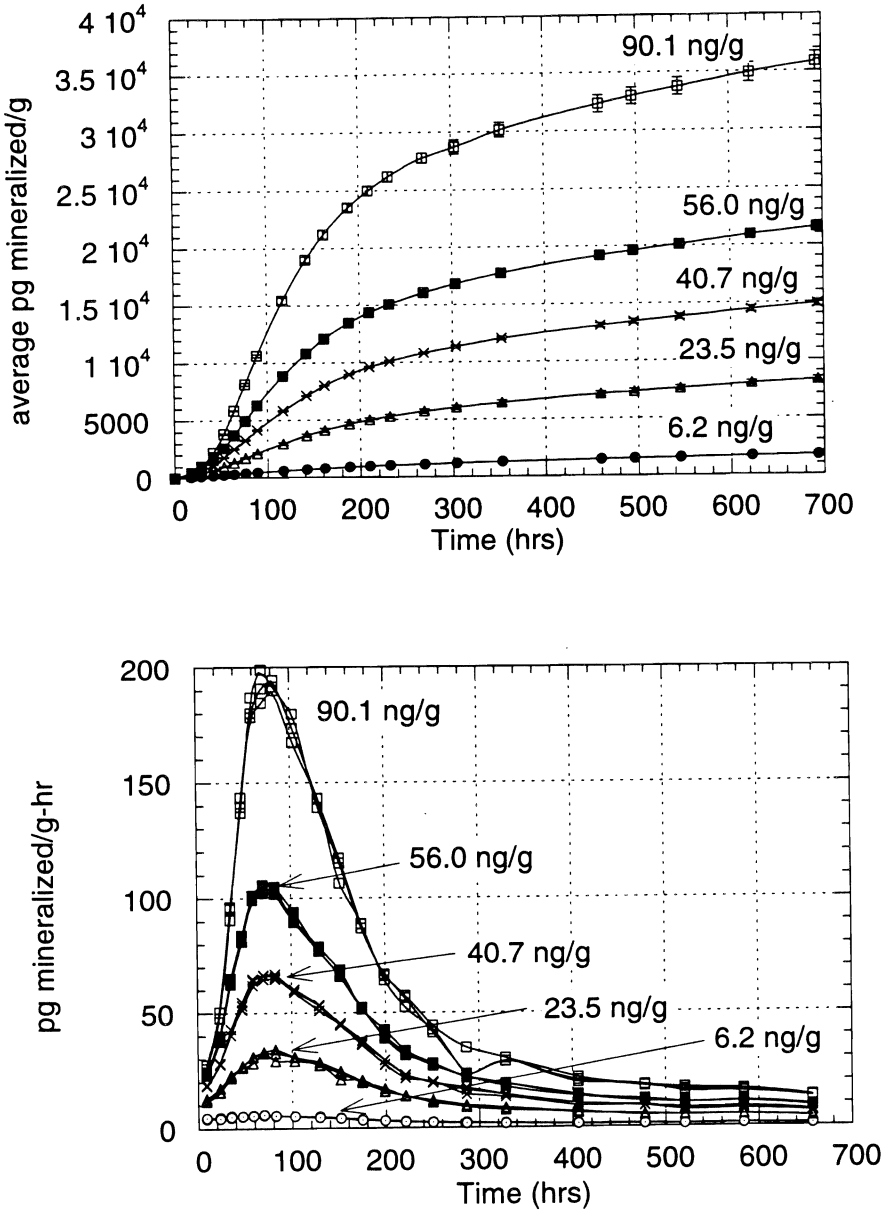

Figure 11. Effect of phenanthrene concentration on biodegradation kinetics in Yolo soil. (a) Total phenanthrene mineralized; (b) Mineralization rate.

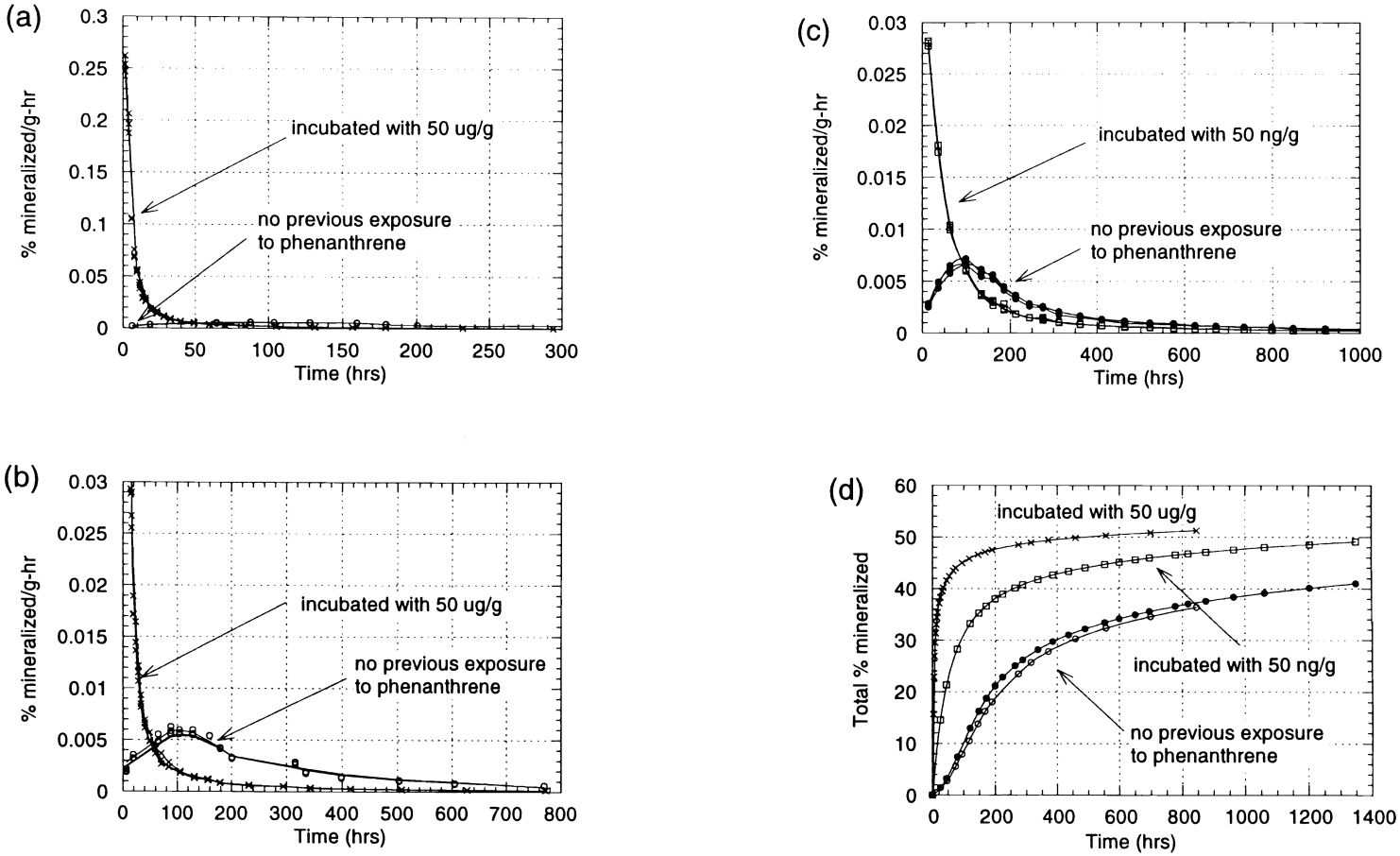

Figure 12. Effect of pre-exposure to phenanthrene on biodegradation kinetics in Yolo soil. (a and b) Soil incubated with 50 µg/g phenanthrene. Two scales shown. (c) Soil incubated with 50 ng/g phenanthrene. (d) All treatments.

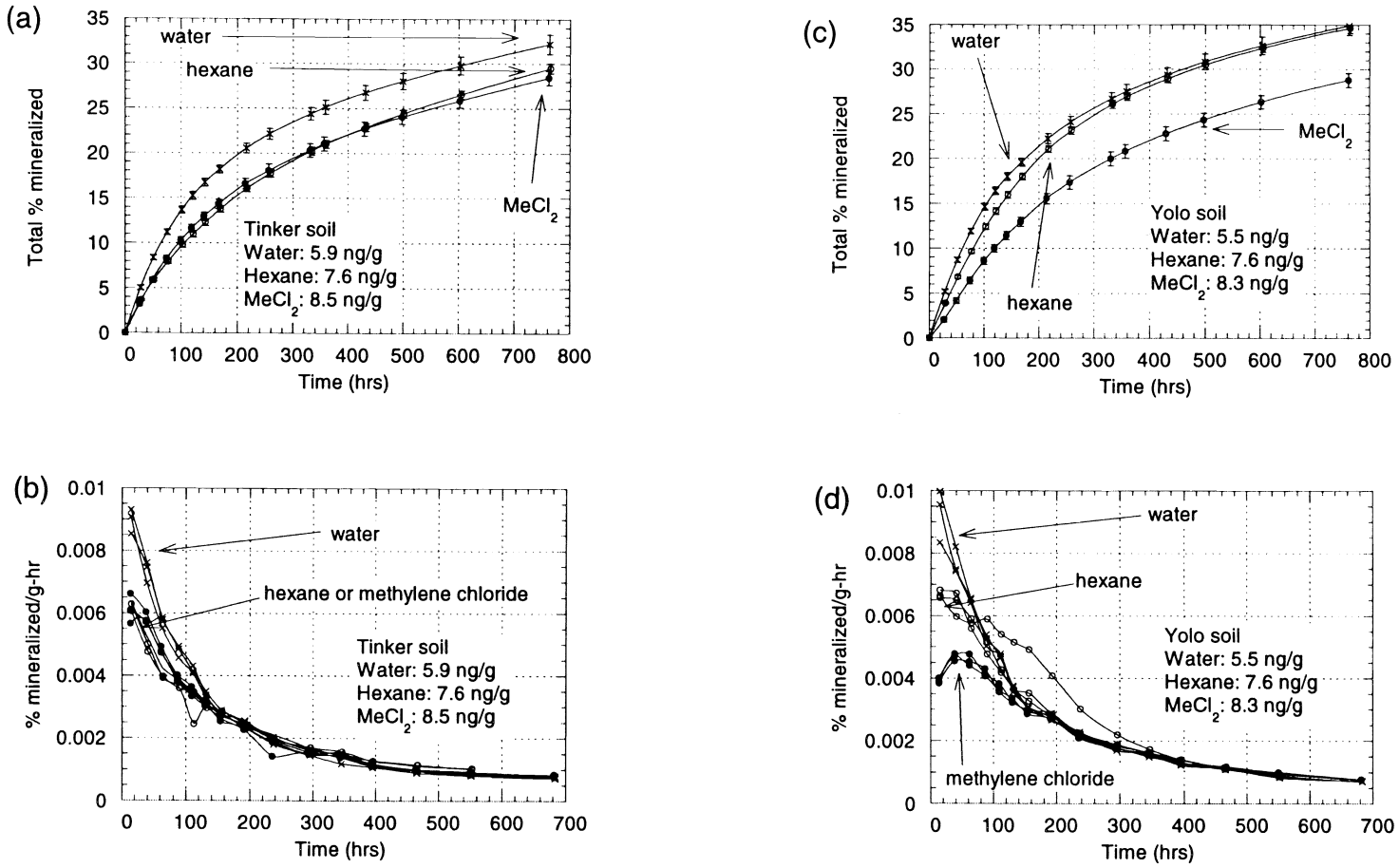

Figure 13. Effect of solvent used to deliver phenanthrene on biodegradation kinetics in Yolo and Tinker soils. (a and b) Tinker soil; (c and d) Yolo soil.

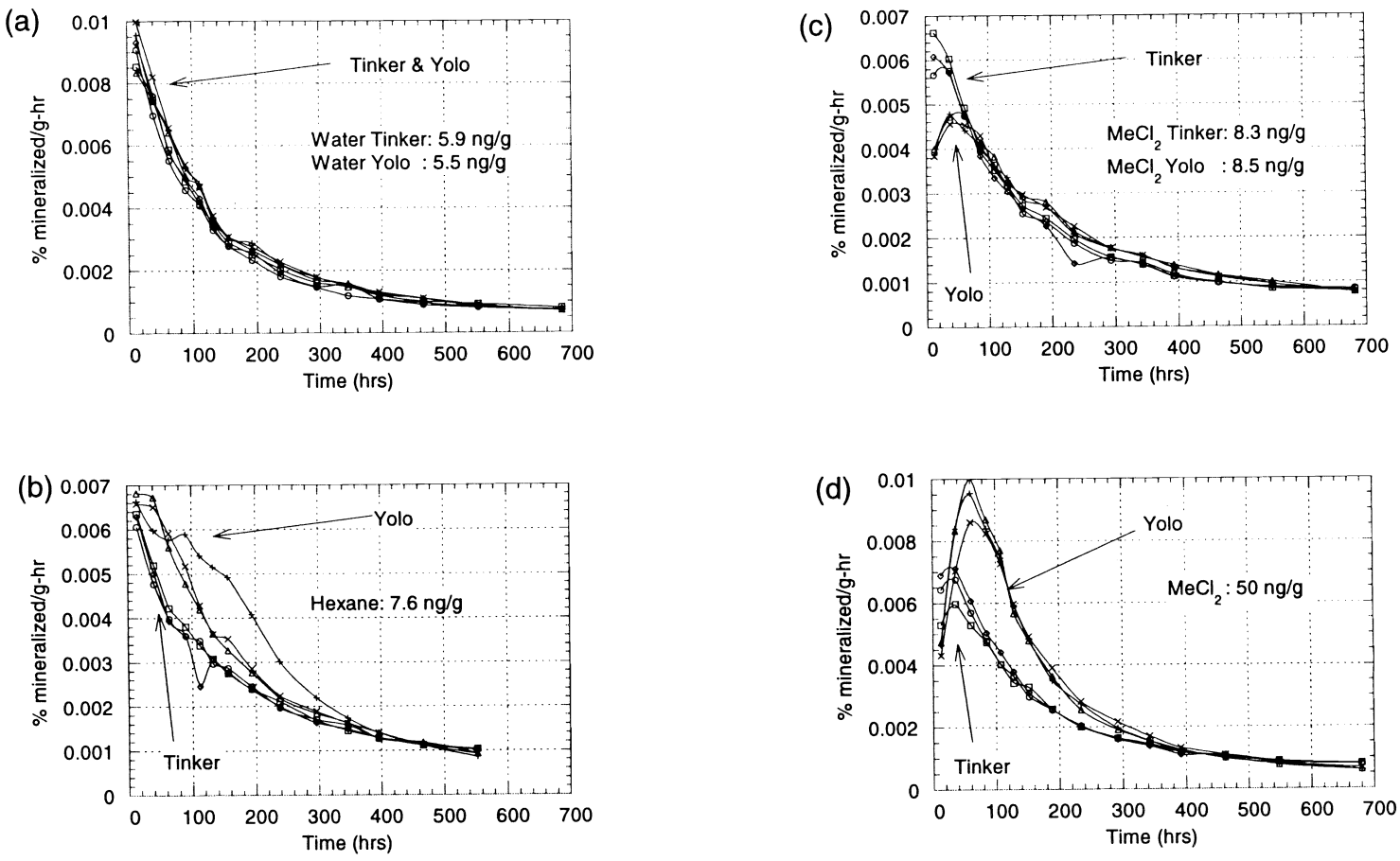

Figure 14. Effect of solvent used to deliver phenanthrene on biodegradation kinetics in Yolo and Tinker soils. (a) Water; (b) Hexane; (c) Methylene chloride-low; (d) Methylene chloride-high.

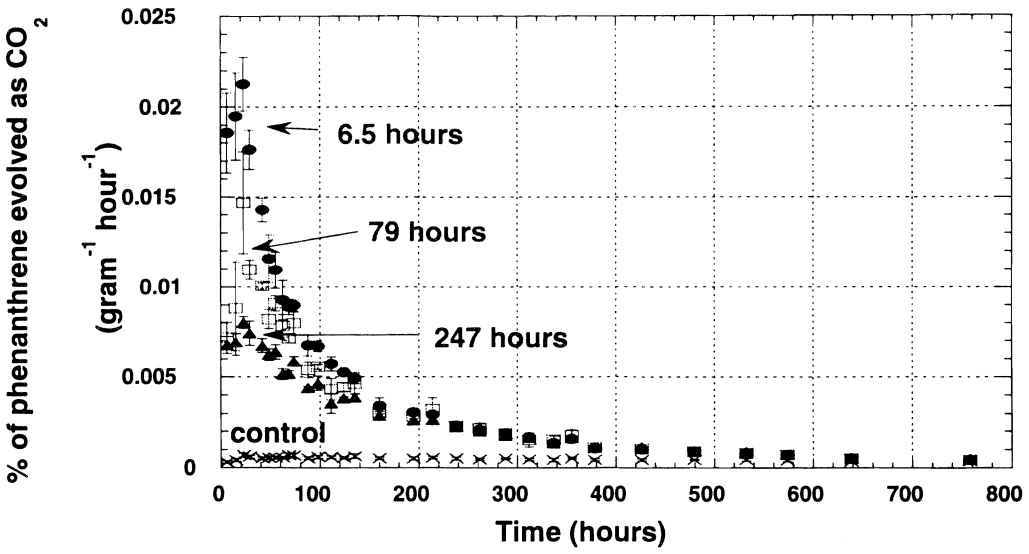

Figure 15. The maximum degradation rate declines as the phenanthrene residence time in soil increases. After 300 hours the rates are very similar.

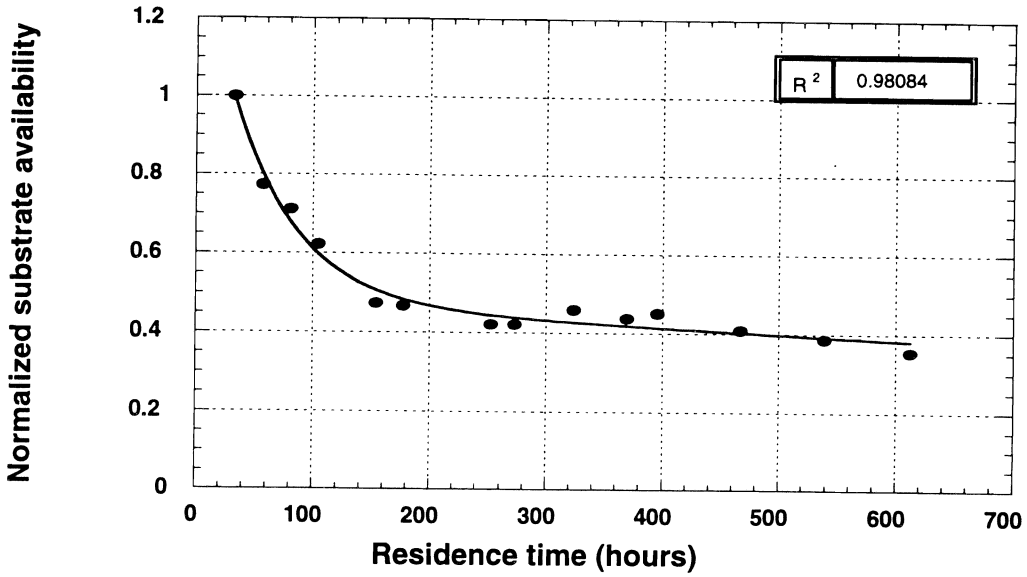

Figure 16. The availability of phenanthrene to a bacterial inoculum declines in a biphasic double exponential pattern.

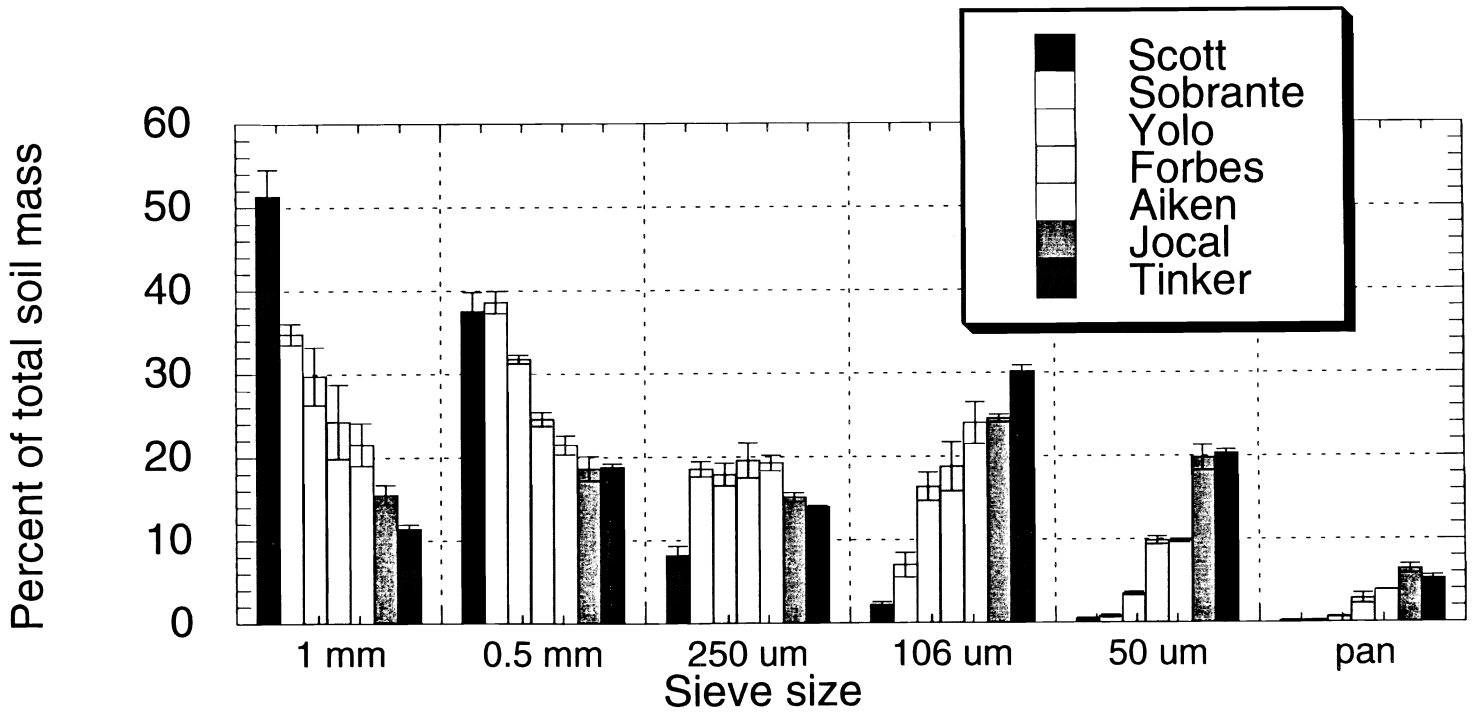

Figure 17. Aggregate size distribution in air dried soils.

Rhizosphere Effects on Degradation of Pesticides in Soil

DAVID E. CROWLEY
Department of Soil and Environmental Sciences, Riverside Campus

Summary

The rhizosphere fortuitously enhances the population numbers and activity of certain microorganisms that degrade xenobiotic soil contaminants. This research examined the ecology of degrader microorganisms in the rhizosphere, and specifically examined the influence of plants on biodegradation of chlorobenzoates, chlordane, polychlorinated biphenyls (PCBs), and the herbicide atrazine. Degradation rates of most xenobiotics examined were not significantly influenced by the presence of a rhizosphere. However, a major benefit of the rhizosphere was to harbor certain degrader organisms at higher cell numbers, thereby shortening the acclimation period. Another benefit may be enhanced transfer of degradative plasmids, or in some instances, enhanced cometabolism of compounds which can not be directly utilized as substrates for microbial growth.

Key Words: biodegradation, microbial ecology, herbicide, phytoremediation, bioremediation.

Project Objectives Addressed in 1995-1996

1. To determine whether plant roots influence the rates of biodegradation or disappearance of chlorobenzoate and other representative chlorinated hydrocarbons from soil.

2. Examine the ecology of a chlorobenzoate-degrading bacterium after introduction into planted and nonplanted soils.

3. Determine the effects of the plant rhizosphere on rates of atrazine disappearance from soil inoculated with an atrazine degrader consortium.

Research Plan and Procedures

Chlorobenzoates

In initial research conducted by our laboratory, chlorobenzoates were chosen as model compounds for studies on the effects of rhizodeposition and selected organic substrates on microbial populations that metabolized the xenobiotic for growth in the absence of supplemental carbon, or that degraded chlorobenzoate by growth-linked metabolism or cometabolism requiring supplemental nutrients. Halogenated benzoic acids have previously been used as model compounds to study the degradation and metabolic pathways of other halogenated aromatic compounds (Hardman, 1991). Chlorobenzoates can either be cometabolized or used as a sole source of carbon and energy. Monosubstituted chlorobenzoates are only moderately recalcitrant, allowing degradation studies to be conducted in a period of several weeks. Along with being model compounds, chlorobenzoates are themselves environmental contaminants. They occur as a result of the use of chlorobenzoate-based pesticides, as breakdown products of other classes of pesticides and as metabolites of polychlorinated biphenyl degradation.

3-Chlorobenzoate

Experiments were conducted with soil containing indigenous microorganisms capable of degrading the model compound 3-chlorobenzoate (3-CB) (Haby and Crowley, 1996). The results showed degradation of 3-CB in 1:1 soil:water slurries from ryegrass rhizosphere soil that had not been previously exposed to 3-CB had a faster initial rate of 3-CB degradation than nonrhizosphere soil. This rhizosphere effect could be simulated in nonrhizosphere soil using glucose, mannitol, or benzoate. A long term experiment further showed that the population size of microorganisms that degraded 3-CB in the absence of supplemental carbon (catabolizers), and those that degraded 3-CB in the presence of supplemental carbon, e.g., via growth-linked metabolism or cometabolism, were enriched by 40- and 250-fold, respectively, in rhizosphere soil. In contrast, planted and nonplanted microcosms that were repeatedly exposed to 3-CB over 24 wk were similarly enriched for 3-CB degraders, which had a MPN of 4×10^8 g^{-1} soil. Our results

suggested that under conditions where there is not constant exposure of the microbial population to 3-CB as a carbon source, carbon provided by rhizodeposition may enhance the population numbers of microorganisms that degrade 3-CB by cometabolic or growth-linked metabolism, and thereby promote rapid depletion of 3-CB from soil during short term or low level exposure to the xenobiotic.

2,5-Dichlorobenzoate

2,5-DCB is normally a highly recalcitrant substrate and was not significantly degraded in soil unless the soil was bioaugmented with a degrader bacterium. Genes for catabolism of this compound are carried on a catabolic plasmid pPB111, which was originally isolated from *Pseudomonas putida* P111, and transferred by conjugation to *P. fluorescens* 2-79RL (Crowley et al., 1996). The major benefit of the plant rhizosphere was to promote a greater rate of degradation and to improve long-term stability of the plasmid in *P. fluorescens* 2-79 RLD. Part of the difference in the rate of 2,5-DCB disappearance appeared to be due to plant uptake of the compound, but the major effect appeared to involve enhancement of degradation activity. In the presence of plants, the xenobiotic was completely mineralized after 4 days, whereas, in nonplanted soil 2,5-DCB disappeared after 7 days to 14 days. One possibility for the enhanced disappearance rate may have been that the plasmid was more stably maintained in the rhizosphere, which is supported by the fact that most of the introduced bacteria continued to carry the plasmid even after the 2,5-DCB substrate was gone. Another benefit may have been enhanced transfer of the degradative plasmid to the indigenous microflora.

Polychlorinated Biphenyls

In research supported both by the Kearney Foundation and the U.C. Toxic Substances Training and Research Program, plant compounds that induced *Arthrobacter* sp. strain B1B to cometabolize polychlorinated biphenyls (PCBs) were identified using a screening assay based on the formation of 4,4'-dichlorobiphenyl ring-fission product. A chemical component of spearmint (*Mentha spicata*), *l*-carvone, induced *Arthrobacter* sp. strain B1B to cometabolize Aroclor 1242, resulting in significant degradation of 26 peaks in the mixture, including selected tetra- and penta-chlorobiphenyls (Gilbert and Crowley, 1997). Evidence for PCB biodegradation included peak disappearance, formation of the phenylhexedienoate ring-fission product, and chlorobenzoate accumulation in the culture supernatant. Carvone was not utilized as a growth substrate, and was toxic at concentrations greater than 500 mg L^{-1}, suggesting that carvone was metabolized as a detoxification mechanism. Several compounds structurally-related to *l*-carvone, including limonene, *p*-cymene, and isoprene, also induced cometabolism of PCBs by *Arthrobacter* sp. strain B1B. A structure-activity analysis showed that chemicals with an unsaturated *p*-menthane structural motif caused the strongest cometabolism activity. These data strongly suggests that certain plant-derived isoprenoids are natural substrates for the enzymes encoded by the *bph* genes.

Atrazine

Among the various xenobiotics that may have enhanced degradation in the rhizosphere, atrazine is a particularly good candidate since, like most hydrophobic compounds, it accumulates on clay and organic matter in the upper soil horizon occupied by plant roots. At normal application rates, it is present at relatively low concentrations that may preclude the growth and maintenance of an effective degrader population size (Pahm and Alexander, 1993). This latter problem is particularly problematic for atrazine, which has a highly oxidized triazine ring that provides no energy for microbial growth (Cook, 1987). Thus, atrazine-degrader organisms can only acquire energy by utilizing carbon in the side chains attached to the ring or by growth on other carbon compounds contained in soil organic matter or root exudates. Atrazine has also been shown to serve as a nitrogen source for microbial growth (Alvey and Crowley, 1995; Mandelbaum et al., 1995), which may be enhanced by plant uptake of nitrogen and simultaneous deposition of carbon, thereby providing a selective advantage for microorganisms that are able to derive nitrogen from the triazine ring.

Studies in our laboratory showed that despite optimistic scenarios for enhanced atrazine biodegradation in the rhizosphere, rates of atrazine biodegradation were not significantly improved by the presence of plants when atrazine degraders were added to soil at a high population density (Alvey and Crowley, 1996). Bioaugmentation of soil contaminated with 6 ppm atrazine resulted in mineralization ca. 75-80% of that applied in 4 wk in the presence or absence of plants. The only benefit of the plants was to slow the decline in population size of the consortium over that which occurred in bulk soil without plants. Thus if atrazine degraders were ever utilized for removing atrazine residues at the end of a growing season, there might be some benefit to utilizing plants in conjunction with bioaugmentation. This might also be employed for bioaugmentation of riparian strips to reduce atrazine runoff into surface waters. However, these data again point to the consistent observation that the primary benefit of the rhizosphere is to harbor the degrader organisms at a larger population size that may shorten the acclimation period rather than enhancing the actual rate of degradation by the degrader organisms.

Data from our experiments showed that corn plants themselves may have been responsible for transformation of the parent compound to nonphytotoxic hydroxyatrazine, since high levels of hydroxyatrazine accumulated in the rhizosphere even under axenic conditions. Differences in the level of hydroxyatrazine formation between greenhouse and growth chamber experiments further revealed the importance of environmental conditions on the rate of hydroxyatrazine transformation mediated by plants (Alvey and Crowley, 1996). Further incubation of the planted soils under fallow conditions demonstrated that hydroxyatrazine was a relatively transient molecule with subsequent formation of hydroxylated N-dealkyl metabolites. These data highlight some of the complexity that must be considered in evaluating disappearance of xenobiotics from soil or in characterizing rhizosphere effects on biodegradation by soil microorganisms.

In soils where atrazine is present at concentrations that will support direct growth of a degrader population it has been shown that bioaugmentation results in high levels of degradation. Mandelbaum and coworkers (1995) inoculated soils from a hazard waste site and found ca. 65% disappearance of the atrazine upon inoculation with the atrazine mineralizing *Pseudomonas sp.* in 3 wk (51). Other studies have demonstrated similar rates of mineralization of atrazine in soil, Alvey and Crowley found 60 % mineralization of 1000 ppm of atrazine in soil after inoculation with a consortium and Kontchou and Gschwind found 60 % mineralization of 10 ppm in soil (Yanze-Kontchou and Gschwind, 1995). These data suggest that bioaugmentation alone might be sufficient for remediation of atrazine contaminated soils.

Results and Discussion

Results of experiments examining the influence of plants on biodegradation of chlorobenzoates, other chlorinated hydrocarbons, and atrazine are summarized in Table 1. Each of the compounds examined in this research showed a different possible effect of plants on the rate of disappearance of these contaminants from soil. With 3-CB, there was fortuitous enrichment of microorganisms that could directly utilize 3-CB as a carbon source, or that could degrade 3-CB in the presence of supplemental carbon. However, this beneficial effect was observed only in soils that had not been previously exposed to the contaminant, where the main benefit of the rhizosphere was to shorten the acclimation phase. After acclimation to the xenobiotic, the compound was degraded within a few days irrespective of the presence of plants. In the case of a more recalcitrant chlorobenzoate, 2,5-DCB, plants significantly increased the rate of disappearance of the contaminant only after the introduction of the catabolic genes into the soil. In these experiments, the 2,5-DCB catabolic genes were carried on a plasmid contained in a rhizosphere colonizing pseudomonad. The main benefit of the rhizosphere was to increase the survival of the degrader, and possibly to enhance plasmid transfer to the indigenous microflora.

In the case of chlordane and 4,4 dichlorobiphenyl, there was no effect of plants since microorganisms capable of degrading these compounds were either not present or were inactive in these soils. Lastly, detailed studies were conducted on atrazine, another recalcitrant compound which requires the presence of an active degrader population in order to be degraded. In research on this herbicide, an atrazine degrader consortium was isolated from soil previously exposed to the contaminant. When the consortium was inoculated into a nonhistory soil at a high population density, atrazine was rapidly degraded in either the presence or absence of plants. The main benefit of the rhizosphere was to enhance the long term survival of the consortium, which in soils receiving pulses of atrazine would help to shorten the acclimation phase that occurs prior to rapid degradation of the contaminant.

The rhizosphere is commonly perceived as a site of high microbial activity and bacterial population numbers. Microbial population densities in the rhizosphere are typically measured at 10^9 cells per gram of soil or root (Curl and

Truelove, 1986), a number as great as that obtained in nutrient rich media used to culture cells in the laboratory and 100 to 1000-fold greater than occurs in bulk soil. However, high numbers do not necessarily translate to high activity for all microorganisms associated with the rhizosphere. Rhizosphere ecologists have long recognized that much of the rhizosphere is oligotrophic, containing stationary phase or very slow dividing bacteria that are growth limited by lack of carbon substrates (Bowen and Rovira, 1976; van Elsas and van Overbeek, 1993). In actuality, the only sites of relatively high microbial activity are confined to the root tips or sites of lateral root emergence where microorganisms have received a temporary pulse of carbon provided by root exudates or root cell lysates. These spatial variations in nutrient availability, as well as differences in the composition of plant derived compounds in different zones may impact both growth-linked and cometabolic degradation of xenobiotics.

Different root zones can also influence the heterogeneity of the rhizosphere community, which reflects microbial succession after the primary colonization of new roots. Early studies of the rhizosphere microbial community suggested that pseudomonads were the predominant microorganisms associated with plant roots, comprising anywhere from 30 to 90% of the culturable organisms isolated on agar media (Vancura, 1980). More recent studies using media that select for oligotrophic microorganisms or DNA probing methods show that there is tremendous diversity in the community of microorganisms associated with roots, and that these communities vary for different plant species, or even for the same plant species in different soils (Laguerre et al., 1996). Microbial communities associated with individual plants may even differ from one root to the next, depending on stochastic events that lead to the successful colonization of a particular root by different microorganisms. Redox and gas diffusion gradients, as well as the structure and transition of microbial communities in a biofilm that extends radially from the root surface further delimit environmental conditions that affect microbial transformations of xenobiotics. Lastly, protozoa and nematode grazing of bacteria associated with the root surface, results in turnover of microorganisms, release of nitrogen mineralized from the microbial biomass, and changes in the types and quantities of substrates that are available to competing microorganisms in the rhizosphere over time.

An illustration of the differences in microbial activity that occur along plant roots is shown in Fig. 1, in which roots of bean plants were inoculated with a root-colonizing pseudomonad containing a bioluminescence marker. In this marker, light production is regulated by a ribosomal promoter, such that light is produced only when the bacterium is actively growing. This organism also carried a plasmid which conferred the ability to degrade the recalcitrant xenobiotic, 2,5-dichlorobenzoate (Crowley et al., 1996). The soil used for this study had been uniformly inoculated with the degrader, and contaminated with the xenobiotic prior to transplanting the plants into the microcosms. After three days, the plants were removed and exposed to x-ray film for autophotography to locate actively growing cells. As shown in the Fig. 1, growth-linked bioluminescence of the pseudomonad was apparent only at the root tips and at sites of lateral root emergence. Several root tips did not show any

bioluminescence and were colonized only at very low population densities by the degrader organism. Other locations were found to contain high population densities, but the cells were not bioluminescent, indicating that the cells were in stationary phase.

To further investigate the physiological status of this microorganism in different locations of the rhizosphere, we developed novel methods to quantify the relationship between the starvation state of this bacterium and expression of its bioluminescence marker (Marschner and Crowley, 1996). Starvation-related changes in cell physiology include a decrease in physiological activity (Kurath and Morita, 1983), as well as sharp decreases in ATP, protein, DNA, and RNA per cell (Morita, 1993). When starved cells are subsequently provided with nutrients, one of the first events in their recovery is induction of rRNA required for production of new proteins. This leads to an longer lag phase in starved cells, which increases in proportion to the degree of prior starvation (Amy et al., 1983). In *Pseudomonas fluorescens* 2-79RL, stationary phase cells are nonbioluminescent, whereas during recovery from starvation the first step prior to cell division is to synthesize new ribosome. Since the bioluminescence genes are coupled to a ribosomal promoter, the onset of light production marks the end of lag phase. In principle, this methodology is similar to other luminescence-based marker and reporter systems that have been used to assay the activity of pseudomonads in the rhizosphere and in soil (Meikle et al., 1994).

Typical data showing the physiological status (lag phase duration) and cell numbers of *P. fluorescens* 2-79 are shown in Fig. 2. Short lag phases (line graph data) are observed primarily at locations behind plant root tips or at sites of lateral root emergence, reflecting the relative availability of carbon in these root zones. In soil and on older root parts, the lag phase ranges from 3 to 16 h depending on the degree of starvation and concomitant reduction in physiological status. Population densities (bar graph data) are highest in the zone of elongation 3 cm behind the root tip, and decline on the older root parts as the bacterium is displaced by other indigenous bacteria that are presumably better adapted to low carbon availability. Pulse-labeling by providing the plants with $^{14}CO_2$ allows us to quantify the relative amounts of carbon in different roots zones using a modified filter-paper technique.

Altogether, these studies show the heterogeneity of the plant rhizosphere in terms of physiological status and microbial distribution. Our data also reveal that there may be tremendous differences in the physiological status of microorganisms in the rhizosphere than under laboratory conditions in rich media where xenobiotic degraders are frequently characterized. Although further study is necessary to extend these observations, the rapid decline to a status reflecting extreme starvation shows that the rhizosphere is a crowded, highly competitive, oligotrophic environment.

Conclusions

The successful application of plant-microbial systems to bioremediation problems requires an understanding of rhizosphere ecology to predict the ways in which plants influence microbial biodegradation of specific xenobiotics. There are numerous scenarios by which plants might affect the biodegradation process (Fig. 3). As reviewed by Alexander (1994), there are several aspects of biodegradation which can be considered independently; including acclimation, microbial population sizes and growth kinetics, bioavailability, and environmental factors, all of which contribute to the rate of degradation. In some instances, plants might directly influence biodegradation by promoting growth-linked degradation or by enhancing cometabolism via rhizodeposition of cosubstrates that induce the enzymes for catabolism of soil contaminants. Plants may also have an indirect influence on biodegradation processes; for example, by creating microenvironments that are conducive to increased genetic exchange of degradative plasmids. Finally, plants may physically alter the soil environment for xenobiotic degradation by altering pH and redox conditions in the rhizosphere, or by influencing the spatial arrangement of microbial communities that develop in the vicinity of plant roots. To optimize the processes that control the rates of degradation, it is important to understand the specific ways in which plants might influence microbial ecology.

Although there is increasing evidence that plants may sometimes enhance the biodegradation of xenobiotics (Schnoor et al., 1995), it should be kept in mind that there are also circumstances where plants may have no effect on biodegradation, or even inhibit biodegradation. For example, when a compound can be used as a growth substrate, there are probably very few instances where plants will benefit the degradation rate if the indigenous microflora has already acclimated to the substrate. This was observed in our studies with chlorobenzoates and atrazine. Even in experiments with 2,5-DCB, the primary factor causing disappearance of this recalcitrant compound was bioaugmentation with a degrader organism, not the effects of plants on the activity of this degrader.

While shorter acclimation periods may be important for rapid degradation of contaminants that are briefly exposed to soil microorganisms before transport into groundwater, acclimation is probably not beneficial for phytoremediation of waste sites in which the indigenous microflora have experienced long term exposure to the contaminant. However, if the degrader microorganisms are dependent on specific plant exudate components or other rhizodeposition products for cometabolism, the rhizosphere may exert a real effect on the disappearance of the contaminant. In some cases, there may also be a priming effect in which the rhizosphere fortuitously enhances the growth of a degrader organism to a population size that subsequently becomes effective for metabolizing a contaminant otherwise present at a level too low to support growth of the degrader.

The overall findings of this research indicate that phytoremediation of organic xenobiotics has promise as a technique for cleanup of various classes of chemical compounds, but that there are many circumstances where plants may have no real beneficial effect. When a compound is being considered for cleanup using phytoremediation, it is important to consider its bioavailability and the potential pathway by which it will be broken down, and the best ways in which the plant-microbial system can be manipulated to achieve this purpose. This will likely vary for every class of chemical compounds that are targeted for remediation.

References

Alexander, M. 1994. Biodegradation and Bioremediation., Academic Press. San Diego, CA.

Alvey, S. and D.E. Crowley. 1995. Influence of organic amendments on biodegradation of atrazine as a nitrogen source. J. Environ. Qual. 24:1156-1162.

Alvey, S. and D.E. Crowley. 1996. Survival and activity of an atrazine-mineralizing bacterial consortium in rhizosphere soil. Environmental Sci. Technol. 30:1596-1603.

Amy, P.S., C. Pauling, and R. Y. Morita. 1983. Recovery from starvation by a marine *Vibrio* sp. Appl. Environ. Microbiol. 45:1685-1690.

Bowen, G. D., A.D. Rovira. 1976. Microbial colonization of plant roots. Ann. Rev. Phytopath. 14:121-144.

Cook, A. M. 1987. Biodegradation of s-triazine xenobiotics. FEMS Microbiol. Rev. 46:93

Crowley, D. E., M. V, Brennerova, C. I. Irwin, V. Brenner, and D. D. Focht. 1996. Rhizosphere effects on biodegradation of 2,5-dichlorobenzoate by a bioluminescent strain of root-colonizing Pseudomonas fluorescens. FEMS Microbiol. Ecol. 20:79-89.

Curl E. A. and B. Truelove. 1986. The Rhizosphere. Springer-Verlag, NY.

Gilbert, E. S. and D. E. Crowley. 1997. Natural plant compounds that induce PCB degradation by *Arthrobacter* B1B. Appl. Environ. Microbiol. In press.

Haby, P. and D. E. Crowley. 1996. Biodegradation of 3-chlorobenzoate as affected by rhizodeposition and selected carbon substrates. J. Environ. Qual. 25:304-310..

Hardman, D. J . 1991 Biotransformation of haogenated compounds. Crit. Rev. Biotechnol. 11:1-40.

Laguerre, G., F. Allard, and P. Lemanceau. 1996. The composition of fluorescent pseudomonad populations associated with roots is influenced by plant and soil type. Appl. Environ. Microbiol. 62:2449-2456.

Mandelbaum, R. T., L. P. Wackett, and D. L. Allan. 1995. Isolation and characterization of a *Pseudomonas* sp. that mineralizes the s-triazine herbicide atrazine. Appl. Environ. Microbiol. 61:1451-1457.

Marschner, P. and D. E. Crowley. 1996. Physiological activity of a bioluminescent *Pseudomonas fluorescens* (strain 2-79) in the rhizosphere of mycorrhizal and nonmycorrhizal pepper (*Capsicum annum)*. Soil Biol. Biochem. 28:869-876.

Meikle, A., K. Kilham, J. I. Prosser, and L. A. Glover. 1992. Luminometric measurement of population activity of genetically modified *Pseudomonas fluorescens* in the soil. FEMS Microbiol. Lett. 99:217-220.

Morita, R. Y. 1993. Bioavailability of energy and the starvation state. In: S. Kjelleberg (Ed.) Starvation in Bacteria. Plenum Press, New York.

Pahm, M. A. and M. Alexander. 1993. Selecting inocula for the biodegradation of organic compounds at low concentrations. Microbial Ecol. 3:275.

Schnoor, J. L., L. A. Licht, S. C. McCutcheon, N. L. Wolfe, and L. H. Carreira. 1995. Phytoremediation of organic and nutrient contaminants. Env. Sci. and Technol. 29:318-323.

van Elsas, J. D. and L. S. van Overbeek. 1993. Bacterial responses to soil stimuli. In: S. Kjelleberg (Ed.) Starvation in Bacteria. Plenum Press, New York.

Vancura, V. 1980. Fluorscent pseudomonads in the rhizosphere of plants and their relation to root exudates. Folia Microbiol. 25: 168-173

Yanze-Kontchou, C., and N. Gschwind. 1994. Mineralization of the herbicide atrazine as a carbon source by a *Pseudomonas* strain. Appl. Environ. Microbiol. 60:4297-4303.

Table I. Influence of plants on degradation rates of selected xenobiotics and final population numbers of culturable degrader organisms.

Chemical	% Disappearance		Degrader Cell Numbers**		Plant
	No plants	Plants	No Plants	Plants	
3-CB*	100	100	5×10^4	1×10^7	ryegrass (12)
2,5-DCB	63	100	5×10^2	8×10^4	bean (18)
chlordane	0	0	0	0	Bermuda grass
4,4'-DCDB	<1	<1	9×10^6	1.8×10^7	ryegrass
atrazine	84	71	270	8100	corn (32)

*Abbreviations: 3-CB 3-chlorobenzoate; 2,5-DCB 2,5-dichlorobenzoate; 4,4'-DCDB 4, 4'-dichlorobiphenyl (PCB). **Microcosms were bioaugmented with *P. fluorescens* 2-79RLD for experiments lasting 14 to 21 d with 2,5-DCB, and with *Arthrobacter* sp B1B in 50 d studies with 4, 4'-DCDB. Atrazine disappearance was measured as mineralization ($^{14}CO_2$). Atrazine degrader cell numbers are based on most probable number assays of an atrazine-degrading bacterial consortium after 4 wk. 3-CB degradation was studied for indigenous microorganisms after 6 months in soil continuously exposed or nonexposed to the xenobiotic; chlordane biodegradation experiments were conducted with soil containing an indigenous microflora that had been exposed to ca 100 ppm chlordane for several years.

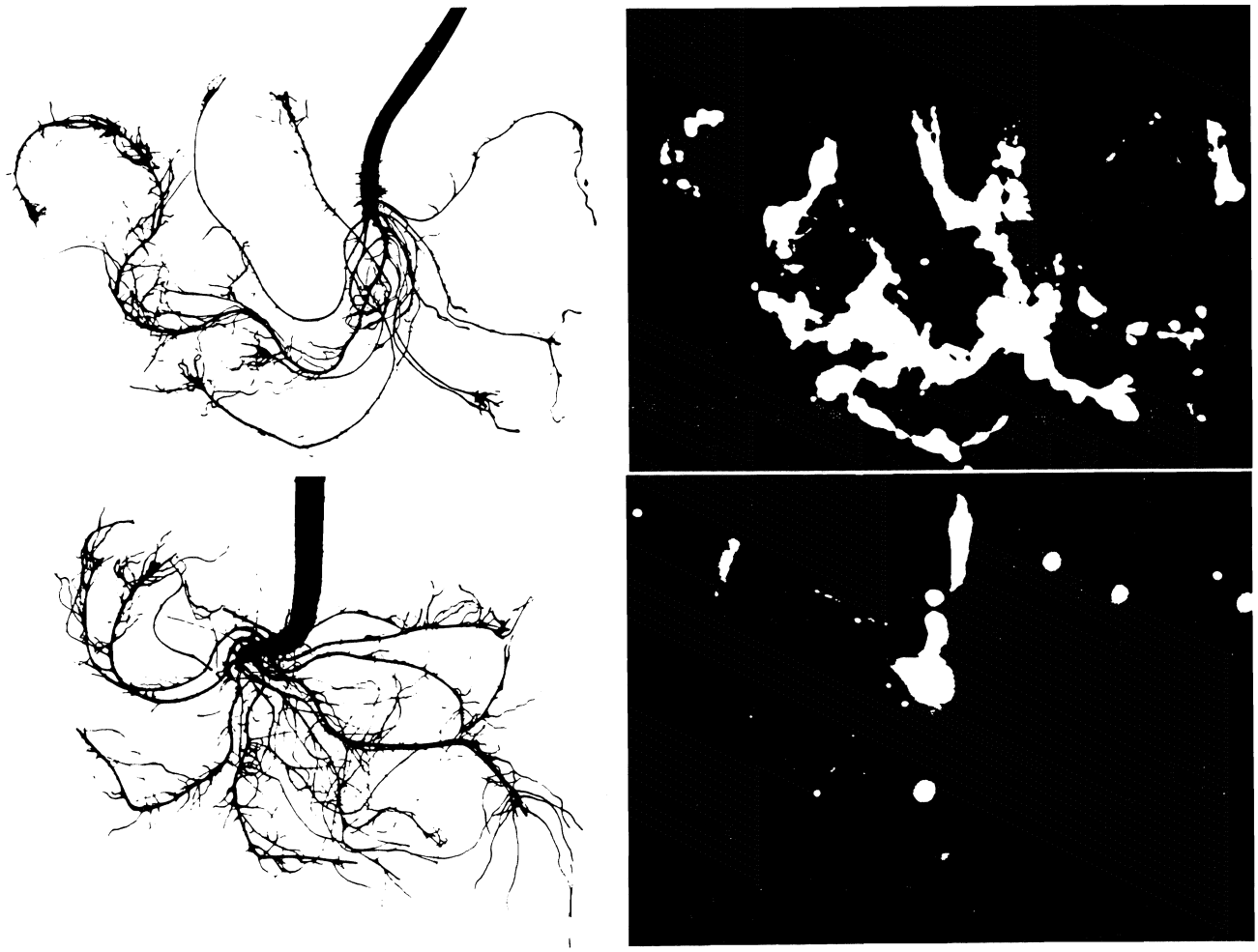

Figure 1. Autophotograph of bean roots colonized by *Pseudomonas fluorescens* 2-79RLD containing a bioluminescence marker. Plants were cultured for 3 days and 10 days in soil microcosms containing 10 mg kg^{-1} 2,5-dichlorobenzoate and inoculated with 10^6 cfu g soil. Film exposure times were 3 and 36 h for autophotographs A and B respectively.

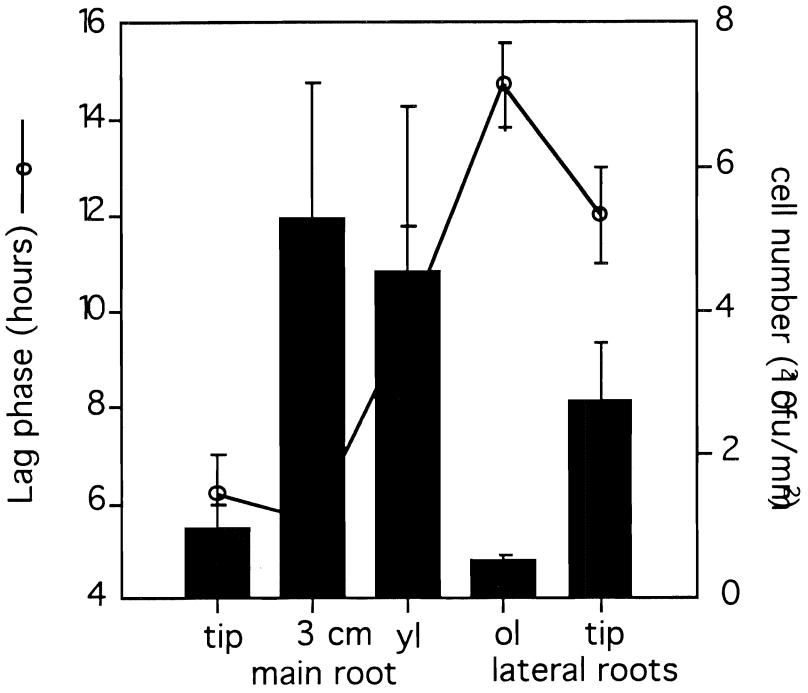

Figure 2. Length of lag phase (line graph) and population density (bar graph) of *Pseudomonas fluorescens* 2-79RL in different root zones (tip: seminal root apex; 3 cm from apex; yl: young lateral roots including sites of lateral root emergence; ol: older suberized lateral roots; tip lateral: non elongating secondary root tip).

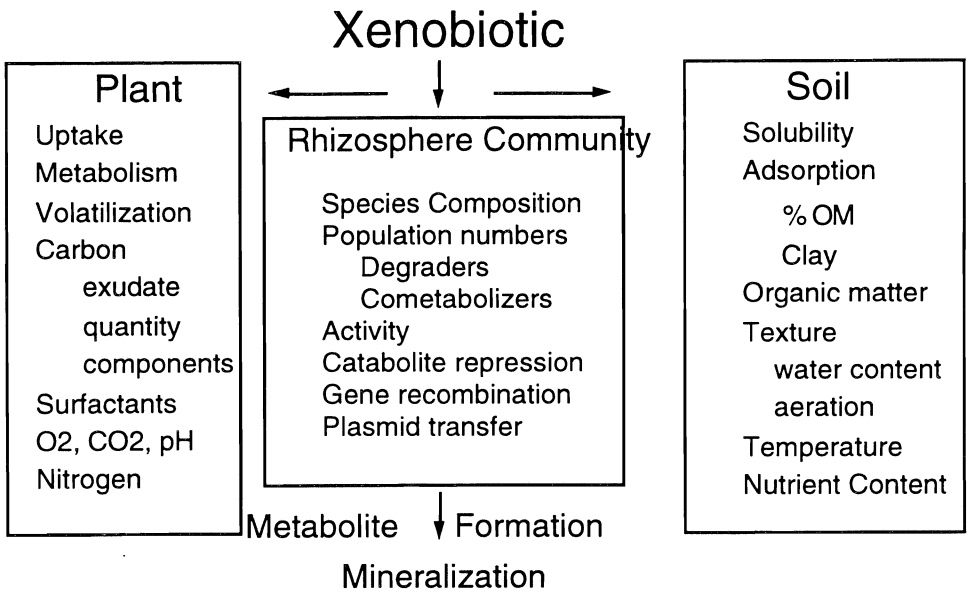

Figure 3. Conceptual model of plant and soil influences on bioavailability and biodegradation of xenobiotic soil contaminants by microbial communities in the plant rhizosphere.

The Effects of a Chlorinated, Volatile Hydrocarbon (1,1,1-TCA) on the Diversity and Function of the Microbial Community in Surface and Subsurface Soil

M. K. FIRESTONE AND K. A. DUNKIN
Department of Environmental Science, Policy and Management, Berkeley Campus

Summary

Microbial community structure and activity were examined in surface soil and subsurface material from a hazardous waste site at Los Alamos National Laboratory, New Mexico. The numbers and activities of bacteria were generally low, however measurable activities were detected and viable bacterial cells were present The distribution of the microbial community was spatially heterogeneous with a few localized pockets of activity.

To assess the impact of a model volatile chlorinated hydrocarbon on a soil microbial community, a method for application of reverse sample genome probing (RSGP) was developed. Isolates from surface soil were the source of bacterial genomic standards used on master filters. The probe, whole community DNA obtained form the soil microbial community, was labeled and hybridized against the standards in order to assess changes in the genomic composition of the community. In a preliminary application, surface soil was exposed to two concentrations of the chlorinated hydrocarbon, 1,1,1-TCA and the effect of this exposure was evident through RSGP analysis.

Key Words: chlorinated hydrocarbons, 1,1,1-trichloroethane, subsurface microbial ecology, reverse sample genome probing

Project Objectives Addressed in 1995-1996

To measure the changes in microbial community diversity and function in surface and subsurface soils exposed to a model chlorinated-hydrocarbon, 1,1,1-trichloroethane (TCA).

Research Plan and Procedures

To examine the activity of the microbial community in samples taken from the subsurface of the contaminated Materials Waste Disposal Area L at Los Alamos National Laboratory, New Mexico, bacterial numbers were determined using plate counts and direct counts. Activities of the microbial community were determined as nitrification potentials, denitrification potentials, respiration, dehydrogenase activity, utilization of ^{14}C-acetate and ^{14}C-glutamate. The potential for the microbial community to degrade 1,1,1-trichloroethane (1,1,1-TCA), a major contaminant at the site, was evaluated.

To assess the impact of chlorinated hydrocarbon contaminants on microbial community composition in soil a new technique for the application of reverse sample genome probing (RSGP) was developed. Reverse sample genome probing surveys the composition of the microbial community by using the whole community DNA as a probe. Gram negative, aerobic soil bacteria were isolated from the surface soil at the disposal site. Seventy five individual bacterial genomes were selected and spotted onto replicated master filters. These "standards" were used as indicators of the bacterial community of interest. A procedure to label the community DNA with a non-radioactive label using random primed extension was developed for use on DNA extracted from soil. Whole community DNA was obtained from microbial community of the surface soil overlying the waste disposal area; the community DNA was then labeled and hybridized against the standards on the master filter. Standard genomes present in sufficient quantity in the community DNA were identified. Finally a soil community was exposed to the volatile chlorinated hydrocarbon 1,1,1-trichloroethane (1,1,1-TCA) and changes in the microbial community were evaluated using RSGP.

Site Description and Sampling

The study site was located at the Los Alamos National Laboratory on the Pajarito Plateau, New Mexico. The vegetation at the site was pinion-juniper woodland. The site was the historical location for disposal of non-radioactive chemical waste into the subsurface through shafts and pits. Two vertical boreholes were drilled in Material Disposal Area L in November of 1993 and April 1995. Procedures for subsurface sampling and sample handling are described in Dunkin (1996).

Surface soil was collected from an area located 0.5 km north east of Materials Disposal Area L,. The first sampling was made in May 1994 and the second in Sept 1994. Bacterial isolates were obtained from both samples.

Counts and Isolations

Numbers of viable cells were determined on agar plates as colony forming units (CFU's) using 5 different media/isolation procedures are described in Dunkin (1996). Direct counts were performed using serial dilutions from the plating procedure; standard acridine orange fixation and counting procedures were used for microscopic bacterial enumeration (Dunkin, 1996).

To assemble a collection of isolated and purified bacteria for RSGP analysis, individual colonies were randomly chosen from dilution plates with between 30 and 100 CFU and standard isolation procedures applied.. Purified isolates were stored in glycerol in 96-well plates at -50°C. The 103 isolates were scored for 24 physiological attributes (Dunkin, 1996).

Activity Assays

Subsamples of subsurface material were assayed for 1,1,1-TCA degradation potential using gas chromatography with a flame ionization detector (Dunkin, 1996). To assess microbial activity in subsurface soils: nitrification potential was determined as rates of ammonium oxidation (Schimel, Firestone, and Killham, 1984); denitrification of added nitrate in the presence of excess carbon, acetylene and reduced oxygen tension was assayed by gas chromatography; community dehydrogenase activity was measured using the reduction of iodonitotetrazolium violet (INT) to INT-formazan (Trevors, Mayfield, and Innis 1982); community respiration was measured with an automated respirometer attached to a gas chromatograph (Brooks and Paul 1987); and utilization of ^{14}C-substrates was done using [2-^{14}C]-Acetic Acid and L-{U-^{14}C-glutamic acid}.

RSGP method

Extraction of community DNA from soil was accomplished using a procedure modified from the direct extraction procedure of Xia, et.al. (1995). The soil DNA extraction method developed was unusual in that it did not rely on physical disruption to lyse cells and it required only 4 g soil as compared to about 100 times that for most other methods. CTAB (cetyl trimethylammonium bromide) was used to separate DNA from polysaccharides resulting in cleaner DNA than many other procedures. The DNA extracted was sufficiently pure so that other commonly used cleanup procedures were not needed (Dunkin, 1996).

Extracted community DNA was labeled using a procedure derived from the commercially available Genius system for non-radioactive probe development (Boehringer-Mannheim, IN). This procedure involved the synthesis new DNA from community DNA; the new DNA incorporates digoxigenin coupled dUTP to allow visualization of the probe. Modifications optimized the procedure for soil community DNA with a very broad G+C content.

Extraction of genomic DNA from the pure cultures was accomplished by relatively standard procedures. The oligotrophic soil bacteria used here were generally slower growing and more difficult to lyse than those commonly used in molecular studies (Dunkin, 1996). Culture DNA standards were immobilized onto positively charged nylon membranes after heat denaturation resulting in 300 to 600 ng DNA in each spot. Soil community DNA was used as a positive control for hybridization and *Candida maritima* NRRL Y-7899 isolated from sea water was used as the negative control.

Labeled soil community DNA was hybridized onto the standard DNA immobilized on the membranes using standard procedures. Again the procedures required optimization for the broad G+C content of the soil DNA (Dunkin, 1996). The chemiluminescent substrate (1,2-dioxetane) was activated by alkaline phosphatase and detected by exposure to x-ray film.

Test soil was exposed to concentrations of TCA (50 mg l^{-1} and 33 mg l^{-1}). Batch reactors were incubated statically for 800 hr at 27 C and soil community DNA was extracted.

Soil Physical Characteristics and Statistics

Physical characteristics of the surface soil and subsurface material were determined using standard methods reported in Dunkin (1996). Linear regression analysis to determine rate constants was performed using Statview statistical software (Abacus Concepts, Berkeley, CA). Rates were considered to be significantly different from zero at $p = 0.05$.

Results

Subsurface Material

The subsurface material from both cores were from the same lithological unit of Bandelier tuff about 26 m below the surface. They were composed of slightly-welded, ash flow tuff from the Tshirege member which is thought to have flowed approximately 1.1 mil yr ago from the Valles Caldera (IT Corporation 1987). The subsurface material was unconsolidated and was light gray to light pink in color. Material from both boreholes was dry with water potentials of about -1 J kg-1 for one core and less than -5 J kg -1 in samples from the second core. Water contents reflected the low water activities (Table 1). The pH values of the two boreholes differed by more than 1 pH unit; pH 7.6 for samples from 54-1009 and pH 9.0 for samples from 54-1018. This difference might have been due to the location of 54-1009 which was directly adjacent to one of the hazardous waste disposal pits. This pit was used for many years as a disposal site for a wide variety of materials, mostly unrecorded, some of which may have been very acidic (V. Trujillo, personal communication). The low bulk density (1.23 g cm^{-3}) is due to the large number of vesicles common in tuffaceous materials. Total C and N values were extremely low, with C at or below 0.06% and N below detection.

Contaminant Concentrations

Thermal desorption gas chromatography-mass spectroscopy (TDGCMS) was used to analyze adsorption gas samples taken at a sampling well near 54-1009 which was contaminated with an organic vapor plume consisting primarily of 1,1,1-trichloroethane (1,1,1-TCA), trichloroethylene (TCE), and tetrachloroethene (PCE) among other contaminants (J. Sollid, personal communication, Table 2). The chloroflorocarbons, CFC 11 and CFC 113 were also present in this area (Table 2).

The gas phase of cores from borehole 54-1009 were also analyzed at Berkeley using a gas chromatograph with a flame ionization detector, showing several peaks. One peak corresponded to the retention time for a standard injection of 1,1,1-TCA but without the additional information provided by mass spectroscopy, the chromatograms alone cannot identify unknown components. However, the chromatograms do confirm the presence of volatile hydrocarbons in these samples at the time of analysis. Borehole 54-1018 was subsequently used as a monitoring well in a pilot gas extraction project and actual gas concentrations from the well were made available (Table 2). Vapor phase contamination at borehole 54-1018 was measured using down well photoacoustic radiometry (PAR) for the major contaminants: 1,1,1-TCA, TCE, CFC 113 and CFC 11 (J. Sollid, personal communication, Table 2). The data demonstrate the presence of contaminants in borehole 54-1018 at a magnitude similar to the concentrations in the borehole 54-1009 area.

Numbers of Active and Total Cells

The material from borehole 54-1009 contained very low numbers of colony forming units (CFU's); counts were always below 20 CFU's per plate for the lowest dilutions (Table 3). Three months after the initial plating, 60% of the plates had no detectable growth, indicating that the microorganisms were not simply growing slowly.

CFU values for samples from 54-1018, were highly variable (Table 3). The numbers of CFU's from the S2 sample ranged from below detection for heat tolerant bacteria to 7 X 103 CFU's g^{-1} when plated on King's B medium. The colonies from S2 were dominated by smooth and opaque - yellow, orange, red and pink colored colonies; while colonies on King's B media were uniformly greenish but not fluorescent under UV illumination.

These results are indicative of a highly variable spacial distribution of viable microbes in the subsurface. High spacial variability of viable cells has been noted by others in studies of the subsurface (Haldeman et al. 1993; Russell et al. 1994) and the spacial distribution seems to be independent of the variability in subsurface physical characteristics (Colwell 1989; Haldeman and Amy 1993; Kieft et al. 1993; Kieft et al. 1995). The standard method of plate counting has traditionally relied on homogenization in order to reduce variability but recent work by Stevens and Holbert (1995) has demonstrated that homogenization of subsurface material resulting in reductions of cell density

may inhibit outgrowth of cells possibly due to cell growth density-dependence phenomena.. In samples from the subsurface, low numbers of cells and the apparent patchy distribution could reduce the efficacy of standard dilution procedures. Further studies on both subsurface cell distribution and the nature of density dependence are needed to determine if the standard methods used in plate counts are inappropriate for subsurface or other low cell-density environments.

Acridine orange direct-count estimates of total cell numbers in samples from 54-1009 were below the detection limit of 10,000 cells g^{-1} (Table 3). Total cell numbers in 54-1018 were variable by sample sleeve (Table 3). These results further support the spatially variable nature of cell distribution in this subsurface environment.

Only about 0.1% of the total cells counted were culturable under the conditions used. This percentage is low, especially when compared to the 10% culturable common in surface soil. Many of the cells visible in direct counts could have been dead. Any sort of density-dependence response may also reduce the numbers of CFU's thus influencing the proportion of cultural cells. The selectivity of media was also important in determining the numbers of viable cells. Since the subsurface environment was oligotrophic, media relatively low in carbon were used. The majority of CFU's were recovered on the most oligotrophic media. One tenth TSA has been used in determining surface soil CFU's and 1% PTYG media has been preferred in the Department of Energy's deep subsurface microbiology program. However the numbers of CFU's on these two media were essentially the same.

Heat-resistant bacterial-forms did not seem to be a component of the bacterial communities as no CFU's were found on any of the heat treated plates. This is in contrast to surface soil communities where a large proportion of the microbial community is able to form heat resistant spores. Working with deep subsurface volcanic tuff, Haldeman et al, (1993) were also unable to recover spore forming microorganisms by heat treatment.

Biodegradation Potential of 1,1,1-TCA

Degradation potential of 1,1,1-TCA was tested in batch reactors of subsurface material. Concentrations of added 1,1,1-TCA remained within 2% of the sterile controls in all samples tested. Degradation of 1,1,1-TCA has been measured in a contaminated subsurface aquifer material under both methanogenic and sulfate reducing conditions (Klecka, Gonsior, and Markham 1990). In contrast, 1,1,1-TCA contaminated vadose zone material (depth not given) tested in batch reactors with prior enrichment of methanotrophic bacteria showed no degradation of 1,1,1-TCA (Broholm, Christensen, and Jensen 1991). In a series of studies, Bouwer and McCarty found that 1,1,1-TCA was degraded by a mixed, methanogenic culture seeded from sewage sludge with acetate as the primary carbon substrate, but no degradation occurred in mixed-denitrifying or aerobic cultures also seeded from sewage sludge (Bouwer and McCarty 1983a; Bouwer and McCarty 1983b).

Activity Assays

Estimates of rates for nitrification and respiration in samples from one borehole were not significantly different from zero (Table 3). Samples from the second borehole had measurable rates of nitrification, respiration and denitrification activity. (Table 3). Dehydrogenase activities ranged from below detection to about 2 times the detection limit for samples from 54-1018. Dehydrogenase assays were repeated 3 times and the pattern and magnitudes were the same each time.

These whole community assays should reflect characteristics of the community in situ. Measurements of respiration rates are used as an index of microbial community size in surface soil assays. Nitrification activity is used as an index of the size of the nitrifying population and is particularly useful to evaluate here since nitrifying organisms have been shown to degrade halogenated hydrocarbons (Vannelli et al. 1990). The low levels of activity in specific samples mirror the low numbers of cells and the low numbers of CFU's.

The presence of measurable denitrification rates in some of the samples indicates that denitrification conditions periodically exist in the subsurface. Oxygen consumption in microsites at 25 m depth may at times exceed rates of recharge from the surface.

In order to test for very low levels of activity, ^{14}C labeled substrates were used.. ^{14}C-CO2 evolved from acetic acid or glutamic acid was measured. after 1 month of incubation. While generally extremely low, the percentage of labeled substrate mineralized reached 2% of the glutamate for the most active sample, 54-1018.

Surface Soil

The surface soil was an alfisol sandy-loam of the Hackroy series (clayey, mixed mesic lithic, aridic Haplustaff). Nitrification potentials averaged 0.053 $\mu g\ g^{-1}\ hr^{-1}$; respiration rates were 1.92 $\mu g\ CO_2\text{-}C\ g^{-1}\ hr^{-1}$; and dehydrogenase activity was 2.97 $\mu g\ g^{-1}\ hr^{-1}$. All of these values are in the low range for surface soils probably reflecting the arid climate and low amount of plant cover at the site. Plate count determinations of aerobic heterotrophs ranged from 4×10^7 (1% PTYG) to 4×10^6 (King's B).

Extraction of community DNA from Exposed Soil

Yield of DNA averaged 7.2 (1.4 S.E.) µg DNA g-1 soil for 4 samples from 4 different batch reactors. The DNA was largely unsheared with the majority of fragments moving more slowly than 12.3 Kb fragments in a 1% agarose gel. The DNA was successfully restricted with *Eco* R1 restriction enzyme indicating the absence of enzyme-inhibiting contamination. Probe yield from extracted

community DNA ranged from 10 to 100 ng per reaction. X-ray images of the hybridized filters were analyzed with laser densitometry.

To detect the bound probe, a chemiluminescent substrate was activated by alkaline phosphatase (conjugated to a digoxigenin-specific antibody) to produce light which was detected by exposure to x-ray film. Sensitivity of detection was determined by quantification of standard masses on a laser densitometer and was about 0.1 pg of target DNA (Dunkin, 1996).

Images of film exposed to RSGP membranes from two levels of TCA-exposed test soil may be digitized and evaluated. The positive control hydridized strongly in both cases, confirming the probe was homologous to the template DNA and that hybridizing conditions were met. The negative control provides an estimate of the background hybridization which occurred under the experimental conditions. In the soil exposed to the lower concentration of TCA, 7 of the 78 standard genomes had absorbance greater than the negative control. In contrast, only one of the standards hybridized exceeded the negative control in the soil sample exposed to the higher TCA concentration. Loss of community diversity (as determined using characteristics of isolated organisms) is known to be an effect of exposure to pollution (Atlas and Bartha 1987) . It is interesting that an apparent shift in the bacterial community can be see using only 78 standard genomes on the membrane; this is a very small percentage of the total number of bacterial community members.

While the results reported here are encouraging, it should be clearly understood that a substantial amount of additional work is necessary before we know whether the method will be an effective means of observing changes in microbial community composition in soil. First and foremost, the replicability of the results must be documented. If the method proves to be reproducible, then we may have a relatively simple and direct method to characterize microbial community composition in soil.

Discussion

Many microbial ecologists and bioremediation specialists desire to gain a better understanding of the composition and function of the microbial community in soil. Hazardous materials in surface and subsurface soils can commonly be altered to more benign components if the microbial community contains the appropriate metabolic capabilities and if the soil environment and contaminant characteristics can be managed to promote microbial activity. Bioremediation may be accomplished through the introduction of organisms into the system or through the manipulation of indigenous microorganisms. For either approach, a thorough understanding of the ecology of the microbial community is essential to the effective and predictable implementation of bioremediation.

To understand the ecology of the soil microbial community both the community composition and function should be considered. The components of the community define the metabolic potential and to some extent, community stability upon disturbance. Community function includes the cycling and transformations of N, P, and S, degradation of xenobiotic and biotic compounds,

and flux of biogenic gases. Understanding function is important to predicting the system-wide effects of disturbances and to evaluating the ability of a community to degrade the contaminants.

The microbial communities of a subsurface hazardous waste site contaminated with chlorinated solvents and CFC's were examined . Microbial numbers and activities were generally low, however a few measurable activities were detected and viable bacterial cells were present. The distribution of the microbial community was spatially heterogeneously with a few localized, slightly-active pockets of organisms in this deep, dry location. Understanding the origin of and characterizing the active pockets of microbes in the subsurface is basic information for potentially manipulating or managing microbial communities to promote biodegradation in the vadose zone.

The status of our understanding of the composition of the microbial community is changing rapidly due to the incorporation of molecular methods. RSGP is a relatively simple, one-step procedure for surveying the composition of the microbial community. The use of known genomes as standards could allow us to follow desirable or competent strains in response to management protocols. While the results reported here are encouraging, it should be clearly understood that a substantial amount of additional work is necessary before we know whether the method will be an effective means of observing changes in microbial community composition in soil.

References

Atlas, R.M. and R. Bartha. 1987. *Microbial Ecology* Second Ed. The Benjamin/Cummings Publishing Co., Inc. Menlo Park, CA.

Bouwer, E. J., and P. L. McCarty. 1983a. Transformations of 1- and 2- carbon halogenated aliphatic organic compounds under methanogenic conditions. Applied and Environmental Microbiology 45 (4):1286-1294.

Bouwer, E. J., and P. L. McCarty. 1983b. Transformations of halogenated organic compounds under denitrification conditions. Applied and Environmental Microbiology 45 (4):1295-1299.

Broholm, K., T. H. Christensen, and B. K. Jensen. 1991. Laboratory feasibility studies on biological in-situ treatment of a sandy soil contaminated with chlorinated aliphatics. Environmental Technology12:279-289.

Brooks, P. D., and E. A. Paul. 1987. A new automated technique for measuring respiration in soil samples. Plant and Soil 101:183-187.

Colwell, F. S., 1989. Microbiological comparison of surface soil and unsaturated subsurface soil from a semiarid high desert. Applied and Environmental Microbiology 55 (9):2420-2423.

Dunkin, K.A. 1996. Microbial communities: subsurface microbial community activities and abundance at two different contaminated sites and development of reverse sample genome probing. Ph.D. Dissertation. 127 pp.

Haldeman, D., and P. S. Amy. 1993. Bacterial heterogeneity in deep subsurface tunnels at Rainier Mesa, Nevada Test site. Microbial Ecology 25:183-194.

Haldeman, D. L., P. S. Amy, D. Ringelberg, and D. C. White. 1993. Characterization of the microbiology within a 21 m3 section of rock from the deep subsurface. Microbial Ecology 26:145-159.

I T Corporation. 1987. Geological assessment of technical area 54 -area G and L, Los Alamos National Laboratory. Project # 301017.02.

Kieft, T. L., P. S. Amy, F. J. Brockman, J. K. Fredrickson, B. N. Bjorndstad, and L. L. Rosacker. 1993. Microbial abundance and activities in relation to water potential in the vadose zones of arid and semiarid sites. Microbial Ecology 26:59-78.

Kieft, T. L., J. K. Fredrickson, J. P. McKinley, B. N. Bjornstad, S. A. Rawson, T. J. Phelps, F. J. Brockman, and S. M. Pfiffner. 1995. Microbiological comparisons within and across contiguous lacustrine, paleosol and fluvial subsurface sediments. Applied and Environmental Microbiology 61 (2):749-757.

Klecka, G. M., S. J. Gonsior, and D. A. Markham. 1990. Biological transformations of 1,1,1-Trichloroethane in subsurface soils and groundwater. Environmental toxicology and chemistry 9:1437-1451.

Russell, C. E., R. Jacobson, D. L. Haldeman, and P. S. Amy. 1994. Heterogeneity of deep subsurface microorganisms and correlations to hydrogeological and geochemical parameters. Geomicrobiology Journal 12:37-51.

Schimel, J. P., M. K. Firestone, and K. S. Killham. 1984. Identification of heterotrophic nitrification in a Sierran forest soil. Applied and Environmental Microbiology 48 (4):802-806.

Stevens, T. O., and B. S. Holbert. 1995. Variability and density dependence of bacteria in terrestrial subsurface samples: implications for enumeration. Journal of microbiological methods 21:283-292.

Trevors, J. T., C. I. Mayfield, and W. E. Innis. 1982. Measurement of electron transport system (ETS) activity in soil. Microbial Ecology 8:163-168.

Vannelli, T., M. Logan, D. Arciero, and A. B. Hooper. 1990. Degradation of halogenated aliphatic compounds by the ammonia-oxidizing bacterium Nitrosomonas europaea. Applied and Environmental Microbiology 56 (4):1169-1171.

Xia, X., J. Bollinger, and A. Ogram. 1995. Molecular genetic analysis of the response of three soil microbial communities to the application of 2,4-D. Molecular Ecology. 4:17-28.

Table 1. Physical characteristics of Los Alamos National Laboratory subsurface material.

Borehole	pH	Water Content	Water Potential	Bulk Density
		kg kg^{-1}	J kg^{-1}	g cm^{-3}
54-1009				
25.9m	7.6	0.025	-1.30	1.23
26.2m	7.7	0.034	-0.98	1.23
26.5m	7.6	0.035	-0.92	1.23
54-1018				
S1	9.0	0.010	<-5	n.d.†
S2	9.0	0.013	<-5	n.d.

† n.d.; Not determined.

Table 2. Subsurface Gas Contaminant Concentrations. Data from J. Sollid, Los Alamos National Laboratory.

		Borehole 54-1010†				Borehole 54-1018‡		
Compound	Abbreviation	6.1m	9.1m	12.2m	15.2m	21.3m	37.2m	42.7m
								mg m^{-3}
1,1,1,- Trichloroethane	1,1,1,- TCA	730	1500	430	1700	316	264	376
Trichloroethene	TCE	390	880	210	550	63	54	74
Trichlorotrifluoroethane	CFC 113	43	72	74	250	91	62	111
Dichloromethane		14	82	7.5	200	n.d.¶	n.d.	n.d.
1,1- Dichloroethene	DCE	34	36	22	180	n.d.	n.d.	n.d.
1,2- Dichloroethane		18	57	2.1	74	n.d.	n.d.	n.d.
1,2- Dichloropropane		25	42	1.2	73	n.d.	n.d.	n.d.
Tetrachloroethene	PCE	84	59	37	54	n.d.	n.d.	n.d.
Chloroform		19	34	2.1	41	n.d.	n.d.	n.d.
Trichloroflouromethane	CFC 11	26	18	23	34	4.8	4.8	6.5
1,1 - Dichloroethane		23	38	2.8	32	n.d.	n.d.	n.d.
Carbon Tetrachloride		2.4	11	1.6	17	n.d.	n.d.	n.d.
Benzene		b.d.§	3	b.d.	15	n.d.	n.d.	n.d.
Dichlorodifluoromethane		2.9	3.3	3.7	10	n.d.	n.d.	n.d.
Toluene		6.8	4	3.7	2.6	n.d.	n.d.	n.d.
Acetone		3.5	b.d.	b.d.	b.d.	n.d.	n.d.	n.d.

† Adsorption gas samples analyzed by Thermal Desorption Gas Chromatography - Mass Spectroscopy.
‡ Analysis by down-well Photo Acoustic Radiometry (J. Sollid, personal communication)
§ b.d.; Below detection.
¶ n.d.; Not determined.

Table 3. Average colony forming units, direct counts, and activity assays for Los Alamos National Laboratory subsurface materials, n = 3. See methods section for descriptions of media and assay procedures.

Borehole	Acridine orange direct counts	1/10 TSA heat shock	King's B Medium	Den potential	Nitrification potential	Respiration
	Cells g^{-1}	----------CFU g^{-1}----------		ng N_2O $g^{-1}hr^{-1}$	µg NO_2^- $g^{-1}hr^{-1}$	µg CO_2-C $g^{-1}hr^{-1}$
54-1009†	b.d.§	<200	n.d.‡	n.d.	b.d.	b.d.
54-1018						
S1	b.d.	<200	200	n.d.	b.d	0.015 (0.004)
S2	4.5 x 10^7	<200	7 x 10^3	13.3 (2.9)	1.9 (0.6)	0.031 (0.005)

†Values represent independent analysis of three depths; 25.9m, 26.2m, and 26.5m.
‡n.d.; Not determined
§b.d.; Below detection

Cometabolism of 1,1-dichloro-2,2-bis(4-chlorophenyl)ethylene (DDE) by *Pseudomonas acidovorans* M3GY Grown on Biphenyl

ANTHONY G. HAY AND DENNIS D. FOCHT
Department of Soil and Environmental Sciences, Riverside Campus

Summary

The pesticide DDT (1,1,1-trichloro-2,2-bis(4-chlorophenyl)ethane) and its breakdown products have been found in at least 310 hazardous waste sites on the EPA's National Priority List (Clement, 1994). The most toxic of these breakdown products, DDE, (1,1-dichloro-2,2-bis(4-chlorophenyl)ethylene) has recently been linked to reports of reproductive system abnormalities in wildlife and humans. DDE has traditionally been viewed as a dead-end metabolite: there are no published reports detailing bacterial metabolism of DDE in either soil or pure culture. In this study, we investigated the ability of *Pseudomonas acidovorans* M3GY to transform DDE and its unchlorinated analog, 1,1-diphenylethylene (DPE). Biphenyl grown cells degraded both DDE and DPE through the standard *meta*-fission pathway. The key intermediate 2-(4-chlorophenyl)-3,3-dichloropropenoic acid was dehalogenated and oxidized through several intermediates to 4-chlorobenzoate, which was subsequently degraded through a *meta*-fission pathway. While strain M3GY could grow on DPE, DPE grown cells could not degrade DDE. This study provides a possible model for biodegradation of DDE in soil by biphenyl-utilizing bacteria.

Key Words: Biodegradation, DDT, PCB, chloroaromatic, bacteria

Project Ojectives Addressed in 1995-1996

To determine if polyaromatic hydrocarbons or DDT related compounds could be enhanced by enrichment of biphenyl-degrading bacteria

Research Plan and Procedures

PAHs Results for enhancement of PAH degradation in soils were negative and are not considered in this report.

Bacterial culture *Pseudomonas acidovorans* M3GY, a recombinant strain constructed by the continuous amalgamated culture method (McCullar et al, 1994), was grown in 1 L of mineral salts medium (Focht, 1994), supplemented with 0.005% yeast extract. Diphenylethylene (DPE, 200 µl) or biphenyl (500 mg) was use as the growth substrate in the presence of 100 mg DDE, which was not utilized as a growth substrate. Cultures were incubated in the dark, on a rotary-platform shaker at 28°C and 200rpm for 20 days.

Metabolite recovery. Recovery of metabolites was achieved by centrifuging 1L of $CaCl_2 2H_2O$ saturated growing cell culture, acidified to pH 8, for 15 minutes at 25,900 g and 4°C. The supernatant was kept on ice, acidified to pH 3 with concentrated HCl, and extracted 4 times with 100 ml cold ethyl ether which had been stored at -25°C and kept on ice during the extraction. The ethyl ether extracts were pooled and then back-extracted 4 times with 40 ml of cold 0.1M NaOH in order to saponify lipids and remove polar moieties. The NaOH fractions were pooled and acidified to pH 3 with 12N HCl then re-extracted 4 times with 30 ml ethyl ether. The pooled ether extracts were then either dried over NaCl and concentrated by rotary evaporation at 4ºC under reduced pressure, or methylated with 10-15 ml of an etheral solution of diazomethane, then concentrated by roto-evaporation.

GC-MS and GC-FTIR analysis A Hewlett-Packard model 5890 gas chromatograph with an HP 5965B Fourier Transform Infrared detector and an HP 5890 G.C. with an HP 5971 Mass Selective detector was used to identify the metabolites. The injector temperature was held at 200°C. The initial oven temperature was 37°C, but was immediately ramped to 250°C at 10°C/min and held at 250°C for 20 min. Helium was the carrier gas at a flow rate of 0.25 ml/min. A 30 m DB-5 ms capillary column with an inner diameter of 0.322 µm was used. The flow cell and transfer line were held at 250°C. The ion source and quadruple were held at 100 and 250°C respectively.

Soil incubations To determine if biphenyl or cymene enhanced biodegradation of DDE in soil, 100 g of Altamont soil were spiked with ^{14}C-DDE (0.454 mCi, 11.6 mg) and treated accordingly: 1) control, 2) cymene (4.0 g), 3) biphenyl + N (18), 4) biphenyl (4.0 g) + inoculation with strain M3GY (10^8 cells/g), 5) biphenyl (4.0 g) + continuous inoculation (10^8 cells/g per week). $^{14}CO_2$ was monitored by trapping in 2 M NaOH (18), and total recovery of DDE was determined after 60

days by extraction of soil with a hexane/acetone (1:1, v:v) solution, and counted by scintillation (Beckman LB5000TD). Viable plate counts were done in triplicate at 0 and 30 days on biphenyl-mineral salts agar plates (18).

Results

Supernatants from DDE+BP cultures had a characteristic yellow color (λ_{max}399) that was absent in biotic or abiotic controls. This color persisted under basic to neutral conditions but was abolished under acidic conditions (<pH 5). This color, which is characteristic of *meta* ring-fission products, reached its maximal absorbance (O.D.=1.5) after 20 days. No yellow color was observed in the supernatant of the DDE+DPE cultures.

Unmethylated extracts from the supernatant of DDE+DPE grown cells yielded 9 metabolites that were identifiable by GC-MS and GC-FTIR analysis. Benzophenone was present in large quantities and was by far the most abundant metabolite, although it could not support growth of strain M3GY. No chlorinated metabolites were identified from the DPE grown culture. Extracts from supernatants of cells grown on DDE + BP, were analyzed as methylated derivatives, and without derivatization. Eight metabolites were identified by their mass spectra.

Addition of biphenyl or cymene raised the numbers of biphenyl degraders to 10^7/g to 10^8/g in comparison to 104/g observed in the unamended control (data not shown). Nevertheless, these substrates did not enhanced transformation of DDE (Table 1), or evolution of $^{14}CO_2$ levels above background levels (data not shown).

Discussion

Although limited mineralization of DDE has been demonstrated by fungi (Bumpus et al., 1993), this is the first published report detailing ring fission of DDE, long considered a dead-end metabolite and/or conversion product of DDT (Kaushik, 1991; Nadeau et al.,1994, World Health Organization, 1989). Based on the information contained herein we propose a pathway for the cometabolic mineralization of DDE by *P. acidovorans* M3GY grown on biphenyl (Fig. 1). Oxidation of 4-chloroacetophenone to 4-chlorobenzoate (4-CBa), would indicate eventual mineralization as the dehalogenation of the latter has been demonstrated by this strain (McCullar et al., 1994).

Our study also suggests a possible mechanism for the production of 4-CBa from DDT as observed by (Nadeau et al., 1996) Aldolase activity on the DDT ring-fission product could produce 3,3,3,4'-tetrachloroatropic acid. Decarboxylation and subsequent oxidation could yield 2,2,2,4'-tetrachloroacetophenone which could be metabolized in a similar manner to 4-chloroacetophenone, an intermediate in the DDE pathway which is degraded to 4-CBa.

Although DDE was clearly biodegradable in culture, it was recalcitrant in soil despite inoculation with strain M3GY and addition of biphenyl (Table 1). Inasmuch as the Kow for DDE is ten times higher than that for DDT and is similar to that for hexa and heptachlorobiphenyls, it is conceivable that availability, rather than enzyme specificity is a major factor in the recalcitrance of DDE in the environment. This raises the intriguing possibility that enzyme modification to broaden dioxygenase attack on chlorinated aromatic hydrocarbons may be irrelevant, and that uptake (e.g., surfactants) deserves more consideration as a limiting factor.

In conclusion, these results demonstrate that DDE can be degraded by bacteria in pure culture when the correct pathway is induced. Biphenyl was capable of affecting this induction, while the more structurally similar compound, DPE, was not. This indicates that traditional approaches to analogue enrichment and cometabolism induction may need to be re-evaluated in that the most similar analog (DPE) did not induce for the cometabolism of DDE.

References

Bumpus, J. A., R. H. Powers, and T. A. Sun. 1993. Biodegradationn of DDE (1,1-dichloro-2,2-bis(4-chlorophenyl)ethyene. Mycological Research. 97(1):95-98.

Clement, I. C. 1994. Toxicological Profile for DDT, DDE, and DDD tp-93/05. U.S. Department of Health and Human Services, Public Health Services, Agency for Toxic Substances and Disease Registry.

Focht, D. D. 1994. Microbiological procedures for biodegradation research, p. 407-426. *In* R. W. Weaver, J. S. Angle, and P. S. Bottomley (eds.), Methods of Soil Analysis, Part 2. Microbiological and Biochemical Properties. Soil Science Society of America, Madison, WI.

Kaushik, C. P. 1991. Persistence and metabolism of HCH and DDT in soil under subtropical conditions. Soil Biol. Biochem. 23(2):131-134.

McCullar, M. V., V. Brenner, R. H. Adams, and D. D. Focht. 1994. Construction of a novel polychlorinated biphenyl-degrading bacterium: utilization of 3,4'-dichlorobiphenyl by *Pseudomonas acidovorans* M3GY. Appl. Environ. Microbiol. 60:3883-3839.

Nadeau, L. J., F. M. Menn, A. Breen, and G. S. Sayler. 1994. Aerobic degradation of 1,1,1,-trichloro-2,2-*bis*(4-chlorophenyl)ethane (DDT) by *Alcaligenes eutrophus* A5. Appl. Environ. Microbiol. 60:51-55.

World Health Organization. 1989. DDT and its derivatives-environmental aspects. World Health Organization, Geneva, Switzerland.

Table 1. Recovery (%) of ^{14}C-DDE from Altamont soil after 30 days.

Treatment	Control	Cymene	BP & N	Bl &S I	BP &Cl
Mean	80.17	79.08	83.65	82.50	86.59
Standard Deviation	3.88	0.41	3.01	3.02	2.43

BP Biphenyl
N Nitrogen addition
SI Single inoculation
CI Continuous inoculation

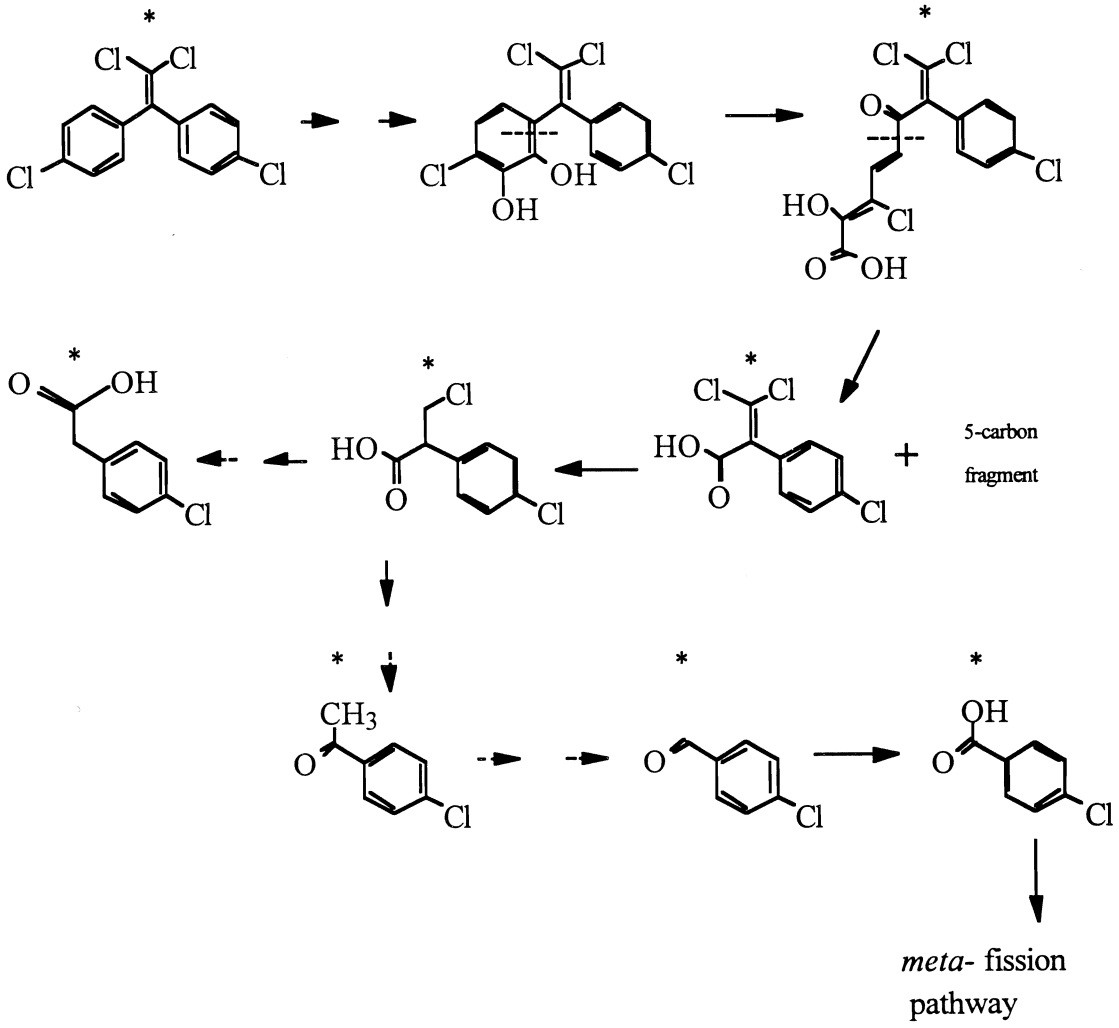

Figure 1. Proposed *meta*-cleavage pathway for degradation of DDE. Dashed arrows denote one or more undetermined steps. Asterisk indicates identity confirmed by GC-MS. The hypothetical catechol is suggested by identification of the acid catalyzed phenolic product.

Chemical Factors Affecting Colloid-Mediated Transport of Organic Pollutants in Soils

GARRISON SPOSITO
Department of Evironmental Science, Policy, and Management
Berkeley Campus

Summary

Dynamic and static light scattering measurements, as well as electrophoretic mobility measurements, were made on dilute suspensions of Na-illite in NaCl solutions of varying concentration and pH. The electrophoretic mobility of Silver Hill illite and Hanford soil illite decreased similarly in absolute value with increasing NaCl concentration and decreasing pH. The critical coagulation concentrations (at pH 8) were near 40 and 300 mol m^{-3} NaCl for the two illites, respectively. Both the specimen and the soil illite formed fractal floccules, the fractal dimension for the former lying between 1.8 and 2.1, depending on chemical conditions, whereas that for the latter lay between 2.0 and 2.4. Flocculation kinetics for the two illites showed significant differences from those observed typically for model synthetic colloids.

Key Words: colloid stability, electrophoretic mobility, flocculation, fractal dimension, groundwater quality, illite, light scattering

Project Objectives Addressed in 1995-1996

To perform light-scattering experiments on flocculating suspensions of specimen and soil illitic colloids under varying conditions of electrolyte concentration and pH, and to evaluate the light-scattering data in terms of transport -or reaction-control kinetics and fractal concepts.

Research Plan and Procedures

Clay stock suspensions

Materials. Silver Hill illite obtained from the Source Clays Repository of the Clay Mineral Society was used as a specimen clay mineral. The following unit-cell formula has been calculated from ICP analysis, assuming the anion $O_{20}(OH)_4$ (Newman and Brown, 1987, section 1.3.2.3):

$$K_{1.44}Na_{0.12}M_{0.021}(Si_{6.81}Al_{1.19})\,[Al_{2.86}Fe_{0.67}Mg_{0.47}]O_{20}(OH)_4$$

Hanford sandy loam (coarse-loamy, mixed, non-acid, thermic Typic Xerorthent) was used as the source of soil illite (Heil and Sposito, 1993).

Colloid surface preparation. Washing procedures are necessary to obtain a known surface state of the above materials (saturation of cation-exchange sites and dissolution of surface inorganic coatings). The procedures of Sposito and Levesque (1985) and Heil and Sposito (1993) were used for the Silver Hill and the Hanford soil illite, respectively, but with the samples being washed with a mixed solution of NaCl and KCl instead of $NaClO_4$ and $KClO_4$. The KCl is used to prevent desorption of structural K^+ from illite.

Preparation of the colloidal suspension. To recover a colloidal size fraction, the last washing was done at a low concentration of NaCl (2 mol m^{-3} for Silver Hill illite and 5 mol m^{-3} for Hanford illite, respectively). The suspension is then centrifuged on a Sorvall SS-3 automatic centrifuge to recover the desired size fraction in the supernatant suspension. Sodium bicarbonate ($NaHCO_3$) is added in order to bring the suspension to pH 8.0.

Dry mass measurement. The stock suspensions were oven-dried in order to determine the mass-concentration of solid material. Samples for light scattering experiments must be dilute enough to be in the flocculation domain, but not in the gelation domain.

The primary particle size distributions, measured by light scattering, were bimodal in all stock suspensions, but in those used for kinetics experiments, the smallest mode (< 100 nm) was predominant. The z-average mean diameter of the primary particles (effective hydrodynamic radius, see below) was 86 nm (Silver Hill illite, kinetics experiments), 75 nm (Hanford illite, kinetics experiments), 370 nm (Silver Hill illite, electrophoretic mobility measurements) or 200 nm (Hanford illite, electrophoretic mobility measurements).

Electrophoretic mobility measurements.

Measurements were performed on a Zetaphometer II apparatus (Sephy Instruments, France). The temperature was held constant at 25°C. The incident light source was a 5 mW He-Ne laser operating at 632.8 nm wavelength and adjusted to illuminate the stationary level in the rectangular sample cell. Light scattered by the suspended particles is collected by a CCD camera mounted on top of an optical microscope, set to focus at the stationary level as well. The depth of focus being about 5 μm, contributions from scattering centers lying outside the stationary level are minimized and accurate measurements of electrophoretic mobility are possible. The speed, v, of the particles is determined automatically from snapshots of their positions at known time intervals. The electrophoretic mobility,

$$u \equiv v / E \qquad (1)$$

is then calculated, with E being the magnitude of the electric field in the sample cell.

A sample preparation consisted of mixing a NaCl solution adjusted to the desired pH value with the colloidal sample adjusted to the same pH. The volume ratios were such as to yield always the same particle mass concentration. This concentration was 0.088 g (kg suspension)$^{-1}$ for Hanford illite and 0.015 g (kg suspension)$^{-1}$ for Silver Hill illite. The sample was then stirred 5 min using a magnetic bar and readjusted to the desired pH value, since the pH changes upon mixing the two preparations. Electrophoretic mobility measurement followed immediately.

Atrazine (2-chloro-4-ethylamino-6-isopropylamino-s-triazine), a widely-applied post-emergent herbicide (Wierinck and Verstraete, 1990), was also equilibrated with the Hanford illite stock suspension used for electrophoretic mobility measurements. The atrazine-Hanford illite mixture had a mass concentration in colloids of 0.22 kg (suspension)$^{-1}$, an atrazine concentration of 0.050 mol (kg suspension)$^{-1}$ and a pH value of 5.0. Equilibration time was 4d. Under these pH and concentration conditions, close to maximum binding of atrazine to humic acid has been observed (Wang et al., 1991).

Light scattering experiments.

Measurements were performed on a Malvern PCS 100 light-scattering goniometer. The incident light source was a 35 mW He-Ne laser operating at 632.8 nm wavelength with vertical polarization. The temperature was held constant at 25°C. Flocculation was initiated by mixing 10 or 15 ml of Silver Hill and Hanford illite stock suspension, respectively, with a volume of NaCl solution that resulted in the desired dilution. The NaCl solution was adjusted to pH 8.0 beforehand. Mixing was done systematically by pouring the NaCl solution onto the colloidal suspension, then rotating the vial five times clockwise and five times counterclockwise. This procedure diminished variations in initial

conditions from mixing. Once mixed, the preparation was poured into a cylindrical Burchard cell. From mixing to first measurement, the delay was constant and equal to 45 s in order to let the preparation return to Brownian motion conditions. The data acquisition time varied from 6 s to 120 s, depending on reaction kinetics.

The variation of the total scattering intensity with scattering vector **q** was measured between scattering angles of 15° and 150°. ($0.00345\ nm^{-1} < q < 0.0255\ nm^{-1}$). The time used for acquisition was 10 s, including 10 sub-scans that allow a dust-discrimination procedure. A measurement was made every 3° and the total data acquisition time was about 8 min for each intensity [I(q)] curve. Measurements were made continuously during the flocculation process in order to follow the evolution of the apparent fractal dimension of the floccules.

Particle size measurement. The theoretical approach to particle size measurement was described in our 1994-95 Kearney Foundation of Soil Science Annual Technical Report. Improvements have been made in order to take into account the contributions of polydispersity in the cluster size distributions and of rotational diffusion of the clusters to the decay of the autocorrelation function. Figure 1 is a schematic representation of the change of the ratio D_{eff} / D_T , where D_T is the average cluster translational diffusion coefficient and D_{eff} is the effective diffusion coefficient calculated by the usual cumulant analysis (see 1994-95 Annual Technical Report) which takes into account rotational diffusion contributions. The graph has been reproduced from Lin et al. (1990). These authors studied the influence of rotational diffusion on average-size measurements by dynamic light scattering and came to the conclusion that for $qR_h << 1$, no contribution is observed. For $qR_h >> 1$, the contribution of rotational diffusion is constant, and D_{eff} / D_T is a constant greater than 1.0 (see Fig. 1). For $qR_h \approx 1$, a transition domain exists. These findings can be interpreted in terms of the inverse of the momentum transfer, q^{-1}, which is the spatial order of magnitude at which the scattering centers are probed (Harrison, 1995). When q is large compared to the scattering centers, light can not "see" their rotations. As q^{-1} decreases (or R_h increases), light is able to resolve rotational motion, unless the scattering centers are homogeneous, in which case their orientations have no effect on the interference of the light waves, and $D_{eff} / D_T = 1$ (Fig. 1). As q^{-1} becomes large, all scatterers (or clusters) are probed internally and a constant, equal contribution is obtained, because of the scaling of the mass anisotropy within the clusters (Lin et al., 1990) and the large relaxation time of rotational diffusion as compared to translation diffusion (Cametti et al., 1989).

To probe polydispersity in the cluster size distribution as flocculation proceeds, and to account for the relaxation times of rotational diffusion, the 64-channels of the Malvern correlator were divided into four parallel sets of 16 channels each. The overall autocorrelation function was obtained from a logarithmic sampling scheme over the four sets, provided by the manufacturer 's software.

Floccule structure measurement. Static light scattering was used as a non-invasive probe of floccule structure measurement. Figure 2 shows static light scattering data for a flocculating suspension of Silver Hill illite (40 mol m^{-3} Na and pH 8.0). The theoretical approach to data interpretation was given in our 1994-95 Kearney Foundation of Soil Science Annual Technical Report. A correction to equation 7 in the 1994-95 report is required: The total scattered light intensity, I(q), is given by

$$I(q) \propto N(M)M^2S(q)P(q) \qquad (2)$$

where M is the mass (number of primary particles) of a cluster and N(M) is the number-distribution of the clusters in the scattering volume (Vicsek, 1989). The symbol S(q) represents the distribution of primary particles within the cluster, or structure factor, whereas P(q) is the form factor, or parameter describing the mass distribution of a single particle. The equation given in the previous report, was correct only for small-angle scattering.

Results and Discussion

Figures 3 and 4 show electrophoretic mobility data for Silver Hill and Hanford illite, as well as Hanford illite equilibrated with atrazine. Both negative and positive value are plotted at a given NaCl concentration, because it was observed that the particles in suspension were moving faster under the first polarization order of the electrodes than they did under the second. All mobilities nevertheless are negative algebraically, indicating a net negative surface charge density. The data showed two trends:

- As the concentration of 1-1 electrolyte increases under given conditions, the electrophoretic mobility decreases.
- At a given NaCl concentration, the electrophoretic mobility decreases as the pH increases (data not shown).

Furthermore, it can be seen that the isoelectric point (pH value at which the electrophoretic mobility vanishes) is not reached, even at pH values as low as 2.0.

Atrazine had no influence on the electrophoretic mobility of Hanford illite; therefore, this compound does not affect the stability of these colloids. A similar result was obtained by monitoring the evolution of size and total scattered light intensity during the 4-day equilibration period of Hanford illite either alone or mixed with atrazine, at different total concentrations. Atrazine was found not to affect the colloids, showing again its lack of effect on stability. The latter experiment was performed at a NaCl concentration around 1 mol m^{-3}, such that the conclusions here can be inferred only from mobility measurements at higher NaCl concentrations.

Electrophoretic mobility data of Silver Hill illite were converted to zeta potentials by modeling the clay platelets as oblate spheroids, following the analysis of Fair and Anderson (1988). The zeta potential at the face of the clay was found with estimations of the p.z.n.p.c. (point of zero net proton charge) at different NaCl concentrations. This potential was then transformed to the accessible structural surface charge density via the Gouy-Chapman model (Sposito, 1984). It was found that, at high NaCl concentrations (typically > 100 mol m^{-3}), the distance of the plane of shear from the face of the clay was smaller than 0.5 nm, which is physically unrealistic (McBride and Baveye, 1995). This can be explained by an increase in mobility (relative to isolated clay platelets) from the formation of clusters under these concentration conditions (Miller et al., 1992). It was also found that, under the conditions wherein the model was applicable, the plane of shear was about 2 nm from the face surface of illite, which is physically reasonable, if one considers the result of McBride and Baveye (1995), that five layers of water molecules are strongly bound to the surface of hectorite.

It must also be stated (Fair and Anderson, 1988) that the Smoluchowski equation cannot be used for natural colloids as a conversion from electrophoretic mobility to zeta potential. Unless a model accounting for morphology as well as net surface charge distribution is available, such a conversion is inaccurate. For instance, it was found that the distance of the plane of shear would lie over 5 nm away from the clay face surface if the zeta potential of this face were to be calculated with the Smoluchowski equation.

Finally, it can be seen from Figs. 3 and 4 that Hanford illite colloids have a somewhat lower mobility in absolute value than Silver Hill colloids. Yet the ccc (critical coagulation concentration) of Hanford illite is much higher than that of Silver Hill illite. All things being equal between these two materials, this would mean that the stability of Hanford illite has to be explained by other means than electrostatic repulsion. Steric stabilization between the organic surface coatings of the natural particles has been invoked to explain this result (see, for instance, Heil and Sposito, 1993).

Results obtained from flocculation kinetics studies showed that the natural colloids used did not follow the kinetics observed for synthetic colloids. One example can be seen from Fig. 5, which demonstrates the effect of primary particle concentration on the kinetics of Silver Hill illite. For a stock suspension that has been diluted four times, oscillations appear in the size-evolution of these colloids. Similar patterns are observed in the vicinity of this concentration (40 mol m^{-3} NaCl) and disappear as the diffusion-limited (DLCA) and reaction-limited (RLCA) régimes are attained. This behavior is explained through the help of Fig. 6. At low electrolyte concentrations, the time scale for clusters to coalesce is much higher than the time for their restructuring. At high electrolyte concentrations, this is expected to be true as well, at least for certain values of the initial particle concentration. At intermediate concentrations, coalescence of clusters is first faster than the time needed for restructuring, but as flocculation proceeds, the total number of clusters will decrease and the coalescence time scale will increase, resulting in a vertical upward shift of the blue curve in Fig. 6.

As a consequence, the two time scales will start to overlap. This competition is thought to result in fragmentation of the cluster. Intuitively, fragmentation would be most favored at the ccc, the onset of colloidal destabilization. This is indeed observed for Silver Hill illite, for which the ccc equals, under the present conditions, 43 (mol NaCl) m^{-3} (1994-95 Kearney Foundation of Soil Science Annual Technical Report). At higher concentrations, the two time scales can also compete, but it is believed that the interparticle forces are strong enough to avoid cluster fragmentation. In the case of Hanford illite, decreases in cluster size were observed at certain electrolyte and primary particle concentration. Yet for these colloids, the size increased again almost immediately after it had decreased, which is a different behavior from the one in Fig. 5. These patterns started to appear at 300 mol m^{-3} NaCl concentration, which is in the range of the estimated value of the ccc (1994-95 Kearney Foundation of Soil Science Annual Technical Report).

It was also found that both Hanford and Silver Hill illite floccules could be characterized by a fractal dimension according to the static light scattering curves. For Silver Hill illite, the fractal dimension (D) was found to be 1.83 in both the DLCA and the RLCA régimes at the same high primary particle concentration. No influence of particle concentration on D was observed for RLCA, but D increased to 2.05 in the DLCA régime for a tenfold dilution of the stock suspension. All other values of D were found to lie between these two limiting values for Silver Hill illite. The fractal dimensions of Hanford illite clusters all lay between 2.08 and 2.35 for a stock suspension that was diluted twice. It was found that D decreased from 2.35 under RLCA conditions to 2.10 under DLCA conditions. All values of D given are different from those obtained for synthetic colloids. In addition, the dependence of D on dilution strongly suggests that restructuring occurs, hence a change of reactivity with cluster structure, as well as competition between different mechanisms. In order to explain the oscillating curve in Fig. 6, fragmentation has also to be considered.

References

Cametti, C., P. Codastefano, and P. Tartaglia. 1989. Aggregation kinetics in model colloidal systems: a light scattering study. J. of Colloid and Interface Sci. 131: 409-422.

Fair, M.C. and J. L. Anderson. 1988. Electrophoresis of nonuniformly charged particles. J. of Colloid and Interface Sci. 127:388-400.

Harrison, A. 1995. Fractals in chemistry. Oxford University Press, Oxford.

Heil, D. and G. Sposito. 1993. Organic matter role in illitic soil colloids flocculation: I. Counter ions and pH. Soil Sci. Soc. Am. J. 57:1241-1246.

Lin, M. Y., Lindsay H. M., Weitz, D. A., Klein, R., Ball, R. C. and P. Meakin. 1990. Universal diffusion-limited colloid aggregation. J. Phys.: Condens. Matter 2:3093-3113.

McBride, M. B. and P. Baveye. 1995. Mobility of anion spin probes in hectorite gels: viscosity of surficial water. Soil Sci. Soc. Am. J. 59:338-394.

Miller, N. P., Berg, J. C. and R. W. Brien. 1992. The electrophoretic mobility of a porous aggregate. J. of Colloid and Interface Sci. 153:237-243.

Newman, A. C. D. and G. Brown. 1987. The chemical constitution of clays. *In* A. C. D. Newman (ed) Chemistry of Clays and Clay Minerals. Longman Scientific and Technical.

Sposito, G. 1984. The Surface Chemistry of Soils. Oxford Univ. Press, New York.

Sposito, G. and C. S. Levesque. 1985. Sodium-calcium-magnesium exchange on Silver Hill illite. Soil Sci. Soc. Am. J. 49:1153-1159.

Vicsek, T. 1989. Fractal growth phenomena. World Scientific, Singapore.

Wang, Z., Gamble, D. S. and C. H. Langford. 1991. Interaction of atrazine with Laurentian humic acid. Analytica Chimica Acta. 244:135-143.

Wierinck, I. and W. Verstraete. 1990. Degradation of atrazine by a hydrogenotrophic microbial association. Environ. Technol. 11: 843-852.

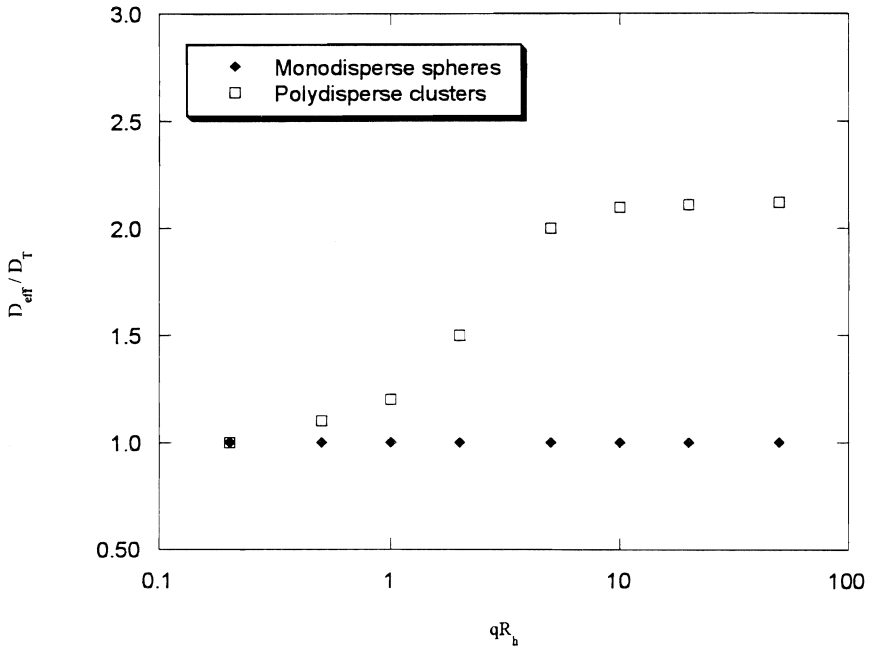

Figure 1. Influence of qR_h on the value of D_{eff}/D_T.

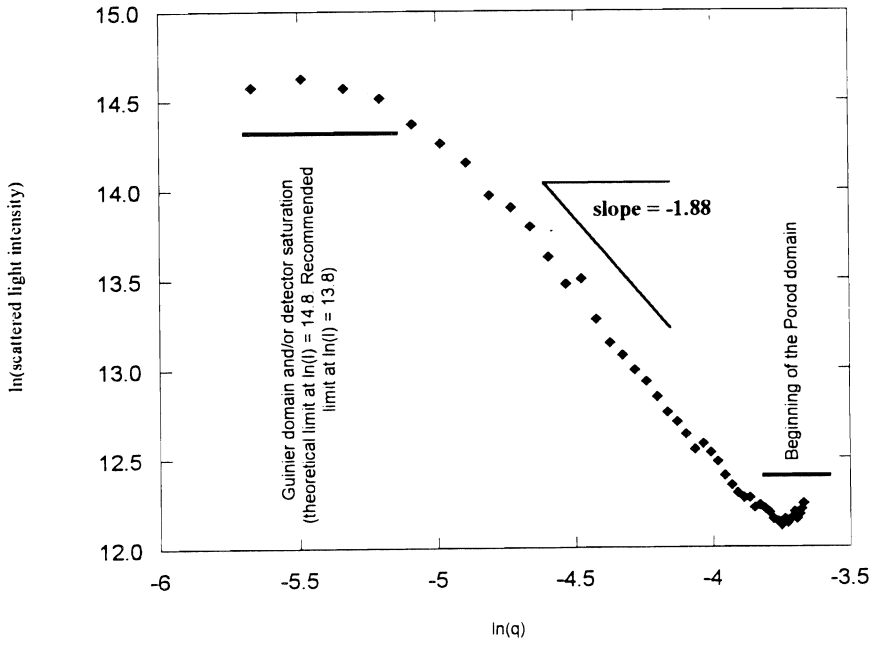

Figure 2. Static light scattering data obtained for a suspension of flocculating Silver Hill illite. The pH value was 8.0 and the NaCl concentration was 40 $mol.m^{-3}$. Particle mass concentration was 47 $mg.kg^{-1}$.

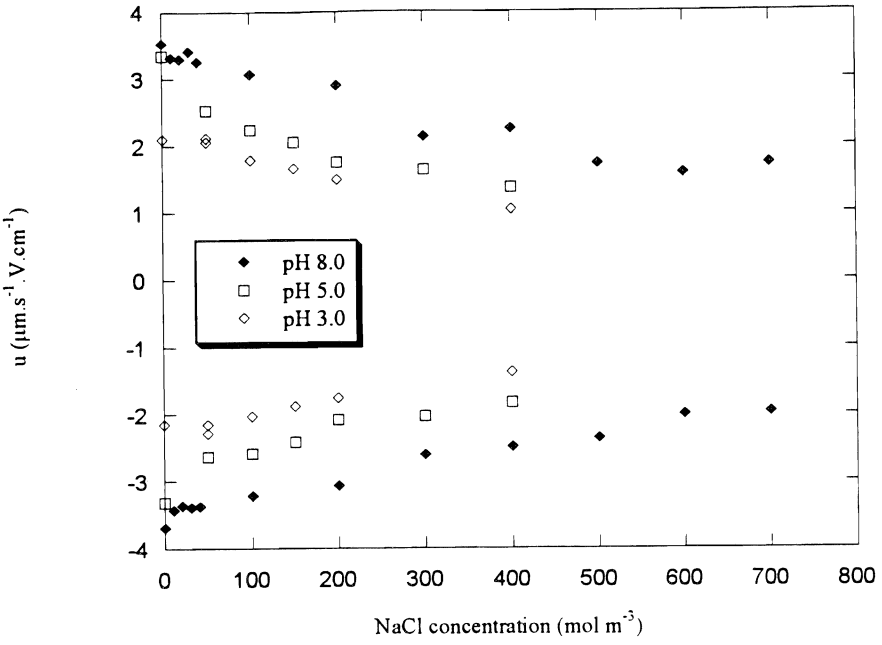

Figure 3. Electrophoretic mobility data for Silver Hill illite as a function of pH and NaCl concentration.

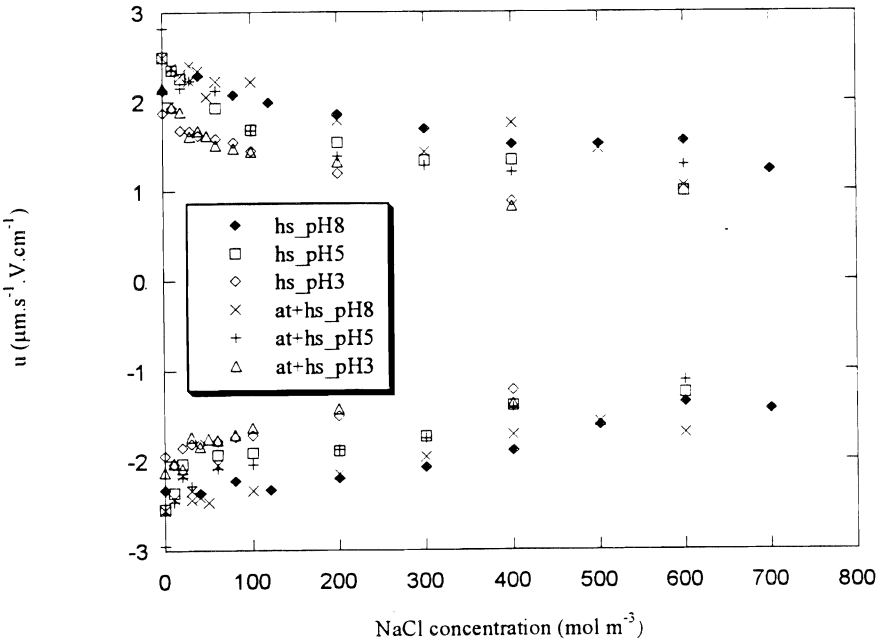

Figure 4. Electrophoretic mobility data for Hanford illite colloids alone (symbol hs_) or reacted with atrazine (symbol at+hs_), as a function of pH and NaCl concentration.

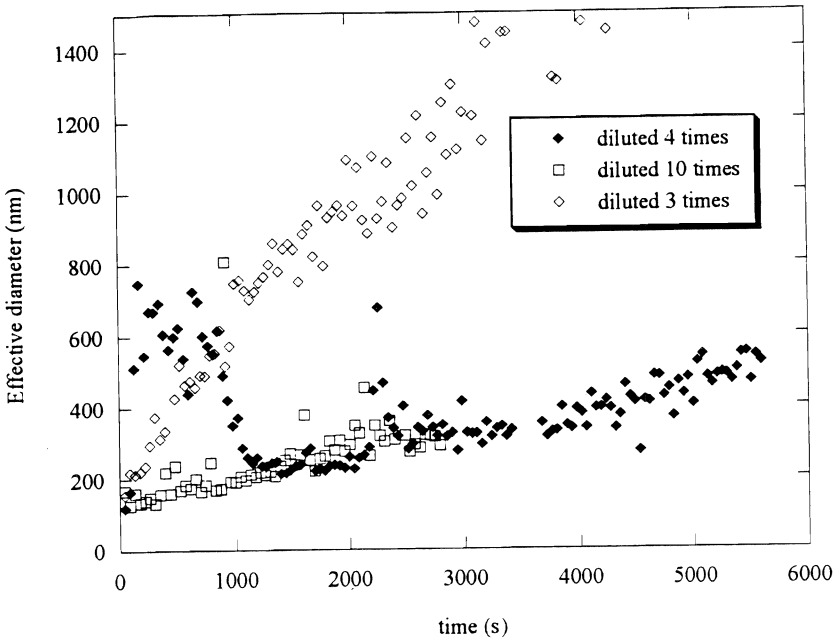

Figure 5. Flocculation kinetics of Silver Hill illite at 40 mol m^{-3} NaCl and pH 8.0. Dilutions are relative to the stock suspension.

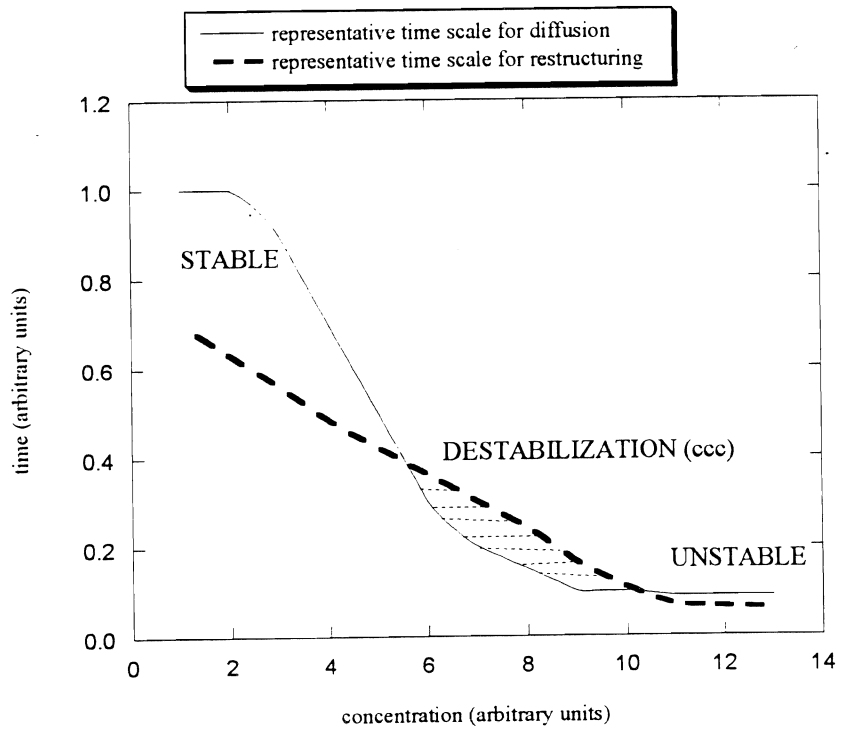

Figure 6. Schematic representation of the competition between floccule growth and restructuring time scales.

Spectroscopic Studies of Herbicide-Humic Substance Complexes in Soils

GARRISON SPOSITO
Department of Environmental Science, Policy, and Management, Berkeley Campus

Summary

Atrazine [6-chloro-*N*-ethyl-*N'*-(1-methylethyl)-1,3,5-triazine-2,4-diamine] reaction pathways with soil humic acid remain controversial. Optical and magnetic resonance spectral data indicate that proton-transfer and hydrogen bonding are as important as electron-transfer in the reaction mechanism of atrazine and humic acid, whereas other *s*-triazines appear to react more strongly by electron-transfer mechanisms. Representative tropical and temperate-zone humic acids were investigated spectroscopically to probe the issue of mechanisms more decisively. They were reacted with 140 mmol m^{-3} atrazine solution at pH < 7 under exclusion of light. Infrared and electron spin resonance spectra of the resulting products gave evidence for proton-transfer and, under certain conditions, electron-transfer mechanisms. These spectroscopic data and those from other published studies were interpreted in terms of molecular properties of both humic acids and *s*-triazines. The results suggested that proton-transfer is favored for humic acids of high acidic functional group content and for *s*-triazines of low basicity. Electron-transfer is favored for humic acids of low acidic functional group content and for *s*-triazines of high basicity. This principle illustrates the importance of specific molecular structure, as opposed to compound class structure, for understanding reactivity between *s*-triazines and humic acids.

Key Words: adsorption, charge-transfer complex, atrazine, electron spin resonance, humic acid, hydrogen bonding, infrared spectroscopy, proton-transfer, symmetric-triazines

Project Objectives Addressed in 1995-1996

Among the post-emergent herbicides, atrazine is the one most commonly applied worldwide to control weeds on both agricultural and non-agricultural land. It is, unfortunately, also very widely detected in water supplies and for this reason is considered to be an important indicator of pesticide contamination in the United States and elsewhere (Ritter et al., 1994; Tindall and Vencill, 1995; Biradar and Rayburn, 1995). Adding to this water quality problem is a growing concern over its potential carcinogenic effects (Biradar and Rayburn, 1995; Patlak, 1996). Laboratory studies (Clay and Koskinen, 1990a,b; Singh et al., 1990; Pignatello and Huang, 1991; Barriuso and Calvet, 1992; Barriuso et al., 1992; Roy and Krapac, 1994) have documented the key role played by pH and soil organic matter in atrazine sorption processes. These studies indicate the relatively weak binding of freshly-applied atrazine as compared to other *s*-triazine compounds, including even its hydrolysis product, hydroxyatrazine [6-hydroxy-*N*-ethyl-*N'*(1-methylethyl)-1,3,5-triazine-2,4-diamine].

Hayes (1970) and Senesi (1992) reviewed the chemical literature on *s*-triazine complexation by soil organic matter, particularly humic substances. Hayes (1970) emphasized the likelihood of proton-transfer (and hydrogen bonding) in the reaction mechanism (Fig. 1b), with the principal proton donor being the carboxyl groups in humic acid. Experimental evidence for this mechanism is provided by the observation of an increased content of carboxylate species in an *s*-triazine/humic acid adduct, relative to humic acid alone. Senesi (1992) added to this pathway a much stronger reaction mechanism involving electron-transfer (Fig. 1c). He pointed out that quinone-like moieties in humic acid have the ability to attract electrons from the secondary amino groups and the triazine ring N to form charge-transfer complexes. The charge-carrier intermediate species would be of the semi-quinone type, stabilized by the molecular structure of the humic acid/*s*-triazine adduct. Evidence for this mechanism is provided by the observation of an increase in the content of stable free radicals of the semi-quinone type (i.e., increased "spin concentration") in the adduct, relative to humic acid alone. Experimental results implying both of these complexation mechanisms are abundant in the literature of *s*-triazine-humic substance interactions (see reviews by Wang et al., 1990, 1991; Senesi, 1992). Partisans for proton-transfer (Gamble et al., 1994) or electron-transfer (Piccolo, 1994) as the dominant complexation mechanism have made the issue controversial.

The objectives of our project were to apply infrared and electron spin resonance spectroscopy to prepared reaction products of atrazine with representative soil humic acids in order to elucidate, with the help of existing spectroscopic published data, the relative importance of proton-transfer vs. electron-transfer:

(1) To apply spectroscopic methods (both optical and magnetic) to characterize the complexes formed between atrazine and humic acid extracted from a California soil and other soil sources.

(2) To interpret the spectroscopic data in terms of reaction mechanisms and to compare these mechanisms among the humic acids investigated.

Research Plan and Procedures

Humic acid samples. The humic acid (HA) samples used in this project were extracted from the Bh horizon of a Canadian Spodosol, the A horizon of a California Entisol, the 0-50 cm depth of a Brazilian Oxisol, and the 2.5-4.0 m depth of a Brazilian Histosol. Conventional extraction and purification methods (Schnitzer, 1982) were employed to obtain HA products with ash contents < 40 g kg^{-1}. The Entisol from which HA was extracted was a Hanford sandy loam (coarse-loamy, mixed, non-acid, thermic, Typic Xerorthent) collected at the Kearney Agricultural Center in the San Joaquín Valley. The Spodosol source was a poorly-drained forest soil (Armadale series) in northeastern Canada. Its humic fraction, available commercially (Contech E.T.C. Ltd., Ottawa, Ontario), was analyzed in detail by Sposito et al. (1982), who found its composition to be consistent with typical HA, in contradiction with the supplier, who labeled it a fulvic acid. Further investigation (Maurice-Johnsson, 1993, p. 152) has indicated the essential correctness of classifying this humic substance as HA. Table 1 lists elemental composition data for the HA samples.

Carboxyl content in the HA samples was determined by the method of Holtzclaw and Sposito (1979) as adapted for naturally-occurring humic substances. Briefly, a 100 mg sample of HA is placed into a 125-mL Erlenmeyer flask equipped with a screw cap. The flask is purged with N_2, 40 mL Milli-Q™ water and 10 ml of 1 mol dm^{-3} $Ca(CH_3CO_2)_2$ stock solution are added, and then the flask is closed tightly and wrapped with Al foil to prevent photoreactions. A blank solution is also prepared using all reagents other than the HA sample to be analyzed. The flasks are shaken moderately for approximately 24 h at room temperature (RT), then are removed and retained for steam distillation. The transfer of the sample for distillation is made by decanting the solution from the Erlenmeyer flask into the vessel of the steam-distillation apparatus and washing the flask with a few mL Milli-Q™ water. Steam generation is adjusted to provide a distillate rate of 6 to 8 mL min^{-1} and a distillate temperature of 22°C upon emergence from the condenser. A 400-mL volume of distillate is collected in a calibrated 500-mL flask, covered, and retained for base titration. The sample and blank solutions are titrated potentiometrically with standardized 100 mol m^{-3} NaOH to pH 8.50. The carboxyl content of the sample is calculated according to the expression:

$$\frac{[\text{volume NaOH(sample)} - \text{volume NaOH(blank)}] \times \text{concentration NaOH}}{\text{ash- and water-free mass of sample}}$$

The steam-distillation step is essential to avoid positive interference from titrating weakly-acidic functional groups in HA that do not react with calcium acetate (Holtzclaw and Sposito, 1979). Carboxyl contents for the HA samples appear in Table 1 (sixth column).

Atrazine-Humic Acid Complexes. Reagent-grade atrazine (98.7% purity, Ciba-Geigy, Greensboro, NC) was dissolved in Milli-Q^{TM} water to prepare a 140 mmol m^{-3} solution that was stored with exclusion of light to preclude photoreactions. Exactly 15 mg of purified HA were reacted with 25 mL of this solution at fixed pH values in the range 2 to 7 (adjusted, as necessary, using $HClO_4$ or NaOH). The sample solutions (designated HAAT) were mixed gently on an arm shaker at RT for 4 d, again with exclusion of light to avoid photoreactions (Pelizzetti et al., 1990). Solid-phase products for use in spectroscopic experiments were obtained by freeze-drying the HAAT solutions. Reference humic acid samples without atrazine (designated HA) were prepared in the same way. The ratio of added atrazine to HA, 0.23 mol atrazine kg^{-1} HA, exceeds the typical maximum complexation capacity of HA for atrazine (Wang et al., 1991). Preliminary experiments indicated that, for pH < 4, about one-third of the added atrazine complexed with HA in the freeze-dried product, while the remainder was merely coprecipitated with HA.

FTIR spectroscopy. Fourier-transform infrared (FTIR) spectra of the HAAT and HA samples were obtained with a Mattson Cygnus 100 FTIR spectrophotometer using 30-mg pellets. Generally, 2 to 3 mg of the HAAT or HA sample was added to 100 mg of KBr and pressed into a pellet.

ESR spectroscopy. Electron spin resonance (ESR) spectra of the HAAT and HA samples were obtained with a Brucker ESR spectrometer operating at X-band frequency (9 GHz) with the sample at RTK. At RT, semiquinone-type free radicals were quantitated using the conventional approximation, intensity $\times$ line width^2 (Wertz and Bolton, 1986). The areas of the ESR peaks were calibrated with that corresponding to the ESR signal of a "strong pitch" reference of known free radical content, obtained from Brucker.

Results

Infrared spectra of the Spodosol and Oxisol HA and HAAT samples appear in Figs. 2 and 3 as representative examples. The HAAT spectra showed a relative enhancement in absorbance near 1600 cm^{-1} as compared to the HA spectra, an effect seen also in the Entisol and Histosol HA and HAAT spectra at pH < 3 (Martin-Neto et al., 1994; Sposito et al., 1996). Absorbance near 1600 cm^{-1} reflects primarily the antisymmetric vibration of carboxylate groups (Stevenson, 1994, p. 312), and its relative enhancement in the HAAT spectra can be attributed to proton-transfer reactions between HA carboxyl groups and the 2,4-diamine groups in atrazine (Senesi et al., 1987). At pH > 2, changes in the spectra near 1100 to 1200 cm^{-1} occurred for the HAAT samples. Given the assignment of this latter wavenumber region principally to C-O stretching vibrations in hydroxylated moieties (Stevenson, 1994, p. 312), and the very low value of 1.68 for the pK_a of atrazine (Weber, 1970), these changes in the spectra may be a signature of hydrogen-bonding interactions between OH groups and deprotonated atrazine (Senesi et al., 1987).

Tables 2 to 5 list ESR parameters measured for the HA samples and their atrazine complexes at varying pH. No significant change in spin concentration was observed for the Spodosol, Oxisol, or Histosol HA upon reaction with atrazine (Tables 2, 4, and 5); whereas, an appreciable increase in spin concentration did occur for the Entisol HA after the reaction (Table 3). Increases in spin concentration signal the formation of charge-transfer complexes between HA and atrazine (Senesi, 1992).

Discussion

Infrared spectra of complexes between atrazine and HA (Figs. 2 and 3) indicate a proton-transfer bonding mechanism (Fig. 1b) was operative at pH < 5. Hydrogen bonding between N in either the secondary amino groups or the triazine ring of atrazine and oxygen-containing functional groups in HA also is likely. These conclusions are in accord with many previous experimental studies of the atrazine-HA interaction [for reviews see Hayes (1970), Senesi and Testini (1982), and Senesi (1992)], as well as with the semi-empirical structure-reactivity correlations of Welhouse and Bleam (1993a,b), which suggest enough delocalization of N lone-pair electron density into the triazine ring to create significant polarity (acidic side-chain NH vs. basic triazine ring), leading to stable hydrogen bond formation. In the same spirit, Gamble et al. (1994) have shown that the atrazine complexing capacity of fulvic acid increases with increasing protonation of its carboxyl groups.

The spin concentration data in Tables 2 to 5, as well as those presented recently by Senesi et al. (1995), who also used ESR to study atrazine complexes with soil HA, suggest that electron-transfer mechanisms (Fig. 1c) play a role of varying importance in the complexation of atrazine by HA. Welhouse and Bleam (1993a) predicted a problematic status for electron-transfer reactions from their semi-empirical structure-reactivity analysis, pointing to the low overall basicity of the atrazine molecule. Basicity among *s*-triazines is determined primarily by the substituent at the 6 position on the triazine ring, with lesser effects coming from those on the secondary amino groups at the 2- and 4-positions (Weber, 1967, 1970). Basicity increases as the electronegativity of a substituent decreases. Thus, for example, the order of increasing pK_a (a useful quantitative measure of basicity) for the series of *s*-triazines, 6-R-N,N′-(1-methylethyl)-1,3,5-triazine-2,4-diamine, is: 1.85 (Cl), 4.05 (SCH_3), 4.28 (OCH_3), 5.20 (OH), where the 6-position substituent R follows in parentheses (Weber, 1967). Atrazine differs from propazine, the first member of this series, only by replacement of the 1-methylethyl group at the triazine-ring 2-position by an ethyl group, with the result that pK_a drops only slightly to 1.68 because of a decrease in the number of C atoms in the alkyl substituent (Weber, 1970). If the Cl at the 6-position on the triazine ring of atrazine is replaced by the less electronegative SCH_3 to create ametryne [6-methylthio-N-ethyl-N′-(1-methylethyl)-1,3,5-triazine-2,4-diamine], the pK_a value rises sharply to 4 (Weber, 1970). With OH in the 6-position to create hydroxyatrazine, it increases to about 5 (Clay and Koskinen, 1990b).

The low basicity of atrazine should inhibit its complexation with HA through electron-transfer mechanisms. Ametryne, being much more basic than atrazine, should be more reactive toward electron-deficient HA moieties. Senesi and Testini (1982) found no change in spin concentration, after reaction with ametryne, in two out of three soil HA samples they investigated, but Senesi et al. (1987) observed a large increase in spin concentration for ametryne complexation by a synthetic HA containing almost no carboxyl groups. Senesi et al. (1987) also noted that prometone [6-methoxy-N,N′-(1-methylethyl)-1,3,5-triazine-2,4-diamine], whose 6-position methoxy group renders it quite basic in the series of pK_a (= 4.28) given above, was highly effective in engaging electron-transfer mechanisms to complex with HA.

The same line of reasoning should apply to hydroxyatrazine. At pH 2.0-2.5, significant hydrolysis of atrazine to form hydroxyatrazine over the four-day reaction period in the present experiments is likely (Li and Felbeck, 1972; Martin-Neto et al., 1994). With a $pK_a \approx 5$ (Clay and Koskinen, 1990b), it remains protonated at pH < 4, with a concomitant lesser tendency to form hydrogen bonds with HA than atrazine. Wang et al. (1991) noted a lack of competition between atrazine and hydroxyatrazine in sorption by HAand suggested that there are different HA reaction sites for the two compounds. The high basicity of hydroxyatrazine, on the other hand, should make it likely to engage in electron-transfer reactions. Hydrolysis of atrazine at pH < 4 in the present experiments may in fact have contributed to the increases in spin concentration observed for the Entisol HA (Table 3).

The spectroscopic data in the present study, taken together with the data from other published studies discussed above, suggest a general guiding principle in the complexation mechanisms of *s*-triazines with soil humic acids: Proton-transfer is favored (and electron-transfer is disfavored) for humic acids of high acidic functional group content and for *s*-triazines of low basicity (e.g., atrazine). Conversely, humic acids of low total acidity and *s*-triazines of high basicity will tend to engage strongly in electron-transfer reactions and only weakly in proton-transfer reactions.

References

Barriuso, E., and R. Calvet. 1992. Soil type and herbicides adsorption. Int. J. Environ. Anal. Chem. 46:117-128.

Barriuso, E., Ch. Feller, R. Calvet, and C. Cerri. 1992. Sorption of atrazine, terbutryn and 2,4-D herbicides in two Brazilian Oxisols. Geoderma 53:155-167.

Biradar, D. P., and A. L. Rayburn. 1995. Chromosomal damage induced by herbicide contamination at concentrations observed in public water supplies. J. Environ. Qual. 24:1222-1225.

Clay, S. A., and W. C. Koskinen. 1990a. Characterization of alachlor and atrazine desorption from soils. Weed Sci. 38:74-80.

Clay, S. A., and W. C. Koskinen. 1990b. Adsorption and desorption of atrazine, hydroxyatrazine, and s-glutathione atrazine on two soils. Weed Sci. 38:262-266.

Gamble, D. S., C. H. Langford, and G. R. Barrie Webster. 1994. Interactions of pesticides and metal ions with soils: Unifying concepts. Rev. Environ. Contam. Toxicol. 135:63-91.

Hayes, M. H. B. 1970. Adsorption of triazine herbicides on soil organic matter, including a short review on soil organic matter chemistry. Residue Rev. 32:131-174.

Holtzclaw, K. M., and G. Sposito. 1979. Analytical properties of the soluble, metal-complexing fractions in sludge-soil mixtures: IV. Determination of carboxyl groups in fulvic acid. Soil Sci. Soc. Am. J. 43:318-323.

Li, G.-C., and G. T. Felbeck. 1972. Atrazine hydrolysis as catalyzed by humic acids. Soil Sci. 114:201-209.

Martin-Neto, L., E. M. Vieira, and G. Sposito. 1994. Mechanism of atrazine sorption by humic acid: A spectroscopic study. Environ. Sci. Technol. 28:1867-1873.

Maurice-Johnsson, P. A. 1993. Hematite dissolution in natural organic acids. Ph.D. dissertation, Stanford University.

Patlak, M. 1996. Estrogens may link pesticides, breast cancer. Environ. Sci. Technol. 30:210A-211A.

Pelizzetti, E., V. Muarino, C. Minero, V. Carlin, E. Pramauro, O. Zerbinati, and M. Tosato. 1990. Photocatalytic degradation of atrazine and other *s*-triazine herbicides. Environ. Sci. Technol. 24:1559-1565.

Piccolo, A. 1994. Interactions between organic pollutants and humic substances in the environment. p. 961-979. *In* N. Senesi and T.M. Miano (ed.) Humic substances in the global environment and implications on human health. Elsevier Science, Amsterdam.

Pignatello, J. J., and L. Q. Huang. 1991. Sorptive reversibility of atrazine and metolachlor residues in field soil samples. J. Environ. Qual. 20:222-228.

Ritter, W. F., R. W. Scarborough, and A. E. M. Chirnside. 1994. Contamination of groundwater by triazines, metolachlor and alachlor. J. Contam. Hydrol. 15:73-92.

Roy, W. R., and I. G. Krapac. 1994. Adsorption and desorption of atrazine and deethylatrazine by low organic carbon geologic materials. J. Environ. Qual. 23:549-556.

Schnitzer, M. 1982. Organic matter extraction. p. 581-594. In A. L. Page (ed.) Methods of soil analysis. Part 2. Chemical and microbiological properties. American Society of Agronomy, Madison, WI.

Senesi, N. 1992. Binding mechanisms of pesticides to soil humic substances. Sci. Total Environ. 123/124:63-76.

Senesi, N., and C. Testini. 1982. Physico-chemical investigations of interaction mechanisms between *s*-triazine herbicides and soil humic acids. Geoderma 28:129-146.

Senesi, N., C. Testini, and T. M. Miano. 1987. Interaction mechanisms between humic acids of different origin and nature and electron donor herbicides: A comparative IR and ESR study. Org. Geochem. 11:25-30.

Senesi, N., V. D'Orazio, and T. M. Miano. 1995. Adsorption mechanisms of s-triazine and bipyridylium herbicides on humic acids from hop field soils. Geoderma 66:273-283.

Singh, G., W. F. Spencer, M. M. Cliath, and M. Th. van Genuchten. 1990. Sorption behavior of *s*-triazine and thiocarbamate herbicides on soil. J. Environ. Qual. 19:520-525.

Sposito, G., K. M. Holtzclaw, C. S. LeVesque, and C. T. Johnston. 1982. Trace metal chemistry in arid-zone field soils amended with sewage sludge: II. Comparative study of the fulvic acid fraction. Soil Sci. Soc. Am. J. 46:265-270.

Sposito, G., L. Martin-Neto, and A. Yang. 1996. Atrazine complexation by soil humic acids. J. Environ. Qual. (In press).

Stevenson, F. J. 1994. Humus chemistry. John Wiley, New York.

Tindall, J. A., and W. K. Vencill. 1995. Transport of atrazine, 2,4-D, and dicamba through preferential flowpaths in an unsaturated clayean soil near Centralia, Missouri. J. Hydrol. 166:37-59.

Wang, Z.-D., D. S. Gamble, and C. H. Langford. 1990. Interaction of atrazine with Laurentian fulvic acid: binding and hydrolysis. Anal. Chim. Acta 232:181-188.

Wang, Z., D. S. Gamble, and C. H. Langford. 1991. Interaction of atrazine with Laurentian humic acid. Anal. Chim. Acta 244:135-143.

Weber, J. B. 1967. Spectrophotometrically determined ionisation constants of 13 alkylamino-*s*-triazines and the relationship of molecular structure and basicity. Spectrochim. Acta 23A:458-461.

Weber, J. B. 1970. Mechanisms of adsorption of *s*-triazines by clay colloids and factors affecting plant availability. Residue Rev. 32:93-130.

Welhouse, G. J., and W. . Bleam. 1993a. Atrazine hydrogen-bonding potentials. Environ. Sci. Technol. 27:494-500.

Welhouse, G. J., and W. F. Bleam. 1993b. Cooperative hydrogen bonding of atrazine. Environ. Sci. Technol. 27:500-505.

Wertz, J. E., and J. R. Bolton. 1986. Electron spin resonance. Chapman and Hall, New York.

Table 1. Chemical composition of the humic acid samples.[†]

Humic acid source	C	H	N	O	COOH
	---------- g kg^{-1} ----------				mol_c kg^{-1}
Spodosol[‡]	564	46	8.6	380	4.7 ± 0.1
Entisol[§]	438	50	42	470	2.7 ± 0.1
Oxisol	440	51	55	454	3.7
Histosol	554	47	25	374	—

[†] ash- and water-free basis; O calculated as 1000-(C + H + N content)

[‡] data from Sposito et al. (1982)

[§] data from E.M. Vieira, USP/IQ, São Carlos, Brazil

Table 2. Electron spin resonance parameters for free radicals in the Spodosol humic acid (g = 2.003).

Sample	pH	Spins 10^{17} g^{-1}	Line width G†
HA	6.7	6.7 ± 0.5	5.3 ± 0.2
HAAT	6.7	6.9 ± 0.5	5.3 ± 0.2
HA	4.6	4.5 ± 0.5	4.8 ± 0.2
HAAT	4.6	4.3 ± 0.5	4.8 ± 0.2
HA	3.2	2.4 ± 0.5	3.5 ± 0.2
HAAT	3.2	3.1 ± 0.5	3.5 ± 0.2
HA	2.0	2.7 ± 0.5‡	3.2 ± 0.2
HAAT	2.0	2.9 ± 0.5‡	3.2 ± 0.2

† 1 gauss (G) = 10^{-4} tesla (T)

‡ smaller sample volumes than at pH > 2

Table 3. Electron spin resonance parameters for free radicals in the Entisol humic acid (g = 2.003).

Sample	pH	Spins $10^{17}g^{-1}$	Linewidth G†
HA	4.5	5.3 ± 0.1	4.5 ± 0.0
HAAT	4.5	5.9 ± 0.3	4.4 ± 0.1
HA	3.5	5.8 ± 0.3	4.3 ± 0.0
HAAT	3.5	7.5 ± 0.3	4.4 ± 0.1
HA	2.5	9.0 ± 1.0	4.0 ± 0.0
HAAT	2.5	13.2 ± 0.8	4.3 ± 0.2

† 1 gauss (G) = 10^{-4} tesla (T)

Table 4. Electron spin resonance parameters for free radicals in the Oxisol humic acid (g = 2.004).

Sample	pH	Spins	Line width
		10^{17} g^{-1}	G†
HA	6.5	1.4 ± 0.3	4.0 ± 0.2
HAAT	6.5	1.3 ± 0.3	4.0 ± 0.2
HA	4.5	1.8 ± 0.3	4.3 ± 0.2
HAAT	4.5	1.6 ± 0.3	4.3 ± 0.2
HA	3.5	1.3 ± 0.3	4.2 ± 0.2
HAAT	3.5	1.4 ± 0.3	4.2 ± 0.2
HA	2.3	1.8 ± 0.3	3.2 ± 0.2
HAAT	2.3	1.9 ± 0.3	3.4 ± 0.2

† 1 gauss (G) = 10^{-4} tesla (T)

Table 5. Electron spin resonance parameters for free radicals in the Histosol humic acid (g = 2.004).

Sample	pH	Spins	Line width
		10^{18} g^{-1}	G†
HA	6.0	1.1 ± 0.1	3.0 ± 0.2
HAAT	6.0	1.1 ± 0.1	3.0 ± 0.2
HA	5.0	1.1 ± 0.1	3.0 ± 0.2
HAAT	5.0	1.1 ± 0.1	3.0 ± 0.2
HA	3.8	1.1 ± 0.1	3.0 ± 0.2
HAAT	3.8	1.0 ± 0.1	3.0 ± 0.2
HA	2.3	0.5 ± 0.1	3.0 ± 0.2
HAAT	2.3	0.6 ± 0.3	3.4 ± 0.2

† 1 gauss (G) = 10^{-4} tesla (T)

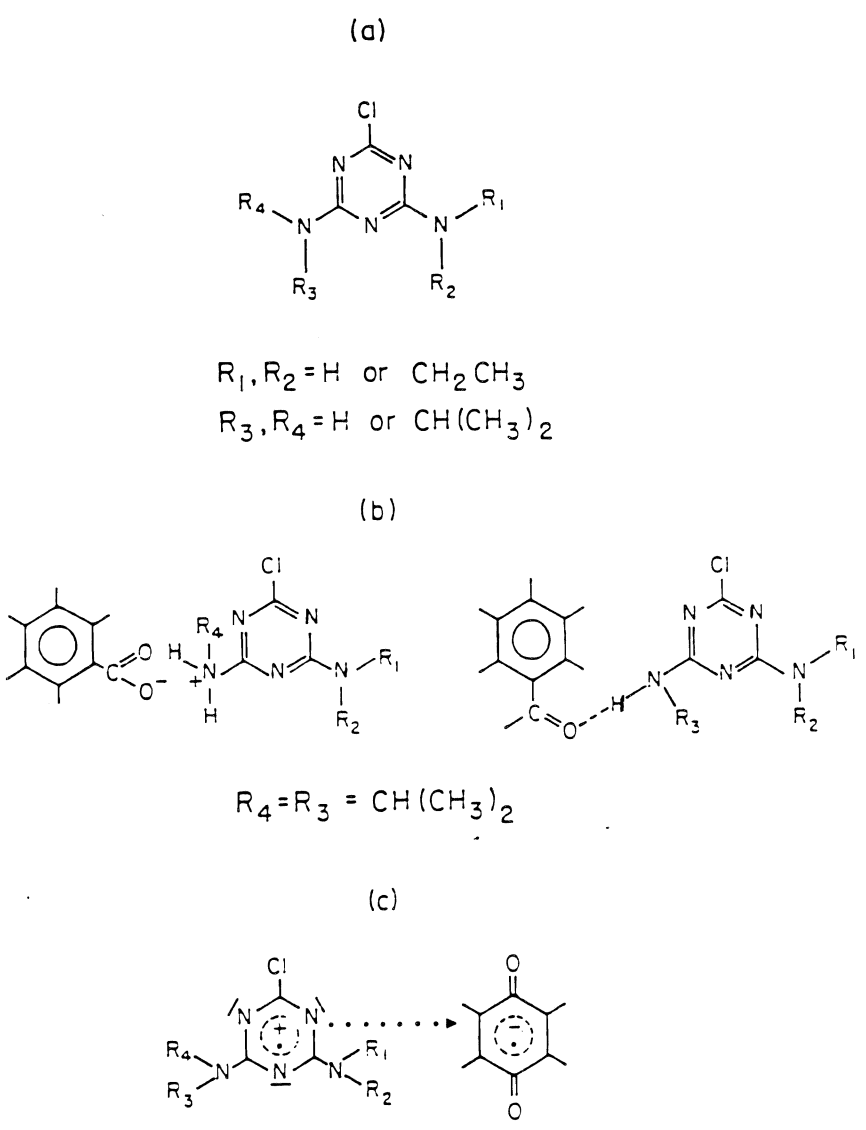

Figure 1. (a) Molecular structure of atrazine. (b) Proton-transfer (left) and hydrogen-bonding (right) mechanisms of bonding to HA moieties. (c) Electron-transfer mechanism of bonding to quinone-like structures in HA.

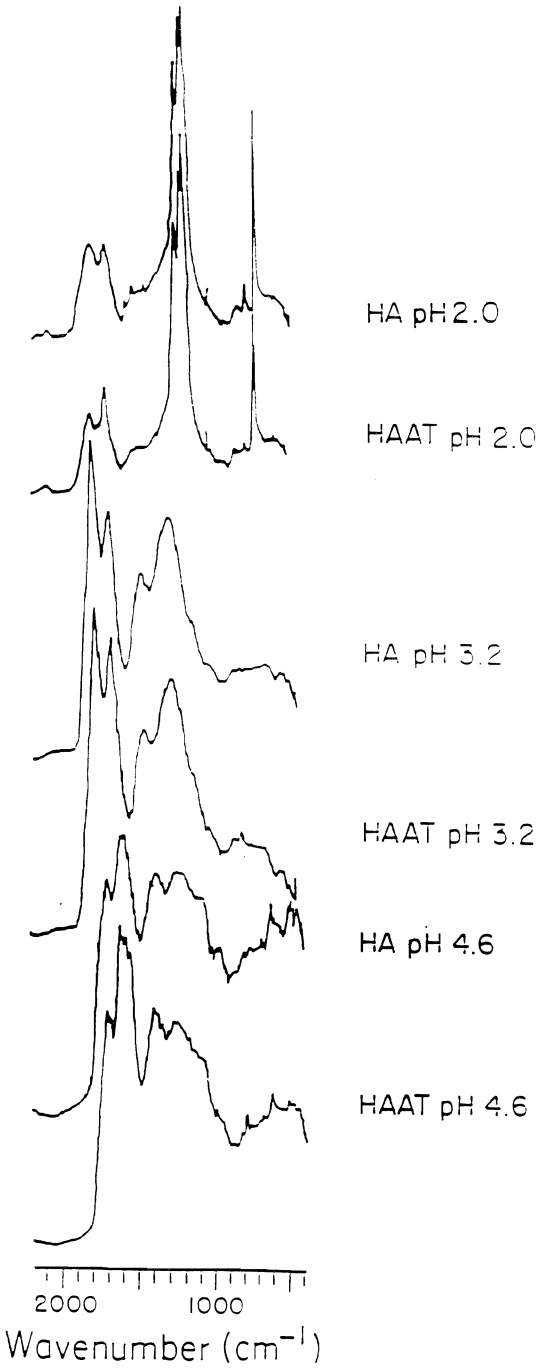

Figure 2. Infrared spectra of the Spodosol HA and HAAT samples.

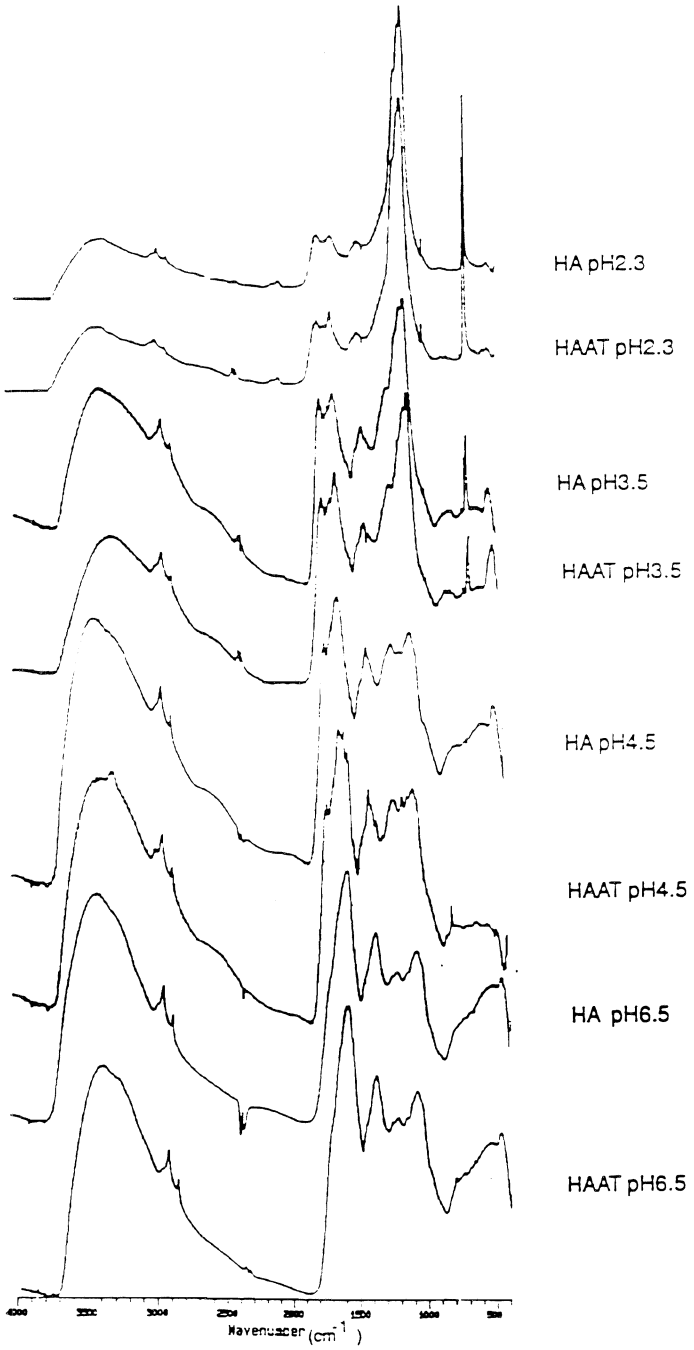

Figure 3. Infrared spectra of the Oxisol HA and HAAT samples.

Factors Influencing Sorptive Properties of Carbonates for Trace Elements in Soils

MAVRIK ZAVARIN AND HARVEY E. DONER
Department of Environmental Science, Policy, and Management, Berkeley Campus

Summary

Soil samples from high terraces near the Panoche Creek, California, were used to investigate the activity of soil carbonate surfaces and to determine whether current aqueous speciation data can model measured equilibrium solution composition. Results indicated that the organically-rich soil horizons are supersaturated with respect to calcite, while extracts from gypsic horizons were found to be at equilibrium with gypsum. Soluble trace and minor elements, such as selenite or silicon, as well as organic solutes, may alter or coat the surfaces of natural carbonates, preventing the surface from catalyzing precipitation of calcite.

Extended X-ray Absorption Fine Structure (EXAFS) data for adsorbed selenite (Se(IV)) indicate an inner-sphere structure, while selenate (Se(VI)) seems to be dominated by an outer-sphere structure. Selenite coprecipitation experiments indicate that calcite forces selenite into a coordination site which is different from crystalline calcium selenite. In addition, calcite may have selectivity-dependent sorption sites which are manifested by changes in Se near-neighbor structure, depending on selenite and carbonate concentrations during coprecipitation. Both Ni and Mn are found to form surface precipitate structures on calcite, which are different from thermodynamically favored mineral phases. Coprecipitated Ni and Mn both form structures which are controlled by the coordination structure of coprecipitating calcite and do not resemble the respective hydroxide or carbonate forms.

The fluorescence ratio method, coupled with x-ray focusing techniques and high flux synchrotron x-ray sources, is a promising technique for 3-D elemental mapping at the micrometer scale. Results from both experimental and theoretical data indicate that resolution in the third dimension can be achieved as low as the micrometer level, though the matrix composition, element of interest, and intensity of the source will control the achievable resolution.

Key Words: Selenium, nickel, manganese, calcite, EXAFS, XANES.

Project Objectives Addressed in 1995-1996

1. Investigate the activity of natural carbonate surfaces and their interaction with soil solutions.

2. Investigate the sorptive properties of calcite with respect to trace and minor elements, particularly Ni(II), Se(IV), Se(VI), and Mn(II).

3. Investigate microscopic and molecular level structure of trace metals and soil minerals using novel synchrotron x-ray techniques

Research Plan And Procedures

A. Macroscopic Analysis of Trace Element Interaction with Calcite

Soil samples from high terraces near the Panoche Creek, California, were used to investigate the activity of soil carbonate surfaces and determine whether current aqueous speciation data can model measured equilibrium solution composition. The site and soils were described previously (Doner and Zavarin, 1995). Water extracts were run in duplicate at soil:water dilution ratios of 1:2, 1:5, 1:10, and 1:50 to test the equilibrium state of the soil solutions and determine mineral dissolution trends. 0.25% CO_2 was used to mimic the approximate CO_2 levels found in soil. Each extract was contained in a plastic bottle and held at 25°C by a shaking constant temperature bath. The 0.25% CO_2 was bubbled through the solution for 24 hours for equilibration. After 24 hours, pH was measured and the samples were extracted, filtered through 0.45 micron filters, and stored. Solutions were analyzed for organic matter and major and minor cations and anions by a UV-persulfate Organic Carbon analyzer and Inductively Coupled Plasma (ICP) spectrometer. The equilibrium program "HYDRAQL" (Papelis, 1988) was used to determine the saturation state of the extract.

Trace element accumulation in synthetic calcite was investigated by pH-stat. The precipitation rate was controlled by using a solution initially supersaturated with respect to calcite and inducing crystal formation by calcite seeds. By monitoring the rate of trace metal removal from solution over time, we arrived at an accurate measure of trace metal incorporation rates. A detailed description of the system was made previously (Doner and Zavarin, 1995). The same pH-stat system was used to prepare samples for detailed molecular-level structural investigation of trace metals in calcite by synchrotron Extended X-Ray Absorption Fine Structure (EXAFS) and X-Ray Absorption Near Edge Structure (XANES).

B. Molecular-Level Organization of Trace Elements in Carbonates

Selenium adsorption isotherms were run as 1:10 solid:solution ratio batch experiments in 0.1M ionic strength solutions. Batch Se concentrations were 100 ppb for both selenite (Se(IV)) and selenate (Se(VI)) and equilibrated for 24 hours, preceded by a calcite equilibration step. Elemental analysis was performed by either HGAAS or ICP spectrometry to determine final trace metal concentration and the equilibrium state of the final solution.

Extended X-ray Absorption Fine Structure (EXAFS) and XANES were used to determine the molecular-level structure of Ni, Se and Mn sorbed and coprecipitated on calcite. Coprecipitation samples were prepared using the pH-stat setup and run as dry calcite powder samples at SSRL. Sorption samples used for EXAFS and XANES were prepared similarly to the sorption isotherm samples except at higher concentrations and equilibration time was reduced to only 1 hour to reduce recrystallization effects. After 1 hour, samples were centrifuged, the supernatant was sampled, and the calcite paste was set into sealed sample holders used for EXAFS data collection. Samples were prepared at the SSRL beam line and run immediately. During this study, we found that commercially available selenate salts contained 0.3-1% Se(IV), which was removed from sorption solutions. This was achieved by equilibrating the solutions with excess calcite: selenite sorbed to the excess calcite, while selenate remained in solution.

C. Investigation into Refining Synchrotron X-Ray Microprobe Elemental Analysis of Natural Samples

With the advent of high flux third generation synchrotron x-ray sources such as the Advanced Light Source (ALS), Lawrence Berkeley National Laboratory (LBNL), European Synchrotron Radiation Facility (ESRF), Grenoble, and the Advanced Photon Source (APS), Argonne, as well as other high flux sources such as the Stanford Synchrotron Radiation Laboratory (SSRL), Stanford, and National Synchrotron Light Source (NSLS), Brookhaven, the Synchrotron X-Ray Fluorescence (SXRF) microprobe has become the technique of choice for 2-D elemental mapping. Due to the high brightness of these sources, elemental mapping can be accomplished at the ppm level. Additionally, focusing mirrors (e.g. multi-layer Kirkpatrick-Baez mirrors (Underwood, 1986a; Underwood, 1986b) and others) have been able to focus the beam to micrometer spot sizes to achieve unprecedented spatial resolution from SXRF microprobes. Though other techniques such as the electron microprobe may have similar if not better spatial resolution and nearly equal detection limits, perhaps the most appealing aspect of the SXRF microprobe is that samples can be run at atmospheric pressures and temperatures and with little sample pretreatment, making it an ideal technique for samples which are sensitive to changes in environmental conditions.

Limestone wedges with heterogeneously distributed Cu and Sn were constructed to test a 3-D elemental analysis technique which uses the $K\alpha/K\beta$ fluorescence ratio to calculate the depth-position of a trace metal in a sample; Fig. 1 is a cross-sectional view of the prepared samples which were constructed such that the depth-position of the trace metal increased across the sample. Results from these samples and a computer program used to model heterogeneous systems were reported previously (Doner and Zavarin, 1995). The model was recently used to mimic the limestone wedge experiments and calculate the effective resolution of this technique.

Results

A. Wet-Chemical Studies of Equilibrium State of Soils from Panoche Creek

Figure 2 is a plot of the equilibrium calcite saturation index (S.I. = log(IAP/Ksp)) for the seven horizons of the Mugatu soil equilibrated at four water:soil ratios. The results indicate that horizons 1 and 3 are supersaturated with respect to calcite at low soil:solution ratios. Horizons 1 and 3 were also found to contain high levels of soluble organics, which are thought to interact strongly with carbonate surfaces (Inskeep, 1986) or possibly create a steady state disequilibrium due to organic matter mineralization (Amrhein, 1987).

Figure 3 is a plot of the equilibrium gypsum saturation index for the seven Mugatu soil horizons. These results suggests that the solubility of Ca^{2+} and SO_4^{2-} species are controlled by gypsum solubility in 2 horizons (5 upper and 5 lower) and that the equilibrium ion activity calculations are able to accurately describe the system. Since the Ca activity seems to be well described in the equilibrium speciation model, we expect that a poor description of either CO_3^{2-} activity or carbonate surface activity is causing a perceived supersaturated state with respect to calcite. In addition to calcite supersaturation, we found several horizons to be supersaturated with respect to barite ($BaSO_4$),ndicating that calcite is not the only slightly soluble mineral whose equilibrium speciation is not well described by solubility constants of the geochemically favored mineral phase and known complexation constants.

B. Selenium Sorption and Coprecipitation on Calcite

Figure 4 is a plot of sorption pH isotherms for selenite and selenate on calcite. As might be expected, selenite sorbs much more strongly than selenate. In fact, selenate sorption was not quantifiable (<10% at all pHs). Selenate is most likely a weakly associated outer-sphere complex on calcite, considering its relative strength of sorption. Partitioning coefficients from our selenite coprecipitation results are listed in Table 1, which also includes partitioning constants for selenite reported by Cowan et al. (1991), Goldberg and Glaubig (1988), and Lipton (1991). Phosphate and nitrate sorption values were also included as a comparison. To compare partitioning constants for sorption and coprecipitation experiments, the following equation was used:

$$Kex = (CO_3^{2-})(MO_z\text{-}X)/(MO_z^{2-})(CO_3\text{-}X) \quad (1)$$

where the activities are related to the solution CO_3^{2-} and metal activity and the surface activity or bulk solid molar ratios, depending on whether the experiments were run as sorption or coprecipitation experiments. Table 1 includes a description of the method used to perform the experiments, which may explain some of the variation among selenite partitioning results from the various authors. Similar selenate coprecipitation experiments were attempted but were too low for quantification.

C. Extended X-Ray Absorption Fine Structure (EXAFS) and X-Ray Absorption Near-Edge Structure (XANES) Studies of Sorption on Calcite

Figure 5 is a plot of the uncorrected Fourier Transforms (FT) of EXAFS data for synthesized calcium selenate (a) and calcium selenite (b). The plots indicate that calcium's second nearest neighbors are visible from Fourier transformed EXAFS and should be detectable in sorption and coprecipitation studies. Figure 6a is a similar EXAFS FT plot of data for pH 7.5 selenate solutions of 100 ppm (Se(VI) equilibrated with calcite. Though the sorption samples seem to indicate possible second-neighbors between uncorrected R-values of 3.2 and 3.6, aqueous selenate has a similar structure. This is also evident in the EXAFS data for the three samples described above, as shown in Fig. 6b. Though some asymmetry in the EXAFS of all samples is evident, especially in the first oscillation, there does not seem to be any significant difference between the EXAFS of the aqueous and sorbed samples.

Figure 7 is the EXAFS FT data for aqueous selenite and two selenite sorption samples. In this case, the inner-sphere structure in the sorption samples is evident in the 10 ppm sorption sample. For the 1000 ppm sorption sample, precipitation of calcium selenite is evident from the peak at the uncorrected R-value of 4, which is related to Se-Se backscatter, and the general similarity in structure to synthesized calcium selenite (Fig. 5b).

Figure 8 is the EXAFS FT data for selenite coprecipitated in different conditions. The structure is clearly different from calcium selenite and some changes in second near-neighbor structure are evident as well. The growth of the peak at the uncorrected R-value of 3.1 seems to correlate with the possible selectivity of selenite for surface sites. A low concentration of Se in solution and high CO_2 concentration leads to a decrease in selenite sorption and higher selectivity; increasing Se in solution and reducing the CO_2 concentration increases selenite sorption and reduces site selectivity.

Figure 9 contains XANES plots for two Ni standards, Ni in solution, Ni sorption, and coprecipitation samples. Though both sorption solutions were supersaturated with respect to the geochemically favored $Ni(OH)_2$ mineral phase, the XANES indicates that the sorbed Ni is neither outer-sphere (compared to the aqueous standard) nor similar to $Ni(OH)_2$. Though the nickelous carbonate is not a crystalline standard, the XANES lineshape of sorbed Ni at both solution concentrations is most similar to it. Coprecipitated Ni has a XANES structure that indicates a different near-neighbor structure than $Ni(OH)_2$ or nickelous carbonate. This would indicate that Ni is forced into a structure that is controlled by the coprecipitating calcite.

Figure 10 contains XANES plots for two Mn standards, Mn in solution, Mn sorption, and coprecipitation samples. During sorption experiments, $Mn(OH)_2$ was the geochemically favored mineral phase. With 5 ppm Mn in solution, we found the Mn XANES of the calcite paste to be indicative of a $MnCO_3$ surface precipitate. With 50 ppm Mn in solution, the Mn XANES of the calcite paste was no longer indicative of a $MnCO_3$ nor a $Mn(OH)_2$ structure. The XANES of Mn

coprecipitated in calcite indicated an altered near-neighbor structure, most likely controlled by the atomic structure of the precipitating calcite.

Though the XANES information indicates structural changes in sorbed and coprecipitated Ni and Mn on calcite, EXAFS analysis will be used to calculate the specific coordination and near-neighbor structure of the metals. EXAFS were collected for these samples, though the results are not discussed here.

D. Testing and Improvement of Trace Metal Quantitative Analysis by Synchrotron X-Ray Microprobe

Figure 11 is a plot of fluorescence results from model samples used to investigate 3-D elemental mapping using Kα/Kβ element fluorescence ratios. These results are highly comparable to experimental data which was described previously (Doner and Zavarin, 1995). The model Sn Kα and Kβ fluorescence difference is unresolvable, while the Cu Kα and Kβ difference is easily resolved within the 200 micrometer overlayer range. Included in this plot is Sn Lα and Lβ fluorescence indicating that, in some cases, an La/Lβ or K/L ratio may be used in the same manner as the Kα/Kβ ratio and, in fact, drastically improves sensitivity of the technique. The mass absorption values used in the model were derived from the empirical equation calculated by Wernisch et al. (1984) from published mass absorption tables by McMaster et al. (1969).

Figure 11 illustrates the potential for using Kα/Kb ratios to determine average depth of elements in heterogeneous samples though the technique's accuracy will be much dependent on the matrix mass absorption at the Kα and Kβ fluorescence energies. We can quantify the sensitivity of this techniques for a simple two-layered system by using the heterogeneous fluorescence equation described elsewhere (Zavarin and Doner, in review). Since the Kα and Kβ fluorescence ratio is of interest, a ratio of the heterogeneous fluorescence at Kα and Kβ energies can be used to quantify the sensitivity of this technique. The values of the constants in the two equations are the same except for the energy of the fluorescence. The resultant equation is:

$$\frac{I_1'(\alpha)}{I_1'(\beta)} = \frac{I_1(\alpha) * e^{-\mu_f'(\lambda_\rho)*\rho_f'*d} * e^{-\mu_f'(\lambda_\alpha)*\rho_f'*d}}{I_1(\beta) * e^{-\mu_f'(\lambda_\rho)*\rho_f'*d} * e^{-\mu_f'(\lambda_\beta)*\rho_f'*d}} \qquad (2)$$

where ρ_f' is the density of the overlayer, d is the thickness of the overlayer, and μ is the sample mass absorption at a particular energy. Equation 2 can be simplified to

$$\frac{I_1'(\alpha)}{I_1'(\beta)} = S * e^{\rho_f*d*(\mu_f(\lambda_\beta)-\mu_f(\lambda_\alpha))} \qquad (3)$$

where S represents that part of the equation which is intrinsic to the relative intensity of Kα and Kβ fluorescence passing through the fluorescing underlayer and the remaining exponential function relates to the contribution of overlayer depth to the Kα/Kβ ratio. If Kα and Kβ are equivalent, or if the overlayer thickness, d, equals 0,

$$S = \frac{I_1(\alpha)}{I_1(\beta)} = \frac{I_1'(\alpha)}{I_1'(\beta)} \tag{4}$$

The depth resolution can be approximated by relating the change in element depth to a detectable change in the Kα/Kβ ratio. Assuming that a 5% change in the Kα/Kβ ratio is detectable and assuming that the matrix mass absorption as a function of energy is smooth and negative between Kα and Kβ energies, then:

$$e^{\rho_f' * d * \left(\mu_f(\lambda_\beta) - \mu_f(\lambda_\alpha)\right)} = 0.95. \tag{5}$$

We can then plot the difference in mass absorption at the Kα and Kβ energies relative to the overlayer thickness at a particular density to understand the sensitivity of this technique for various elements. Figure 12 is a plot of $\mu_f'(\lambda_\alpha) - \mu_f'(\lambda_\beta)$ versus d at the densities of two minerals, hematite (Fe_2O_3) and calcite ($CaCO_3$). Overlain on this plot is the calculated K-shell mass absorption difference for some elements in the first transition metal series as well as Ca, Se, and Sn and the Sn L-shell mass absorption differences. The depth resolution is highest with light elements and decreases with the increasing atomic mass (because the interaction of the fluorescence x-rays with the matrix decreases). The only exception to this trend occurs when the matrix mass absorption switches between K-shell mass absorption and the L-shell mass absorption; this is most evident in the change in depth resolution between Mn and Cu in the Fe_2O_3 matrix. Nevertheless, for most first row transition metals in these light element matrices, the resolution varies between 3 and 25 micrometers (the positioning of the sample at 45 degrees to the beam actually improves the depth resolution by a factor of 0.7). In addition, higher resolution for heavier elements may be possible by using a Lα/Lβ ratio or even a K/L ratio. The K/L ratio may be particularly sensitive though its application would be limited to elements whose K and L-shell fluorescence is detectable and binding energies are within the limits of the x-ray source. It must be noted that no attempt was made to test the element concentration detection limit and that this additional factor will control the experimental detection limit of this technique.

Discussion

A. Macroscopic Analysis of Trace Element Interaction with Calcite

Equilibrium calcite solubility calculations could not describe the solution composition of horizons 1 and 3, while equilibrium solubility calculations for gypsum described the solution composition of the gypsic horizons very well. Soluble trace and minor elements, such as selenite or silicon, as well as organic solutes, may alter or coat the surface of natural carbonates, preventing the surface from catalyzing precipitation of calcite (Inskeep, 1986; Suarez, 1982; Suarez, 1992). Since calcium activity seems to be well described by equilibrium speciation calculations (given that gypsum solubility follows our equilibrium speciation calculations), errors in measuring pH or modeling CO_3^{2-} activity may also have created an apparently supersaturated system.

B. Molecular-Level Organization of Trace Elements in Synthetic Carbonates

Laboratory studies indicated that calcite removes extensive amounts of selenite from solution. Some of the variation in selenite partitioning among the various authors listed in Table 1 is mostly likely due to calcite recrystallization. Calcite recrystallization during sorption experiments would increase the calculated Se partitioning because of continuous formation of new surface sites. This is particularly evident in the data reported by Goldberg and Glaubig (1988), who used high surface area carbonates which are very likely to be affected by recrystallization rates.

Extended X-ray Absorption Fine Structure (EXAFS) data for adsorbed selenite indicated an inner-sphere structure, while selenate seemed to be dominated by an outer-sphere structure. The outer sphere selenate result does not agree with our earlier reports, though it does follow from our pH isotherm results. Some of the inconsistencies between EXAFS results can be explained by our finding that coordination of selenate with Ca^{2+} in solution may create an apparent second near-neighbor structure from $CaSeO_4$ solution complexation or possible multiple scattering effects. In addition, we found selenate salts generally contained 0.3-1% selenite, which has a much higher preference for calcite surface sites and may create an apparent inner-sphere structure in earlier selenate sorption samples.

Selenite coprecipitation experiments indicated that calcite forces selenite into a coordination site which is different from calcium selenite. We also found that calcite may have selectivity-dependent sorption sites, evidenced by the changes in near-neighbor structure with increased selenite loading during coprecipitation experiments. The increased loading of selenite was accomplished by either increasing the Se concentration in solution or decreasing the CO_3^{2-} concentration in solution. This indicates that fits to EXAFS data may result in an average near-neighbor structure due to from at least two possible Se positions in the calcite structure.

Both Ni and Mn were found to form surface precipitate structures on calcite, which are different from thermodynamically favored mineral phases. In particular, Ni XANES indicated a "nickelous carbonate"-like structure while Mn formed a rhodochrosite-like structure at low concentrations and either a mixed or alternate structure at higher concentrations. Coprecipitated Ni and Mn both formed structures which were controlled by the coordination structure of coprecipitating calcite and did not resemble the respective hydroxide or carbonate forms.

C. Microscopic Analysis of Trace Element Deposition in Natural Systems

The fluorescence ratio, (i.e. $K\alpha/K\beta$, $L\alpha/L\beta$, K/L ratios), coupled with x-ray focusing techniques and high flux synchrotron x-ray sources, is a promising technique for 3-D elemental mapping at the micrometer scale. Results from both experimental and theoretical data indicate that resolution in the third dimension can be achieved as low as the micrometer level, though the matrix composition, element of interest, and intensity of the source will control the achievable resolution. Although this study concentrated on the application of $K\alpha/K\beta$ ratios to 3-D elemental analysis, $L\alpha/L\beta$ and K/L ratios may also be used in the same manner and improve resolution, particularly for heavier elements.

Acknowledgments

We wish to thank the many people involved in this research project. Hau-Wai Wong conducted most of the solubility experiments. We wish to especially thank Andrea Foster, as well as others in Gordon Brown's research group, for assistance in running our first samples at SSRL and assistance with the EXAFSPAK (George, 1993) and FEFF (Rehr, 1992) software. Some data analysis was also performed with UWEXAFS software.

References

Amrhein, C., and D. L. Suarez. 1987. Calcite supersaturation in soils as a result of organic matter mineralization. Soil Sci. Soc. of Am. J., 51:932-937.

Cowan, C. E., J. M. Zachara, and C. T. Resch. 1991. Solution ion effects on the surface exchange of selenite on calcite. Geochim. et Cosmochim. Acta, 54:2223-2234.

Doner, H. E., and Mavrik Zavarin. 1995. Factors influencing sorptive properties of carbonates for trace elements in soils, Kearney Foundation of Soil Science Annual Report.

George, G. 1993. EXAFSPAK. Stanford Synchrotron Radiation Laboratory, Stanford.

Goldberg, S., and R. A. Glaubig. 1988. Anion sorption on a calcareous montmorillonitic soil - selenium. Soil Sci. Soc. of Am. J., 52:954-958.

Griffin, R. A., and J. J. Jurinak. 1974. The interaction of phosphate with calcite. Soil Sci. Soc. of Am. Proc., 37:847-850.

Inskeep, W. P., and Paul R. Bloom. 1986. Calcium carbonate supersaturation in soil solutions of calciaquolls. Soil Sci. Soc. of Am. J., 50:1431-1437.

Jurinak, J. J., and Robert A. Griffin. 1972. Nitrate ion adsorption by calcium carbonate. Soil Science, 59:1499-1504.

Lipton, D.S., 1991. Associations of selenium with inorganic and organic constituents in soils of a semi-arid region, Ph.D. Dissertation. University of California, Berkeley.

McMaster, W. H., N. Kerr Del Grande, J. H. Mallett, and J. H. Hubbell. 1969. Compilation of x-ray cross sections. UCRL-50174, Sec. II, Rev. 1, Lawrence Radiation Laboratory, University of California, Livermore.

Papelis, C., Kim F. Hayes, and James O. Leckie. 1988. HYDRAQL: A program for the computation of chemical equilibrium composition of aqueous batch systems including surface-complexation modeling of ion adsoprtion at the oxide/solution interface. Technical Report No. 306, Environmental Engineering and Science Department of Civil Engineering, Stanford University, Stanford, CA.

Rehr, J. J., S.I. Zabinsky, and R. C. Albers. 1992. High-order multiple scattering calculations of x-ray absorption fine structure. Phys Rev. Let., 32:3397-.

Suarez, D. L., and J. D. Rhoades. 1982. The apparent solubility of calcium carbonate in soils. Soil Sci. Soc. of Am. J., 46:716-722.

Suarez, D. L., J. D. Wood, and I. Ibraim. 1992. Reevaluation of calcite supersaturation in soils. Soil Sci. Soc. of Am. J., 56:1776-1784.

Underwood, J., H., Troy W. Berbee, Jr., and C. Frieber. 1986a. X-ray microscope with multilayer mirrors. Applied Optics, 25:1730-1732.

Underwood, J. H. 1986b. High-energy x-ray microscopy with multilayer reflectors. Reviews of Scientific Instruments, 57(8):2119-2123.

Wernisch, J., C. Pohn, W. Hanke, and H. Ebel. 1984. X-Ray Spectrometry, 13: 180.

Zavarin, Mavrik, and Harvey E. Doner. (in review). A novel technique for 3-D elemental mapping by synchrotron x-ray microprobe.

Table 1. Anion sorption partitioning coefficients for calcite.

Element	Method	Kex	Kex high	Kex low	Reference
SeO_3	Pre-equilibrated sorption	0.28	0.43	0.12	Cowan et al., 1991
SeO_3	Seed coprecipitation	0.42	0.29	0.54	present investigation
SeO_3	High surface calcite sorption	3.0	5.0	1.0	Goldberg and Glaubig, 1988
SeO3	Non-equilibrated sorption	2.3	2.6	2.0	Lipton, 1991
SeO_3	Co-precipitation w/o seed	0.0042	0.0056	0.0028	Lipton, 1991
PO_4	Non-equilibrated sorption	3.5	6.0	1.0	Griffin and Jurinak, 1974
NO_3	High surface calcite sorption	0.025	0.040	0.010	Jurinak and Griffin, 1972

$Kex = (CO_3^{2-})(MO_z\text{-}X)/(MO_z^{2-})(CO_3\text{-}X)$
Ion activities used when possible, otherwise concentration was substituted.
Activities of bound metals are in terms of either mol/m^2 or mol/g precipitate.

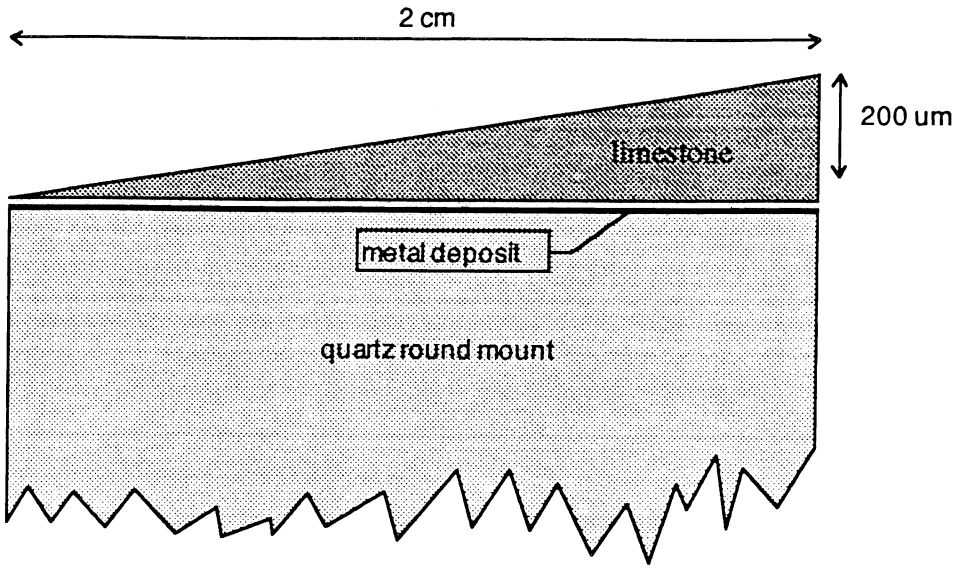

Figure 1. A cross-section of prepared samples used to test 3-D elemental mapping by the synchrotron x-ray microprobe fluorescence ratio method.

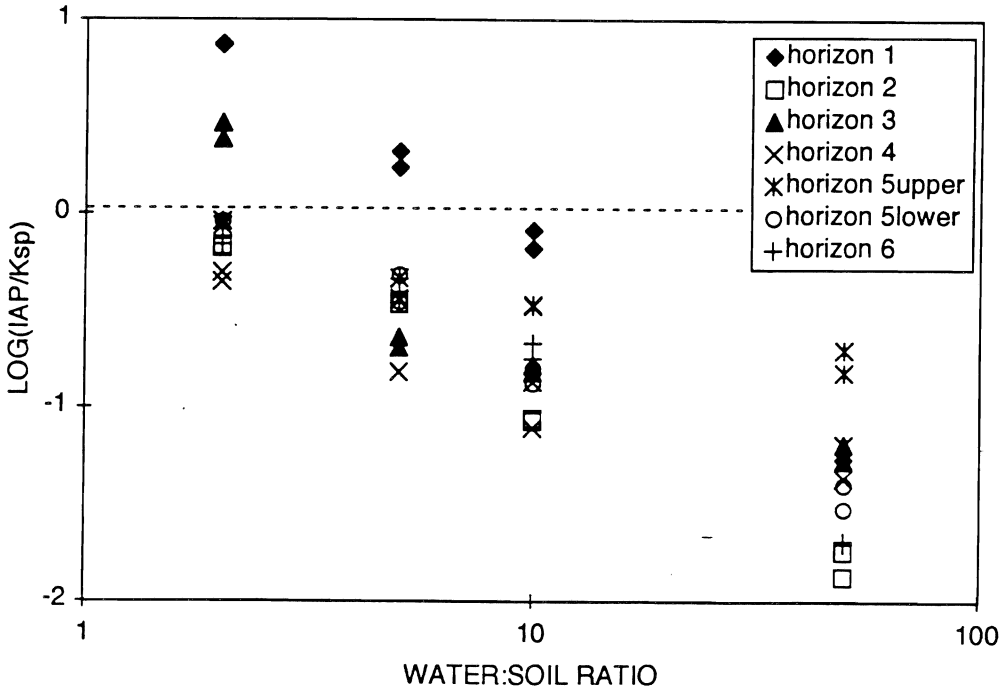

Figure 2. Calcite saturation index (S.I. = log(IAP/Ksp)) versus extract dilution ratio for seven horizons of the Mugatu soil.

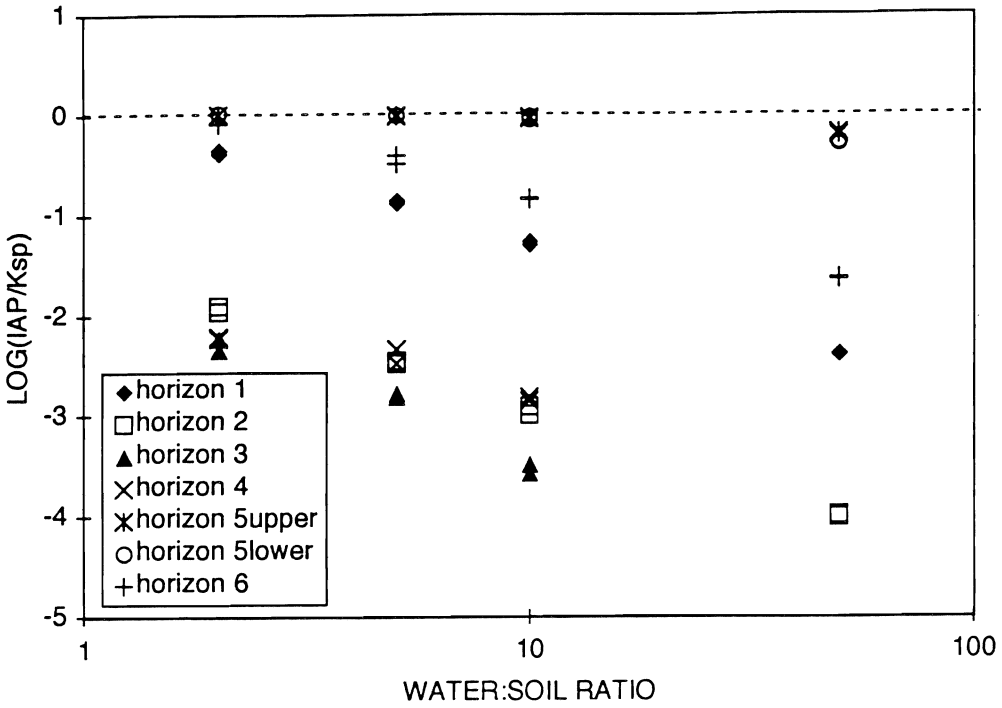

Figure 3. Gypsum saturation index versus extract dilution ratio for seven horizons of the Mugatu soil.

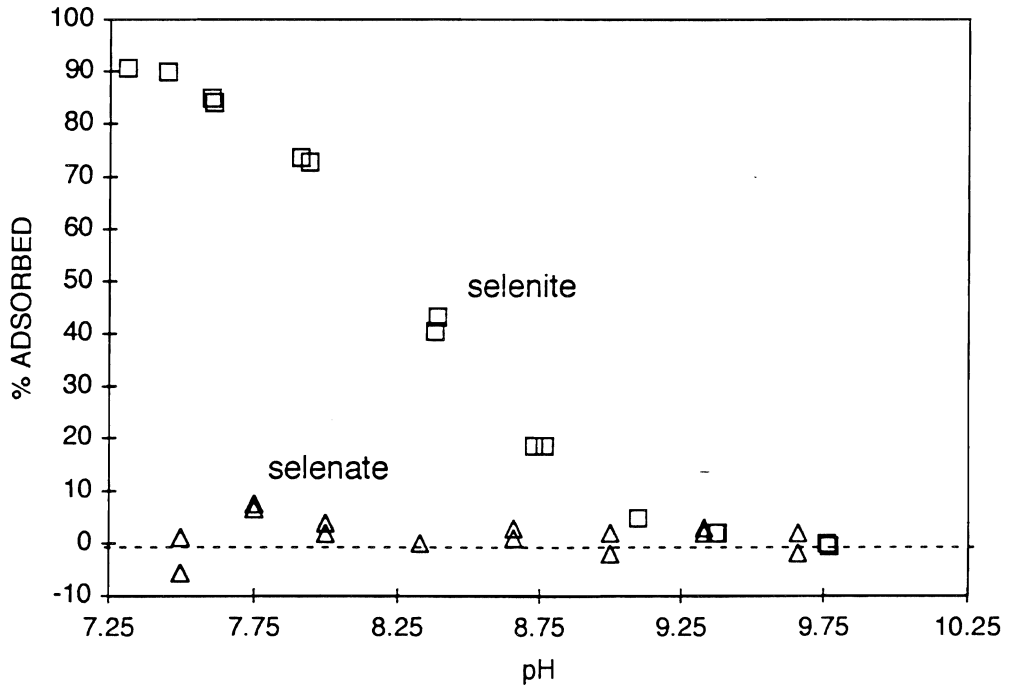

Figure 4. pH isotherms of selenate and selenite in 0.1 M ionic strength calcite equilibrated solutions. The y-axis is percent absorbed relative to a 100 ppb Se starting solution.

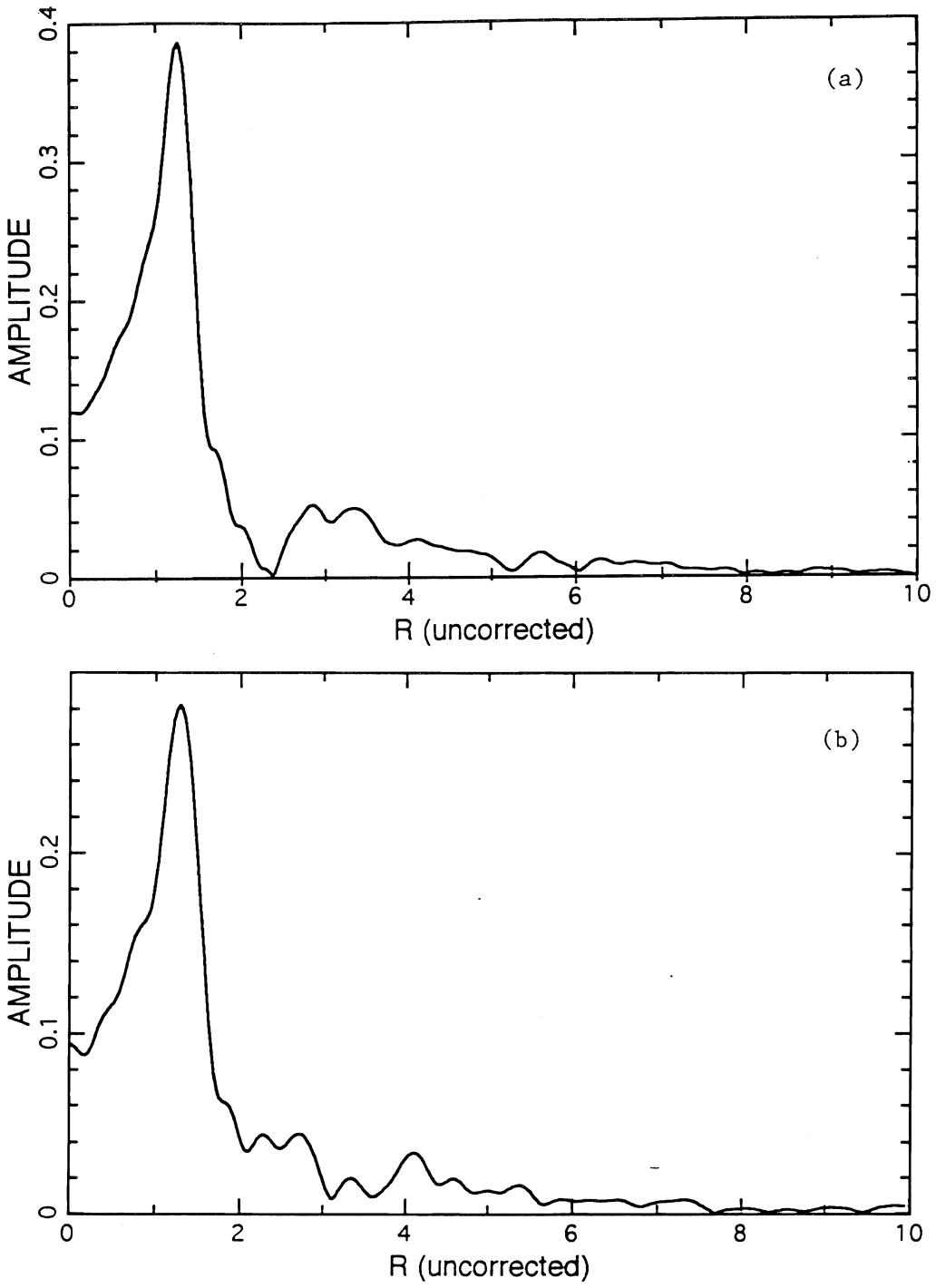

Figure 5. EXAFS Fourier transformed data of synthesized (a) calcium selenate and (b) calcium selenite.

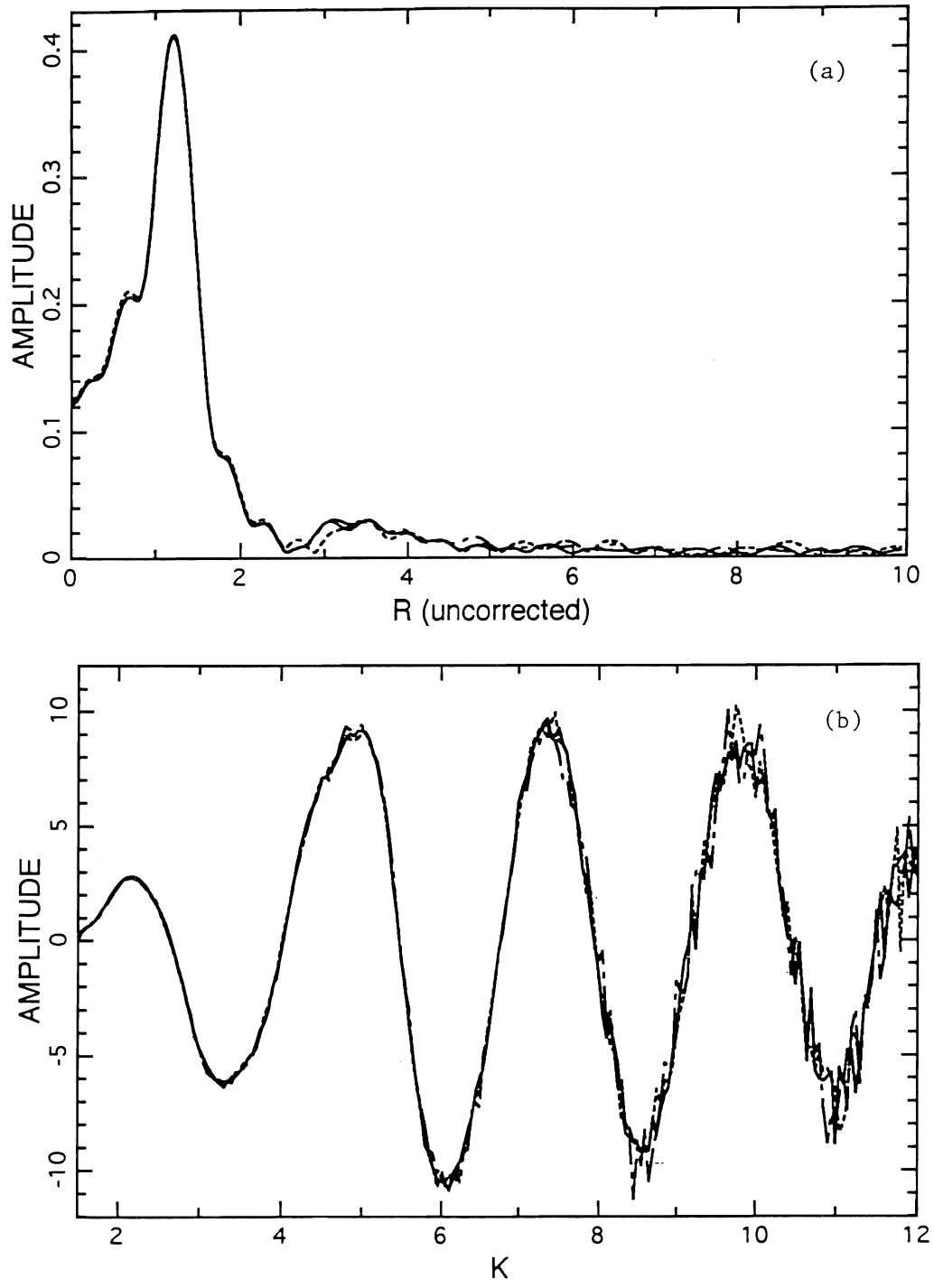

Figure 6. Plots for selenate solution (- - - - - -), selenate sorbed on calcite from 100 ppm solution (– – - - - – –), and selenate sorbed on calcite from 1000 ppm solution (_____): (a) EXAFS Fourier transformed data and (b) EXAFS data. All solutions were at pH 7.5 during experiments.

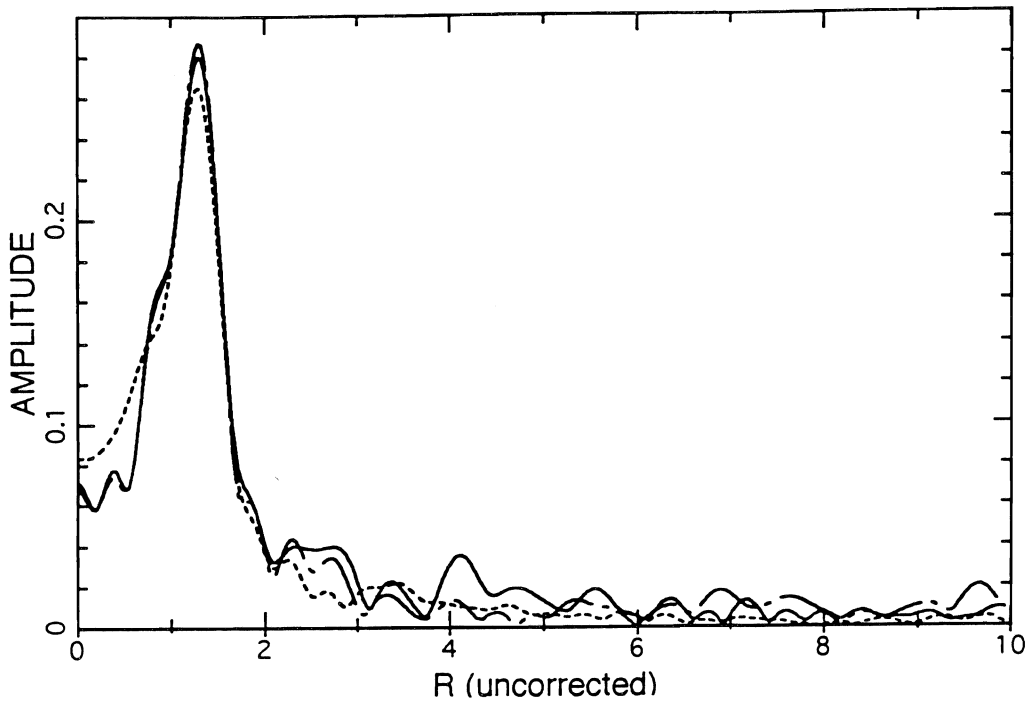

Figure 7. EXAFS Fourier transformed data of - - - - selenite solution, – – – – selenite sorbed on calcite from 100 ppm Se solution, and ——— selenite sorbed on calcite from 1000 ppm Se solution. All solutions were at pH 7.5 during experiments.

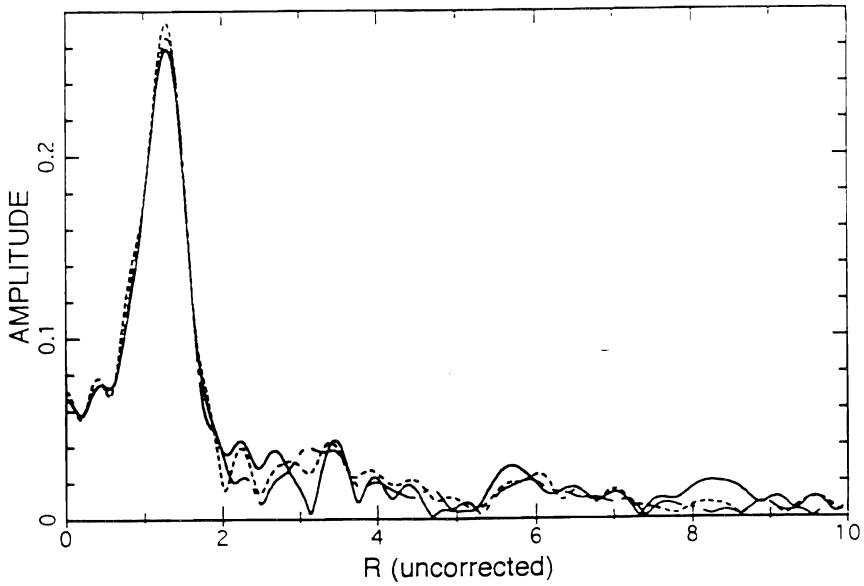

Figure 8. EXAFS Fourier transformed data of ——— 1 ppm solution Se, 0.24% CO_2, coprecipitate, – – – – 10 ppm solution Se, 0.24% CO_2, coprecipitate, and - - - - 10 ppm solution Se, 0.033% CO_2, coprecipitate. All solutions were at pH 7.5 during experiments.

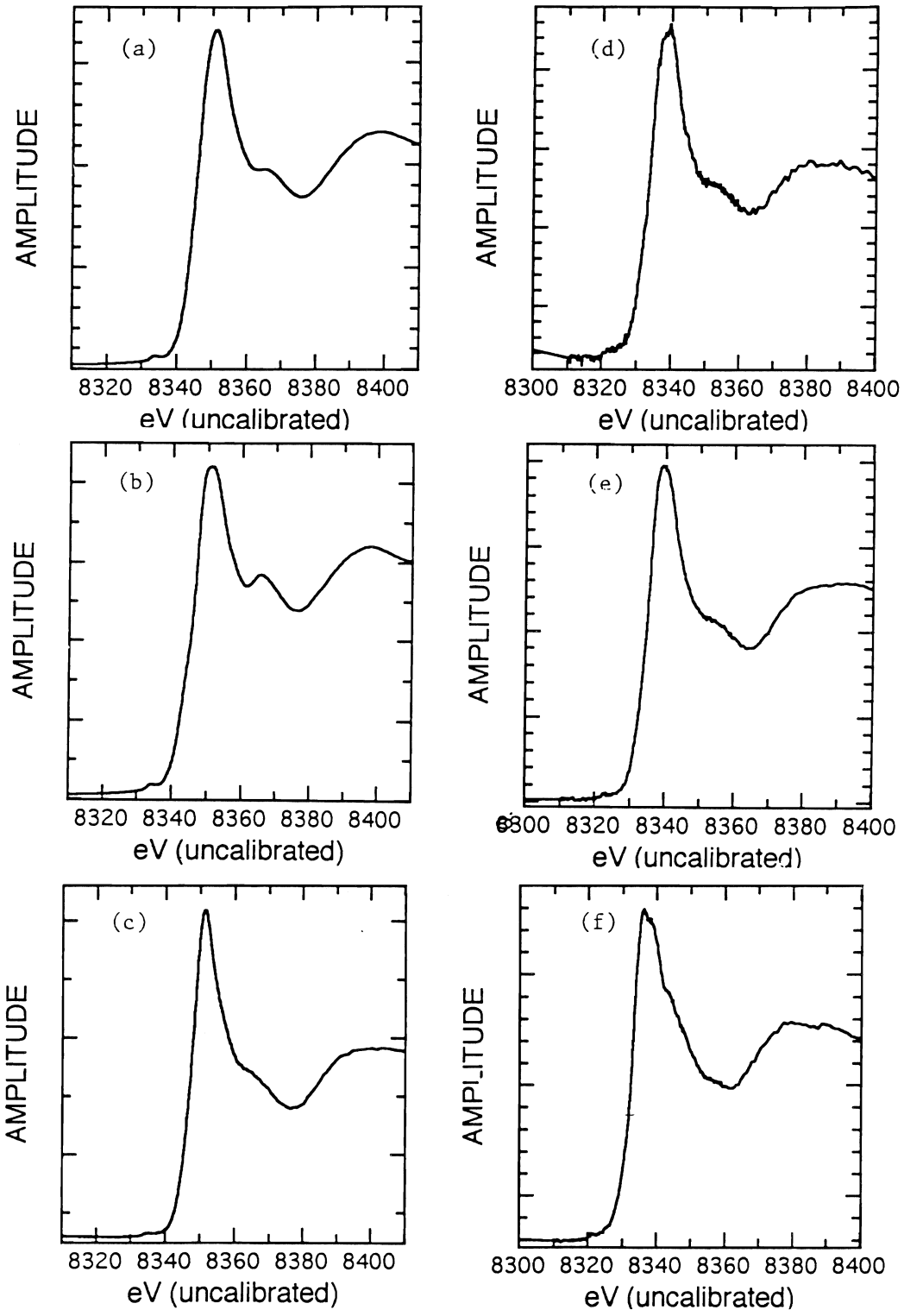

Figure 9. XANES data from (a) nickelous carbonate, (b) $Ni(OH)_2$, (c) aqueous Ni, (d) Ni sorbed on calcite from 5 ppm Ni solution, (e) Ni sorbed on calcite from 50 ppm Ni solution, and (f) Ni coprecipitated in calcite at 500 ppb Ni in solution. All solutions were at pH 7.75 during experiments.

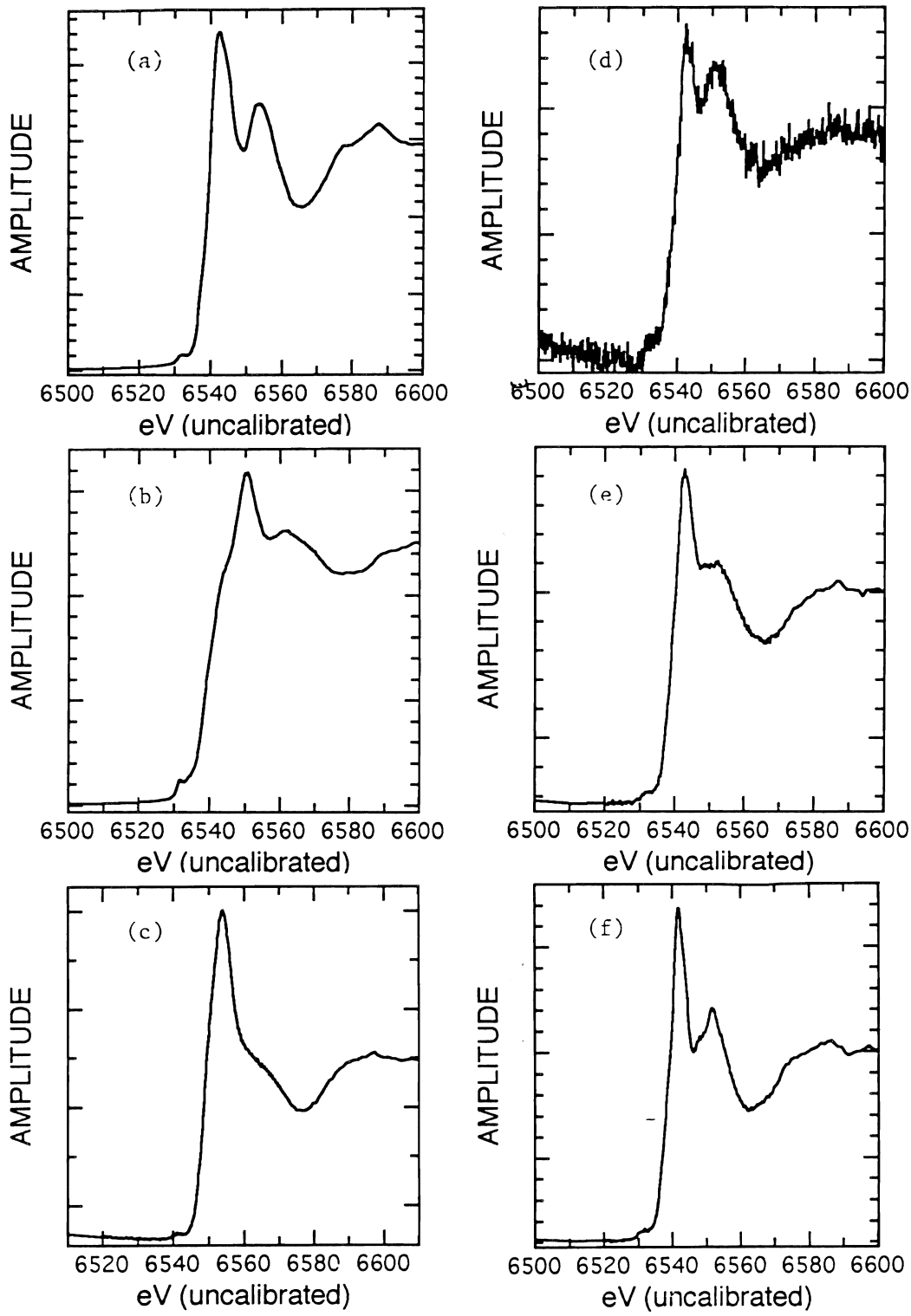

Figure 10. XANES data from (a) rhodochrosite, (b) $Mn(OH)_2$, (c) aqueous Mn II, (d) Mn II sorbed on calcite from 5 ppm Mn II solution, (e) Mn sorbed on calcite from 50 ppm Mn II solution, and (f) Mn coprecipitated in calcite at 500 ppb Mn in solution. All solutions were at pH 7.75 during experiments.

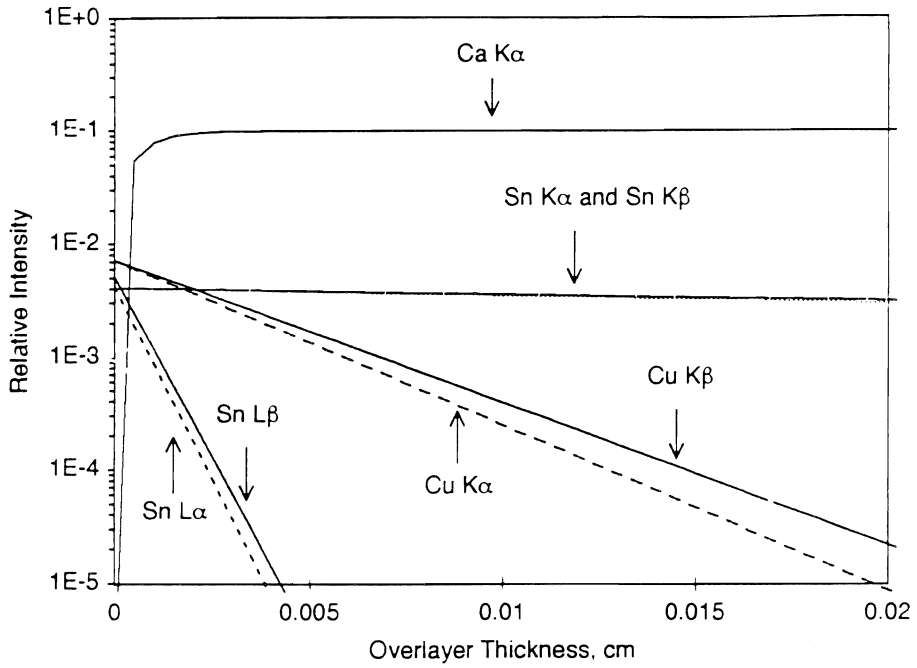

Figure 11. Relative fluorescence versus calcite overlayer thickness for modeled calcite wedges with Cu and Sn metal deposits.

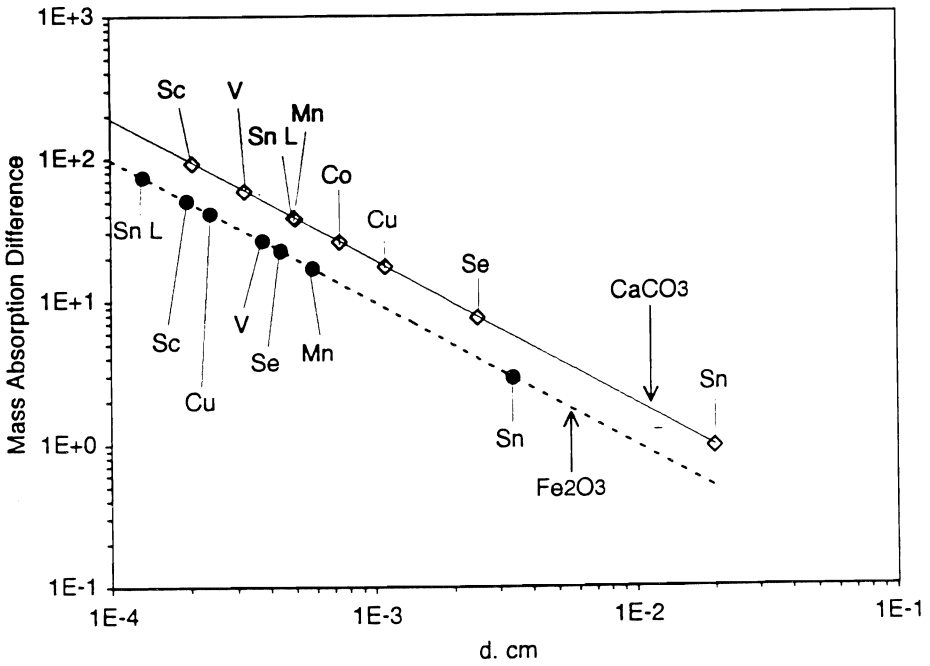

Figure 12. Calculated depth resolution limits (x-axis) for a set of elements in a $CaCO_3$ and Fe_2O_3 matrix. All resolution determinations were carried out using a Kα/Kβ ratio except Sn L shell which is related to Sn Lα/Lβ ratio.

The Effects of a Hydrophobic Soil Layer on the Development of Unstable Flow

J. LETEY, MARCIA CARRILLO, AND SCOTT YATES
Department of Soil and Environmental Sciences, Riverside Campus

Summary

The movement of water through the vadose zone has been found to occur preferentially through certain paths in some soils. The preferential flow can reduce degradation of chemicals and enhance chemical transport to the groundwater. Preferential flow paths can be caused by the presence of macro pores and inclined barriers, and the occurrence of unstable wetting fronts. This project investigated experimentally the effects of a hydrophobic layer near the soil surface on the development of unstable flow. Laboratory experiments were conducted in a specially built Plexiglas rectangular chamber in which effects of hydrophobic soil layers on creating unstable flow were investigated. The development of unstable flow was found to be a function of the water breakthrough pressure of the hydrophobic soil layer, depth of the layer, and depth of ponded water at the surface. The ratio of total water head above the layer to the breakthrough pressure was a determining factor in predicting the development of unstable flow. The greatest degree of instability occurred when that ratio was slighted greater than 1 and decreased as the ratio got larger. The hydraulic conductivity of the hydrophobic soil increased as the depth of water on the surface increased. This was caused by increase in water content in the hydrophobic soil as the depth of ponded water increased. This phenomenon differs from the behavior of wettable soils.

Key Words: preferential flow, breakthrough pressure, hydraulic conductivity, water repellence, infiltration.

Project Objectives Addressed in 1995-1996

1. Determine the effects of degree of hydrophobicity, location and thickness of the hydrophobic layer, and waterflow boundary conditions on the development of unstable flow.

2. Test the validity of the proposed theory on conditions that lead to unstable flow in soil systems.

Research Plan and Procedures

The experiments were conducted on two sandy soils obtained from a field at the University of California Research Station located in Coachella Valley, California. The two sands will be designated as sand 1 for the coarser sand and sand 2 for the finer sand. These sands were made hydrophobic by two methods. In one case various amounts of octadecylamine were applied to the sands. Each sand was treated by mixing 200 g of soil and 100 ml of water containing 0.06, 0.10, and 0.14 g of octadecylamine for sand 1 and 0.20, 0.21, and 0.22 g of octadecylamine for sand 2. The sand-solution mixtures were shaken for 12 hours and then dried at 70°C. The second procedure involved treating sand 1 with solvent extracts of peat moss using ethanol or benzyl alcohol. The extracts were made by mixing 200g of peat with 1.5 L of either solvent. The peat-solvent mixtures were shaken for 24 hours and then filtered through a number 3 Whatman filter. One thousand grams of sand 1 were mixed both with 250 ml and 500 ml of the filtered ethanol extract and with 250 ml of the filtered benzyl alcohol extract. The ethanol extract treated soils were dried under the hood for 24 hours and the benzyl alcohol treatments were dried in 100° C for 72 hours. The octadecylamine created a very stable hydrophobic material which supported a water drop infinitely without penetration. The peat extracted treated materials were less stable and created different water drop penetration times.

A device was designed to measure the pressure required to force water into the hydrophobic sand. This pressure will be referred to as the breakthrough pressure (H_p) and characterized by the height of water that could be supported on the sand surface without water penetration.

Another method of measuring the degree of hydrophobicity was measuring the 90° surface tension. This was accomplished by mixing alcohol and water to different ratios to create a range of surface tensions. The 90° surface tension is the surface tension of the solution which results in water penetration of the sand in five seconds.

The theoretical relationship between the breakthrough pressure and 90 degree surface tension was found to be valid. The breakthrough pressure is dependent both on the degree of hydrophobicity and the effective pore radius of the medium. On the other hand, the 90 degree surface tension is dependent entirely on the degree of hydrophobicity.

A chamber was constructed to measure the effect of a hydrophobic layer on the creation of unstable flow. The chamber was constructed of Plexiglas so that water flow through the soil being tested could be visually observed. The Plexiglas chamber walls were 56 cm wide and 61 cm deep. The rectangular front and back Plexiglas wall plates were 2 cm apart and held together by end plates. The bottom of the chamber was constructed of 60 mesh stainless steel screen mounted on a 0.16 cm thick perforated metal plate for support.

A procedure employing a sand randomizer was developed to minimize layering and sand particle size segregation as the chambers were packed with the sand. The sand randomizer had the same dimensions as the chamber except that it contained two coarse wire mesh grades at 10 cm and 20 cm from the bottom of the extension. These grates randomized the sand as it fell through the extension into the chamber. It lines up on top of the test chamber during packing. Once the sand randomizer was in place, the sand mix was poured evenly into the extension. As the sand passed through the wire screens and fell into the chamber, it rose evenly in the chamber, thus avoiding microlayering.

The chamber was first filled with untreated sand to a given depth. A 1-cm hydrophobic layer was then placed on top of it and covered with untreated sand.

Once the chamber was packed, it was leveled and the water application system placed on the top of the chamber. Water was rapidly and uniformly applied by placing the necessary quantity of water in a specially built tray whose width was equal to that of the chamber. The lip of the tray was placed over the front part of the chamber and water was rapidly poured into the chamber. A constant head was maintained by applying water to the top of the chamber with a pressurized water application system.

Water movement through the sand was recorded using a Panasonic video camera. The video images were digitized using a Jandel Imaging analysis system and analyzed for finger width velocity and percent area wetted by fingers. The flow rate into the chamber was measured by a flow meter connected in-line to the pressurized water application system. The flow rate data were collected by connecting the output signal of the flow meter to a data logger data acquisition system and downloaded to a personal computer for storage.

The following variables were investigated as to their effect on finger formation in this study. Hydrophobic sands with H_p values of 4.0 and 8.1 cm of water were used. Placement of the hydrophobic layer depth, L, of 0, 5, and 15 cm below surface were used. The depth of the ponded water, H_0, had values ranging between 1.5 and 10 cm of water.

In a separate experiment, the steady state water flux of water through a 5 cm hydrophobic layer was measured as a function of ponded water depth. This was done by filling a ten cm diameter plastic column with hydrophobic sand to a

bulk density of 1.41 g/cm^3 . The bottom of the column was covered with a wire screen to hold the sand. Prior to each measurement, the inside of the column was treated with Teflon lubricant to prevent water from preferentially flowing down the column wall. Water was added and maintained at a specific height and the steady state water flux measured. After each experiment, the stand was removed, weighed, dried at 105°C for 24 hours, and reweighed to calculate the volumetric water content. The hydraulic conductivity was calculated using the water flux and the hydraulic head gradient measurements.

Results

A summary of the results is presented in Table 1. Figures 1, 2, and 3 illustrate the water flow patterns observed in 6 of the experiments. No water flowed through the hydrophobic layer until H_0+ L was greater than H_p. In general, finger formation was most pronounced when H_0+L was slightly greater than H_p. When H_0+L was much greater than H_p, stable water flow was observed. The effect of the ratio $(H_0+L)/H_p$ on finger formation is illustrated in Fig. 4. For $(H_0+L)/H_p$ values between 1 and 1.5, fingering in water flow occurred and for values exceeding 1.5, there was stable flow.

At the end of each experiment, the chamber was taken apart and the hydrophobic layer examined. As (H_o+L) increased, the layer became wetter across its entire width (Fig. 3). For experiment 8 which had only a few fingers, the layer was dry except in a few areas where water was observed to penetrate (Fig. 2).

The hydraulic conductivity of the hydrophobic layered sand material was measured in a separate column. The hydraulic conductivity was measured for different values of water depth (H_o) placed at the top of the column. After steady state flow was established, the hydraulic conductivity was calculated using the water flow values and the hydraulic head gradient. A wettable porous media has hydraulic conductivity independent of H_o. However, in the water repellent materials, the hydraulic conductivity increased with hydraulic head (Fig. 5). The water content in the sand was measured at the end of each run. The water content increased with increasing values of H_o. The plot of the hydraulic conductivity and flow rate through the column is illustrated as a function of volumetric water content in Figure 6. Note that the hydraulic conductivity and flux decrease as the water content decreases consistent with well established water flow principles through porous media.

In summary, the increased hydraulic head caused the sand to wet up to higher volumetric water contents which allowed for higher conductivity of water. This behavior is consistent with what would be based upon the capillary rise equation

$$h = 2\gamma \cos\theta / \rho g r \qquad (1)$$

where

h is the height of rise
r is the pore radius
g is gravitation constant
γ is solution-air surface tension
ρ is solution density
θ is contact angle

As the pore radius (r) bec omes smaller, a larger head (h) is required to force water into the capillary tube. Therefore, in a porous media with a mixture of pore radiuses, a low value of h only wets the large pores, thus we get the relationship between increasing sand water content with increasing values of h.

Previous research by other investigators has documented that unstable flow can occur when a media of lower hydraulic conductivity overlies a media of higher hydraulic conductivity. In our experiments, the hydrophobic layer created a restricted hydraulic conductivity as compared to the lower hydraulic conductivity media. This caused the fingering. However, as the value of H_o plus L increased, the hydraulic conductivities through the hydrophobic layer increased such that the hydraulic conductivity of the upper layer became comparable with the lower layer and ingering in the lower layer disappeared..

The sand that had been treated with peat extracts had similar but different results then the more stable hydrophobic sand. The extracts caused the soil to initially repel water and have an H_p value. However, after exposures to water for some time, the sand material wet up. The water drop penetration time, WDPT, was used to characterize the stability of its water repellency.

The same type of water flow experiments were run as previously described for octadecylamine treated sands. The results are summarized in Table 2. The time for water to penetrate the water repellent layer was most affected by WDPT. For a given value of WDPT, the time for water to penetrate the water repellent layer was related to $H_o + L$ as was the case for the stable hydrophobic layer. The main point is that water eventually penetrated the water repellent layer regardless of H_o or L.

The WDPT had a significant influence on finger formation. The WDPT of 150 minutes tended to have more fingers that were persistent in time and space than the lower values of WDPT. The lower WDPT soil formed fingers but they tended to converge with time and depth. Also the fingers once formed tended to widen with time. For all cases, the lower the WDPT and the larger the ratio $(H_o + L)/H_p$ the wider and faster the fingers and in some case no finger developed.

The water flux into the chamber increased with time in all cases (Fig. 7). In all cases, the flux increased with time and then plateaued. The rate of the flux increased and steady state flux both increased as the ratio $(H_o + L)/H_p$

increased. These characteristics are attributed to finger formation in the lower layer with time. As more and more fingers form in the lower layer, the flux to the chamber increased. Furthermore, the velocity and width of finger increased with increasing head above the layer. For the highest $(H_o + L)/H_p$ value, o the fingers formed quickly, tended to be wide and spread fast, and eventually filled the entire chamber. The water flux in the chambers for experiment 3 through 6 are not reported in detail but show similar results.

Table 1. The effect of depth of water ponding, H_o, depth of hydrophobic layer, L; and breakthrough pressure H_p, on finger formation and average water flow rate, J.

Exp. No.	H_o	H_p	L	No. of fingers formed	J
	----------cm----------				cm/sec
1	6	4.0	0	5	.19
2	5	4.0	5	0	>.31
3	5	4.0	15	0	>.31
4	9	8.1	0	3	-
5	8	8.1	5	W**	.19
6	1.5	8.1	5	NP*	0
7	4	8.1	5	7	.03
8	3.5	8.1	5	2	.03
9	5	8.1	5	6	.05
10	7	8.1	5	4	.14
11	10	8.1	5	W**	>.31
12	5	8.1	15	0	>.31

* Water did not penetrate hydrophogic layer
**Wetting front was wavy.

Table 2. The effect of depth of water ponding, H_o; depth of water repellent layer, L; breakthrough pressure, H_p; and Water Drop Penetration Time, WDPT; on the time of water to penetrate the water repellent layer, t_p.

Expt. No.	H_o	L	H_p	WDPT	t_p
	----------cm----------			min.	sec.
1	1.0	0	2.5	1	0
2	2.0	3	2.5	1	0
3	2.5	0	4.0	10	35
4	5.0	0	4.0	10	5
5	2.0	3	4.0	10	8
6	3.0	3	4.0	10	3
7	2.5	0	4.0	150	352
8	5.0	0	4.0	150	48
9	2.0	3	4.0	150	40
10	3.0	3	4.0	150	6

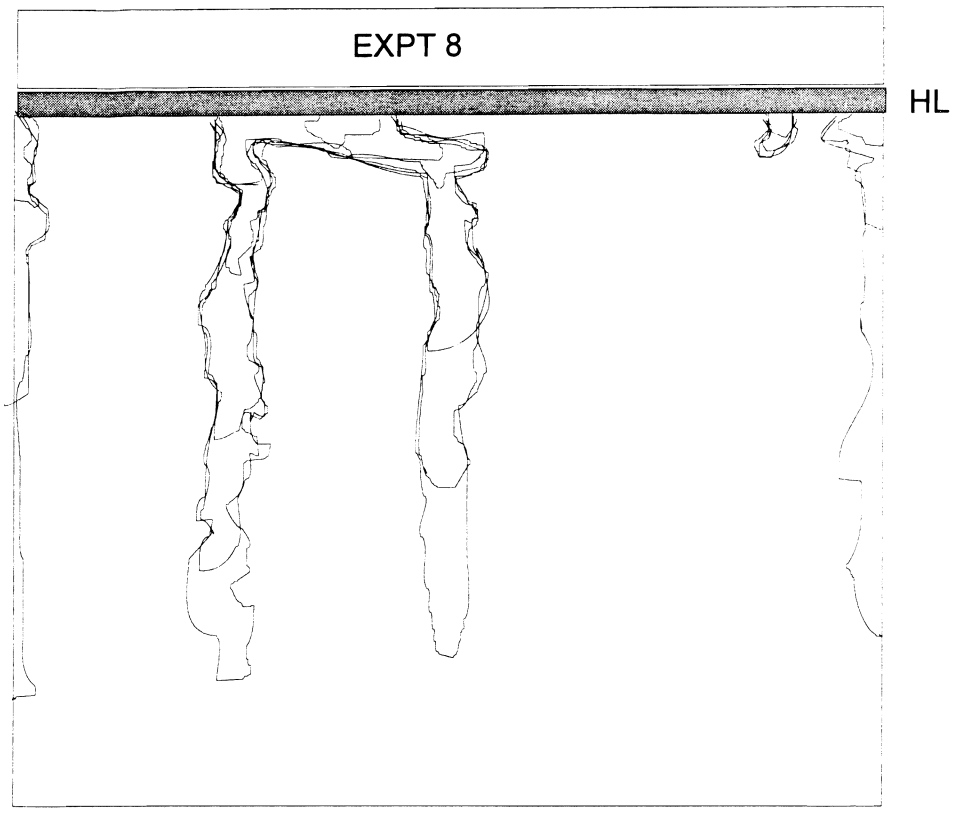

(a)

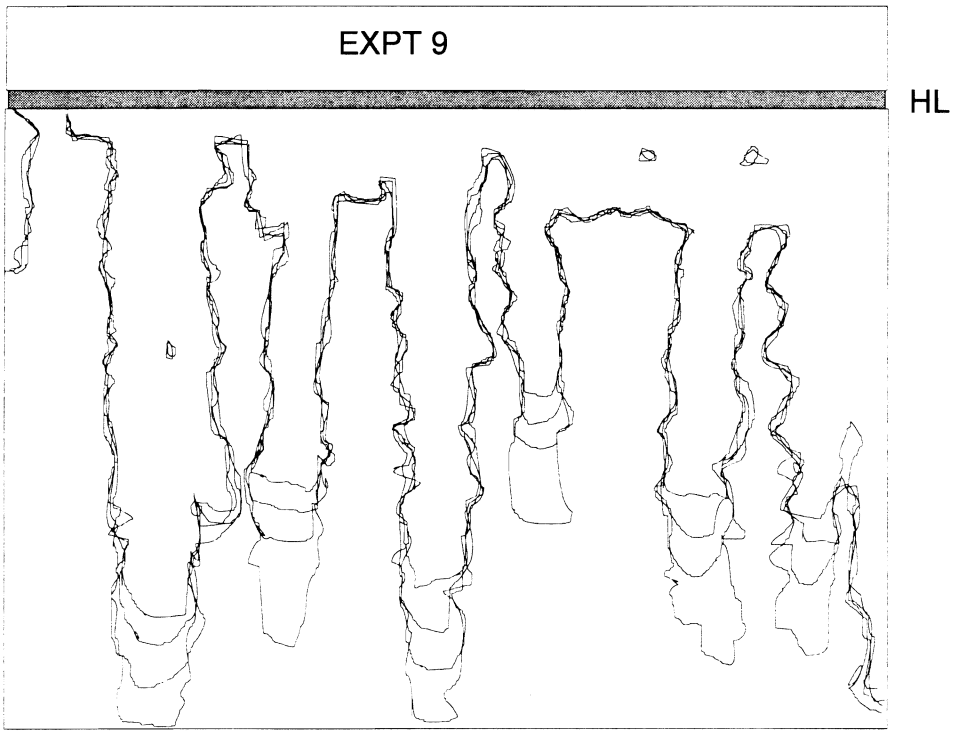

(b)

Figure 1. Infiltration studies: (a) $h_o = 3.5$, $L = 5$, $h_p = 8.1$; (b) $h_o = 5$, $L = 5$, $h_p = 8.1$ HL = Hydrophobic Layer.

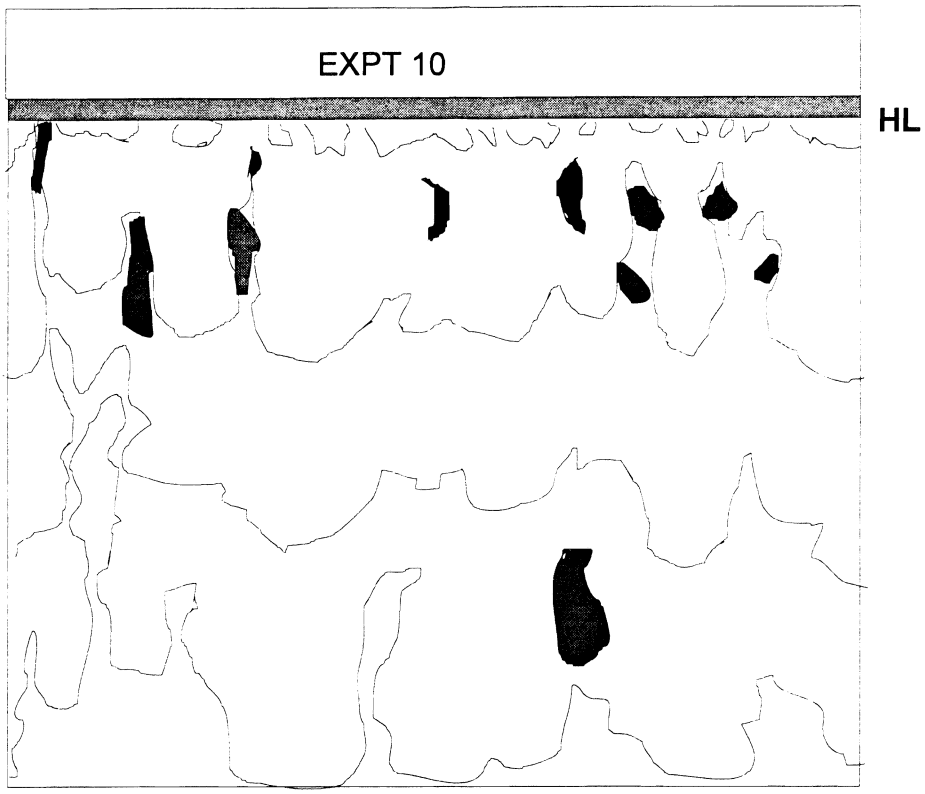

(a)

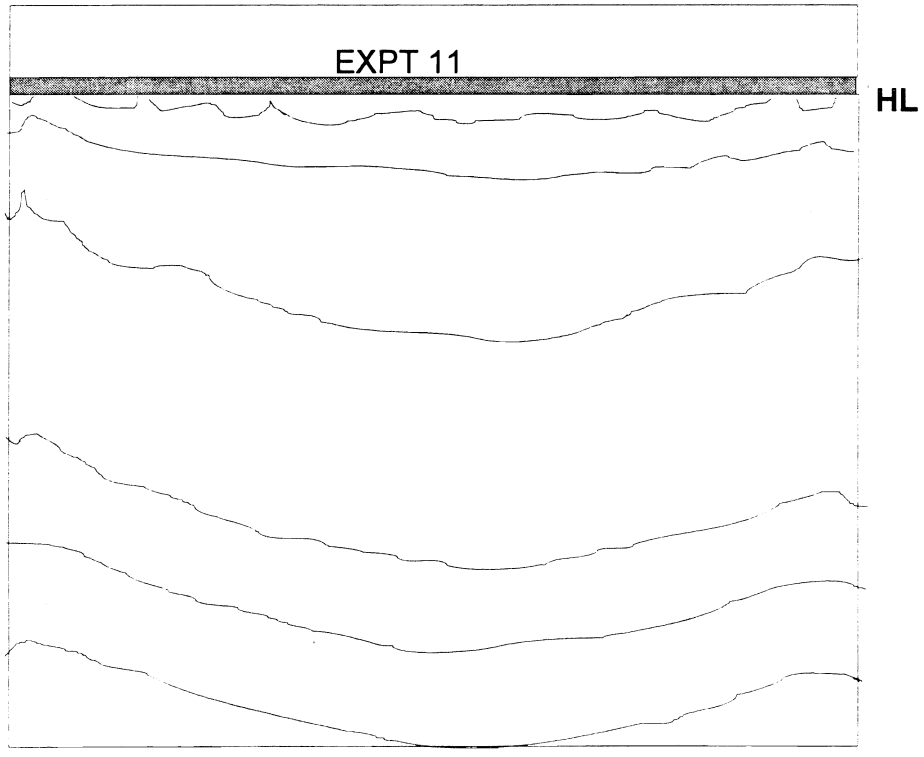

(b)

Figure 2. Infiltration studies: (a) $h_o = 7$, $L = 5$, $h_p = 8.1$; (b) $h_o = 10$, $L = 5$, $h_p = 8.1$ HL = Hydrophobic Layer.

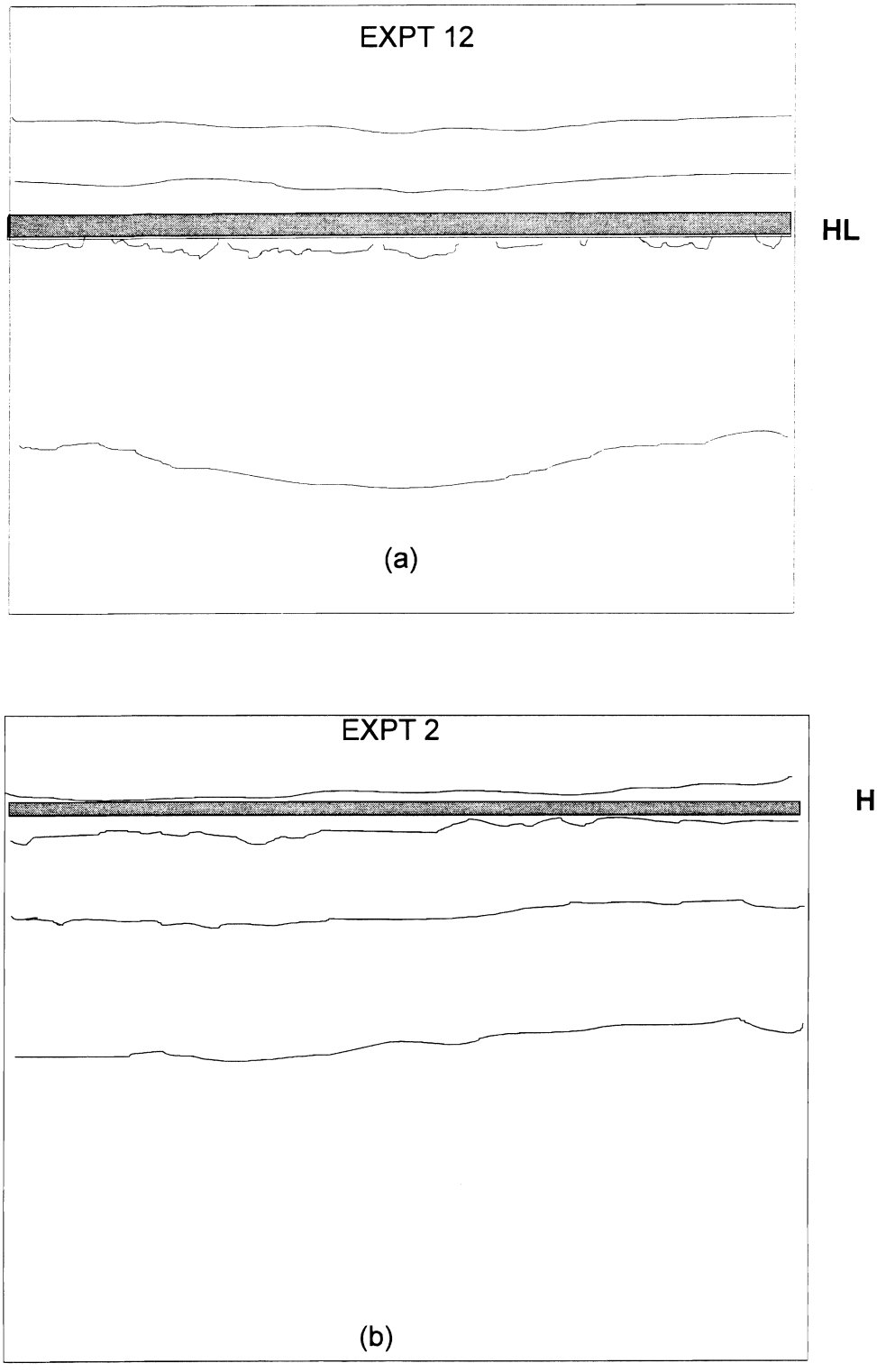

Figure 3. Infiltration studies: (a) $h_o = 5$, $L = 15$, $h_p = 8.1$; (b) $h_o = 5$, $L = 5$, $h_p = 4.0$ HL = Hydrophobic Layer.

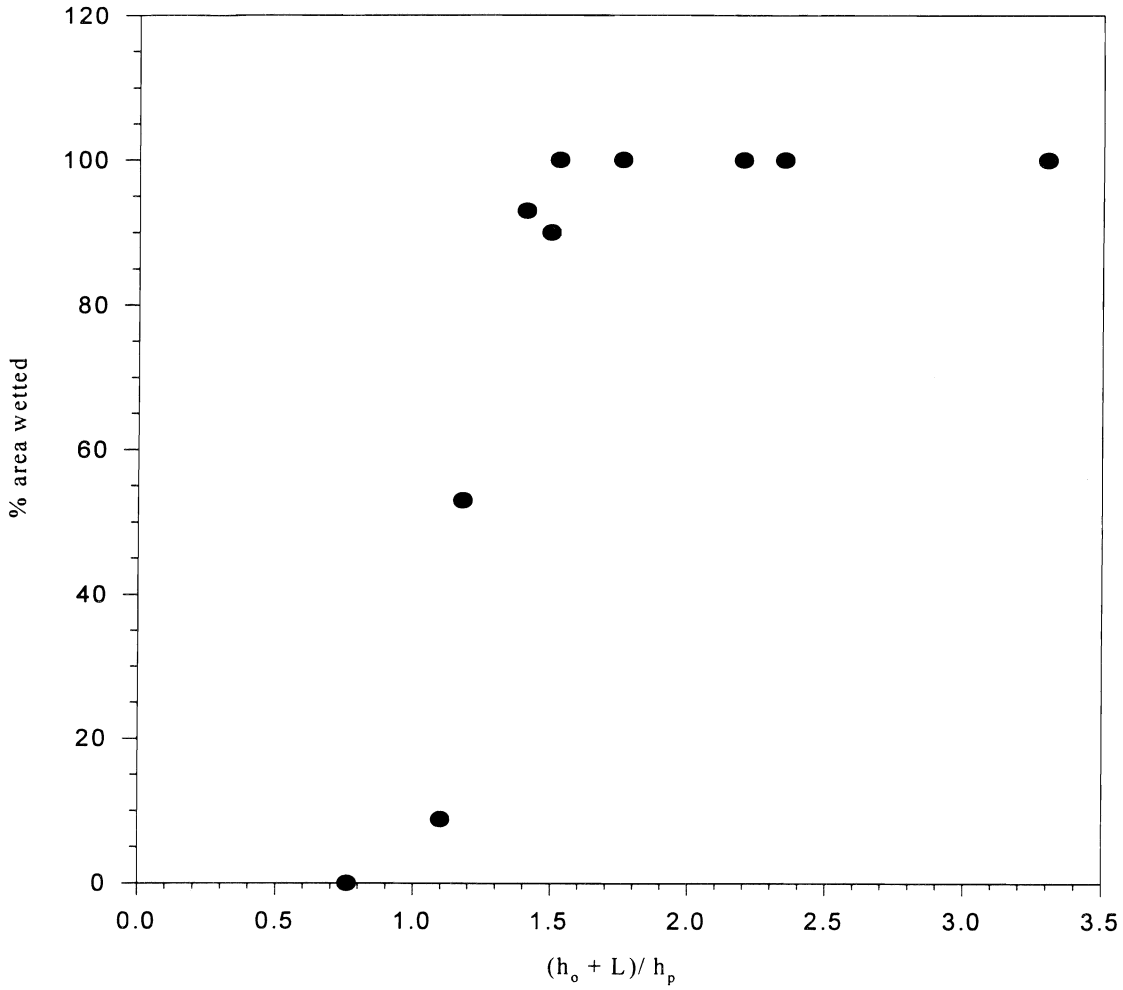

Figure 4. Effects of increasing the ratio$(h_o+L)/h_p$ on fraction of area wetted in a wettable sublayer.

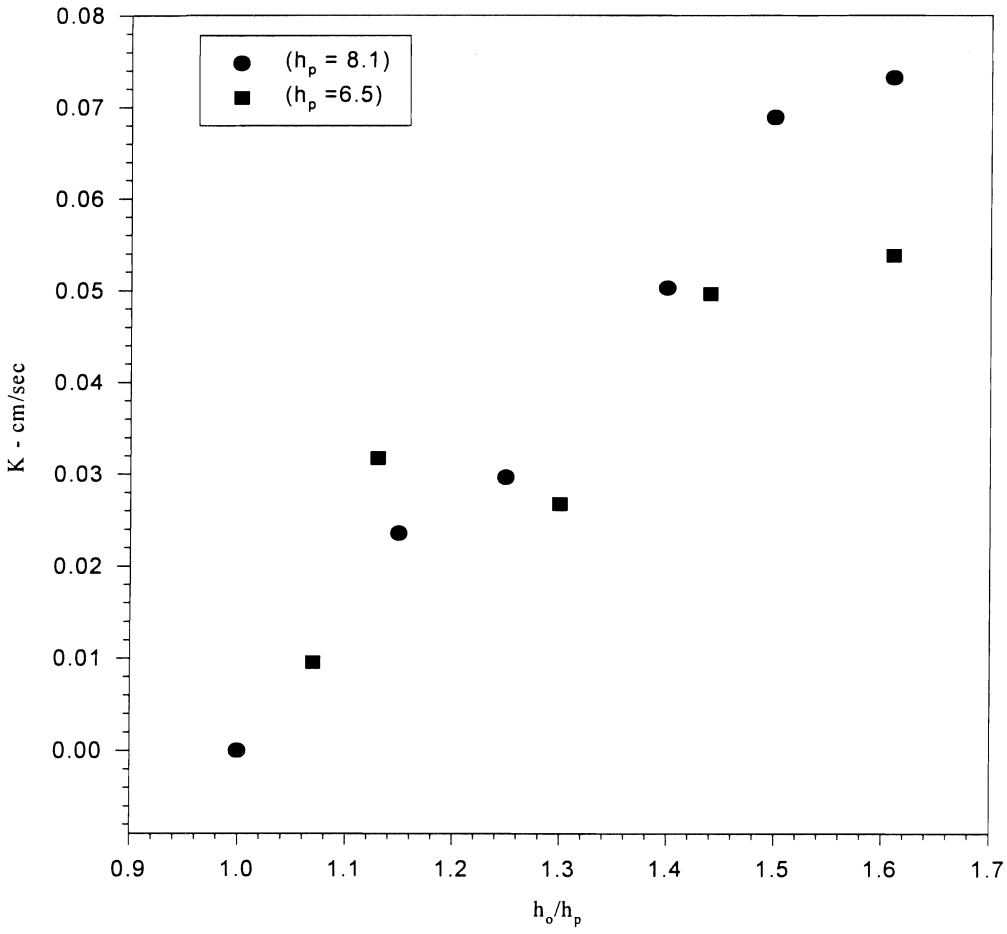

Figure 5. Hydraulic conductivity as a function of h_o/h_p for the column studies conducted. As h_o increases relative to h_p more pores are filled and start to conduct which increases K_{eff}.

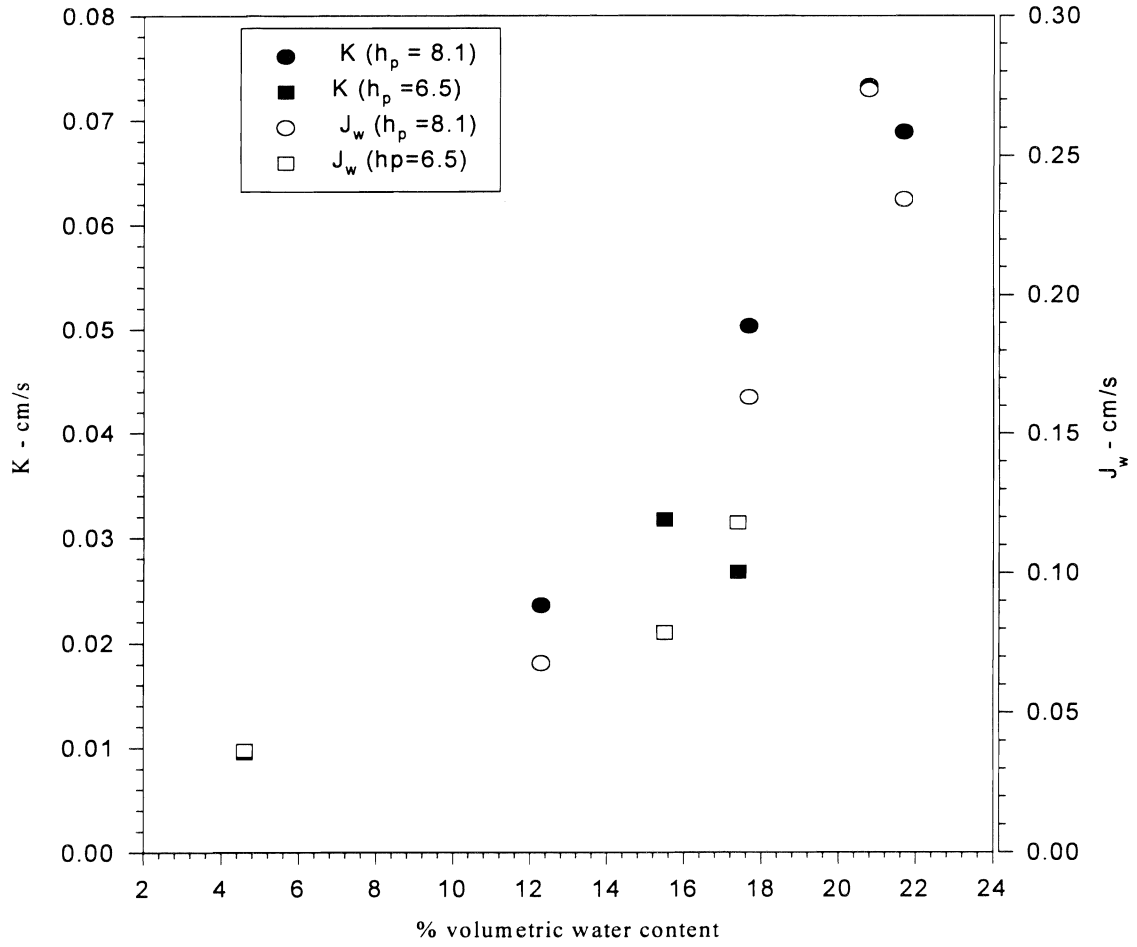

Figure 6. Hydraulic conductivity and column flux as a function of the volumetric water content.

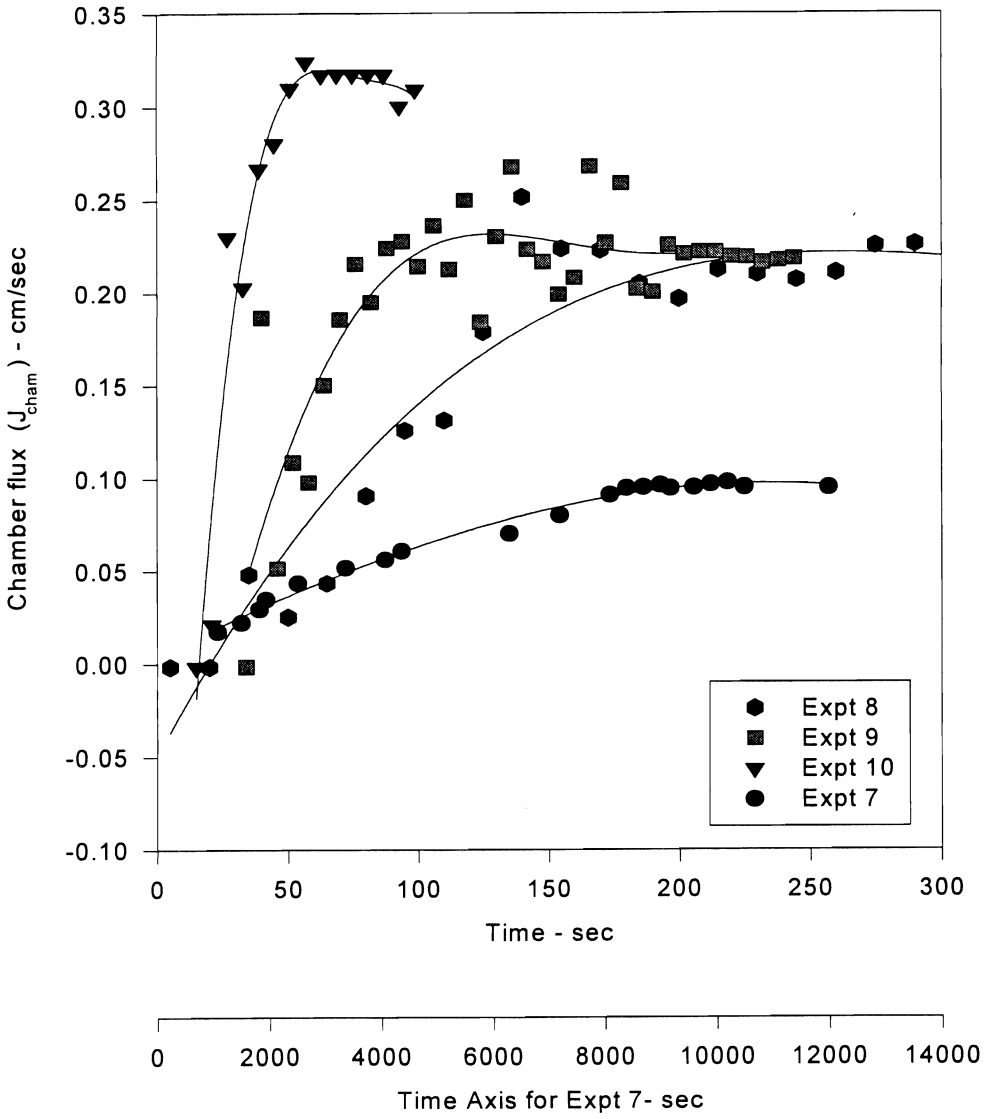

Figure 7. Chamber flux for experiment 7, 8, 9 and 10.

Rotational Conformers as Molecular Probes of Sorptive Interactions at Mineral and Organic Soil Surfaces

WALTER J. FARMER
Deptartment of Soil and Environmental Sciences, Riverside Campus

Summary

The goal of this research is to enhance understanding of sorption/desorption mechanisms at clay and organic matter surfaces, both singly and in combination in a whole soil, that contribute to the unexplained retention of nonpolar organic chemicals. The use of diffuse reflectance infrared spectroscopy in conjunction with chemicals, dihaloethanes, that exhibit isomerization properties represents a novel approach to the investigation of phenomena occurring at heterogeneous surfaces. Variations in conformer populations for these chemicals, indicative of their immediate environment, can be observed *in situ* in their infrared spectra from a kinetic as well as a mechanistic point of view. Over the course of the project, humic substances differing in origin and properties and soils sampled as a function of depth were used as sorbents. Dihaloethane behavior at humic surfaces was found to differ from that with clay minerals and characteristics of both types of behavior were found in spectral series for soils. Evidence for a persistent but slowly accumulated sorbed species was found with all the sorbents. These results, and the effect of water vapor on the spectra of soils, are interpreted in the context of the microstructural properties of the sorbents.

Key Words: humic substances, diffuse reflectance infrared spectroscopy, pollutant persistence, slow sorption

Project Objectives Addressed in 1995-1996

1. Develop a means for comparison of molecular level interaction mechanisms of nonpolar organics with both mineral and humic substances under both dry conditions and in the presence of water vapor.

2. Evaluate the relative importance of interaction mechanisms with individual soil constituents for the retention of nonpolar organic chemicals when the constituents are present in a whole soil.

Research Plan and Procedures

The technique developed utilizes the unique capabilities of diffuse reflectance infrared spectroscopy (DRIFT) to monitor the species of chemical present on the sorbent surfaces as sorption and desorption are proceeding. The methodology as it was used with clay mineral sorbents has been described in detail in previous publications (Aochi et al., 1992; Aochi and Farmer, 1993), but a brief description is included here to facilitate the discussion that follows. The sorbent of interest is in powder form and is sieved to <45um. It is thoroughly mixed using a mixer mill with a diluent matrix. For the studies performed under dry conditions, the matrix is Kbr and the cell of the controlled environment diffuse reflectance cell is purged using a stream of N_2 gas after the sample has been packed in the sampling cup. The sorption process is initiated by introducing vapor phase chemical into the gas stream and spectra are collected as a function of time. When the sorption/desorption experiments are performed in the presence of water, diamond powder is used as the diluent and the sample is preequilibrated with water vapor at 50% RH for 2 h before sorption with the organic chemical begins. The sample is maintained at this RH throughout the experiment. When the selected sorption period has been completed, vapor phase chemical is removed from the flow stream and spectra are once again collected as desorption proceeds. Through the use of spectral subtraction, interferences in each of the collected spectra from absorption bands of the sorbent, unassociated vapor phase chemical in the space surrounding the sample within the chamber, and water vapor are removed. The resulting spectra, therefore, are those of the sorbed chemical only.

The most novel aspect of these experiments is in the use of chemicals, 1,2-dihaloethanes, that exist in multiple conformeric states as molecular probes of the interactions that are occurring. The existence of 1,2-dihaloethanes in two stable rotational conformations, anti and gauche, has been known for some time. Differences in the relative abundance of conformational isomers for these chemicals in different environmental conditions were explained through the use of Onsager relationships (Mizushima, 1954). These relationships mathematically describe the loss in potential energy for a molecule with a dipole moment when it is transferred from a vacuum to a medium with a different dielectric constant. The higher the dielectric constant of the medium, the greater is the loss in potential energy. Because the gauche conformers of

1,2-dihaloethanes possess a dipole moment but the anti conformers do not, as the dielectric constant of the medium increases, the effect of the potential energy loss is a stabilization of the gauche conformation relative to the anti conformation. Bands characteristic of each conformer are present in the infrared spectra of these chemicals. FTIR can be used, therefore, to monitor any changes in conformer populations that may occur as a function of time and the conditions of sorption.

Results

During the first year of this study, time-dependent DRIFT spectra were collected while sorption and desorption of 1,2-dichloroethane (DCA) were in progress on several different humic substances obtained from the International Humic Substances Society. These included soil humic and fulvic acid, Suwannee stream fulvic acid, and peat humic acid. Humic substances were expected to have the opposite effect from clay minerals when they act as sorbents for dihaoethanes. Instead of providing an environment of higher dielectric field with greater affinities for the gauche conformer, these comparatively nonpolar sorbents should exhibit a preference for the anti conformer.

Shown in Fig. 1 are spectra obtained for DCA sorbed on soil humic acid as a function of time. During the 22 h sorption period, the bands in this spectral region are shown to all increase in intensity but change very little in characteristic band shape. Unlike the clay mineral series (Aochi and Farmer, 1993), there were no indications in the spectra of the prominent bands indicating the presence of a liquid phase. The broad multiplet shapes observed during both sorption and desorption are characteristic of low to moderate resolution spectra of chemicals in the vapor phase. The spectra, in fact, appeared to be very similar to that of bulk vapor phase DCA but, as shown using spectral oversubtraction and integrated band area ratios (Kearney Foundation of Soil Science Annual Report, 1995), the species giving rise to them was enriched in the anti conformer as was expected. The preference for the anti conformer was found to decrease as a function of sorption time.

The second important aspect in the sorption series is the delayed appearance of a broad band with maximum intensity at around 1400 cm^{-1}. No comparable band can be found in the spectrum of the bulk vapor phase species. As can be seen in Fig. 2 for DCA sorbed 22 h onto humic and fulvic acids extracted from different sources, similar broad bands appear with all the humic substances. The shape and absolute intensity of the broad band as well as its intensity relative to the other bands in the spectrum, however, vary with the particular humic material used as the sorbent.

Once exposure to the sorptive chemical ceases and only N_2 gas flows through the sample, the vapor phase type bands rapidly diminish (Fig. 3). The 1400 cm^{-1} band, on the other hand, appears to slightly increase in intensity. In fact, as shown by the data plotted in Fig. 4, it continues to increase in intensity as desorption times increase, but the rate of increase is also sorbent

dependent. The figure shows the integrated area of the band as a function of desorption time for soil humic and fulvic acid. The data were collected during three different experiments for each sorbent when the initial condition of the humic sample was (a) stored in a dessiccator, (b) freeze-dried for 2 h, and (c) stored in a vacuum dessicator under vacuum for various lengths of time. Although scatter is apparent, these data demonstrate the consistently greater intensity and a more rapid increase in intensity for the persistent band when fulvic acid is the sorbent.

The most important question, of course, is how mineral and organic sorbents function when they are present in a natural state within particles of whole soil. Studies in the current year under the Kearney Foundation funding are part of an overall plan to address that very question. Shown in Fig. 5 are spectra collected after 0.5, 1, and 22 h of DCA saturated N_2 flow through a sample of Palouse soil, in a matrix of Kbr. The spectra, like those with the humic sorbents, are very similar to that of the bulk vapor phase chemical particularly at short sorption times. Here also, a preference for the anti conformer is indicated by the ratios of the wag bands. This suggests that sorption is dominated by interaction with the natural organic matter present. With longer periods of exposure, however, there is a significant change in the relative intensity of certain regions in the spectrum. This is most easily seen in the region near 1430 cm^{-1}.

The reason for these changes can be understood by referring to the spectral series collected during the desorption shown in Fig. 6. It can be seen from this figure that as the other bands in the spectrum with vapor state character diminish with increasing desorption periods, a single narrow band remains at this frequency. This single band is essentially identical to the one observed in the spectra of DCA sorbed on clay minerals, which was assigned to the scissor vibration of the gauche conformer not in the vapor phase but in the liquid. This indicates that as the sorption process was proceeding, condensation of liquid phase chemical was occurring but at a slower rate than was observed with the clay minerals. Furthermore, some intensity for this band remains even after 24 h of desorption, much longer than with the clay minerals. A similar liquid phase band was not observed in the desorption spectra when humic substances alone were used as sorbents.

Also present in this spectrum is a broad band in the area of 1400 cm^{-1} where the persistent band was observed for both the clay minerals and the humic substances. Although low in intensity, it is consistently present in the desorption spectra and is accompanied by the presence of a second broad band near 1030 cm^{-1}. This suggests that the source of the band could be the network of pores proposed previously in the clay mineral studies (Aochi and Farmer, 1995). Supporting this conclusion is the enhanced intensity found for this band at 1400 cm^{-1} when identical experiments are performed on the same soil after it had been treated to remove organic matter.

The Palouse soil sample discussed above was taken from the top 10" of the soil profile. The organic matter content is 4.2% and the mineralogy is dominated by illite and montmorillonite. When identical experiments were performed on soil sampled from the 18-30" depth with an organic matter content of 2.86%, some differences in intensities were observed and the soil from the lower depth appeared to retain greater quantites of sorbate chemical in the liquid phase. In general, however, the spectral sequences were very similar. Larger spectral differences were observed between the surface and 12-18" samples for Molokai c, a kaolinitic Hawaiian soil high in iron oxides, but the differences here also were in the relative extents of sorbed vapor and liquid.

All of the experiments described above were performed using dry samples and sorptive saturated N_2 flow. One of the objectives of this project was to evaluate the manner in which the sorption mechanism changed when water is present in the system. The addition of water vapor required major modifications to the flow system and the environmental chamber and a change in the diluent matrix as well. All the necessary modifications were completed and several potential matrices were investigated. Each of the matrices was found to have distinct limitations. In order to use the most acceptable of these, diamond powder, it was necessary to increase the concentration of the sample in the matrix to 4%. Even at that concentration, the signal-to-noise ratio of the resulting spectra was far lower than in previous spectra with Kbr.

As demonstrated in a previous publication (Aochi and Farmer, 1993), when higher sorbent concentrations are used, band intensities for the sorbate in the liquid phase are enhanced relative to vapor phase species and the presence of the broad 1400 cm^{-1} band is greatly suppressed. Furthermore, the additional flow of water vapor through the sample reduces the maximum possible partial pressure of sorptive chemical to less than 1, further reducing the observed intensities. Despite these caveats, the spectra presented in Figs. 7 and 8 are highly significant.

Spectra in Fig. 7, were collected after samples of Palouse in a diamond matrix were exposed to a flow of DCA at a partial pressure of 0.5 for 30 min. In the case of the upper spectrum, the sample was preequilibrated at 50% RH for 2 h before DCA was introduced into the flow stream. It is clearly dominated by vapor phase bands with no distinct evidence for the presence of a liquid phase. In contrast, the dry sample exhibits liquid phase bands at 1454 and 1435 cm^{-1} . These bands appear to be approximately equal in intensity and the gauche band (1435 cm^{-1}) is somewhat shifted to higher frequencies than observed previously with the clay minerals and in the desorption spectra for the soils. As sorption progressed, spectra for the dry sample became quite similar in appearance to that of the wet sample but intensities of all of the bands in the spectra continued to be greater for the sorbent in the presence of water throughout the sorption period.

Spectra shown in Fig. 8 were collected after a 22 h sorption period and a 2 h desorption period. While both of the spectra show some residual band intensity at 1454 and 1429 cm^{-1} (note the change in frequency), the lower

frequency band is clearly more intense for the dry sample. The other bands in the spectrum for this sample also appear to be predominantly of liquid phase character while the corresponding bands for the wet sample are still clearly vapor phase in both shape and frequency.

Discussion

Investigations conducted over the last several years in our laboratory have focused on the development of an *in situ* spectroscopic technique that could detect differences in the sorption status of nonpolar organic chemicals not only as a function of the sorbent used but also as a function of time. Impetus for the development of this technology came from the increasing awareness that the sorption/desorption processes for anthropogenic organic chemicals in soil are far more complex and kinetically dependent than previously assumed. Even for very simple chemicals, both processes seem to be comprised at the minimum of a slow and rapid component (see Pignatello, 1996 for a recent review). Evidence indicates that this is true for separate mineral and organic sorbents as well as whole soils.

The chemicals used in these studies are frequently detected as pollutants of groundwater and their retention in soils for periods greater than would be predicted from their physicochemical properties has been documented (Steinberg et al., 1987; Pignatello et al., 1990). Understanding the reasons for the prolonged retention of these particular chemicals, however, is only part of the justification for the investigations discussed here. It is widely held that the persistence of many nonpolar organic chemicals can be attributed to either hindered intraaggregate diffusion or intraorganic transport. These mechanisms imply that the controlling factors lie in characteristics of the sorbent rather than the specific sorbate. Because chemicals with the potential for isomerization exhibit an additional degree of sensitivity to the environment in which they reside, they are also uniquely suited to reveal properties of the sorbents with which they interact. Those properties are likely to affect the fate of any chemical that comes into contact with soil materials, not just dihaloethanes.

Our previous spectroscopic investigations of dihaloethane sorption onto clay sorbents (Aochi et al., 1992; Aochi and Farmer, 1993, 1995) provided evidence that the sorbed chemicals are present in different physical states; a liquid state, a labile vapor state and a persistent vapor state. It was concluded that in each of these states, the sorbed chemicals experience higher effective dielectric fields when they are associated with clay surfaces than when they exist in the bulk state. This conclusion was based on the higher proportion of gauche conformer present in the sorbed chemical relative to the bulk state. While the gauche conformer was in each case preferentially retained during both sorption and desorption processes, the degree of preference depended on the clay used. All of these spectral results are consistent with sorbent porosity as the factor controlling the sorption/desorption process. Both the size of the pores and their interconnection to form a network of pores can determine whether a sorptive is condensed as a liquid, weakly retained in the vapor state, or transported slowly to regions of the clay difficult to both access or egress.

Humic substances, of course, provide a far different sorbent. While the porous nature of clay minerals is universally acknowledged, the organic carbon matrix has been conceptualized in several different ways. In the most simple view, organic matter is thought to behave much like an organic solvent into which sorbate chemicals actually dissolve (see Chiou, 1990 for a summary). A second envisions meshlike humic macromolecules existing in random coil conformations with extensive inter- and intramolecular bonding. When the humic materials are present in aqueous solution or suspension, the more polar functional groups are oriented toward the exterior of the coils and the more hydrophobic portions toward the interior. This orientation may invert as the amount of water present is reduced, which could account for the difficulty of rewetting dried humic substances (Cameron, 1972; Hayes, 1985; Stevenson, 1995).

Wershaw (1986, 1993) has proposed a third structural model in which humic substances are comprised of lipid-like amphiphilic molecular fragments originating from partially decomposed plant polymers. In aqueous media, the amphiphiles form micelle structures in which the hydrophobic portions are located in the central regions and the polar heads are present at the exterior surfaces. In association with soil solids, the amphiphile structures flatten to form flexible bilayer membranes that coat the available surfaces. With both the micelle and membrane structures, the central hydrophobic portions are thought to form a liquid-like interior into which nonpolar chemicals can partition.

Implicit in both of the latter two models is the presence of discrete regions of both high and low polarity that would differ significantly in their affinity for sorptive chemicals. They also suggest the existence of porous structures through which diffusion of chemicals can occur. Rates of diffusion for chemicals sorbed within these structures could be hindered both by the size of the pores and interactions with functional groups that comprise the walls. Data obtained by Schulten and Schnitzer (1995) using pyrolysis mass spectrometry suggest that such membranelike structures for organic matter exist whether it is extracted from or incorporated within a soil.

As stated earlier, the broad multiplet shapes of the labile sorbed species appearing earliest in the sorption process with humic substances as sorbents are characteristic of low to moderate resolution spectra of chemicals in the vapor phase. These shapes are actually band contours that extend over a whole series of bands that are not individually resolved under the spectral conditions (Colthup, 1990). They are only observed for chemicals in the vapor phase because the many bands from which they are comprised arise from rotational transitions of the molecule. Their presence thus implies a fair degree of rotational freedom for the sorbed molecule. Along with the fact that the band frequencies differ only slightly from those of the bulk phase bands, the spectrum of this species is highly suggestive of pockets of sorbate molecules entrapped within pores of the sorbent. Once desorption was initiated, this species was rapidly desorbed leaving only the persistent band at 1400 cm^{-1} . The ease with which this occurs is also consistent with minimal interaction with the sorbent

surfaces. The preference for the anti conformer exhibited by this labile sorbed species with all of the humic sorbents used is consistent with the more nonpolar nature of organic matter compared to mineral surfaces.

The band observed at 1400 cm^{-1} with the humic substances is very similar to the band at 1402 cm^{-1} observed in the spectra of DCA sorbed on clay minerals in band frequency and also in its delayed appearance and its persistence during desorption. This broad band in the earlier studies was interpreted to arise from combined anti and gauche scissor vibrations of sorbate molecules that had diffused into a network of narrow pores within the clay particles. In these regions, they experienced higher dielectric fields because of the proximity of the walls of the pores that resulted in a predominance of molecules in the gauche conformation (Aochi & Farmer, 1995).

In the spectral series with humic sorbents, this band could possibly be accounted for by residual mineral components not removed from the humic materials in the extraction process. The ash content of these materials is, however, extremely low (P. MacCarthy, personal communication). Furthermore, the band is not accompanied by the other persistent band at 1028 cm^{-1} as it was in the DCA/clay spectra. It seems more likely that it is due to the diffusion of sorbate molecules to portions of the organic matrix of greater density, more tightly coiled, or more highly polar. Movement into such regions would certainly be expected to slow the movement of sorbed chemical both into and out of the organic particles.

This interpretation is consistent with the behavior of the band in both the 22 h sorption spectra shown in Fig. 2 and 24h desorption spectra presented in the Kearney Foundation of Soil Science Annual Report for last year. Its intensity was fairly well correlated with generally acknowledged properties of the different humic substances that could result in the formation of such regions (see Malcolm, 1990; Hayes, 1985 for discussions of properties). In general, fulvic acids are higher in O-containing functional groups than humic acids and therefore could be expected to provide more extensive regions with high polarity. Stream fulvic acids (FA) are believed to be lower in O and N than soil FA and higher in C. Aquatic humic substances such as Suwannee stream FA most likely form by different pathways and from different starting materials than terrestrial ones and should thus differ somewhat in structure and behavior. Peat, on the other hand, is believed to form along similar pathways as soil humates and thus humic acids (HA) from the two sources should be quite similar (Steelink, 1985). The most striking evidence for this hypothesis, however, can be found in the data presented in Fig. 4, demonstrating the differences in the behavior of the band with soil HA and FA as sorbents.

Spectral series with whole soils as sorbates indicate that both their mineral and organic constituents are active in the sorption process. The labile vapor phase type bands present from the earliest sampling period show an enhanced proportion of anti conformer and thus indicate the dominance of organic matter. As sorption continues, however, it becomes apparent, especially from the early desorption spectra, that the sorptive chemical is also being

retained as a liquid. The accumulation of the liquid sorbate and also its release during desorption occur at a far slower rate than in the case of clay minerals. All of the soils exhibited a persistent broad band near 1400 cm^{-1} that is accompanied by some band intensity in the 1030 cm^{-1} region. The intensity of this band significantly increases upon treatment of the soils to remove organic matter. Smaller differences in spectral series are observed as the organic matter content diminishes naturally for soils as a function of depth.

Other investigators have suggested that mineral and organic constituents interact in a complex way to form a matrix in which the movement of sorbed chemicals is limited. Wu and Gschwend (1986) suggested that rather than providing specific sites for strong interactions with nonpolar organic chemicals, the important characteristic of minerals may be the way in which they aggregate. The formation of clay domains and the aggregation of those domains with larger mineral grains could result in a network of pores through which diffusion is hindered.

The lack of significant frequency shifts for the liquid and labile vapor phase bands shown here indicates that at least these sorbed species do not experience strong interactions with specific sites on the surfaces of soil particles. For the species giving rise to the persistent band, their presence in a network of pores in which movement is hindered and concentrations increase very slowly is the most plausible explanation. Humic materials present within the aggregate structure appear to further increase hindrance to diffusion by acting as plugs that prevent or impede the movement of organic chemical into and out of much of the existing pore space. It is quite interesting in this context that Fitch and Du (1996) have recently presented electrochemical evidence that humic materials clog pores leading to inner regions of clay coated onto an electrode surface, thereby inhibiting access to those regions.

It has been well established (Chiou and Shoup, 1985; Chiou 1990; Ong and Lion, 1991) that as the water content of a soil sorbent system is increased the dominant sorption mechanisms change along with the relative importance of mineral and organic surfaces. Enhanced band intensities shown here suggest that when the soil sample is allowed to equilibrate with water vapor prior to exposure to sorptive chemical, the pores of the organic carbon matrix expand in size and their sorptive capacity is accordingly increased. As a consequence of the swelling, the humic "plugs" also become more effective in inhibiting access to regions in which condensation of liquid phase chemical or migration within the porous network may occur.

While the role of porosity in sorption processes has been alluded to by a number of investigators (Steinberg et al, 1987; Pignatello, 1989, Ball and Roberts, 1991a,b), both the size of the pores involved and their location within the sorbent particles have not been established (Pignatello et al., 1993). The spectra presented here indicate that pores in a wide range of sizes may contribute to the long term retention of a pollutant chemical. Sorbate condensed as a liquid within mesopores may act as reservoirs for chemical movement into the porous network of the sorbent. The porous network itself can be comprised

of pores of varying size with narrow pores likely to dominate since strong dielectric fields are indicated. Farrell and Reinhardt (1994a,b) invoked enhanced sorption in micropores as an explanation for the persistence of TCE in porous silica particles but provided no estimates of microporosity to support that interpretation. They also did not consider the fact that if micropores are as accessible as larger pore spaces, then entrapment of sorptive chemical within those spaces should occur most rapidly instead of gradually over long periods of time.

References

Aochi, Y. O. and W. J. Farmer. 1995. Spectroscopic evidence for the rate-limited accumulation of a persistent fraction of 1,2-dichloroethane sorbed onto clay minerals. Environ. Sci. Technol. 29:1760-1765.

Aochi, Y. O. and W. J.Farmer. 1993. Conformational dynamics of 1,2-dichloroethane on illite during sorption and desorption. J. Colloid Interface Sci. 161:106.

Aochi, Y. O., W. J. Farmer, and B. L. Sawhney. 1992. *In situ* investigation of 1,2-dibromoethane sorption/desorption processes on clay mineral surfaces by diffuse reflectance infrared spectroscopy. Environ. Sci. Technol. 26:329.

Ball, W. P., and P. V. Roberts. 1991a. Long-term sorption of halogenated organic chemicals by aquifer material. 1. Equilibrium. Environ. Sci. Technol., 25:1223.

Ball, W. P., and P. V. Roberts. 1991b. Long-term sorption of halogenated organic chemicals by aquifer material. 2. Intraparticle diffusion. Environ. Sci. Technol. 25:1237.

Cameron, R. S., B. K. Thornton, R S. Swift, and A. M. Posner. 1972. Molecular weight and shape of humic acid from sedimentation and diffusion measurements on fractionated extracts. J. Soil Sci. 23:394-408.

Chiou, C. T. 1990. In: Humic Substances in Soil and Crop Science; P. MacCarthy (ed) Soil Sci. Soc. Am., Madison, WI.

Chiou, C. T. and T. D. Shoup. 1985. Soil sorption of organic vapors and effects of humidity on sorptive mechanism and capacity. Environ. Sci. Technol. 19:1196.

Colthup, M. B., L. H. Daly., and S. E. Wiberley. 1990. Introduction to Infrared and Raman Spectroscopy, Academic Press, San Diego, CA, 1990.

Farrell, J. and M. Reinhard. 1994a. Desorption of halogenated organics from model solids, sediments, and soil under unsaturated conditions. 1. Isotherms. Environ. Sci. Technol. 28:53.

Farrell, J. and M. Reinhard. 1994b. Desorption of halogenated organics from model solids, sediments, and soil under unsaturated conditions. 2. Kinetics. Environ. Sci. Technol. 28:63.

Fitch, A. and J. Du . 1996. Solute transport in clay media: effect of humid acid. Environ. Sci. Technol. 30:12.

Hayes, M. H. B. 1985. In: G. R. Aiken, D. M. McKnight, R. L. Wershaw, P. MacCarthy (eds). Humic Substances in Soil, Sediment, and Water, Wiley-Interscience, New York.

Malcolm, R. L. 1990. In: P. MacCarthy, C. E. Clapp, R. L. Malcolm, P. R. Bloom (eds). Humic Substances in Soil and Crop Sciences. Soil Science Society of America, Madison, WI.

Mizushima, S. 1954. Structure of Molecules and Internal Rotation, Academic Press, New York.

Ong, S. K., and L. W. Lion. 1991. Mechanisms for trichloroethylene vapor sorption onto soil minerals. J. Environ. Qual. 20:180.

Pignatello, J. J. 1996 Mechanisms of slow sorption of organic chemicals to natural particles. Environ. Sci. Technol. 30:1.

Pignatello, J. J., F. J. Ferrandino, and L. Q. Huang. 1993. Elution of aged and freshly added herbicides from a soil. Environ. Sci. Technol. 27:1563.

Pignatello, J. J., C. R. Frink, P. A. Marin, and E. X. Droste 1990. Field observed ethylene dibromide in an aquifer after two decades. J. Contam. Hydrol. 5:195-214.

Pignatello, J. J. 1989. In: B. L. Sawhney and K. Brown (eds), Reactions and Movement of Organic Chemicals in Soils. SSSA Special Publication No. 22. Soil Science Society of America, Madison, WI.

Schulten, H.-R. and M. Schnitzer. 1995. Three dimensional models for humic acids and soil organic matter. Naturwissen . 82, 487.

Steelink, C. 1985. In: G. R. Aiken, D. M. Mcknight, R. L. Wershaw (eds) Humic Substances in Soil, Sediment, and Water. Wiley-Interscience, New York.

Steinberg, S. M., J. J. Pignatello, and B. L. Sawhney. 1987. Persistence of 1,2-dibromoethane in soils: Entrapment in intraparticle micropores. Environ. Sci. Technol. 21:1201.

Stevenson, F. J. 1995. Humus Chemistry, John Wiley & Sons, New York.

Wershaw, R. L. 1986. A new model for humic materials and their interactions with hydrophobic organic chemicals in soil-water or sediment-water systems. J. Contam. Hydrol. 1:29-45.

Wershaw, R. L. 1993. Model for humus in soils and sediments. Environ. Sci Technol. 27:814-16.

Wu, S.-C. and P. M. Gschwend. 1986. Sorption kinetics of hydrophobic organic compounds to natural sediments and soils. Environ. Sci. & Technol. 20: 717.

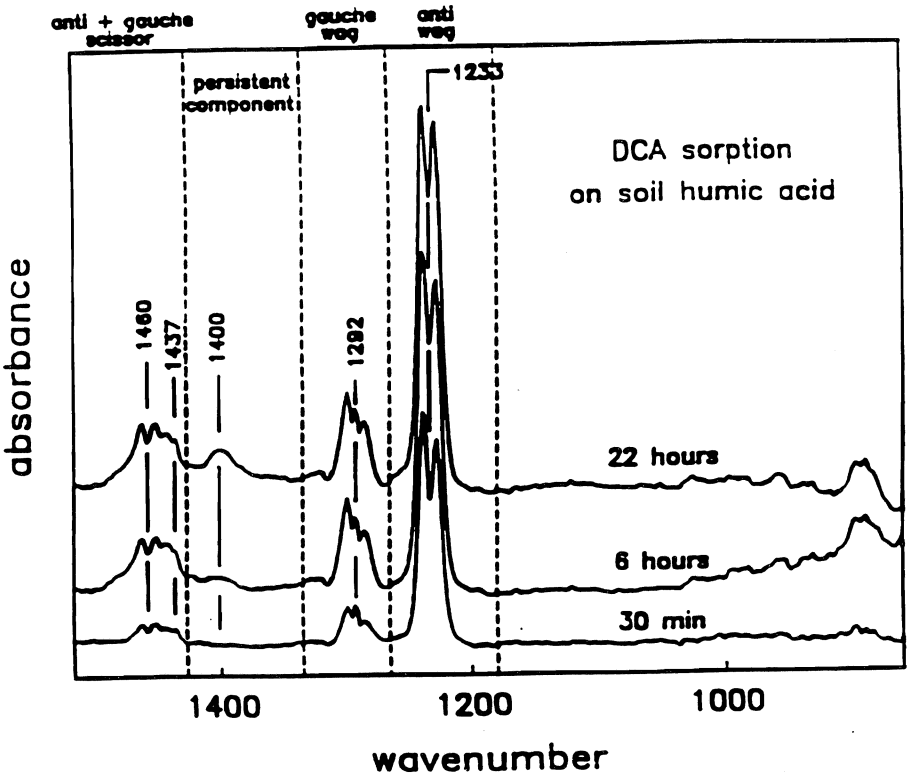

Figure 1. DCA on soil humic acid in KBr after .5, 6, and 22h sorption..

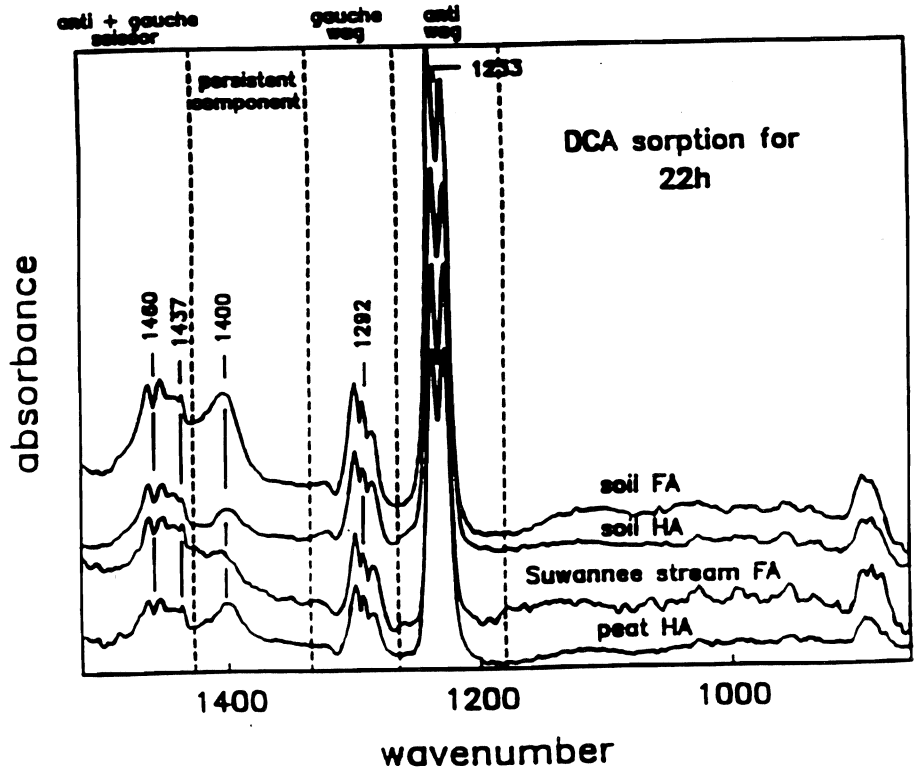

Figure 2. DCA on four different humic materials in KBr after a 22h sorption period.

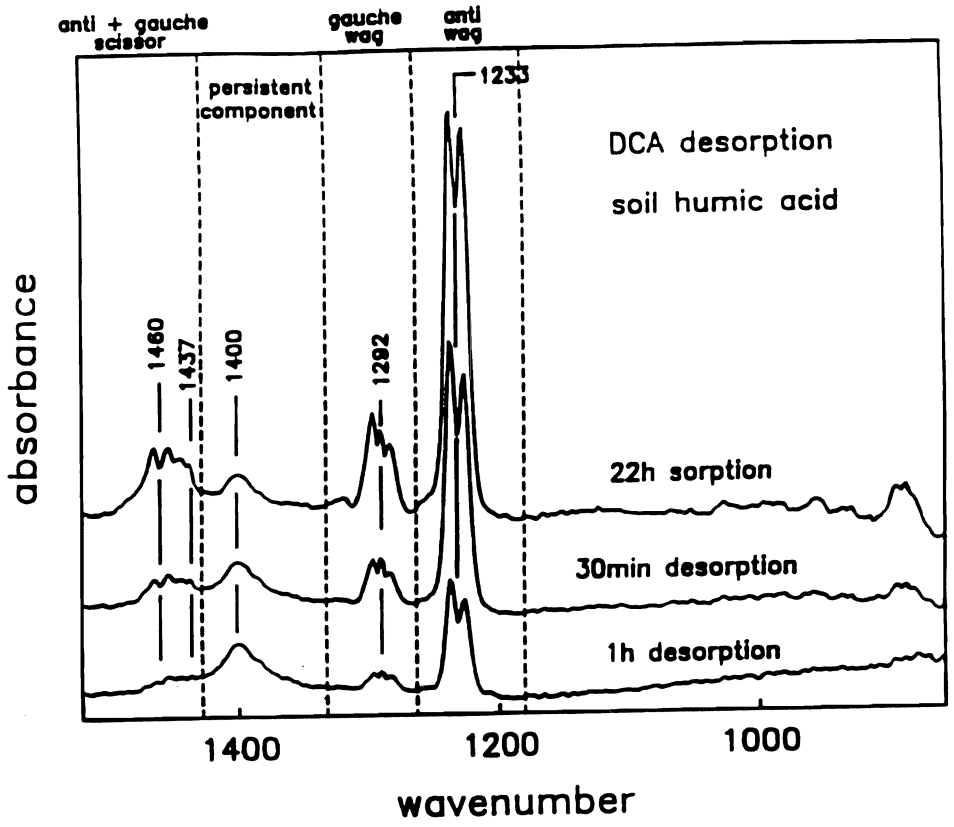

Figure 3. DCA on soil humic acid in KBr after 22h sorption, .5 and 1h desorption.

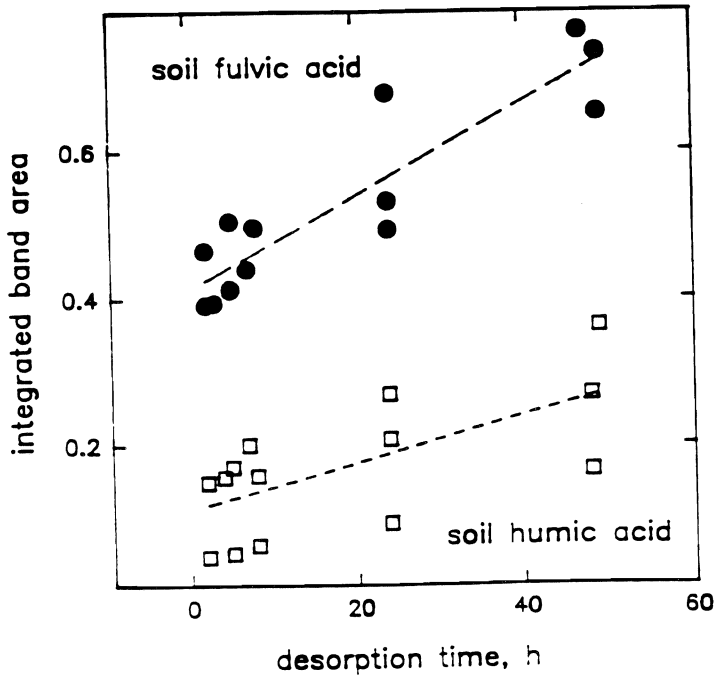

Figure 4. Integrated area of the 1400 cm^{-1} band as a function of time for soil humic and fulvic acid in KBr.

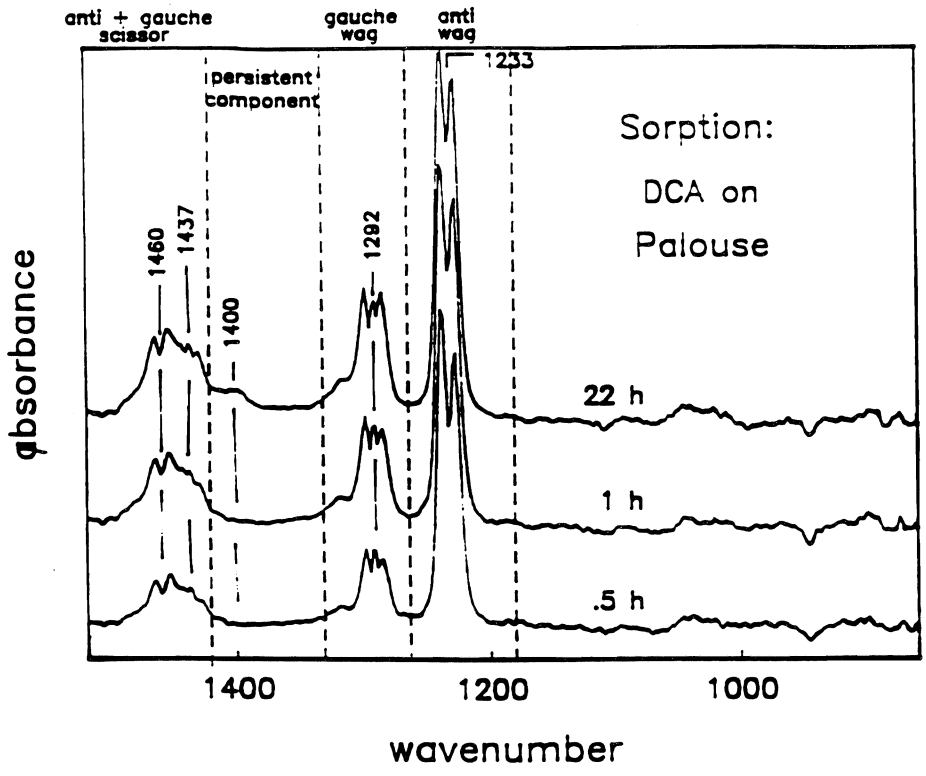

Figure 5. DCA on Palouse soil in KBr after .5, 1, and 22h sorption.

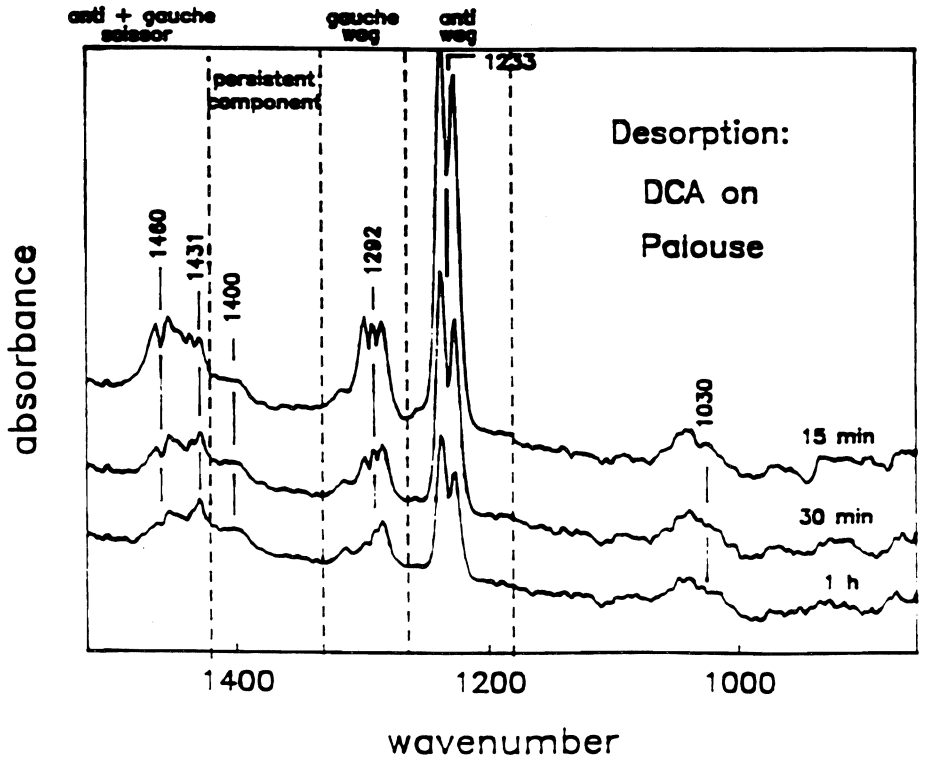

Figure 6. DCA on Palouse soil in KBr after .25, .5, and 1h desorption.

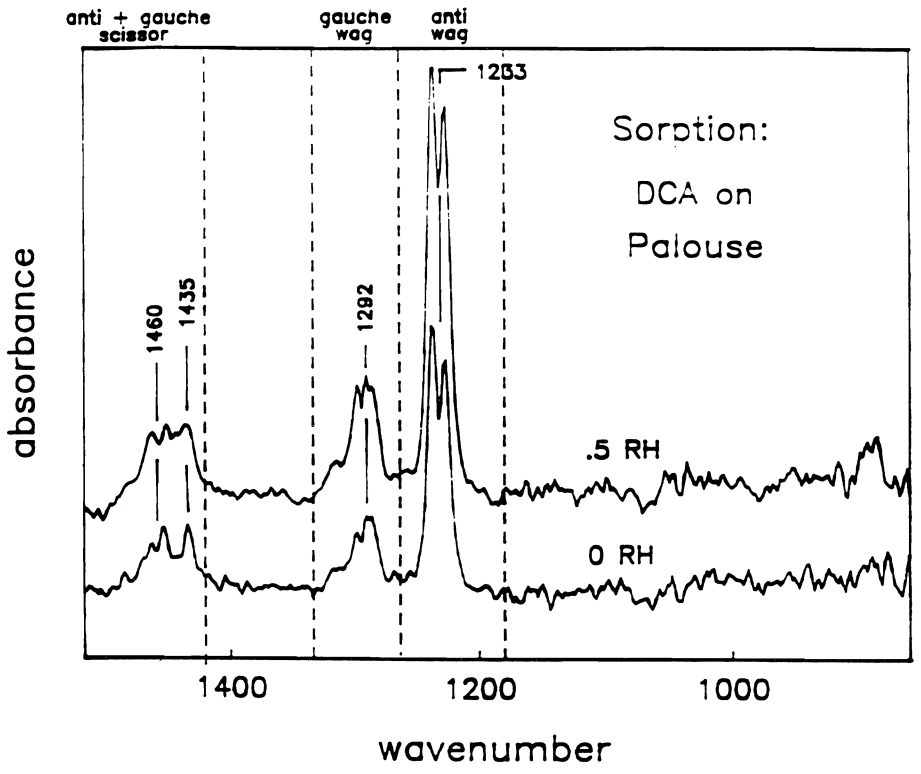

Figure 7. DCA (p/p_o = .5) on Palouse soil in diamond powder after .5h sorption.

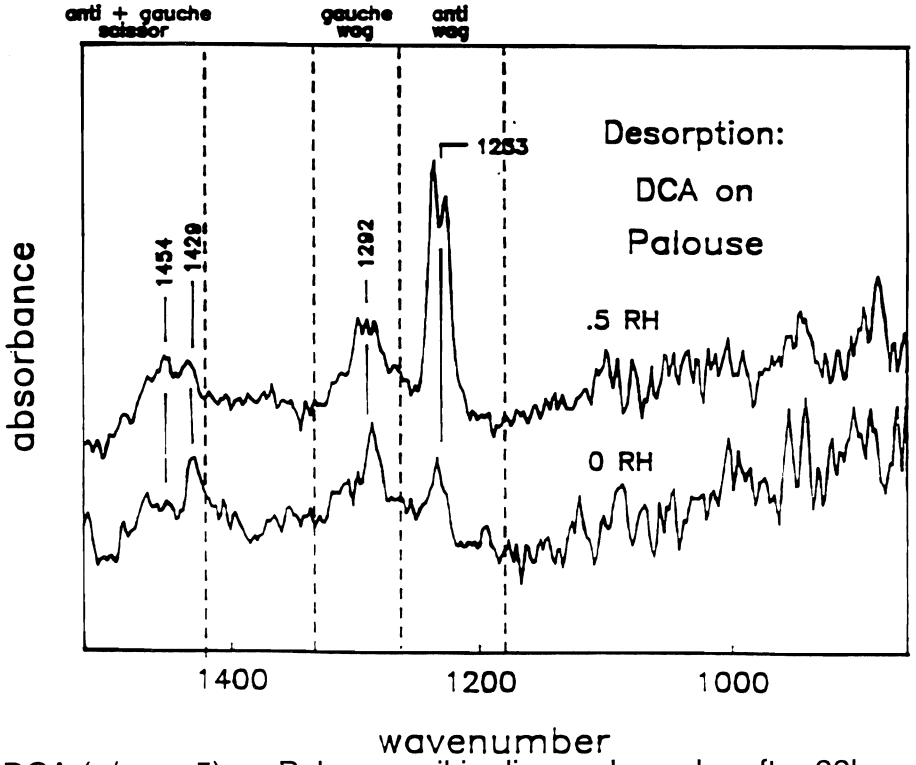

Figure 8. DCA (p/p_o = .5) on Palouse soil in diamond powder after 22h sorption and 2h desorption.

Adsorption-Desorption Kinetics of VOCs onto Pure Clay Minerals

MARK E. GRISMER AND FERGUS MORRISSEY
Department of Land, Air and Water Resources, Davis Campus

Summary

Transient isothermal sorption/desorption experiments using acetone, benzene and toluene onto the pure clay minerals, illite, kaolinite and montmorillonite, suggest sorption kinetics are controlled by rates of inter-particle (macro) diffusional mechanisms, intra-particle (micro) diffusional mechanisms, and kinetics.

Incorporation of macroscopic and microscopic diffusion parameters, and partitioning therein, into a superposed analytical solution of Fick's Second Law, result in precise correlation with experimental isotherms. Correlation coefficients of 0.99 were found between the parameter optimized analytical solution and experimental data. Macroscopic diffusion coefficients ranged from 10^{-2} to 10^{-4} cm^2/min; microscopic diffusion coefficients ranged from 10^{-12} to 10^{-17} cm^2/min; and, the fraction of adsorption occuring on the surface ranged from 30% to 75% of the total sorbed mass, depending on the VOC/mineral combination. Kinetic processes were modelable as Fickian diffusion processes. Adsorption capacities were found to correlate well with mineral specific surface area. Irreversible sorption was observed in relative degrees, most pronounced with the higher specific surface clays.

Due to the length scales associated with the inter-particle (millimeter, particular to the experiments performed) and intra-particle (micrometer) diffusion processes, values of diffusional time constants associated with each process during adsorption/desorption experiments were generally found to be within two orders of magnitude. This result would not be expected if particles larger than a few micrometers (i.e. clay aggregates) comprised part of the sorbing system. Experimental results help to explain the occurrent environmental persistence of VOC-contaminated soils.

Key Words: inter-particle, intra-particle, diffusion, kinetics

Project Objectives Addressed in 1995-1996

1. To develop efficient, precise experimental methods to conduct isothermal sorption experiments with flexible sorbent/sorbate systems.

2. To conduct isothermal sorption/desorption experiments using a range of VOCs and clay minerals.

3. To develop conceptually/physically based mathematical models describing the sorption/desorption response of a sorbent/sorbate system.

4. To determine if sorption occurs instantaneously or if kinetics are involved.

5. To classify the kinetic process mechanism.

Research Plan and Procedures

Laboratory Experiments For the experiments, VOC-saturated nitrogen was "instantaneously" introduced into the headspace of an oven-dry, pure clay mineral system, initially void of sorbate. The bottom boundary of the system was represented by a no flux boundary. Headspace concentration was maintained constant throughout the sorption phase and until the desorption phase when pure nitrogen gas replaced the VOC. The experimental setup/procedure was configured for maximum simplicity with regard to duplicating the initial and boundary conditions of an existing analytical solution of the diffusion equation. Gravimetric experiments were conducted using acetone, benzene and toluene, exhibiting a wide range of equilibrium vapor pressures, and oven-dried; illite, kaolinite and montmorillonite, exhibiting a wide range of specific surface areas, in an isothermal room set at 25°C. Three trials, each with varying profile thickness (macroscopic diffusion length scale, l_a), were conducted for each of the 9 mineral/VOC system combinations for a total of 27 experiments. Sorption/desorption experiments were conducted until equilibrium was reached for at least one of the three trials. Data, consisting of system mass, were collected at 10 second intervals with experiments lasting on the order of one to several hours, depending on the particular system and profile thickness.

Independent non-reactive gas diffusion experiments were performed in order to determine the diffusive properties, D_p and D_m values, of the clay mineral. Based on these values, the rate of adsorption could theoretically be modeled by their use in the analytical solution of the diffusion equation if, adsorption were instantaneous, D were not a function of sorbed concentration, and Fickian diffusion prevails. Departure of the observed results from this instantaneous solution then, provides information on adsorption/desorption mechanisms.

Results

Sorption/desorption results for the three individual trials (for all VOC/mineral systems) corresponding to the same VOC/mineral, collapse into a single curve when plotted on a Boltzman transformed abscissa, in accordance with Fickian diffusion and instantaneous adsorption (Crank, 1968). When plotted on a conventional time scale, the thinner profile will naturally adsorb/desorb a greater fraction of material by mass due to the diffusion process exposing the mineral to more sorbate in an equal amount of time. Boltzman transforming (plotting the sorption data vs $(t)^{1/2}/l$), compensates for this, thereby normalizing the data. The attached Figs. 1 and 2 illustrate the sorption isotherm for the trials of the acetone/ montmorillonite system on a conventional time and reduced time basis, respectively.

In order to model the sorption data, modification of the analytical solution was necessary. It was found that by adding an additional term, one representing a microscopic, or intra-particle adsorptive process (length scale represented by l_i), and splitting the adsorbed mass between intra-particle (l) and inter-particle (1-l) diffusion, the data could be modeled precisely. An optimization program was utilized to determine the parameters of best fit (D_a, D_i, l). The resulting equation which, when fitted with the appropriate system parameters, represents all of the experimental observations is:

$$\frac{Mt}{M\infty} = \lambda\left[1 - \frac{8}{\pi^2}\sum_{n=0\rightarrow\infty}\frac{1}{(2n+1)^2}e^{-\frac{D_a(2n+1)^2\pi^2t}{l_a^2}}\right] + (1-\lambda)\left[1 - \frac{8}{\pi^2}\sum_{n=0\rightarrow\infty}\frac{1}{(2n+1)^2}e^{\frac{D_i(2n+1)^2\pi^2t}{l_i^2}}\right] \quad (1)$$

This equation describes the rate of mass accumulation/adsorption. The lead term (l) represents the mass fraction sorbed onto the surface of the mineral particles, while the second term represents the remainder of sorbed material, that sorbed intra-particle. These terms together then, represent mass adsorption and intra-particle adsorbtion, respectively. Length scale values for the lead term, l_a, represent the bulk profile thickness, while l_i represents the thickness of an individual particle. Particle size was assumed to be 1 mm, and D_i is based on that assumption.

Figures 3 and 4 illustrate agreement between the parameter-optimized computer-generated data points based on the analytical model (Model) and the actual experimental values (Data) for the toluene/illite (sorption) and toluene/kaolinite (desorption) systems. Table 1 represents a complete summary of the optimized parameters.

Desorption

The optimization process was able to show the amount of irreversibility during the desorption process. The term (mfl) in Table 1 represents the maximum fractional loss. For instance, in the example illustrated in Fig. 4, the mfl of the total sorbed mass was only 91%, the remaining 9% irreversibly

sorbed or at least desorbed at an exceedingly slow rate, and controlled by non-Fickian processes.

Methodology for the analysis of the desorption process was identical to that of the sorption process. Differences between the adsorption and desorption processes are manifested by the differences in the effective diffusion values listed in Table 1. The mechanisms appear to be quite similar in all other respects.

Kinetics

As stated, the D_p values were determined experimentally using a non reactive gas, Freon 112. Using the fraction of material sorbed to the surface of each clay mineral, (I, determined during the optimization process) calculating the Retardation Factor, R and determining D_R for each VOC/mineral system, and comparing this value to the D_a for the adsorption phase, provided information on the actual kinetics of the sorption process on the surface.

Because the data match the analytical solution of a Fickian diffusion process, and D_R is not equal to D_a, it is theorized that the kinetic mechanisms have the same physical interpretation as a diffusion mechanism, i.e. the process is fundamentally based on the binomial probability distribution, or random walk model. The effective diffusion found is equal to the diffusion of a non-reactive gas divided by a constant.

Table 2 provides the relationship between the effective diffusion coefficient representing instantaneous adsorption and the observed effective diffusion coefficient.

Correlation between the specific surface area and sorption capacity is illustrated in the following Fig. 5 for acetone systems. Figure 6 illustrates the relative sorption of acetone by the clay minerals. The same trend occurs for the other VOCs as well.

References

Crank, J and G. S. Park (eds.) 1968. Diffusion in Polymers. Academic Press, New York, N.Y. 452 pp.

Table 1. Summary of Results

VOC/MINERAL SYSTEM	ADSORPTION PHASE					DESORPTION PHASE			
	D_a	D_2	I	S	R^2	D_a	D_i	mfl	R^2
	cm^2/min	cm^2/min	%	%		cm^2/min	cm^2/min	%	
ACETONE/ILLITE	$6.0\ E^{-4}$	$6.0\ E^{-12}$	34	3	.996	$1.7\ E^{-3}$	$4.7\ E^{-13}$	60	.999
ACETONE/KAOL.	$3.4\ E^{-2}$	$5.1\ E^{-11}$	76	0.3	.998	$3.0\ E^{-3}$	$3.7\ E^{-17}$	75	.992
ACETONE/MONT.	$6.3\ E^{-4}$	$6.3\ E^{-12}$	28	11	.999	$1.7\ E^{-5}$	$2.1\ E^{-14}$	30	.999
BENZENE/ILLITE	$2.8\ E^{-3}$	$1.9\ E^{-12}$	60	5	.999	$6.5\ E^{-4}$	$2.3\ E^{-12}$	90	.999
BENZENE/KAOL.	$9.0\ E^{-3}$	$8.2\ E^{-13}$	68	0.9	.999	$1.4\ E^{-2}$	$3.6\ E^{-12}$	100	.998
BENZENE/MONT.	$2.6\ E^{-4}$	$1.8\ E^{-13}$	56	15	.995	$2.9\ E^{-4}$	$2.1\ E^{-13}$	70	.998
TOLUENE/ILLITE	$9.0\ E^{-4}$	$2.5\ E^{-12}$	40	5	.999	$1.1\ E^{-4}$	$1.9\ E^{-12}$	80	.999
TOLUENE/KAOL.	$1.7\ E^{-2}$	$1.4\ E^{-11}$	33	0.9	.999	$9.1\ E^{-3}$	$3.6\ E^{-11}$	91	.999
TOLUENE/MONT.	$3.5\ E^{-4}$	$2.1\ E^{-13}$	35	10	.999	$9.1\ E^{-6}$	$7.4\ E^{-13}$	70	.999

Table 2. Theoretical vs. Optimized D_R For Sorption Process.

	Acetone			Benzene			Toluene		
Mineral	Theoretical cm^2/min Dthry/Dopt	Optimized	Ratio cm^2/min	Theoretical cm^2/min	Optimized cm^2/min	Ratio Dthry/Dopt	Theoretical cm^2/min	Optimized cm^2/min	Ratio Dthry/Dopt
Mont.	$3.8\ E^{-3}$	$6.3\ E^{-4}$	6.0	$1.3\ E^{-2}$	$2.6\ E^{-4}$	50	$1.0\ E^{-2}$	$3.5\ E^{-4}$	29
Illite	$1.5\ E^{-2}$	$6.0\ E^{-4}$	25	$4.4\ E^{-2}$	$2.8\ E^{-3}$	16	$2.1\ E^{-2}$	$9.0\ E^{-4}$	23
Kaol.	$7.6\ E^{-2}$	$3.4\ E^{-2}$	2.2	$2.2\ E^{-1}$	$9.0\ E^{-3}$	24	$1.5\ E^{-1}$	$1.7\ E^{-2}$	8.8

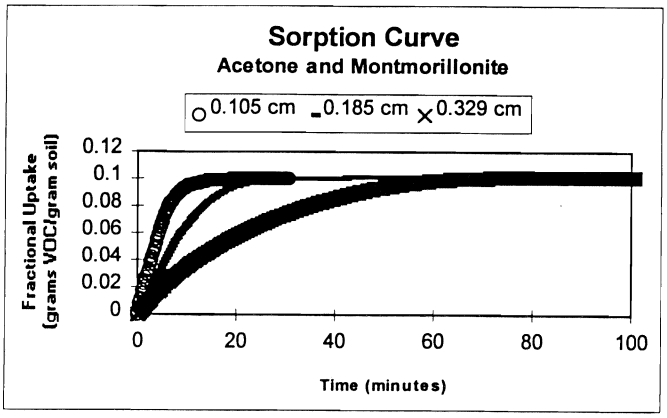

Figure 1. Sorption curve - acetone and montmorillonite.

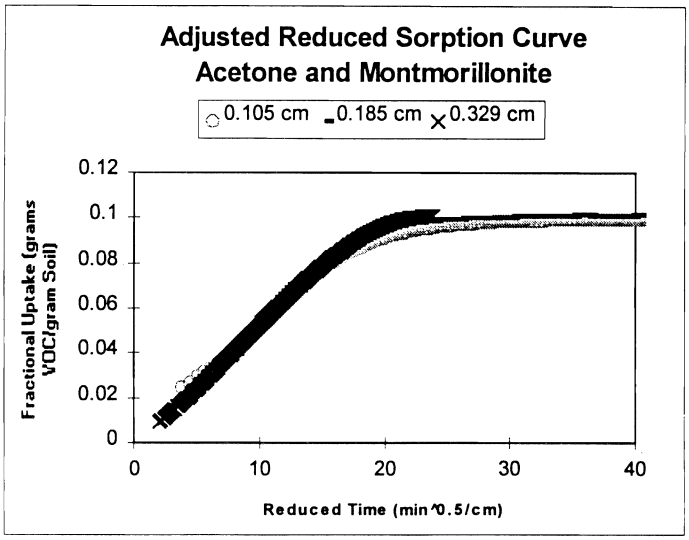

Figure 2. Reduced sorption curve - acetone and montmorillonite

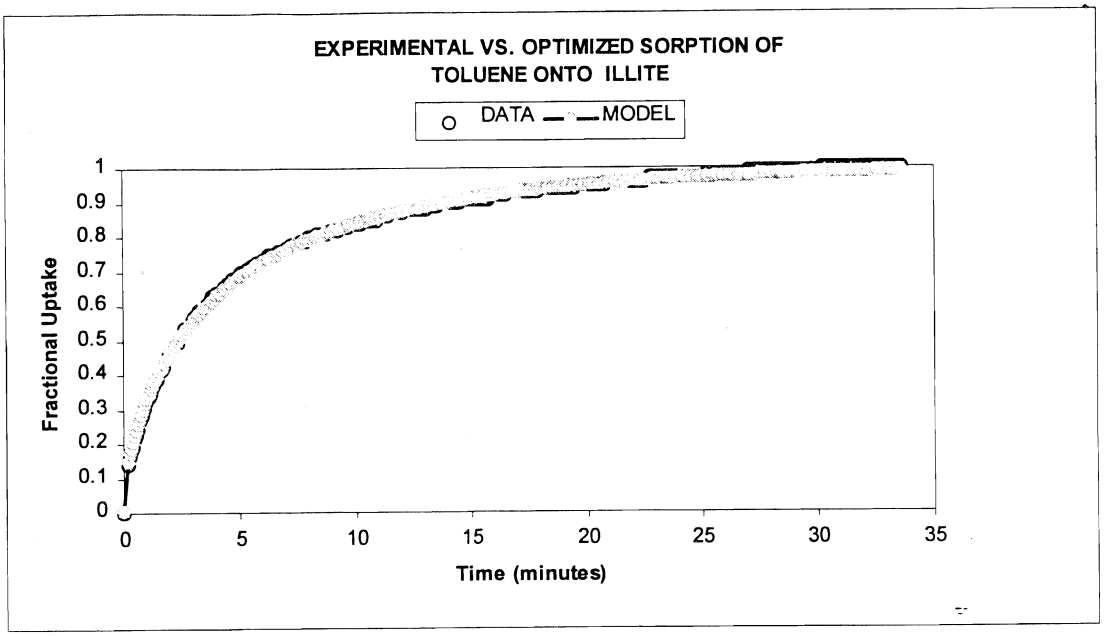

Figure 3. Experimental vs. optimized analytical sorption response.

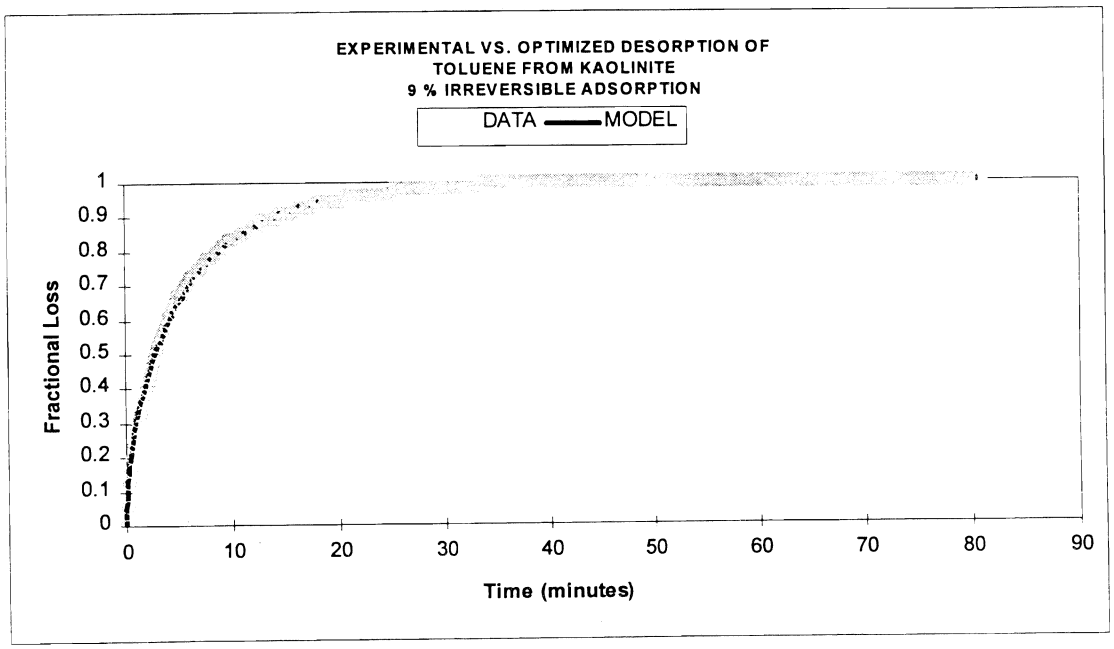

Figure 4. Experimenal vs. optimized analytical desorption response.

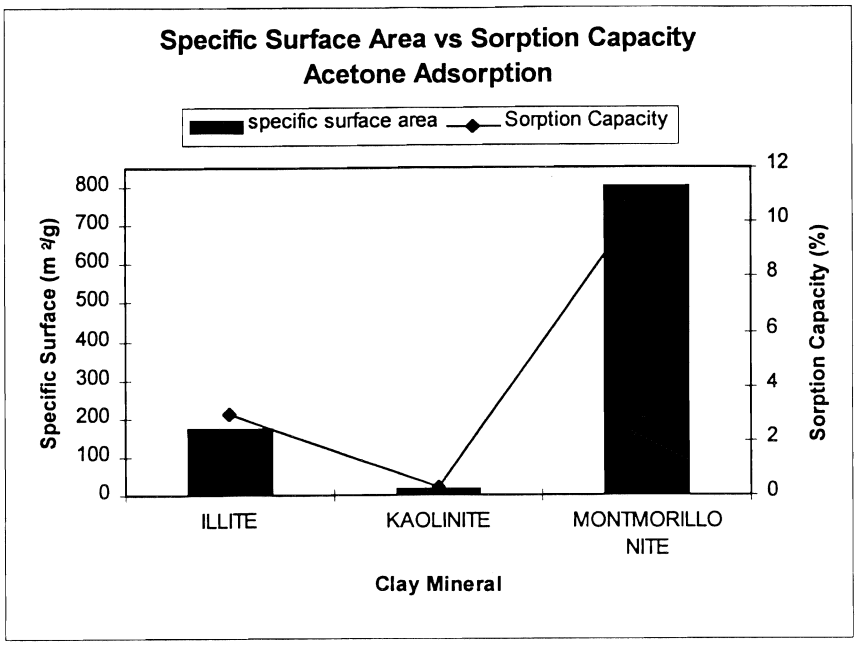

Figure 5. Specific surface area vs. acetone sorption capacity.

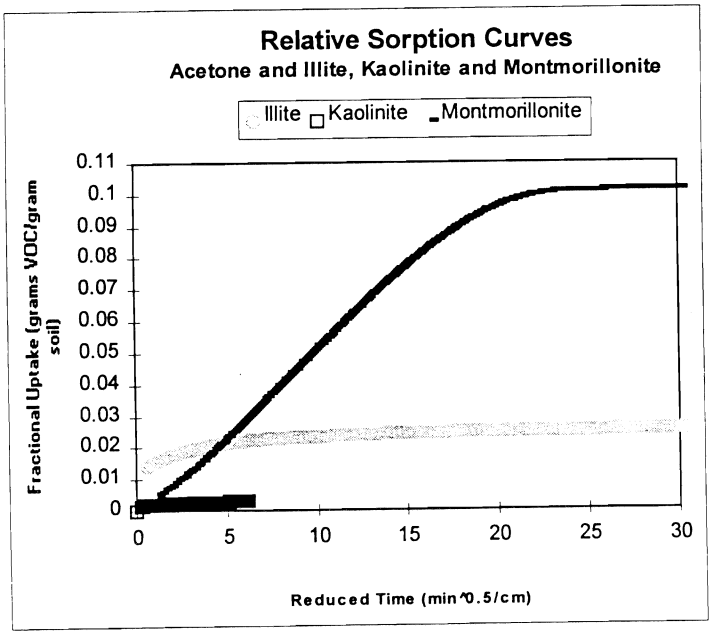

Figure 6. Relative adsorption rate of acetone.

Water Flow and Virus Transport in Weathered Bedrock

C. SCOTT FRAZIER, ROBERT C. GRAHAM, MARYLYNN V. YATES, AND MICHAEL A. ANDERSON
Department of Soil and Environmental Sciences, Riverside Campus

Summary

Rural residential developments in upland areas of California are often located on thin soils underlain by weathered, fractured bedrock. These developments typically use septic tanks for on-site waste treatment, but little is known of the potential for contaminant transport or attenuation within weathered bedrock. Viruses are of particular concern because their colloidal size makes them highly susceptible to transport. While weathered granitic bedrock can have unsaturated hydraulic conductivities within the acceptable range for on-site wastewater treatment, systems frequently fail, producing saturated conditions. In this study, fractures within weathered granitic rock were found to strongly influence the movement of MS2 bacteriophage, used as a surrogate for human enteric viruses. Applied under ponded conditions, a suspension of MS2 was channeled rapidly and deeply through bedrock fractures with little retardation in the weathered rock matrix. While weathered granitic rock can be used for septic tank leach fields, extra care must be taken to avoid excessive effluent loading rates, since resulting preferential flow increases the potential for groundwater or surface water contamination.

Key Words: weathered granitic rock, contaminant transport, on-site waste disposal

Project Objectives Addressed in 1995-96

1. To quantify movement of MS2 bacteriophage and Br^- in weathered bedrock.

2. To relate their observed movement to the morphological properties of the weathered bedrock.

Research Plan and Procedures

The study site was on a nearly level ridge top in the foothills of the San Jacinto Mountains. Soils at the site are loamy, mixed, mesic, shallow Typic Haploxeralfs underlain by a thick zone of weathered tonalite. The bedrock begins at a depth of 7 cm and can be divided into 4 horizons: the BCrt horizon (7-17 cm depth) with 26% clay, the Cr1 horizon (17-45 cm) with 16% clay, the Cr2 horizon (45-88 cm) with 11% clay, and the Cr3 horizon (88-110 cm) with 8% clay. In all of these horizons the rock is weathered such that it can be dug with some difficulty using a spade and chunks of it can be crumbled to sand-sized pieces using bare hands, although it does become harder with depth. Another important feature of the bedrock is that it is dissected by joints that yield vertical and horizontal fractures spaced about 20 cm apart. In many places, these fractures are filled with a sandy loam material, but when the bedrock is dry, cracks one or two millimeters wide are often present. The fractures are sites for preferential root growth (Sternberg et al., 1996) and have a higher organic carbon content (~0.55%) than the weathered rock matrix (~0.05%). In the Cr horizons, the fracture walls have coatings that contain more clay than the matrix.

To investigate the extent and pathways of virus transport, an aqueous tracer suspension of bacteriophage MS2 (5×10^{11} PFU [plaque forming units] L^{-1}), NaBr (1600 mg L^{-1} as Br^-), and a strongly adsorbing organic dye (food coloring with FD&C Blue #1; a 1:4 dye:water ratio) was applied to the weathered bedrock. This was accomplished by removing the thin soil cover to expose the BCrt horizon over a 2 x 2 m area. A PVC cylinder (70 cm high with a 61 cm inside diameter) was sealed to the bedrock surface with silicone gel. A float valve was used to maintain a 5 cm hydraulic head within the cylinder. A total of 77.8 L of suspension was applied over 8.75 hours. The tracer suspension had a pH of 4.23, an EC of 2.45 dS m^{-1} and ranged in temperature from 14°C to 19°C over the course of the application period.

Eight hours after the application was completed, a trench was excavated to expose a vertical cross-section of the bedrock affected by the infiltrating suspension. A wire grid with 7.5 x 7.5 cm cells was used to map the bedrock morphology, the wetting front, and the areas stained by dye. Samples were collected from the cells to include the visible wetted zone, the wetting front, and a few cells beyond. Additional samples were collected from fractures stained with dye. All samples were sealed in sterile polyethylene bags, placed in coolers at 4°C, and transported to the lab where they were stored at -4°C until

they were assayed for MS2 bacteriophage and Br^- within 1 to 22 days. A second set of samples was used to determine gravimetric water content. Background levels of Br^-, MS2, and moisture were determined from samples taken by auger in the surrounding unaffected areas.

A contour mapping software package, SURFER, was used to illustrate the two-dimensional spatial distribution of the tracers on the weathered bedrock trench wall. A geostatistical software package (Yates and Yates, 1990) was used to generate semivariogram plots from the tracer data sets to determine appropriate variogram model to use in SURFER for each data set.

Results

The distribution of the tracers in the weathered bedrock is shown in Fig. 1. The organic dye adsorbed strongly to the weathered bedrock surface and to the surfaces of fractures infiltrated by the tracer suspension. Most of the dyed fractures were continuous to the bedrock surface. The Br^- plume was much wider in the BCrt and Cr1 horizons, where the fracture density was greatest, than in the Cr2 and Cr3 horizons (Fig. 1A). The highest Br^- concentrations were coincident with dyed fractures or at the bedrock surface. The distribution of MS2 bacteriophage generally resembled that of Br^-, except that it was laterally more heterogeneous in the BCrt and the plume was more restricted in the upper part of the profile (Fig. 1B). It should be noted, however, that the apparent greater lateral spreading for Br^-, especially in the 0 to 30 cm depth range, may be an artifact of the kriging procedures used. Since the Br^- concentrations at the wetting front were generally not equal to zero (whereas MS2 concentrations usually were), the SURFER plotting program may have overestimated the Br^- concentrations beyond the wetting front boundaries. The mean MS2 bacteriophage concentration in fracture samples was 4.4 $\log_{10}$ PFU g^{-1}; whereas, the mean concentration in the weathered rock matrix was 2.6 $\log_{10}$ PFU g^{-1}. Concentrations of MS2 near fractures at the base of the sampled profile were as high as concentrations at the surface.

The maximum lateral distance from the fracture planes at which the tracers were detected in the rock matrix varied with depth (Fig. 2). In the upper two bedrock horizons (the BCrt and Cr1), the MS2 bacteriophage, Br^-, and the applied water were all detected at the same distance into the matrix, on the order of 12 to 19 cm from the fracture surface. In the lower part of the profile (the Cr2 and Cr3 horizons), the Br^- and applied water were found farther into the rock matrix (approximately 22 - 24 cm from a fracture surface) than the MS2 bacteriophage (17 cm for the Cr2 horizon, 9 cm for the Cr3), and this difference was exaggerated with depth.

Discussion

The dye was retarded by adsorption reactions at, or near, the surfaces along which the tracer suspension entered the matrix. Specifically, the dye marked the application surface, where the suspension was ponded, and the vertical fracture planes in the bedrock (Fig. 1). Thus, the dye tracer recorded the application surface and the fractures as the initial flow paths of the suspension before it moved into the weathered rock matrix.

Bromide is a conservative tracer, closely following the movement of the water in which it is dissolved. Bromide concentrations were highest near the application surface, partly because this part of the profile was wettest, and therefore retained the most Br^- solution, and partly because some evaporative concentration occurred. The contour map of Br^- concentrations (Fig. 1A) shows "ridges" of relatively high Br^- concentrations, roughly following the vertical fractures, while the lowest values are on the margins of the plume and centered in the bedrock matrix between fractures. Thus, the distribution of Br^- in the profile indicates that although water penetrated throughout the rock matrix, it did not move uniformly, but was instead strongly influenced by preferential flow in fractures.

For the MS2 bacteriophage, the lateral distribution relative to the fractures is more restricted than for Br^-, although not so much as for the dye (Figs. 1, 2). The zones of high concentrations of MS2 along fractures and low concentrations between fractures suggest that the movement of the bacteriophage into the rock matrix from the preferential flow paths is retarded. Channeling of the tracer suspension along fractures rapidly carried the MS2 bacteriophage deep into the weathered bedrock.

Previous results from this project (Graham et al., 1996), indicated that weathered granitic bedrock can provide unsaturated hydraulic conductivities within the range that is acceptable for on-site wastewater treatment. Although on-site waste disposal systems are designed to operate under unsaturated conditions, systems frequently fail, producing saturated conditions. The results presented here demonstrate that the morphologic features of weathered granitic rock, specifically the fractures, impart hydraulic characteristics that can strongly influence the movement of contaminants. Because the MS2 bacteriophage exhibits structural features, size dimensions, and adsorptive behavior similar to those of many important human enteric viruses, it is often used as a surrogate to investigate the environmental behavior of viruses that pose a threat to human health (Goyal and Gerba, 1979; Snowdown and Cliver, 1989; Powelson et al., 1991). Under saturated conditions, viruses in suspension are channeled rapidly and deeply through bedrock fractures with little retardation in the weathered rock matrix. While weathered granitic bedrock can be used for septic tank leach fields, extra care must be taken to avoid system failure and the potential for preferential flow of contaminants to ground or surface waters.

References

Goyal, S.M., and C.P. Gerba. 1979. Comparative adsorption of human enteroviruses, simian rotavirus, and selected bacteriophages to soils. Appl. Environ. Microbiol. 38:241-247.

Graham, R.C., M.V. Yates, and M.A. Anderson. 1996. Water flow and virus transport in weathered bedrock. p. 141-146. *In* Reactions of Toxic Pollutants in Soil Systems, Kearney Foundation of Soil Science 1994-95 Annual Report.

Powelson, D.K., J.R. Simpson, and C.P. Gerba. 1991. Effects of organic matter on virus transport in unsaturated flow. Appl. Environ. Microbiol. 57:2192-2196.

Snowdon, J.A., and D.O. Cliver 1989. Coliphages as indicators of human enteric viruses in groundwater. Crit. Rev. Environ. Control. 19: 231-249.

Sternberg, P.D., M.A. Anderson, R.C. Graham, J.L. Beyers, and K.R. Tice. 1996. Root distribution and seasonal water status in weathered granitic bedrock under chaparral. Geoderma 72:89-98.

Yates, S.R., and M.V. Yates. 1990. Geostatistics for waste management: A user's manual for the GEOPACK (version 1.0) geostatistical software system. Robert S. Kerr Environ. Res. Lab., Office of Research and Development, USEPA. Ada, OK.

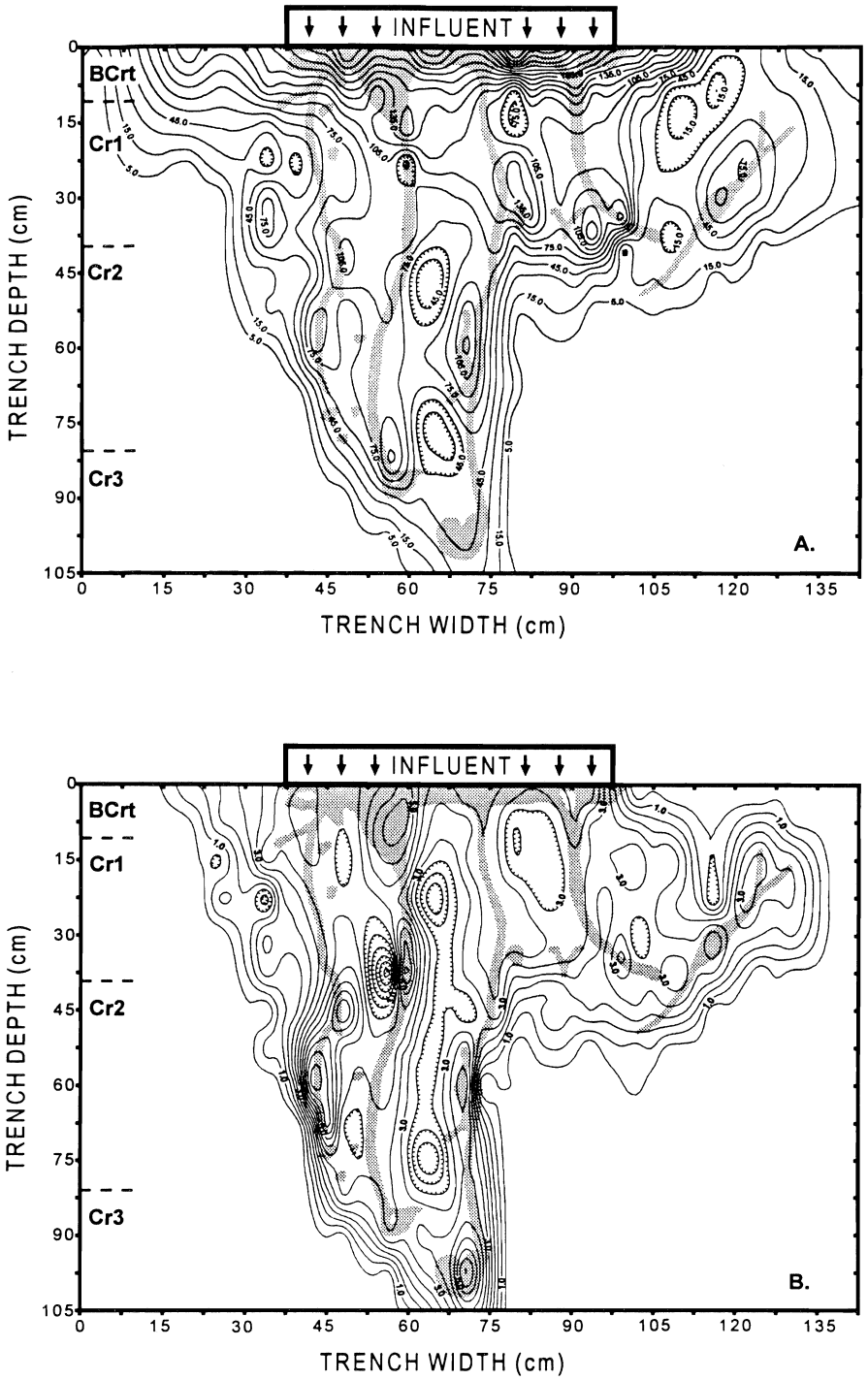

Figure 1. Spatial distribution of tracers on the weathered bedrock trench exposure: (A) bromide with concentrations in mg kg^{-1}; (B) MS2 bacteriophage with concentrations expressed as log_{10} PFU g^{-1}. The gray shading represents the areas stained by dye. The location of the influent cylinder is shown at the tops of the diagrams.

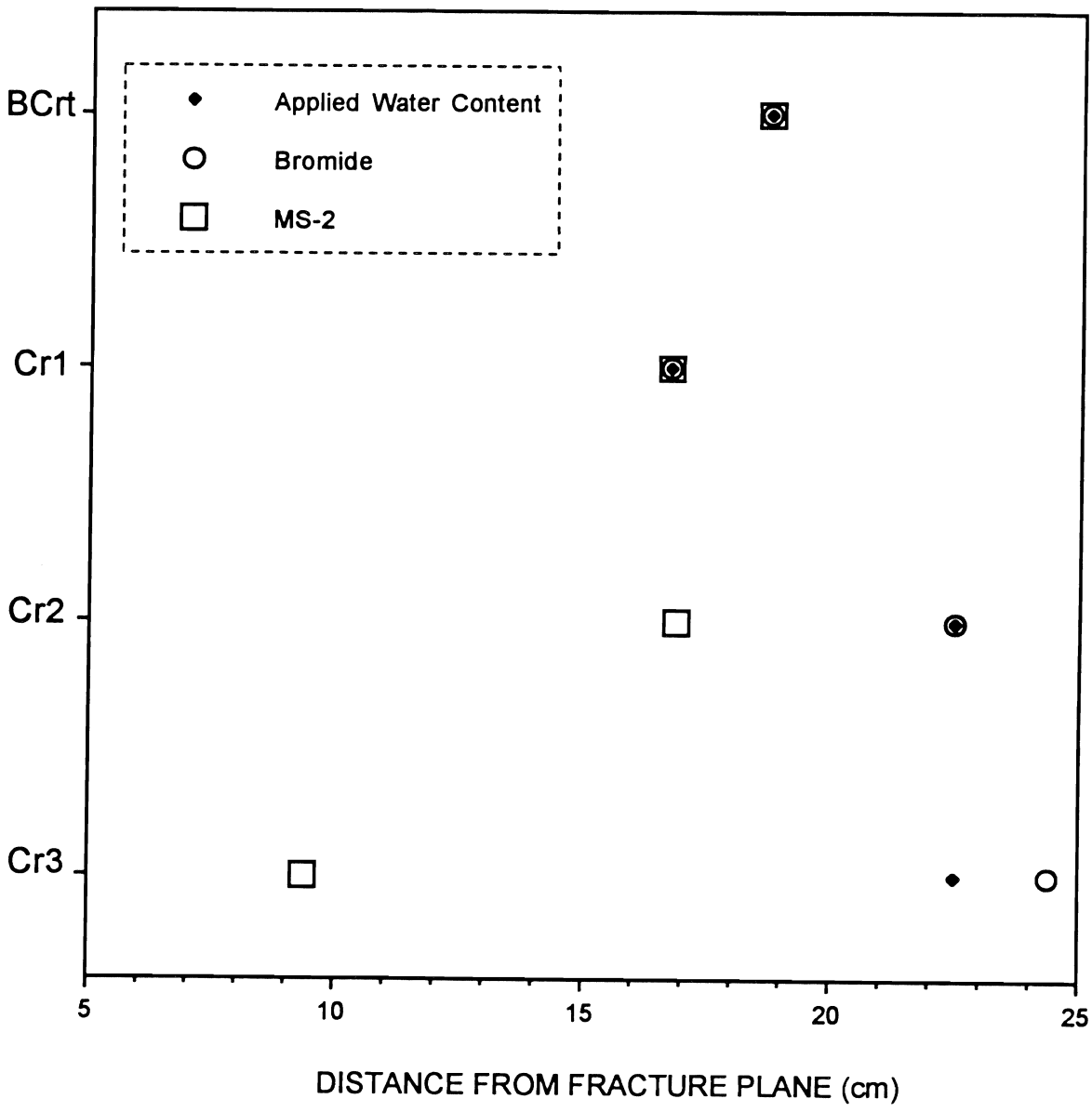

Figure 2. The aximum distance from the dyed fractures at which bacteriophage, bromide (Br^-), and applied water were detected in the weathered bedrock matrix.

Kinetics of Metal Fixation at Soil Carbonate Mineral Surfaces

WILLIAM H. CASEY[1] AND PETER A. ROCK[2]
Department of Land, Air and Water Resources, Davis Campus
Department of Chemistry, Davis Campus

Summary

Phytoremediation of metal-contaminated soil involves planting and periodic harvesting of metal-sequestering plants. Plants, mychorrhizae, and other microbes release oxalate (e.g., Graustein et al., 1977; Malujczuk and Cromack, 1982; Lapeyrie, 1988, Cromack et al., 1979), which is one of the most important, and certainly the most conspicuous, organic metal-complexing agent in soils. The high concentrations of oxalate in forest soils (≈90 g/m^2) led us to wonder if it plays a similar role in controlling movement of toxic heavy metals. This possibility was evaluated by determining new values of $\Delta G\,^\circ_f[PbC_2O_4(s)]$, $\Delta G\,^\circ_f[CdC_2O_4{\cdot}3H_2O(s)]$, $\Delta G\,^\circ_f[ZnC_2O_4{\cdot}2H_2O(s)]$, and $\Delta G\,^\circ_f[Hg_2C_2O_4(s)]$. These values were determined via amalgam electrodes that offer several advantages over traditional solubility methods. These advantages include measurements of the $\Delta G\,^\circ_f$ values without appeal to complicated models of solute speciation, the absence of a liquid-liquid junction, and verification of the cell reaction by Nernstian response of the electrode. We couple this experimental work to theoretical treatments of metal-uptake by carbonate minerals. These theoretical calculations have the potential to yield estimates of excess Gibbs energies of mixing that are more accurate than can be measured.

Key Words: thermodynamics, electrochemistry, geochemistry, soil chemistry, solubilities.

Project Goals Addressed in 1995-1996

1. To instruct students in electrochemical methods for determining thermodynamic properties of minerals and solutes that are superior to the standard solubility experiments.

2. To determine thermodynamic properties of minerals and aqueous solutions by determining $G\,°_f[PbC_2O_4(s)]$, $\Delta G\,°_f[CdC_2O_4{\cdot}3H_2O(s)]$, $\Delta G\,°_f\,[ZnC_2O_4{\cdot}2H_2O(s)]$ and $\Delta G\,°_f[Hg_2C_2O_4(s)]$.

3) To establish a theoretical framework for predicting the extents of metal uptake by soil carbonate minerals, that is, the excess Gibbs energies of mixing $[\Delta G^E_{mix}\}$metal contaminants into the lattices of aragonite and calcite.

Research Plan and Procedures

Thermodynamic Properties of Heavy-Metal-Oxalate Minerals

The thermodynamic properties of calcium monohydrate [Whewellite, $CaC_2O_4{\cdot}H_2O(s)$] are well known because of the role that this mineral plays in plant nutrition (e.g., Graustein et al., 1977) and in forming kidney stones (Finlayson et al., 1971). We took advantage of this fact to construct an electrochemical cells of the type:

$$Pb(Hg,2\text{ -phase})/PbC_2O_4(s),CaC_2O_4{\cdot}H_2O(s)CaCl_2(aq,m)Hg_2Cl_2(s)Hg(l) \qquad (1)$$

that use the well-known $\Delta G\,°_f\,[CaC_2O_4{\cdot}H_2O(s)]$ value to determine the relatively poorly known value of $\Delta G\,°_f\,[PbC_2O_4(s)]$. Once the value of $\Delta G\,°_f\,[PbC_2O_4(s)]$ is estimated from a cell containing Whewellite, $\Delta G\,°_f$ values for the other heavy-metal oxalate phases, such as $ZnC_2O_4{\cdot}2H_2O(s)$, $CdC_2O_4{\cdot}3H_2O(s)$ and $Hg_2C_2O_4(s)$ can be estimated from electrodes containing the appropriate corresponding metal amalgam, such as:

$$Zn(Hg,sat.)/ZnC_2O_4{\cdot}H_2O(s)/Na_2C_2O_4(aq,m)/PbC_2O_4(s)/Pb(Hg,2\text{ -phase}) \qquad (2)$$

or

$$Pb(Hg,2\text{ -phase})/PbC_2O_4(s)/Na_2C_2O_4(aq,m)/Hg_2C_2O_4(s)/Hg(l) \qquad (3)$$

Application of the Nernst equations to the cell reactions yields uncommonly simple equations for the respective values of E°, and hence the values of $\Delta G\,°_f$ for the unknown solid.

Thermodynamics Properties of Solid-Solution Carbonate Minerals

The extent that calcium-carbonate minerals take up metal impurities reflects the difference in energies of the solid-solution ($Ca_xM_{1-x}CO_3$) relative to that of the pure calcium-carbonate mineral ($CaCO_3$) and the pure metal-carbonate mineral (MCO_3). This extent could be calculated if better estimates of the lattice energies of forming the solid solution were available. This energy can be resolved into separate contributions from polarization, repulsion, and electrostatic energies.

In order to develop a general theory for predicting Gibbs excess energies for metal-carbonate solid solutions, it is necessary to first examine the formation of pure metal-carbonate minerals. We consider the condensation of ions from the gas phase:

$$M^{2+}(g) + CO_3^{2-}(g) \rightarrow MCO_3(s). \qquad (4)$$

To date, changes in the electrostatic and polarization energies have been calculated for metal-carbonate minerals where M = Ca, Cd, Fe, Mg, and Mn as a function of the charge on oxygens in the mineral lattice and in the $CO_3^{2-}(g)$ reactant. The electrostatic contribution to lattice energy was calculated via a point-charge pairwise interaction approach.

The change in lattice energy due to polarization was determined in a two-step process. First the oxygen polarizabilities of the pure metal-carbonate minerals were determined from the crystal refractive indices by employing the Lorentz local field model (see Lawless and DeVries, 1964). Next, a self-consistent method was employed to determine the oxygen-dipole moment in both $MCO_3(s)$ and $CO_3^{2-}(g)$. With this information, the polarization energy is computed.

The calculation of the repulsive contribution to the lattice energy was calculated using a potential of the form: $\Delta U_{repulsive} = AR^{-9}$ (Slater, 1939). The quantity A is a constant while R represents the distance of closest approach between M^{2+} and CO_3^{2-} in $MCO_3(s)$. By using the following equilibrium condition:

$$\frac{d}{dR}\left[\Delta U_{electrostatic} + \Delta U_{polarization} + \Delta U_{repulsive}\right] = 0 \qquad (5)$$

the value of the constant A can be determined.

Results

Heavy-Metal-Oxalate Minerals

The new values for $\Delta G\,^{\circ}_f[PbC_2O_4(s)]$, $\Delta G\,^{\circ}_f\,[ZnC_2O_4{\cdot}2H_2O(s)]$, $\Delta G\,^{\circ}_f\,[HgC_2O_4(s)]$, and $\Delta G\,^{\circ}_f\,[CdC_2O_4{\cdot}3H_2O(s)]$ are given in Table 1. These new values of $\Delta G\,^{\circ}_f$ [were employed in multicomponent speciation calculations to examine whether the soil solutions in oxalate-rich environments could reach equilibrium with heavy-metal oxalate solids if contaminated with heavy metals. The possibility that the metal concentrations could be controlled by oxalato complexes was evaluated by including complexation constants taken from Martell and Smith (1977, 1982) (Table 3).

In this modeling, we use the soil solution compositions of spodosols reported by Dahlgren et al. (1989) (Table 3). One μmole/kg is used as the total dissolved concentration of each heavy metal in the solutions described in Table 3. While these concentrations are relatively high, even for polluted soils, the same essential results would be observed if smaller concentrations were modeled, as we show. The total dissolved oxalate concentrations are difficult to estimate because in most studies the concentrations are reported per mass of soil or plant material (e.g., Graustein et al., 1977; Cromack et al., 1979; Malajczuk and Cromack, 1982). Inskeep and Comfort (1986) calculate a range of concentrations near the roots hairs of *Pinus radiata* of 4-1640 mM. The estimated value depends sensitively on the author's assumptions about rates of transport away from the root hairs and rates of microbial degradation. Because sampling of the soil solution is difficult, the local concentrations are likely to be much higher than the average value. Dissolved oxalate concentrations of 35 μM were measured (Dahlgren et al., 1991) for spodosols and we therefore consider a total dissolved concentration of 100 mm to be reasonable for the modeling calculations.

Properties of Solid-Solution Carbonate Thermodynamics Minerals

The modeling effort is coming to fruition, although much work remains to be done. In Table 5, we report the calculated values of oxygen polarizabilities for a range of metal-carbonate minerals. In Table 6, we report the variation of the electrostatic and polarization energies as a function of the charge on the oxygen (an independent varible in this case). As one can see, the energy contributions are very sensitive to the partial charge assigned to the oxygen which, in this case, we determined through calculations using the Gaussian 94 molecular-orbital modeling program, using the 6-31++G* basis set.

Discussion

Heavy-Metal-Oxalate Minerals in Nature

The $CdC_2O_4 \cdot 3H_2O(s)$ and $ZnC_2O_4 \cdot 2H_2O(s)$ solids are sufficiently soluble (Table 4) that they probably would never form in natural systems, unless the soil metal concentrations approach millimolar concentrations of dissolved metal, which is unlikely even in highly contaminated environments. Soil solutions, however, could easily reach equilibrium with $PbC_2O_4(s)$. Although $Hg_2C_2O_4(s)$ is highly insoluble, it is unlikely to form because most small concentrations of dissolved chloride ion would lead to formation of calomel, a much more stable solid than $Hg_2C_2O_4(s)$. While the heavy-metal oxalate phases could form during soil detoxification by plants or microbes, the resulting solids would not be in equilibrium with the adjacent soil solution at reasonable chemical conditions (Table 4).

References

Allison, J. D., D. S. Brown, and K. J. Novo-Gradac. 1991. MINTEQA2/PRODEFA2-A geochemical assessment model for environmental systems: Version 3.0 users manual. USEPA Report 600/3-91/021. Center for Exposure Assessment and Modeling, Office of Research and Development, Environmental Research Laboratory, Athens, GA.

Cromack, K. Jr., P. Sollins, W. D. Graustein, K. Speidel, A. W. Todd, G. Spycher, C. Y. Li, and R. L. Todd. 1979. Calcium oxalate accumulation and soil weathering in mats of the hypogeous fungus *Hysterangium crassum*. Soil Biol. Biochem. 11:463-468.

Dahlgren, R. A. and F. C. Ugolini. 1989. Effects of tephra addition on soil processes in spodosols in the Cascade Range, Washington. Geoderma 45:331-355.

Dahlgren, R. A., K. A. Vogt, and F. C. Ugolini. 1991. The influence of soil chemistry on fine root aluminum concentrations and root dynamics in a subalpine Spodosol, Washington State, USA. Plant and Soil 133:117-129.

Driscoll W., P. Mushak, J. Garfias, and S. J. Rothenberg. 1992. Reducing lead in gasoline- Mexico's experience. Environ. Sci. and Technol. 26:1702-1705.

Finlayson, B., L. L. Hench, and L. H. Smith. 1971. Urolithiasis, Physical Aspects, National Academy of Science, Washington, D.C.

Graustein, W. C., K. Kromack Jr., and P. Sollins. 1977. Calcium oxalate-occurence in soils and effect on nutrient and geochemical cycles. Science 198:1252-1254.

Inskeep, W. P. S. D. and Comfort. 1986. Thermodynamic predictions for the effects of root exudates on metal speciation in the rhizosphere. J. Plant Nutrition 9:3-7.

Latimer, W. M. 1952. The oxidation states of the elements and their potentials in aqueous solutions. 2nd. ed. Prentice-Hall, Englewood Cliffs, NJ.

Lawless, W. N. and R. C. DeVries. 1964. J. Phys. Chem. 25:1119.
Lapeyrie, F. 1988. Oxalate synthesis from soil bicarbonate by the mycorrhizal fungus Paxillus involutus. Plant and Soil 110:3-8.
Malajczuk, N., and K. Cromack Jr. 1982. Accumulation of calcium oxalate in the mantle of ectomycorrhizal roots of *Pinus radiata* and *Eucalyptus marginata*. New Phytol. 92:527-531.
Martell, A. E., and R. M. Smith. 1977. Critical Stability Constants: Organic Ligands. Plenum Press, New York/London.
Martell, A. E., and R. M. Smith. 1982. Critical Stability Constants: First Supplement. Plenum Press, New York/London.
Moore J. N. and S. N. Luoma. 1990. Hazardous wastes from large-scale metal extraction. Environ. Sci. and Technol. 24:1279-1285.
Naumov, G. B., B. N. Ryshenko, and I. L. Khodakovsky. 1974. Handbook of Thermodynamic Data (translated by G. J. Soleimani, edited by I. Barnes and V. Speltz), U.S. Geol. Surv. Wat. Res. Rept. 74-001, p. A-74.
Slater, J.C. 1939. Introduction to Chemical Physics, p. 389, McGraw-Hill, New York.
Vosburgh, W. C. and J. F. Beckman. 1940. The solubility of cadmium and zinc oxalates in salt solutions. J. Amer. Chem. Soc. 62:1028-1031.
Wagman, D. D., W. H. Evans, V. B. Parker, R. H. Schumm, I. Halow, S. M. Bailey, K. L. Churney, and R. L. Nuttall. 1982. The NBS tables of chemical thermodynamic properties: selected values for inorganic and C_1 and C_2 organic substances in SI units. J. Phys. Chem. Ref. Data, 11 (Supplement 2), 392 pp.

Table 1. Experimental $\Delta G\,^{\circ}_{f}$ values at 25.0°C for heavy-metal oxalate solids compared with estimates from selected other studies. The value for $\Delta G\,^{\circ}_{f}$ [$CaC_2O_4 \cdot H_2O$(s)] reported by Wagman et al. (1982) was used in the calculations of $\Delta G\,^{\circ}_{f}$ values for other phases and is not a new result.

Phase	K_{sp}	$\Delta G\,^{\circ}_{f}$ (kJ mol^{-1})	Source
PbC_2O_4(s)	$8.3*10^{-12}$	-754.4	Latimer, 1952
	$8.4*10^{-10}$	-750.1	Wagman et al., (1982)
	$2.95*10^{-11}$	-758.70	this study
	$7.2*10^{-11}$	-749.8	Naumov et al., (1971)
$Hg_2C_2O_4$(s)	$1.00*10^{-13}$	-588.7	Latimer (estimate; 1952)
	$1.73*10^{-12}$	-587.51	this study
$ZnC_2O_4 \cdot 2H_2O$(s)	$1.28*10^{-9}$	-1345.95	Vosburgh and Beckman, 1940
	$1.37*10^{-9}$	-1345.8	Wagman et al., 1982
	$1.06*10^{-9}$	-1346.45	this study
$CdC_2O_4 \cdot 3H_2O$(s)	$1.44*10^{-8}$	-1507.66	Vosburgh and Beckman, 1940
	$1.42*10^{-8}$	-1507.7	Wagman et al., 1982
	$1.84*10^{-8}$	-1507.05	this study

Table 2. Equilibrium constants for the complexation of Ca^{2+}(aq), Cd^{2+}(aq), Pb^{2+}(aq), and Zn^{2+}(aq) by oxalate from Martell and Smith (1977, 1982). The constants correspond to 298.2 K and I=0.1 M, except for some which I = 1.10[1] or I = 2.0[2].

Reaction		log β
$ox^{2-} + H^+$	$= Hox^-$	1.04
$ox^{2-} + 2H^+$	$= H_2ox°$	3.82
$ox^{2-} + Ca^{2+}$	$= Ca(ox)°$	1.66[1]
$2ox^{2-} + Ca^{2+}$	$= Ca(ox)_2^{2-}$	2.69[1]
$ox^{2-} + Cd^{2+}$	$= Cd(ox)°$	2.61[2]
$2ox^{2-} + Cd^{2+}$	$= Cd(ox)_2^{2-}$	4.11[2]
$3ox^{2-} + Cd^{2+}$	$= Cd(ox)_3^{4-}$	5.06[2]
$ox^{2-} + Pb^{2+}$	$= Pb(ox)°$	3.32[3]
$2ox^{2-} + Pb^{2+}$	$= Pb(ox)_2^{2-}$	5.03[3]
$ox^{2-} + Zn^{2+}$	$= Zn(ox)°$	3.48
$2ox^{2-} + Zn^{2+}$	$= Zn(ox)_2^{2-}$	5.48
$2ox^{2-} + Hg_2^{2+}$	$= Hg2(ox)_2^{2-}$	6.98[1]

[1]1.0 M $NaClO_4$; [2]1.0 M $NaNO_3$; [3]1.5 M KNO_3

Table 3. Concentrations (μmole/kg) of chemical constituents in the simulated soil solution in spodusols from Findlay Lake, Washington (from Dahlgren et al., 1989). DOC corresponds to dissolved organic carbon and HZ refers to the soil horizon of the sample of soil solution.

pH	Al	Si	Ca	Mg	K	Na	Cl	NO_3	SO_4	HCO_3	DOC	HZ
3.88	61	123	156	63	129	92	107	19	87	0	6758	Oa
3.99	63	550	52	46	116	151	316	6	125	0	1986	E
4.36	40	341	40	23	26	96	146	3	69	0	706	Bhs
4.98	16	111	9	9	8	37	52	3	15	35	261	Bs
5.30	23	164	39	40	22	94	96	2	76	42	175	C

Table 4a. The percentage of the total dissolved concentration present as a selected solute species and saturation indices for the hypothetical soil solutions in Table 3.

	Species	Horizon #1 (%)	Horizon #2 (%)	Horizon #3 (%)	Horizon #4 (%)	Horizon #5 (%)
Oxalate	$C_2O_4^{2-}$	41.3	47.6	67.7	89.2	96.5
	$HC_2O_4^-$	58.2	52.1	32.2	10.5	2.9
Cd(II)	Cd^{2+}	96.3	93.8	95.3	96.3	94.7
	$CdC_2O_4^o$	1.2	1.3	2.0	2.9	2.9
	$CdCl^+$	tr	2.4	1.2	tr.	tr.
	$CdSO_4^o$	1.6	2.3	1.4	tr.	1.6
Zn(II)	Zn^{2+}	90.5	88.9	85.3	81.4	80.2
	$ZnSO_4^o$	1.2	1.8	1.0	tr.	1.1
	$ZnC_2O_4^o$	8.2	9.3	13.6	18.2	18.5
Ca(II)	Ca^{2+}	98.7	98.1	98.7	99.4	98.5
	$CaSO_4^o$	1.2	1.7	1.0	tr.	1.2
Pb(II)	Pb^{2+}	90.9	88.8	87.3	85.8	83.3
	$PbC_2O_4^o$	5.7	6.4	9.6	13.3	13.3
	$PbSO_4^o$	3.0	4.3	2.6	tr.	2.8
Hg(I)	Hg_2^{2+}	98.2	97.8	94.0	94.0	94.1
	$(Hg)_2C_2O_4$	1.8	2.2	6.0	6.0	5.9

Table 4b. The saturation indices (Q_{sp}) and solubility products (K_{sp}) correspond to reactions of the form:

$$ML_x(s) = M^{2+}(aq) + x\ L^{-\frac{2}{x}}(aq).\ \text{espressed as log}\ \frac{Q_{sp}}{K_{sp}}$$

Reaction Products	log	log	log	log	log
Whewellite	+ 0.43	- 0.12	-0.52	- 0.55	+ 0.1
$Cd(OH)_2$ (A)	-13.05	-11.85	-11.08	- 9.83	- 9.20
$Cd(OH)_2$ (C)	-12.97	-11.77	-11.00	- 9.47	- 9.12
$CdC_2O_4 \cdot 3H_2O$	-3.80	-2.75	-2.56	- 2.41	- 2.40
Hg_2Cl_2(s) Calomel	+3.80	+4.74	+4.09	+ 3.2	+ 3.7
$Hg_2C_2O_4$	+1.24	+1.30	+1.48	+ 1.63	+ 1.62
$Hg_2(OH)_2$	-3.56	-3.36	-2.61	- 1.65	+ 0.7
$PbCO_3$(s) Anglesite	-2.48	-2.33	-2.55	- 3.19	- 2.52
PbC_2O_4(s)	+0.01	+0.06	+0.24	+ 0.38	+ 0.38
ZnO(s) Zincite	-9.49	-9.28	-8.54	- 7.3	- 6.9
$ZnC_2O_4 \lozenge 2H_2O$	-1.59	-1.54	-1.37	- 1.25	- 1.24
$Zn(OH)_2$(A)	-10.80	-10.59	-9.85	- 8.62	- 7.99

Table 5. Calculated values of the oxygen polarizabilities in the carbonate lattice (calcite structure) for a range of metal-carbonate minerals. The polarizabilities are in units of 10^{-30} m^3.

Metal Carbonate	Parallel Oxygen	Perpendicular Oxygen
$CaCO_3$	1.322	1.171
$CdCO_3$	1.328	1.045
$FeCO_3$	1.378	1.202
$MgCO_3$	1.322	1.195
$MnCO_3$	1.367	1.207

Table 6. Contributions of electrostatic and polarization energies to the lattice energies (see Eqn. 5) units of kJ mol^{-1}.

Oxygen Charge	$\Delta U_{electrostatic}$	$\Delta U_{polarization}$
-0.90	-2957.87	63.52
-0.91	-2997.87	59.02
-0.92	-3038.43	53.25
-0.93	-3079.46	46.20
-0.94	-3120.93	37.87
-0.95	-3162.77	28.27
-0.96	-3204.90	17.40
-0.97	-3247.29	5.24
-0.98	-3289.89	-8.18
-0.99	-3332.63	-22.89

The Soil Chemistry of Iodine

J. A. WARNER, R. A. DAHLGREN AND W. H. CASEY
Department of Land, Air and Water Resources, Davis Campus

Summary

The Chernobyl accident contaminated approximately 20 percent of Byelorussia (37,500 km^2) with fallout particles containing radioactive iodine (Lukashev, 1993; Hoshi et al., 1994). This radioactive iodine may be inhaled by humans or ingested with contaminated food. Exposure to even small amounts of radioiodine is hazardous, particularly for children, since it is preferentially stored in the thyroid gland. Correspondingly, incidence rates of childhood thyroid cancer have increased by a factor of six in the Ukraine since the Chernobyl accident (Likhtarev et al., 1995). Elevated levels of radioiodine are also found in soils and in the atmosphere near nuclear fuel reprocessing plants (Hauschild and Aumann, 1989; Robens et al., 1989; Stewart and Wilkens, 1985) and in areas where nuclear weapons testing occurs. The U.S. Nuclear Regulatory Agency is particularly concerned about the mobility of radioiodine in the shallow engineered pits that are proposed to store low-level radioactive waste (e.g., Schulz et al., 1994). These pits are to be lined with layers of relatively reactive and impermeable clays, possibly soils, intended to prevent the migration of waste constituents (Gu and Schulz, 1991; Schulz et al., 1992). Volcanic soils are being investigated because they commonly contain high concentrations of noncrystalline inorganic materials, such as imogolite and ferrihydrite, that have relatively large specific surface areas (700-1000 m^2/g) and appreciable anion exchange capacity under acidic conditions (Parfitt, 1980; Schulz et al., 1992; Shoji et al., 1993).

The agricultural industry is also concerned with the biogeochemistry of iodide now that pressure is building to eliminate methyl bromide as a soil fumigant because of its ozone-destroying properties and high volatility. Roughly 20-60% of the atmospheric burden of methyl bromide originates from soil fumigation (Lobert et al., 1995; Wong, 1991). Methyl iodide is being tested as a replacement for methyl bromide (Liyanage et al., 1993; J.J. Sims, University of California-Riverside, personal communication, 1996) because it has a much lower vapor pressure, a low natural flux (mostly from the oceans), and because it hydrolyzes rapidly in natural waters. The factors controlling iodine chemistry in the soil environment were investigated by performing sorption studies on volcanic soils and noncrystalline components of the inorganic fraction of these soils. Rates of iodide retention by volcanic-ash soils were slow and did not attain a steady-state after 300 h. The reaction of iodide with the volcanic-ash soils was consistent with a rapid initial uptake by imogolite and ferrihydrite, followed by a slower reaction of soil organic matter with oxidized forms of iodide. Under our experimental conditions, iodide was likely oxidized slowly by dissolved oxygen to molecular iodine. The slow rate of iodination was consistent with the continual formation and reaction of $I_2(aq)$ or HOI(aq) by titration with soil organic matter.

Key Words: iodine, volcanic soils, soil organic matter, adsorption, imogolite

Project Objectives Addressed in 1995-1996

1. To determine the sorption affinity, reaction kinetics and speciation of iodine partitioned to soil materials following additions of iodide.

2. Comparison of reaction of iodide with a series of volcanic-ash soils to the noncrystalline materials that constitute much of the inorganic fraction of these soils.

Research Plan and Procedures

Twelve soil samples were selected for study from the vicinity of Mount Shasta in northern California. Soil samples were passed through a 2-mm sieve to remove coarse fragments and the <2-mm fraction was refrigerated (3°C) at field-moisture water content for the duration of the study.

A subsample of the field-moist soil samples was air dried for solid-phase characterization. Soil pH, organic carbon, anion exchange and surface area were determined on all soil samples. Selective dissolution was used to characterize noncrystalline materials and secondary iron-oxide composition as follows: (i) sodium pyrophosphate (Al_p, Fe_p), one 16 h extraction; (ii) acid-ammonium oxalate (Al_o, Fe_o, Si_o), one 4 h extraction at pH 3 in the dark; and (iii) citrate dithionite (Fe_d), one 16 h extraction at 23°C . Iron, aluminum, and silicon concentrations in all extracts were measured by inductively coupled plasma (ICP) spectroscopy.

Iodide sorption to synthetic imogolite and ferrihydrite was examined as a function of equilibration time (0.5-240 h), pH (4-8) and initial iodide concentration (0.025-1 mmol/L). For the kinetic study, 0.5 g (dry weight equivalent) of synthetic imogolite (pH=5.5) or 2.0 g of ferrihydrite (pH=4.0) were added to 50 mL of solution containing 1 mmol/L sodium iodide and 100 mmol/L sodium perchlorate. Experiments were conducted in the dark at 20°C with end-over-end mixing at two cycles per min. A 1.5 mL subsample of the suspension was collected at 0.5, 1, 12, 24, 72, 144, and 240 h. These subsamples were centrifuged and filtered through a 0.2 μm syringe filter and analyzed for iodide [I^-(aq)], iodate [IO_3^-(aq)], and active iodine which consists of molecular iodine [I_2(aq)], hypoiodous acid [HOI(aq) or OI^-(aq)], and the triiodide ion [I_3^-(aq)] (APHA, 1985).

Iodide Sorption by Volcanic-Ash Soils

Iodide sorption as a function of the initial iodide concentration was determined for synthetic imogolite and ferrihydrite. The pH was maintained at 5.5, which was the pH of maximum sorption for imogolite and also the approximate pH of the soil suspensions from the volcanic soils used in this study. Iodide was incrementally added as sodium iodide (0.1 *M*) in order to obtain, in the absence of sorption, the following aqueous concentrations: 0.025, 0.05, 0.1, 0.25, 0.3, 0.4, 0.5, 0.75, and 1 mmol/L. Suspensions were allowed to equilibrate 30 min

following addition of each sodium iodide increment and 1.5 mL of suspension was collected prior to addition of the next increment. Samples were centrifuged, filtered and analyzed as described above.

A subsample of each field-moist soil was sterilized to assess the role of microbial metabolism in iodine retention by soils. Two methods of sterilization were compared since sterilization methods have been shown to alter soil physical and chemical properties (Wolf et al., 1989; Muramatsu et al., 1990). A subsample of each soil was sterilized by gamma-irradiation from a ^{60}Co source. The Mudwell soil was also sterilized by autoclaving the sample twice, 24 h apart, each time for 1 h at 120°C. In both methods, the soils were maintained at field-mois water content to avoid any alterations that may result from drying of soils.

Ten grams (dry weight equivalent) of sterilized or non-sterilized soil were placed in a 65 mL high density polyethylene bottle. Sufficient sodium perchlorate and sodium iodide were added to obtain a final solution volume of 50 mL containing 1 mmol/L sodium iodide and 100 mmol/L sodium perchlorate. A 1.5 mL subsample of the suspension was collected at 6, 12, 36, 84, 132, 228 and 300 h. Analysis was performed as above for iodine species.

The pre- and post-kinetic experiment soil samples were extracted with 0.016 *M* sodium dihydrogen phosphate (soluble + sorbed) and 0.1 *M* sodium hydroxide (soluble + sorbed + organically complexed) solutions in order to recover iodine retained by the solid-phase (Whitehead, 1973). Although these extraction techniques are not exclusively specific for a given solid-phase iodine pool, they do serve as a basis for comparison among contrasting soils and treatments. Three grams of soil (dry weight equivalent) were reacted with 50 mL of extraction solution for 16 h with gentle shaking on a reciprocating shaker. Total iodine was determined on the A and Bw horizons of the Mudwell soil following the kinetic study by refluxing 2 g of soil with 2 *M* sodium hydroxide for 45 min (Whitehead, 1973). All extracts were centrifuged, filtered through a 0.2 μm filter, and digested using 2% potassium persulfate (1:9, sample:reagent) to destroy soluble organic matter. Iodate was measured colorimetrically (APHA, 1985). The amount of iodine entrained in the solution-phase of the moist soils was subtracted from the total iodine extracted by these methods to determine the amount of iodine retained by the solid phase.

Rate Studies using Laboratory-grade Humic Acid

The rate of reaction of aqueous solutions of molecular iodine with Aldrich sodium humate was first characterized at pH values between 3.6 and 6.6 and at initial molecular iodine concentrations ranging from $1x10^{-5}$ M to $1x10^{-4}$ M, using a batch technique. All experiments were conducted in the dark at 25 ± 0.2°C in a background ionic strength of 9.2 mM $NaClO_4$. The pH was initially adjusted using either 0.1 M $HClO_4$ or NaOH and was subsequently controlled by a titrimeter solution of 0.1 N NaOH. An Orion 94-53 iodide selective electrode paired with an Orion 90-02 double junction Ag/AgCl reference electrode was used to monitor changes in iodide concentration. A HP 8452A diode array spectrophotometer was used to simultaneously monitor the triiodide absorbance

at 351 nm and molecular iodine at 460 nm. Experiments were initiated by the addition of 5 mL of a 0.5 g/L solution of Aldrich sodium humate to a reaction vessel containing 5 mL of 50 mM I^- and 115 mL of 10 mM $NaClO_4$ in a 25°C water bath. In separate experiments the humate was replaced by distilled, deionized water, and either N_2 or air was bubbled slowly through the solution. Measurement of I_2(aq) and I^-(aq) concentrations were also performed colorimetrically (APHA, 1985).

Results

The twelve soil samples selected for study provide a range of chemical and mineralogical properties representative of soils formed from volcanic ejecta in northern California (Table 1). Organically complexed iron and aluminum (pyrophosphate-extractable) were generally very low (<9 g/kg). Allophane/imogolite concentration in the <2-mm fraction, estimated from Si_o x 7.14, ranged between 14 and 192 g/kg and was most abundant in the Harris and Modoc Bw horizons. The percentage of allophane/imogolite in the clay fraction ranged between 5 and 80%. Imogolite, rather than allophane, was the dominant allophanic clay as revealed by TEM (Takahashi et al., 1993). The Fe_o/Fe_d ratio indicates a wide range in the degree of iron oxide crystallinity, from <20% in the Bartle and Mudwell soils to >85% in the Modoc soil. The noncrystalline fraction is composed primarily of ferrihydrite which ranges in concentration between 9 and 26 g/kg (Fe_o x 1.7). Dehydrated tubular halloysite (0.7 nm) was the dominant crystalline mineral in the A horizon of all soils, while hydrated halloysite (1.0 nm) was often a co-dominant mineral with dehydrated halloysite in the Bw horizons.

Iodide Adsorption by Imogolite and Ferrihydrite

The adsorption of iodide by imogolite and ferrihydrite was rapid and reached a steady-state within 30 min. The amount of iodide adsorbed onto ferrihydrite and imogolite as a function of pH displayed different patterns (Fig. 1a). The pH of maximum iodide adsorption by imogolite was pH=5.5 (2.25 mmol/kg). The sorption density decreased slightly to a relatively constant value for pH<5.5 (75% of maximum), showed a minimum at pH 7 and displayed a gradual increase at pH>7 (Fig. 1a). Iodide sorption onto ferrihydrite increased with decreasing pH (Fig. 1a). Unlike imogolite, no maximum in sorbed concentration was observed for ferrihydrite. Sorption of iodide onto natural imogolite was indistinguishable from adsorption onto synthetic imogolite (Fig. 1a).

Iodide sorption by imogolite and ferrihydrite over the initial aqueous concentration range of 0.025-1.0 mmol/L shows that iodide sorption increases in a near-linear fashion as the initial iodide concentration increases (Fig. 1b). It is clear from Fig. 1b that the maximum sorption capacity of imogolite and ferrihydrite was not exceeded at the 1 mmol/L initial concentration. For any given initial iodide concentration, imogolite displays a 3-to 4-fold greater sorption of iodide than ferrihydrite on a mass basis.

Iodide Sorption by Volcanic-Ash Soils

In sharp contrast to the adsorption experiments with synthetic ferrihydrite and imogolite, the adsorption of iodide by non-sterilized soils was quite slow. The concentration of iodide in a soil suspension typically did not reach a steady-state value within 300 h of reaction (Fig. 2), even though the clay mineralogy is often dominated by imogolite, which showed rapid equilibration. Only for a single soil (Bartle Bw) did the iodide concentration appear to reach a steady-state value in 300 h. There was no appreciable change (±0.2) or trend (increase or decrease) in pH values of the soil suspensions between the initial and 300 h measurements (Tables 1 and 2).

The extent of reaction also differed among the soils in the series. The total iodide retained by the soils varied from 0.55 mmol/kg for the Bartle Bw horizon, which was the only soil to achieve a steady-state concentration in 300 h, to 2.95 mmol/kg for the Mudwell Bw horizon. Most importantly, the extent of reaction was not predictable at any given reaction time from soil organic matter content ($p=0.68$ at 300 h), the concentration of imogolite ($p=0.31$) or ferrihydrite ($p=0.97$), surface area ($p=0.86$), or any combination of these parameters. The only soil chemical parameter significantly correlated with iodide retention was pH ($p=0.03$) which showed an inverse relationship (Table 2). Likewise, it is difficult to predict whether the A or Bw horizon from a given soil had a greater retention capacity.

Sterilization of the soils via either gamma-irradiation or autoclaving changed the rate of the reaction and reduced the amount of iodide retained by the soils (Table 3). The autoclaving sterilization method resulted in a greater reduction in iodide retention compared to the gamma-irradiation technique, especially for the organic-rich A horizon. On average, the amount of iodide retained by the gamma-irradiated soils was half that of the non-sterilized soils and, in many cases, a 2-3 fold decrease in the extent of reaction was observed after sterilization. With the exception of the Mudwell A horizon, all gamma-irradiated soils had similar iodide-retention capacities (0.5 - 0.7 mmol/kg) at 300 h. These values fall within the range that could be explained by anion exchange (AEC < 1 mmol/kg). In all cases, the soils exhibited rates of reaction with iodide that were much slower than for synthetic imogolite and ferrihydrite, which obtained a steady-state within 30 min.

Soils contained no detectable phosphate extractable iodine and <4.4 μmol/kg of sodium hydroxide extractable iodine (Table 3). Following the kinetic experiments, the phosphate extraction recovered from 0.4 to 25.2% of the iodide retained by the soils (Table 3). The mean values were 7.6% for the sterilized soils and 11.3% for the non-sterilized soils. Even reaction of the soils with 0.1 *M* sodium hydroxide, which partially extracts humic substances, could not recover all of the iodide retained during the 300 h equilibration. The sodium hydroxide extraction recovered, on average, 46% of the iodine sorbed by the non-sterilized soil and 25% of the iodine sorbed by the sterilized soil. In order to check for the possibility that iodine was lost as a volatile species (e.g., I_2, CH_3I), the final

equilibrated suspensions from the Mudwell A and Bw horizons were refluxed with 2.0 *M* sodium hydroxide. This treatment recovered essentially all (98%) of the iodide retained during the sorption experiments indicating that iodine is clearly retained by the soil in a nonlabile form rather than being lost by volatilization.

Rate Studies using Laboratory-grade Humic Acid

Rates of reaction between aqueous solutions of molecular iodine [I_2(aq)] and laboratory grade sodium humate were relatively fast compared to similar experiments using aqueous solutions of iodide. During mixing of an aqueous iodide and humate solution for 72 hours, no detectable change in iodide concentration was measured by either colorimetry or an iodide electrode.

The rates of reaction of aqueous molecular iodine solutions increased with an increase in pH (Fig. 3). At the highest pH value of 6.6, equilibrium was reached with respect to the triiodide ion after 20 hours. Similar experiments which varied the initial iodide concentration indicated that the reaction rate decreased with increasing iodide concentration.

The oxidation of iodide was investigated under experimental conditions similar to those used in the rate studies. Figure 4 shows a plot of the absorbance of triiodide at 351 nm versus the reaction time for a dilute solution of iodide (2 mM) saturated with air at pH 5.5. No formation of I_3^- was observed in the absence of O_2.

Discussion

Iodide Reaction with Imogolite and Ferrihydrite

Imogolite and ferrihydrite have ZPC values of approximately 6.5 and 6.9 (Parfitt, 1980), respectively, and sodium chloride adsorption isotherms indicate a point of zero net charge (PZNC) of 8.4-8.5 for synthetic imogolite (Clark and McBride, 1984; Su et al., 1992). Thus, these noncrystalline components and the soils containing these components will have some positively charged sites at the experimental conditions. The increasing iodide sorption below pH 7 is consistent with increasing surface charge density of positive sites below the ZPC. The sorption minimum at pH 7 for imogolite is not readily explained; however, Whitehead (1973) showed an identical relationship for certain soil components. Decreased iodide sorption by imogolite below pH 5.5 is due to its solubility under strongly acidic conditions. Similar results for iodide sorption as a function of pH were shown by Whitehead (1974) for freshly precipitated ferric and aluminum oxides. The adsorption reaction is relatively rapid (<30 min) suggesting that iodide sorption is not diffusion -imited, such as could occur if iodide were slowly migrating down the imogolite tubes. Intercalation of ions into imogolite tubes has been suggested by experimental data; however, no independent verification was possible (Clark and McBride, 1984).

Due to differences in experimental protocols, it is not possible to compare directly the iodide sorption results of this study to other studies of anion sorption by imogolite and ferrihydrite. Iodide would be expected to form primarily outer-sphere complexes similar to chloride and perchlorate. The sorption capacity of synthetic imogolite for chloride and perchlorate from 0.01 *M* solutions was shown to range between 250-450 mmol/kg in the pH range 6-8 (Clark and McBride, 1984; Su et al., 1992). Thus, the 0.1 *M* background electrolyte of sodium perchlorate employed in this study would be expected to have an appreciable competitive effect on iodide sorption. For inner-sphere complex forming anions, such as phosphate, a 100 μmol/L solution reacted with imogolite and ferrihydrite resulted in sorption of 100 and 200 mmol PO_4/kg, respectively (Theng et al., 1982; Parfitt, 1989). In this study, iodide sorption from a 100 μmol/L solution was 0.5 and 0.25 mmol/kg for imogolite and ferrihydrite, respectively (data not shown). These comparisons suggest that iodide is weakly sorbed relative to other common anions.

Sorption of Iodide by Volcanic-Ash Soils

We find little similarity between the reaction of iodide onto volcanic soils and adsorption onto the noncrystalline phases that make up much of the clay-size fraction of some of these soils. The initially rapid uptake of iodide (6 h retention) is consistent with retention at the surface of noncrystalline materials, but a second, slower reaction proceeds to fix the majority of the iodide from solution with time. The amount of anion exchange capacity was <1 mmol/kg, which is consistent with the 6 h iodide retention values that ranged between 0.07 and 0.52 mmol/kg. When the iodide retention capacity of the noncrystalline components for each soil was calculated from imogolite and ferrihydrite concentrations at the appropriate pH value for each soil, based on the iodide retention values of the pure phases, from 0.05 to 0.61 mmol/kg of iodide retention was predicted. These values are similar in magnitude to the 6 h iodide retention values and are consistent with retention by the noncrystalline material fraction of the soil.

While the rapid retention (6 h values) of iodide may be due to reaction with the noncrystalline components of the clay fraction, the slower reaction that continues to 300 h can not be explained by retention to noncrystalline materials. The calculated noncrystalline material retention capacity for iodide averaged only 17% (range 2-58%) of the 300 h iodide retention values. Thus, reaction with imogolite and ferrihydrite can not explain the much higher sorption capacities of these soils. The halloysite component of the clay fraction is not expected to have a significant iodide retention capacity based on previous research that has shown layer silicate clays to have a negligible iodide retention capacity (Raja and Babcock, 1961; Whitehead, 1974). Furthermore, the slow reaction kinetics do not appear to be accounted for by coverage of reactive mineral surfaces by organic films since A (organic-rich) and B (low organic matter) horizons display similar iodide retention kinetic characteristics.

The 2- to 3-fold decrease in iodide sorption following sterilization is difficult to interpret mechanistically because several soil microbiological, physical and chemical properties may change as a result of autoclaving or gamma irradiation (e.g. Wolf et al., 1989). In general, autoclaving and gamma irradiation result in a small reduction in pH and soil organic matter concentrations, structural changes in soil organic matter, reduced surface area, large increases in extractable Mn and increases in soluble and extractable organic matter. The pH was not altered in this study, probably due to the strong pH buffering capacity originating from the variable charge minerals and organic matter. While dissolved organic matter concentrations were not measured in this study, the color of the filtrate appeared similar between sterilized and non-sterilized treatments. An increase in soluble organic matter could result in aqueous complexation of iodide, which would hinder sorption and iodide transformations leading to sorption (e.g., iodide to iodine). Similarly, enhanced concentrations of Mn may affect iodine redox reactions, as evidenced by the 68 mV decrease in redox potential following gamma irradiation. This decrease in redox would hinder the transformation of iodide to $I_2(aq)$, the species believed to be active in the reaction with organic matter. Structural changes in organic matter may also result in the loss or alteration of reactive sites. Of particular interest to this study are factors that inhibit the free-radical pathway to reaction with organic matter (Huang and Lu, 1991). Chemical degradation of amitrole in soil was greatly reduced by sterilization because it destroyed the free radical-generating mechanism required for degradation (Kaufman et al., 1968). This same phenomenon could explain the observed results with iodide in this study since free radical scavengers were shown to greatly retard iodide reaction with soil organic matter (Huang and Lu, 1991). This could be due to inhibition of iodide oxidation, as shown by Kimura et al. (1995) and Kimura et al. (1994). In their studies, the radical scavengers acrylamide and acrylonitrile were found to decrease the rate of iodide oxidation. Suppression of soil enzyme activity (McLaren et al., 1957) related to iodide transformations may similarly lead to decreased iodide retention by organic matter as has been observed in marine settings (Price and Calvert, 1977; Ullman and Aller, 1980; Wong, 1991).

Iodide is oxidized in highly acidic solutions at room temperature (typically $[H^+] > 0.1$ M) via,

$$4H^+(aq) + O_2(aq) + 6I^-(aq) \leftrightarrow 2I_3^-(aq) + 2H_2O(l) \qquad [1]$$

The rate of this reaction increases with increasing acidity in both uncatalyzed and some catalyzed reactions (Kimura, et al. 1994; Kimura, et al. 1995). The reaction is catalyzed by a number of species including light, copper(II) ions, nitrous acid, vanadyl (VO^{2+}), and iron(III). Catalysis by a given metal ion may be a function of whether the metal ion can itself be reduced by iodide and subsequently reoxidized by oxygen (Sellers, 1985). Figure 4 of this study indicates that iodide oxidation can occur at pH 5.5 in dilute solutions of iodide ([I-]=2 mM) over several hours. We consider it likely that in the soil sorption experiments, occurring over 300 hours, iodide is being oxidized and subsequently reacting with the soil organic matter.

We find no evidence for loss of iodine by volatilization and little evidence that the rates of iodide uptake are controlled by microbes. While we cannot rule out a microbial influence, any iodide-peroxidase activity in these microbes must be quite low; the effect of microbes may be passive, as was concluded by Sheppard and Thibault (1992). Changes in iodide reactivity of soils following sterilization by autoclaving and gamma-irradiation have been reported previously and attributed to changes in the chemical properties of organic matter in the soil, which is possible in our case as well (Muramatsu et al, 1990).

Several important points need to be summarized: (i) there is no similarity between the rates and extents of iodide retention by the volcanic soils and the constitutive minerals imogolite and ferrihydrite, even though these materials make up a considerable fraction of the clay mineralogy for some soils; (ii) retention kinetics are much slower than shown for specific and non-specific anion adsorption mechanisms; (iii) iodide retained by the soil is largely nonlabile, and can be completely extracted only with boiling 2*M* sodium hydroxide treatment; (iv) soil reactivities are attenuated by sterilization, but sterilization does not stop the fixation, or appreciably slow the rate of reaction, of iodide with the soil; (v) reactivities of a particular soil sample are not predictable from the amount of organic matter, imogolite and ferrihydrite concentrations, surface area, or oxalate-extractable iron and aluminum, as shown in other studies; (vi) aqueous molecular iodine solutions readily react with laboratory-grade humic acid with much faster kinetics than iodide-only solutions; and (vii) iodide oxidation has been demonstrated to occur at pH 5.5 under our experimental conditions.

References

APHA. 1985. Iodide/Iodine. In *Standard Methods for the Examination of Water and Waste Water, 16th ed.,* pp. 364-372. American Public Health Association, Washington D.C.

Clark, C. J. and M. B. McBride. 1984. Cation and anion retention by natural and synthetic allophane and imogolite. Clays & Clay Miner. 32:291-299.

Gu, B. and R. K.Schulz. 1991. Anion retention in soils: Possible application to reduce migration of buried technetium and iodine. NUREG/CR-5464, U.S. Nuclear Regulatory Commission, 19 pp.

Hauschild, J. and D. C. Aumann. 1989. Iodine-129 in the environment of a nuclear fuel reprocessing plant: V. The transfer of ^{129}I and ^{127}I in the soil-pasture-cow-milk/meat pathway, as obtained by field measurements. J. Environ. Radioactivity 9:145-162.

Hoshi, M., M. Yamomoto, H. Kawamura, and K. Shinohara. 1994. Fallout radioactivity in soil and food samples in the Ukraine-measurements of iodine, plutonium, cesium and strontium isotopes. Health Phys. 67:187-191.

Huang, T. S. and F. J. Lu. 1991. Iodide binding by humic acid. Environ. Toxic. Chem. 10:179-184.

Kaufman, D. D., J. R Plimmer, P. C Kearney, J. Blake, and F. S. Guardia. 1968. Chemical versus microbial decomposition of amitrole in soil. Weed Sci. 16:266-272.

Kimura, M., M. Tokuda, and K. Tsukahara. 1994. Kinetics and mechanisms of the copper(II)-catalyzed oxidation of iodide ion in the presence of molecular oxygen in aqueous acid media. Bull. Chem. Soc. Jpn., 67:2731-2735.

Kimura, M., T. Hara, and K. Tsukahara. 1995. Kinetics and mechanisms of the vanadium(IV)-catalyzed oxidation of iodide ion in the presence of molecular oxygen in an acid solution. Bull. Chem. Soc. Japan. 68:2853-2857.

Lukashev, V. K. 1993. Some geochemical and environmental aspects of the Chernobyl nuclear accident. Appl. Geochem. 8:419-436.

Likhtarev, I.A., B. G. Sobelev, I. A. Kairo, N. D. Tronko, T. I. Bogdanova, V. A. Oleinic, E. V. Epshtein, and V. Bera. 1995. Thyroid cancer in the Ukraine. Nature 375:365.

Liyanage, C., D. A. Luvisi, and D. O. Adams 1993. The glutathione content of grape berries is reduced by fumigation with methyl bromide or methyl iodide. Am. J. Enol. Viticult. 44:8-12.

Lobert, J. M., J. H. Butler, S. A. Montzka, L. S. Geller, R. C. Myers, and J. W. Elkins. 1995. A net sink for atmospheric CH_3Br in the east Pacific Ocean. Science 200:1002-1005.

McLaren, A. D., L. Reshetko, and W. Huber. 1957. Sterilization of soil by irradiation with electron beam and some observations on soil enzyme activity. Soil Sci. 83:497-502.

Muramatsu, Y., S. Uchida, P. Sriyotha, and K. Sriyotha. 1990. Some considerations on the sorption and desorption phenomena of iodide and iodate on soil. Water, Air & Soil Pollut. 49:125-138.

Parfitt ,R. L. 1980. Chemical properties of variable charge soils. p. 167-194. In B. K. G. Theng, (ed.) Soils With Variable Charge. New Zealand Society of Soil Science, Lower Hutt.

Parfitt, R. L. 1989. Phosphate reactions with natural allophane, ferrihydrite and goethite. J. Soil Sci. 40:359-369.

Price,N. B. and S. E. Calvert. 1977. The contrasting geochemical behaviors of iodine and bromine in recent sediments from the Namibian shelf. Geochim. Cosmochim. Acta 41:1769-1775.

Raja, M. E. and K. L. Babcock. 1961. On the soil chemistry of radio-iodine. Soil Sci. 91:1-5.

Robens, E., J. Hauschild, and D. E. Aumann. 1989. Iodine-129 in the environment of a nuclear fuel reprocessing plant IV: ^{129}I and ^{127}I in undisturbed surface soils. J. Environ. Radioact. 9:17-29.

Schulz, R. K., E. O'Donnell, and E. C. Duckart. 1992. Anion retention in soil: Possible application to reduce migration of buried technetium and iodine. NUREG/CR-5974, 19 pp.

Schulz ,R. K., R. W. Ridky,. and E. O'Donnell. 1994. Control of water infiltration into near-surface LLW disposal units. NUREG/CR-4918, 21 pp.

Sellers, R. M. 1985. A data base for the reaction kinetics of iodine in aqueous solution In A. M. Deane and P. E.Potter (eds.)Proceedings of the Specialists' Workshop on Iodine Chemistry in Reactor Safety, AERE R 11974, Harwell, England.

Sheppard, M. I. and D. H. Thibault. 1992. Chemical behaviour of iodine in organic and mineral soils. Applied Geochem. 7:265-272.

Shoji, S., M. Nanzyo, and R. A. Dahlgren. 1993. Volcanic Ash Soils: Genesis, Properties and Utilization. Elsevier, New York, 288 pp.

Stewart, S. P. and B. T. Wilkens. 1985. Areal distribution of ^{129}I in West Cumbrian soils. J. Environ. Radioact. 2:175-182.

Su, C., J. B. Harsh, and P. M. Bertsch. 1992. Sodium chloride sorption by imogolite and allophane. Clays Clay Miner. 40:280-286.

Takahashi ,T., R. A. Dahlgren, and P. van Sustern. 1993. Clay mineralogy and chemistry of soils formed in volcanic materials in the xeric moisture regime of northern California. Geoderma. 59:131-150.

Theng, B. K. G., M. Russell, G. J. Churchman, and R. L. Parfitt. 1982. Surface properties of allophane, halloysite, and imogolite. Clays Clay Miner. 30:143-149.

Ullman, W. J. and R. C. Aller. 1980. Dissolved iodine flux from estuarine sediments and implications for the enrichment of iodine at the sediment-water interface. Geochim. Cosmochim. Acta. 44:1177-1184.

Whitehead, D.C. 1973. Studies on iodine adsorption in British soils. J. Soil Sci. 24:260-270.

Whitehead, D.C. 1974. The sorption of iodide by soil components. J. Sci. Food. Agric. 25:73-79.

Wolf,D. C., T. H. Dao, H. D. Scott, and T. L. Lavy. 1989. Influence of sterilization on selected soil microbiological, physical, and chemical properties. J. Environ. Qual. 18:39-44.

Wong, G.T.F. 1991. The marine geochemistry of iodine. Rev. Aquatic Sci. 4:45-73.

Table 1. Selected soil characterization data for the <2 mm fraction of soils used in iodide sorption studies.

Soil/ Horizon	pH	Org. C g/kg	Sfc Area m^2/g	Al_p†	Fe_p	Al_o	Fe_o	Si_o	Fe_d	Fe_o/Fe_d	All/Img‡	Ferrihyd‡	All/Im% of clay§	Crystalline minerals
				---------- g/kg ----------							----- g/kg ------			
Bartle														
A	6.92	27	70.5	6	1	27	6	8	40	0.15	57	10	27	Ht(7)[a] 2:1
Bw	6.32	5	54.6	1	1	6	5	2	77	0.07	14	9	5	Ht(10)[a] Ht(7)>Gb
Edson														
A	5.79	71	19.0	7	2	28	15	9	25	0.60	64	25	21	Ht(7)>>2:1
Bw	5.93	11	27.9	3	1	28	15	14	29	0.52	99	25	48	Ht(7)
Harris														
A	6.02	82	21.3	9	1	32	6	9	16	0.38	64	10	28	Ht(7)>>2:1
Bw	6.21	13	60.3	3	<1	40	7	21	29	0.24	149	12	65	Ht(7)>Gb>2:1
McGavic														
A	5.80	82	15.5	9	2	20	5	5	12	0.42	36	9	24	Ht(7)>>2:1
Bw	6.25	29	38.0	5	1	32	7	12	18	0.39	85	12	36	Ht(10)[a]Ht(7)
Modoc														
A	6.12	54	8.0	5	1	15	6	4	7	0.86	28	10	29	Ht(7)>>2:1
Bw	6.09	20	31.3	4	1	50	15	27	16	0.94	192	26	80	Ht(10)Ht(7)>Gb>2:1
Mudwell														
A	6.12	38	29.1	5	2	14	6	3	29	0.21	21	10	11	Ht(7)>Gb>2:1
Bw	6.34	5	55.2	2	1	7	7	3	57	0.12	21	12	9	Ht(10)[a] Ht(7)>Gb

†Subscripts p, o, and d refer to pyrophosphate, oxalate, and dithionite-citrate extractable components, respectively.
‡Calculated by Si_o x 7.1; Calculated by Fe_o x 1.7
§Allophane/imogolite as a percentage of the total clay fraction
¶Ht(10)=hydrated halloysite, Ht(7)=dehydrated halloysite, 2:1=hydroxy-Al interlayered 2:1 minerals, Gb=gibbsite

Table 2. The final (300 h) pH and Eh of soil suspensions in the iodide retention experiment with volcanic soils.

Soil/ Horizon	Treatment	pH	Eh --mV--
Bartle			
A	Non-sterilized	5.47	542
A	Sterilized	5.85	440
Bw	Non-sterilized	6.04	505
BwSterilized		Insufficient sample	
Edson			
A	Non-sterilized	5.38	448
A	Sterilized	5.34	491
Bw	Non-sterilized	5.68	429
Bw	Sterilized	5.56	307
Harris			
A	Non-sterilized	5.64	432
A	Sterilized	5.59	337
Bw	Non-sterilized	6.33	412
Bw	Sterilized	6.25	338
McGavic			
A	Non-sterilized	5.30	470
A	Sterilized	5.06	379
Bw	Non-sterilized	5.80	445
Bw	Sterilized	5.62	383
Modoc			
A	Non-sterilized	5.21	463
A	Sterilized	5.27	394
Bw	Non-sterilized	5.78	444
Bw	Sterilized	5.63	418
Mudwell			
A	Non-sterilized	5.35	465
A	Sterilized	5.05	453
Bw	Non-sterilized	5.34	472
Bw	Sterilized	5.75	438

Table 3. Comparison of the amount of iodide retained during the 300 h equilibration to the amount of iodine recovered by extraction methods following equilibration. Note that pretreatment NaOH extractable iodine concentrations are extremely low relative to the amount retained during sorption experiments.

Soil/ Horizon	NaOH Pre-Treat	Iodide retention		NaH_2PO_4		NaOH	
		Sterile	Non-Ster.	Sterile	Non-Ster.	Sterile	Non-Ster.
	mol/kg	---- mmol/kg ----		--- % of retained iodide extracted ---			
Bartle							
A	0.34	0.78	1.67	0.4	3.7	8.5	20.2
Bw	0.55	N/A	0.55	N/A	5.1	N/A	12.5
Edson							
A	4.32	0.54	1.84	6.7	2.5	21.4	49.6
Bw	1.20	0.75	1.65	8.3	11.3	16.3	44.9
Harris							
A	0.57	0.75	1.56	1.8	4.4	31.3	43.4
Bw	0.21	0.68	0.85	10.6	25.2	24.4	63.6
McGavic							
A	0.81	0.72	2.06	18.4	14.8	22.3	59.9
Bw	0.62	0.53	1.70	15.7	14.2	42.5	68.3
Modoc							
A	0.28	0.66	0.95	4.2	16.6	53.7	50.4
Bw	0.07	0.78	1.27	10.2	13.9	19.4	49.9
Mudwell							
A	0.34	1.65	2.27	3.5	6.3	40.5	46.8
Bw	0.43	0.76	2.95	3.3	17.1	24.3	42.9

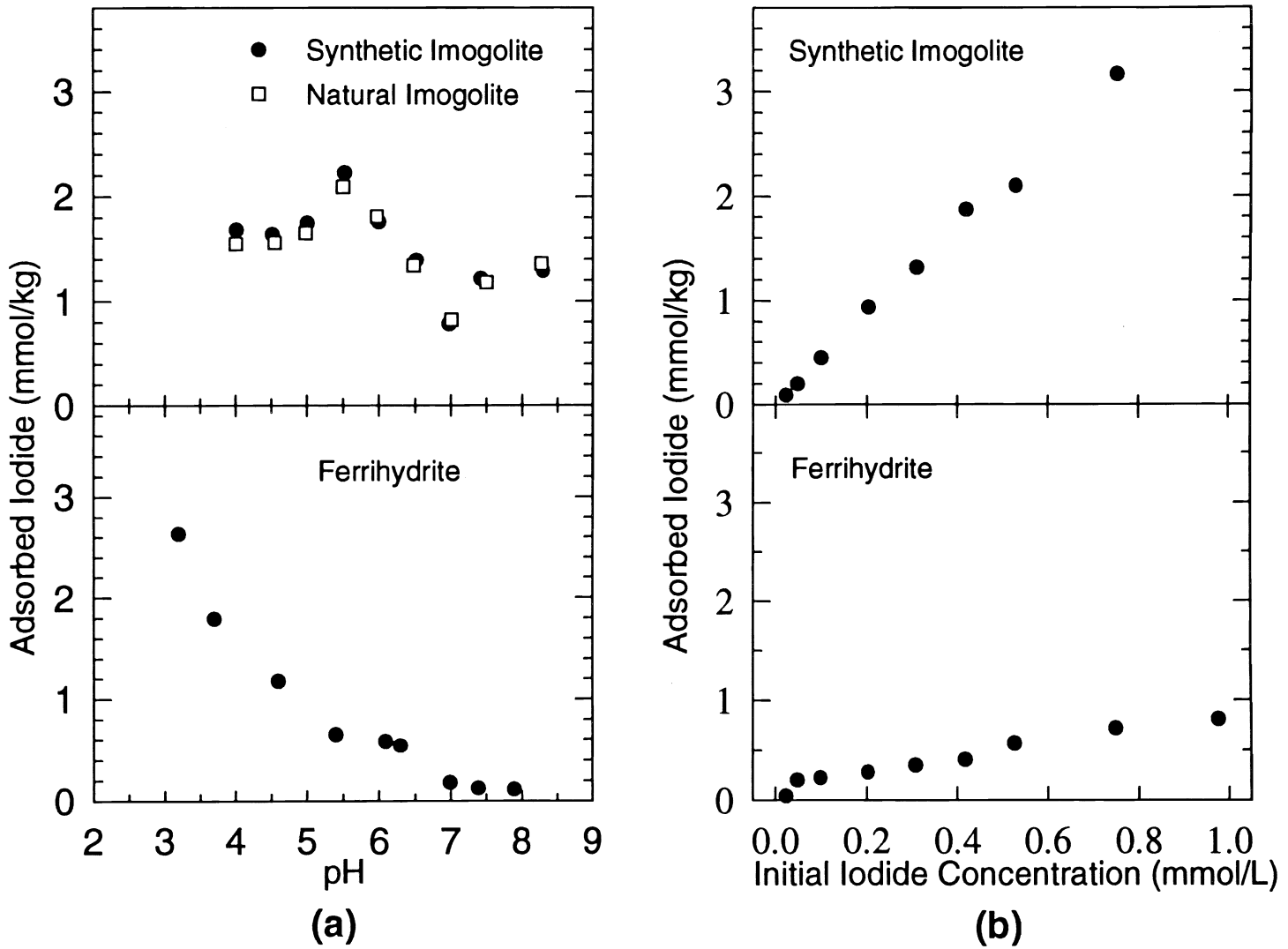

Figure 1. (a) Iodide sorption to synthetic imogolite, natural imoglite and ferrihydrite as a function of pH, $[I^-]_i$ = 0.5 mmol/L. (b) Sorption isotherms for iodide on synthetic imogolite and ferrihydrite, $[I^-]_i$ = 1.0 mmol/L at pH = 5.5.

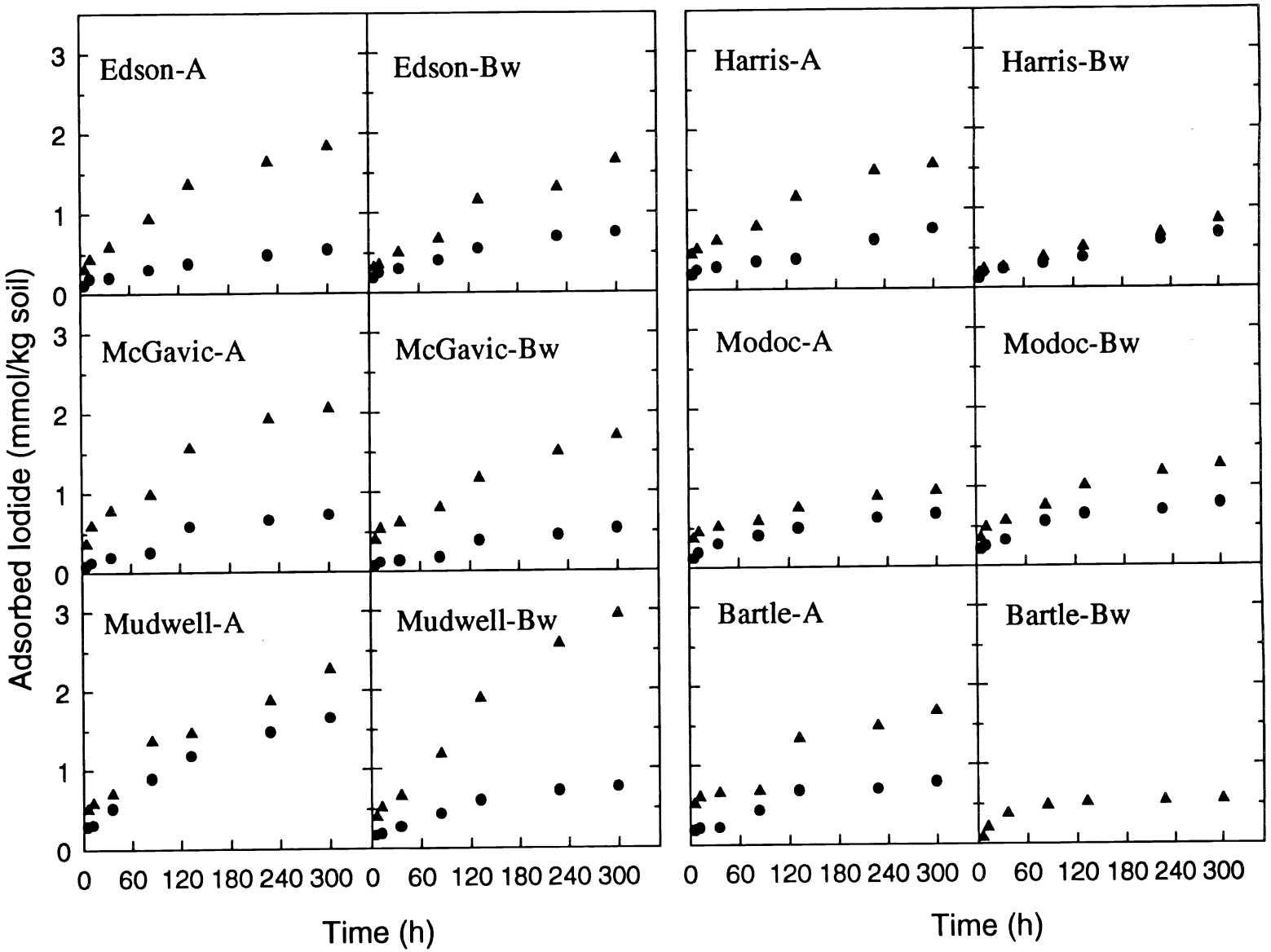

Figure 2. Iodide retention characteristics by nonsterilized (▲) and gamma-irradiated (●) A and Bw horizons from six volcanic soils, $[I^-]_{i,T}$ = 1 mmol/L. There was insufficient sample to gamma-irradiate the Bartle Bw horizon.

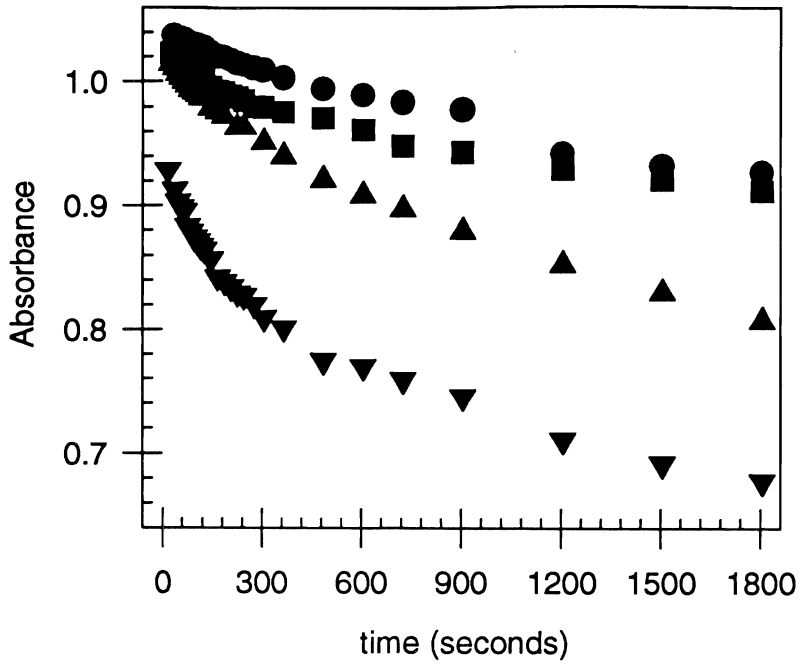

Figure 3. Plots of absorbance of I^-_3(351 nm) against time. Conditions: 0.02 g/L lab-grade sodium humate, $[I_2] = 3.6 \times 10^{-5}$ M. $[I^-] = 4 \times 10^{-3}$ M, ionic strength = 9.2 mM $NaClCO_4$, 25°C and dark, pH = 3.6 (●), 4.6 (■), 5.6 (▲), and 6.6 (▼).

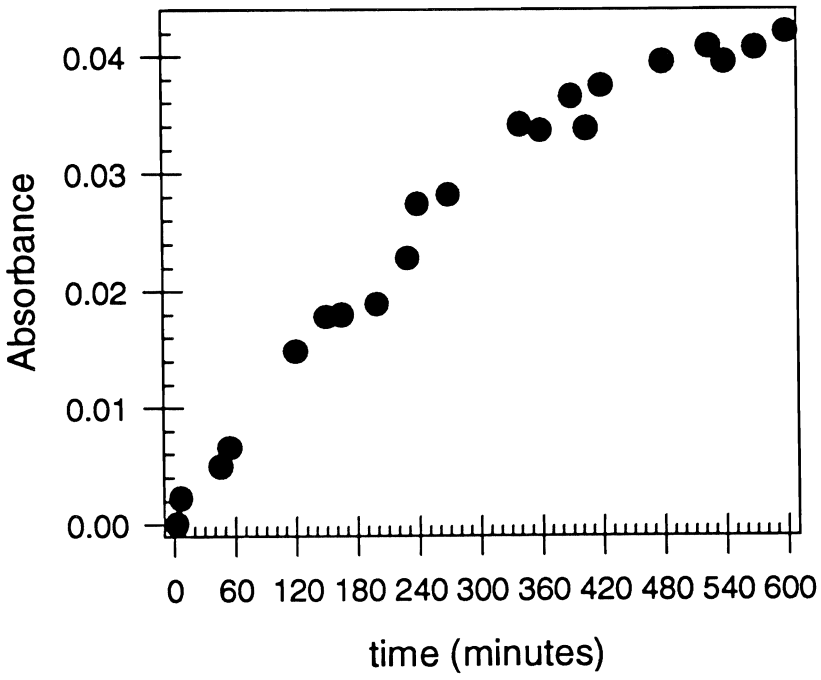

Figure 4. Plot of absorbance of I^-_3 (351 nm) against time. Conditions $[I^-] = 2 \times 10^{-3}$ M, pH 5.5, air-sat., background ionic strength = 90.2 mM $NaClCO_4$, 25°C and dark.

A Spectroscopic Study of Bonding Structures and Redox Transformation of Arsenate and Arsenite on Goethite Surfaces

XIAOHUA SUN AND HARVEY E. DONER
Department of Environmental Science, Policy and Management, Berkeley Campus

Summary

The bonding structures and redox transformation of arsenite (As(III)) and arsenate (As(V)) on goethite (α-FeOOH) were studied by Transmission-Fourier Transform Infrared (T-FTIR) and Attenuated Total Reflectance-FTIR (ATR-FTIR) spectroscopy. ATR-FTIR spectra of deuterated goethite showed three bands of OD stretch, corresponding to singly, doubly and triply coordinated OH hydroxyls on the goethite surface. Both FTIR modes provided similar structural information for arsenic adsorption. Arsenate and arsenite oxyanions replaced two singly coordinated surface OH groups (A-type) to form binuclear bridging complexes. Their effects on doubly (C-type) and triply (B-type) coordinated surface OH groups were different, however. As(III) mainly reacted with C-type OH groups, while As(V) reacted with B-type OH groups. These reactions may be attributed to hydrogen-bonding and/or chemical bonding. Sequential extraction results showed that relatively strong chemical extraction was necessary to remove 75 to 80% of total adsorbed arsenic from the goethite samples treated with arsenite or arsenate and aged in air dry condition. The strong retention of As(III) and As(V) is most likely caused by the formation of binuclear complexes with goethite. We applied the FTIR-deuteration and solution chemistry methods to investigate the adsorption and oxidation of As(III) on the goethite surface. The results indicated that at low pH, the As(V)/As(III) ratio in the solid phase was higher than in the solution phase. Some As(III) could be oxidized to As(V) and adsorbed on the goethite surface. As(III) adsorbed on goethite under air dry conditions was not very stable. After twenty days, more than 20% of adsorbed As(III) was oxidized to As(V). Birnessite was a very active oxidant for the As(III) to As(V) transformation reaction, both in solutions and on the goethite surface. This study suggested that the adsorption-oxidation system composed of goethite and birnessite may be significant in decreasing the arsenic toxicity in terrestrial environments.

Key Words: Arsenate, arsenite, adsorption, goethite, FTIR, deuteration, binuclear bonding, sequential extraction, oxidation, birnessite.

Mixtures of As(V) and As(III) adsorbed on goethite were prepared by reacting 30 mg goethite with 200 µl As(V) (Na_2HAsO_4) and As(III) ($NaAsO_2$) solutions of various concentrations at pH 5.5 to give the total adsorption density (As(V) + As(III)) of 150 µmol As/g goethite at different As(V)/As(III) ratios. After equilibrating for one hr, films of both untreated and treated goethite were prepared by evaporating a suspension on the surface of the AgCl pellet, placing the pellet inside an IR cell with KBr windows, evacuating the IR cell to 0.002 torr, and treating with D_2O vapor. The T-FTIR spectrum was collected using a Matson Galaxy 3000 FTIR Spectrometer.

Suspensions for adsorption studies were prepared by dispersing 50 mg goethite in 10 ml 0.01 M NaCl solutions. The initial As(V) (Na_2HAsO_4) or As(III) ($NaAsO_2$) was added in solutions at the rate of 12.5 mM. The pH was adjusted with NaOH or HCl, then shaken at the room temperature (25 $\pm$ 2°C) for 2 hrs. The samples were centrifuged (10,000 x g) for 10 min. in a Sorvall RC2-B Centrifuge and filtered. Aliquots were taken and As(III) and As(III) + As(V) were determined by a Perkin-Elmer 2280 atomic absorption spectrophotometer and a Varian VGA-76 hydride generator.

Suspensions for oxidation studies were prepared by adding 1.5 ml 100 µmol/ml As(III) ($NaAsO_2$) solutions to the 150 ml goethite suspensions which contained 1.0 g goethite and 0.01 M NaCl, producing 150 mmol As(III)/g goethite. The pH was adjusted and controlled by HCl or NaOH additions to 5.0 or 8.0 while constantly stirring. Suspension samples were collected at different times up to 100 hrs. The samples were centrifuged and As(III) and As(III) + As(V) in supernatant solutions were determined as described above. About 30 mg slurry samples were collected for FTIR studies as above.

The reaction of As(III) with birnessite in goethite suspensions was carried out by using the same treatment as in the stirred experiment. After As(III) reacted with goethite for one hr in suspensions, birnessite was added at the rate of 5% (w/w of goethite) to the system. Suspension samples were collected at different time intervals and centrifuged. The aqueous phases of the centrifuged samples were taken and As(III) and As(III)+As(V) were determined as previously described. Thirty mg of the slurry samples were collected for FTIR studies as above.

For the air-dry treatment, the sample was prepared by evaporating a 100 µl As(III) - goethite suspension (As(III) = 150 µmol/g, pH=7.0) on the surface of the AgCl pellet. The pellet was placed into an IR cell with KBr windows, exposed to air for different periods of time, evacuated to 0.002 torr. and treated with D_2O vapor. The T-FTIR spectrum was then collected.

Results

Bonding structures of As(V) and As(III) on goethite

Figure 1a shows T-FTIR scans of D_2O-treated goethite at different pH values. From this we can see that pH has little effect on IR absorbance. The addition of arsenate and arsenite caused the reduction in intensity of the 2584 cm^{-1} band (Fig. 1b and c). When the concentration of arsenic reached 200 μml/g, the 2584 cm^{-1} peaks were almost removed completely by both forms of arsenic. This indicates that both oxidation states of arsenic react strongly with A-type groups. In the As(V) treated sample (Fig. 1b) a new peak appeared at 2686 cm^{-1}. With increased As(V) coverage on goethite, the band at 2701 cm^{-1} decreased and the band at 2686 cm^{-1} increased in intensity. In addition, another band at 2713 cm^{-1} appeared with the 200 μmol As(V) g^{-1} goethite treatment. When the content of As(V) reached 400μmol/g, the original 2701 cm^{-1} peak was no longer apparent. It may have split into the main band at 2686 cm^{-1} and the small band at 2713 cm^{-1}. At the same time, As(III) slightly reduced the 2701 cm^{-1} peak (Fig. 1c). The effect of As(III) on the 2701 cm^{-1} peak was different from that of As(V) (Fig. 1b). With the increase of the As(III) concentration, this peak became broad. At the higher As(III) treatment, the 2701 cm^{-1} band could no longer be detected. These results support the hypothesis that the bonding mechanisms of As(V) and As(III) to B- and C- type hydroxyls may be very different.

Using the same deuteration treatment as with the T- FTIR method, we observed a different IR spectrum of pure goethite by the ATR-FTIR method (Fig. 2a). Besides the bands at 2701 and 2584 cm^{-1}, there was an additional band at 2681 cm^{-1}, which has not been reported before for a pure goethite system. We postulate that the new band is due to the absorbance of C- type OH groups exchanged with D_2O, and that the 2701 cm^{-1} band is the absorbance of B- type OD groups. By the T-IR method, it is probable that the 2701cm^{-1} peak Parfitt et al. (1976) observed was B-type hydroxyls. Different pH treatments did not affect the absorbance of the three kinds of hydroxyls.

Figure 2b and 2c are ATR-FTIR spectra of goethite treated with As(V) and As(III). The reactions of the A-type OH with both As(V) and As(III) were similar as found in the T-FTIR. Two hundred μmol/g As(V) and As(III) nearly eliminated the 2584 cm^{-1} band. As(V) adsorption also decreased the band at 2701 cm^{-1}. Such a reaction may be attributed to chemical bonding or/and hydrogen-bonding. The effect became greater as the As(V) concentration was increased. However, the band at 2681 cm^{-1} remained in the same position, suggesting As(V) reacted mainly with B-type hydroxyls. This is comparable to the transmission mode in which As(V) decreased the 2701 cm^{-1} peak, leaving the 2686 cm^{-1} band. The reaction of As(V) with B-type hydroxyls decreased absorbance, and this reaction may also decrease the interaction between B- and C-type hydroxyls. So the absorbance of C-type hydroxyls at 2681 cm^{-1} could be observed from transmission mode spectra. For As(III), we can see it mainly perturb the band at 2681 cm^{-1}. The band at 2701 cm^{-1} remained at all

treatment levels. This was also similar to what we found in transmission mode. Thus, the information about arsenic adsorption interactions on goethite from two modes of IR spectra support each other.

Figure 3 shows the distributions of extractable As(III plus V) from the goethite samples treated with As(III) or As(V) and aged to 20 days and then extracted with 0.25 M KCl, 0.1 M NaOH and 1.0 M NaOH at 70 ^{o}C. The amounts of total As(III plus V) extracted by 0.25 M KCl from dry, aged goethite were very small (0.1% for the As(V) treatment and 0.3% for the As(III) treatment). The sequential extraction results showed that relatively strong chemical extraction was necessary to remove 75 to 80% of adsorbed arsenic (III + V) from both arsenite and arsenate aged goethite samples.

Arsenic adsorption and oxidation

Figure 4 shows the T-FTIR spectra of surface deuterated goethite treated with 150 μmol/g arsenic in different As(V)/As(III) ratios. The goethite treated with 100% As(III) (150 μmol As(III)/g) (Fig. 4) has a band at 2701cm^{-1}. Based on the previous assignment, this is the absorbance band of deuterated triply coordinated (B-type) hydroxyls. As seen in previous results, an adsorption band at 2686 cm^{-1} band was observed from the As(V)-treated goethite. As the As(V)/As(III) ratio increased, the intensity of the 2686 cm^{-1} band increased while the 2701 cm^{-1} band decreased.

Table 1 shows the results of As(III) reacted with goethite suspensions at pH 5 and 8. The initial adsorption of As(III) on goethite was very fast; more than 90% of the maximum was adsorbed after one hr. After 100 hrs, a small amount of As(V) may have been present in the pH 5.0 treatment solution, while none was detected in the pH 8.0 treatment. Figure 5 shows the IR spectra of the solid phase at different time intervals. From it we can see that no obvious change is visible within 50 hrs. However, after 100 hrs, a small peak appeared at 2686 cm $^{-1}$ in the lower pH treatment. Figure 6 shows that the adsorption envelopes of As(III) and As(V) on goethite as a function of pH are quite different. The adsorption of As(V) decreased as pH increased while As(III) adsorption reached a maximum at pH 7 to 7.5.

The addition of 5% birnessite (w/w of goethite) to the As(III)-goethite system resulted in nearly complete depletion of As(III) in solution (Table 2) within 50 min. The IR spectra of solid phases show that most As(III) adsorbed on the goethite surface was transformed to As(V) (Fig. 7) after 10 min reaction time and one hr deuteration period.

Under air-dry conditions (Fig. 8) more than 20% of the adsorbed As(III) on goethite was oxidized to As(V) after 20 days.

Discussion

High-resolution TEM studies indicate that (110) rather than (100) and (010) faces dominate the crystals in synthetic goethite (Schwertmann, 1984). The adsorption of phosphorus on goethite (Torrent et al. 1990) showed that the surfaces of different goethite crystals have similar adsorption capacities and the average adsorption density is 2.51 μmol P m^{-2}. These data agree well with the binuclear complex model on (110) faces:

$$\frac{1OH}{0.30\,nm \times \left(1.00^2 + 0.46^2\right)^{1/2}\,nm} \times \frac{1.0\,mol}{6.023 \times 10^{23}} \times \frac{10^{18} - nm^2}{1.0\,m^2} \times \frac{P}{2} = 2.5\,\mu mol\,P\,m^{-2}$$

(a = 0.46 nm, b = 1.00 nm, c=0.30 nm)

Torrent et al. (1990) concluded that P adsorption essentially took place on (110) faces. Our goethite has a specific surface area of 80 m^2/g giving a calculated A-type hydroxyl density of 400 mmol/g on the (110) face, which means the adsorption capacity for the binuclear complex is 200 mmol/g. Assuming the binuclear complex model on (110) faces, we may propose some possible bonding structures of As(V) and As(III) on goethite surfaces. We know from IR spectra that the addition of about 200 mmol/g arsenic caused the 2584 cm^{-1} band to disappear. This suggests that one $H_2AsO_4^-$ or $H_2AsO_3^-$ ion, like phosphate, replaced two adjacent A-type hydroxyls on (110) faces, forming a binuclear complex on the surface of goethite. Figure 9 shows possible bonding structures of the As(V) anion on the (110) surface of goethite (generated from ATOMS, Copyright 1995, Eric Dowty): one $H_2AsO_4^-$ replaced two adjacent singly coordinated hydroxyls and interacted with a B-type hydroxyl as discussed below:

The O-O distance in $H_2AsO_4^-$ is 0.28 nm (Waychunas et al., 1993), a little shorter than the distance between two contiguous A-type hydroxyls along the goethite c axis (0.30 nm). Thus, there should be some changes in the shape of the FeOOH octahedral to compensate for the strain created by As(V) adsorption. The EXAFS studies (Waychunas et al., 1993, 1995; Manceau, 1995) showed evidence that the bridging arsenate was attached to adjacent apices of edge-sharing Fe oxyhydroxyl octahedral. This conclusion is compatible with IR data observed here. No information was available from EXAFS about the perturbation of As(V) on B-type hydroxyls. Based on their studies, Waychunas et al. (1995) indicated that EXAFS may neglect weakly bonded or randomly connected complexes, and the important tool at this time for unravelling assignments may be IR spectroscopy. Trinuclear complexes cannot be excluded by EXAFS data, because some of these structures have As-Fe distances similar to those in binuclear complexes. Transmission and ATR-IR spectra showed that As(V) could react with B-type hydroxyls and decrease their absorbance in IR spectra. The mechanisms of this reaction may be attributed to H-bonding (Fig. 9a) or trinuclear bonds (Fig. 9b). Because of the small size of

As(V) anions, trinuclear complexes may create more strain in the FeOOH octahedral compared to binuclear complexes and, thus, be difficult to form. All samples here were dried by evacuation before collecting spectra. The dehydrated condition may favor trinuclear complexes.

The O-O distance in $H_2AsO_3^-$ is 0.32 nm (Walter, 1950), so the replacement of two contiguous A-type hydroxyls by As(III) would also introduce a change in the shape of the goethite oxyhydroxyl octahedral. The IR spectra indicated that $H_2AsO_3^-$ can react with C-type hydroxyls. A possible adsorbed structure of $H_2AsO_3^-$ on the (110) face of goethite is shown in Fig. 10. Similar to As(V), one $H_2AsO_3^-$ replaced two adjacent singly coordinated hydroxyls, forming a binuclear complex on the surface of goethite. Unlike As(V), $H_2AsO_3^-$ reacted with C-type hydroxyls instead of B-type hydroxyls. The only possibility of this reaction is the formation of H-bonds because the distance between A- and nearest C-type hydroxyls is 0.48 nm (calculated from ATOMS), 0.16 nm farther than the O-O distance in $H_2AsO_3^-$.

The aging-extraction result shows that about 11% and 14% of adsorbed arsenic can be extracted from As(V)-and As(III)-treated goethite by 0.1M NaOH. This fraction of arsenic may be specifically adsorbed with weak affinity, such as mononuclear complexes. EXAFS studies (Waychunas et al., 1993) indicated that mononuclear arsenate accounts for about 30% of all As-Fe correlations on the ferrihydrite surface. The mononuclear complexes were also observed at low As/Fe ratio (0.001-0.01) on goethite. This compares with a ratio of 0.003 used in our study. The largest fractions for both oxidation states were extracted by 1.0 M NaOH at 70°C. Hingston et al. (1974) found that phosphate was significantly less extractable at room temperature than fluoride. They proposed that phosphate formed binuclear complexes on goethite compared to mononuclear complexes of fluoride. Because of the chemical similarities of phosphorus and arsenic, the fractions extracted by 1.0 M NaOH at 70°C here may be mainly associated with binuclear adsorbed species which can not be desorbed by 0.1 M NaOH at room temperature. This fraction accounts for 75% of the total arsenic in the As(V)-treated sample and 78% in the As(III) treated sample. Thermodynamically, the strength of binuclear bonding is stronger than mononuclear bonding (Hingston et al., 1974). However, the research of Waychunas et al. (1993) suggested that initially populated sites have a geometry that allows simultaneously binuclear and mononuclear arsenate binding. The residual fractions could include trinuclear complexes and/or arsenic precipitated on the goethite surface. The extraction results (Fig. 3) also show that little difference exists between the fractional distributions of arsenic in both arsenate- and arsenite-treated goethite. Interpretation of chemical extraction results always requires caution. For example, the alkaline environment used here might cause As(III) oxidation. Rapid re-adsorption of the oxidized As(III) to As(V) is possible, but less likely in the strong alkaline environment (Fig. 6).

According to thermodynamic calculations, the oxidation of As(III) by Fe(III) should be favorable in low pH (Oscarson et al., 1980), but no evidence from calorimetry and X-ray photoelectron spectroscopy (Oscarson et al., 1981a) showed the redox reaction occurred between Fe(III) and As(III) in 72 hrs at pH 6.9. Here, after 100 hrs at pH 5, a small peak appeared at 2686 cm $^{-1}$ in IR spectra of As(III)-treated goethite (Fig. 5a). By comparing this to Fig. 4, we estimate 10-20% of As(III) that adsorbed on goethite was transformed to As(V). This ratio is higher than in solution phase (Table 2).

H_3AsO_3, the predominant species of arsenite at low pH, is a very weak acid (pK_{a1}= 9.3). The adsorption of this undissociated acid is much less than $H_2AsO_4^-$, the main species of arsenate. From the adsorption results we can see that at low pH, any As(V) oxyanions produced from the oxidation of As(III) in the solution can be selectively adsorbed by goethite and enriched in the solid phase (Foster et al., 1995). So it would be very inaccurate if we only use the As(V)/As(III) ratio in solution to evaluate the oxidation of As(III) in goethite suspensions. At pH 8, no detectable As(V) was observed by FTIR (Fig. 5b). Thermodynamically, the oxidation of As(III) on goethite would not be expected to occur at high pH (Scott 1991).

Studies (Oscarson et al., 1981b) have shown that the manganese (Mn) oxides, which are widely distributed in soils and sediments, are very effective oxidants responsible for the oxidation of As(III) to As(V). Birnessite is one of the most common Mn oxides in terrestrial and aquatic environments (Moore et al., 1990). The depletion (oxidation and adsorption) of As(III) in the birnessite suspension is rapid, with a time scale of minutes (Scott and Morgan, 1995). Scott and Morgan (1995) described the mechanism of As(III) oxidation by birnessite as a surface reaction with three steps: (1) As(III) adsorption, (2) oxidation of As(III) to As(V), and (3) desorption of As(V). Table 2 also shows that the pH influence on the reaction between aqueous As(III) and birnessite is slight. Unlike iron oxides, Mn oxides are capable of As(III) oxidation over a wide pH range in natural waters (Scott and Morgan, 1995).

In general, the adsorption and redox transformation of arsenic at the water-goethite interface could include the following four processes (Fig. 11): (1) the adsorption and desorption of As(III), (2) the redox transformation between As(III) and As(V) in the solution, (3) the adsorption and desorption of As(V), and (4) the redox transformation between As(III) and As(V) on goethite. The oxidation of As(III) to As(V) in solution by the addition of birnessite will disturb the equilibrium. As the result, more As(III) will be desorbed from the goethite surface, oxidized by birnessite in the solution, and then readsorbed as As(V). Finally, all the adsorbed As(III) will be replaced by As(V). However, in this study, the transformation rate of the adsorbed As(III) on goethite was too fast to be only attributed to the oxidation in the liquid phase, because our previous study (Sun and Doner, 1996) indicated that both As(III) and As(V) formed binuclear adsorption complexes on goethite surfaces, which were not so easily desorbed. There are several other possible reactions that can be used to explain this result: (1)Sung and Morgan (1981) reported that the γ-FeOOH surface could act as a catalyst in the oxidation of Mn(II) by oxygen. The Mn(II) produced from

redox reactions in the solution may be adsorbed on goethite, then oxidized by oxygen to Mn(IV). The newly formed Mn(IV) on the goethite surface could oxidize adsorbed As(III) on the goethite surface directly. (2) Manganese oxides are present in both the colloidal and non-colloidal particle-size fractions (Oscarson et al., 1981c). The colloidal fraction of synthetic birnessite may be active enough to oxidize the adsorbed As(III) on the goethite surface. (3) Some other surface reactions could occur during the one hour evacuation and deuteration process.

The electron transfer should be more difficult in dry samples than in solutions. However, after twenty days, more than approximately 20% of the adsorbed As(III) was oxidized to As(V). Because the sample was aged in the air, we cannot say if the oxidant is Fe(III), oxygen in the air, or a microbe process. As(III) in distilled, demineralized water is very stable; no oxidation of As(III) was observed after 37 days (Tallman and Shaikh, 1980). Eary and Schramke (1990) reported a half-time of one year for As(III) oxidation by oxygen in atmosphere. The spectroscopic evidence here shows that the goethite surface plays an important role in As(III) oxidation, either as a catalyst or a direct oxidant.

Conclusion

(1) By ATR-FTIR and deuteration techniques, we identified singly, doubly and triply coordinated OH groups on goethite surfaces.

(2) In evacuated, dry samples, the major fractions of adsorbed arsenate and arsenite replaced singly coordinated hydroxyls (A-type) and may have formed inner-sphere binuclear complexes on the (110) faces of goethite. Their reactions with B and C-type hydroxyls were different. Arsenate reacted with B-type hydroxyls; while arsenite reacted with C-type hydroxyls. These reactions probably formed H-bonds and/or trinuclear complexes.

(3) The sequential extraction study showed that after aging for 20 days under air-dry conditions, the chemical extraction results for As(III)-and As(V)-treated goethite samples were very similar. The various extractable fractions of As may be associated with different bonding mechanisms to goethite. However, the method seems to be insensitive to the roles of B- and C-type hydroxyls in As adsorption.

(4). The IR spectral difference between As(III) and As(V) was used to investigate the oxidation of As(III) on the goethite surface. The results indicated that at low pH, some of As(III) could be oxidized to As(V) and adsorbed on the goethite surface. Because of higher adsorption capacity of As(V) compared to As(III) at low pH, the As(V)/As(III) ratio in the solid phase is higher than in the liquid phase. Thus, it is not accurate to evaluate the As(III) oxidation only by the As(V)/As(III) ratio in solutions.

(5). Birnessite can actively oxidize As(III) to As(V), and influence the As forms both in solution and on the goethite surface. The transformation mechanism of adsorbed As(III) needs to be investigated further. The oxidation rate of As(III) to As(V) on the goethite surface by birnessite was faster than expected considering it was a purely solution controlled process.

(6). The adsorbed As(III) in the air-dry condition was not very stable. More than 20% of adsorbed As(III) was oxidized to As(V) after 20 days. Because As(III) in pure water is very stable in the air, we may conclude that the goethite surface may play an important role in its oxidation.

References

Atkinson, R. J., A. M. Posner, and J. P. Quirk. 1968. Crystal nucleation in Fe(III) solutions and hydroxide gels. J. Inorg. Nucl. Chem. 30:2371-2381.

Eary, L. E. and J. A. Schramke. 1990. Rates of inorganic oxidation reactions involving dissolved oxygen, In D. C. Melchior and R. L. Bassett, (eds.) Chemical Modeling of Aqueous Systems II. , ACS Symp. Ser. 416:379-396.

Foster, A. L., G. E. Brown, Jr., G. A. Park, and D. E. Voigt. 1995. X-ray absorption near-edge spectroscopic (XANES) analysis of As-contaminated soil. SSRL 95, 22nd annual users meeting. Poster abstract. p. 23.

Glaubig, R. A. and S. Goldberg. 1988. Determination of inorganic arsenic(III) and arsenic(III plus V) using automated hydride-generation atomic-absorption spectrometry. Soil Sci. Soc. Am. J., 52:536-537.

Heilman, M. D., D. L. Carter and C. L. Gonzalez. 1965. The ethylene glycol monethylether (EGME) technique for determining soil-surface area.Soil Sci. 100:409-413.

Hingston, F. J., A. M. Posner, and J. P. Quirk. 1974. Anion adsorption by goethite and gibbsite II Desorption of anions from hydrous oxide surfaces. J. Soil Sci. 25:16-26.

Hunter, D. B. and P. M. Bertsch. 1994. *In situ* measurements of tetraphenylboron degration kinetics on clay mineral surface by IR. Environ. Sci. Technol. 28:686-691.

Igbene, A. O. 1985. Adsorption characteristics and mechanisms of A-amino acids on goethite (α-FeOOH). Ph.D. Thesis. Univ. of California, Berkeley. (Univ. of Michigan Microfilm No. 8524995).

Johnston, S. E. and W. M. Barnard. 1979. Comparative effectiveness of fourteen solutions for extracting arsenic from four western New York soils. Soil Sci. Soc. Am. J. 43:304-308.

Lumsdon, D. G., A. R. Fraser, J. D. Russell, and N. T. Livesey. 1984. New infrared band assignments for the arsenate ion absorbed on synthetic goethite (α-FeOOH). J. Soil Sci. 35: 381-386.

Manceau, A. 1995. The mechanism of anion adsorption on iron oxides: Evidence for the bonding of arsenate tetrahedra on free $Fe(O, OH)_6$ edges. Geochim. Cosmochim. Acta. 59:3647-3653.

McKenzie, R. M. 1971. The synthesis of birnessite, crytomelane, and some other oxides and hydroxides of manganese. Mineral. Magazine. 38:493-502.

Moore, J. N., J. R. Walker, and T. H. Hayes. 1990. Reaction scheme for the oxidation of As(III) to As(V) by birnessite. Clay and Clay Minerals. 38:549-555.

Oscarson, D. W., P. M. Huang, and W. K. Liaw,. 1980. The oxidation of arsenite by aquatic sediment. J. Environ. Qual. 9:700-703.

Oscarson, D. W., P. M. Huang, C. Defosse, and A. Herbillon. 1981a. Oxidative power of Mn(V) and Fe(III) oxides with respect to As(III) in terrestrial and aquatic environments. Nature. 291:50-51.

Oscarson, D. W., P. M. Huang, and W. K. Liaw. 1981b. Role of manganese in the oxidation of arsenite by freshwater lake sediments. Clay and Clay Minerals. 29:219-225.

Oscarson, D. W., J. S. Rogers., P. M. Huang, and W. K. Liaw. 1981c. The nature of selected prairie lake and stream sediments. Int. Revue Hydrobiol. 66:95-107.

Parfitt, R. L., J. D. Russell, and V. C. Farmer. 1976. Confirmation of the surface structures of giethite (a-FeOOH) and phosphated goethite by infrared spectroscopy. J. of the Chem. Soc. Far. I72 :1082-1087.

Schwertmann, U. 1984. The influence of aluminium on iron oxides: IX. Dissolution of Al-goethites in 6 M HCl. Clay Miner. 19:9-19.

Scott, M. J. 1991. Kinetics of adsorption and redox processes on iron and manganese oxides: reactions of As(III) and Se(IV) at goethite and birnessite surfaces. Environmental Quality Laboratory. EQL Report No. 33. California Institute of Technology.

Scott, M. J. and J. J. Morgan. 1995. Reactions at oxide surface. 1. Oxidation of As(III) by synthetic birnessite. J. Environ. Qual. 29:1898-1905.

Sun, X. and H. E. Doner. 1996. An investigation of arsenate and arsenite bonding structures on goethite by FTIR. Soil Sci. (accepted).

Sung, W. and J. J. Morgan. 1981. Oxidative removal of Mn (II) from solution catalyzed by the lepidocrocite surface. Geochim. Cosmochim. Acta. 45:2377-2383.

Tallman, D.E. and A. U. Shaikh. 1980. Redox stability of inorganic arsenic(III) and arsenic(V) in aqueous solution. Anal. Chem. 52:196-199.

Torrent, J., V. Barron, and U. Schwertmann. 1990. Phosphate adsorption and desorption by goethite differing in crystal morphology. Soil Sci. Soc. Am. J. 54:1007-1012.

Traina, S. J. and H. E. Doner. 1985. Copper-Manganese (II) exchange on a chemically reduced birnessite. Soil Sci. Soc. Am. J. 49:307-313.

Walter, H. 1950. Structural Chemistry of Inorganic Compounds. Elsevier Publishing Company, Inc. 127 pp.

Waychunas, G. A, B. A. Rea., C. C. Fuler, and J. A. Davis. 1993. Surface chemistry of ferrihydrite: Part 1. EXAFS studies of the geometry of coprecipitated and absorbed arsenate. Geochim. Cosmochim. Acta. 57 :2251-2269.

Waychunas, G. A, B. A. Rea., J. A. Davis, and C. C. Fuler 1995. Geometry of sorbed arsenate on ferrihydrite crystalline FeOOH: Re-evaluation of EXAFS results and topological factors in predicting geometry, and evidence for monodenate complexes. Geochim. Gosmochim. Acta. 59 : 3655-3661.

Table 1. The concentration changes of As(III) in solutions after different reaction times in goethite suspensions.

	pH = 5.0		pH = 8.0	
t(hrs)	As(III) (mM)	$\frac{As(III)}{(As(III)+(As(V))}$	As(III) (mM)	$\frac{As(III)}{(As(III)+(As(V))}$
0	1.25	1.00	1.25	1.00
1.0	0.67	1.00	0.31	1.03
5.0	0.66	1.01	0.29	0.97
10.0	0.64	0.99	0.28	1.00
50.0	0.61	0.96	0.29	1.03
100.0	0.59	0.95	0.28	1.00

Table 2. The concentration changes of As(III) in solutions after different reaction times in goethite suspensions with the addition of birnessite.*

	pH = 5.0		pH = 8.0	
t**(min)	As(III) (mM)	$\frac{As(III)}{(As(III)+(As(V))}$	As(III) (mM)	$\frac{As(III)}{(As(III)+(As(V))}$
0	0.67	1.00	0.31	1.00
10	0.13	0.20	0.17	0.53
20	0.09	0.13	0.10	0.33
30	0.07	0.11	0.07	0.17
40	0.04	0.06	0.04	0.12
50	0.02	0.03	0.02	0.06
100	0.02	0.03	0.02	0.06

*The initial As(III) = 1.25 mM, adsorbed on goethite suspensions for one hour before the addition of birnessite.
**After the addition of birnessite.

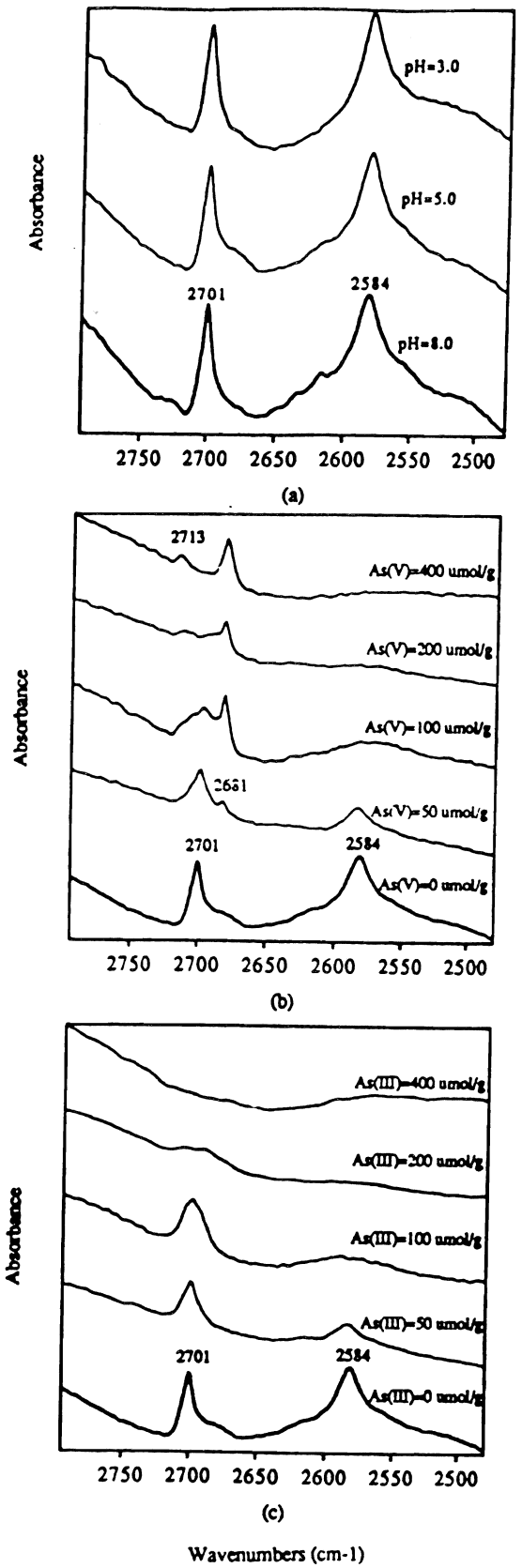

Figure 1. The T-FTIR absorbance spectra of surface deuterated goethite. (a) pure goethite at different pH values, (b) treated with As(V), (c) treated with As(III).

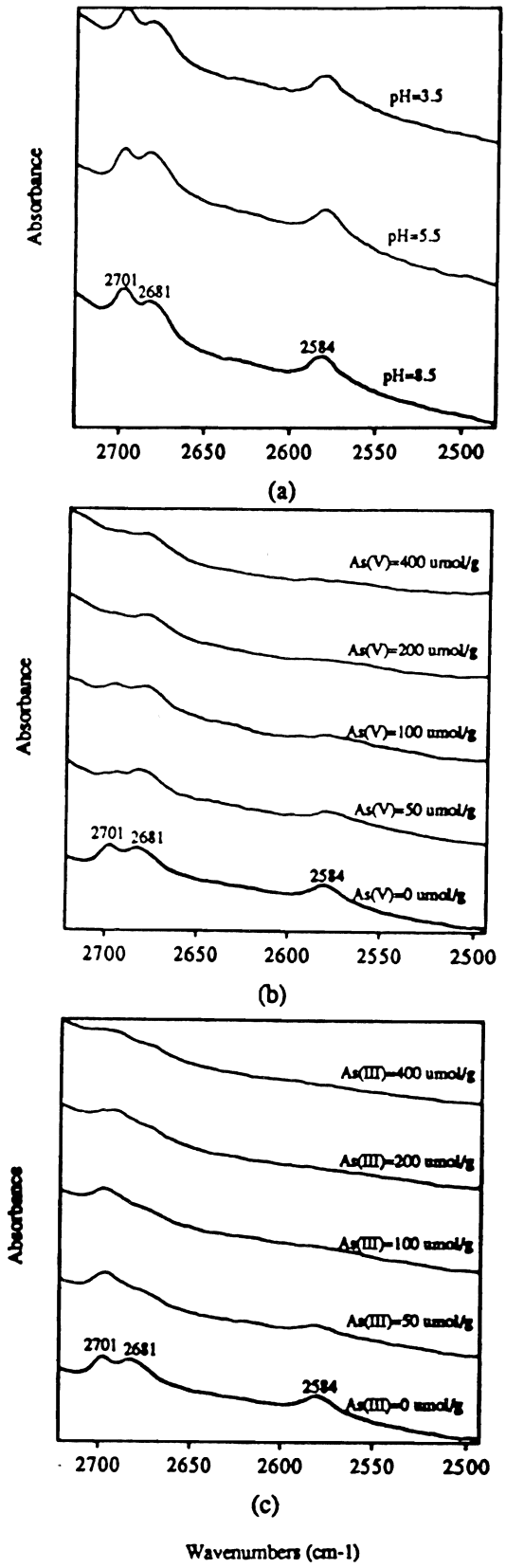

Figure 2. The ATR-FTIR absorbance spectra of surface deuterated goethite. (a) pure goethite at different pH values, (b) treated with As(V), (c) treated with As(III).

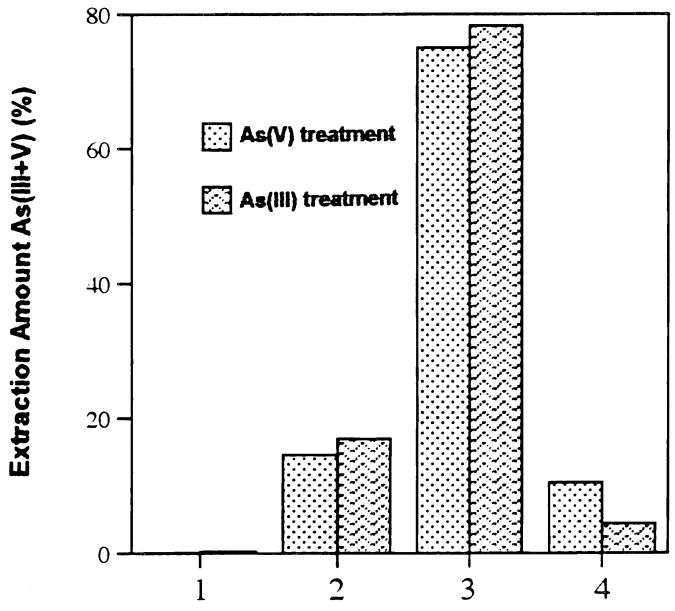

Figure 3. The sequential extraction of air-dry goethite treated with arsenic at As(III) = AS(V) = 25 μmol/g
1. 0.25 M KCl
2. 0.1 M NaOH
3. 1.0 M NaOH at 70°C
4. residual.

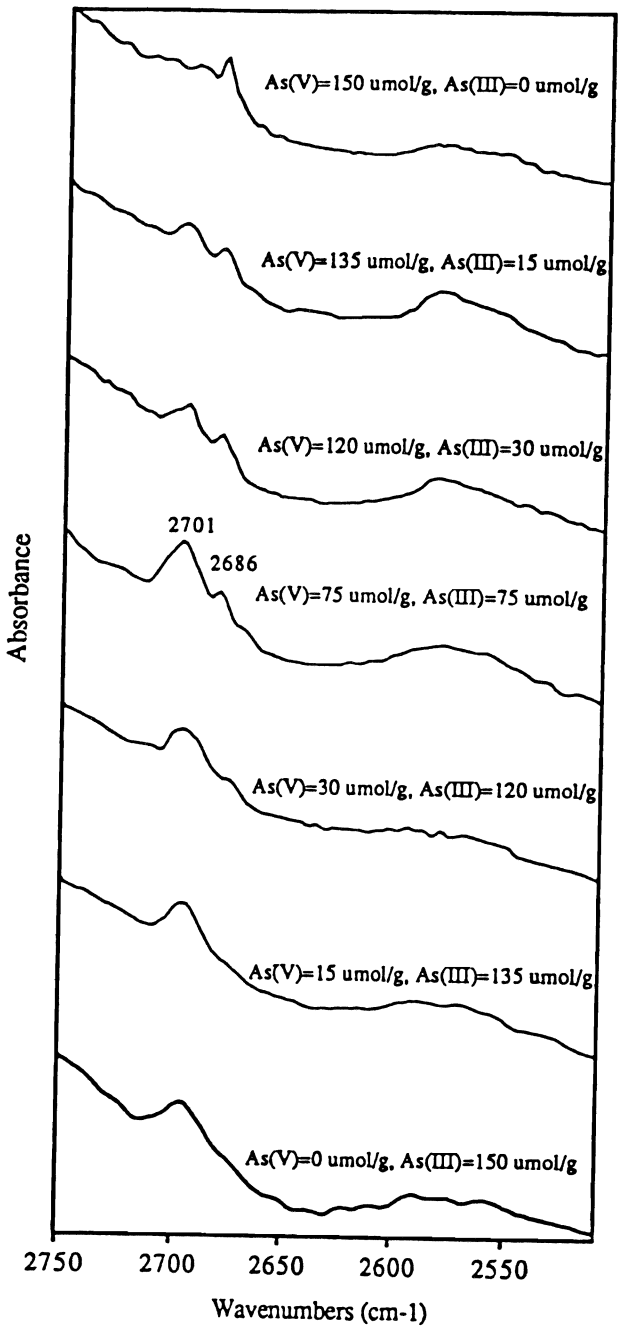

Figure 4. The T-FTIR absorbance spectra of surface deuterated goethite treated with As(III) and As(V) at As(III)+As(V) = 150 μmol/g, pH = 5.5.

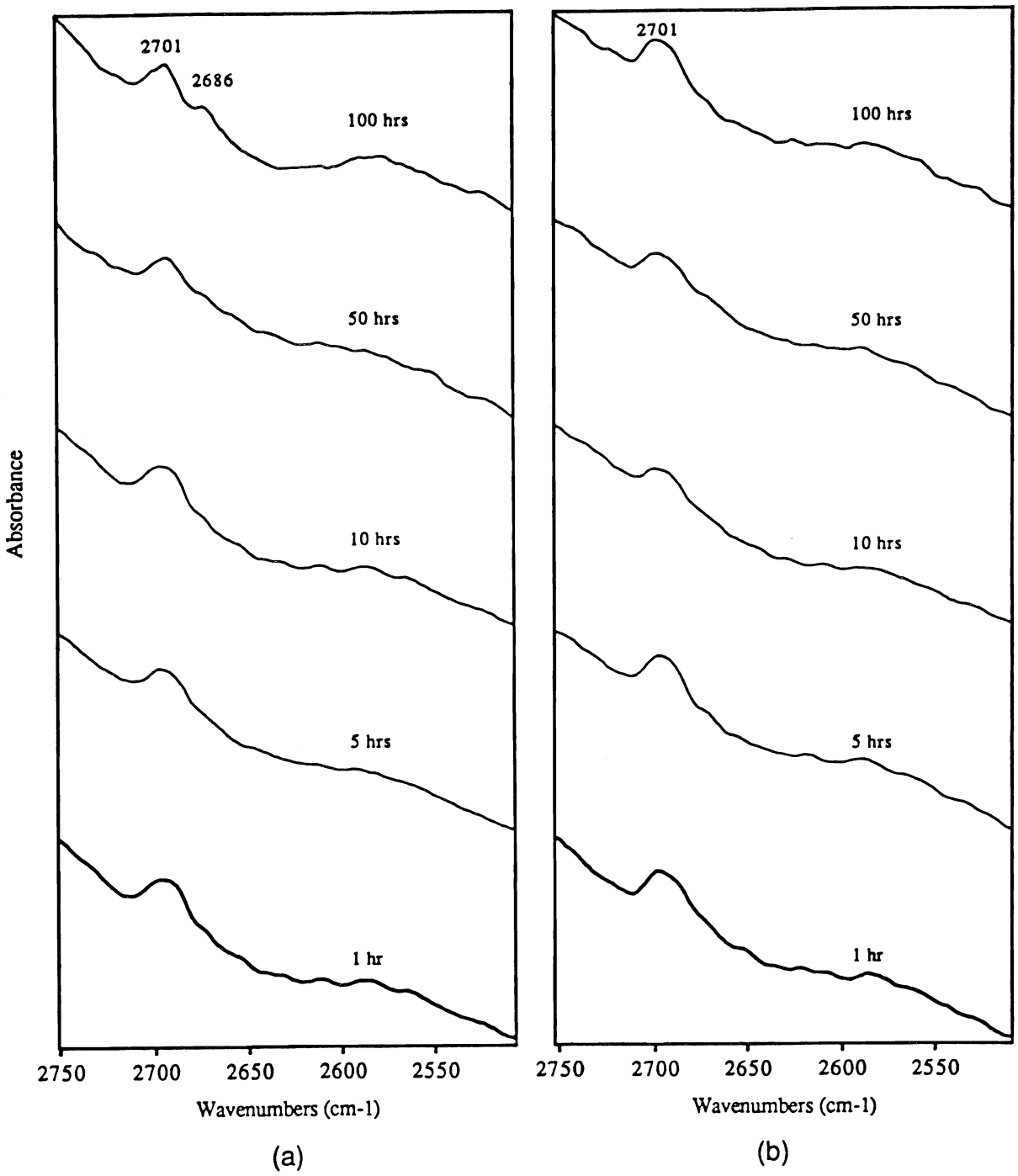

Figure 5. The T-FTIR absorbance spectra of surface deuterated goethite treated with As(III) at 150 μmol/g. (a) pH = 5.0, (b) pH = 8.0.

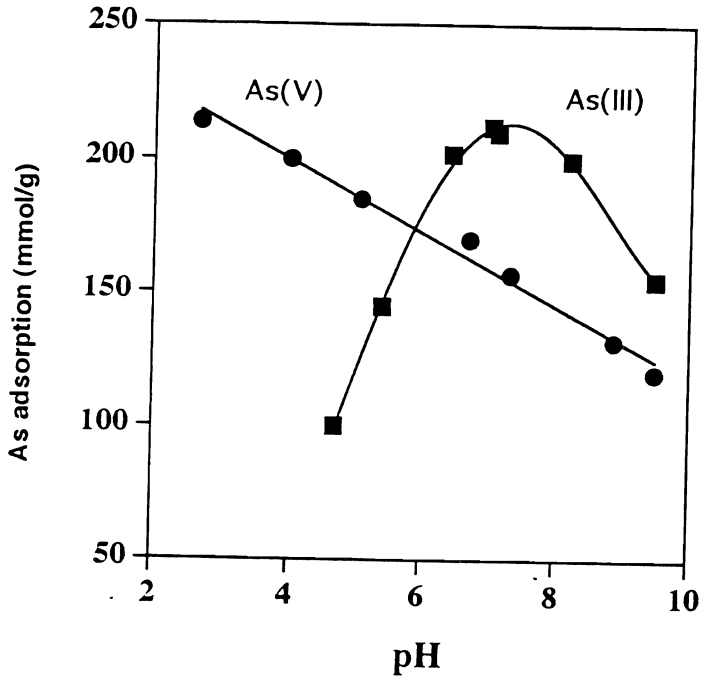

Figure 6. The adsorption of As(III) and As(V) on goethite. $As(III)_T=As(V)_T=12.5$ mM, goethite = 5.0 mg/ml, in 0.01 M NaCl.

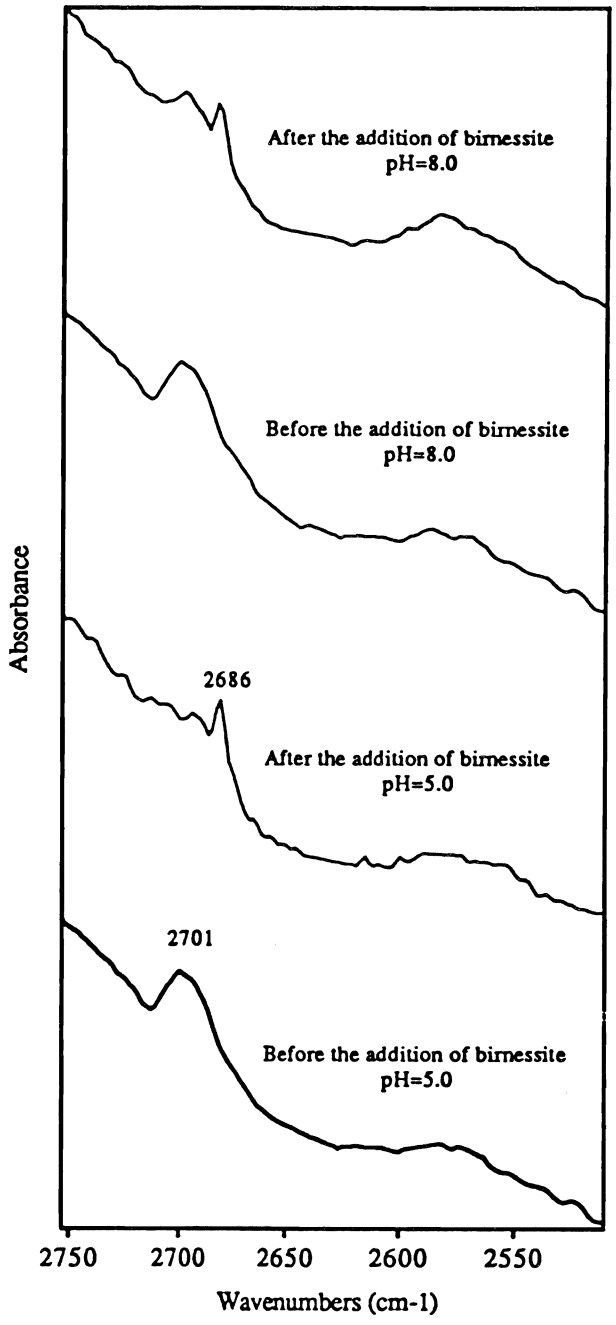

Figure 7. The T-FTIR absorbance spectra of surface deuterated goethite treated with As(III) at 150 μmol/g for one hour and added 5% birnessite (w/w of goethite) for ten minutes.

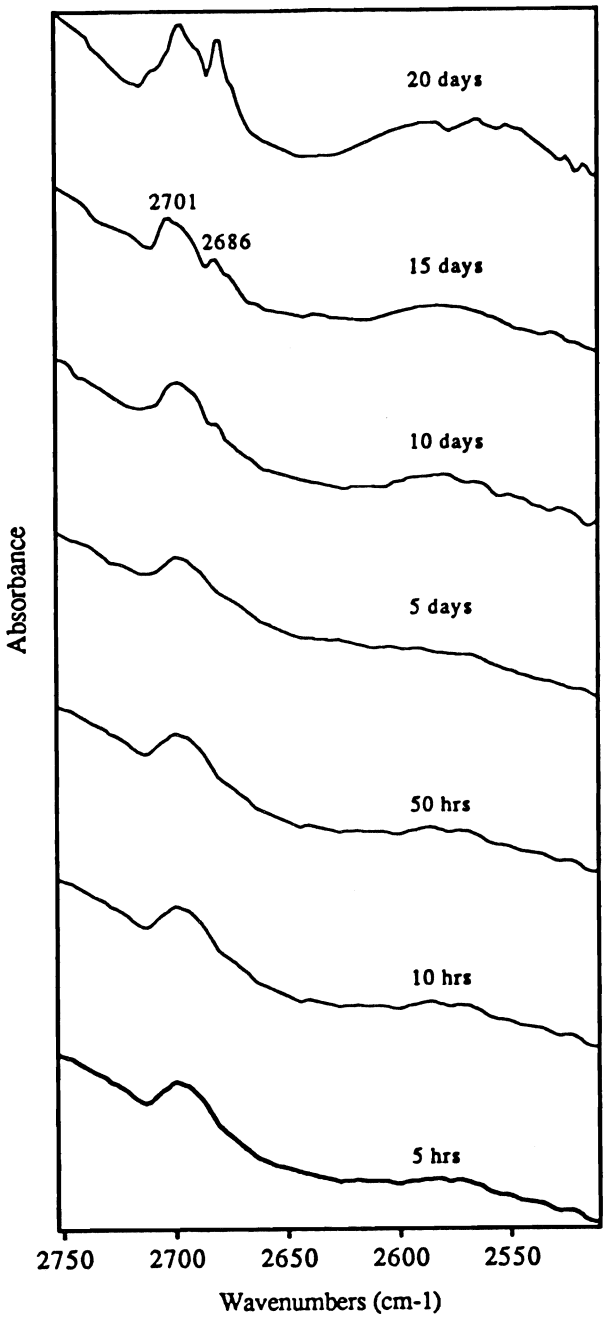

Figure 8. The T-FTIR absorbance spectra of surface deuterated goethite treated with As(III) at 150 μmol/g and kept in air-dry condition at different time intervals; initial pH = 7.0.

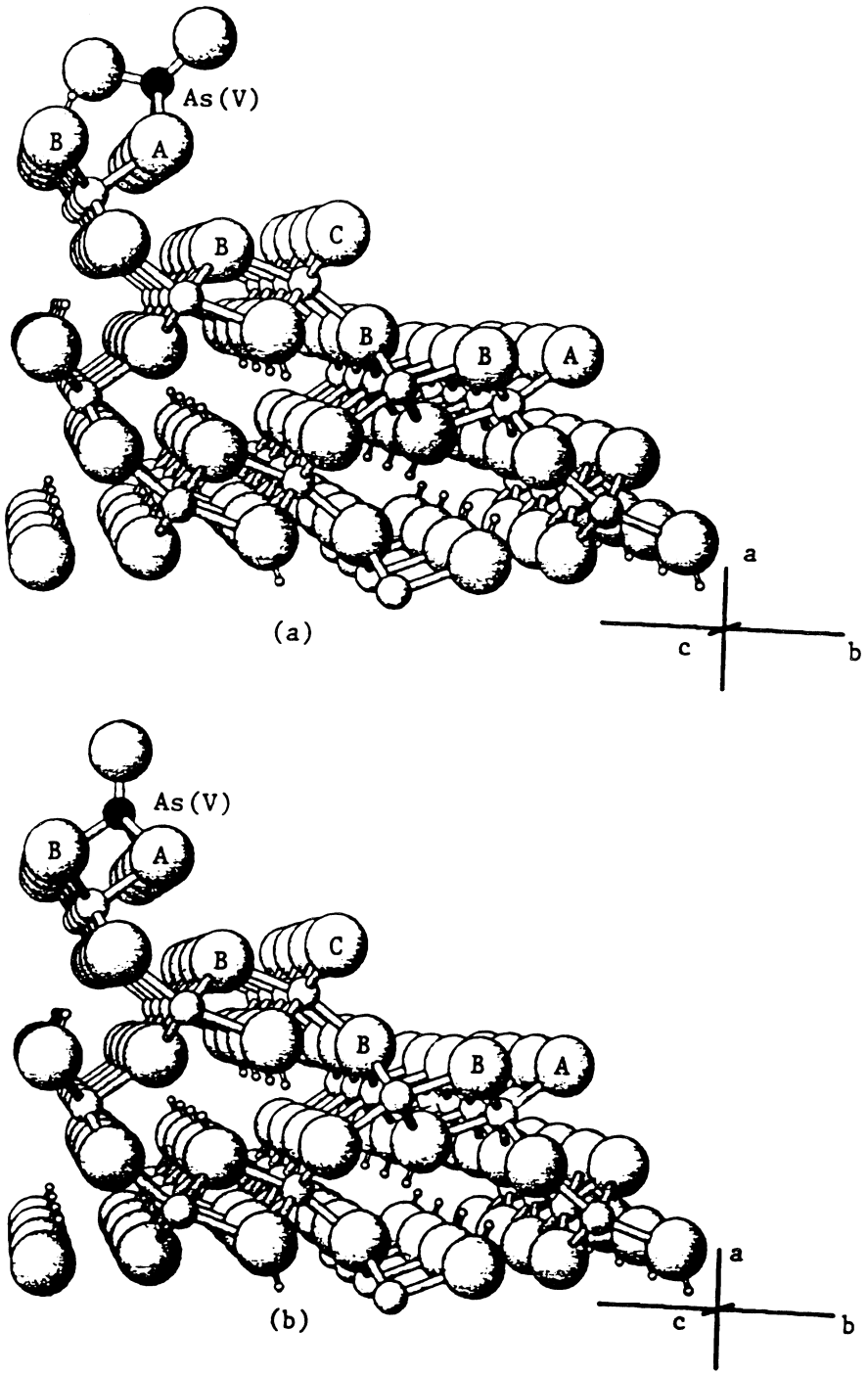

Figure 9. As(V) possible bonding structures on (110) faces of goethite.
(a) Binuclear complex with two A-type hydroxyls and H-bonding with a B-type hydroxyl.
(b) Trinuclear complex.

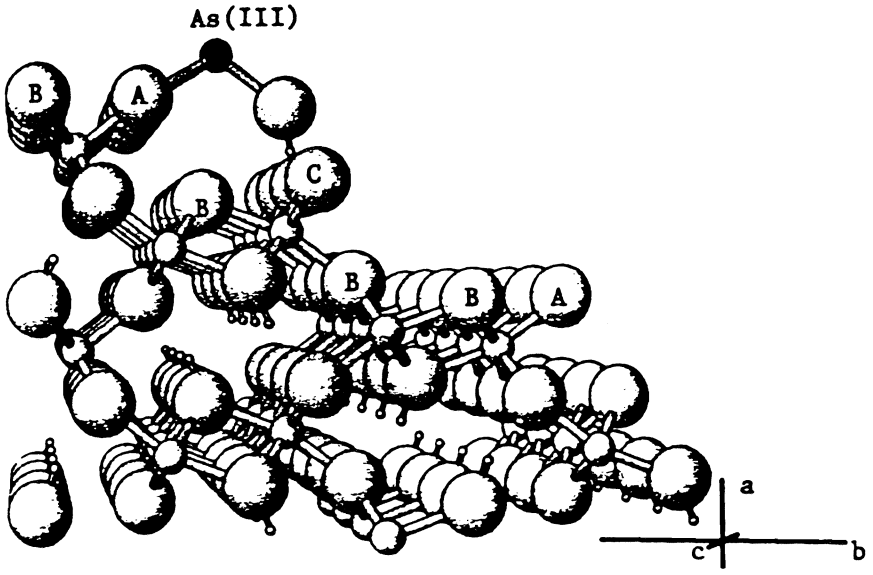

Figure 10. As(III) possible bonding structures on (110) face of goethite. Binuclear complex with two A-type hydroxyls and H-bonding with a C-type hydroxyl.

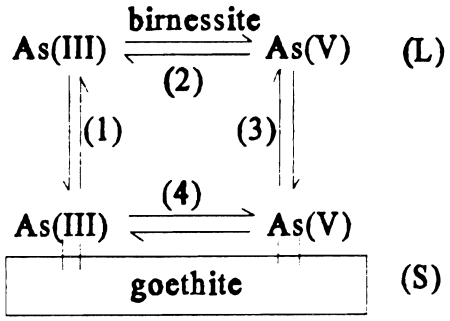

Figure 11. The reactions of As(III) and As(V) at water-goethite interfaces.

A Geometric Approach to Soil Pollution

CARLOS E. PUENTE
Department of Land, Air and Water Resources, Davis Campus

Summary

This research deals with the geometric quantification of the concentration patterns that are observed when a pollutant migrates within the soil. The objective of this project is to test if the dynamics of actual plumes could be properly described (predicted) following the time evolution of surrogate parameters that allow a close geometric representation of observed concentration patterns. In particular, this research focuses on the mathematical description of vertically-averaged two-dimensional concentration patterns as measured on ten dates at the Borden site.

Close encodings of the chloride and bromide plumes at the Borden site have been achieved employing the fractal-multifractal framework developed by Puente (1992, 1996). The excellence of the representations is expressed by close geometric agreements between real and modeled plume snapshots, which in turn result in close correspondence of plume moments of orders one to four, for all times. The most variable fractal-multifractal parameters for the plumes are the coordinates by which fractal interpolating functions pass (localization parameters). It turns out that these surrogate parameters basically exhibit a linear growth in time and follow closely the tracers' center of mass and their dispersion. A complete study of alternative prediction schemes shows that some of the future plumes, besides being geometrically reasonable and non-Gaussian, have their first two moments close to those predicted via stochastic theories, e.g. Dagan (1984).

Key Words: pollution transport, contaminant transport, fractals, multifractals.

Project Objectives Addressed in 1995-1996

1. A sensitivity analysis study of the fractal-multifractal parameters for the chloride concentrations for the ten dates at the Borden site, varying the objective function that defines the nonlinear inverse optimization problem.

2. A complete study of alternative forecasting scenarios based on fractal-multifractal parameter trends for the ten chloride patterns at the Borden site.

Research Plan and Procedures

Proper description (interpolation, estimation, prediction, simulation, etc.) of hydrologic information in space and time is crucial for the understanding and quantification of the phenomena at hand and its consequences. A common trait of these data sets, typical in pollution studies, is that they are complex. They exhibit "heterogeneities," "anisotropies" and "intermittencies" which preclude a simple mathematical description. The typical approach for many years has been to understand such variability based upon well-founded physical principles, i.e. partial differential equations which express conservation laws, and to couple them with stochastic methods to account for the inherent lack of knowledge on some aspects of the model, such as parameters or boundary conditions.

Instead of concentrating on the detailed geometry of data sets per-se, state of the art stochastic procedures center their attention on "relevant statistics" of the patterns at hand (i.e. means, variances, spatial correlations, extremes, etc.). Assumptions like stationarity and ergodicity are often used to aid in the development of theories, even though it is common to have phenomena which provide but a single spatial pattern (as in groundwater properties). Despite substantial progress throughout the years, the problem of understanding and predicting soil pollution still remains unsolved. Although modern stochastic methods provide a viable representation of complex data, more often than not (given their assumptions) they result in "smoothed," "distorted" and/or "unreal" representations of observed patterns. All these approximations may be unacceptable if prevailing dynamic conditions are sufficiently nonuniform and nonlinear.

This work attempts to model plume dynamics by capturing explicitly the geometrical features observed in pollution studies, i.e. "shades of concentrations". The idea is to reproduce the "complex," "jagged" and "intricate" patterns as deterministic fractal transformations of turbulence-related distributions (multifractal probability measures), (Puente, 1992). The basis for the representation is the belief that the geometric effects may be filtered out properly by proper encoding, which in turn would allow visualizing the evolution of the plume based upon few surrogate parameters. Capturing geometry may

be the key because, after all, the observed patterns are mere unique reflections of ongoing physico-chemical mechanisms taking place within the porous medium.

As part of an earlier project funded by the Kearney Foundation of Soil Science, suitable surrogate parameter sets for a fractal-multifractal description of pollution patterns were catalogued. (See Kearney Foundation of Soil Science Annual Reports for 1991-92, 1992-93, and 1993-94). Observed spatial snapshots are normalized and then interpreted as derived distributions obtained, transforming a simple (binomial) multifractal measure by means of a three-dimensional fractal interpolating function whose graph looks like a wire. The surrogate parameters of the fractal-multifractal representation include: (a) the coordinates of points in three dimensions by which the fractal interpolation function passes (localization parameters); (b) the sequences of ups and downs and the angles that determine the final shape of the fractal interpolating function (scalings and rotations, regularity parameters); and (c) the quantities that dictate how to recursively construct the multifractal measure (intermittency parameters). At the end, a compact deterministic description of the derived measure is found, despite the complex and seemingly random nature of the target pattern (Puente, 1996).

Results

Figure 1 includes the best surrogate parameters for the ten chloride frames measured at the Borden site. Not included are the intermittency parameters which are all equal to 0.5 for all dates, indicating that all patterns are encoded as fractal transformations of uniform distributions. The best parameters were obtained solving an inverse optimization problem, which minimizes a suitable "distance" between a real concentration profile and a pattern generated via the fractal-multifractal procedure. Such a distance, even though varied from frame to frame, contained common statistical qualifiers for the records, which included: (i) moments of orders up to four on both spatial axes, (ii) spatial cross correlations of orders up to two, (iii) moments of orders up to four computed from the concentration's axis, (iv) autocorrelation functions, which included: horizontal, vertical, transverse, and isotropic, (v) entropy, (vi) level excursions, and (vii) differences between real and fitted records at the scale of the measurements and also when records are aggregated over larger scales. The surrogate parameters minimized squared differences of weighted sums of the aforementioned attributes and relied on a preliminary fit based on the multidimensional simplex method (Press et al., 1989) and on a refinement of these parameters via simulated annealing (Otten et al., 1989).

Figure 2 includes observed chloride concentrations for the last day of observations, 647 after injection, and predictions via the last five of the following six alternative forecasting schemes based on Fig. 1: (i) linear regression of all surrogate parameters using the last two dates as reported in Fig. 1, (ii) linear regression of all surrogate parameters but using the last 5 frames on Fig. 1, (iii) the same but only using all ten dates, (iv) linear regression of coordinates and scalings from all 10 dates while fixing the rotations at the average values from

all days, (v) linear regression for coordinates only and from the last 2 frames while fixing the scalings and rotations to averages from the last 2 days, and (vi) the same as the previous scenario (v) but having the scalings from a linear regression. Figures 3 and 4 present the corresponding predictions for all six scenarios, 725 and 800 days after injection. Figure 5 compares the most used moments, i.e. the covariance tensor, for all days (either interpolated or predicted) via the six scenarios against those of the actual records and their best fractal-multifractal fit. Such a figure also includes the approximation obtained via the stochastic model of Dagan (1984), as reported by Freyberg (1986).

Discussion

A detailed sensitivity analysis of the surrogate parameters for days 63 and 462 revealed that the obtained parameters, reported in Fig. 1, are indeed the best that have been found. For those two dates, and for the others as well, all the seven groups of statistics mentioned before are nicely preserved. When a variety of objective functions are defined so that they include only some of the seven sets of attributes, e.g. moments and entropy, etc., the "best" parameters obtained give either close agreement with those reported in Fig. 1 or they provide solutions which are not better than those in Fig. 1. This happens both geometrically and statistically with both optimization procedures. In order to verify further the goodness of the best solutions, wider parameter simplexes were defined and then used on both days. For this exercise, it was found that again the solutions of the alternative inverse problems via alternative objective functions did not improve the solution whose parameters are reported in Fig. 1. Overall, when a "good" simplex is used, the obtainable fractal-multifractal patterns are similar to the best, irrespective of the combination of attributes used to define an objective function. When the parameter simplex is "wide", on the other hand, alternative objective functions clearly influence the overall shape and precision of the patterns that can be found. The results suggest that interactive experimenting with a catalog of shapes is indeed essential before any optimization procedure becomes effective.

As seen in Fig. 2, a close representation of the observed plume at day 647, Fig. 2 (a) is found only when using a scheme which relies on regressions based on the last two dates (Fig. 2f). Although usage of all dates on the regression preserves the overall trend of the plume (Fig. 2 c, d), these schemes give smoothed patterns which do not preserve the width and details of the original plume. Usage of the last five dates (Fig. 2b), and a representation having averaged scalings and rotations based on the last two dates (Fig. 2e), also give smooth approximations which appear reasonable, if measurement errors are accounted for. Of all the schemes, regression on all surrogate attributes based on the last two dates, not shown, is best. Such a pattern has as parameters those given in Fig. 1 and faithfully reproduces the observed measurements.

As seen in Figs. 3 and 4, predictions for days 725 and 800 follow the trends found for day 647. Plumes 3(a), 4(a), 3(f), and 4(f), both obtained via regressions of at least coordinates and scalings, exhibit similar heterogeneous behavior in terms of detail and possible plume splitting for future times. Notice the strong geometric influence of these patterns on the one seen at day 647. As for the other schemes, it is clear that the detail they provide varies: While Figs. 3(b), 4(b), 3(e), and 4(e) give a plume whose shape is quite open, and only vaguely reminiscent of the initial pattern for day 647, regression schemes which use surrogate parameters from all days. [Figs. 3(c), 4(c) 3(d), and 4(d)] continue being quite elongated.

The covariance tensor as given by its longitudinal, transverse and cross correlation terms exhibits interesting behavior for alternative prediction scenarios. As seen in Fig. 5, and as hinted in Figs. 3(b,e) and 4(b,e), schemes based on regression of the last five dates (triangles) and regression of coordinates via the last two while fixing both scalings and rotations (hexagons) give both an increasing growth on transverse variance, which clearly deviates from those predicted by Dagan's model. In regard to the other schemes, it is clear from Fig. 5 that all of them can be considered reasonable approximations of the trends predicted via the stochastic model. Curiously, the patterns that appear to be most "reasonable" by eye, i.e. regression of all surrogate parameters from the last two dates (squares) and the same idea but fixing rotations (circles), give the closest agreement in both longitudinal and transverse variances (with squares being more consistent than circles in cross-correlation) in regards to the stochastic model.

It is remarkable that the assumption-free geometric procedure provides predictions which are consistent with those given via stochastic ideas and specific assumptions. The geometric detail provided by the geometric method comes as an advantage over stochastic methods, which are limited by their analytical tractability and which result, as in the case of Dagan's model, in Gaussian (i.e. elliptical) plumes which are not found in practice. The influence of the predictions on the observed plumes, as shown in Figs. 2, 3, and 4, shows that the geometric procedure may be successful only if patterns gathered are stable enough to allow extrapolation of the plume as it samples larger regions in space. Possible stability criteria have been identified as it has been observed that reasonable predictions correspond to smooth variations on a variety of qualifiers based on the surrogate parameters of the geometric procedure. Among those qualifiers, there are indices which determine whether a plume is Gaussian or not (Puente and Klebanoff, 1994). In regard to geometric predictability, it is worth noticing that trying to approximate the plume at day 647 employing data from the past results in patterns which do not resemble the observed elongated shape, irrespective of the prediction scheme used.

References

Dagan, G., 1984. Solute transport in a heterogeneous porous formation. J. Fluid Mech. 145:151-177.

Freyberg, D. L. 1986. A natural gradient experiment on solute transport in a sand aquifer. 2. Spatial moments and the advection and dispersion of nonreactive tracers. Water Resour. Res. 22(13):2031-2046.

Otten, R. H. J. M. and L. P. P. P. van Ginneken. 1989. *The Annealing Algorithm.* Kluwer Academic Publishers, Boston..

Press, W. H., B. P. Flannery, S. A. Teukolsky, and W. T. Vetterling 1989. Numerical Recipes. Cambridge University Press.

Puente, C. E. 1992. Multinomial multifractals, fractal interpolators, and the Gaussian distribution. Physics Letters A. 161:441-447..

Puente, C. E. and A. Klebanoff. 1994. Gaussians everywhere. Fractals 2(1):65-79..

Puente, C. E. 1996. A new approach to hydrologic modeling: derived distributions revisited. J. Hydr. In press.

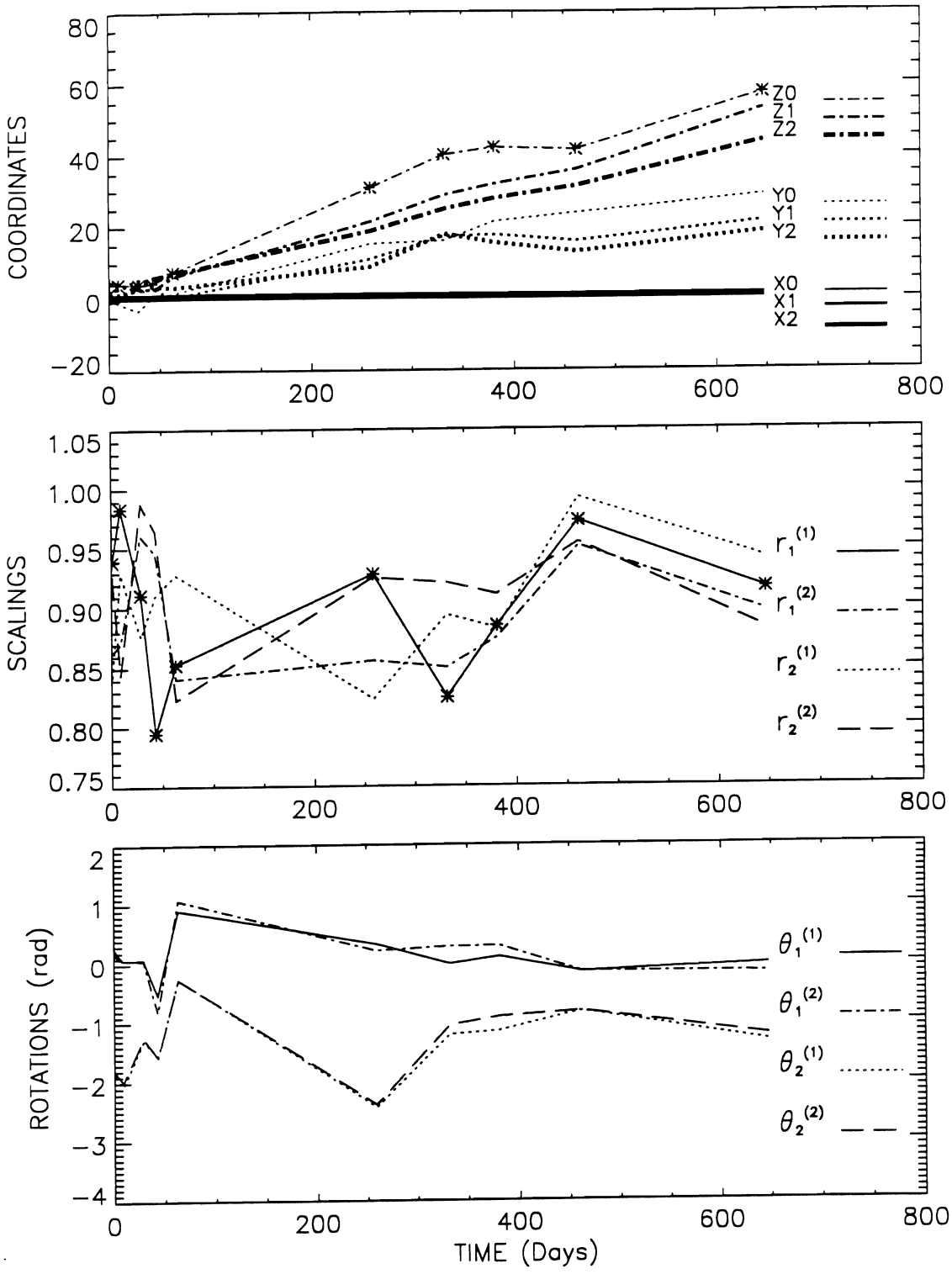

Figure 1. Fractal-multifractal surrogate parameter evolution for the ten chloride concentration profiles measured at the Borden site.

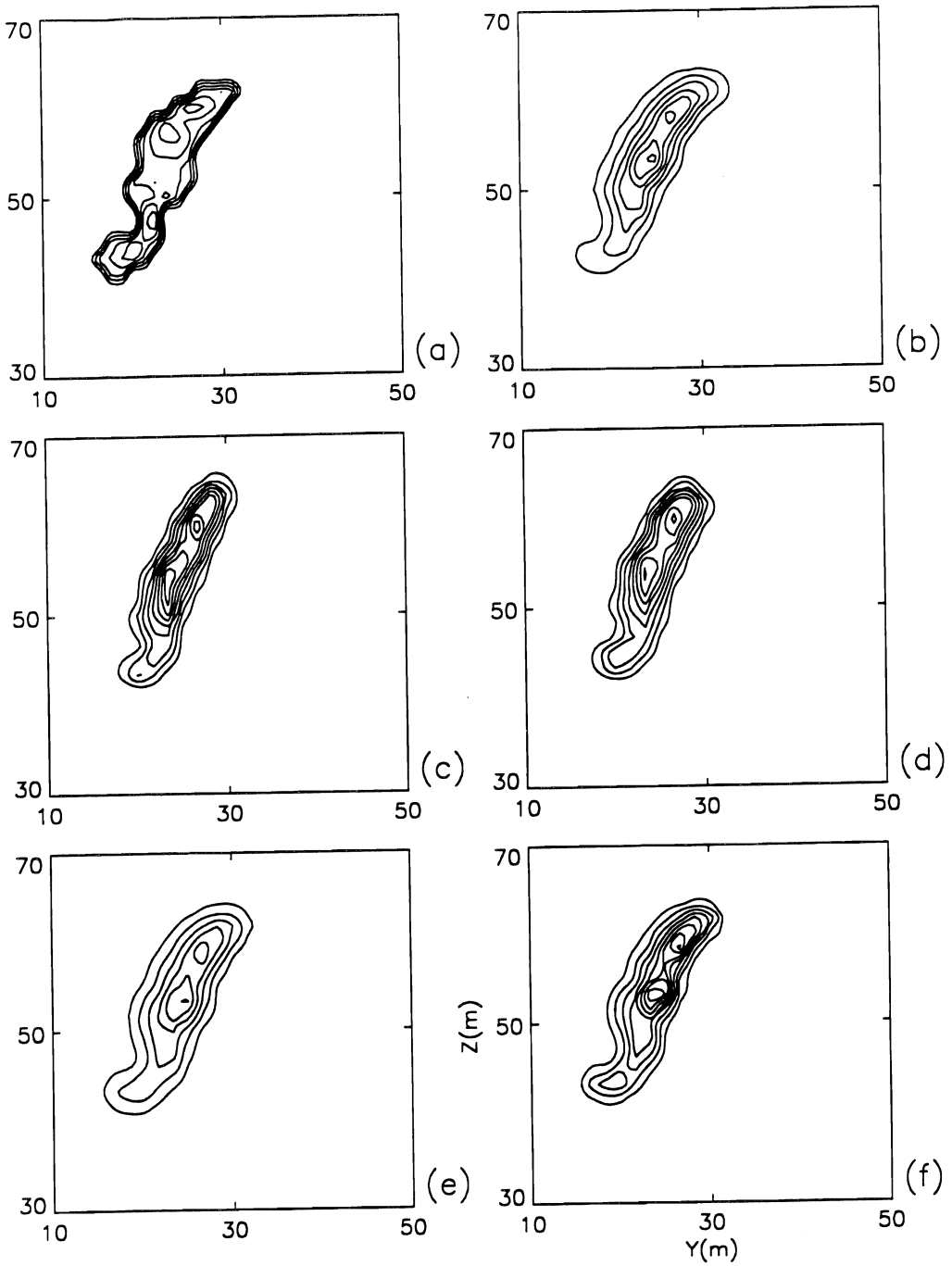

Figure 2. Observed and fitted chloride profiles via alternative interpolating schemes for day 647. (a) Observed records, (b) via regressions on all surrogate parameters using the last 5 dates on Fig. 1, (c) same as (b) but using all 10 frames available, (d) via linear regression of coordinates and scalings from all 10 dates while fixing the rotations at the average values from all days, (e) via linear regression for coordinates only and from the last 2 frames while fixing the scalings and rotations to averages from the last 2 days, and (f) same as (e) but having the scalings from a linear regression.

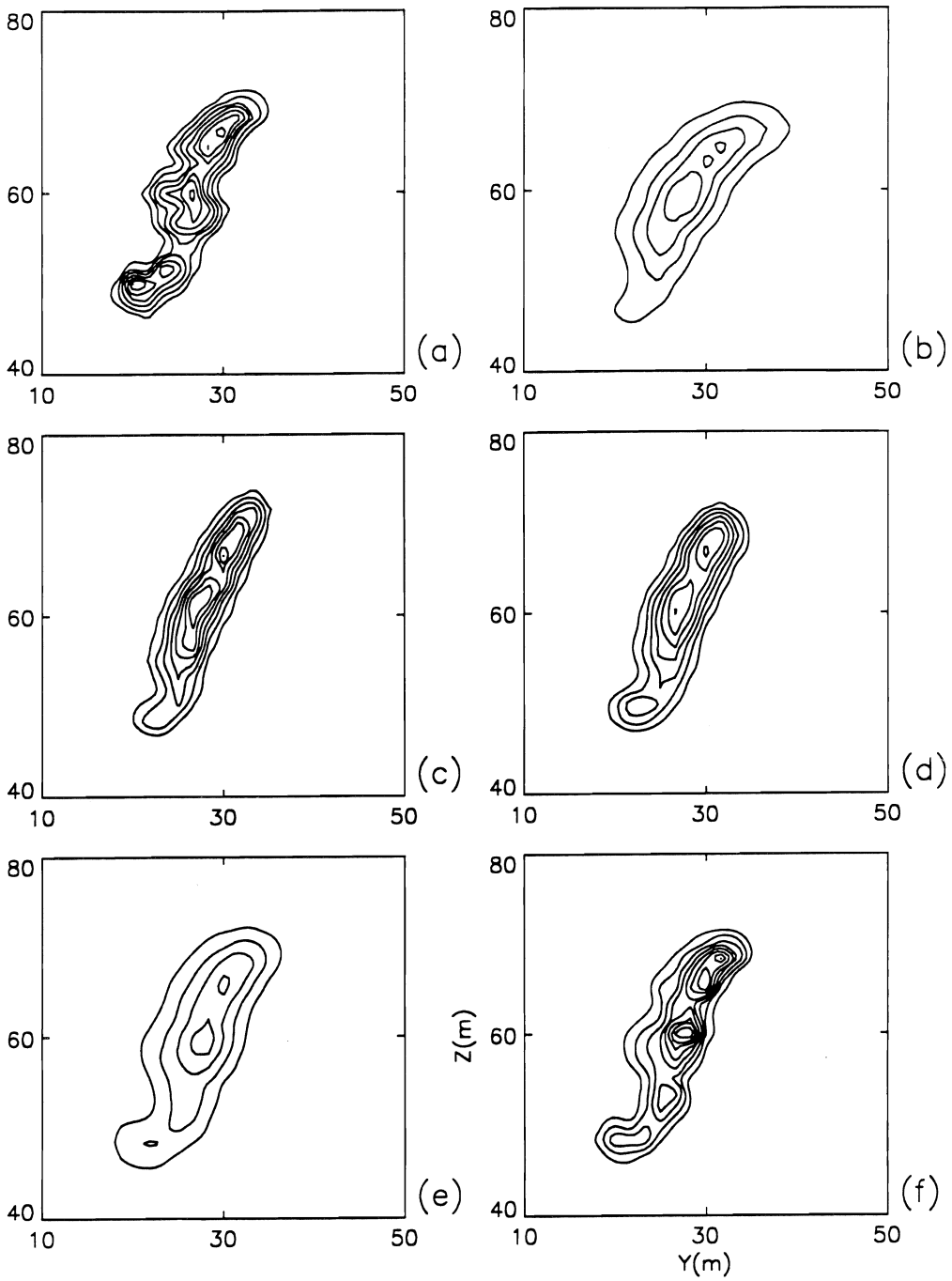

Figure 3. Predicted chloride profiles via alternative interpolating schemes for day 725. (a) Via regressions on all surrogate parameters using the last 2 dates on Fig. 1, (b) same as (a) but using the last 5 dates, (c) same as (a) but using all 10 frames available, (d) via linear regression of coordinates and scalings from all 10 dates while fixing the rotations at the average values from all days, (e) via linear regression for coordinates only and from the last 2 frames while fixing the scalings and rotations to averages from the last 2 days, and (f) same as (e) but having the scalings from a linear regression.

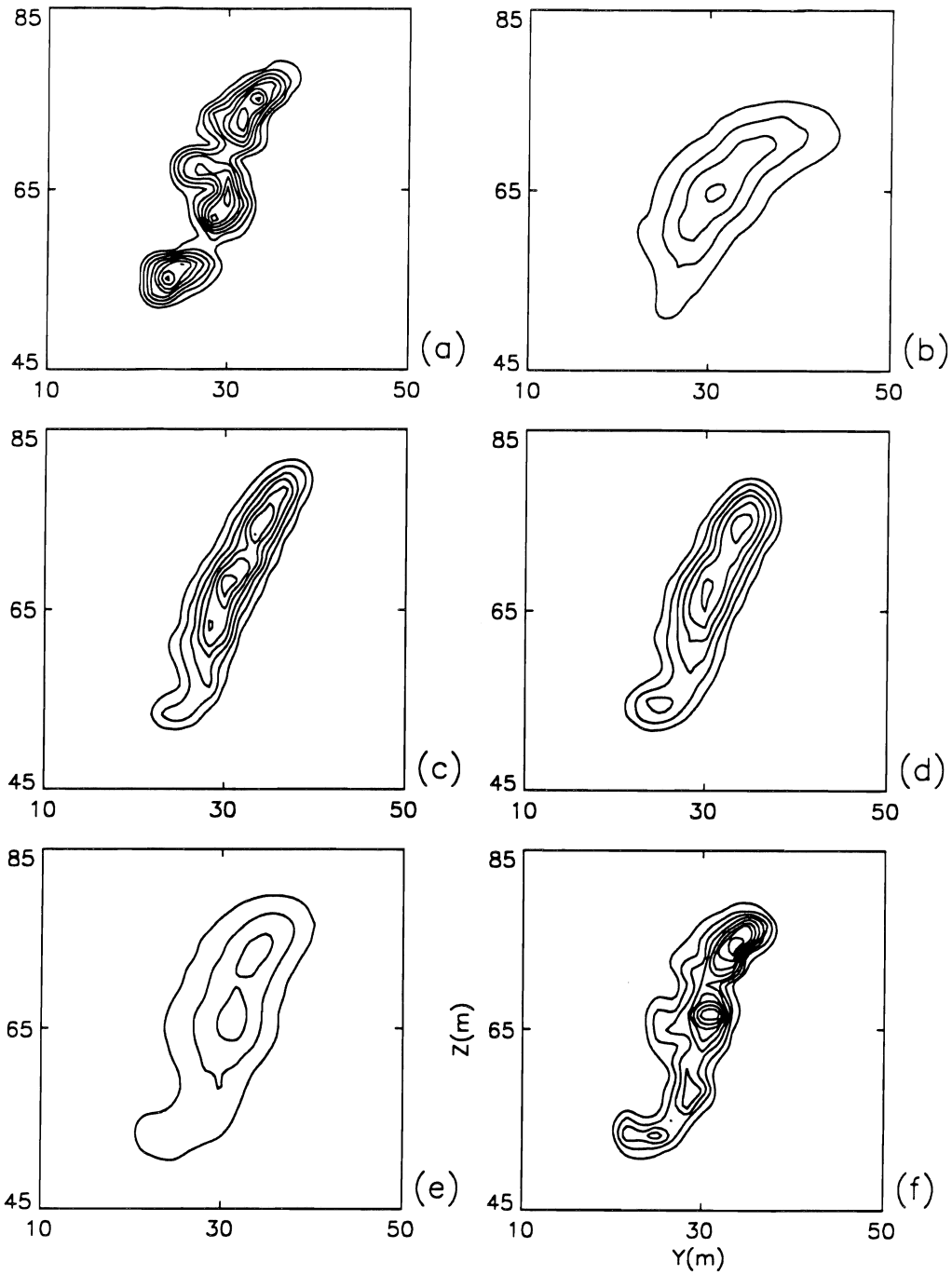

Figure 4. Predicted chloride profiles via alternative interpolating schemes for day 800. (a) Via regressions on all surrogate parameters using the last 2 dates on Fig. 1, (b) same as (a) but using the last 5 dates, (c) same as (a) but using all 10 frames available, (d) via linear regression of coordinates and scalings from all 10 dates while fixing the rotations at the average values from all days, (e) via linear regression for coordinates only and from the last 2 frames while fixing the scalings and rotations to averages from the last 2 days, and (f) same as (e) but having the scalings from a linear regression.

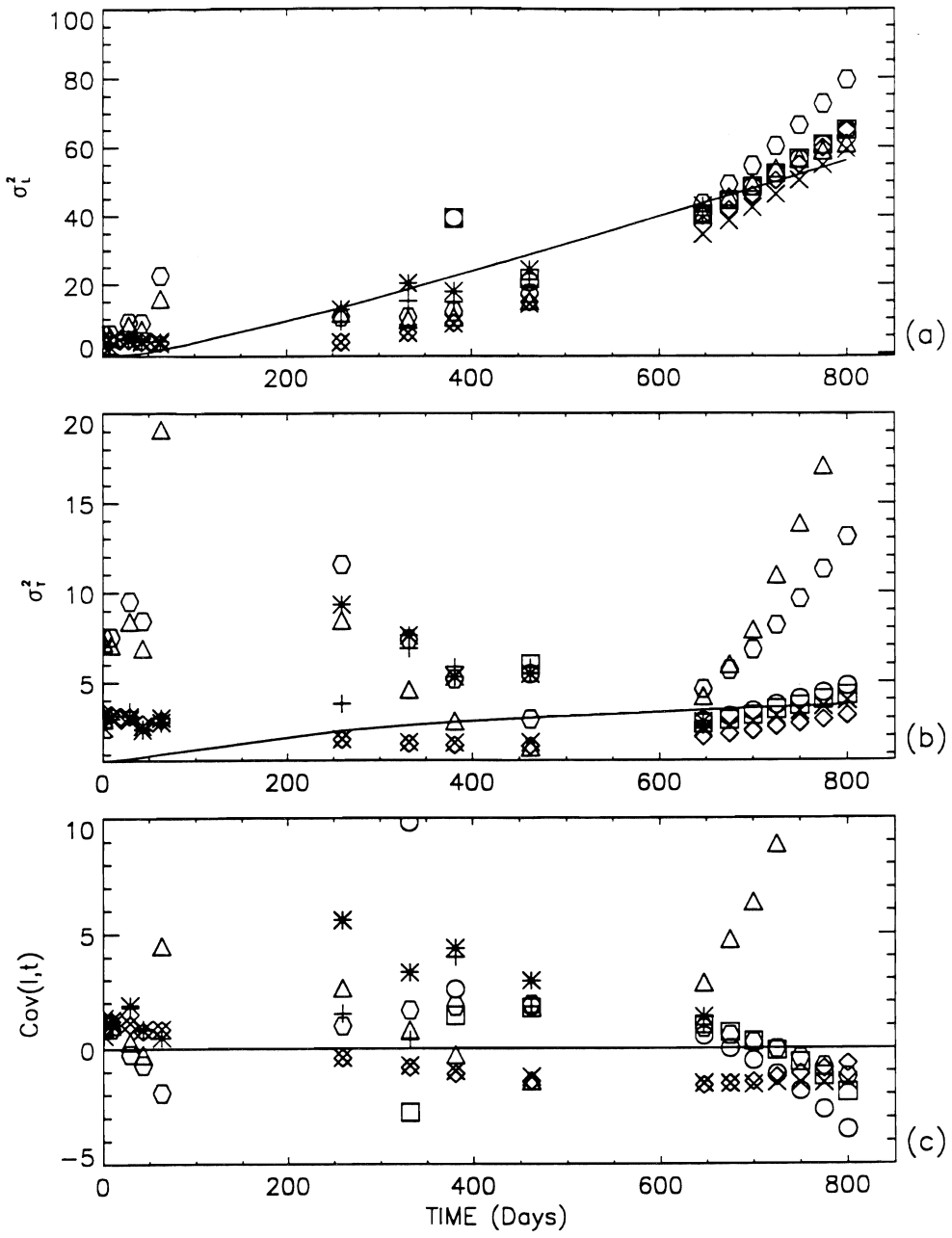

Figure 5. Interpolated and predicted covariance tensor for alternative interpolating schemes. Via regressions on all surrogate parameters using the last 2 dates on Fig. 1, (squares), using the last 5 dates (triangles), using all 10 frames available (diamonds), via linear regression of coordinates and scalings from all 10 dates while fixing the rotations at the average values from all days (times), via linear regression for coordinates only and from the last 2 frames while fixing the scalings and rotations to averages from the last 2 days (hexagons), and also the last 2 days but having the scalings from a linear regression (circles). Also included in the figure are observed values (asterisks) and Dagan's model covariances (solid line).

Macroscopic Dispersivity with a Linear Trend in the Log Conductivity

TROY T. REID[1], ROY B. LEIPNIK[1], HUGO A. LOAICIGA[2], AND MIGUEL A. MARINO[3]
[1]*Department of Mathematics, Santa Barbara Campus*
[2]*Department of Geography, Santa Barbara Campus*
[3]*Department of Land, Air and Water Resources, Davis Campus95616*

Summary

Recently, the development of effective conductivity in the presence of a deterministically linear trend in the log hydraulic conductivity and a "small" stochastic perturbation hve been investigated. The model of these processes was coupled with the transport phenomena of solutes to produce spectral equations governing macroscopic dispersivity. A general relationship was derived governing the coefficients of the macrodispersivity tensor in terms of an integral equation. Analysis was performed using standard assumptions on the hydraulic parameters. The auto-covariance of the stochastic perturbation in the log hydraulic conductivity was chosen to be Gaussian in nature, rather than the usual exponential model. Numerical emulation of sedimentary deposition examined the macrodispersivities as a function of correlation scales, microdispersivities, and the slope of the log conductivity. The result was that the ratio of the horizontal to the vertical macrodispersivities tends to decrease monotonely as a function of the slope of the log conductivity, or the horizontal correlation scales, or the longitudinal microdispersivity.

Key Words: macroscopic dispersivity, log conductivity, groundwater, stochastic analysis, spectral analysis.

Project Objectives Addressed in 1995-1996

The transport of particulates via groundwater flow in heterogeneous media is of great interest for environmental protection and to water resource management. Due to the variability inherent in a heterogeneous porous medium, its characteristics, in particular the hydraulic conductivity,.are modeled as random fields, The transport process at large scales (i.e. at field scales of hundreds or thousands of meters, see (Gelhar, 1993) is then characterized by the macrodispersivity tensor through a Fickian law. Expressions for the coefficients of the macrodispersivity tensor can be derived by coupling the following three stochastic differential equations, having both random variables and a random coefficient (the hydraulic conductivity):

a. the steady-state fluid flow equation,
b. Darcy's equation governing the hydraulic head, and
c. the steady-state transport equation.

The steady-state case is assumed, as normally done, since subsurface groundwater flow occurs at large time scales and has usually evolved into a steady-state, (see Gelhar and Axness, 1993) who analyze the unsteady case and rationalize this assumption. Also, the solutes are assumed to be ideal tracers, which do not react with the groundwater to produce changes in fluid viscosity or fluid density. Details concerning the case of a non-ideal tracer can be found in Welty and Gelhar (1991).

The heterogeneity of the porous medium is manifested in modeling the logarithm of the hydraulic conductivity as a deterministic mean superimposed upon with a "small" random field. All other random variables in the stochastic differential equations are modeled in the same fashion: a random field superimposed on a deterministic mean. These other random fields are dependent on the log conductivity field through the stochastic differential equations. Gelhar and Axness (1983) performed their analysis under the assumptions that the deterministic portion of the log conductivity field is constant and that the random portion is characterized by an exponential model of its auto-covariance function. This constant assumption seems too restrictive; experimental results (Rehfeldt et al., 1992) suggest the need for spatial trends in the deterministic portion of the log conductivity field.

The technical possibility of including spatial trends is shown by the recent focus on the development of effective conductivity in the presence of linear trends (Loaiciga et al., 1993, 1994, 1996). Recently, macrodispersivity in the presence of a linear trend in the log conductivity has been analyzed in Indelman and Rubin (1995); (however using an exponential model for the auto-covariance). Their method generated moments of the solutions of the stochastic differential equations using Green's functions. The theory of Fourier/Spectral representation, used by Loaiciga et al., (1993, 1994, 1996), on the first two of these stochastic differential equations, furnishes an alternate approach that allows certain generalizations, discussed below, to be made easily. The spatial

trend in the log conductivity will be assumed to be dominated by a linear trend within, say, one or two log conductivity scales, the usual distance for field-scale experiments to be considered essentially infinite.

The development of the basic equations has been kept as general as possible. The standard assumptions governing the hydraulic parameters were then applied (e.g. the orientation of the x_1-axis with the direction of the mean fluid flow, the form of the local dispersivity tensor under this orientation, etc.) and the analysis was performed. The hope is that in the future, these standard assumptions can be further generalized. One improvement in the stage of explicit calculation was to model the random field in the log conductivity by a Gaussian auto-covariance function, instead of the linear exponential model. The mathematical cost is not severe.

Research Plan and Procedures

The macrodispersivity tensor, $\underline{A}$, having components, A_{mn}, is defined using a version of Fick's Law governing dispersive flux,

$$\sum_{n=1}^{3} A_{mn} G_n = \frac{1}{q} \cdot \overline{c' q'_m} \tag{1}$$

where G_n are the components of the mean concentration gradient; q is the magnitude of the mean specific discharge vector; c' is the random field associated with the concentration field; and q'_m, m = 1, 2 or 3, are the components of the random field associated with the specific discharge vector (Gelhar, 1993). The term, $\overline{c' q'_m}$, represents the mean dispersive flux of the tracers in the x_m-direction and can be written as an integral of an expectation value of quantities governed by the three stochastic differential equations mentioned above. This gives

$$\sum_{n=1}^{3} A_{mn} G_n = \frac{1}{q} \int_{\Re^3} E\left[dZ_{c'}(\bar{k})\, dZ^*_{q'_m}(\bar{k}) \right] d^3k \tag{2}$$

(note: z^* represents complex conjugation of z.) The terms, $dZ_{c'}$ and $dZ_{q'_m}$, are the spectral representations of the stochastic processes in the concentration field and in the specific discharge vector, respectively. These terms are related to the stochastic process in the log conductivity field through these stochastic differential equations. In particular, Darcy's equation states that

$$q_m = -K \frac{\partial \phi}{\partial x_m} \tag{3}$$

where q_m is a component of the specific discharge vector represented by a deterministic mean, $\vec{\bar{q}}$, plus a zero-mean stochastic process, q'_m; K is the hydraulic conductivity whose logarithm is modeled as a constant, F, plus a linear trend, $\vec{b}\cdot\vec{x}$, plus a zero-mean stochastic process, f; and ϕ is the hydraulic head represented by a deterministic mean, H, (which is assumed to have an essentially constant gradient, $-\vec{J}$) plus a zero-mean stochastic process, h. Using these representations in Darcy's equation and dropping terms of second order and higher in the stochastic processes yields the following relationship

$$q'_m = -e^{F+\vec{b}\cdot\vec{x}} \left(\frac{\partial h}{\partial x_m} - J_m f \right) \tag{4}$$

At this point, the spectral representation of the stochastic processes is introduced:

$$h\left(\vec{x}\right) = \int_{\Re^3} e^{j\vec{k}\cdot\vec{x}}\, dZ_h\left(\vec{k}\right) \tag{5}$$

$$f\left(\vec{x}\right) = \int_{\Re^3} e^{j\vec{k}\cdot\vec{x}}\, dZ_f\left(\vec{k}\right) \tag{6}$$

$$q'_m\left(\vec{x}\right) = \int_{\Re^3} e^{j\vec{k}\cdot\vec{x}}\, dZ_{q'_m}\left(\vec{k}\right) \tag{7}$$

where $j = \sqrt{-1}$. Using fairly standard manipulations of the Fourier/Spectral transform, (4) becomes

$$dZ_{q'_m}\left(\vec{k}\right) = -\frac{e^F}{(2\pi)^3}\left[jl_m\, dZ_h\left(\vec{l}\right) - J_m\, dZ_f\left(\vec{l}\right)\right]\Big|_{\vec{l}=\vec{k}+j\vec{b}} \tag{8}$$

Before proceeding along these lines, the steady-state fluid flow equation is used to express dZ_h in terms of dZ_f. The steady-state fluid flow equation in 3-D can be written in terms of the log conductivity as

$$\sum_{i=1}^{3}\left[\frac{\partial}{\partial x_i}(\log K)\frac{\partial \phi}{\partial x_i} + \frac{\partial^2 \phi}{\partial x_i^2}\right] = 0 \tag{9}$$

The same analysis as performed with Darcy's equation can now be applied to this version of the steady-state fluid flow equation to yield the following relationship (Loaiciga et al., 1996), who derive a similar equation with the denominator rationalized,

$$dZ_h\left(\vec{k}\right) = \frac{j\vec{J}\cdot\vec{k}}{j\vec{b}\cdot\vec{k} - k^2}\, dZ_f\left(\vec{k}\right) \tag{10}$$

This is used to eliminate dZ_h in (8), resulting in:

$$dZ_{q'_m}\left(\vec{k}\right)=\frac{e^F}{8\pi^3}\left(\frac{j\vec{J}\cdot\vec{l}}{j\vec{b}\cdot\vec{l}-l^2}+J_i\right)dZ_f\left(\vec{l}\right)\Bigg|_{\vec{l}=\vec{k}+j\vec{b}} \tag{11}$$

Next, a similar analysis is performed on the steady-state transport equation to express $dZ_{c'}$ in terms of dZ_f. The steady-state transport equation states that

$$\sum_{i=1}^{3}\frac{\partial}{\partial x_i}\left[\sum_{j=1}^{3}\underline{E_{ij}}\frac{\partial c}{\partial x_j}-cq_i\right]=0 \tag{12}$$

where the $\underline{E_{ij}}$ are the coefficients of the local dispersivity tensor (assumed to be constant multiples of the mean specific discharge) and where c is the concentration of the tracers (see, for example, Gelhar and Axness, 1983). Let the specific discharge be represented as before, and let the concentration be represented by a deterministic mean, C, plus a zero-mean stochastic process, c'. The mean concentration is further specialized to have a constant gradient, $\frac{\partial C}{\partial x_i}=-G_i$, (Gelhar and Axness, 1983). It is hoped that this restriction may be relaxed in future analysis since the terms introduced in modeling the concentration gradient linearly can be dealt with in the same fashion presented; however, they become considerably lengthier.

The spectral representation of the stochastic processes is introduced, as before, and a similar analysis as with Darcy's equation is performed. This includes using a previous result, (11), to eliminate the dependence on the stochastic process associated with the specific discharge vector. The following equation is then derived,

$$dZ_{c'}\left(\vec{k}\right)=\frac{e^F}{8\pi^3}\;\frac{1}{\vec{l}^{\,T}\,\underline{E}\,\vec{l}+j\vec{l}\cdot\vec{q}}\left(\frac{(\vec{J}\cdot\vec{l})(\vec{G}\cdot\vec{l})}{j\vec{b}\cdot\vec{l}-l^2}+\vec{G}\cdot\vec{J}\right)dZ_f\left(\vec{l}\right)\Bigg|_{\vec{l}=\vec{k}+j\vec{b}} \tag{13}$$

Results

This result, (13), the complex conjugate of (11), and the Fickian relationship, (2), are combined to yield a rather general equation governing the coefficients of the macrodispersivity tensor. This equation can be simplified for special applications in five respects. First, we impose the orthogonality condition of the spectral process, dZ_f, i.e. that

$$E\left[dZ_f\left(\vec{\xi}\right)dZ_f\left(\vec{\mu}\right)\right]=\delta\left(\vec{\xi}-\vec{\mu}\right)S_{ff}\left(\vec{\xi}\right) \tag{14}$$

where δ is the dirac delta function and S_{ff} is the spectral auto-covariance function associated with the log conductivity field. Second, the summation in (2) can be uncoupled and the right-hand side of (2) is reduced to the following integral for the coefficients of the macrodispersivity tensor:

$$A_{mn}=\frac{e^{2F}}{64\pi^3\bar{q}}\int_{\Re^3}\frac{\Theta_n\left(\vec{k}\right)\Theta_m^*\left(\vec{k}\right)}{\vec{k}^T\,\underline{E}\,\vec{k}+j\vec{k}\cdot\vec{q}}S_{ff}\left(\vec{k}+j\vec{b}\right)d^3k \tag{15}$$

Here,

$$\Theta_n\left(\vec{k}\right)=\left(J_n-\frac{\vec{J}\cdot\left(\vec{k}+j\vec{b}\right)\left(k_n+jb_n\right)}{k^2+j\vec{b}\cdot\vec{k}}\right) \tag{16}$$

While (15) and (16) can be handled by standard methods of mathematical physics, the conclusions would be difficult to interpret without further specialization. Thus, thirdly, the coordinate system will be oriented to put the mean specific discharge vector in the form,

$$\vec{\bar{q}} \;=\; \langle \bar{q},0,0\rangle \tag{17}$$

Fourth, the local dispersivity tensor under this orientation is assumed to be of the form

$$\underline{E}=\begin{pmatrix}\alpha_1 & 0 & 0\\ 0 & \alpha_2 & 0\\ 0 & 0 & \alpha_3\end{pmatrix}\bar{q},\qquad \alpha_1,\alpha_2,\alpha_3>0 \tag{18}$$

(See Gelhar and Axness (1983), who work with the further specialization into longitudinal and transverse dispersivity.) Fifth, as mentioned before, the spectral auto-covariance is chosen to be Gaussian in nature, in particular of the form

$$S_{ff}\left(\vec{k}\right)=\frac{\lambda_1\lambda_2\lambda_3\,\sigma_f^2}{8\pi^{\frac{3}{2}}}\exp\left[-\frac{\lambda_1^2k_1^2}{4}-\frac{\lambda_2^2k_2^2}{4}-\frac{\lambda_3^2k_3^2}{4}\right] \tag{19}$$

which follows from the Gaussian auto-covariance function

$$R_{ff}\left(\vec{x}\right)=\sigma_f^2\exp\left[-\frac{x_1^2}{\lambda_1^2}-\frac{x_2^2}{\lambda_2^2}-\frac{x_3^2}{\lambda_3^2}\right] \tag{20}$$

Using these choices, the integral in (15) becomes,

(21)

$$A_{mn} = \frac{e^{2F}\sigma_f^2\lambda_1\lambda_2\lambda_3}{64\pi^{\frac{3}{2}}\bar{q}^2}\exp\left(\sum_{i=1}^{3}\frac{\lambda_i^2 b_i^2}{4}\right)\int_{\Re^3}\frac{\Theta_n\left(\vec{k}\right)\Theta_m^*\left(\vec{k}\right)}{\sum_{i=1}^{3}\alpha_i k_i^2 + jk_1}\exp\left(-\sum_{i=1}^{3}\frac{\lambda_i^2 k_i^2}{4} + j\sum_{i=1}^{3}\frac{\lambda_i^2 b_i k_i}{2}\right)d^3k$$

Numerical Results: To emulate typical sedimentary deposition, numerical experiments were conducted on this problem in the case where the linear trend in the log conductivity was in the vertical direction. The local dispersivities were chosen to be simplified into longitudinal and transverse dispersivities only (see comment after (18)). A further reduction was made by eliminating the mean hydraulic head gradient in terms of the mean specific discharge vector, via the mean of Darcy's equation, (3). The computations were performed on a Sun computer (SunOS 5.4). Considering the fact that the integrations were over three-dimensional space, the time it took to calculate each data point was rather lengthy (several hours of CPU time, per data point).

Under all of these assumptions the essential parameters are the linear trend in the log conductivity, $\vec{b} = \langle 0,0,b \rangle$, the local dispersivities, α_L and α_T, and the correlation scales, λ_1, λ_2 and λ_3 (for which horizontal isotropy is assumed). All of the other parameters just provide scaling factors which are eliminated by considering the ratio of the macrodispersivities, A_{11}/A_{33}. Due to the horizontal isotropy in the correlation scales, $A_{22} \cong A_{11}$ (actually, A_{11} is slightly larger than A_{22} due to the orientation of the mean specific discharge vector in the x_1-direction, but not appreciably).

Discussion

The analysis of the macrodispersivity coefficients for the special applications mentioned in the results is almost complete (see Appendix). The method allows the choice of a Gaussian auto-covariance function at little extra cost, over the perhaps less defensible exponential assumption. Some natural extensions to the method include a non-diagonal form of the local dispersivity tensor (see (18)), accounting for shearing effects; a more general form of the Gaussian auto-covariance function (see (19)) to drive these shearing effects; and a higher-order model of the mean concentration gradient to include at least a linear term.

Figures 1 and 2 show that the ratio of the horizontal to vertical macrodispersivities tends to decrease as either the slope in the log hydraulic conductivity increases or as the horizontal correlation scales increase, and that the ratio tends to decrease less for larger values. Comparison of Figs. 1 and 2 shows that this ratio of horizontal to vertical macrodispersivities decreases as the longitudinal microdispersivity increases. Figures 3 and 4, and their comparison, reaffirm the trends previously mentioned.

Appendix A. Analytical results can be continued by considering the following integral,

$$\text{(A1)}\qquad \int_{\Re^3} \frac{\exp\left(-\sum_{i=1}^{3}\eta_i k_i^2 + j\sum_{i=1}^{3}\beta_i k_i\right)}{\left(\sum_{i=1}^{3}\alpha_i k_i^2 + jk_1\right)\left(\sum_{i=1}^{3}k_i^2 + j\sum_{i=1}^{3}b_i k_i\right)\left(\sum_{i=1}^{3}k_i^2 - j\sum_{i=1}^{3}b_i k_i\right)} d^3k$$

where the parameters, η_i and β_i, are introduced to take care of the remaining polynomial in the numerator, which was left out (via differentiation after the fact). The Gaussian nature of the integrand can now be utilized by eliminating the quadratic denominators through a Laplace-like transformation, yielding

$$\text{(A2)}\qquad \int_{\Re^3}\int_0^\infty\int_0^\infty\int_0^\infty \exp\left[-\sum_{i=1}^{3}(\eta_i+\alpha_i r+s+t)k_i^2 + j\sum_{i=1}^{3}(\beta_i-\delta_{i1}r-b_i s+b_i t)k_i\right] dr\,ds\,dt\;\; d^3k$$

After interchanging the order of integration, the integrals over k-space can be evaluated, giving

$$\text{(A3)}\qquad \int_0^\infty\int_0^\infty\int_0^\infty \prod_{i=1}^{3}\left\{\sqrt{\frac{\pi}{\eta_i+\alpha_i r+s+t}}\exp\left[-\frac{(\beta_i-\delta_{i1}r-b_i s+b_i t)^2}{4(\eta_i+\alpha_i r+s+t)}\right]\right\} dr\,ds\,dt$$

Upon rotating the r,s-plane 45°, (24) yields

$$\text{(A4)}\qquad -\frac{1}{2}\int_0^\infty\int_0^\infty\int_{-v}^{v}\prod_{i=1}^{3}\left\{\sqrt{\frac{\pi}{\eta_i+\alpha_i r+v}}\exp\left[-\frac{(\beta_i-\delta_{i1}r-b_i w)^2}{4(\eta_i+\alpha_i r+v)}\right]\right\} dw\,dv\,dr$$

An additional integration can be performed on (25), to give

$$\text{(A5)}\qquad -\frac{\pi^2}{4}\int_0^\infty\int_0^\infty \frac{\exp\left[\frac{\theta^2-\phi\psi}{\phi}\right]\left\{erf\left(\sqrt{\phi}v+\frac{\theta}{\sqrt{\phi}}\right)-erf\left(-\sqrt{\phi}v+\frac{\theta}{\sqrt{\phi}}\right)\right\}}{\sqrt{\phi}\quad\prod_{i=1}^{3}\left\{\sqrt{\eta_i+\alpha_i r+v}\right\}} dv\,dr$$

where

$$\text{(A6)}\qquad \phi=\sum_{i=1}^{3}\frac{b_i^2}{4(\eta_i+\alpha_i r+v)},\qquad \theta=\sum_{i=1}^{3}\frac{b_i(\delta_{i1}r-\beta_i)}{4(\eta_i+\alpha_i r+v)},\qquad \psi=\sum_{i=1}^{3}\frac{(\delta_{i1}r-\beta_i)^2}{4(\eta_i+\alpha_i r+v)}$$

References

Gelhar, L. 1993. Stochastic Subsurface Hydrology. Prentice Hall, Englewood Cliffs, NJ

Gelhar, L. and C. Axness. 1983. Three-dimensional stochastic analysis of macrodispersion in aquifers. Water Resources Research, 19(1):161-180.

Indelman, P. and Y. Rubin. 1995. Flow in heterogeneous media displaying a linear trend in the log conductivity. Water Resources Research. 31(5): 1257-1265.

Loaiciga, H., R. Leipnik, M. Marino, and P. Hudak. 1993. Stochastic groundwater flow analysis in the presence of trends in heterogeneous hydraulic conductivity fields. Mathematical Geology 25(2):161-176.

Loaiciga, H., R. Leipnik, P. Hudak, and M. Marino. 1994. Effective hydraulic conductivity of nonstationary aquifers. Stochastic Hydrology and Hydraulics 8:1-17.

Loaiciga, H., R. Leipnik, P. Hudak, and M. Marino. 1996. 1-, 2- and 3-dimensional effective conductivity of aquifers. Mathematical Geology, 28(5): 563-584.

Rehfeldt, K., J. Boggs, and L. Gelhar. 1992. Field study in a heterogeneous aquifer, 3. Geostatistical analysis of hydraulic conductivity. Water Resources Research 28:3309-3324.

Welty, C. and L. Gelhar. 1991. Stochastic analysis of the effects of fluid density and viscosity variability on macrodispersion in heterogeneous porous media. Water Resources Research 27(8): 2061-2075.

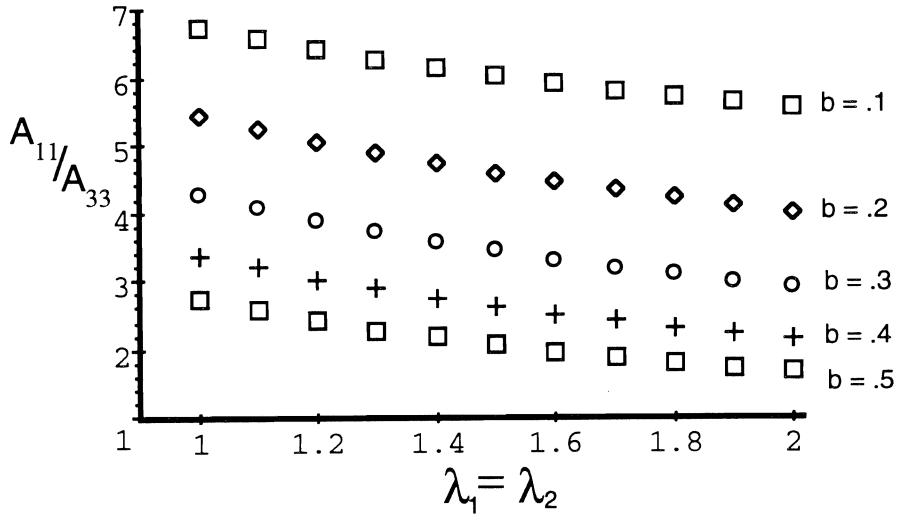

Figure 1. Graph of the ratio of longitudinal macrodispersivity (A_{11}) to the transversal macrodispersivity in the vertical direction (A_{33}) as a function of the correlation scale in the x-y plane ($\lambda_1 = \lambda_2$) for various levels of the trend in log-conductivity (b), and longitudinal dispersivity $\alpha_L = 6$, transversal dispersivity $\alpha_T = 1$, and vertical corfrelation scale $\lambda_3 = 0.5$.

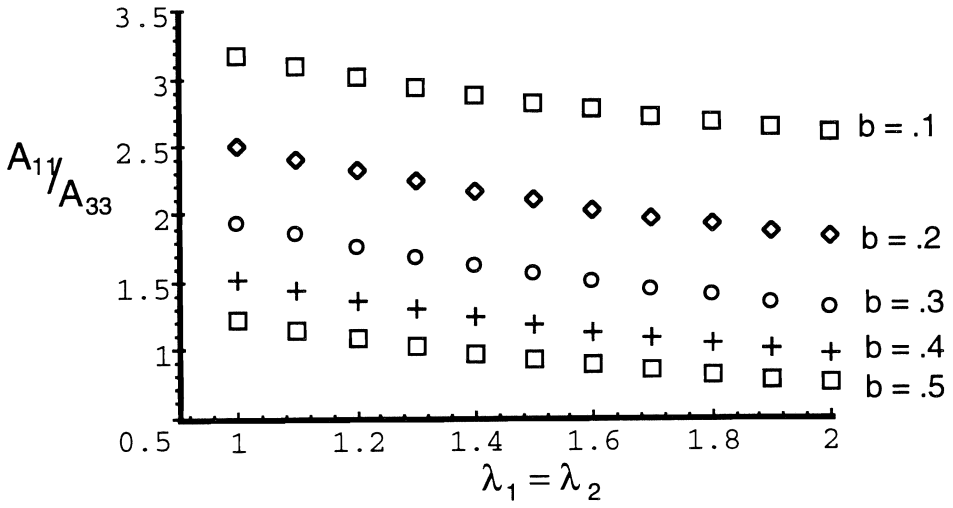

Figure 2. Graph of the ratio of longitudinal macrodispersivity (A_{11}) to the transversal macrodispersivity in the vertical direction (A_{33}) as a function of the correlation scale in the x-y plane ($\lambda_1 = \lambda_1$) for various levels of the trend in log-conductivity (b), and longitudinal dispersivity $\alpha_T = 1$, and vertical correlation scale $\lambda_3 = 0.5$.

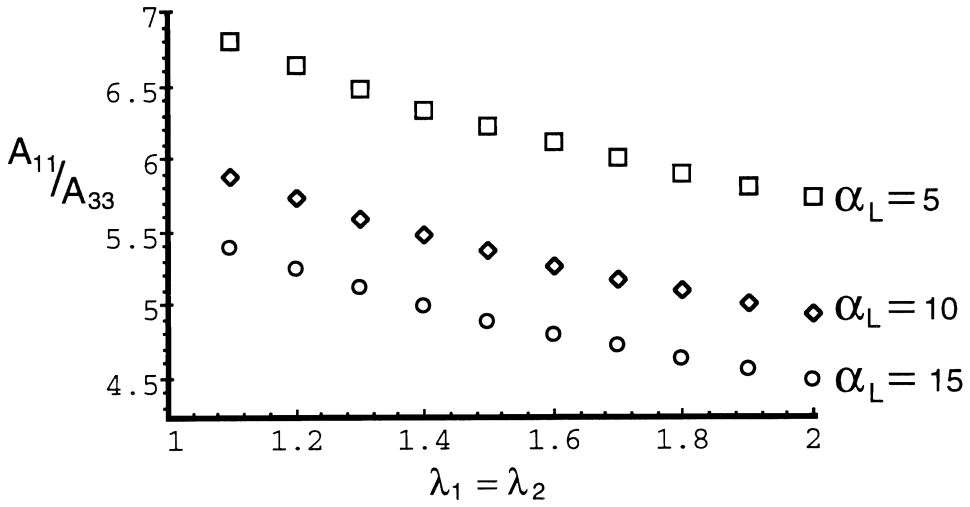

Figure 3. Graph of the ratio of longitudinal macrodispersivity (A_{11}) to the transversal macrodispersivity in the vertical direction (A_{33}) as a function of the correlation scale in the x-y plane ($\lambda_1 = \lambda_2$) for various levels of the longitudinal dispersivity α_L, and trend in log-conductivity b = 0.1, transversal dispersivity α_T = 1, and vertical correlation scale λ_3 = 0.5.

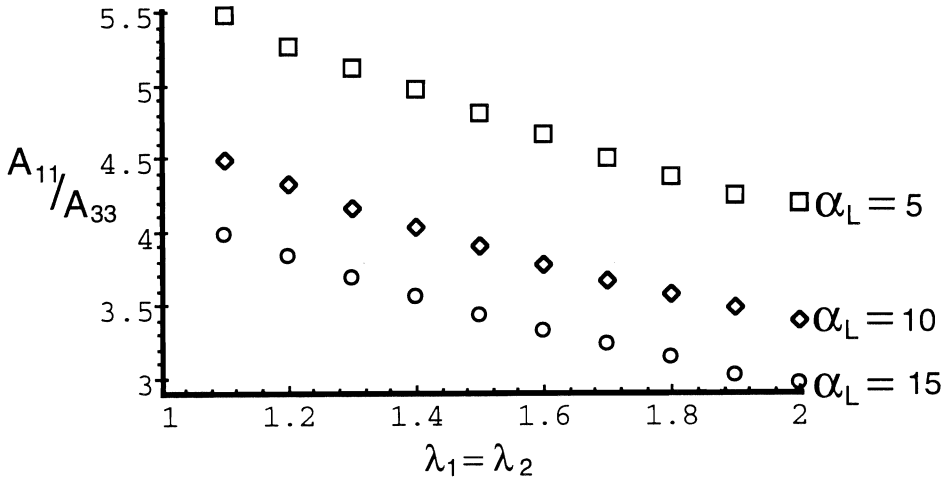

Figure 4. Graph of the ratio of longitudinal macrodispersivity (A_{11}) to the transversal macrodispersivity in the vertical direction (A_{33}) as a function of the correlation scale in the x-y plane ($\lambda_1 = \lambda_2$) for various levels of the longitudinal dispersivity α_L, and trend in log-conductivity b = 0.2, transversal dispersivity α_T = 1, and vertical correlation scale λ_3 = 0.5.

Development and Testing of a Micro-Tensiometer

JAN W. HOPMANS AND THEODORE C. HSIAO
Department of Land, Air and Water Resources, Davis Campus

Summary

To better understand transport mechanisms in soils, noninvasive, nondestructive measurement methods have been developed. Recent x-ray computed tomography applications by Clausnitzer et al. (1995) demonstrated that specialized instrumentation allows the nondestructive measurement of soil water distribution and root architecture at spatial scales ranging from 20 to 200 μm. The objective of such investigations is to increase understanding of water flow and contaminant and nutrient transport in soils and between soils and plant roots. Although the tomographic studies allow visualization of the spatial arrangement of soil particles, soil pores, soil water, and fluid-solid interfaces, they do not provide the direction of flow, the driving force, and their spatial variations. For that, tensiometric measurements will be needed. However, regular tensiometers are too large in size and will not give information on the magnitude and spatial variation of soil water pressure at the pore-size and root-size scales as measured with the CT-scanning instrument. For that purpose, a micro-tensiometer is needed.

Recent developments in computed-tomography (CT) of x-ray attenuation and NMR imaging have offered the opportunity to study water flow and transport in soils at a spatial scale of 10-20 μm. The objective of this one-year research project was to develop a micro-tensiometer for pore-water pressure measurements in water-saturated pores of unsaturated porous media. Such a micro-tensiometer, in combination with CT-measurements, will aid in the elucidation of mechanisms governing microscopic flow in porous media as well as between soils and plant roots. The tip of the capillary of the tensiometer is of a size smaller than the diameter of water-filled pores (5 μm), thereby allowing direct measurement of the pore-water pressure. Measurements were conducted in a porous medium of glass beads with a diameter in the range between 0.25 and 0.5 mm. The results of the present system were only partially successful. Micro-tensiometric measurements correlated well with applied suction values up to a soil water pressure of -50 cm. However, when larger suctions were applied, the pressure as measured by the transducer did not respond to decreasing microscopic soil water pressure measurements. This is likely the result of a loss of hydraulic contact between the capillary of the micro-tensiometer and the water-filled pores.

Key Words: soil water potential, vadose zone, microscopic measurements, water tension in pores

Project Objectives Addressed in 1995-1996

To develop and test the micro-tensiometer technique for pore-water pressure measurements in unsaturated porous media.

Research Plan and Procedures

A micro-probe connected to a pressure transducer was used to measure positive turgor pressures in single plant cells (Husken et al., 1978). The technique was brought to UC Davis in the late 1980's (French and Hsiao, 1993). In these studies, the pressure probe consisted of a capillary tube with a tip of approximately 3-5 μm outside diameter, which was introduced into a plant cell to measure positive cell turgor pressures. Using the same technology, a capillary probe was designed to measure capillary pressures in porous media. The probe consists of a 1-mm glass capillary with a 5 μm outside diameter tip connected to a minimum displacement pressure transducer. Rigid tubing between the capillary and the transducer and complete water filling of the measurement system resulted in fast response time and insignificant exchange of water between the water-filled pores and the capillary. In principle, the minimum soil water pressure measurement at which such a micro-tensiometer is operational is controlled by the air-entry value of the capillary (e.g. for a capillary with a 20 μm inside diameter tip, the air entry value is about 150 cm), and the size of the water-filled pores. The capillary probe is inserted in the water-filled pores with the help of a microscope. The size of the glass beads was between 0.25-0.5 mm. Glass bead size and water-filled pores were measured with a micrometer scale in the eyepiece of the microscope.

The setup and measurements with the micro-tensiometer were done in a constant temperature room to minimize pore-water pressure variations due to temperature changes. The microprobe consists of a microcapillary tube, a pressure block with the pressure transducer and a micro-manipulator (Fig. 1), which allowed for the positioning of the capillary tip in all three major directions.

The microscope was an Olympus zoom stereoscope (Model SZ-Tr) with a total magnification of 21-210X. The capillary was connected with the transducer (Model V, Sensotec) by a flexible metal tube (0.125 mm inside diameter), filled with deionized water. The transducer has a steel diaphragm, thereby minimizing changes in volume as caused by pressure variations, and has an accuracy of 0.25 % FSO (30 mV). This accuracy allowed an approximate accuracy of 3 cm water pressure for a pressure range of 0-1000 cm. The pressure transducer was attached to a pressure block, which allowed easy flushing and de-airing of the pressure measurement system. A 10 VDC single-channel conditioner provided a stable output to the pressure transducer. The output signal from the transducer in millivolts was digitized and displayed. The pressure transducer was calibrated in the range from 0-200 cm suction, by insertion of the micro-tensiometer in water with 10 cm suction increments.

Micro-tensiometric measurements in the glass beads were carried out in a 5-cm internal diameter and 7-cm length PVC column, on which a nylon membrane was glued at the bottom. The glass beads were fully saturated initially, by wetting from the bottom through the membrane. Different soil water potentials were achieved by various suction increments applied to the bottom of the PVC column. After the capillary was inserted in a water-filled pore, it remained in that position for a sequence of suction increments. In doing so, the tip was carefully positioned in a specific water-filled pore, whose size was small enough to remain water-filled for all suction increments. Applied suction increments were 0, 5, 10, 15, 20, 25, 30, 50 and 100 cm. The whole experiment was replicated five times (i.e., the micro-probe was inserted in five different pores), and the data were averaged.

Results and Discussion

In concept, we hypothesized that a capillary with a tip of 5 μm diameter should be small enough to measure directly pore water pressures in pores of 30 μm diameter or larger, equivalent to a pore pressure of -100 cm. Unless there is no hydraulic continuity between the capilllary and the water-filled pore, the transducer reading should detect changes in pore-water pressure. Moreover, its response should be quick, since the present design does not require any significant water exchange between the pore and the capillary of the micro-tensiometer. During the calibration of the pressure transducer, response times were one minute or smaller.

The comparison of the tensiometric measurements with the suction applied to the nylon membrane of the glass beads columns for five suction increments are presented in Fig. 2. Despite the fact that care was taken for the measurement system to be completely air-free, micro-tensiometric results were successful only in the range from saturation to -50 cm, corresponding to the soil water pressure in water-filled pores of 60 micrometer diameter or smaller. The pressure transducer would not respond to increasing suction changes, as if the tip of the capillary was disconnected from the meniscus of the water-filled pore. This could have been the case, given the difficulty experienced to determine whether a pore was water-filled or drained. The use of dyes to improve the contrast between air- and water filled pores was not successful.

Although our data show that the present technique is physically correct, we are slightly unsatisfied with the limited range of the micro-tensiometer so far. We are, however, optimistic about the future success of the technique. We believe that the instrument setup can be improved to maintain hydraulic continuity with the pore water. The possibility of measuring soil water pressures at the pore-size scale will offer a broad spectrum of opportunities in soil and plant science. The ability to measure soil water pressure in water-filled pores and in water films surrounding soil particles and their spatial and temporal variability will offer a new perspective on the conceptualization of flow and transport mechanisms in the vadose zone. In addition, we would be able to study the interactions between plant roots and the soil water. For example, application of the micro-tensiometer technique will allow water potential

gradient measurements across the root-soil interface, thereby making it possible to determine experimentally the root-water uptake distribution and its spatial and temporal variation.

References

Clausnitzer, V., D. A. Heeraman and J. W. Hopmans. 1995. Noninvasive observation of pore-scale transport and plant roots with X-ray computed tomography. Proceedings of Kearney Foundation of Soil Science Conference on Vadose Zone Hydrology: Cutting Across Disciplines, Davis, CA , September 1995.

French, J., and T. C. Hsiao. 1993. Hydraulic propagation of pressure along immature and mature xylem vessels of roots of *Zea mays* measured by pressure probe techniques. Planta 190: 263-270.

Heeraman, D. A., J. W. Hopmans and T. C. Hsiao. 1995. Pore water pressure measurement using a micro-tensiometer. Agron. Abstracts. Amer. Soc. Agron., p. 206, St. Louis, MO. Oct. 29-Nov. 3, 1995.

Husken, D., E. Steudle, and U. Zimmerman. 1978. Pressure probe technique for measuring water relations of cells in higher plants. Plant Physiology. 61:158-163.

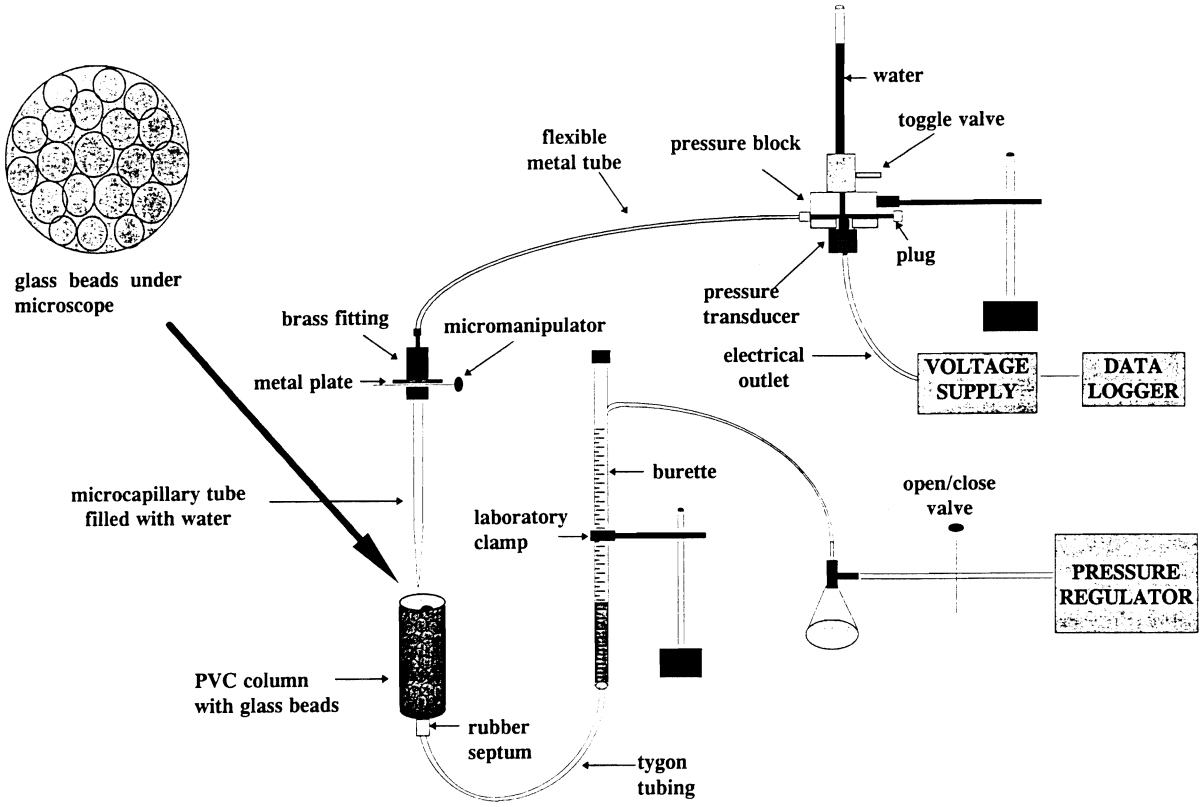

Figure 1. Experimental setup of micro-tensiometer measurements.

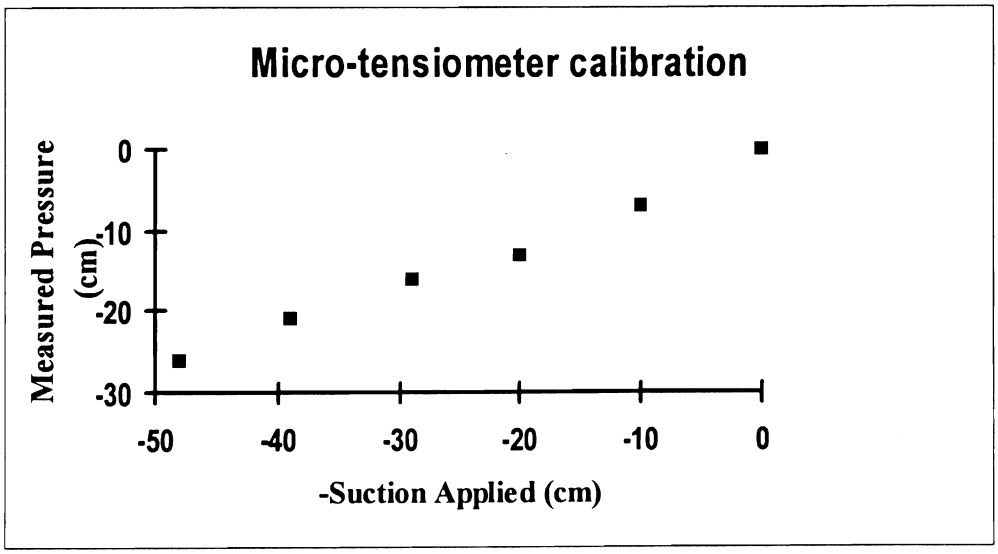

Figure 2. Soil water pressure as measured with the micro-tensiometer, compared with suction increments applied to PVC column with glass beads.

Development of a Screening Model for Fate of Nonaqueous Phase Liquids in Soil

WILLIAM A. JURY
Department of Soil and Environmental Sciences, Riverside Campus

Summary

This study developed a mathematical screening model to determine the environmental fate of a nonaqueous phase liquid (NAPL) that is trapped in the soil or in ground water. Processes represented in the model include dissolution, advective-dispersive transport, vapor phase movement, leaching to ground water, volatilization to the atmosphere, and degradation. The model was formulated to produce relative assessments of the behavior of different chemicals subjected to the same standard initial and boundary conditions in the soil (finite mass suspended in soil or trapped in ground water), and requires only the basic chemodynamic environmental fate properties that characterize organic liquids in soil. These include: water solubility, Henry's constant, organic carbon partition coefficient, degradation half-life, and NAPL density. Simplified analytic and more complex numerical versions of the screening models were constructed using the process descriptions for NAPL dissolution developed from a previous Kearney Foundation study. The model can be used to obtain preliminary information relative to waste cleanup strategies, exposure assessment from an existing spill, or identification of the time of release of an existing waste spill. It can also be used to compare the behavior of different chemicals subjected to the same natural or forced remediation methods.

Key Words: mass transfer, dissolution, soil vapor extraction, NAPL

Project Objectives Addressed in 1995-1996

1. To develop analytical and numerical NAPL screening models to use in assessing the environmental fate of chemical spills.

2. To develop versions of the NAPL screening model that are applicable to specific cleanup or design problems (e.g. soil-vapor extraction)

3. To develop an inventory of fate properties for common NAPLs

4. To analyse the NAPLs using the screening models to determine trends and identify NAPLs with unusual environmental behavior.

Results: Objective 1

The problem setting represented by the model is a medium initially containing a finite homogeneous supply of immiscible NAPL trapped in the pores of a soil of uniform water content θ. The NAPL is located in a subsurface layer of finite thickness overlain by clean soil, such as might occur from a leaking storage tank (Fig. 1).

The model, which is an extension of the dissolved chemical screening model of Jury et al. (1983, 1984a,b,c), assumes that the NAPL releases mass to the surrounding water phase by a rate-limited dissolution process in the NAPL zone, and can move through the soil in the dissolved or vapor state. Loss to the atmosphere occurs by volatilization. Two scenarios are represented in the screening model: dissolution during continuous downward leaching, and soil vapor extraction of chemical by upward moving air.

The Governing Equations. The governing equations for the system are the chemical mass balance and the flux equations. These are different, depending on whether or not NAPL is present.

Mass Balance Equation. The NAPL material is assumed to obey the mass balance equation

$$\frac{\partial C_t}{\partial t} + \frac{\partial \Omega}{\partial t} + \frac{\partial J_s}{\partial z} + \mu C_t = 0 \qquad (1)$$

where C_t is the total chemical mass per soil volume in the dissolved, sorbed, and vapor phases, Ω is the total chemical mass per soil volume in the NAPL phase, J_s is the solute mass flux equation, and μ is the first-order decay rate. It is assumed that no degradation occurs directly in the NAPL liquid.

Chemical Storage Relations. The total resident concentration within a unit soil volume is assumed to consist of immiscible NAPL and the three phases of miscible NAPL (dissolved, gaseous, and sorbed)

$$C_t + \Omega = \rho_b C_a + \theta C_\ell + a C_g + \eta \rho N \tag{2}$$

where η is the volume of NAPL per volume of soil, ρN is the NAPL fluid density (assumed to be a constant for a given compound), ρb is soil bulk density, θ,a are volumetric water and air contents, C_a (mass per soil mass), C_ℓ (mass per soil solution volume), C_g (mass per soil air volume) are the sorbed, dissolved, and vapor phases of chemical concentration

Flux Equations. For generality, it is assumed that the chemical can diffuse in the dissolved and vapor phases, and can also advect with moving bulk soil solution or soil air. We can write these equations as follows:

$$J_s = -D_g^8 \frac{\partial C_g}{\partial z} - D_\ell^8 + \frac{\partial C_\ell}{\partial z} + J_a C_g + J_w C_\ell \tag{3}$$

where J_w, J_a are soil water and soil air flux rates, and D_ℓ^8, D_g^9 are soil dissolved and vapor diffusion coefficients.

Partitioning Relations. To simplify the analysis for screening purposes, we will assume linear, equilibrium partitioning of the sorbed, dissolved, and gaseous phases. These relations can be written as follows:

$$C_8 = K_d C_\ell = f_{oc} K_{oc} C_\ell \tag{4}$$

$$C_g = K_H C_\ell \tag{5}$$

If we combine (1)-(5), we may write the general chemical transport equation as

$$\frac{\partial C_t}{\partial t} + \rho N \frac{\partial \eta}{\partial t} = D_E \frac{\partial^2 C_t}{\partial z^2} - V_E \frac{\partial C_t}{\partial z} + \mu C_t \tag{6}$$

where

$$D_E = \frac{D_\ell^8 + K_H D_g^8}{R_\ell} \tag{7}$$

$$V_E = \frac{J_w + K_H J_a}{R_\ell} \tag{8}$$

$$R_\ell = \rho b f_{oc} K_{oc} + \theta + a K_H \tag{9}$$

Rate-limited Dissolution. We assume that NAPL fluid enters the surrounding soil water by rate-limited dissolution. We express this process as

$$\frac{\partial \Omega}{\partial t} = \rho N \frac{\partial \eta}{\partial t} = \alpha\left(C_\ell - C^*\right) \tag{10}$$

where C^* is the solubility of the NAPL in water and α is a mass transfer coefficient, which may depend on the local geometry and on the NAPL concentration. We may rewrite (10) in terms of the total miscible concentration C_t as

$$\frac{\partial \Omega}{\partial t} = \rho N \frac{\partial \eta}{\partial t} = \alpha_E\left(C_t - C_t^*\right) \tag{11}$$

where $\alpha_E = \alpha/R$, $C_t = C^*/R$.

With this addition, we may write the chemical transport equation in the NAPL region as

$$\frac{\partial C_t}{\partial t} + \alpha_E\left(C_t - C_t^*\right) = D_E \frac{\partial^2 C_t}{\partial z^2} - V_E \frac{\partial C_t}{\partial z} - \mu C_t \tag{12}$$

Dissolution Models. Rate-limited NAPL dissolution has been studied extensively by researchers over the past 25 years. The most common way of modeling the rate coefficient α is to develop empirical relations among dimensionless groups of variables known to influence the mass transfer process. Chief among these variables are the following:

- Sherwood number $Sh = k_\ell \ell_c / \mathcal{D}$
- Reynolds number $Re = \ell_c J_w / \nu_w$
- Schmidt number $Sc = \nu_w / \mathcal{D}$
- Peclet number $Pe = Re \times Sc = \ell_c J_w / \mathcal{D}$

where ℓ_c is a characteristic length scale, $\mathcal{D}$ is the diffusion coefficient of the dissolved NAPL in water, k_ℓ is the local mass transfer coefficient, and ν_w is the

kinematic viscosity of water. The relationship between the local mass transfer coefficient and the overall rate coefficient α is

$$\alpha = k_\ell \, a \tag{13}$$

where a is the NAPL specific surface area.

The mass transfer correlation used in the screening model is the Wilson and Geankopolis (1966) relationship

$$Sh = 1.09 \frac{Pe^{1/3}}{\theta} \tag{14}$$

which translates into

$$k_\ell = 1.09 \frac{J_w^{1/3} \mathcal{D}^{2/3}}{\theta \ell_c^{2/3}} \tag{15}$$

However, it is not physically reasonable for k_ℓ to vanish as $J_w \rightarrow 0$. To handle this case, we have added 0.55 to (14), as used by Pfannkuch (1984), which produces

$$k_\ell = 1.09 \frac{J_w^{1/3} \mathcal{D}^{2/3}}{\theta \ell_c^{2/3}} + 0.55 \frac{\mathcal{D}}{\ell_c} \tag{16}$$

In the dissolving spheres model, the NAPL is envisioned as a group of identical spheres of initial diameter d_0. Thus, the sphere density ξ is given by the ratio η_0 of the initial NAPL volume per soil volume and the volume of a sphere $\pi d_0^3 / 6$

$$\xi = \frac{6\eta_0}{\pi d_0^3} \tag{17}$$

and the specific surface area a is

$$a = \pi d^2 \xi = \frac{6\eta_0 d^2}{d_0^3} \tag{18}$$

We may relate Ω to the sphere diameter d by

$$\frac{\Omega}{\Omega_0} = \left(\frac{d}{d_0}\right)^3 \rightarrow d = d_0 \left(\frac{\Omega}{\Omega_0}\right)^{1/3} = d_0 \bar{\Omega}^{1/3} \tag{19}$$

This produces the following relations for the surface area and rate coefficient:

$$a = \frac{6\eta_0 d^2}{d_0^3} = \frac{6\eta_0}{d_0} \bar{\Omega}^{2/3} \tag{20}$$

$$\alpha = k_\ell a = \left[6.54 \frac{\eta_0 J_w^{1/3} \mathcal{D}^{2/3}}{\theta d_0 \ell_c^{2/3}} + \frac{3.3\eta_0 \mathcal{D}}{d_0 \ell_c} \right] \bar{\Omega}^{2/3} \tag{21}$$

Characteristic Length ℓ_c. There are two obvious choices for the characteristic length ℓ_c: the constant initial sphere diameter d_0 and the variable local sphere diameter d at time t. These give rise to two different expressions for the rate coefficient.

1. If we set the characteristic length equal to the initial sphere diameter d_0, we may write the final form of (21) as:

$$\alpha_1 = \left[6.54 \frac{\eta_0 J_w^{1/3} \mathcal{D}^{2/3}}{\theta d_0^{5/3}} + \frac{3.3\eta_0 \mathcal{D}}{d_0^2} \right] \bar{\Omega}^{2/3} \tag{22}$$

2. If we set the characteristic length equal to the local sphere diameter d, we may write the final form of (21) as:

$$\alpha_2 = 6.54 \frac{\eta_0 J_w^{1/3} \mathcal{D}^{2/3}}{\theta d_0^{5/3}} \bar{\Omega}^{4/9} + \frac{3.3\eta_0 \mathcal{D}}{d_0^2} \bar{\Omega}^{1/3} \tag{23}$$

Note that these two forms are identical at t = 0.

We may now rewrite the transport equations (6)-(11) in the form

$$\frac{\partial \bar{C}_t}{\partial t} + \frac{\partial \bar{\Omega}}{\partial t} = D_E \frac{\partial^2 \bar{C}_t}{\partial z^2} V_E \frac{\partial \bar{C}_t}{\partial z} + \mu \bar{C}_t \tag{24}$$

$$\frac{\partial \bar{\Omega}}{\partial t} = \omega \alpha_E \left(\bar{C}_t - 1 \right) \tag{25}$$

where $\bar{C}_t = C_t / C_t^*$, $\bar{\Omega} = \Omega / \Omega_0$, and $\alpha_E = \alpha_E(\bar{\Omega}) = \alpha_1 / R$ or α_2 / R

Results: Objective 2

Two options are available in the model: soil-vapor extraction and dissolution during leaching. Soil-vapor extraction consists of an upward movement of air at a specified flux to the volatilization boundary at the surface, while the lower boundary is constrained to zero flux. The dissolution simulation consists of downward water flow at a specified rate to a lower boundary either at C=0 (water table) or dC/dz = 0 (free drainage).

All simulations use the following initial condition for the NAPL

$$\begin{aligned} \eta(z,0) &= 0 && 0 < z < L \\ \eta(z,0) &= \eta_0 && L < z < H + L \\ \eta(z,0) &= 0 && H + L < z < P \end{aligned} \qquad (26)$$

The corresponding condition for the total solution concentration is

$$\begin{aligned} C_t(z,0) &= C_i * C_t^* \frac{z}{L} && 0 < z < L \\ C_t(z,0) &= C_i * C_t^* && L < z < H + L \\ C_t(z,0) &= C_i * C_t^* * \frac{P - z}{P - H - L} && H + L < z < P \end{aligned} \qquad (27)$$

where P is the maximum depth used in the numerical simulation, and C_i is a flag that can be set equal to 1 or 0 by the user.

The upper boundary condition for the concentration is

$$C_t(0,t) = 0 \qquad (28)$$

It has been shown (Jury et al., 1984b) that (28) is sufficient to represent the upper boundary condition for category 1 compounds, to which NAPLs normally belong. This condition is essentially equivalent to placing a stagnant air boundary layer over the soil surface for compounds with a large Henry's constant.

The lower boundary at z = P is somewhat artificial and the boundary condition applied there depends on the physical constraints of the problem. The screening model provides three different options for the lower boundary at z = P:

$$C_t(P,t) = 0; \quad \text{Option 1} \quad (29)$$

$$\partial C_t / \partial z(P,t) = 0; \quad \text{Option 2} \quad (30)$$

$$J_s(P,t) = 0; \quad \text{Option 3} \quad (31)$$

Option 1 or 2 should be used with the downward leaching simulation under free drainage; option 2 should be used with the downward leaching simulation if a water table is present at z = P; and option 3 should be used with the soil vapor extraction case.

Results: Objective 3

The screening model requires numerical values for the following soil properties: Henry's constant, water solubility, NAPL density, organic C partition coefficient, and degradation half life. Data for a select set of chemicals has been obtained and are tabulated in Table 1.

Results: Objective 4

Dissolution During Leaching. In this representation, chemicals are placed in a 10 cm thick layer located 10 cm below the soil surface. Water is added at a steady rate of 10 cm/d and flows downward under free drainage. Option 1 for the lower boundary condition is applied at z = 50 cm. Three chemicals, benzene, carbon tetrachloride, and nitrophenol, are placed in the screening simulation for 50 d at a constant NAPL volume fraction of $\eta_0 = 0.05$.

Figure 2 shows the profiles of relative NAPL (η/η_0) and solution (C_ℓ/C^*) concentrations at 5 d intervals. As shown in the figure, the chemicals are dissolved at different rates under the same conditions, owing to the difference in their NAPL densities and water solubility. Figure 3 shows the cumulative mass of chemical leached past z=50 cm during the period of the simulation.

Volatilization During Vapor Extraction. In this representation, chemicals are placed in a 10 cm thick layer located 10 cm below the soil surface. Air is forced upward at a steady rate of 100 cm/d. Option 3 for the lower boundary condition is applied at z = 50 cm. Three chemicals, benzene, carbon tetrachloride, and nitrophenol, are placed in the screening simulation for 350 d at a constant NAPL volume fraction of $\eta_0 = 0.05$.

Figure 4 shows the profiles of relative NAPL (η/η_0) and solution ((C_ℓ/C^*)) concentrations at 35 d intervals. As shown in the figure, the chemicals are removed at different rates under the same conditions, owing to the difference in their Henry's constants and water solubility.

Figure 5 shows the cumulative mass of chemical volatilized during the period of the simulation. Here the situation is reversed, compared to the previous simulation, and nitrophenol loses the least mass under the same conditions. The reason for this is that it has the smallest Henry's constant and therefore releases the least mass into the moving air stream.

Discussion

The model developed has potential application to a variety of pollution cleanup situations, and may also be useful in analyzing residuals found in old waste dumps or spill sites. It is also a useful educational tool. Although the model uses a particular mass transfer relation and a sphere model, screening model results probably do not depend too closely on the specific model used. Several approximate indices discussed below are also useful for NAPL classification.

Dissolution Time Index. One of the important design variables for a NAPL in soil is the time required to remove the compound by dissolution. This depends on the removal rate, which is a function of the water solubility of the compound, and the extent of dissolution that occurs as the water flows through the NAPL mass. Assuming that the water is able to reach saturation during transport, then the NAPL flux escaping the mass is

$$J_s = C_\ell^* J_w \tag{32}$$

For a NAPL of density ρ_N occupying a layer L of soil at a volume fraction η_0, it would require a dissolution time

$$t_d = \frac{\rho_N \eta_0 L}{C_\ell^* J_w} \tag{33}$$

to remove the NAPL at this rate, or equivalently, the number of pore volumes of leaching would be

$$PV = \frac{J_w t_d}{L\theta} = \frac{\rho_N \eta_0}{C_\ell^* \theta} \equiv \xi_L \tag{34}$$

Thus, the parameter ξ_L is a useful index of leaching efficiency for a compound. This rate however is an underestimate, since the outflow concentration is not always saturated. It can be used in lieu of the model for simple screening calculations, and provides an accurate estimate of the relative ease of NAPL removal during leaching.

A corresponding index for air stripping may be determined by realizing that the maximum flux that may be removed by the air flow is

$$J_s = K_H * C^*_\ell J_a \tag{35}$$

For a NAPL of density ρ_N occupying a layer L of soil at a volume fraction η_0, it would require a time

$$t_d = \frac{\rho N \eta_0 L}{K_H C^*_\ell J_a} \tag{36}$$

to remove the NAPL at this rate, or equivalently, the number of pore volumes of air flow would be

$$PV = \frac{J_a t_d}{La} = \frac{\rho N \eta_0}{K_H C^*_\ell a} \equiv \xi_A \tag{37}$$

Table 2 presents values for ξ_L, ξ_A for the chemicals in the data base, for the case where $\theta = 0.5$ (leaching), $a = 0.5$ (vapor extraction), and $\eta_0 = 0.5$. Notice that the rank order for efficiency of the process changes between leaching and vapor extraction. This implies that the type of process used for NAPL removal is very chemical-specific and that a group of compounds located together may require more than one removal method.

The Fortran computer program for the screening model is available upon request from the author.

References

Jury, W. A., W. F. Spencer, and W. J. Farmer. 1983. Model for assessing behavior of pesticides and other trace organics using benchmark properties. I. Description of model. J. Environ. Qual. 12:558-564.

Jury, W. A., W. J. Farmer, and W. F. Spencer. 1984a. Model for assessing behavior of pesticides and other trace organics using benchmark properties. II. Chemical classification and parameter sensitivity. J. Environ. Qual. 13:567-572.

Jury, W. A., W. F. Spencer, and W. J. Farmer. 1984b. Model for assessing behavior of pesticides and other trace organics using benchmark properties. III. Application of screening model. J. Environ. Qual. 13:573-579.

Jury, W. A., W. F. Spencer, and W. J. Farmer. 1984c. Model for assessing behavior of pesticides and other trace organics using benchmark properties. IV. Review of experimental evidence. J. Environ. Qual. 13:580-585.

Pfannkuch, H. O., 1984. Determination of the contaminant source strength from mass exchange processes. In: Petroleum Hydrocarbons and Organic Chemicals in Ground Water. Natl. Water Well Assn. Worthington, OH p. 444-458.

Wilson, E. J. and C. J. Geankoplis, 1966. Liquid mass transfer at very low Reynolds numbers in packed beds. Ind. Eng. Chem. Fundam. 5:9-14.

Table 1. Environmental fate properties for a select set of nonaqueous phase liquids

Chemical	C_ℓ^*	ρ_N	K_H	K_{OC}	$t_{1/2}$
	mg/m^3	mg/m^3		cm^3/g	g
BENZENE	.179E+01	.879E+03	.220E+00	.830E+02	.160E+02
BIPHENYL	.750E-02	.118E+04	.660E-01	.140E+05	.365E+02
BROMOBENZENE	.450E-01	.150E+04	.620E-02	.150E+03	.365E+02
CARBON TETRACHLORIDE	.805E+00	.160E+04	.940E+00	.110E+03	.365E+02
CHLOROBENZENE	.470E+00	.111E+04	.150E+00	.150E+03	.365E+02
ETHYL CHLORIDE	.571E+01	.921E+03	.615E+00	.250E+02	.300E+02
CHLOROFORM	.800E+01	.150E+04	.120E+00	.290E+02	.100E+03
DICHLOROETHANE	.920E+01	.126E+04	.380E-01	.220E+02	.900E+02
DICHLOROMETHANE	.200E+01	.134E+04	.128E+00	.130E+02	.100E+03
NAPHTHALENE	.317E-01	.115E+04	.500E-01	.130E+04	.300E+01
NITROBENZENE	.190E+01	.120E+04	.100E-02	.710E+02	.365E+02
NITROPHENOL	.113E+02	.148E+04	.100E-02	.610E+02	.160E+02
TETRACHLOROETHYLENE	.150E+00	.162E+04	.847E+00	.608E+03	.100E+02
TOLUENE	.535E+00	.867E+03	.270E+00	.980E+02	.220E+02
TRICHLOROETHANE	.124E+00	.133E+04	.146E+01	.113E+03	.365E+03
TRICHLOROETHYLENE	.110E+01	.146E+04	.374E+00	.150E+03	.400E+01
VINYL CHLORIDE	.900E-01	.920E+03	.440E+00	.560E+02	.180E+03
O-XYLENE	.155E-00	131E+04	.280E+00	.500E+02	.300E+02

Table 2. Indices for dissolution and vapor extraction times for the chemicals in Table 1.

Chemical	ξ_L	Rank	ξ_A	Rank
BENZENE	49.	5	223.	4
BIPHENYL	15733.	18	238384.	17
BROMOBENZENE	3333.	16	537634.	18
CARBON TETRACHLORIDE	199.	10	211.	2
CHLOROBENZENE	236.	11	1574.	10
ETHYL CHLORIDE	16.	3	26.	1
CHLOROFORM	19.	4	156.	3
DICHLOROETHANE	14.	2	360.	6
DICHLOROMETHANE	67.	7	523.	7
NAPHTHALENE	3628.	17	72555.	16
NITROBENZENE	63.	6	63158.	15
NITROPHENOL	13.	1	13097.	14
TETRACHLOROETHYLENE	1080.	15	1275.	11
TOLUENE	162.	9	600.	8
TRICHLOROETHANE	1073.	14	735.	9
TRICHLOROETHYLENE	133.	8	355.	5
VINYL CHLORIDE	1022.	13	2323.	12
O-XYLENE	845.	12	3018.	13

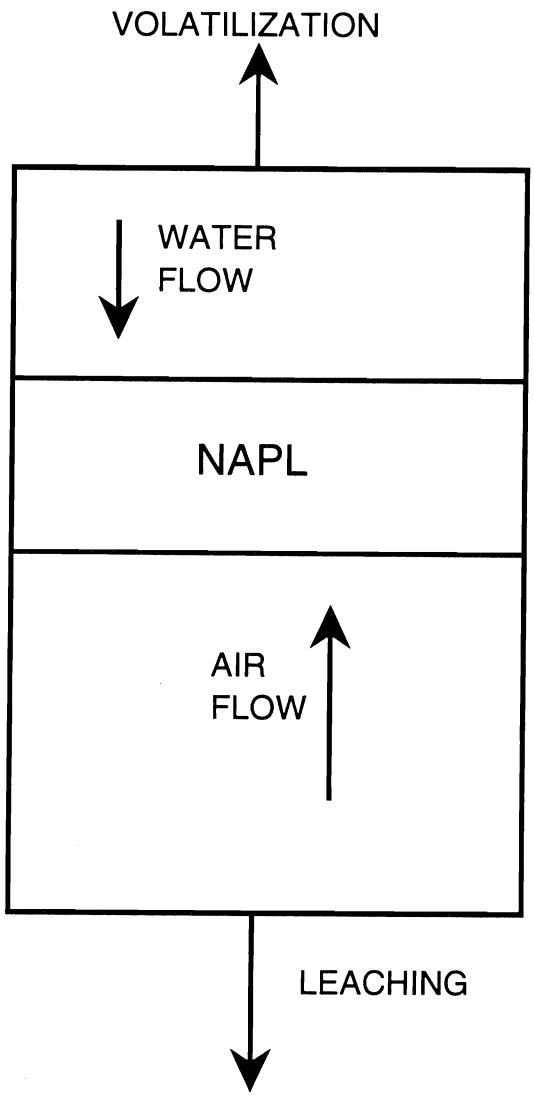

Figure 1. Schematic of the NAPL screening model scenario.

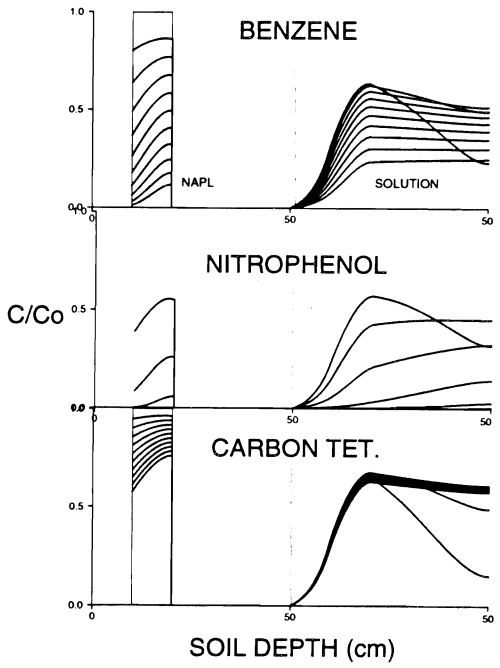

Figure 2. Output of chemical profiles from screening model calculation 1.

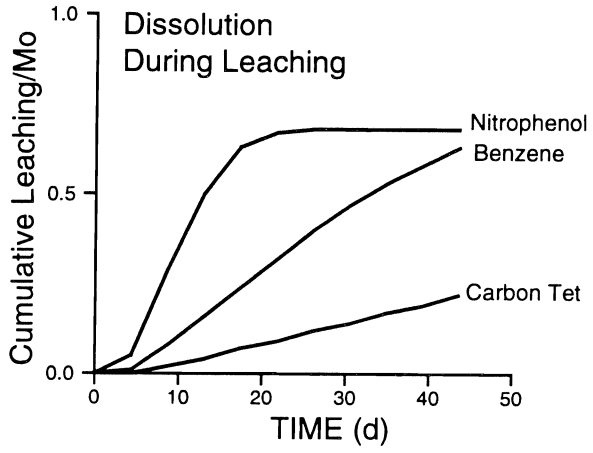

Figure 3. Output of cumulative leaching from screening model calculation 1.

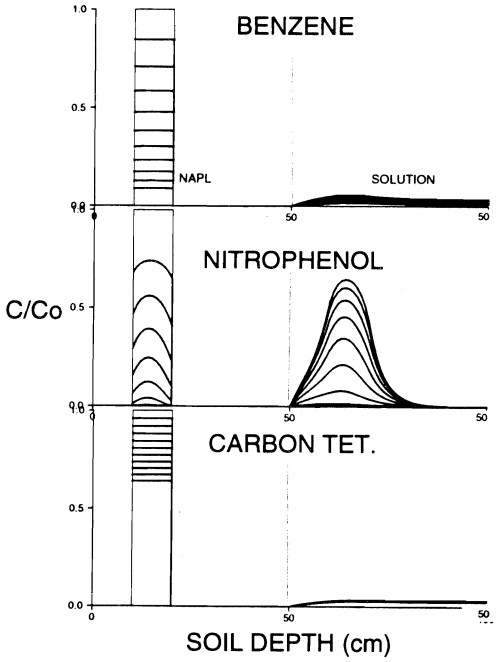

Figure 4. Output of chemical profiles from screening model calculation 2.

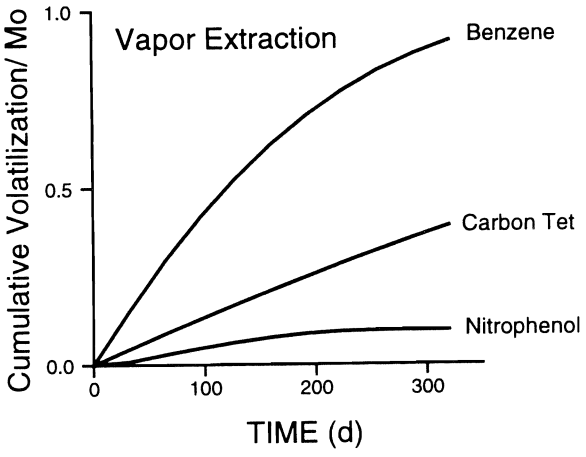

Figure 5. Output of cumulative leaching from screening model calculation 2.

Uncertainty of Reactive DBCP Transport in Soils

THOMAS HARTER, SOUHEIL EZZEDINE AND KENNETH K. TANJI
Department of Land, Air, and Water Resources Davis Campus

Summary

Uncertainty in predicting DBCP leaching through the vadose zone is determined by the spatial variability of hydraulic conductivity, water content and chemical soil properties. In this study, we analyzed the importance of spatial variability in sorption and degradation processes relative to the importance of spatial variability in physical soil properties with respect to DBCP transport and prediction uncertainty. A numerical Monte Carlo-based model and a first-order stochastic analytical solution are developed to predict the evolution of a hypothetical DBCP plume under conditions of spatially variable water content, hydraulic conductivity, and retardation coefficient. The correlation between the retardation coefficient and hydraulic conductivity is critical to the DBCP spreading and we investigated three principal conditions: no correlation between the hydraulic conductivity (physical heterogeneity) and the sorption coefficient (chemical heterogeneity), positive correlation, and negative correlation. Positive correlation significantly reduces the vertical solute spreading, while negative correlation enhances vertical solute spreading. The effect increases with mean sorption strength, which is dependent on the organic carbon content of the soil. A high degree of soil layering (large anisotropy ratio) may entirely erase the effects of variable sorption under conditions of positive correlation between chemical and physical heterogeneity. In the opposite case of negative correlation, it does not alter, however, the effects of variable sorption on solute spreading. Irrespective of the degree of soil layering, chemical heterogeneity has no measurable impact on horizontal solute spreading.

Key Words: stochastic methods, Monte Carlo simulations, reactive solute transport, macro- dispersion

Project Objectives Addressed in 1995-1996

1. Develop a first-order stochastic analytical solution for flow and reactive transport solutes with a spatially variable water content and retardation coefficient.

2. Adopt an existing computer code (model) for flow and non-reactive transport in random heterogeneous porous media to take into account the spatial variability of water content, a geochemical partitioning coefficient, and first-order decay.

3. Perform Monte Carlo simulations of flow and reactive solutes in unsaturated porous media to assess the effect of the geochemical and physical heterogeneity on plume spreading.

Research Plan and Procedures

Background

Contamination by agricultural and industrial activities has become a severe problem for groundwater quality (Leistra and Boesten, 1989; Cohen, 1991). Notorious examples are pesticides and organic contaminants. As a consequence, water resources managers, environmental and agricultural agencies, as well as farmers receive considerable governmental and public pressure to asses the risk of the contaminants and their consequences for soil and groundwater quality. Because of the complexity of the processes involved in the transport of pesticides through the unsaturated and saturated zone, and the limited data usually available for regional-scale modeling, parameter uncertainty must be considered when predicting groundwater quality. Here, a stochastic approach was chosen to take into account the scarcity of measurements and the uncertainty in predicting pesticide transport and, specifically, DBCP transport. Stochastic approaches have been utilized in groundwater hydrology for more than two decades. Unlike deterministic models, they provide quantitative representations of data variability and prediction uncertainty. Most experimental and theoretical studies have focused on inert solutes (e.g., chloride). However, the fate of DBCP and other pesticides in soils is also subject to reactive processes. Processes identified as being the primary determinants of pesticide behavior in soils include: (i) microbial degradation of pesticides by soil organisms and chemical reactions; ii) pesticide sorption by mineral and organic constituents of the solid matrix; iii) uptake of the pesticide by plant roots; iv) and volatilization of the pesticide. Field-scale investigations have provided evidence that reactive processes (i) and (ii) are subject to significant spatial variability (cf. Mackay et al. 1986, Rao et al. 1986, Robin et al. 1991). The impact of spatially variable sorption on pesticide transport in unsaturated media with spatially variable water content has received relatively little attention to date and is the focus of this investigation. Here, we shall consider only the overall mean pesticide spreading, measured in terms of spatial moments. Breakthrough curves and statistical moments of concentrations are currently under investigation.

3.2. Mathematical Problem Statement

Unsaturated Flow: The governing equation for flow in variably saturated porous media is given by

$$\frac{\partial}{\partial x_i}\left[K_{ij}(x,\psi)\frac{\partial \psi(x,t)}{\partial x_j}\right]=\frac{\partial \theta(x,\psi)}{\partial t} \qquad i,j=1,2,3 \tag{1}$$

where $x=(x_1,x_2,x_3)$ is the cartesian coordinate system and x_1 is directed vertically downward; x_2 lays in the vertical cross section and perpendicular to x_1 and x_3 is oriented into the domain; t is time; $\Psi(x,t)= h(x,t)+x_1$ is the capillary pressure head; $\theta(x, h(x,t))$ is the volumetric moisture content, which is a function of soil water tension (see below); $K=K(x, h)$ is the unsaturated hydraulic conductivity assumed to be isotropic locally; and h is the suction head. Note that boldface letters denote vectors. Our coordinate system is chosen such that x_1 denotes the long term mean (vertical) flow direction.

Relationship among hydraulic conductivity, soil water tension, and water content: To perform a meaningful mathematical analysis, it is assumed that the local $K(x,h(x))$ and $\theta(x,h(x))$ parameterization can be described by the Gardner-Russo parametric expressions (Russo, 1988). Although other models, such as the parametric expressions by van Genuchten (1980) better match conductivity and retenion curves over the entire range of measurable soil water tension, the Gardner-Russo model is chosen here for its universal applicability and mathematical simplicity:

$$K(x)=K_s(x)\exp(-\alpha(x)h(x)) \tag{2}$$

$$\theta(x)=\Delta\theta\exp\left(\frac{1}{2}\alpha(x)h(x)\frac{2}{m+2}\right)\left\{1+\frac{1}{2}\alpha(x)h(x)\right\}^{\frac{2}{m+2}} \tag{3}$$

where $\Delta\theta=\theta s-\theta r$; θs and θr are the saturated and residual water contents, respectively; Ks is the saturated hydraulic conductivity; α is the soil parameter related to the pore size distribution; and m is a parameter related to tortuosity.

We limit our investigation to transport under steady-state unsaturated flow conditions. Therefore, $q_i(x,t)=q_i(x)$, $\theta(x,t)=\theta(x)$, and $h(x,t)=h(x)$. Then equation (1) can be expanded as follows:

$$\nabla.q(x)=0, \quad \text{and} \quad q_i(x)=-K(x)\frac{\partial \psi(x)}{\partial x_i}, \quad i=1,2,3 \tag{4a,b}$$

Solute transport: Transport of reactive solutes through porous media is governed by the reactive advection-dispersion equation:

$$\frac{\partial}{\partial x_i}\left(D_{ij}\frac{\partial c(x,t)}{x_j}\right) - q_i(x,t)\frac{\partial c(x,t)}{\partial x_i} - \lambda(x,t)c(x,t) = \theta(x,\psi)R(x,t)\frac{\partial c(x,t)}{\partial x_i} \qquad (5)$$

where D_{ij} is the local dispersion tensor computed as a function of the local flux q(x,t):

$$D_{ij}(x,t) = (\alpha_L - \alpha_T)\frac{q_i(x,t)q_j(x,t)}{q} + \alpha_T q(x,t)\delta_{ij} + D_0 \qquad (6)$$

α_L is the longitudinal dispersivity,and a_T is the transverse dispersivity. δ is the Kronecker symbol; D_0 is the apparent molecular diffusion; and λ is a spatially variable, non-selective, first-order decay rate. The retardation coefficient, R, and is related to the spatially variable equilibrium sorption coefficient, k_d, by

$$R(x,t) = 1 + \rho_b(x,t)\frac{k_d(x,t)}{\theta(x,t)} \qquad (7)$$

where ρ_b is the bulk density of the porous media.

For simplicity, we assume that $\lambda(x,t)$ and R(x,t) are spatially variable but temporally constant. Bulk density is constant in time and space.

The advective non-reactive seepage velocity at x is related to the specific flux q_i by

$$u_i(x) = \frac{q_i(x)}{\theta(x)} \qquad (8)$$

Similarly, the reactive seepage velocity at x is given by Kabala and Sposito, (1991), Dagan (1989), Bellin et al. (1993), and Russo, (1993).

$$u_i^r(x) = \frac{u_i(x)}{R(x)} = \frac{q_i(x)}{R(x)\theta(x)} \qquad (9)$$

In most stochastic theories of non-reactive transport (e.g., Russo, 1993, 1995a-b; Harter and Yeh, 1996), the variability of $\theta(x)$ in (5-8) is neglected and assumed to be equal to its mean. In this report, we investigate reactive solute transport without neglecting soil water potential-dependent variability of water content.

Stochastic Analytical Model

Velocity covariances: Several field studies (Hoeksema and Kitanidis, 1984) have shown that the log-conductivity (Y=ln K) displays a simpler correlation structure than the conductivity, and hence, we shall work with the log-transform of the conductivity. In line with first order, linearized theories (Dagan, 1982; Gelhar and Axness, 1983; Russo, 1993; Yeh et al., 1985a-b]; Mantoglou and Gelhar, 1985) the unsaturated hydraulic conductivity is assumed to follow a lognormal distribution. In order to model their spatial variability, Y and h are defined here as random space functions (RSFs).

Now, we define the log-transformed Y(x)=lnK(x) and decompose it into Y(x)=<Y(x)>+Y'(x), where angle brackets denote the expected value operator, and h(x)=<h(x)>+h'(x). Hence Y' and h' represent the fluctuations of Y and h about their respective means, <Y(x)> and <h(x)>. For purposes of deriving a closed-form analytical solution, we shall assume small variability of the log-conductivity, and we shall use the linearized flow equation in order to relate between Y' and h'. Under these conditions, h' becomes a linear function of Y', and their crosscovariance can be easily defined [Yeh et al., 1985a-b]. Likewise, following previous definitions, we now have $q_i(x)= <q_i(x)> +q_i'(x)$.

To simplify matters and to distinguish among the magnitudes of the spatial variability of α, θ, h, K and Ks on one hand and m and $\Delta\theta$, on the other hand, only the former parameters were considered as normally or lognormally distributed, and as second-order stationary RSFs characterized entirely by their first two statistical moments (mean, variance, and correlation structure), while the latter two parameters were considered as deterministic constants, uniform throughout the flow domain. This simplification is justified due to the relatively small variability of m and $\Delta\theta$ under natural conditions.

Similar to the unsaturated hydraulic conductivity, one can assume, with reasonable approximation:

$$a(x) = \ln\alpha(x) =< a(x) > +a'(x); \quad < a'(x) >= 0 \tag{10}$$

$$f(x) = \ln K_s(x) =< f(x) > +f'(x); \quad < f'(x) >= 0 \tag{11}$$

$$\theta(x) =< \theta(x) > +\theta'(x); \quad < \theta'(x) >= 0 \tag{12}$$

where a' and f' are the fluctuations of the lognormally distributed α and K about their respective means.

Using equation (4), replacing h by <h>+h' and K by exp(<Y>+Y'), expanding all the perturbation term in Taylor series, the covariances of specific flux, up to first terms, are given by

$$C_{q_{ij}}(r) = K^{G^2}\left\{\delta_{i1}\delta_{j1}C_Y(r) - \delta_{i1}\frac{\partial C_{Yh}(r)}{\partial r_i} + \delta_{j1}\frac{\partial C_{Yh}(-r)}{\partial r_i} - \frac{\partial^2 C_h(r)}{\partial r_i \partial r_j}\right\} \qquad (13)$$

where r=x-y, $C_Y(r)$ is the covariance of unsaturated hydraulic logconductivity; $C_{Yh}(r)$ is the crosscovariance of unsaturated hydraulic logconductivity and suction head; $C_h(r)$ is the covariance of the suction head; and k^G is the geometric mean of lnK. Similarly, the non-reactive velocity covariances depending on water content are

$$C_{u_i}(r) \le u_i'(x)u_j'(y) \ge \frac{1}{<\theta>^2}\left\{C_{q_{ij}}(r) - <u_j> C_{q_i\theta}(r) - <u_i> C_{q_j\theta}(-r) + <u_i><u_j> C_\theta(r)\right\} \qquad (14)$$

and the reactive velocity covariances are

$$C^r_{u_{ij}}(r) = \frac{1}{<R>^2<\theta>^2}\left\{\frac{<q_i><q_j>}{<\theta>^2}C_\theta(r) + \frac{<q_i><q_j>}{<R><\theta>}C_{R\theta}(r) - \frac{<q_i>}{<\theta>}C_{\theta q_j}(r) + \frac{<q_i><q_j>}{<R><\theta>}C_{R\theta}(-r) + \frac{<q_i><q_j>}{<R>^2}C_R(r) - \frac{<q_i>}{<R>}C_{Rq_j}(r) - \frac{<q_j>}{<\theta>}C_{\theta qi}(r) - \frac{<q_j>}{<R>}C_{Rq_j}(r) + C_{q_{ij}}(r) - \right\} \qquad (15)$$

The C_{uiq}, C_q, C_{Rq}, and C_{Rqj} are the crosscovariances between pore velocity and water content, the covariance of water content, the crosscovariance between the retardation factor and water content, and the crosscovariance between specific flux (velocity) and the retardation factor, respectively. For the chosen parametric expression (Gardner-Russo model, Eq. (2) and (3)), and an arbitrary model characterizing the correlation between saturated hydraulic conductivity and partitioning coefficient (e.g. $k_d=k_d^G\exp(\pm Y')$, where k_d^G is the geometric mean of k_d), we have developed mathematical expressions for these (cross)covariances (Ezzedine and Harter, manuscript in preparation).

Spreading of reactive solute mean concentration plume: Using a Lagrangian description of the motion of a reactive particle in a steady state flow field, the particle trajectory X(t), is a solution of the kinematic equation dX(t)/dt=V(X), where X(t=0)=a and V=<U>+u is the Eulerian velocity, <U> is its expected value and u is random fluctuation with respect to its mean. <U> is assumed constant uniform in space and time. Neglecting pore scale dispersion,

for a solute particle injected into the flow field at time t=0 and location X=a, within a release volume V_0, the trajectory X(t) at time t is given by (Dagan, 1989):

$$X(t;a) = a + Ut + \int_0^t u[X(t';a)]dt' \tag{16}$$

Assuming ergodic conditions and Lagrangian and Eulerian stationarity and homogeneity, Dagan (1982, 1984) shows that we can approximate the actual trajectory of the particle path by its mean trajectory. Therefore

$$X(t;a) = a + Ut + \int_0^t u[Ut']dt' \tag{17}$$

Under the aforementioned assumptions, for fixed a, the particle displacement mean, <X(t)>, and by a first-order approximation in the velocity covariances, the particle displacement covariances $X_{ij}(t)=<X'_i(t)X_j'(t)>$ where X' is the fluctuation with respect to the mean <X> of X, are given by (Dagan, 1989):

$$< X(t) >= Ut \tag{18}$$

$$X_{ij}(t) = \int_0^t \int_0^t u_{ij}(Ut', Ut'')dt'\,dt''; \quad a = 0 \tag{19}$$

$u_{ij}(r)$ can be either C_{uij} (14) or C_{uij}^r (15). The macrodispersion coefficients are (Dagan, 1989):

$$D_{ij}(t) = \frac{1}{2}\left(\frac{dX_{ij}(t)}{dt}\right) \tag{20}$$

Stochastic Numerical Method

The purpose of also developing a numerical model is to simulate the transport of reactive solutes in unsaturated porous media without the restriction to small variability. The numerical stochastic approach is based on Monte Carlo simulation: for each single realization of a physically and chemically variable soil, generated numerically according to the statistical properties defined from field measurements, equations for flow and transport will be solved using a numerical model capable of solving the highly nonlinear flow equation and high-resolution transport problem. Statistical analysis of all realizations and their solutions provide the basis for comparison with the analytical solutions derived in the previous section.

A two-dimensional numerical model was used for the simulation of water flow and chemical transport through variably saturated porous media. The nonlinear flow equation is solved using the Galerkin finite-element technique with either the Picard or the Newton iteration scheme. A continuous velocity field is obtained by separate application of the Galerkin technique to Darcy's equation. The model was adopted to include a linear equilibrium sorption model with a first-order loss term to describe the chemical behavior of the reactive solute. The advective part of the transport equation is solved with one-step backward particle tracking while the dispersive part is solved by the regular Galerkin finite-element technique. To improve the efficiency of the numerical model an enhanced solution routine was built in that allows the use of either preconditioned conjugate-gradient-like (CG) or bi-conjugate-gradient-stabilized (BiCGStab) methods for the iterative solution of the systems of linear simultaneous equations.

The random field either for the saturated hydraulic logconductivity (Ks, Eq. (2)), or for the pore size distribution parameter (α, Eqs. (2-3)) is performed using an efficient random field generator based on Gutjahr's work (1989) using fast Fourier transform (FFT) technique.

Case Study

We investigated reactive transport under conditions of either positively or negatively correlated k_d vs Ks. Although variability of the first-order decay is implemented in both the numerical and analytical methods, we initially assumed that degradation was uniform in space and time. To assess the effect of varying k_d and its degree of correlation with the saturated hydraulic conductivity on the plume spreading, calculations have been performed with three values of k_d^G, namely, 0.4, 0.8, and 10. These values were selected to present a small (k_d^G=0.4) and a large (k_d^G=10) mean sorption coefficient, and an intermediate case where k_d^G=0.8. These values are similar to values reported for DBCP (Fry and Istok, 1994). Note that the sorption coefficient for DBCP and other pesticides is primarily dependent on the organic carbon content of the soil, which varies in space within and between soil types.

Varying degrees of anisotropy were also investigated to assess the effect of soil layering on vertical and horizontal spreading of the reactive solute. Therefore, three different axisymmetric anisotropy ratios were chosen, n=1 (no layering), 3, and 6, based on field observations reported in the literature.

To analyze the effect of the degree of textural variability in soils, three different values of σ_f^2, σ_f^2 =0.5, 1.0, and 1.5, have been chosen. The σ_a^2 is superimposed by the ratio $\zeta = \sigma_f \sigma_a$. Such variability of the saturated hydraulic conductivity has been reported in several field studies. Few of these studies have reported significantly higher variability in saturated hydraulic conductivity. Also, the first-order approximation is known to be valid at best for the smallest of

the three chosen values for σ_f^2, In our analysis we assessed the validity of the analytical model for soils with higher variability.

A complete overview of the simulated cases is given in Table 1. From simulation to simulation, statistical input parameters were varied systematically one by one. Apart from parameters in Table 1, which determine heterogeneity of physical and chemical properties, other parameters were kept constant in all simulations. Porosity was 20%, the mean of $\ln\alpha$=a was -4.605, and its variance was σ_a^2 = 0.1. The saturated water content was θs=0.3, and the residual water content was θr=0.1. The size of the domain expressed in integral scale was $13I_x x 25I_z$. The parameter m in the Gardner-Russo model was the same for all cases simulated.

As mentioned before, the transport in heterogeneous porous media can be represented in terms of spatial moments. Under ergodic conditions, the first- and second-order spatial moments are equal to the statistical mean and variance of the particle trajectory. Thus, plume spreading is assessed by calculation of the second order moments X_{ii}, i=1,2 as functions of time. For the sake of the comparison, X_{ii} are shown in dimensionless form by dividing X_{ii} by I_z^2. Time is made dimensionless by multiplying t by V/<R> I_z where V is the Eulerian velocity and <R> is the mean retardation coefficient given by $1+k_d^G$ $\exp(s_f^2,/2)$.

Results and Discussions

Effect of k_d^G and the degree of correlation between k_d and Ks ($\pm$1)

The dimensionless longitudinal (vertical) plume spreading as a function of dimensionless time is shown in Fig. 1 for a solute with small sorption, k_d^G=0.4, and either positive or negative correlation between k_d and Ks. Also shown is the plume spreading of a non-reactive solute under the same unsaturated conditions. The non-reactive case, k_d^G=0, has been discussed iextensively n Harter and Yeh (1996). Clearly, there is strong dependency between longitudinal spreading and degree of correlation ($\pm$1) between physical heterogeneity (characterized by Ks) and chemical heterogeneity (characterized by k_d). In the case of positive correlation, the plume spreading in the longitudinal direction is significantly smaller than both the non-reactive case (k_d^G=0) and the case of negative correlation between k_d vs. Ks. This can be explained by the opposite effects that chemical and physical heterogeneity have on the displacement of a solute. A positive correlation between the two implies large velocities in pore areas with strong adsorption and low velocities in pore areas with small adsorption. Thus, in areas where water moves relatively fast, the displacement of the pesticide is slowed down by stronger adsorption; conversely, adsorption and, hence, retardation of the pesticide relative to water flow is weaker where water flow is slow. Adsorption buffers the effects of spatially variable water flux on the spreading of the pesticide plume.

On the other hand, negative correlation between sorption and saturated hydraulic conductivity enhances the plume spreading relative to the spreading of an inert plume. Negative correlation implies that adsorption and retardation are relatively weak in areas of high water flux, while they are relatively strong in areas of very low water flux, which further slows the movement of an already slowly moving pesticide in soils. It is worthwhile to point out that the impact of sorption heterogeneity at a given average sorption strength is larger when chemical and physical heterogeneity are negatively correlated than when they are positively correlated.

The effect of average sorption strength on pesticide spreading is depicted in Fig. 2 for both positive and negative correlation between k_d and Ks. As would be expected, the larger the average sorption strength becomes, the more plume spreading deviates from that of a non-reactive solute. In the case of positive correlation, it becomes smaller; in the case of negative correlation, it becomes larger than the vertical spreading of non-reactive solutes.

Horizontal spreading of the solute plume appears to be affected only slightly by chemical heterogeneity. Indeed, the first-order analytical solution predicts that there is no effect on transverse, horizontal plume spreading. Figure 3 shows the numerical results for the transverse, second-order moment X_{22} as a function of dimensionless time. In both the positively and negatively correlated cases, higher mean sorption strengths almost unnoticeably increased transverse spreading. However, these small differences may also be due to the relatively small number of Monte Carlo simulations (N = 100). Bellin et al. (1992) observed the same problem for saturated porous media in which as many as 1500 realizations were necessary to stabilize the more sensitive second moment X_{22}.

In theoretical work related to solute transport in saturated groundwater, the correlation between sorption strength and hydraulic conductivity has also been found to be a prominent factor. When correlated positively, solute spreading is inhibited, but it may be greatly enhanced when the two are negatively correlated. Because larger specific surface areas can accompany smaller permeabilities and lower overall medium reactivity and vice versa, many heuristic and theoretical arguments have been used to support models of negative correlation between the two quantities. Although other compositional, structural, and geochemical factors may also be relevant, supportive data are sparse and possibly inconclusive (Robin et al., 1991; Tompson, 1993).

We point out that under unsaturated conditions, the correlation between the chemical partitioning coefficient and unsaturated hydraulic conductivity is also a function of the average flux rate or moisture content in the soil. For example, in a heterogeneous sandy soil with interbedded clayey loam, water flux under wet conditions will be concentrated in the sand portions of the soil, where hydraulic conductivity is large, while adsorption is low (negative correlation). Once the soil dries out, hydraulic conductivity in the sand will drop drastically and water flux will concentrate towards the clayey-loam portion of the soil, where hydraulic conductivity is still relatively high, while adsorption

coefficients are also higher (positive correlation). In the same soil, transport behavior and spreading of DBCP will therefore depend strongly on the mean flux rate.

Effect of the anisotropy ν

The effect of soil layering or anisotropy ratio n=1,3 and 6 on the longitudinal displacements X_{11} for both correlations (± 1) are shown in Figs. 4 and 5. Results are compared to non-reactive analytical solutions (Harter, 1994). Soil layering reduces the degree of vertical spreading of a solute relative to the non-layered case (isotropic soil). This is independent of the reactive characteristics of the solute. However, for positively correlated physical and chemical heterogeneity, a high degree of soil layering diminishes the difference between solute spreading of a non-reactive solute and that of a mildly sorptive solute (Figure 4). In contrast, for soils with negative correlation between k_d and Ks (Figure 5), the difference between non-reactive and reactive solution appears to be independent of the degree of anisotropy or soil layering.

Conclusions

- We have developed an analytical model capable of predicting DBCP transport in soils with variable water flow, water content, hydraulic conductivity, and sorption strengths. The analytically determined covariance and cross-covariance functions give important information about the spatial continuity of reactive processes and solute transport behavior in soils. Such information is useful in stochastic inverse modeling (conditioning) and in the design of field sampling strategies.
- It was shown that spatial variability of the sorption coefficient may have a significant impact on solute spreading. For a positively correlated hydraulic conductivity and sorption coefficient, solute spreading in the vertical direction will be diminished. However, under such conditions, the impact of chemical variability vanishes in highly stratified soils (high anisotropy) and DBCP transport may be approximated by non-reactive solute transport. Under unsaturated conditions, such correlation may occur when the soil is dry. In most wet soils, the hydraulic conductivity and adsorption coefficient are likely to be negatively correlated. This will greatly enhance the spreading of the mean solute plume, when compared to non-reactive solute transport. Soil stratification will reduce vertical spreading, but not the relative difference between spreading of a reactive and a non-reactive solute.
- Horizontal spreading of DBCP or other pesticides is not affected by the degree of chemical heterogeneity in the soil.
- Both horizontal and vertical solute spreading are higher in soils with larger spatial variability in the saturated hydraulic conductivity.

References

Bellin, A., P. Salandin, and R. Rinaldo. 1992. Simulation of dispersion in heterogeneous porous formations: Statistics, first-order theories, convergence of computations. Water Resour. Res. 28:2211-2227.

Bellin, A., A. Rinaldo, W. J. P. Bosma, S. E. A. T. M. van der Zee, and Y. Rubin. 1993. Linear equilibrium adsorbing solute transport in physically and chemically heterogeneous porous formations. 1. Analytical solutions. Water Resour. Res. 29:4019-4030.

Cohen, S. 1991 Results of the national pesticide survey. Groundwater Monitoring. 11:85-87.

Dagan, G. 1989. Flow and transport in porous formations. Springer-Verlag.

Dagan, G. 1982. Stochastic modeling of groundwater glow by unconditional and conditional probabilities. 2. The solute transport. Water Resour. Res. 18(4):385-848.

Fry V. A. and J. D. Istok. 1994. Effects of rate-limited desorption on the feasibility of in situ bioremediation. Water Resour. Res. 30(8):2413-2422.

Gelhar, L. W., and C. L., Axness. 1983. Three-dimensional stochastic analysis of macro-dispersion in aquifers. Water Resour. Res. 19(1):161-180.

Gutjahr, A. L. 1989. Fast Fourier transforms for random field generation. Project report for Los Alamos grant to New Mexico Tech., No. 4-R58-2690R, Dept. of Math., New Mexico Tech., Socorro, NM.

Harter, T. 1994. Unconditional and conditional simulation of flow and transport in heterogeneous, variably saturated porous media. PhD Dissertation, Univ. of Arizona.

Harter, T. and C J. Yeh. 1996. Stochastic analysis of solute transport in heterogeneous, variability saturated soils. Water Resour. Res. 32(6):1585-1595.

Hoeksema, R. J, and P. K. Kitanidis, 1984. An application of the geostatistical approach to the inverse problem in two-dimensional groundwater modeling. Water Resour. Res. 27(3):341-351.

Kabala, Z. J. and G. Sposito. 1991. A stochastic model of reactive solute transport with time varying velocity in a heterogeneous aquifer. Water Resour. Res. 27:341-350.

Leistra M. and J. Boesten. 1989. Pesticide contamination of groundwater. Agric. Ecosyst. Environ. 26:269-389.

Mackay D. M., W. P. Ball, and M. G. Durant. 1986. Variability of aquifers sorption properties in a field experiement on groundwater transport of organic solutes: Methods and preliminary results, J. Contam. Hydrol. 1(1/2):119-132.

Mantoglou, A. and L. W. Gelhar. 1985. Large scale models of transiant unsaturated flow and contaminant transport using stochatsic methods. Dept. Of Civil Eng., MIT, R85-2.

Rao, P. S. C., K. Evardson, L.T. Ou, R. E. Jessup, P. Nkedi-Kizza and A. G. Hornsby. 1986. Spatial variability of pesticide soprtion and degradation, In W. Y. Garner, R. C. Honeycutt, H. N. Nigg (eds.) Evaluation of Pesticides in Groudwater, ACS Symp. Ser. 315, 100-115.

Robin, M. J., E. A. Sudicky, R. W. Gillham and R. G. Kachanoski. 1991. Spatial variability of strontium distribution coefficients and their correlation with

hydraulic conductivity in the Candian force base Borden aquifer. Water Resour. Res. 27(10):2619-2632.

Russo, D. 1988. Determining soil hydraulic properties by parameter estimation: On the selection of a model for the hydraulic properties, Water Resour. Res. 24:453-459.

Russo, D. 1995a. On the velocity covariance and transport modeling in heterogeneous anisotropic porous formations. 2. Unsaturated flow. Water Resour. Res. 31:139-145.

Russo, David. 1995b. Stochastic analysis of the velocity covariance and the displacement covariance tensors in partially saturated heterogeneous anisotropic porous formations. Water Resour. Res. 31:1647-1658.

Russo, David. 1993. Stochastic modeling of solute flux in a heterogeneous partially saturated porous formation. Water Resour. Res. 29:1731-1744.

Tompson, Andrew F. B. 1993. Numerical simulation of chemical migration in physically and chemically heterogeneous porous media. Water Resour. Res. 29:3709-3724.

Van Genuchten M.T.A. 1980. A closed form equation for predicting the hydraulic conductivity of unsaturated soils. Soil. Sci. Soc. Am. J. 44:892-898.

Yeh, T. -C., L. W. Gelhar, and A. L. Gutjahr. 1985a. Stochastic analysis of unsaturated flow heterogeneous soils: 1. Statistically isotropic media, Water Resour. Res. 21:447-456.

Yeh, T. -C., L. W. Gelhar, and A. L. Gutjahr. 1985b. Stochastic analysis of unsaturated flow heterogeneous soils: 2. Statistically anisotropic media with variable α. Water Resour. Res. 21:457-464.

Table 1. Cases treated and simulated

	k_d^G			ν			σ_f^2			Correlation		
	0.4	0.8	10	1	3	6	0.5	1.0	1.5	+1	-1	0
anisotropy	√			√	√	√		√		√	√	N†
k_d^G	√	√	√	√				√		√	√	N
σ_f^2	√			√			√	√	√	√	√	N

†N not treated in this paper; under investigation

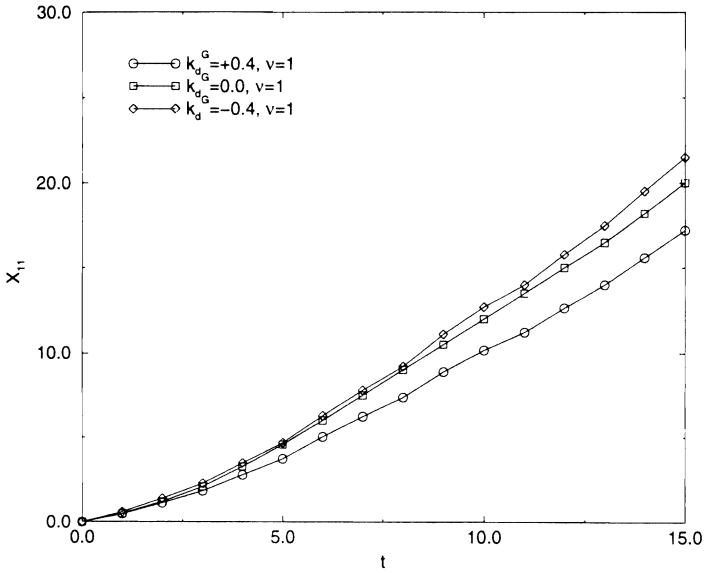

Figure 1. Effect of the correlation between k_d and K_s on X_{11}. Read K_d^G - -0.4: negative correlation (-1) and $K_d^G = 0.4$.

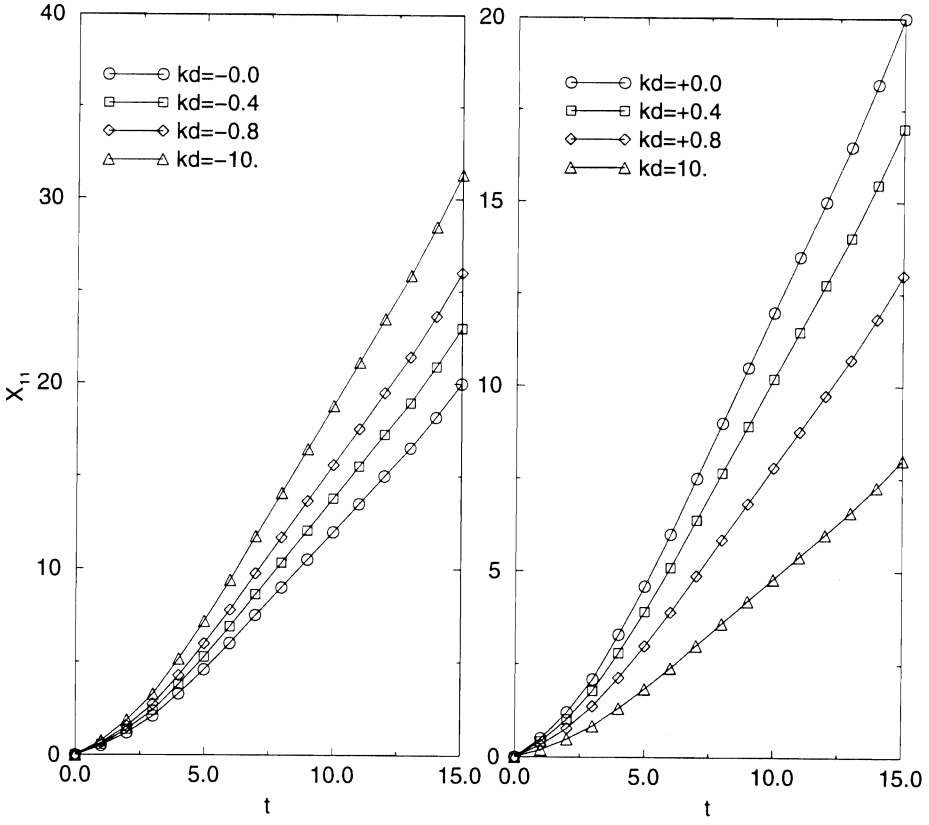

Figure 2. Effect of k_d and correlation on the longitudinal spreading X_{11}.

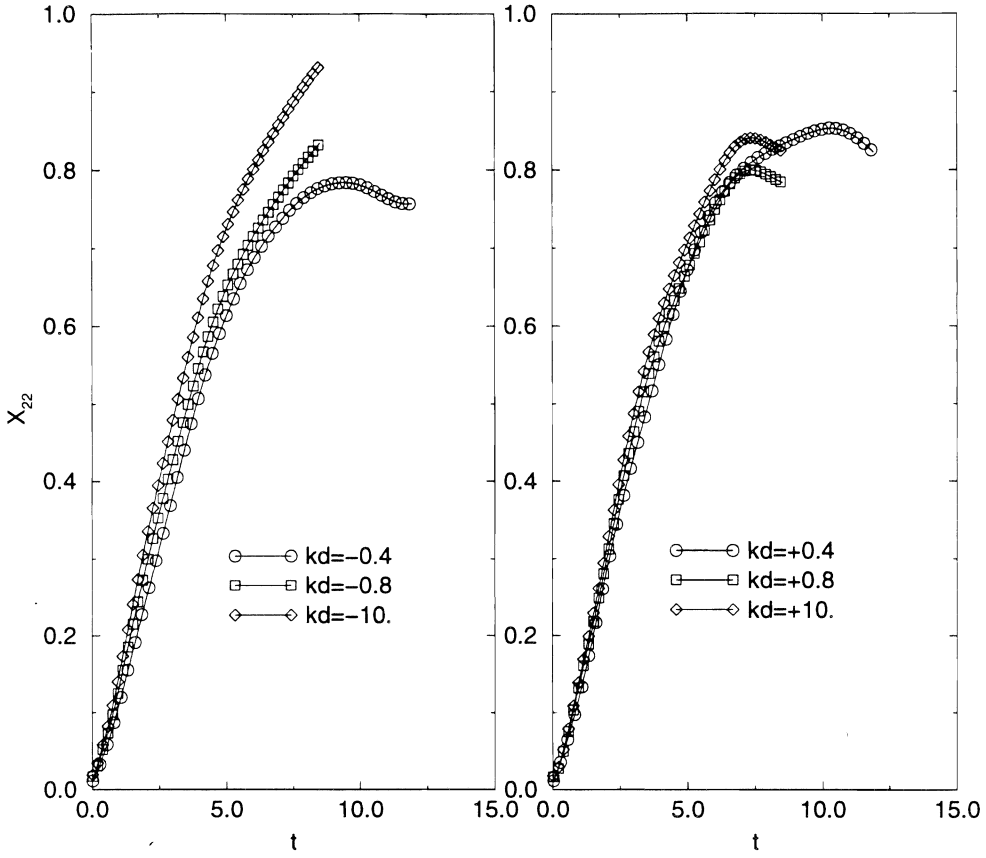

Figure 3. Effect of k_d and correlation on the longitudinal spreading X_{22}.

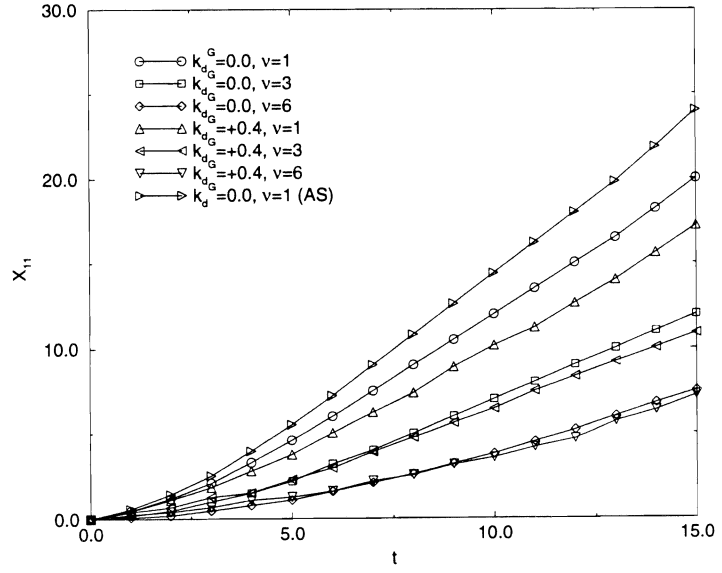

Figure 4. Effect of ν on the longitudinal spreading X_{11}, positive correlation.

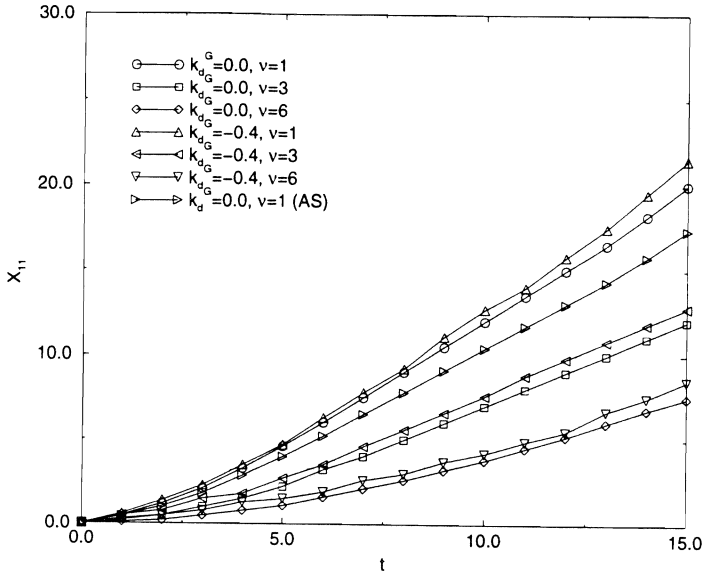

Figure 5. Effect of ν on the longitudinal spreading X_{11}, negative correlation.

The Use of Conditional Simulation to Identify the Sensitive Areas for Nitrate Leaching

LAOSHENG WU, WILLIAM A. JURY, AND LEHUA PAN
Department of Soil and Environmental Sciences, Riverside Campus

Summary

Nitrogen fertilizer-induced nitrate leaching is a serious water pollution problem caused by agriculture. Complete field monitoring of nitrate leaching is costly and time consuming while limited field monitoring often does not provide conclusive results because of spatial variation of soil properties that affect nitrate leaching processes. An alternative is to use computer simulation models, based on limited measurements, and to extrapolate the information to field areas where no measurements were made. However, traditional computer simulation methods are subject to uncertainty because of spatial variability of soil properties. The objective of this one-year research project was to find an efficient way to reduce the uncertainty of nitrate leaching prediction by computer modeling. The research consisted of three parts: (1) developing a numerical program to simulate a spatially variable hydraulic conductivity field with or without conditioning; (2) developing an efficient, process-based numerical model to simulate transient water flow and nitrate transport in heterogeneous soil; and (3) conducting Monte Carlo simulation using the above programs to evaluate the effects and efficiency of different conditioning methods in reducing the prediction uncertainty and identifying the sensitive areas for nitrate leaching.

The Kriging-type conditioning based on the measurement values (knowing 30% of the blocks) successfully identified the major features of the spatial pattern so that the conditioning significantly reduced the prediction uncertainty of the total leaching rate. The identification-type conditioning was able to identify the "real" distribution of hydraulic conductivity from 10,000 possible realizations that had the same statistical properties, provided only 8% of the blocks were known and if the standard deviation of the measurements was less than 0.2. Our results showed that the identification-type conditioning is the only method that can provide accurate point prediction. The simulation also showed that the wetting and nitrate advance fronts were not even for a heterogeneous profile although the applied water at the surface was uniform. Their spatial patterns varied with the spatial distribution pattern of the hydraulic conductivity. It is unlikely to have accurate estimation of the nitrate leaching rate without a proper modeling method.

Key Words: conditional simulation, stochastic approach, nitrate transport, unsaturated flow, soil spatial variability, transient flow, Monte Carlo simulation

Project Objectives Addressed in 1995-1996

1. To compare outputs from conditional and unconditional simulations.

2. To demonstrate the advantage of conditional simulation in reducing the uncertainty of identifying the sensitive areas for nitrate leaching.

3. To develop a model (based on the conditional simulation technique) that can be used as a tool for selecting irrigation schemes for soil with spatial variability so that nitrate leaching can be minimized.

Research Plan and Procedures

Simulation of Hydraulic Conductivity Field A unidimensional unconditional simulation program was developed to generate the random hydraulic conductivity field based on the spectral method (Pardo-Iguzquiza et al., 1992):

$$T_s(x) = 2\sum_{i=1}^{N}\left[S(\omega_i)\Delta\omega\right]^{1/2}\cos(\omega_i x + \phi_i) \qquad (1)$$

where, $T_s(x)$ is the simulated value of the normalized hydraulic conductivity at point x; $S(\omega)$ is the spectral density function, which is the cosine transformation of the covariance function C(h) of the measured data; N, i, and ω are the number of harmonics used, the harmonic number, and the frequency, respectively; $\Delta\omega(=\Omega/N)$, ϕ_i, and Ω are the discretization frequency, the independent random angles uniformly distributed between 0-2π, and the band frequency of the process [-Ω, Ω], respectively. The simulated hydraulic conductivity fields were then calculated as:

$$K_s(x) = \hat{K}\exp\left(T_s(x)\,\sigma_{lnK}\right) \qquad (2)$$

where $\hat{K}$ and σ_{lnK} are the average hydraulic conductivity and the standard deviation (STD) of ln(K), respectively. The simulated fields have the same mean, variance, histogram, and variogram of the measured data. A spherical model was used to describe the spatial structure of the hydraulic conductivity field. The distribution of the hydraulic conductivity is assumed to be log-normal with variance and correlation range being 0.36 and 300 cm, respectively. A profile of 3,000 cm wide by 110 cm deep was assumed to be homogeneous vertically but heterogeneous horizontally. Ten thousand realizations of the hydraulic conductivity fields were generated.

Conditioning the Hydraulic Conductivity Field The basic idea of conditioning is to utilize the information contained in the measured data more completely. Two conditioning methods were used to reduce the prediction uncertainty. The conventional conditioning method is to honor the value of the measured data using the Kriging technique (Journal and Huijbregts, 1978) as follows:

$$T_{sc}(x) = T_s(x) + \sum_{i=1}^{Num} \lambda_i \left[T(x_i) - T_s(x_i) \right] \tag{3}$$

where and T_{sc}, T_s, and T are the conditionally simulated, the unconditionally simulated, and the measured normalized hydraulic conductivities, respectively. λ_i is the Kriging coefficient while Num is the number of points of Kriging neighborhoods. The x_i denotes the ith location of the measurement points. We will call this type of conditioning method Kriging-type conditioning (simply, KT-conditioning).

The real hydraulic conductivity field is only one of the many possible realizations that share the same statistical properties. Therefore, one can also take the conditioning as a procedure to identify the realizations that are closest to the real one. Hence, we proposed a new conditioning method. The new method is to select a subset of unconditionally simulated hydraulic conductivity fields according to the following criterion:

$$\sigma_{ms}^2 = \frac{1}{M-1} \sum_{i=1}^{M} \left[\ln\left(K_s(x_i)\right) - \ln\left(K(x_i)\right) \right]^2 \le \sigma_m^2 \tag{4}$$

where, M is the number of the measurement points, while σ_m is the SD of the measurement error. We will call this type conditioning method as identification-type of conditioning (simply, IT-conditioning). A combined method using (3) and (4) can be employed when the measurement noise is larger than zero.

Simulation of Transient Water Flow A 2-D numerical model was developed to simulate transient water flow through the root zone based on the Richards equation:

$$\frac{\partial \theta}{\partial t} = \nabla \cdot \left[K(\psi) \nabla \psi \frac{\partial K}{\partial z} - S \right] \tag{5}$$

where θ, ψ, z, and t are volumetric water content, water pressure head, depth, and time, respectively. Both the hydraulic conductivity, K, and volumetric water content, θ, are strongly nonlinear functions of ψ. The sink term, S, is the volume of water removed per unit time from a unit volume of soil due to plant uptake, which can be expressed as (Simunek and van Genuchten, 1994):

$$S(\psi, x, z) = a_r(\psi, x, z)\, b(x, z)\, L_t T_p \tag{6}$$

where the water stress response function $a_r(\psi)$ is a prescribed dimensionless function of the soil water pressure head ($0 \leq a_r \leq 1$), and b(x, z) is the normalized water uptake distribution which represents the relative root distribution over the profile. T_p and L_t are the potential transpiration rate and the width of the soil surface associated with the transpiration process, respectively.

The following water retention and hydraulic conductivity models were used (van Genuchten, 1980) in simulations:

$$Se = \frac{\theta - \theta_r}{\theta_s - \theta_r} = \left[\frac{1}{1+(\alpha|h|)^n}\right]^m \tag{7}$$

and

$$K = K_s\, Se^{\frac{1}{2}}\left[1-\left(1-Se^{\frac{1}{m}}\right)^m\right]^2 \tag{8}$$

where, θ_r = 0.0286 c m^3/cm^3, θ_s = 0.366 cm^3/cm^3, a = cm^{-1}, n = 2.239, and m = 1 - 1/n (Berino fine sand) for this research. K_s is the saturated hydraulic conductivity and is assumed to be spatially variable.

A numerical solver for (5) was developed based on the finite volume method, incorporating the transformed pressure head based method and the optimal relaxation method (Pan and Wierenga, 1996).

Simulation of Transient Nitrate Transport The governing equation for nitrate transport is:

$$\frac{\partial(\theta C)}{\partial t} = \nabla\cdot[\theta D\nabla C] - \nabla\cdot(qC) - SC - \mu(C) \tag{9}$$

where, C, q, and D are the nitrate concentration, the Darcian flux, and the local dispersion coefficient, respectively. The nitrate degradation rate, $\mu(C)$, has the form:

$$\mu(C) = \frac{\mu_{max}\, C^{\beta}}{1+\mu_k\, C} \tag{10}$$

where, μ_{max} is the maximum degradation rate for a given microbial community and its surrounding environmental factors. μ_k and β are empirical rate coefficients which specify the reaction type.

For z-direction (vertical), the component of D in (9) is given by:

$$\theta D_z = \nu q_z + \theta D_m \tau$$
$$\tau = \frac{\theta^{7/3}}{\theta_s^2} \qquad (11)$$

where,ν, D_m, and τ are the dispersivity, molecular diffusion coefficient, and tortuosity factor, respectively. The same equation describes the horizontal direction, but the subscripti z in (11) is replaced by x.

The finite volume method was also used to solve (9). A modified bi-conjugate gradient method was used as a linear solver (Press et al., 1992). In order to eliminate the numerical oscillation or the numerical diffusion due to extreme local Peclet number, the power-law scheme, based on the local Peclet number, was used in calculation of the solute flux through the interface between two neighboring cells (Patanker, 1980).

Monte Carlo Simulation of Nitrate Leaching Through Root Zone: A Case Study

Nitrate leaching of a 30 m long by 1.1 m deep transect in the field was simulated. The soil is a Berino fine sand whose hydraulic parameters were shown above. The geometric mean of K_s is 0.3757 cm/min, while the horizontal standard deviation of $\ln K_s$ is 0.6; otherwise, the soil is homogeneous. An infiltration event with a magnitude of 0.025 cm/min was uniformly applied at the surface for 250 realizations of both unconditionally and conditionally simulated hydraulic conductivity fields with/without plant uptake. Therefore, 1,000 simulations were conducted. The duration of the infiltration event was 2,400 minutes for all cases. Both water and nitrate leaching fluxes were calculated by the total amount that passed the depth of 100 cm during infiltration. The horizontal and the vertical grid sizes were 30 cm and 2.5 cm, respectively. Thus, the number of total nodes was 100x44. A fixed time step of 6 minutes was used for all cases. For the cases with plant uptake, the potential evapotranspiration (ET) rate was set to be 5 mm/day and the relative root distribution decreased from the surface to the depth of 100 cm.

Results

The hypothetical K_s field was assumed to have a correlation range of 300 cm. Figure 1a shows 5 selected realizations along with the "real" distribution depicted by measured data. Although they all had the same statistical properties, their spatial distribution details, however, varied tremendously.

When 30 out of 100 blocks were measured, the same realizations in Fig. 1a were conditioned to become similar to the real distribution (Fig. 1b) using KT-conditioning techniques.

Figure 2a shows the dimensionless flux of water through the plane of 100 cm depth. The dimensionless flux is defined as the ratio of the average flux at the depth of 100 cm over the average infiltration flux at the surface. Both conditional and unconditional ensemble means of 250 realizations closely agreed with the real leaching curve. The homogeneous profile had a much steeper leaching curve than the heterogeneous profiles. Similar results are shown in Fig. 2b for nitrate. Figure 3 shows the uncertainty of the model predictions due to lack of K information for the cases in Figs. 2a and 2b. Figures 2c and 2d show the ensemble means of water and nitrate leaching for the cases with root uptake at potential ET = 5 mm/day.

Figures 4a and 4b show the dimensionless root uptake rates of water and nitrate, respectively. Again, the dimensionless root uptake rate is the ratio of the simulated root uptake rate over the infiltration rate.

Figure 5 shows the values of σ_{ms} calculated based on (4) for 500 realizations that have the smallest σ_{ms} within a group of 10,000 realizations, assuming that 30%, 15%, 8%, and 4% of blocks were known. The value of σ_{ms} increases with the number of the known blocks. In other words, the more information we know, the more accurate estimation of the real distribution we can have.

Figures 6a and 6b show the contours of water content and nitrate concentration profiles, respectively, after 10 hours of infiltration. The irrigation rate at the surface was uniformly distributed and constant. However, the water distribution and the wetting front were not uniform. Neither was the nitrate distribution.

Figures 7a, 7b, and 7c show the relative water flux at a depth of 100 cm at three different locations. At x=735 cm, the water flux predicted with KT-conditioning agreed well with the real flux, while the prediction with unconditional simulation was similar to that of the homogeneous profile (Fig. 7a). However, the prediction with KT-conditioning underestimated the water flux at x=1485 cm (Fig. 7b) and overestimated the flux at x=2235 cm (Fig. 7c). The IT-conditioning successfully identified the real distribution of K. Therefore, the predictions with IT-conditioning agreed with the real flux perfectly. Figure 7d shows the prediction errors of the unconditional and the conditional methods for these point predictions. KT-conditioning reduced the prediction errors for observation points 1 and 2 (obs1 & obs2) but increased the prediction errors at point 3 (obs 3). On the other hand, the prediction errors with IT-conditioning were essentially zero.

Discussion

The difference between individual realizations can be very large even though their statistical properties (say, the variograms) are the same (Fig.1a). Obviously, the spatial pattern of the "real" distribution of K was approximated well by the 30 measurement blocks which were uniformly distributed over the space. The KT-conditioning based on these measurement values successfully identified the major features of the spatial pattern (Fig.1b). In other words, the major higher or lower conductivity area could be identified by the KT-conditioning.

For a heterogeneous conductivity profile, a homogeneous assumption predicted much steeper average leaching curves for both water and nitrate than the real curves (Figs. 2a and 2b). If these leaching curves are evaluated as breakthrough curves, one might describe the nitrate transport as having a larger effective dispersivity. However, there is no such effective parameter for water transport. Note that, in reality, both water flow and nitrate transport are transient. Both conditional and unconditional simulations of 250 realizations produced very similar ensemble means and agree with the real leaching curves very well (Figs. 2a and 2b). However, conditioning significantly reduced the overall prediction uncertainty (Fig. 3).

The results from the cases with root uptake were very similar to those from the cases without root uptake, except that the dimensionless leaching flux no longer reached unity (Figs. 2c and 2d). The predicted root uptake rates of conditional, unconditional, and homogeneous cases were all very similar with the real uptake rates (Fig. 4).

Figure 5 illustrates the 500 smallest σ_{ms} of 10,000 realizations for four different information levels. If the measurement error level (σ_m) is less than 0.2, only the real one can be selected from 10,000 realizations as the qualified K field by IT-conditioning (4) even though only 8% blocks were known. This means that the real K field is well identifiable for these cases. Of course, the set of possible realizations with the same variogram is theoretically unbounded. However, the conditioning (4) results in a much smaller subset of possible realizations that need to be simulated by process-based modeling. This result is of great significance in Monte Carlo simulation practices. The KT-conditioning by itself does not reduce the number of possible realizations.

The contour of water content plotted in Fig. 6a shows an uneven wetting front corresponding to the spatial distribution of hydraulic conductivity. The higher the K_s, the deeper the wetting front advanced. The contour of nitrate concentration showed a front pattern similar to that of the wetting front. However, unlike the uniform distribution of nitrate concentration near the surface, the distribution of water content near the surface was not uniform but had a pattern corresponding to the spatial variation of hydraulic conductivity. The lower the hydraulic conductivity, the higher the water content. In the field, it is common practice to measure nitrate leaching only at a few points of a certain

depth. The uneven wetting and nitrate advancing fronts plotted in Figs. 6a and 6b imply that validating a model with field-measured data and estimating the leaching flux by measurements are very difficult and complicated unless the soil properties are characterized well. The stochastic approach is subject to significant high uncertainty if the comparison is made in terms of the point measurements instead of the total or average leaching rates below a certain depth.

Furthermore, if comparison is made based on the point measurements, the KT-conditioning can be subject to significant errors even though its overall performance is better than that of the unconditional prediction (Fig. 7). If the saturated conductivity at the observation point is known exactly (obs 1 in Fig. 1b), the prediction with the KT-conditioning agrees with the real observation very well (Fig. 7a). Otherwise, the effects of the KT-conditioning are uncertain (Figs. 7b and 7c). When K_s at the nearest conditioning point was larger than that of the observation point (obs 2 in Fig. 1b), the KT-conditional prediction underestimated the leaching flux (Fig. 7b). When K_s at the nearest conditioning point was smaller than that of the observation point (obs 2 in Fig. 1b), the KT-conditional prediction overestimated the leaching flux (Fig. 7c). These phenomena are partially related to the weighted averaging property of the Kriging estimator. Figure 7d shows the similar prediction errors which were defined as the standard deviation of difference between the predicted and the real observation. As expected, the unconditional predictions were always close to the uniform predictions. Obviously, the IT-conditioning predicted the real observations, provided K in 8% or more of the blocks was known, because it could identify the real distribution of K (Fig. 5). Therefore, the proposed IT-conditioning is most accurate in terms of point observations.

Conclusions

The differences between individual realizations were very large, although their statistical properties are the same. The KT-conditioning based on the measurement values successfully identified the major features of the spatial pattern so that conditioning significantly reduced the prediction uncertainty. If the measurement noise level (σ_{ms}) was less than 0.2, only the real one was selected from 10,000 realizations as the qualified possible K field by IT-conditioning even though K in only 8% of the blocks was known. This result implies that in theory one needs only a single realization from 10,000 realizations to get an uncertainty-free prediction with this type of conditioning. Practically, one may not be so lucky but the IT-conditioning can lead to a much smaller subset of possible realizations that needs to be simulated by process-based models which will significantly improve the efficiency of Monte Carlo simulation practices.

For the heterogeneous conductivity profile, the homogeneous assumption predicted much steeper average leaching curves for both water and nitrate than the real curves. Both conditional and unconditional simulations of 250 realizations provided very similar ensemble means and agreed with the

real leaching curves very well. The KT-conditioning significantly reduced the overall prediction uncertainty. However, in terms of the point observations, the effectiveness of the KT-conditioning will depend on whether or not the hydraulic conductivity at the observation location is exactly known, while the IT-conditioning is still very successful under such conditions.

The contours of water content and nitrate concentration in the profile during a uniform irrigation showed that the wetting and nitrate advancing fronts were not even for the heterogeneous profile and their spatial patterns varied with the spatial distribution pattern of the hydraulic conductivity. Identifying the spatial distribution of the hydraulic conductivity using conditional Monte Carlo methods, especially the IT-conditioning, is possible and essential for identifying the sensitive areas for nitrate leaching, designing site-specific optimal irrigation and fertilization methods, and accurately evaluating the total leaching rate based on some measured data.

References

Journal, A. And Ch. Huijbregts. 1978. Mining Geostatistics, Academic Press, New York.

Pan, L. and P.J. Wierenga. 1996. Improving numerical modeling of two-dimensional water flow in variably saturated and heterogeneous porous media. Soil Sci. Soc. Am. J. (In press).

Pardo-Iguzquiza, E., M. Chica-Olmo, and J. Delgado-Garcia. 1992. SICON1D: A Fortran-77 program for conditional simulation in one dimension. Computer & Geosciences 18(6):665-688.

Patanker, S.V. 1980. Numerical Heat Transfer and Fluid Flow. McGraw-Hill. New York.

Press, H.M., Saul A. Teukolsky, W.T. Vetterling, and B.P. Flannery. 1992. Numerical Recipes in Fortran (2nd ed.). Cambridge University Press. New York.

Simunek J. and M. Th. van Genuchten. 1994. The CHAIN_2D code for simulating the two dimensional movement of water, heat, and multiple solutes in variably-saturated porous media. Research Report No. 136. USSL, ARS, USDA, Riverside, CA.

van Genuchten, M. Th. 1980. A closed-form equation for predicting the hydraulic conductivity of unsaturated soils, Soil Sci. Soc. Am. J. 44:892-898.

EXAMPLES OF UNCONDITIONAL K FIELD

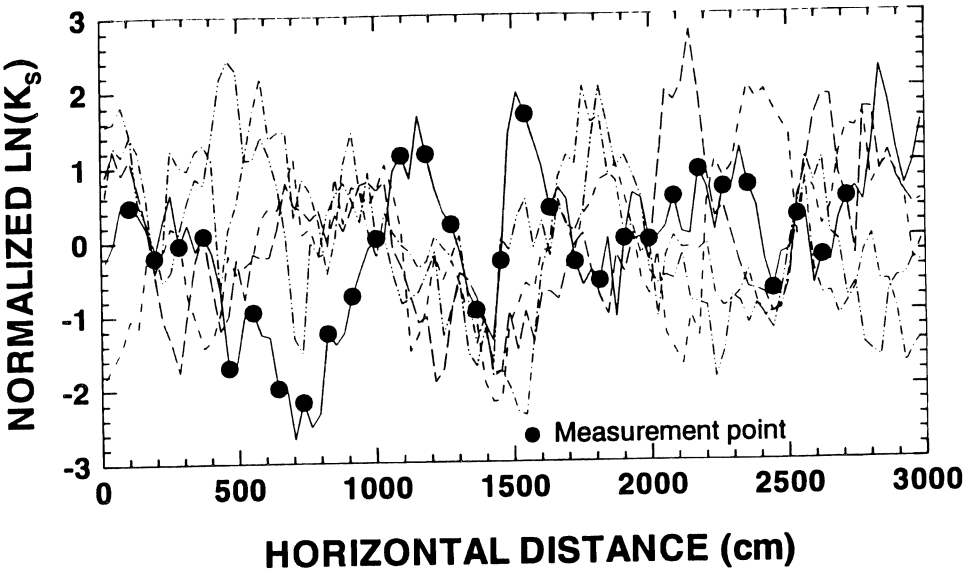

EXAMPLES OF CONDITIONAL K FIELD

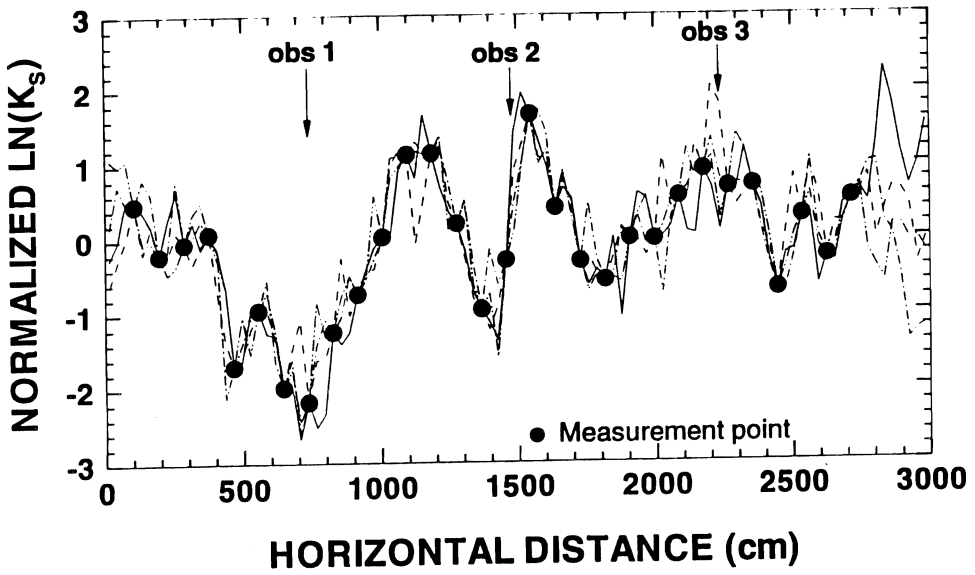

Figure 1. Examples of simulated (dimensionless) saturated hydraulic conductivity field: (a) unconditional; (b) conditional (with 30% known). The solid circles are the measured data points while the solid line is the hypothetical "real" field.

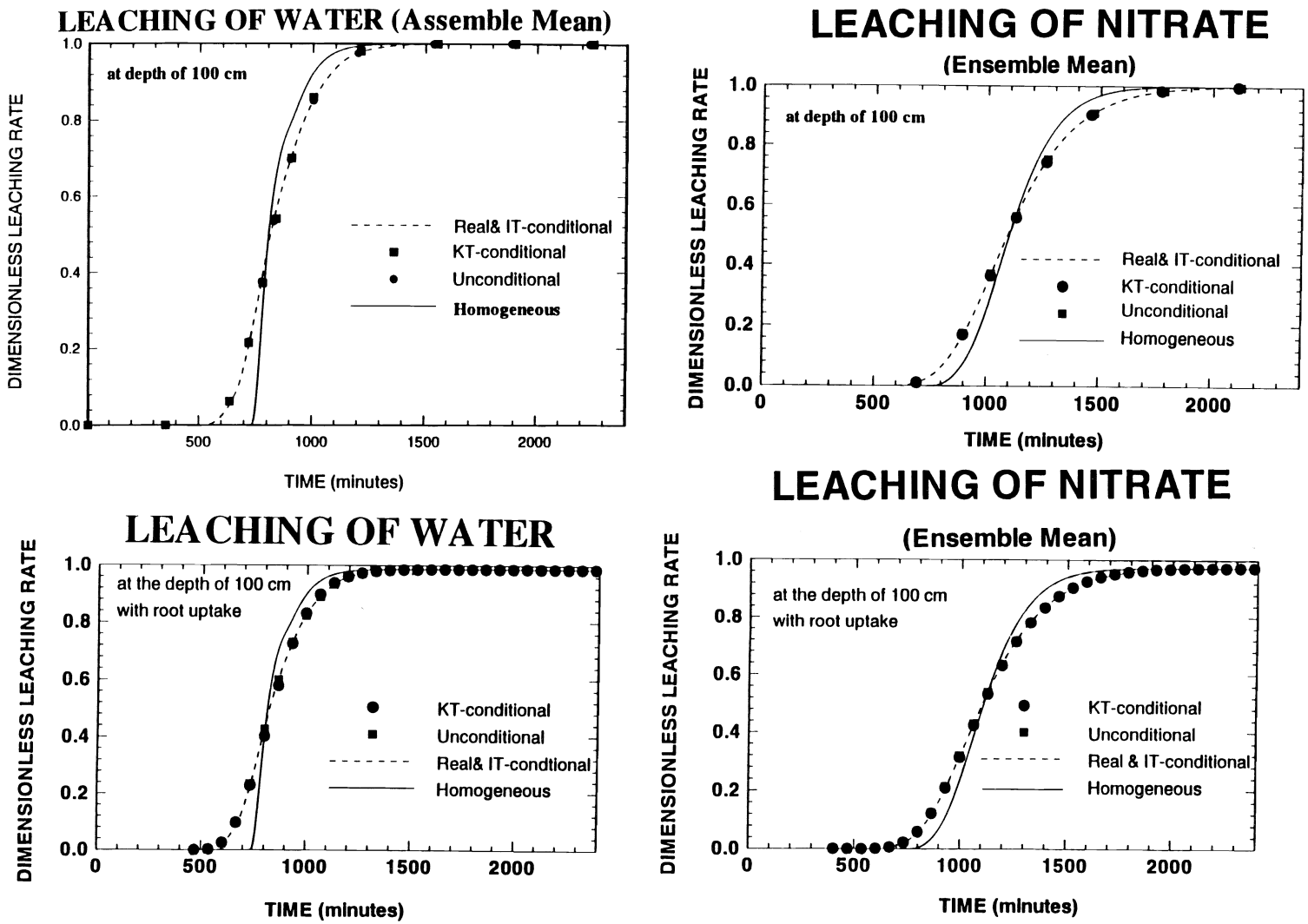

Figure 2. Simulated mean leaching curves at the depth of 100 cm compared with those of the homogeneous profile and the real profile: (a) leaching rate of water without root uptake; (b) leaching rate of nitrate without root uptake; (c) leaching rate of water with root uptake; (d) leaching rate of nitrate with root uptake. The dimensionless leaching rates were all calculated as the ratio of the simulated leaching rate to the infiltration rate. The rate is defined as the average rate over the width of 3,000 cm. The number of realizations is 250.

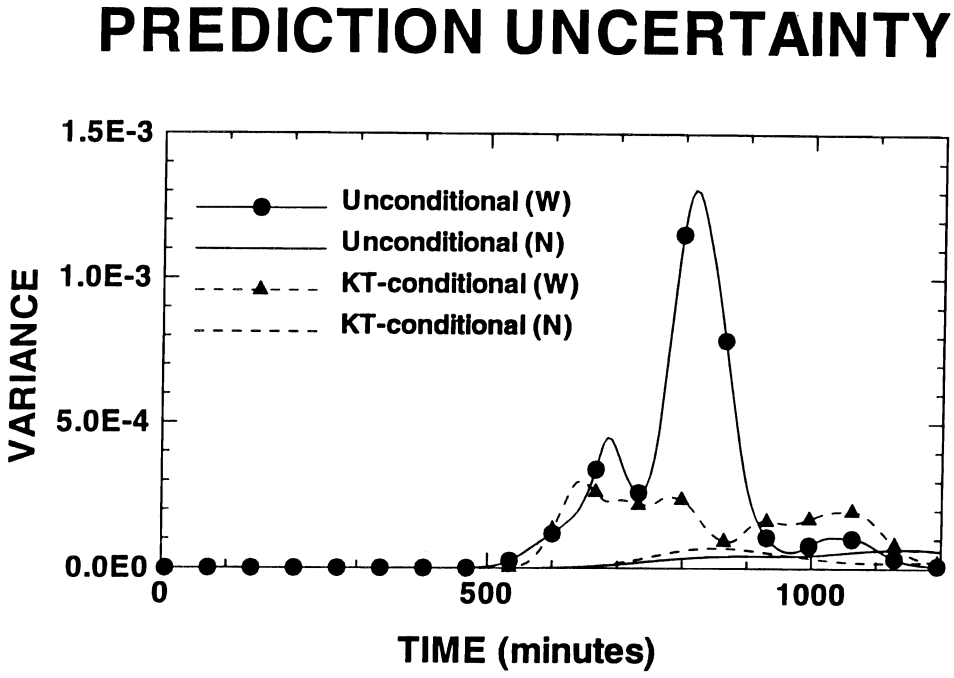

Figure 3. The variance of the Kriging-type conditional and the unconditional predictions corresponding to the cases in Figs. 2a, 2b, 2c, and 2d. The identification-type conditional prediction has zero variance.

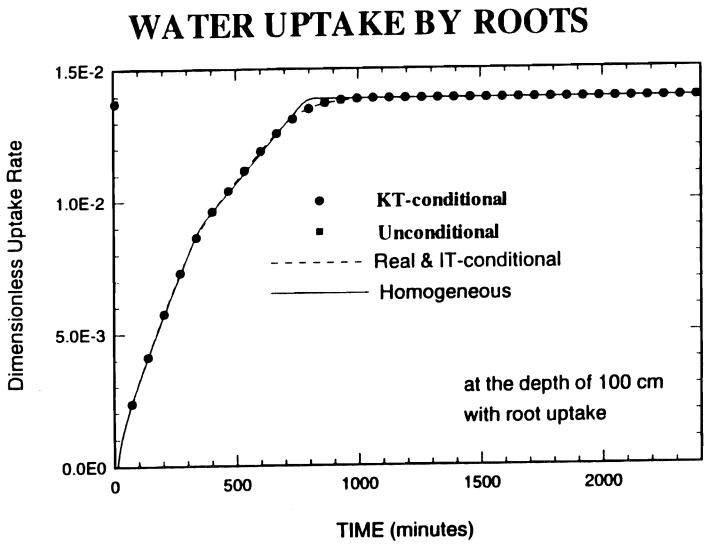

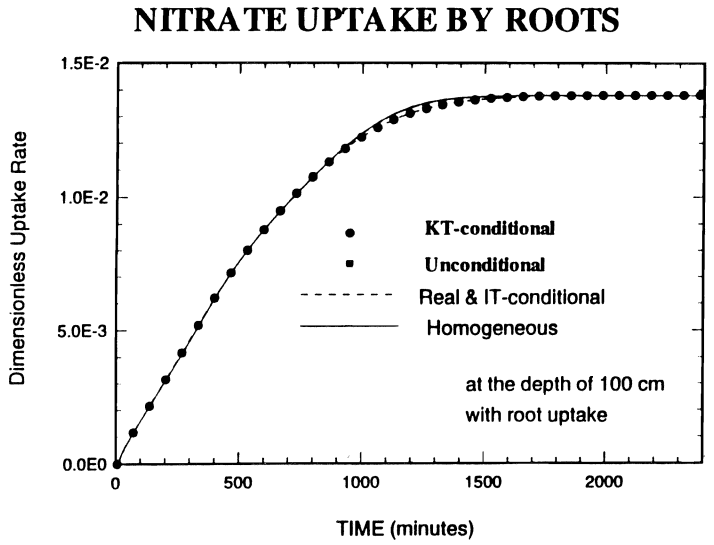

Figure 4. The mean dimensionless root uptake rates compared with those of the homogeneous profile and the real profile: (a) water uptake; (b) nitrate uptake. The dimensionless rate was also calculated as the ratio of root uptake to the infiltration rate.

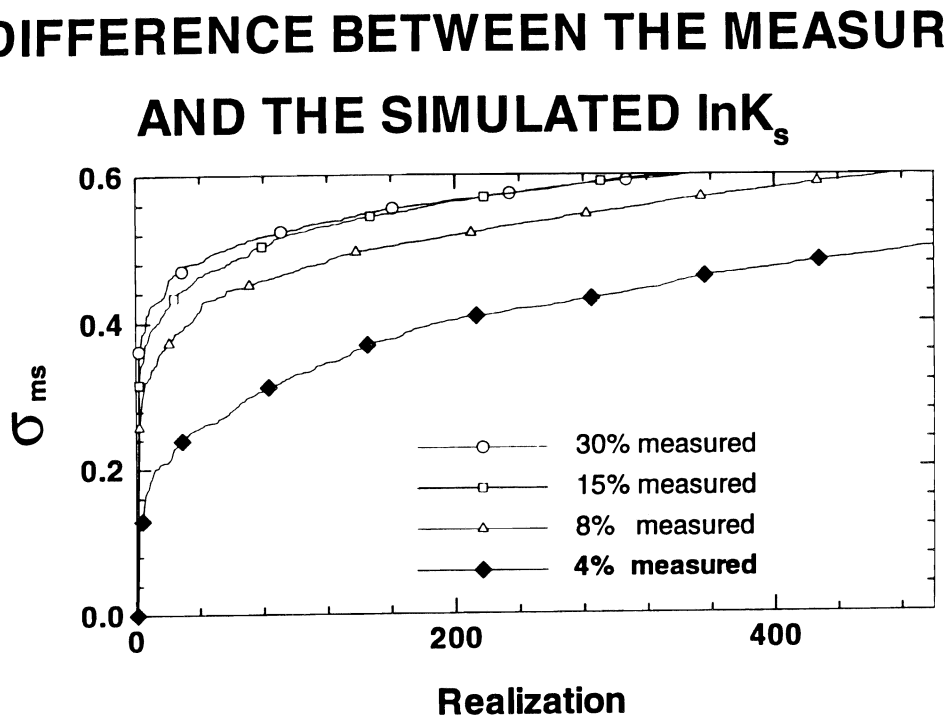

Figure 5. The calculated σ_{ms} based on (4) for the 500 realizations that had smallest σ_{ms} within a group of 10,000 realizations, assuming different information levels.

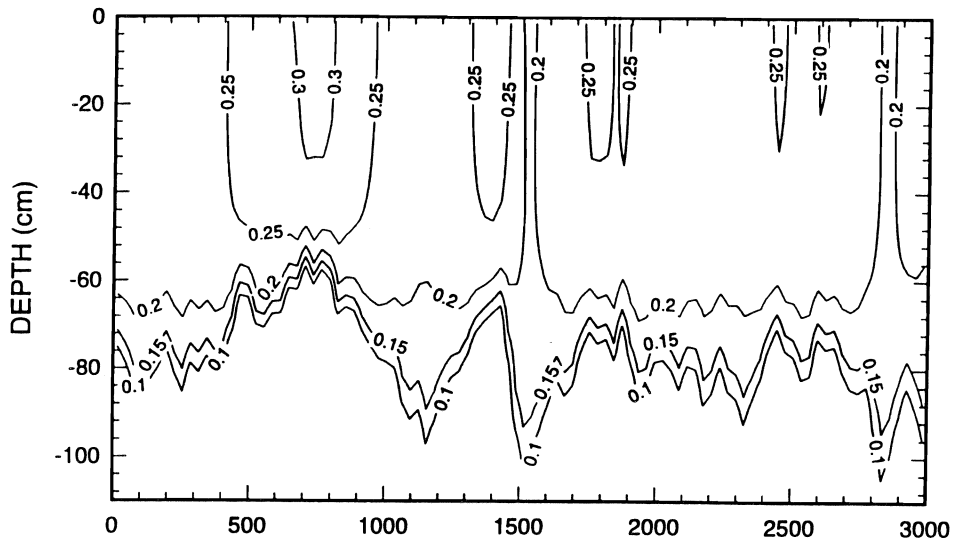

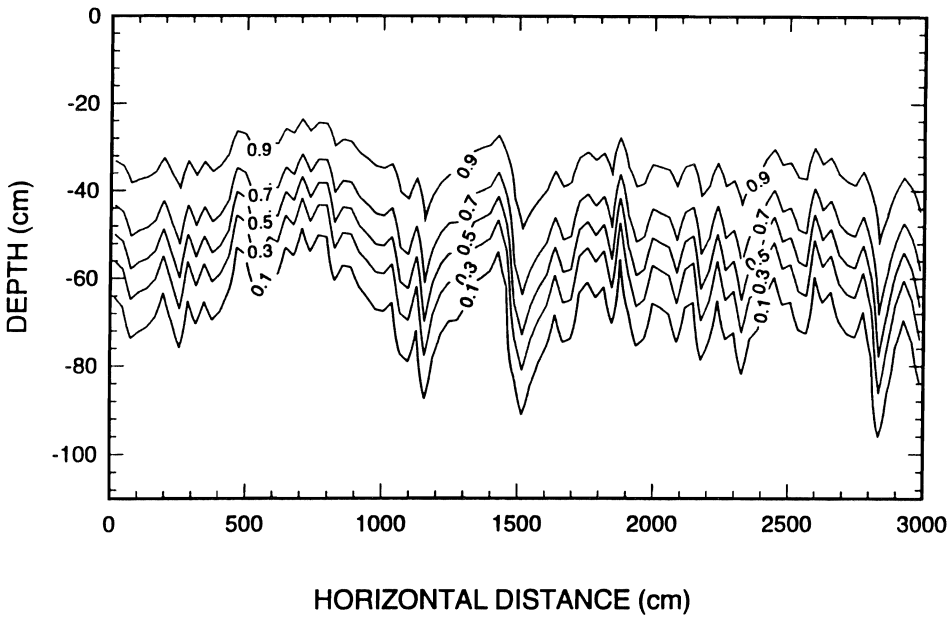

Figure 6. Contours of water content (a) and relative nitrate concentration (b) after 10 hours of infiltration.

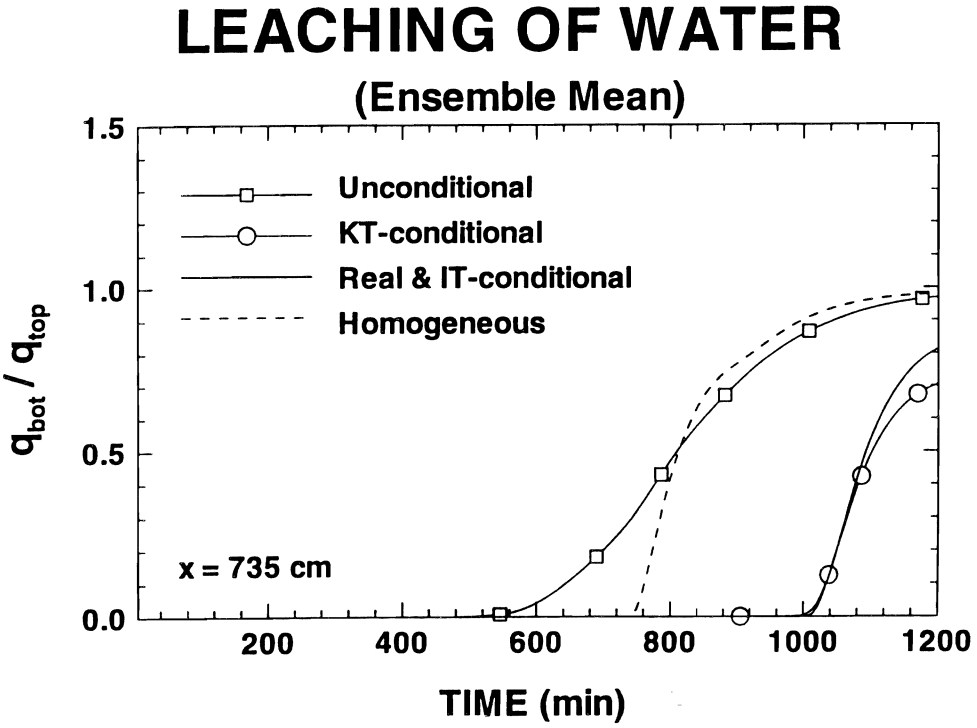

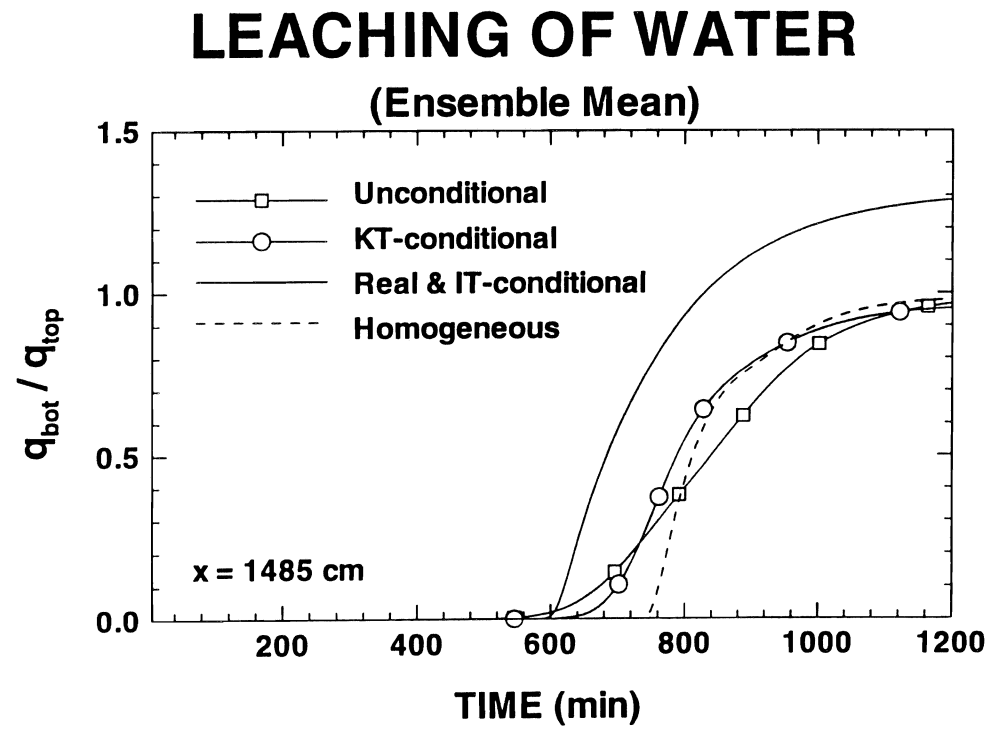

Figure 7a,b. Predicted leaching flux and prediction errors. (a) at point (x=735 cm, z=-100 cm); (b) at point (x=1485 cm, z=-100 cm).

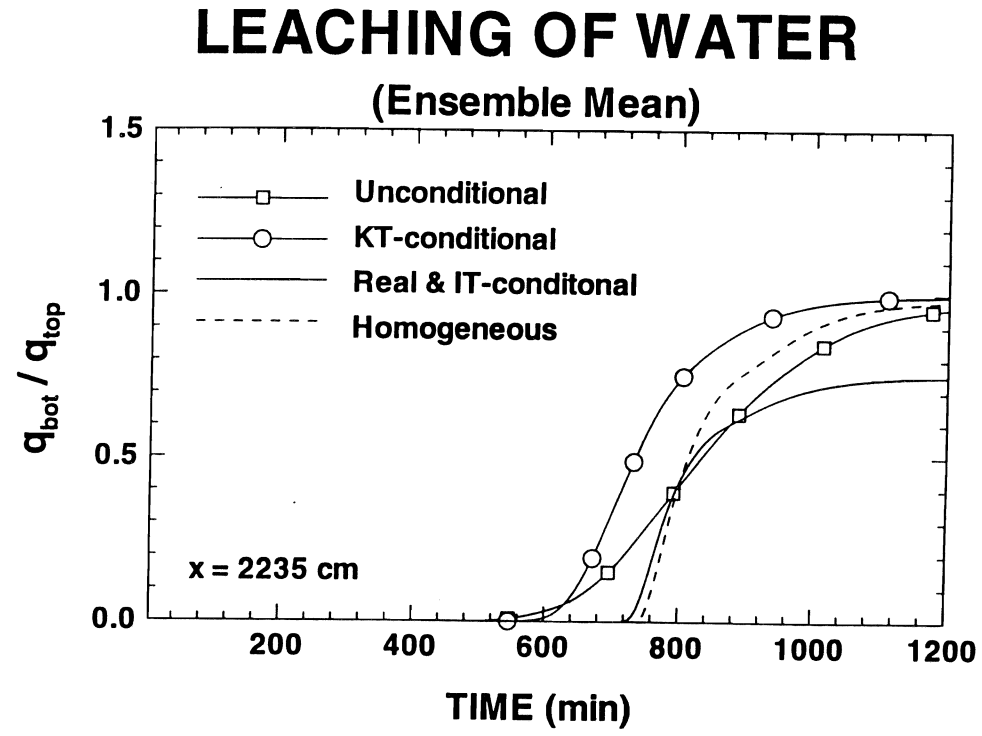

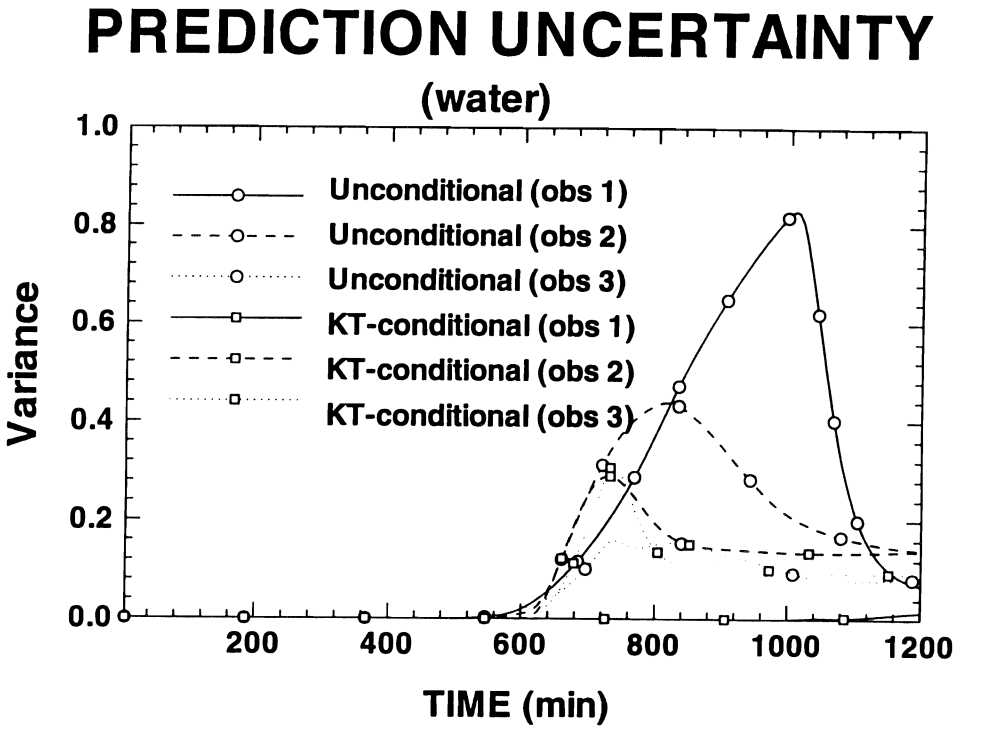

Figure 7c,d. Predicted leaching flux and prediction errors. (c) at point (x=2235 cm, z=-100 cm); (d) prediction errors.

Development of a Sensor for Rapid Determination of Soil Mineral Nitrogen

SHRINI K. UPADHYAHA AND DAVID SLAUGHTER
Department of Biological and Agricultural Engineering, Davis Campus

Summary

The objective of this investigation is to determine the possibility of rapidly sensing soil mineral-N content using the near infrared (NIR) reflectance technique. Particular emphasis is placed on data analysis techniques such as Partial Least Square (PLS) and Principal Component Analysis (PCA) to relate soil mineral-N to absorbance data obtained using NIR spectroscopy. Simulation studies were conducted to determine the ability of PLS and PCR techniques to determine whether these techniques could relate NIR spectral data to soil nitrate content in the presence of interfering effects and experimental noise. The simulation studies revealed that both PLS and PCR techniques are quite robust in predicting soil nitrtate contents, provided the calibration set included the same interfering effects. These techniques fail completely if the prediction set contains interfering effects which are not included in the calibration set. This result implies that a site-specific calibration is necessary for this technique to work successfully. Laboratory tests using Yolo loam and Capay clay soil samples as well as verification tests using field soils (Yolo loam and Capay clay) mixed with nitrogen fertilizer indicated that soil mineral-N contents can be determined reasonably well using the NIR technique. If one desires an unmistakable nitrate signature, it is preferable to use IR range where strong antisymmetric stretch vibration band, ν_3, and its second weaker overtone are located .

Key Words: Soil mineral-N, NIR, PLS, PCR

Project Objectives Addressed in 1995-1996

The specific objective of this investigation is to determine the possibility of rapidly sensing soil mineral-N content using the NIR reflectance technique. The long range goal of this study is to use the NIR technique to develop a portable, soil mineral-N sensor to determine soil mineral-N *in-situ*.

Research Plan and Procedures

Robustness of Analysis Techniques. NIR reflectance of soil samples in the range of 1800 to 2500 nm is not only influenced by the soil mineral-N content but also by soil moisture content, soil organic matter content, soil texture, and perhaps other chemical constituents which are unknown. Proper calibration to obtain soil mineral-N is very critical for successful application of this technique. The laboratory tests with artificially enriched soil samples (with mineral-N) simply indicate if NIR absorbance spectroscopy can detect soil mineral-N content. Since a real soil sample contains many constituents which may all influence spectral response, calibration using real soil samples is of critical importance. In essence, spectral response over many wavelengths (in our case 1800 nm to 2500 nm in increments of 2 nm) is obtained and unknown factors are intrinsically eliminated using techniques such as a PLS technique (i.e. 350 pieces of independent information in the 1800 to 2500 nm range are sufficient to eliminate up to 349 experimental error-free interfering factors, although in reality a minimization technique has to be utilized to eliminate perhaps a handful of interfering effects in the presence of experimental error). Several simulations were conducted to determine the robustness of the PCR and PLS techniques. The following simulation summarizes the main outcome of the simulation study. The NIR response corresponding to an eight component system (i.e. eight chemicals influence NIR response) was simulated in which the chemical of interest, say nitrate ions, was two orders of magnitude less sensitive compared to the one that responds readily to NIR such as water. A normally distributed error of the same order of magnitude as the response due to the chemical of interest was added to the NIR response to simulate experimental error. Calibration equations were established using both the PCR and PLS techniques. These calibration equations were used to predict the chemical of interest in new situations, which also contained responses due to the same eight chemicals. Finally, the calibration equation derived from simulated data containing the NIR response due to eight chemicals was used to predict the chemical of interest (say nitrate) from the simulated NIR response of a ten component system (eight previously considered and two additional chemicals). These two additional chemicals were not a part of the original calibration. The results of this study established the strength and weakness of both the PCR and PLS techniques.

Laboratory tests. Based on our preliminary study, we selected two soils [Yolo loam (31% sand, 52% silt, and 17% clay) and Capay clay(8% sand, 59% silt, and 33% clay)] and three sources of nitrogen (ammonium sulfate, calcium

nitrate, and ammonium nitrate) for conducting laboratory tests. Soil samples were brought from the field and oven dried at 105°C for 24 hours to reduce microbial activity. Then the soil samples were ground and sieved using a 30 mesh sieve. Soil belonging to different types of soil was divided into three batches for treating with different types of fertilizers (ammonium sulfate, calcium nitrate and ammonium nitrate). Each batch was further divided into eleven samples of which ten were mixed with predetermined amounts of one of the three fertilizers to yield soil samples with nitrogen contents of 10, 20, 30, ..., 100 ppm, respectively. The eleventh sample which had no added inorganic nitrogen was considered as the control. These soil samples were allowed to sit at room temperature for five days to allow added mineral-N to distribute evenly within the soil. After five days, the samples were dried and ground once again and stored in a freezer in zip-lock bags. Each of these samples was further subdivided into two experimental units one of which was sent to the DANR Analytical Laboratory for a complete soil analysis. These soil samples were analyzed for texture, NH_4-N, NO_3-N and total N. However, DANR laboratory results for NO_3^- did not agree well with the sample preparation technique (i.e. samples with higher added fertilizer did not show higher nitrate content). So a HPLC technique was used to analyze soil samples under the guidance of Dr. Sham Goyal, Agronomy and Range Science Specialist at the UC Davis campus. Sixty-six experimental units (two soils x three fertilizer types x eleven nitrogen levels) were further subdivided to create ten subsamples. NIR responses from ten subsamples were averaged to obtain a mean response with much less variability.

All 660 subsamples were analyzed using the NIR technique over 1100 to 2500 nm wavelengths using a NIR systems spectrophotometer (model 6500). Soil samples were placed in the spectrophotometer and spectral responses were obtained by a completely automated system. A PLS technique was used to analyze the NIR absorbance data.

NIR Tests with Field Soil. In the second phase of this study, calibration with field soil samples were conducted. A 15m X 16.5 m plot was marked off in a Yolo loam field on the UC Davis campus. The plot was divided into ten 1.65m strips and an increasing amount of calcium nitrate fertilizer was sprayed to each successive strip to produce different nitrate concentrations. The first strip received zero pass of the sprayer, the second strip received one pass, ..., and the tenth strip received nine passes. Following the application of the fertilizer, the strips were rotary tilled to mix the fertilizer with soil. Five soil samples were obtained from each strip after five days. The soil samples were sieved, oven dried, and stored in a freezer until they were tested. Each soil sample was divided into ten subsamples and tested with the NIR spectrophotometer. After the NIR test all subsamples corresponding to a sample were mixed together and a 2 g sample was removed to determine the nitrate content by the HPLC method. A similar procedure was used for the soil samples from the Capay clay field except for an additional step as soon as the samples were brought to the laboratory. The soil samples were sieved to remove large clods, and 400 g of soil from each sample was mixed with distilled water and allowed to sit for two days at room temperature. Then the sample

was dried, ground, and mixed throughly and stored in a zip-lock bag in a freezer. This addional step was introduced to ascertain uniform distribution of mineral-N in the soil. The NIR absorbance spectra were obtained for all thousand subsamples (500 Capay clay and 500 Yolo loam) using the spetrophotometer.

Results and Discussion

Robustness of Analysis Techniques. Figure 1 shows the ability of the PCR technique to predict NO_3^- concentrations from an eight component system using 20 wavelengths even when the NIR response due to NO_3^- is two orders of magnitude smaller than the largest chemical constituent. The coefficient of multiple determination was very high (0.95) and the standard error was about 7 ppm. Figure 2 shows the predictive ability of the technique when 100 different data points were used to cross validate the model. However, the technique completely failed when an attempt was made to predict NO_3^- concentration in a ten component system when the calibration set derived from the eight component system shown in Fig. 1 was used for prediction purposes (Fig. 3). These results clearly indicate that prediction is good only on systems with similar composition. This implies that site-specific calibration is necessary to successfully use this technique. Figures 4 through 6 show similar results when a PLS technique was used. Since the PLS algorithm is somewhat simpler and is widely available on NIR machines, we decided to use the PLS technique to analyze all our spectral data.

Laboratory Test Results. Figures 7 through 12 show the results of laboratory calibration obtained using two different soils and three different sources of fertilizers. Note each data point on these curves represents the average response of ten subsamples. Results are extremely good for all cases with a standard error of about six ppm when calcium nitrate was used as the nitrate source and less than 2.5 ppm for all other cases. Figures 13 and 14 show the effect of pooling two sources of nitrogen in a given soil. The coefficient of multiple determination decreased and the standard error increased. Figures 15 and 16 show the effect of pooling across soil types. The results were very good for ammonium nitrate but not so good for calcium nitrate. These results further confirm that this technique is applicable for a given soil type only and site-specific calibration is necessary.

Although the laboratory results were very encouraging, we had to confirm that what we considered as nitrate response was not actually due to ammonium in the ammonium nitrate and calcium in the calcium nitrate (or more likely calcium carbonate, which could have formed spontaneously). Since ammonium sulfate responds in the NIR region, the ammonium theory is quite credible. To verify these possibilities, we decided to study the NIR response of sodium nitrate (monovalent), calcium nitrate (divalent), and aluminum nitrate (trivalent). Our discussion with several analytical chemists (Ms. Alla Kloss, Analytical Chemist, and Dr. Ron Fawcett, Professor, Chemistry Dept.) on the UC Davis campus indicated that we should use solvents which have very little NIR response in the 1800 - 2300 nm range and that salts of interest should

dissolve readily in the solvents selected. Based on these criteria, dimethyl sulfoxide(DMSO), acetone, and methanol were selected as solvents. The NIR transmission spectra of the three nitrate salts in these three solvents revealed that there was a strong absorption peak at low nitrate concentrations at 1942 ppm. When a high concentration of sodium nitrate was used, the absorption peak disappeared. When the test was repeated with 0,50,100,150, and 250 ppm nitrate concentration in DMSO using sodium nitrate, the absorption peak was observed at 1942 nm. However, this peak tended to be unstable. Further investigation revealed to us that nitrate ion is polar and exhibits four vibration modes in the IR region (Vogt and Finlayson-Pitts, 1994). These four vibration modes are symmetric stretch, ν_1, at 9524 nm, out-of-plane bending, ν_2, at 12034 nm, antisymmetric stretch, ν_3, at 7194 nm, and in-plane bending, ν_4, at 13889 nm. Of these four, ν_1 is IR inactive and is usually very weak. The antisymmetric stretch, ν_3, is usually very strong. In a typical IR spectra strong peak due to ν_3, weak peaks due to ν_1 and ν_2, and certain overtones such as $(\nu_1+\nu_4)$ at 5650 nm, $(\nu_1+\nu_3)$ at 4098 nm, and $2\nu_3$ at 3671 nm are clearly visible. The third overtone of $(\nu_1+\nu_4)$ lies at 1941.5 nm! In the range of 1800 to 2300 nm, the following overtones are likely - second overtones of $(\nu_1+\nu_3)$, $(\nu_2+\nu_3)$, $(\nu_1+\nu_2+\nu_4)$, and third overtones of $(\nu_1+\nu_2)$, $(\nu_1+\nu_4)$, $(\nu_2+\nu_4)$. Unfortunately, many other salts such as carbonates also have overtone absorption peaks in the same range. As we have demonstrated, the PLS or the PCR technique extracts the nitrate information, provided proper calibration technique is followed.

Field Soil Test Results. Figure 17 shows a plot of HPLC-determined nitrate values versus NIR-predicted nitrate values obtained from a calibration set using the PLS technique for the Yolo loam soil. Figure 18 is a cross validation set obtained using the calibration set shown in Fig. 16. The results are reasonably good but not as good as the laboratory test results. Figures 19 and 20 are similar plots for the Capay clay soil. The results are slightly better in this case, perhaps reflecting the improved sample preparation technique for the laboratory nitrate analysis. Note that in Figs. 19 and 20 we have shown only the 0 to 100 ppm range for nitrate concentration, although the full set contained nitrate values up to 300 ppm. We selected the 0 to 100 ppm range, since it is the range of practical interest. The standard error of prediction was about 8 ppm for the Yolo loam soil and 9.4 ppm for the Capay soil.

Additional work. We are currently conducting some additional work in the mid NIR and far NIR ranges to determine whether it is possible to use ν_3 or $2\nu_3$ as an unmistakable signature of nitrate.

References

Vogt, R. and B. J. Finlayson-Pitts. 1994. A diffuse reflectance Infrared Fourier Transform Spectroscopic (DRIFTS) Study of the Surface Reaction of NaCl with Gaseous NO_2 and HNO_3. J. Phys. Chem. 98:3747-3755.

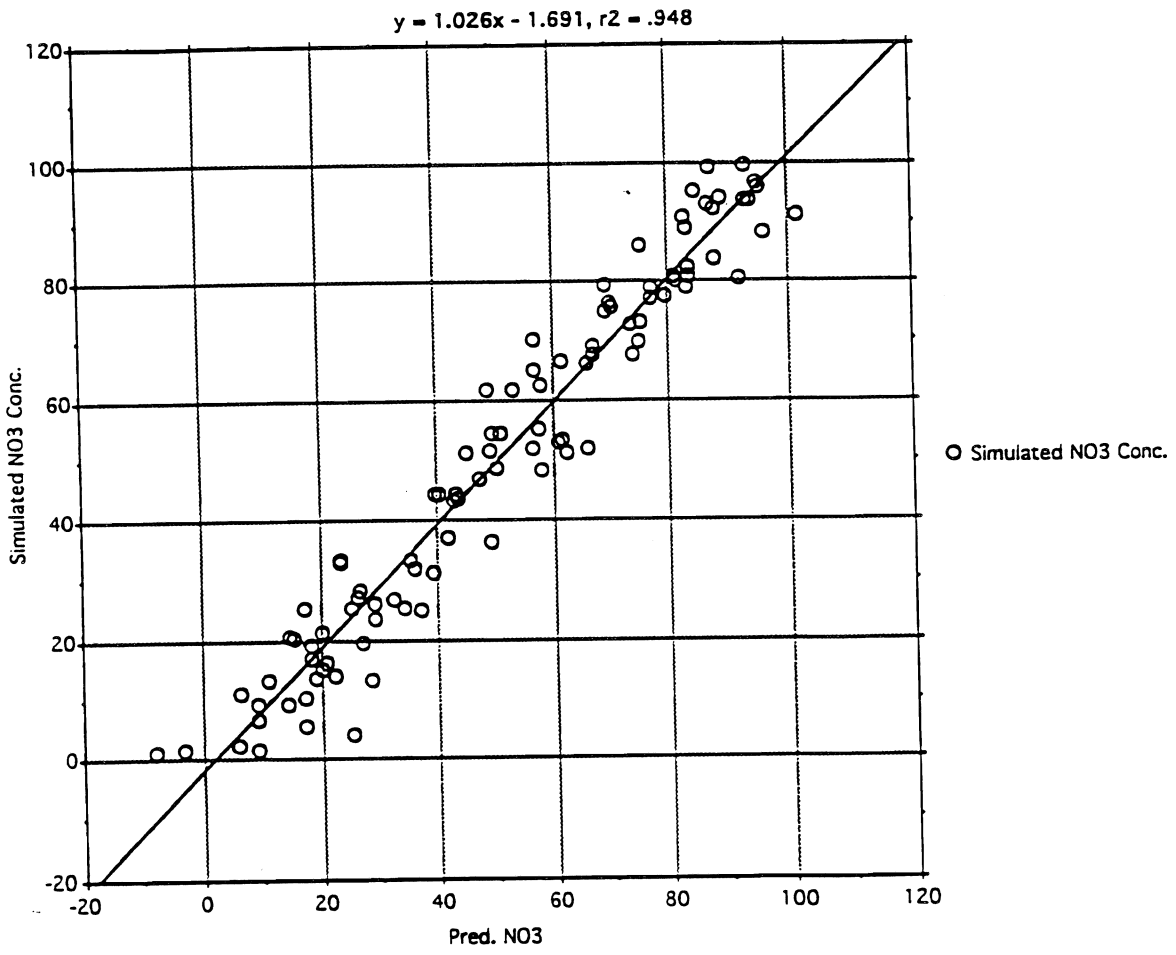

Figure 1. Predicted versus simulated nitrate concentrations in an eight component system when spectral responses at 20 wavelengths were used to develop a calibration equation using a Principal Component Regression (PCR) technique.

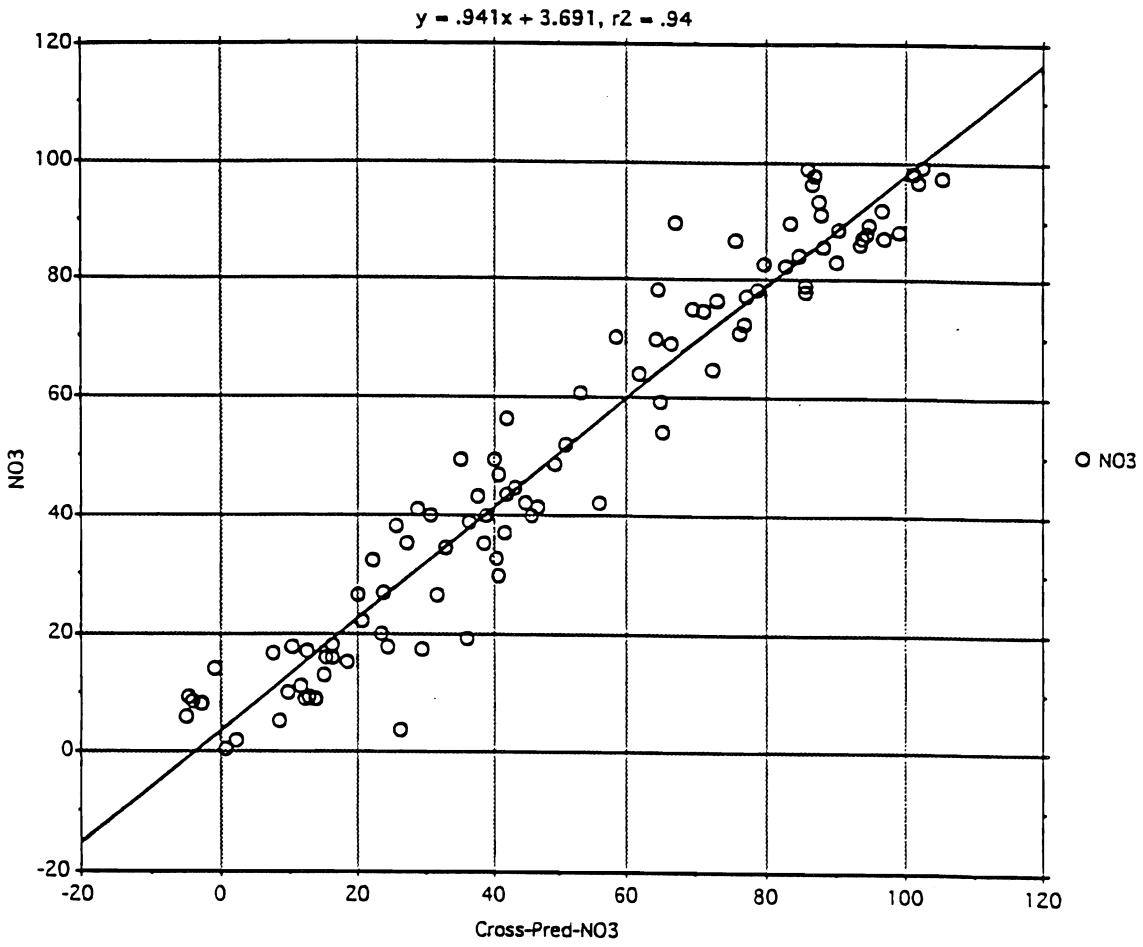

Figure 2. Predicted versus simulated nitrate concentrations in an eight component system when a calibration equation, derived from the PCR technique and based on the spectral responses at 20 wavelengths of the same eight component system, was used to cross validate the model with different data points.

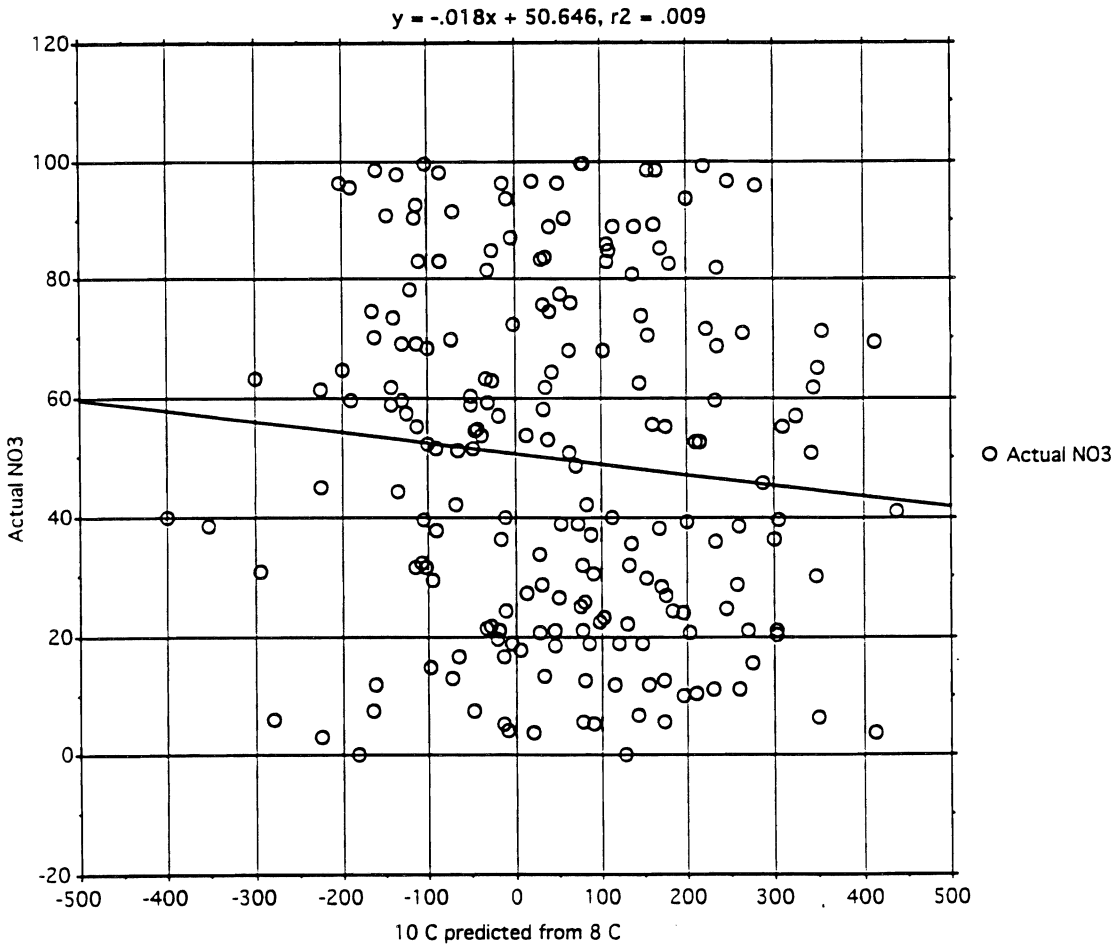

Figure 3. Predicted versus simulated nitrate concentrations in a ten component system when a calibration equation, derived from the PCR technique and based on the spectral responses at 20 wavelengths of an eight component system, was used to cross validate the model. The technique failed completely in this case.

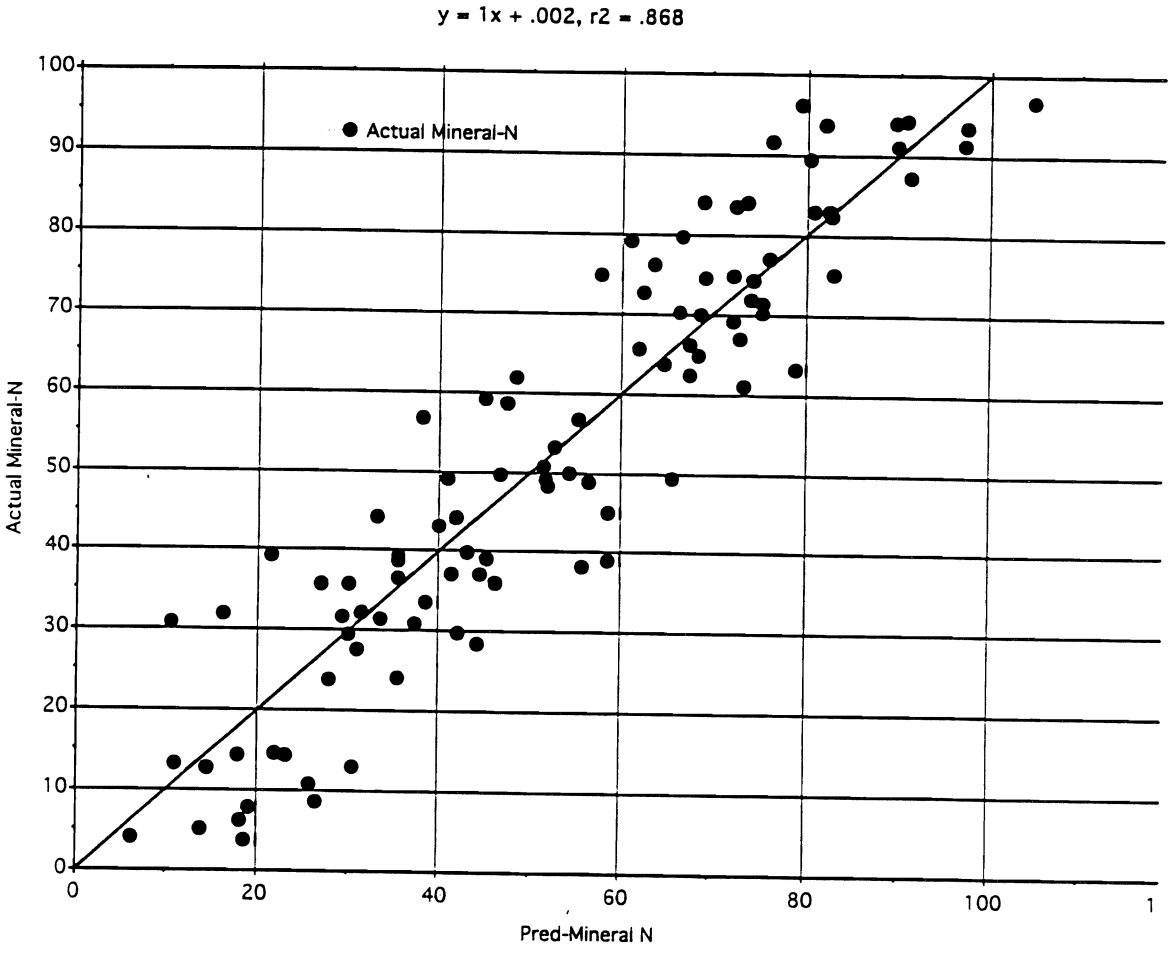

Figure 4. Predicted versus simulated nitrate concentrations in an eight component system when spectral responses at 20 wavelengths were used to develop a calibration equation using a Partial Least Square (PLS) technique.

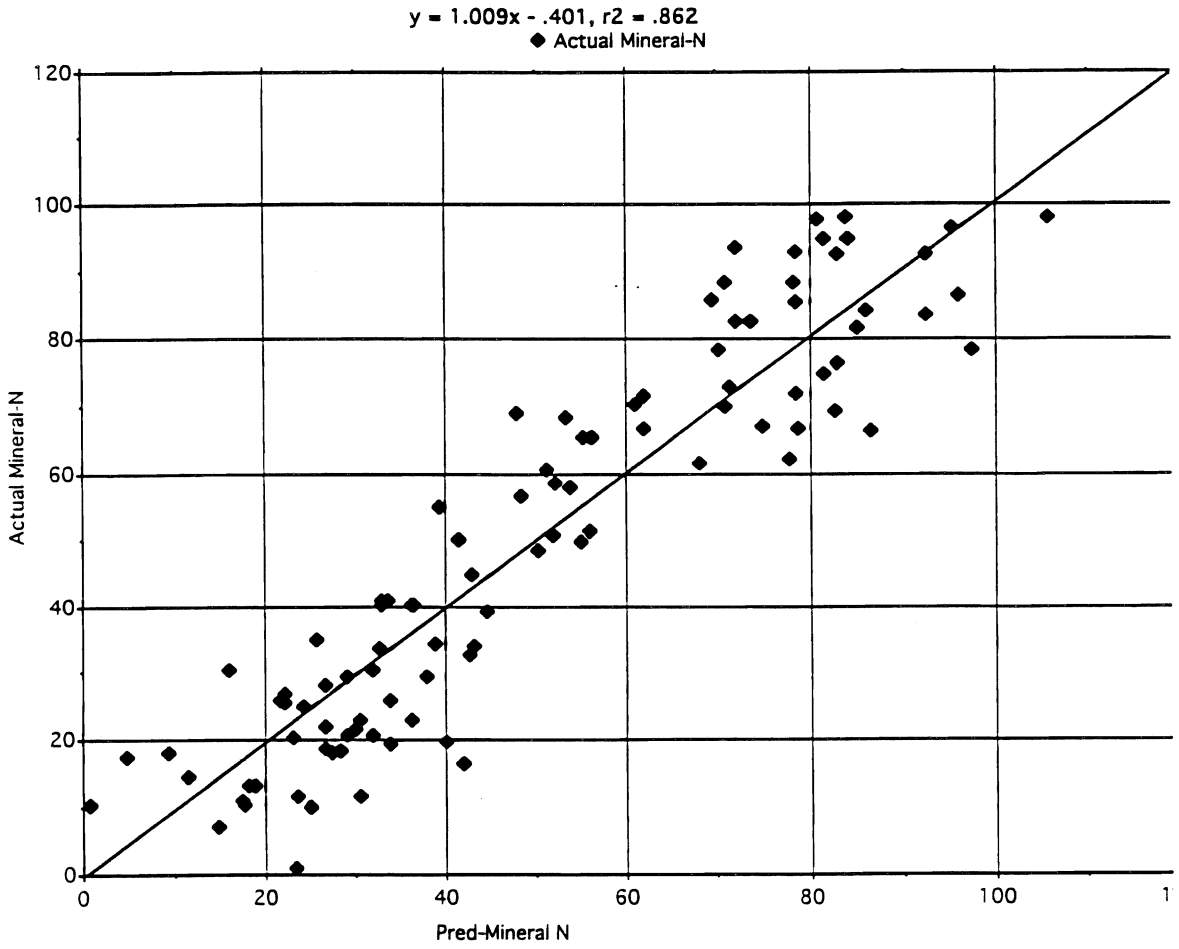

Figure 5. Predicted versus simulated nitrate concentrations in an eight component system when a calibration equation, derived from the PLS technique and based on the spectral responses at 20 wavelengths of the same eight component system, was used to cross validate the model with different data points.

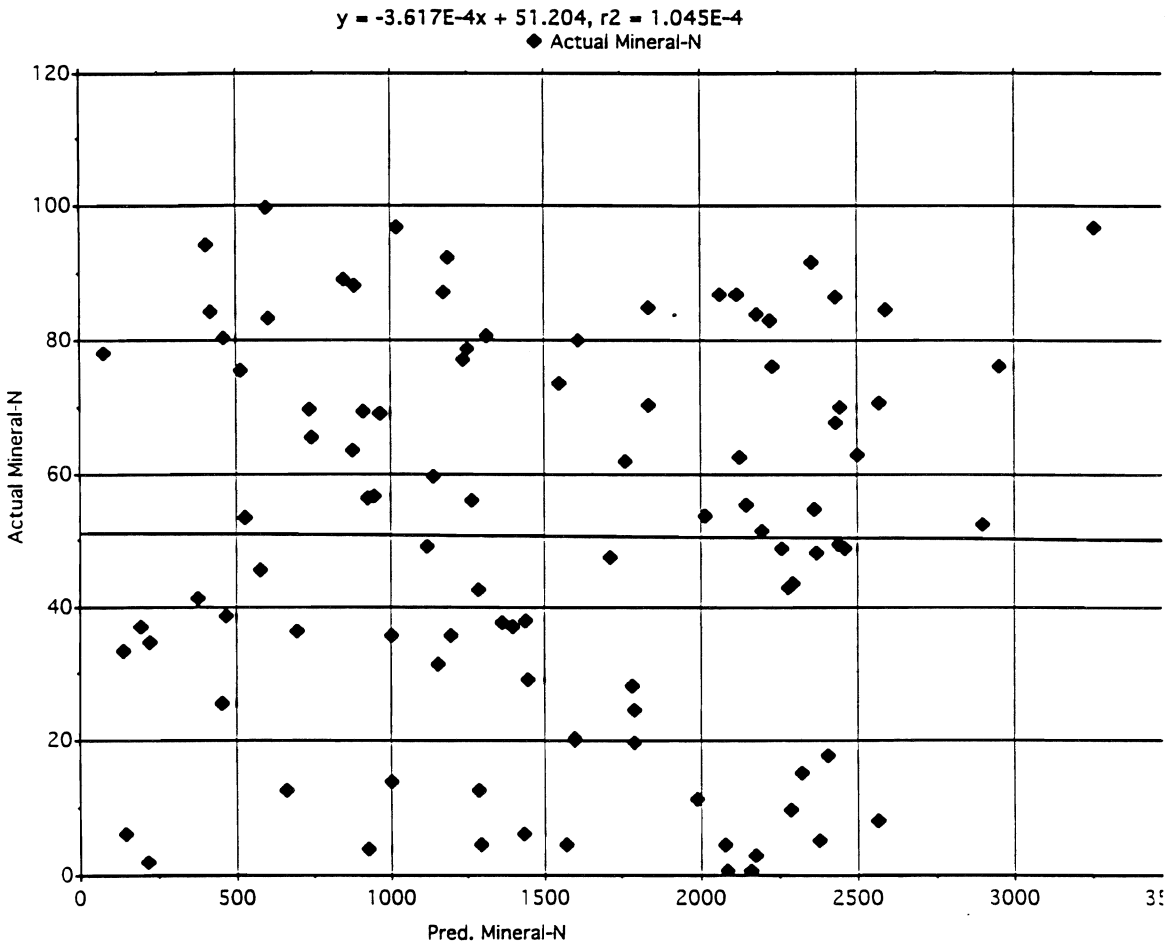

Figure 6. Predicted versus simulated nitrate concentrations in a ten component system when a calibration equation, derived from the PLS technique and based on the spectral responses at 20 wavelengths of an eight component system, was used to cross validate the model. The technique failed completely in this case.

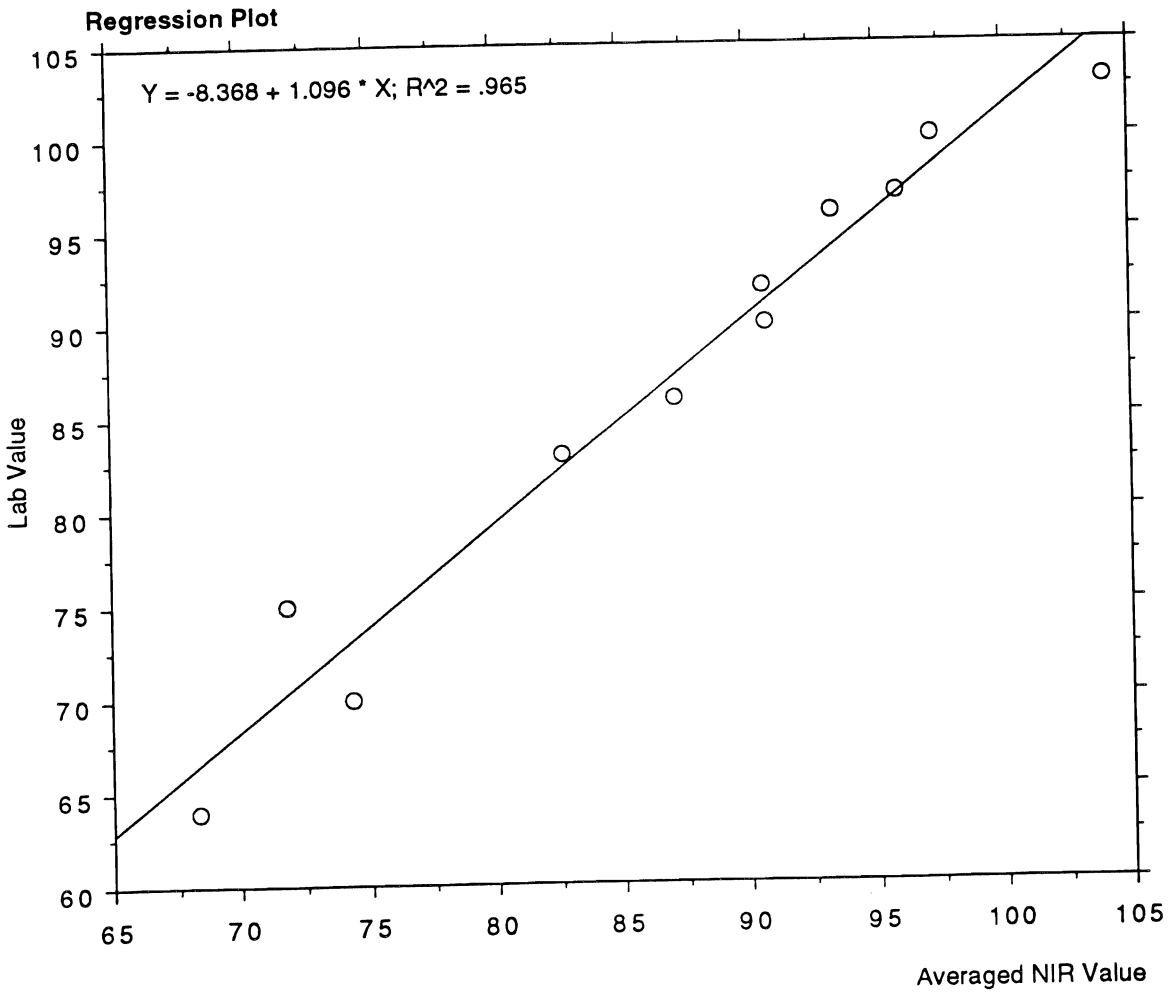

Figure 7. Predicted versus measured nitrate concentrations in a Yolo loam soil when ammonium nitrate was used as a source of mineral-N to spike soil and a PLS regression was used to develop a calibration equation. Each data point is an average of 10 subsamples. The coefficient of multiple determination was 0.965 and the standard error was 2.5 ppm.

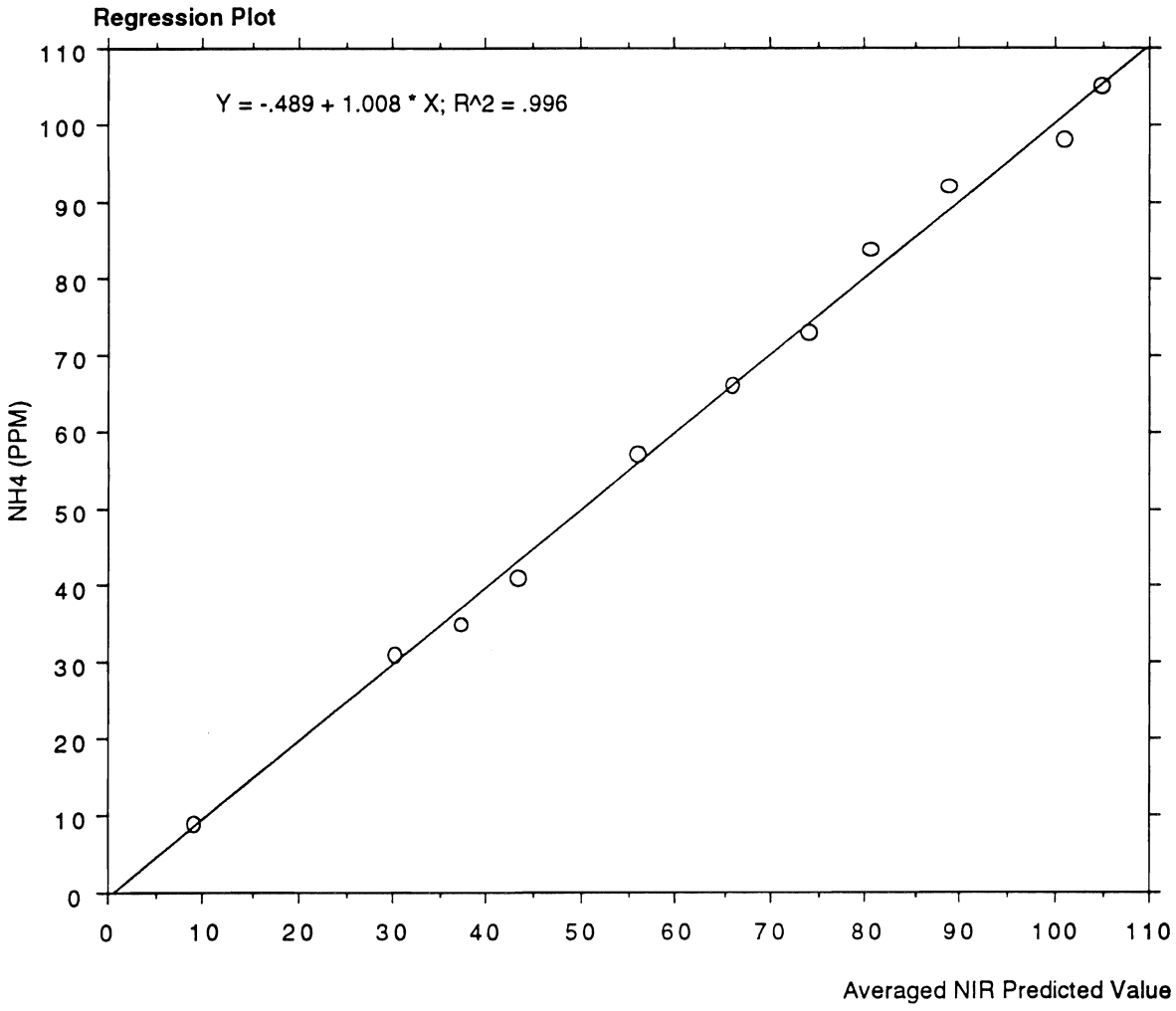

Figure 8. Predicted versus measured ammonium concentrations in a Yolo loam soil when ammonium sulfate was used as a source of mineral-N to spike soil and a PLS regression was used to develop a calibration equation. Each data point is an average of 10 subsamples. The coefficient of multiple determination was 0.996 and the standard error was 2 ppm.

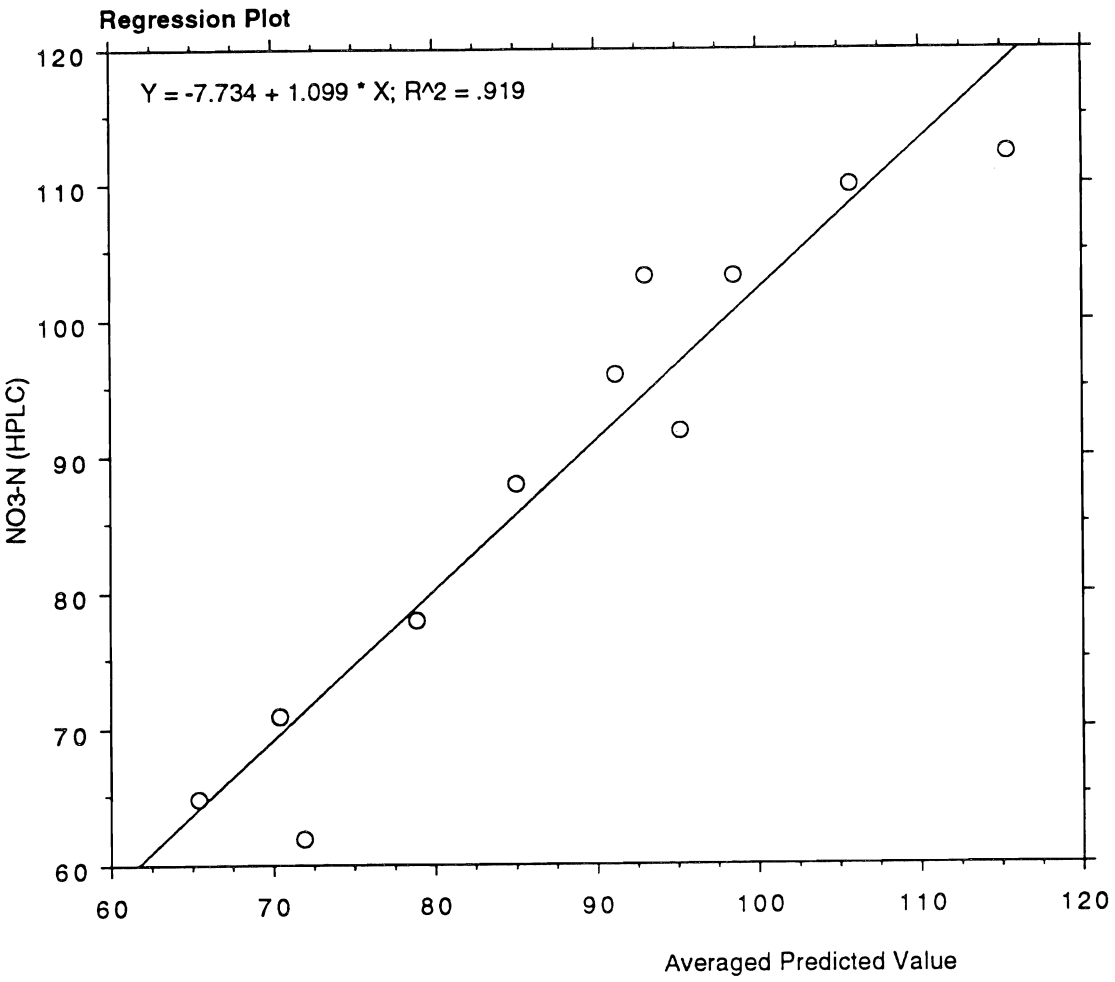

Figure 9. Predicted versus measured nitrate concentrations in a Yolo loam soil when calcium nitrate was used as a source of mineral-N to spike soil and a PLS regression was used to develop a calibration equation. Each data point is an average of 10 subsamples. The coefficient of multiple determination was 0.919 and the standard error was 5.4 ppm.

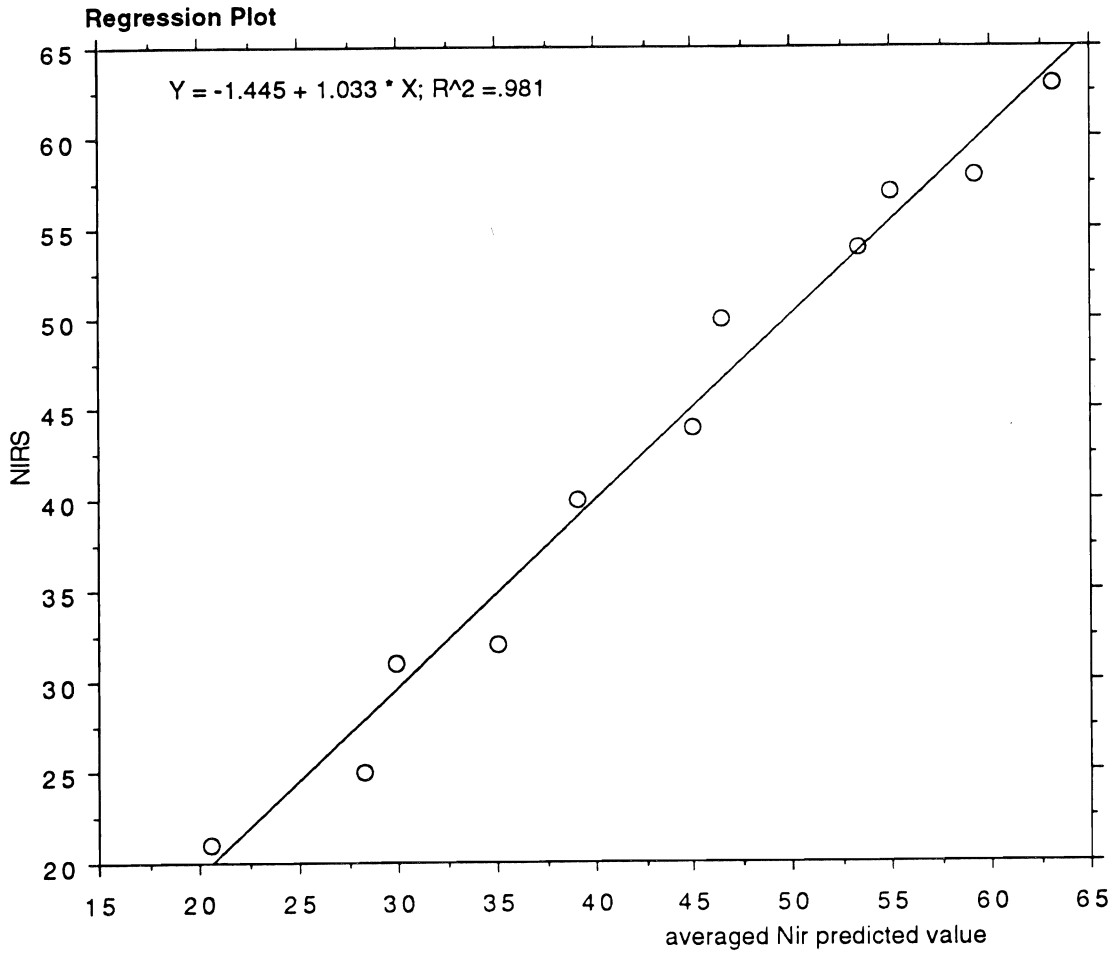

Figure 10. Predicted versus measured nitrate concentrations in a Capay clay soil when ammonium nitrate was used as a source of mineral-N to spike soil and a PLS regression was used to develop a calibration equation. Each data point is an average of 10 subsamples. The coefficient of multiple determination was 0.981 and the standard error was 2 ppm.

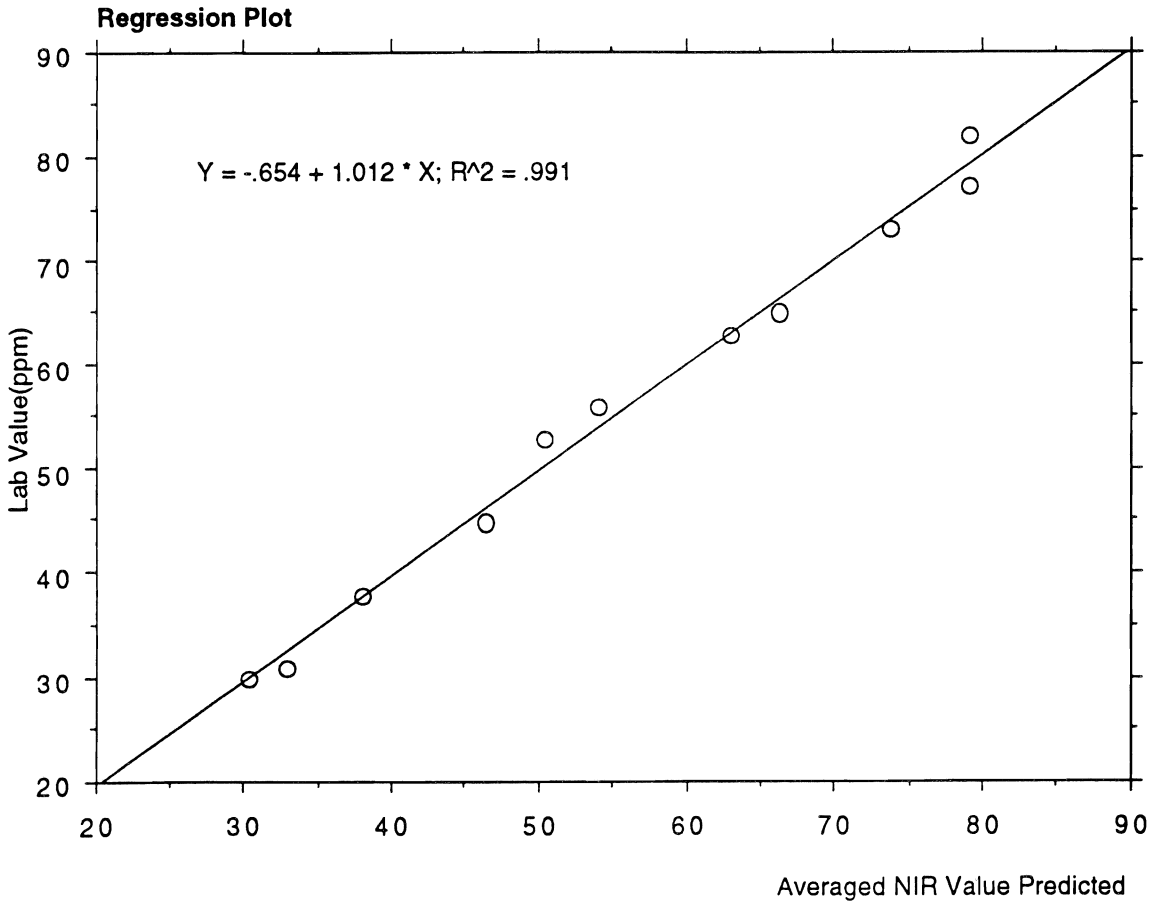

Figure 11. Predicted versus measured ammonium concentrations in a Capay clay soil when ammonium sulfate was used as a source of mineral-N to spike soil and a PLS regression was used to develop a calibration equation. Each data point is an average of 10 subsamples. The coefficient of multiple determination was 0.991 and the standard error was 1.8 ppm.

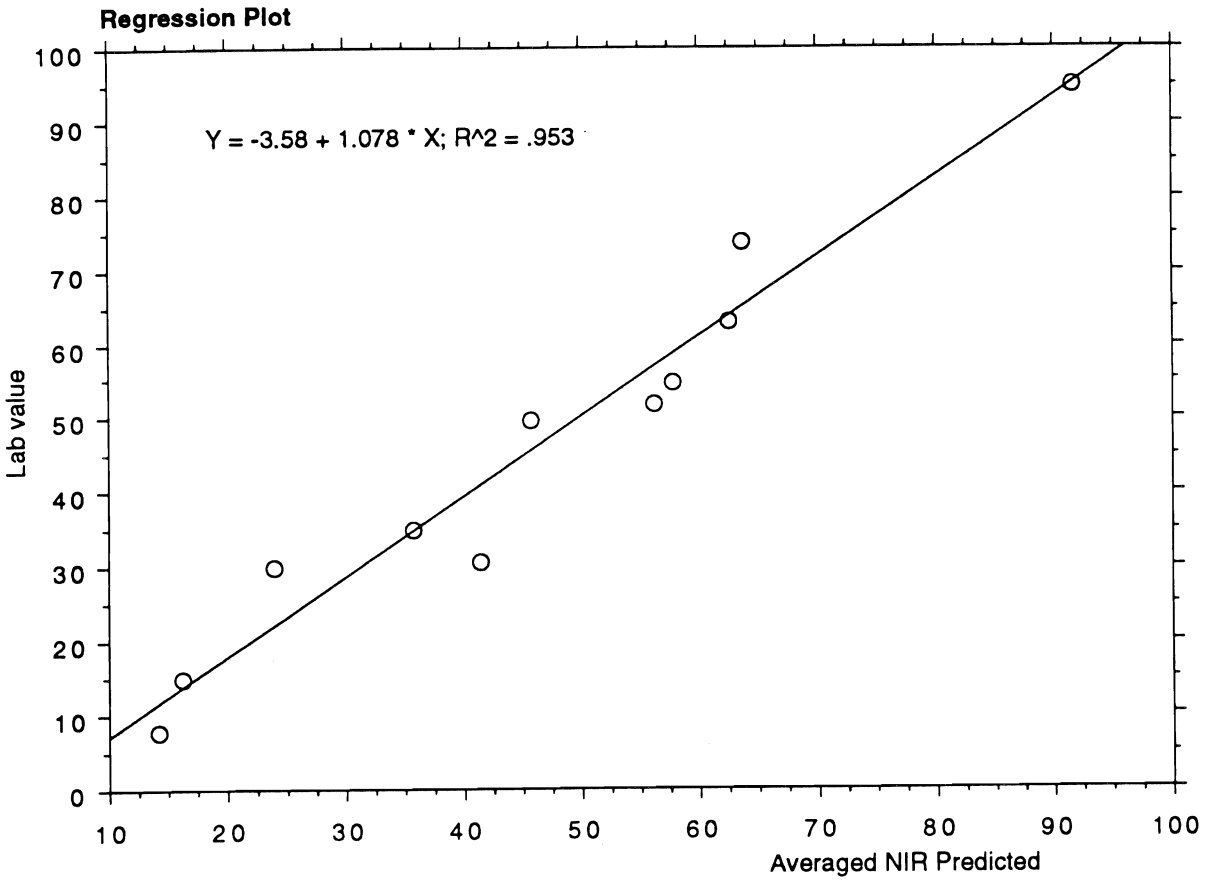

Figure 12. Predicted versus measured nitrate concentrations in a Yolo loam soil when ammonium nitrate was used as a source of mineral-N to spike soil and a PLS regression was used to develop a calibration equation. Each data point is an average of 10 subsamples. The coefficient of multiple determination was 0.95 and the standard error was 6 ppm.

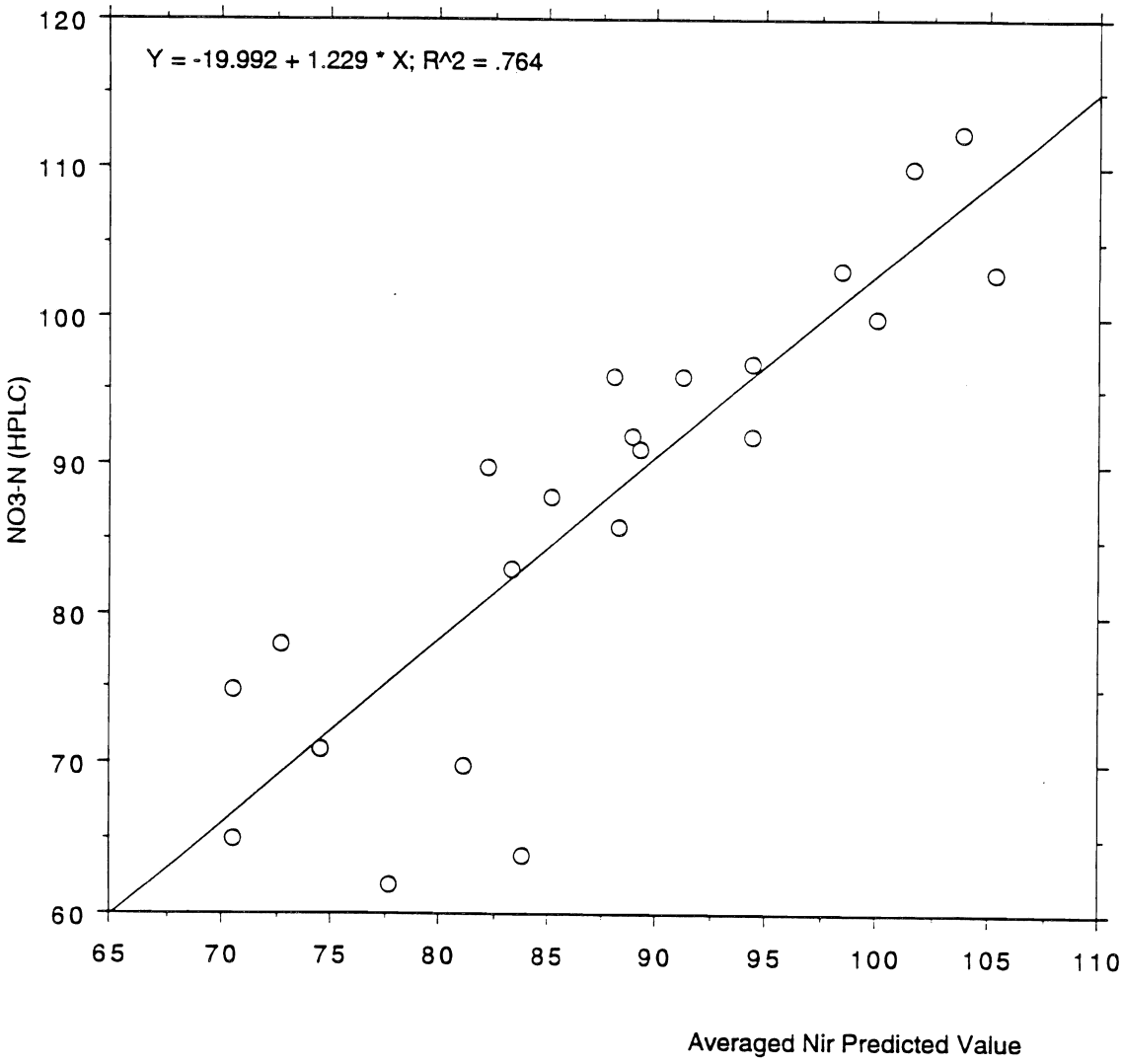

Figure 13. Predicted versus measured nitrate concentrations in a Yolo loam soil when data from soil spiked with both calcium nitrate and ammonium nitrate were pooled together and a PLS regression was used to develop a calibration equation. Each data point is an average of 10 subsamples. The coefficient of multiple determination was 0.764 and the standard error was 7.4 ppm.

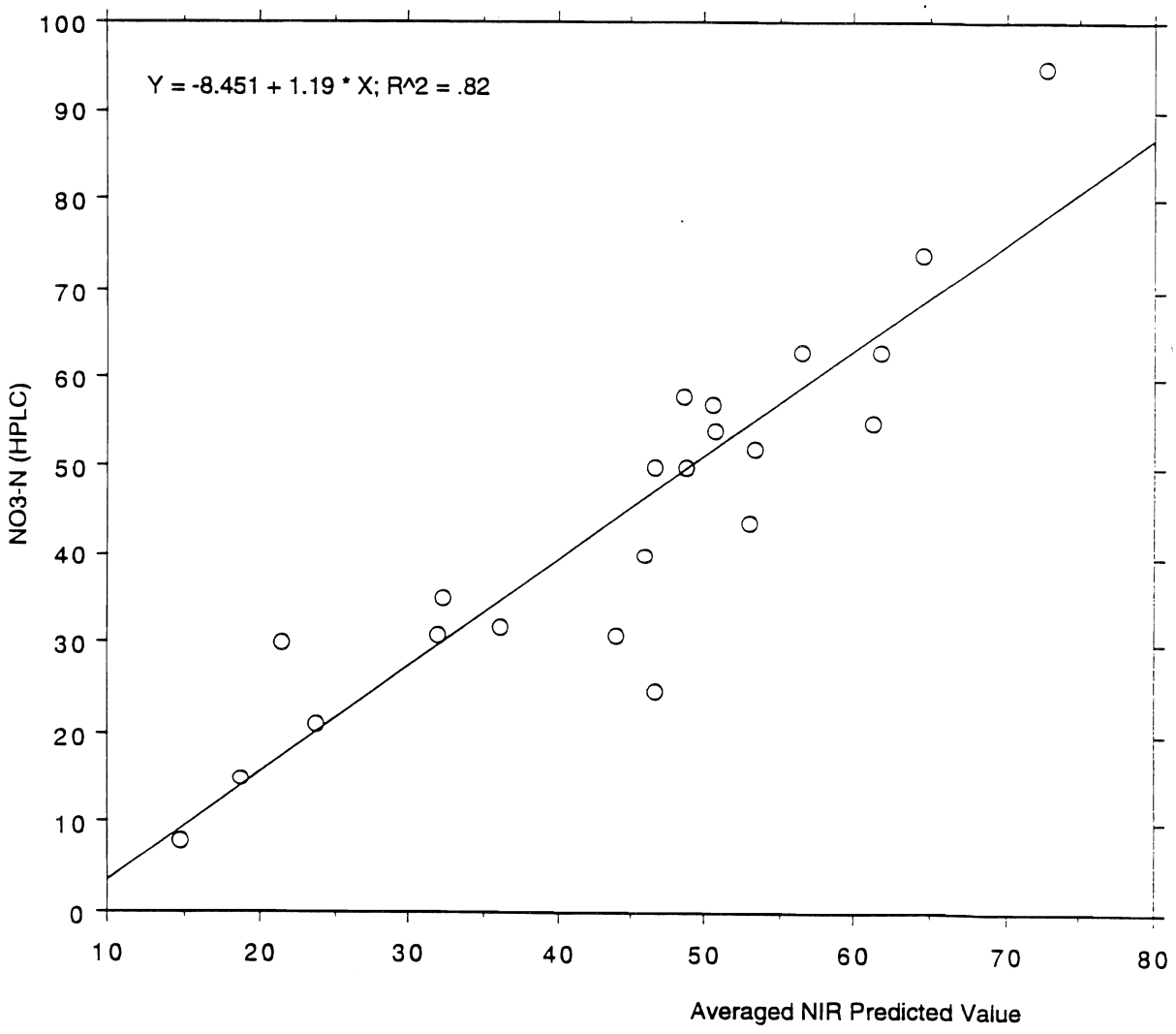

Figure 14. Predicted versus measured nitrate concentrations in a Capay clay soil when data from soil spiked with both calcium nitrate and ammonium nitrate were pooled together and a PLS regression was used to develop a calibration equation. Each data point is an average of 10 subsamples. The coefficient of multiple determination was 0.820 and the standard error was 8.9 ppm.

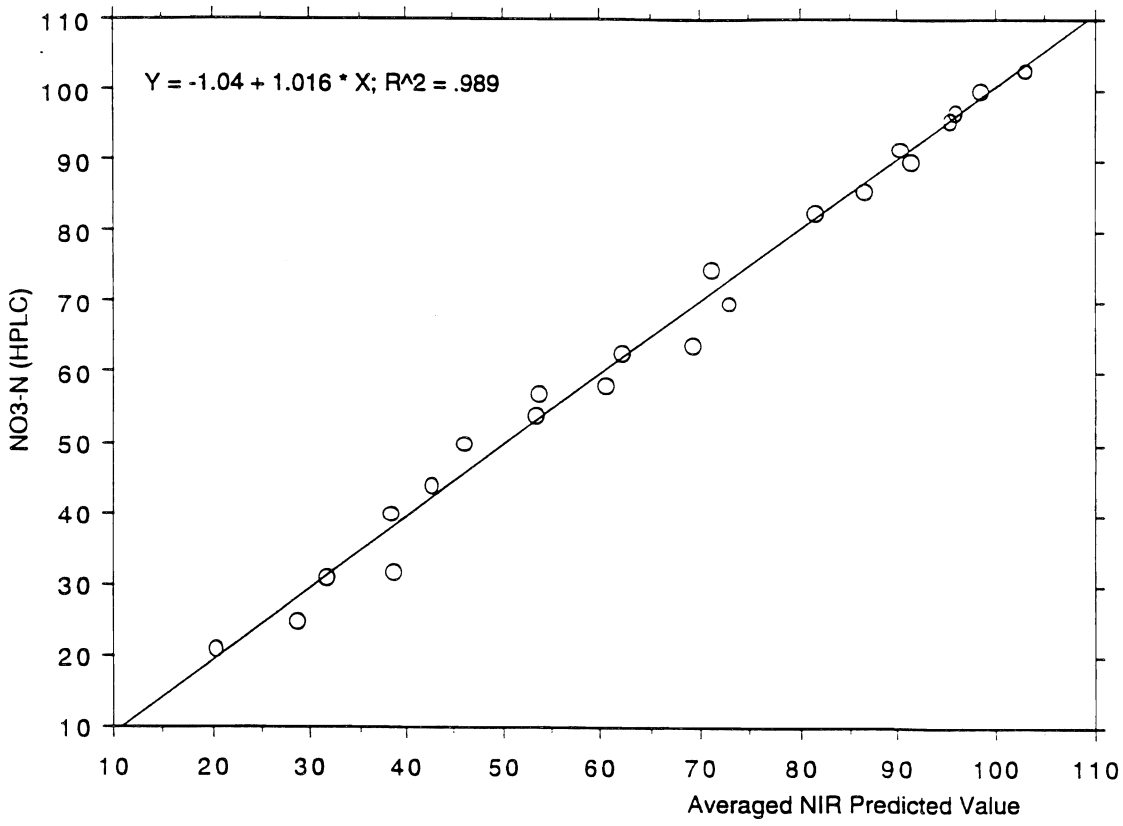

Figure 15. Predicted versus measured nitrate concentrations when data from soil spiked with ammonium nitrate in both a Yolo loam and a Capay clay soil were pooled together and a PLS regression was used to develop a calibration equation. Each data point is an average of 10 subsamples. The coefficient of multiple determination was 0.989 and the standard error was 2.8 ppm.

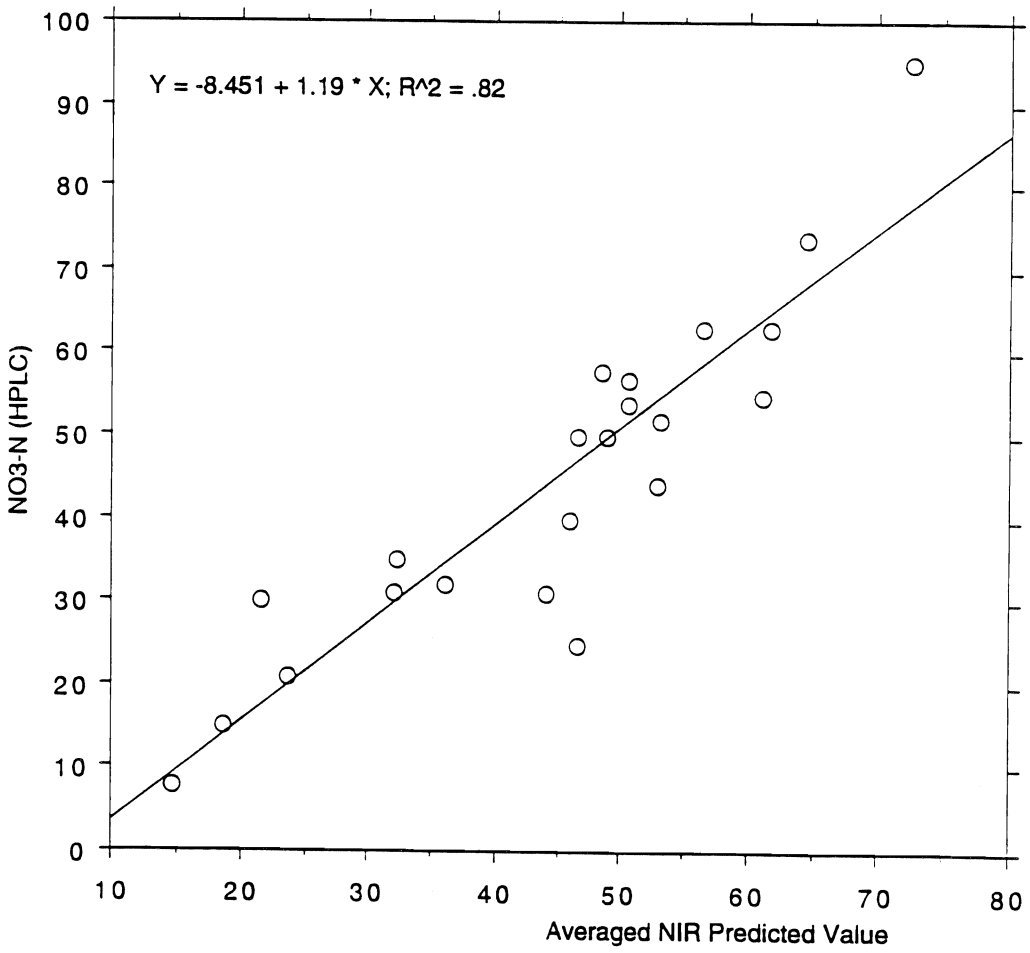

Figure 16. Predicted versus measured nitrate concentrations when data from soil spiked with calcium nitrate in both a Yolo loam and a Capay clay soil were pooled together and a PLS regression was used to develop a calibration equation. Each data point is an average of 10 subsamples. The coefficient of multiple determination was 0.82 and the standard error was 8.9 ppm.

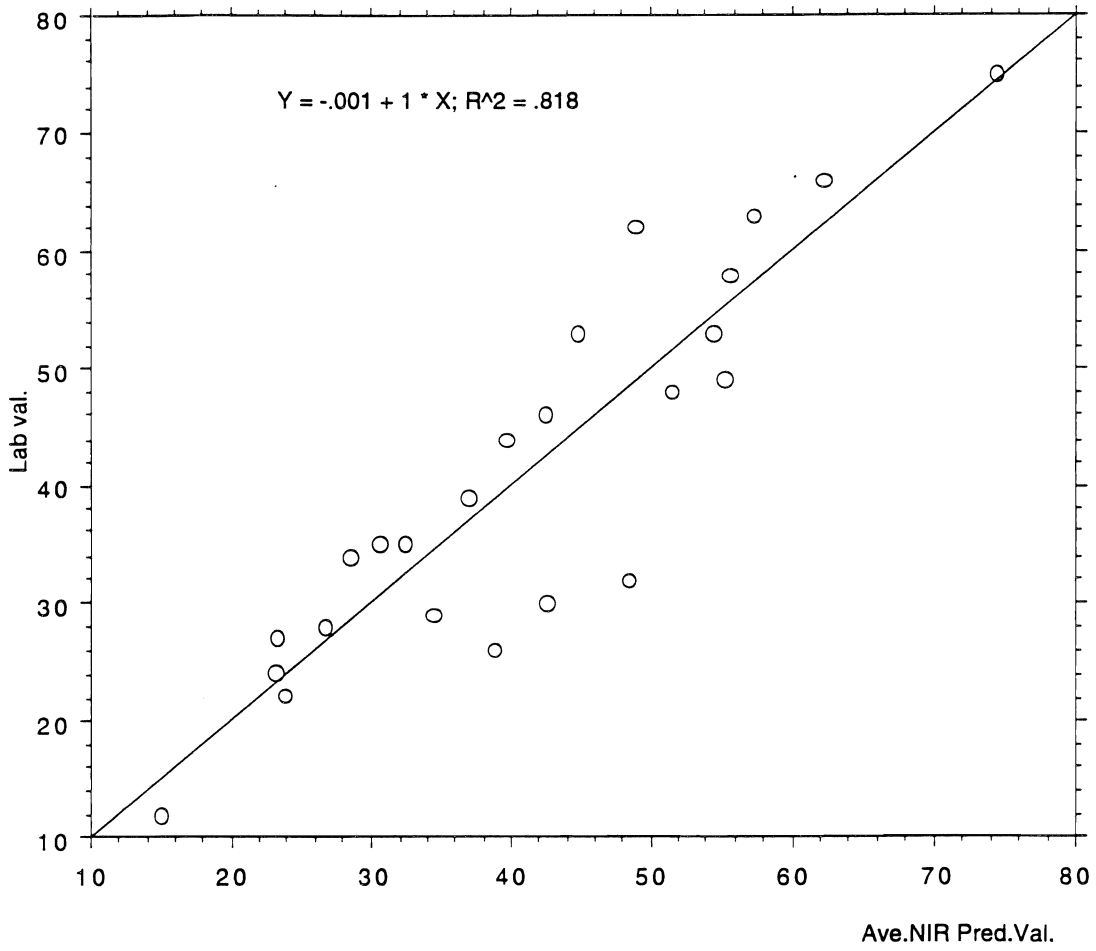

Figure 17. Predicted versus measured nitrate concentrations in a Yolo loam soil when calcium nitrate was used as a source of mineral-N in the field and a PLS regression was used to develop a calibration equation. Each data point is an average of ten subsamples. The coefficient of multiple determination was 0.818 and the standard error was 7 ppm.

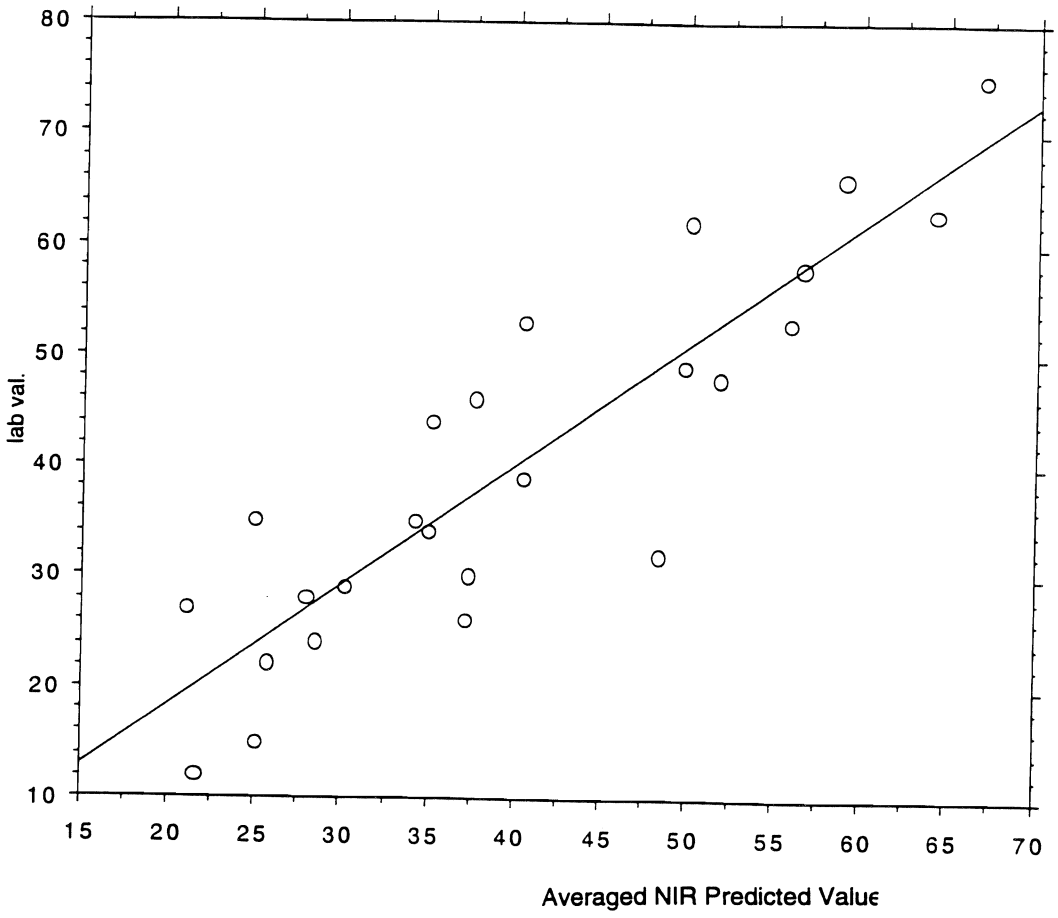

Figure 18. Predicted versus measured nitrate concentrations in a Yolo loam soil when calcium nitrate was used as a source of mineral-N in the field and cross validation was accomplished using the calibration equation developed employing a PLS regression shown in Figure 17. Each data point is an average of ten subsamples. The coefficient of multiple determination was 0.785 and the standard error was 7.7 ppm.

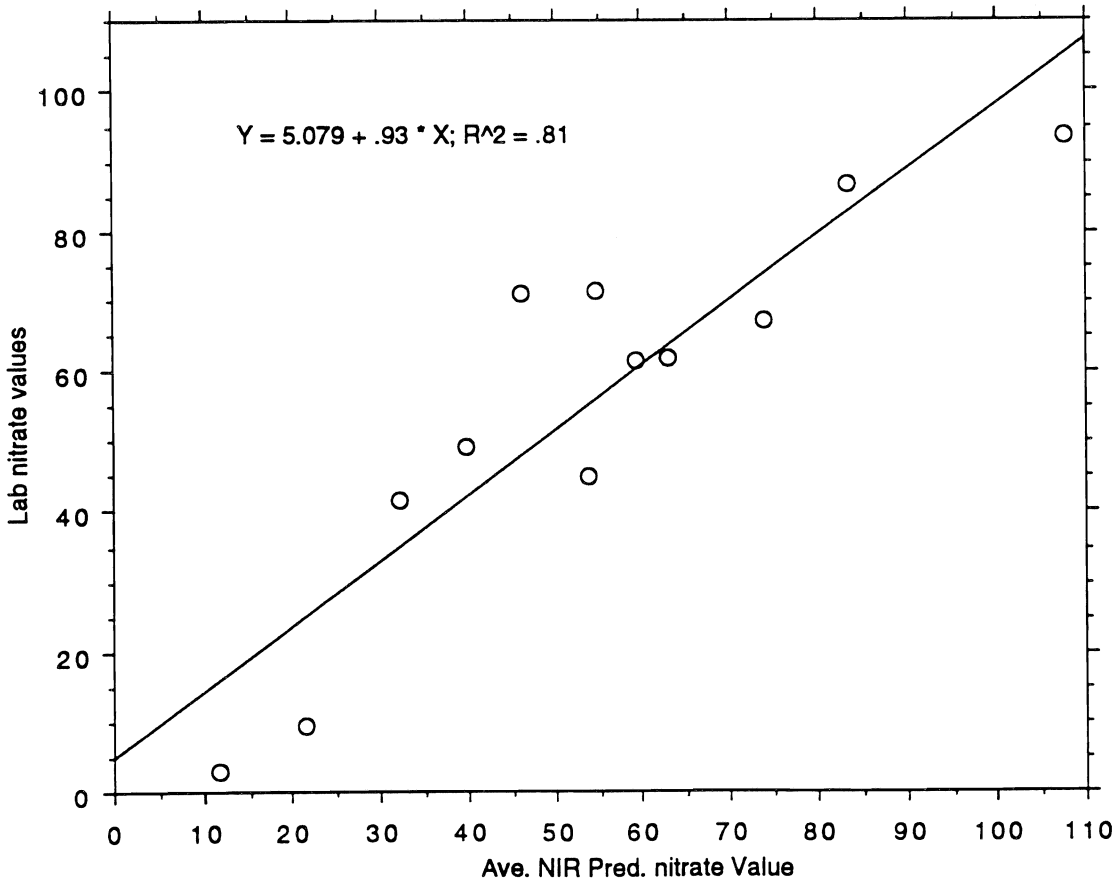

Figure 19. Predicted versus measured nitrate concentrations in a Capay clay soil when calcium nitrate was used as a source of mineral-N in the field and a PLS regression was used to develop a calibration equation. Each data point is an average of ten subsamples. The coefficient of multiple determination was 0.81 and the standard error was 12.6 ppm.

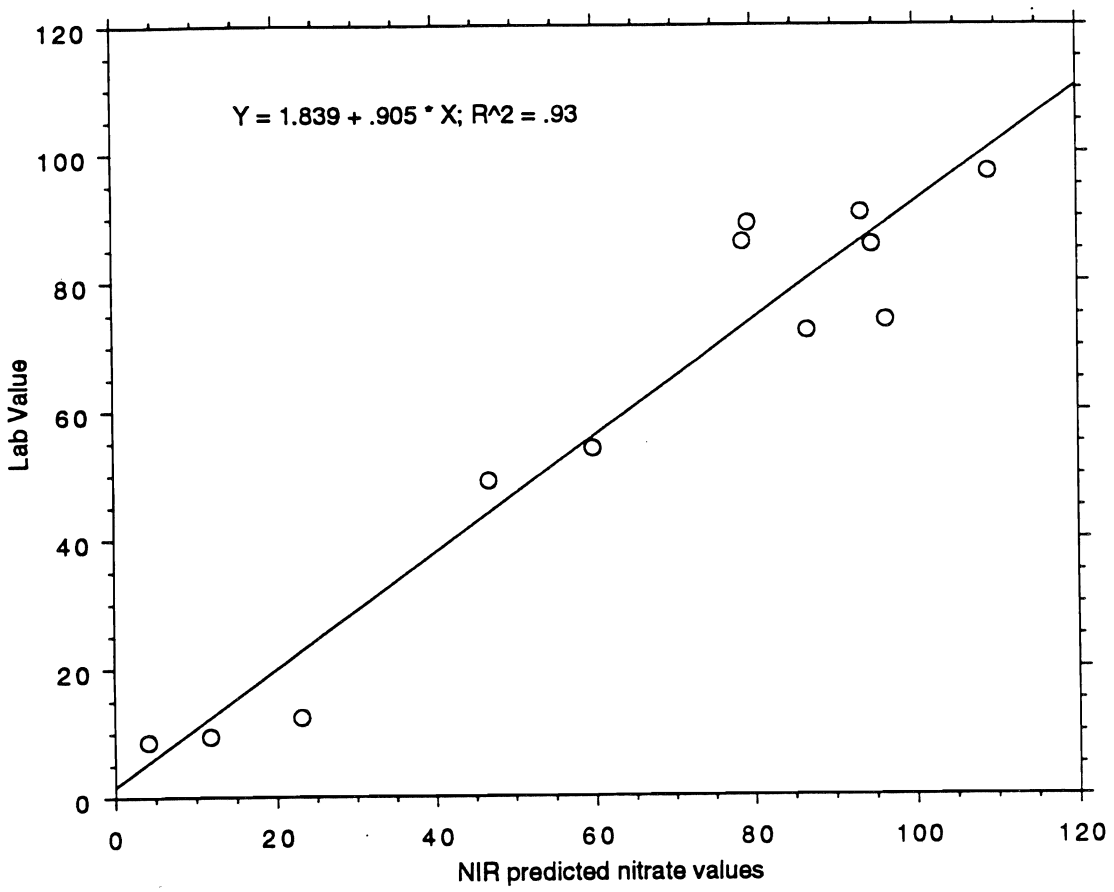

Figure 20. Predicted versus measured nitrate concentrations in a Capay clay soil when calcium nitrate was used as a source of mineral-N in the field and cross validation was accomplished using the calibration equation developed employing a PLS regression shown in Figure 19. Each data point is an average of ten subsamples. The coefficient of multiple determination was 0.93 and the standard error was 9.4 ppm.

Composition and Distribution of Fugitive Dust from Central Valley Crop Management Systems

HEIKE CLAUSNITZER, MICHAEL J. SINGER AND RANDAL J. SOUTHARD
Department of Land, Air and Water Resources, Davis Campus

Summary

Collection of respirable dust (RD) at the implement source was finished with a total of 482 samples from 29 farming operations in two growing seasons. Land preparation operations such as land planing, ripping, plowing, and disking, produced significantly higher dust concentrations than most cultivation operations. We found that on average, for all eight crop and management systems, land preparation operations accounted for 67% of all operations, but produced 82% of the RD. The higher RD production of the land-preparation operations is explained by the fact that they require much more implement contact with the soil than cultivation and harvest operations.

By comparing the seven 2-year crop rotations, we found that the difference in RD production among the systems was primarily due to the increased number of operations and a shift in timing of land preparation operations to the drier and hotter season. In both years, the organically grown crops produced 15 to 40% more RD than the conventionally grown crops. The difference was caused by the tight spring schedule of growing the winter cover crop and preparing for the main crop, thereby postponing dust-intensive land preparation operations to drier and hotter times.

Preliminary work on the comparison between the source soil mineralogy and the RD mineralogy showed a very good correlation, which represents the base for a possible mineralogical distinction of RD from different operations on the same plot.

Key Words: respirable dust, PM-10, air quality, agricultural dust, dust mineralogy

Project Objectives Addressed in 1995-1996

1. Finish field sampling to obtain a representative number of RD measurements of all farming operations for each crop.

2. Compare RD production from the 1994 season to the 1995 season.

3. Evaluate crop and management systems with regard to RD production.

4. Compare the mineralogy of bulk soil to RD fraction.

Research Plan and Procedures

Sample Collection

A detailed description of the field location and the methods for sampling RD were given in the 1995 Kearney Foundation of Soil Science Annual Report of this project (Clausnitzer et al., 1995).

The sampling site consists of seventy-two 4097m^2 field plots with eight different crop and management systems. These systems are organically and conventionally managed tomato and corn, fertilized and unfertilized winter wheat, a fallow rotation, and a winter-legume-cover crop. These systems are arranged in seven 2-year rotations [fallow/wheat, fallow/fertilized wheat, winter-legume-cover crop (wlcc)/wheat, fertilized wheat/conventional tomato, conventional corn/tomato, wlcc and conventional corn/conventional tomato, and organic corn/tomato).

For the RD sampling in 1995, Higgins-Dewell cyclones (BGI Inc., Waltham, MA; Model No. BGI-4) made of stainless steel were employed. Duplicate samples were obtained with two samplers attached to each implement in close proximity and at the same height (on average 97 cm) above the ground. RD was usually sampled on Teflon filters (2-μm pore size; Gelman Science, Ann Arbor, MI), and for some analysis techniques on PVC filters (5-μm pore size; Gelman Science) or quartz filters (Pallflex, Putnam, CT). RD samples were obtained for every operation on each crop and the different management types.

Weather data in 1995 were measured directly at the sampling site.

Laboratory Analysis

RD sample filters were weighed on a 6-digit Cahn 28 Automatic Electrobalance (Analytical Technology, Inc., Boston, MA) with an accuracy of 0.01 μg.

Identification of the source soil mineralogy was accomplished by using standard x-ray-diffraction methods (Janitzky, 1986).

For the RD particles, filters were viewed under a scanning electron microscope (SEM, JSM 840A); then, the elemental composition of single particles was determined by Energy Dispersive X-Ray Spectrometry (EDAX, Link AN 10000). Standard minerals were x-rayed as well. Subsequently, interpretation of the sample particles was based on the comparison to standard mineral pattern and standard-mineral-composition equations (Berry and Mason, 1959). In addition, RD samples were sonicated off the filter in distilled water and mounted on TEM grids (Lacey Carbon on Formvar 150 mesh, Ted Pella Inc., Redding, CA). The grids were observed under the TEM where particle size was determined; an electron-diffraction pattern was obtained; and elemental composition of the same particle was acquired.

Results and Discussion

Dust amounts

Table 1 gives an overview of the 29 farming operations (482 samples) with the average RD concentration and the exact number of single and duplicate samples. The table also includes all measured implement factors, environmental conditions, and sampler locations correlated to the date and time. The operations in the first column are sorted by date. The fourth column contains the number of single and duplicate samples. The abbreviations in the management column are explained at the bottom of the table. The start time gives the daytime range when the samples were collected and the sample time gives the average sampling periods. The sampler height is recorded as the distance from the soil surface to the sampler opening.

The number of samples and the variety of climate and soil conditions for each operation assure that the RD concentrations collected over the last two growing seasons are representative. All these data are only single-point measurements on the implement and are not to be interpreted for off-site purposes.

Several operations were combined due to similarities of the implement regardless of the crop. RD concentrations of these 14 combined operations are graphically represented in ranked order in Fig. 1. Table 2 contains a detailed explanation of the combined operations, their average RD concentration, their standard deviation, and the combined number of samples. High dust concentrations were observed and significant differences were shown among operations. Land preparation operations (land planing, ripping, plowing, disking) ranked highest. The corn harvest ranked high also, primarily due to the high plant biomass and dryness of the plants at the time of harvest as well as due to the dust on the leaves collected over the growing season. The dust concentrations should further be viewed with regard to the number and position of workers involved in each operation. Several land preparation operations

were practiced in open cab tractors, which substantially affected drivers. The corn and wheat harvest were accomplished with air-conditioned harvesters, which greatly lowered dust concentrations for the driver. The tomato harvest involved a number of people close to the dust source, who experienced visibly discomforting symptoms (i.e. irritations of the eyes, nose, and skin).

Climate and soil conditions have a dramatic influence on dust production. For example, operations with high coefficients of variation, such as harrowing, cultivation, seeding, and stubble disking, represent sampling over a wide range of environmental conditions (Table 2). The disking of stubble into the soil includes the disking of (1)vetch/pea in the spring, (2) the wheat stubble in mid-summer, and (3) the corn stubble in fall. Consequently, the soil moisture ranged from the extremes of wet winter rain to dry summer and included fall when soil was either very dry or already moist from the first winter rain. All other climate variables, such as humidity, wind speed, and soil and air temperature had similar wide ranges ranged through the sampling season. Operations with low coefficients of variation suchg as ripping, plowing, and wheat harvest, included a narrower range of soil and climate conditions.

Twenty seven operations were monitored at an average height of 82 cm above the ground. Wheat and corn harvest could only be measured at 230 cm and 220 cm, respectively. Although the sampled RD concentrations of these two operations may be lower compared to other operations because of sampler height, the values allow us to rank them among the RD-producing operations.

In comparing land preparation operations (i.e. disking, ripping, harrowing, and listing) with cultivation and harvest operations, we found that on average, for all eight crop and management systems, land preparation operations accounted for 67% of all operations, but produced 82% of the RD (Figs. 2 and 3). Conversely, the cultivation and harvest operations accounted for 33% of the operations but produced only 18 % of the RD. Depending on the crop, the percentage of total operations that was land preparation ranged from 53% for the wheat crops to 80% for the winter-legume-cover crop (wlcc). Correlatively, the RD concentration produced by land preparation ranged from 75% for the wheat crops to 96% for the wlcc. These data indicate that the percentage of RD concentration produced by land preparation stayed relatively constant above the actual percentage of land preparation operations (Figs. 2 and 3).

The higher RD production of the land preparation operations is explained by the fact that they require much more implement contact with the soil than cultivation operations. In particular, the land leveling operations necessary for the furrow irrigation add considerably to the RD production of each crop. Another reason for the difference in RD production is that cultivation operations are practiced under plant-tolerable soil moisture conditions (up to 10%); whereas, land preparation operations are preferably done under drier conditions (up to 7%).

Figure 4 shows the RD production for the 1994 growing season for the eight crop and management systems. Each bar represents the sum of the RD concentrations of all operations for a particular cropping system. RD production was indexed with reference to fallow fields (index=1.0), which were disked five times that year to discourage weeds. The bars representing the RD production are divided in sections that display RD concentrations from operations done on soil with less than or more than 5% soil moisture. RD production was a function of the number of operations and various environmental influences. For purposes of a better interpretation, the following detailed discussion of Fig. 4 is from the 1995 Kearney Annual Report (Clausnitzer et al., 1995).

When the fallow RD production is utilized as a baseline, growing a winter-cover crop nearly tripled the dust produced. The wheat and the conventionally managed tomato crops increased dust production to two and a half times the baseline and with the cultivation of organically grown tomatoes and conventionally grown corn dust production increased three and a half times over the baseline. Cultivation of organically managed corn increased dust production four times above the baseline.

The differences in RD production among crops were mainly due to inherent plant growth characteristics and the management system, which influences the number of operations performed. The inherent crop differences are especially well expressed in the comparison of the corn and tomato crops with a similar number of operations. The corn crop produced approximately 20% more RD than the tomato crop, chiefly due to higher plant biomass and dryness during harvest and additional postharvest operations. Among the crops studied , tomato and corn were the most intensively cultivated, thereby yielding the highest RD amounts.

In addition to the number of operations compared to the fallow, the number of operations during the dry season is clearly a major influence on RD production. Comparing the winter cover crop with the fallow, we found that the increase in the total number of operations in the wlcc during the dry season caused the tripled increase in RD production, even though the actual number of operations only doubled. The combined influence of operating during the dry season and crop differences is disclosed in an evaluation of the RD production from the wheat and the conventionally managed tomato crops. Both have similar RD concentrations even though the wheat crop requires only two-thirds as many farming operations. The cause is the higher percentage of wheat operations during the summer and the increased plant mass and dryness compared to the tomato crop. The seasonal influence is further demonstrated by the 20% increase in RD production from the organically grown corn and tomato crops compared to their conventionally grown counterparts. The increase can be attributed solely to the delayed cultivation schedule of the main crop because of the incorporation and decomposition time necessary for the preceding winter cover crop as a fertilizer source.

Similar to Fig. 4 for 1994, Fig. 5 displays the RD production for 1995. The weather experienced in the Sacramento Valley in 1995 was unusual in that the winter rains lasted well into the month of May and the cultivation of crops had to be managed differently. At our sampling site,the weather-induced changes in cultivation management included spraying a herbicide instead of tilling the fields and having to disk and land plane additionally to work the soil back to a manageable condition. The additional disking and land preparation operations caused the sum of RD concentrations to go up significantly in 1995 compared to 1994. The fallow fields were only disked twice and treated once with a herbicide which produced less dust than the fallow field disking in 1994. Based on these circumstances, the index numbers of the crop and management systems are higher in 1995. Otherwise, relations between the crop and management systems are similar to the 1994 season except for the fields of the wlcc and the organically grown tomatoes. The wlcc and the organically grown tomatoes were most affected by an adverse soil structure and had to be tilled more often.

The high RD production of the wlcc was caused by disking the plots 13 additional times and land planing them eight additional times as compared to 1994. The winter wheat required only one additional disking and two additional land-planing operations with regard to soil structure improvement and dust production. The conventionally grown corn and tomato crops had some additional tilling operations done during the wet spring in the fallow period. All soil structure-related operations in the organically grown crops were performed in the dry fall, which is the main difference in RD production when compared to their conventional counterparts. In fall, the organically grown corn was disked five times and land planed only once in comparison to the organically grown tomatoes which had four disking and three land-planing operations. As a result, the organically grown tomatoes had a much higher RD production.

Similar to 1994, the organically grown crops produced more RD than the conventionally grown crops. The RD increase ranged from 15% for the organically grown corn to 40% for the organically grown tomatoes compared to the conventionally grown crops.

A comparison among the seven 2-year crop rotations can be seen in Fig. 6. The fallow/wheat rotation was chosen for the index of 1.0. RD concentrations for this figure are from the 1994 season only because, as explained above, 1994 was a more representative year for the Sacramento Valley than 1995. The increase in RD production is primarily due to the increased number of operations and a shift in land preparation operations done during the drier and hotter season.

Source soil and dust particle characteristics

The mineralogy of the surface horizon from 12 LTRAS-plots was determined by x-ray diffraction (Table 3). The clay (<2 μm) and the combined fine and medium silt fraction (2-20 μm) were analyzed separately as was a

mixture of 0-10 μm particles to better correlate the mineralogy of this source-soil fraction to the collected dust-particle-size range.

The predominant clay mineralogy is:

- Smectite
- Smectite intergrades
- Minor amounts of primary minerals

The predominant silt mineralogy is:

- Quartz
- Plagioclase feldspars
- Mica
- Minor amounts of secondary minerals

The mineralogy of the 0-10 μm size fraction included the major constituents of both fractions (not shown in Table 3). No significant differences in the mineralogy within the fractions were found among the plots.

Mineralogical comparison of the RD to the source soil is imperative; however, mineralogy analysis of the RD particles is an extremely time intensive and cost restrictive process. Ten to 100 particles were photographed and analyzed under the SEM from each of seven RD samples. One RD sample taken during the soil-ripping operation on plot No.6-8 was chosen to illustrate the mineralogy and to provide a comparison with the source soil. All scanning-electron micrographs were image-scanned to determine particle sizes. Out of the 80 particles analyzed on this one sample, minerals with five and more occurrences are displayed with their major lengths in Fig. 7. The mineral particle sizes are spread over the whole sampling range. Their means matched well with the manufacturer-quoted cut point of the sampling cyclones ($\leq 4\mu m$). At a 95% confidence level, the sizes of the five mineral types are not statistically different from each other.

Figure 8 shows an example of the interpretation method for the elemental composition in which the elements from a standard mineral are compared to the sample spectrometry pattern. Table 3 gives the mineral composition of the 80 sample particles determined in this way. Based on the SEM/EDAX analysis, the predominant RD mineralogy on this land preparation sample is composed of

- Mica
- Montmorillonite
- An intergrade of Biotite to Montmorillonite
- Quartz

For this soil-ripping sample, source soil mineralogical analyses correlated very well with the mineralogical analyses of the RD.

With the recent completion of the first TEM analyses, we will be able to confirm further the EDAX-spectrometry pattern from the SEM work by getting combined information on the elemental composition, the size, and the crystallography of the same sample particle.

Conclusions

The RD concentrations presented from each farming operation should enable estimation of the RD production for furrow irrigated crops in a Mediterranean climate, where the soil texture of the uppermost horizon is predominantly clay loam. For furrow irrigated crops other than tomato, corn, and wheat, land-preparation and cultivation operations should be similar. Only for harvest and possible post harvest operations would predictions have to be made. RD production for different crop rotations could be calculated as well.

The RD concentrations differ significantly among the 29 sampled farming operations. Therefore, operations with high RD concentrations, such as land preparation (land planing, ripping, plowing, and disking) and harvest (tomato and corn harvest), should be performed with the understanding that these operations have the greatest potential for reducing air quality.

The cultivation of each crop and its specific set of operations need to be more carefully evaluated within the existing climate constraints. Although management systems with winter-cover crops can have advantages to sustainable crop production and human health, they require special attention in a semiarid Mediterranean climate where an increase in RD concentration was observed. We found this increase to be approximately 20% in an average year with a dry spring, which results in a delayed spring schedule of the main crop. For a growing season with a very long wet period in the spring, the increase in RD production is due to additional soil tillage in the dry fall, and was found to range from 15 to 40%.

The measured RD concentrations reveal existing differences among farming operations, but without further spatial distribution studies no conclusion can be drawn about the impact on air quality or human health off-site from these operations.

Although preliminary results from the RD mineralogy determination showed similar minerals as in the source soil, additional analysis is needed for detailed conclusions. Ongoing research of several farming operations from the same plot will determine further if different operations affect the dust composition as compared to the source soil. The manufacturer-quoted cut point of the sampling cyclones ($\leq 4\mu m$) was confirmed because all particles were evenly distributed over the whole sampling range. The major minerals were also found over all sizes of the RD range.

References

Berry, L.G., and B. Mason. 1959. Mineralogy. 1st ed. W. H. Freeman and Company, San Francisco, CA.

Clausnitzer, H., M.J. Singer, and R. J. Southhard. 1995. Composition and distribution of fugitive dust from Central Valley crop management systems. p. 217. 1994-95 Annual Report Kearney Foundation of Soil Science, Riverside, California.

Janitzky, P. 1986. Preparation of soil samples for X-ray diffraction analysis. p.16-18. In M.J. Singer and P. Janitzky (eds.) Field and Laboratory Procedures Used in a Soil Chronosequence Study. US Geological Survey Bulletin 1648. US Gov. Printing Office, Washington, DC.

Table 1. Averages of 29 operations (482 samples) were 444 (183 duplicates + 78 singles = 261) samples are in 21 operations with more than five samples -- collected March 31, 1994 to November 22, 1995.

operation/ dust source	dust [mg/m3 air]	op. #	# of samp. d = dup	manage-ment *	date	start time	samp. time [min]	sampler height [cm]	tract. speed [m/s]	trac-tor [rpm]	soil moisture before [%]	soil moisture after [%]	air temp. [oC]	humi-dity [%]	soil temp [oC]	wind speed [m/s]	wind dir. 0-360	tractor working dir.
AVERAGES OF OPERATIONS WITH FIVE OR MORE SINGLE SAMPLES:																		
mowing vetch/pea	1.753	1	4d+5	t, c, wh	April	8-18	26	78	1.3	2250	tire contact only		19.1	51	17	4.8	246	N/S
disking vetch/pea into soil	0.314	2	4d+7	t, c, wh	April	9-16	28	106	1.9	1800	12 -14	-	18.9	41	16	4.7	274	N/S
1st finish disking	3.788	3	13d+15	t,c,wh,f	April-Aug	7-16	23	77	1.6	2200	2 - 5	3 -12	22.5	47	20	3.6	288	all
2nd &3rd finish disking	4.936	4	7d+6	c, f, wlc	April-Aug	8-15	26	77	1.8	2500	2 - 4	3 -10	22.8	49	21	2.6	274	all
land planing	13.604	5	12d+6	all t/c	April/Sept	7-16	30	86	2.2	3500	1 - 7	-	20.7	54	18	2.0	237	S/4NE/SW,NSEW
listing - plant bed	1.437	6	9d+4	all t/c	April	8-18	23	72	1.6	-	2 - 7	-	16.2	47	16	3.4	226	N/S
corn seeding	0.833	7	10d+1	com&org	April-May	8-16	29	52	1.3	2000	2 - 5	-	23.1	50	18	2.5	229	N/S
spring-tooth harrowing	0.697	8	6d+6	all t/c	April-May	8-16	16	54	2.4	2100	6 -17	-	18.2	53	18	3.1	222	N/S
cultivation	1.092	9	9d+13	all t/c	May-June	7-17	32	62	1.7	2045	1 - 7	6 -15	21.6	48	21	4.3	210	N/S
cultivation & furrow cutting	0.662	10	15d	all t/c	May-July	7-16	33	81	1.7	1953	1 -10	6 -11	23.3	56	24	2.1	179	N/S
injected fertilization w. furrow cutting	0.787	11	6d+2	com t&c	May	8-14	38	65	1.5	2100	2 - 7	4 - 7	18.7	62	21	2.7	189	N/S
wheat harvest	1.124	12	4d+7	all wh	June/July	10-15	26	237	0.8	-	tire contact only		25.3	41	23	2.0	171	N/S
swathging wheat	1.575	13	4d+1	all wh	July	13-16	18	167	1.9	-	tire contact only		26.6	39	25	2.5	152	N/S
baling wheat	2.289	14	8d	all wh	June/July	13-16	24	148	2.5	1000	tire contact only		28.7	35	24	2.9	165	N/S
disking wheat stubble into soil	7.158	15	10d+1	all wh	July/Aug	7-16	32	100	2.3	-	1 - 3	-	27.4	43	24	3.0	223	E/W,N/S
tomato harvest - 75cm above surface	3.681	16	9d+1	com&org	Aug/Sept	7-17	46	75	1.1	-	2 - 6	-	27.1	42	23	3.3	181	N/S
ripping 1st & 2nd	9.885	17	15d	all t	Sept/Oct	10-16	19	74	1.5	2120	3 - 6	-	22.7	34	18	2.0	244	E/W,N/S
corn harvest	6.688	18	14d+2	com&org	October	11-16	17	220	1.0	2300	tire contact only		26.2	25	18	6.5	343	N/S
disking corn stubble into soil	1.610	19	7d+1	com&org	October	7-11	30	92	2.2	2200	5 -18	-	13.8	47	16	2.3	150	E/W,N/S
plowing	6.463	20	6d	c&o corn	October	8-14	26	78	2.9	-	9 -10	-	18.9	49	17	3.1	171	N/S
wlcc &wheat seeding	1.640	21	11d	all wh	November	8-15	28	76	1.0	-	3 - 5	-	19.7	55	14	1.3	225	N/S
OPERATIONS WITH LESS THAN FIVE SAMPLES:																		
tomato harvest-130cm above surface	0.502	16a	4d	org. t 95	August	7-16	91.6	130	1.2	-	3 - 6	-	22.6	52	23	2.0	162	N/S
compost spread	1.128	22	3	org. t	April	8-13	47	70	1.7	2100	tire contact only		15.0	33	13	2.7	324	N/S
leveling tomato bed	2.746	23	1	com. t	4-Apr-94	14	18	66	-	-	4.2	-	24.4	10	17	8.0	334	N/S
cutting irrigation furrows	1.365	24	2	com. c	7-Apr-94	7-9	20	68	1.3	2100	4 - 5	12 -13	8.2	86	14	3.3	356	N/S
tire dust during dry fertilizer application	0.308	25	2	com. c	7-Apr-94	12-14	18	107	1.8	-	tire contact only		17.4	44	15	2.6	319	N/S
tomato transplanting	0.192	26	1	org.	21-Apr-95	8	20	75	0.1	-	7.8	-	12.4	40	15	9.4	347	N/S
surface breakup & herbizide incorporation	0.556	27	2d+1	c&o corn	May	10-16	16	110	2.6	-	5 - 6	-	18.5	45	18	4.5	207	N/S
mowing down corn stems	5.290	28	4	org. c	October	13-15	16	100	0.9	-	tire contact only		29.0	21	17	3.9	356	N/S
ADDITIONALLY MONITORED OPERATION:																		
rototilling road - weed removal	47.766	29	5d+1	road	June	9-14	18	57	1.2	2067	3 - 4	5 - 6	23.5	51	22	3.6	167	E/W,N/S
				* c&o t&c = com. & org. corn & tomato, wh +wheat, f fallow, wlc = winter legume cover crop														

Table 2: Comparison of 14 farming operations with their averages, standard deviations, coefficient of variation, and number of single and duplicate (d) samples.

Operation	Average	Standard Deviation	Coefficient	Number of
	--- Resp. Dust [mg/m^3 air] ---		of Variation	Samples
Land Planing	13.604	11.881	0.87	12d +6 = 18
Ripping	9.885	3.052	0.31	15d = 15
Corn Harvest	6.688	3.558	0.53	14d +2 = 16
Plowing	6.463	2.927	0.45	6d = 6
Finish Disking (1st, 2nd, and 3rd)	4.152	2.717	0.65	20d + 21 = 41
Tomato Harvest	3.681	2.073	0.56	9d + 1 = 10
Stubble Disking (corn, wheat, wlcc)	3.169	4.466	1.41	21d + 9 = 30
Wheat Straw Op. (swathing and baling)	2.014	1.112	0.55	12d +1 = 13
Mowing Vetch	1.753	1.289	0.74	4d + 5 = 9
Listing	1.437	1.617	1.13	9d + 4 = 13
Seeding (corn, wheat, wlcc)	1.236	1.108	0.90	21d + 1 = 22
Wheat Harvest	1.125	0.308	0.27	4d + 7 = 11
Cultivation (including fertilization & cultivation with furrow cutting)	0.895	0.889	0.99	30d + 15 = 45
Harrowing	0.697	0.633	0.91	6d + 6 = 12

Table 3: Mineralogy based on X-ray diffraction analysis of two particle size fractions from the A horizon of 12 LTRAS plots.

	Fine and Medium Silt (2-20 μm)		Clay (<2 μm)	
Plot #	Primary Minerals (most abundant)	Secondary Minerals (least abundant)	Primary Minerals (least abundant)	Secondary Minerals (most abundant)
1-2	Q, PF, M	K, CV, V	Q, PF, M: m, b	S, CS, V, C, K
2-3	Q, PF, M	K, CV, V	Q, PF, M: m, b	S, CS, CV, V, C, K
2-4	Q, PF, M	K, CV, V, Se	Q, PF, M: m, b	S, CS, C, K
3-7	Q, PF, M	K, CV, V, Se	Q, PF, M: m, b	S, CS, C, K
4-4	Q, PF, M	K, CV	Q, PF, M: m, b	S, CS, CV, V, K
5-4	Q, PF, M	K, CV	Q, PF, M: m, b	S, CS, CV, V, K
6-4	Q, PF, M	K, CV	Q, PF, M: m, b	S, V, K
6-5	Q, PF, M	K, V, Se	Q, PF, M: m, b	S, CS, CV, C, K
6-8	*Q, PF, M*	*K, CV, V*	*Q, PF, M: m, b*	*S, CS, CV, V, K*
7-8	Q, PF, M	K, CV, V, Se	Q, PF, M: m, b	S, CS, C, K
8-8	Q, PF, M	K, CV, V, Se	Q, PF, M: m, b	S, CS, C, K
8-9	Q, PF, M	K, CV, V	Q, PF, M: m, b	S, V, C, K

Q = quartz; PF = plagioclase feldspar; M = mica; m = muscovite; b = biotite
CS = chlorite-smectite intergrade; V = vermiculite; Se = serpentine
S= smectite; K = kaolinite; CV = chlorite-vermiculite intergrade

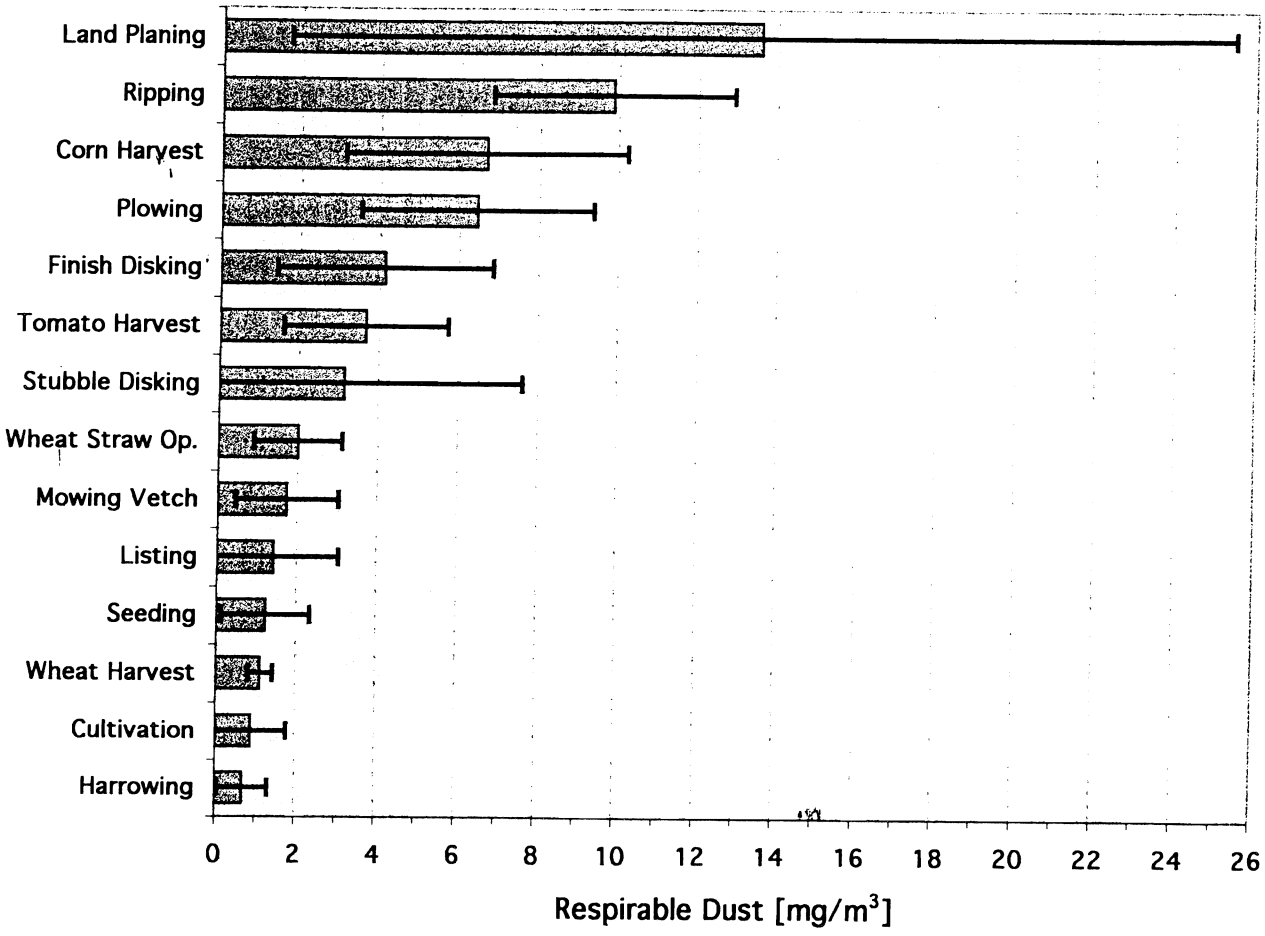

Figure 1. Average respirable dust (RD) concentrations and their standard deviations from 14 farming operations.

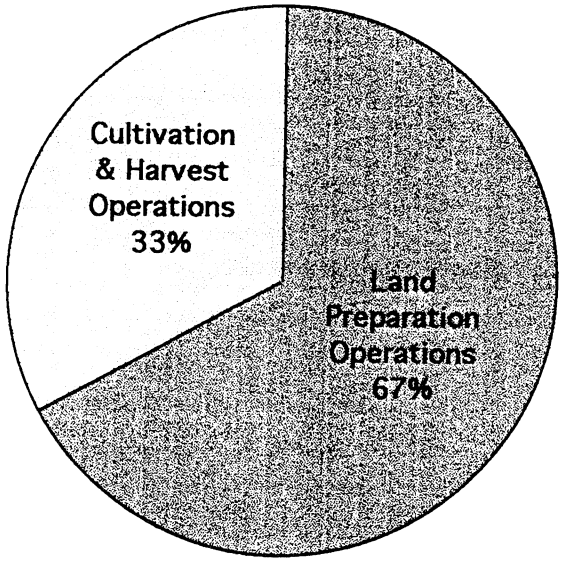

Figure 2. Percentage of number of operations for the average of the 1994 and 1995 growing seasons.

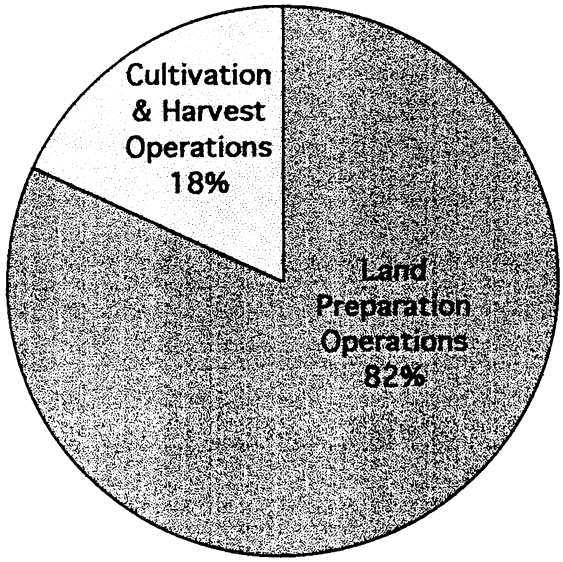

Figure 3. Percentage of respirable dust from operations for the average of the 1994 and 1995 growing seasons.

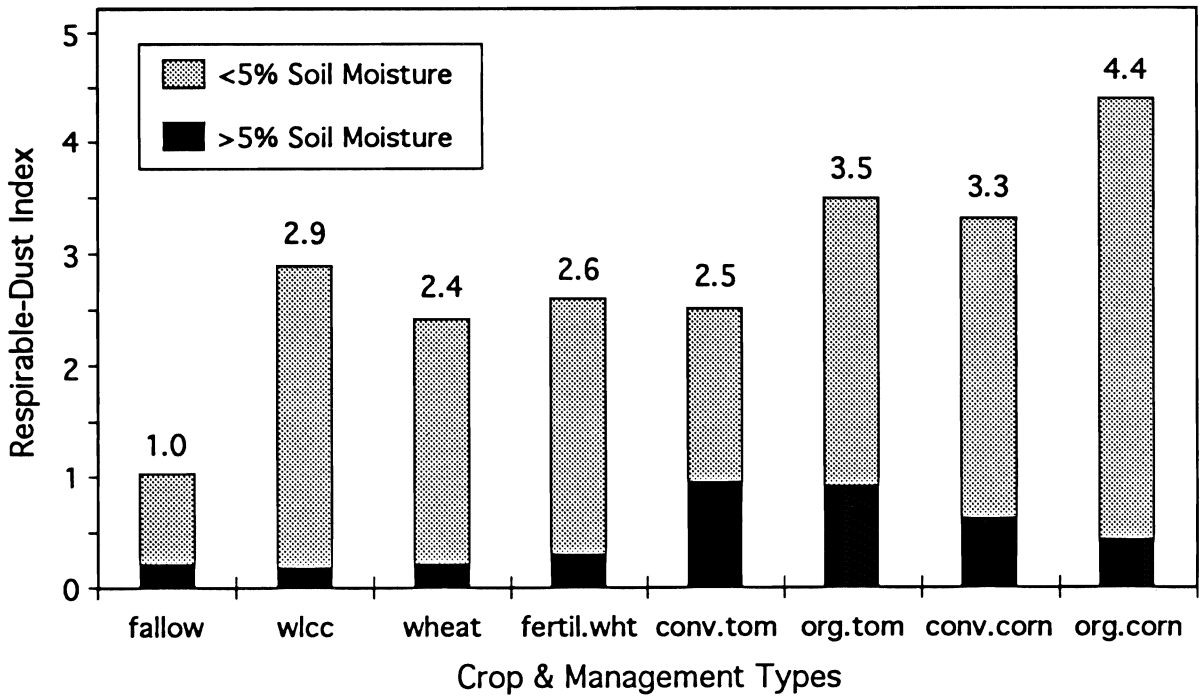

Figure 4. Index of potential respirable dust (RD) production over the 1994 growing season for different crop and management types relative to fallow fields (disked five times).

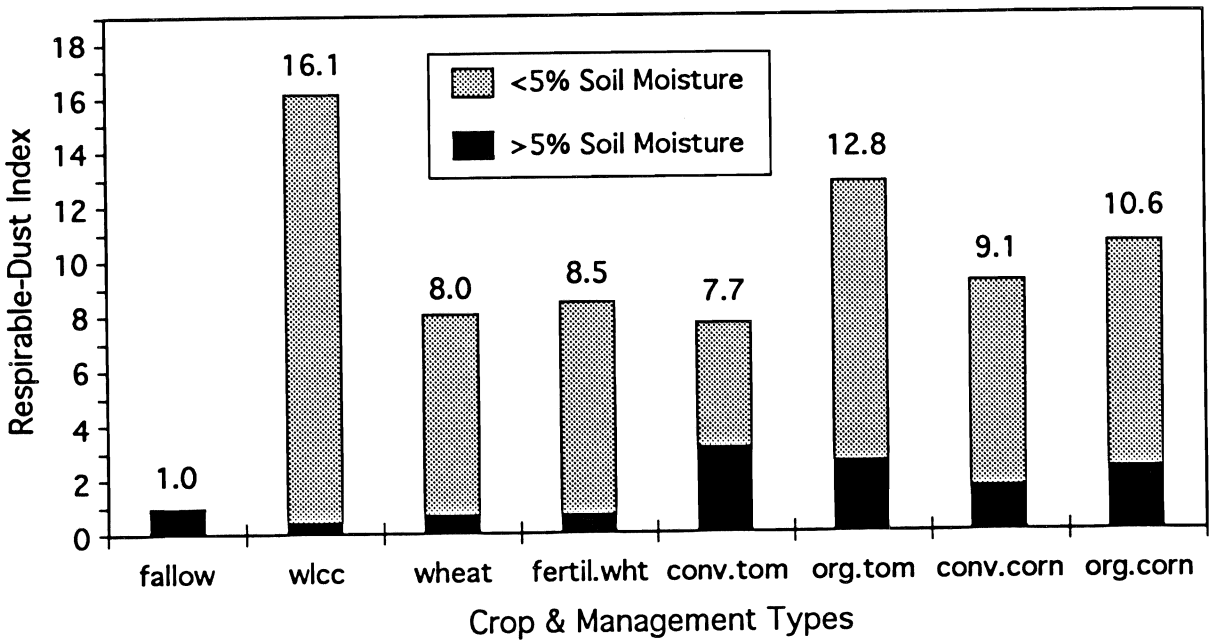

Figure 5. Index of potential respirable dust (RD) production over the 1995 growing season for different crop and management types relative to fallow fields (one herbicide treatment and two diskings).

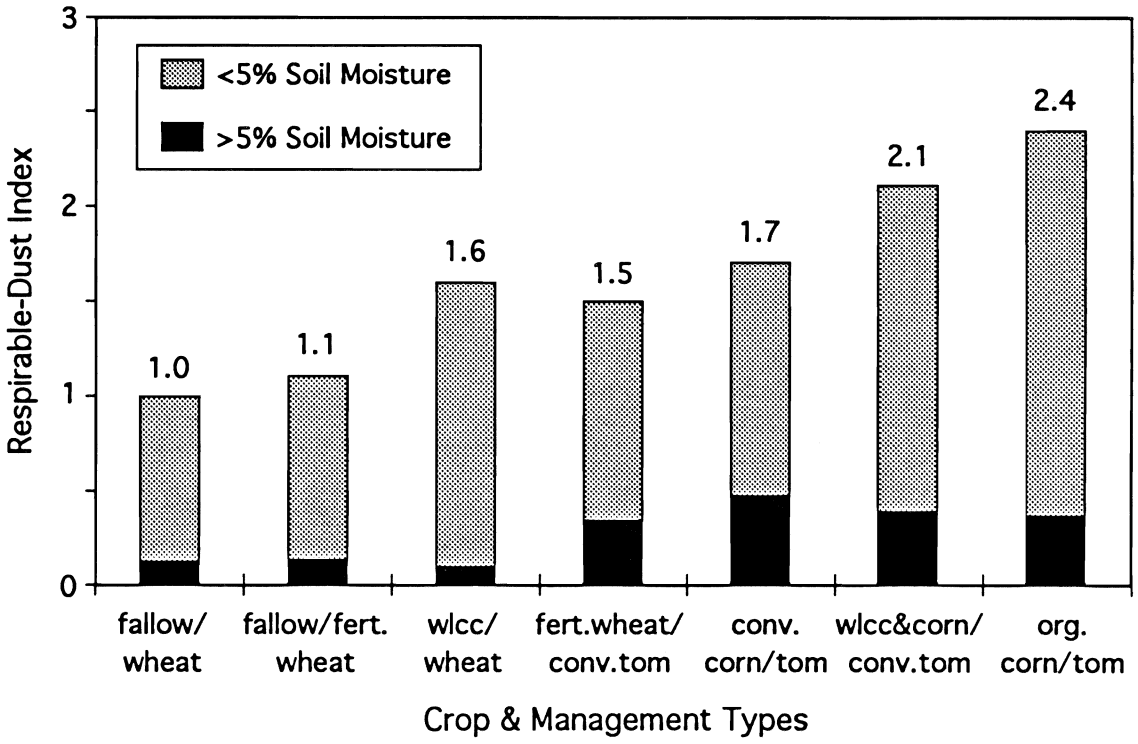

Figure 6. Index of potential respirable dust (RD) production for a 2-year rotation with 1994 season operations for differrent LTRAS crop and management types (fallow/wheat plots equal 1.0)

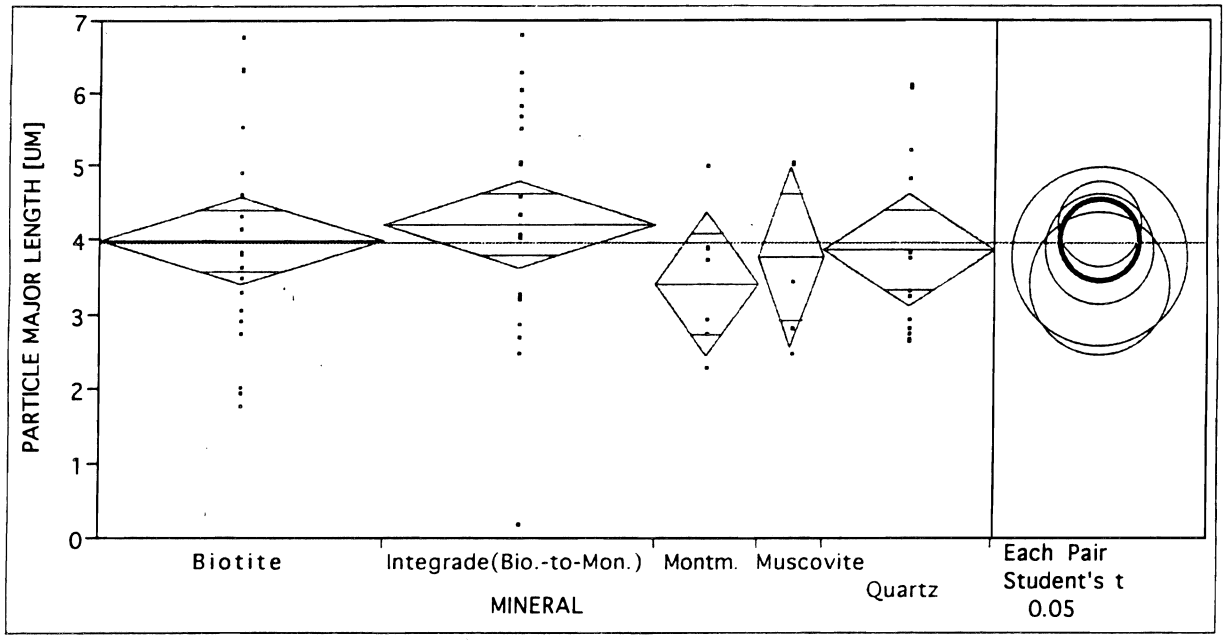

Figure 7. Statistical comparison of the major lengths of the five main mineral groups from the soil-ripping operation sample.
Diamond width is proportional to sample size; diamond height equals 95% probability range for mean (horizontal bar). For the Student's t-test, a representative (Biotite) was chosen for the average dust amount (thick circle). If mineral lengths would be significantly different, their circles had to be at a ≥ 90 degrees intersection angle. The circle size equals the diamond size.

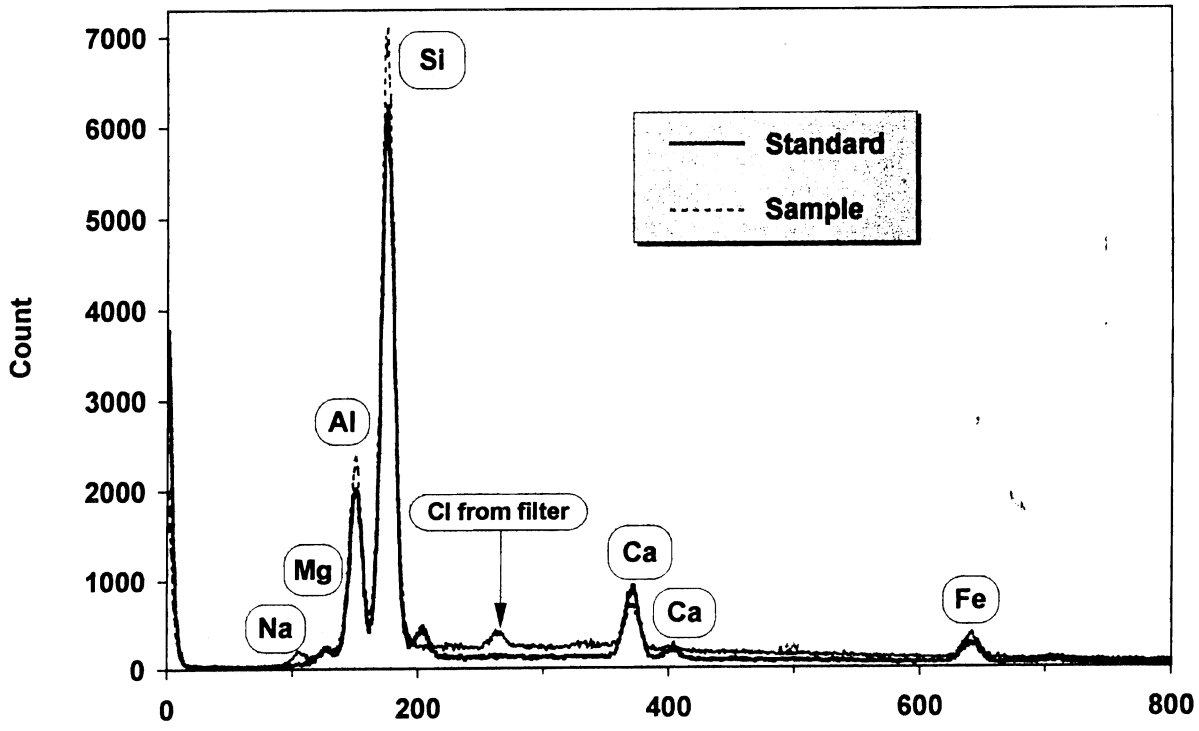

Figure 8. Particle identification accomplished by comparing the elemental composition of the sample to a standard mineral pattern-Montmorillonite in this case.

Objective, Organization and Function of
The University of California
Kearney Foundation of Soil Science

Adopted August 4, 1969
Revised June 30, 1982

Objective

The Kearney Foundation of Soil Science shall focus its program and support research in definitive missions in the fields of soils, plant nutrition, and water science.

Organization

A. The Kearney Foundation of Soil Science is administratively responsible to the Vice President-Agricultural and University Services (A&US) through the Director of the Agricultural Experiment Station and the Associate Director of the Agricultural Experiment Station located on the campus on which the Director of the Foundation is resident.

B. The Kearney Foundation of Soil Science is administered for the Division of Agricultural Sciences by a Director with policy guidance by an Advisory Committee and assistance from a Technical Committee.

1. The Director is appointed by the Vice President-A&US, after approval by the Dean and Associate Director of the Agricultural Experiment Station and the Chancellor of the campus on which the Director is to be resident. The Advisory Committee will propose a slate of candidates for the position of Director to the Vice President-A&US for his consideration.

2. The Advisory Committee of the Kearney Foundation is appointed by the Vice-President-A&US and is responsible to him through the Director of the Agricultural Experiment Station for guidance of the Foundation. The Chairman of the Committee is the Associate Director of the Agricultural Experiment Station at the location where the Director of the Foundation resides. The remaining members are the chairmen, or designees, of the Departments of Land, Air and Water Resources at Davis, Plant and Soil Biology at Berkeley, Soil and Environmental Sciences at Riverside, and one representative from a crop production department, one representative from Agricultural Economics and one representative from Agricultural Extension.

3. The Technical Committee of the Kearney Foundation is appointed by the Vice President-A&US. The Technical Committee shall consist of the Foundation Director as Chairman and four to seven other individuals. Individuals will be selected for the Technical Committee on the basis of their expertise on the Kearney Foundation mission subject matter with consideration for appropriate campus, cooperative extension and possibly non-university representation.

4. The Foundation Director may employ necessary administrative, technical or clerical staff to accomplish the Kearney Foundation goals, but there shall be no permanent staff for the Foundation. The Foundation Director will submit an annual report as prescribed by the University for Multi-campus Research Units.

Functions

A. The function of the Kearney Foundation is to encourage and support research and information dissemination on a specific definitive mission approved by the Vice President-A&US upon the recommendation of the Advisory Committee for a period of five years. The mission shall be one of public concern on which useful contributions are likely to be made in a five-year period. Successive missions will be selected each five years with a new Director for each mission.

B. The Foundation Director shall (1) keep faculty and cooperative extension individuals on various campuses informed on the Foundation goals and objectives and on funding opportunity from the Foundation, (2) solicit research proposals from UC investigators and with help from the Technical Committee develop a proposal funding priority list for review by the Advisory Committee, (3) allocate funds, after review by the Advisory Committee, to accomplish the Foundation mission, (4) be responsible for administrative details including preparation of appropriate reports, (5) assist faculty members to seek funds from sources other than Kearney Foundation that will contribute to the Foundation mission, (6) encourage information dissemination on the mission subject matter to appropriate segments of society, and (7) prepare "wrap-up" document(s) which synthesize the information gained during the five year mission.

C. The Advisory Committee shall (2) advise the Foundation Director when needed, (2) recommend research policy, (3) evaluate progress on the mission research, (4) review recommended allocation of funds by Foundation Director, (5) encourage inter-campus coordination and cooperation to make optimum use of resources and facilities, (6) select a definitive five year research mission to succeed an existing mission, and (7) nominate qualified candidates for a succeeding Director of the Foundation.

D. The Technical Committee shall (2) assist the Director in defining research priorities, (2) evaluate and develop a priority rating on research proposals, and (3) provide advice as requested by the Foundation Director on matters related to technical subject matter.

General Operational Guidelines

A. Recommended missions and Foundation Director candidates are to be submitted to the Director of the Agricultural Experiment Station and the Vice President-A&US by July 1 preceding the final year of an existing research mission. The new mission and Director-designate are to be selected as soon thereafter as possible to enable the Director-designate to plan the program for activation the following July 1.

B. The Director will manage and authorize expenditures of all funds transferred to the Kearney Foundation as of July 1 of the last year of the mission. Any funds transferred into the Kearney Foundation after that time will be used to accomplish the goals of the succeeding mission.

C. The Director normally will use the year after the five year mission period to "wrap up" the mission by holding symposia, preparing publications, etc. Funds to accomplish this task must be reserved from the budget specifically assigned tot he mission during the preceding five years. The immediate past Kearney Foundation Director will report to the Vice President-A&US through the appropriate Dean and Advisory Committee on progress and budgetary expenditures in achieving wrap up of the mission. At the appropriate time, the mission will be considered complete, the Director formally released from responsibility and any unexpended funds will revert back to the Kearney Foundation for use in subsequent missions.

D. The Director and members of the Advisory and Technical Committees are eligible to submit proposals for funding. They must, however, be excluded from discussion or action related to the particular project.

E. Normally extramural contracts or grants supporting activities consistent with the Kearney Foundation mission will be assigned directly to the Department of the scientist serving as PI rather than to the Kearney Foundation. When an outside agency makes an offer or solicits a proposal from the Foundation Director, the Director will make that information known to the Advisory Committee.

F. Kearney Foundation resources are to supplement Agricultural Experiment Station budgets and provide incentives for research redirection. Because of the temporary nature of the funds, funding of non-career employees such as post-doctoral appointments, research assistantships and part time laboratory helpers is strongly encouraged and routinely approved. Justified funding for career employees with supplemental employee benefit costs must be approved by the Advisory Committee.

Kearney Foundation of Soil Science Advisory Committee

Dr. John M. Duniway
Chair, Department of Plant Pathology
Professor of Plant Pathology and Plant Pathologist
University of California
Davis, CA 95616
(916) 752-0324 or (916) 752-4269

Dr. Mary K. Firestone
Chair, Department of Environmental Science, Policy and Management
Professor of Soil Microbiology
University of California
Berkeley, CA 94720
(510) 642-3677

Dr. Steven Grattan
Cooperative Extension Water Relations Specialist
Department of Land, Air, & Water Resources, Hydrologic Science Section
University of California
Davis, CA 95616
(916) 752-1130

Dr. William A. Jury
Chair, Department of Soil & Environmental Sciences
Professor of Soil Physics and Soil Physicist
University of California
Riverside, CA 92521
(909) 787-5134

Dr. Keith C. Knapp
Professor of Resource Economics
Department of Soil & Environmental Sciences
University of California
Riverside, CA 92521
(909) 787-4195

Dr. Lanny J. Lund
Associate Dean, Agricultural Experiment Station
College of Natural and Agricultural Sciences
Chair, Kearney Foundation of Soil Science Advisory Committee
Professor of Soil Science and Soil Scientist
Department of Soil & Environmental Sciences
University of California
Riverside, CA 92521
(909) 787-7291 or (909) 787-3859

Dr. Randal J. Southard
Associate Professor of Soil Genesis and Morphology, and
Director, Soil Science & Biogeochemistry Program
Department of Land, Air & Water Resources
University of Calfiornia
Davis, CA 95616
(916) 752-7041

Kearney Foundation of Soil Science Technical Committee

Dr. Andrew C. Chang
Chair, Kearney Foundation of Soil Science Technical Committee
Director, Kearney Foundation of Soil Science
Professor of Agricultural Engineering and Agricultural Engineer
Department of Soil & Environmental Sciences
University of California
Riverside, CA 92521
(909) 787-5325

Dr. Arthur L. Craigmill
Cooperative Extension Toxicology Specialist
Department of Environmental Toxicology
University of California
Davis, CA 95616
(916) 752-2936

Dr. Dennis D. Focht
Professor of Soil Microbiology and Soil Microbiologist
Department of Soil & Environmental Sciences
University of California
Riverside, CA 92521
(909) 787-3446

Dr. Jan W. Hopmans
Associate Professor of Water Management and Assoc. Water Management Specialist
Director, Hydrologic Science Section, Department of Land, Air & Water Resources
University of Calfornia
Davis, CA 95616
(916) 752-3060 or (916) 752-0453

Dr. John G. McColl
Professor of Forest Soils
Department of Environmental Science, Policy and Management
University of California
Berkeley, CA 94720
(510) 642-1028 or (510) 643-6088

Dr. T. Ishwar Murarka
Senior Program Manager, Land and Water Quality Studies
Electrical Power Research Institute
P. O. Box 10412
Palo Alto, CA 94303
(415) 855-2150

Dr. Albert L. Page
Professor of Soil Science and Chemist
Department of Soil & Environmental Sciences
University of California
Riverside, CA 92521
(909) 787-3654

Dr. Martinus Th. Van Genuchten
Adjunct Professor of Soil Physics
Department of Soil & Environmental Sciences
United States Salinity Laboratory
University of California
Riverside, CA 92521
(909) 369-4847

Index of Principal Investigators

Dr. Michael A. Anderson
Assistant Professor of Soil Chemistry and Assistant Soil Chemist
Department of Soil & Environmental Sciences
University of California
Riverside, CA 92521
(909) 787-3757

Marcia L. K. Carrillo
Graduate Research Assistant
Department of Soil & Environmental Sciences
University of California
Riverside, CA 92521
(909) 787-5105

Dr. William H. Casey
Professor and Aqueous Geochemist
Department of Land, Air & Water Resources, Soil Science & Biogeochemistry Section
University of California
Davis, CA 95616
(916) 752-3211

Heike Clausnitzer
Postgraduate Researcher
Department of Land, Air & Water Resources, Soils & Biogeochemistry Section
University of California
Davis, CA 95616
(916) 752-6081

Dr. David E. Crowley
Assistant Professor of Soil Science and Assistant Soil Chemist
Department of Soil & Environmental Sciences
University of California
Riverside, CA 92521
(909) 787-3785

Randy A . Dahlgren
Associate Professor and Associate Pedogist & Soil Mineralogist
Department of Land, Air & Water Resources, Soil Science & Biogeochemistry Section
University of California
Davis, CA 95616
(916) 752-2814

Dr. Harvey E. Doner
Professor of Soil Chemistry
Department of Environmental Science, Policy, and Management
University of California
Berkeley, CA 94720
(510) 642-4148

Kristie A. Dunkin
Graduate Student Researcher
Department of Soil Science
University of California
Berkeley, CA 94720
(510) 624-6847

S. Ezzedine
Post Graduate Researcher
Kearney Agricultural Center
9240 S. Riverbend Avenue
Parlier, CA 93648
(209) 646-6500

Dr. Walter J. Farmer
Professor of Soil Science and Chemist
Department of Soil & Environmental Sciences
University of California
Riverside, CA 92521
(909) 787-3756

Dr. Mary K. Firestone
Department of Environmental Science, Policy and Management
Professor of Microbiology
University of California
Berkeley, CA 94720
(510) 642-3677

Dr. Dennis D. Focht
Professor of Microbiology
Department of Soil & Environmental Sciences
University of California
Riverside, CA 92521
(909) 787-3446

C. S. Frazier
Graduate Research Assistant
Department of Soil & Environmental Sciences
University of California
Riverside, CA 92521
(909) 787-3751

Dr. Robert C. Graham
Professor of Soil Mineralogy
Department of Soil & Environmental Sciences
University of California
Riverside, CA 92521
(909) 787-3751

Dr. Mark E. Grismer
Associate Professor & Associate Agricultural Drainage Engineer
Department of Land, Air, & Water Resources, Hydrologic Science Section
University of California
Davis, CA 95616
(916) 752-3243

Thomas Harter
CE Hydrology/Hydrogeology Specialist
Kearney Agricultural Center
9240 S. Riverbend Avenue
Parlier, CA 93648
(209) 646-6569

Anthony G. Hay
Graduate Research Assistant
Department of Soil & Environmental Sciences
University of California
Riverside, CA 92521
(909) 787-3446

Dr. Jan W. Hopmans
Director & Associate Professor of Water Management
Department of Land, Air, & Water Resources, Hydrologic Science Section
University of California
Davis, CA 95616
(916) 752-3060 or (916) 752-0453

Dr. Theodore C. Hsiao
Professor and Plant Physiologist
Department of Land, Air, & Water Resources, Hydrologic Science Section
University of California
Davis, CA 95616
(916) 752-0691

Dr. William A. Jury
Professor of Soil Physics
Department of Soil & Environmental Sciences
University of California
Riverside, CA 92521
(909) 787-5134

Dr. Roy B. Leipnik
Professor of Mathematics
Department of Mathematics
University of California
Santa Barbara, CA 93106
(805) 893-2738 or (805) 893-2171

Dr. John Letey
Associate Director, Centers for Water and Wildland Resources
Professor of Soil Physics and Soil Physicist
Department of Soil & Environmental Sciences
University of California
Riverside, CA 92521
(909) 787-5105 or (909) 787-4327

Dr. Hugo A. Loaiciga
Professor of Geography/Hydrology
Department of Geography
University of California
Santa Barbara, CA 93106
(805) 893-8053 or (805) 893-3663

Dr. Miguel A. Marino
Professor of Water Science and Ground Water Hydrologist
Department of Land, Air & Water Resources, Hydrologic Science Section
University of California
Davis, CA 95616
(916) 752-0684 or (916) 752-0453

Fergus Morrissey
Graduate Research Assistant
Department of Land, Air & Water Resources, Hydrologic Science Section
University of California
Davis, CA 95616
(916) 752-3243

Lehua Pan
Visiting Post Graduate Researcher
Department of Soil & Environmental Sciences
University of California
Riverside, CA 92521
(909) 787-34664

Dr. Carlos E. Puente
Associate Professor of Hydrologic Science and Associate Hydrologist
Department of Land, Air, and Water Resources
University of California
Davis, CA 95616
(916) 752-0689 or (916) 752-0453

Troy T. Reid
Postgraduate Researcher
Department of Mathematics
University of California
Santa Barbara, CA 93106
(805) 893-8053

Dr. Peter A. Rock
Professor of Chemistry
Department of Chemistry
University of California
Davis, CA 95616
(916) 752-0940

Dr. Kate M. Scow
Assistant Professor of Soil Science and Assistant Soil Microbial Ecologist
Department of Land, Air, & Water Resources, Soils & Biogeochemistry Section
University of California
Davis, CA 95616
(916) 752-4632 or (916) 752-1406

Dr. Michael J. Singer
Professor of Soil Science
Department of Land, Air, & Water Resources, Soils & Biogeochemistry Program
University of California
Davis, CA 95616
(916) 752-7499

Dr. David Slaughter
Associate Professor
Department of Biological & Agricultural Engineering
University of California
Davis, CA 95616
(916) 752-5553

Dr. Randal J. Southard
Associate Professor of Soil Genesis and Morphology, and
Director, Soils & Biogeochemistry Program
Department of Land, Air, & Water Resources
University of California
Davis, CA 95616
(916) 752-7041

Dr. Garrison Sposito
Professor of Soil Physical Chemistry
Department of Environmental Science, Policy and Management
University of California
Berkeley, CA 94720
(510) 643-8297 or (510) 643-9171

Xiaohua Sun
Graduate Student Researcher
Department of Environmental Science, Policy and Management
University of California
Berkeley, CA 94720
(510) 643-4148

Professor Kenneth K. Tanji
Professor and Water Scientist
Department of Land, Air & Water Resources, Hydrologic Science Section
University of California
Davis, CA 95616
(916) 752-6540

Dr. Shrini K. Upadhyaya
Professor
Department of Biological & Agricultural Engineering
University of California
Davis, CA 95616
(916) 752-8770

Jeffrey Warner
Research Assistant
Department of Land, Air & Water Resources
Soil & Biogeochemistry Section
University of California
Davis, CA 95616
(916) 752-3073

Dr. Laosheng Wu
Assistant Professor of Soil Science
Department of Soil & Environmental Sciences
University of California
Riverside, CA 92521
(909) 787-4664

Dr. Marylynn V. Yates
Associate Professor of Environmental Microbiology and
Associate Cooperative Extension Agronomist -- Groundwater Quality
Department of Soil & Environmental Sciences
University of California
Riverside, CA 92521
(909) 787-5488

Dr. Scott Yates
Adjunct Associate Professor
USDA-ARS, U. S. Salinity Laboratory
450 W. Big Springs Road
Riverside, CA 92507
(909) 369-4803

Mavrik Zavarin
Graduate Student
Department of Environmental Science, Policy, and Management
University of California
Berkeley, CA 94720
(510) 642-3794

OFFICE OF THE DIRECTOR
KEARNEY FOUNDATION OF SOIL SCIENCE
UNIVERSITY OF CALIFORNIA
RIVERSIDE, CA 92521
(909) 787-5325